

2

ANNUAL REPORT
University Research Initiative

Contract No.: N00014-92-J-1808

March 1992 - April 1993

AD-A266 396

S **DTIC**
ELECTE
JUN 21 1993
A **D** **ttt**

The Processing and Mechanical Properties of High Temperature/ High Performance Composites

by

A.G. Evans & F. Leckie
University of California,
Santa Barbara

University of Pennsylvania
Harvard University
Washington State University
Carnegie Mellon University
University of Virginia

This document has been approved
for public release and sale; its
distribution is unlimited.

93 6 12 03 9

93-13754
||||| ||| ||| |||

Book 3 of 5:

**CONSTITUENT PROPERTIES
AND
MACROSCOPIC PERFORMANCE: MMCs**

SUMMARY OF TABLE OF CONTENTS

EXECUTIVE SUMMARY

BOOK 1: CONSTITUENT PROPERTIES OF COMPOSITES

BOOK 2: CONSTITUENT PROPERTIES AND MACROSCOPIC
PERFORMANCE: CMCs

BOOK 3: CONSTITUENT PROPERTIES AND MACROSCOPIC
PERFORMANCE: MMCs

BOOK 4: CONSTITUTIVE LAWS AND DESIGN

BOOK 5: PROCESSING AND MISCELLANEOUS PROPERTIES

DTIC QUALITY INSPECTED 5

Accession For		
NTIS GRA&I		<input checked="" type="checkbox"/>
DTIC TAB		<input type="checkbox"/>
Unannounced		<input type="checkbox"/>
Justification		
By <i>per A216146</i>		
Date <i>10/1/85</i>		
Distribution/Avail		
DTIC (if not available)		
A-1		

BOOK 3

CONSTITUENT PROPERTIES AND MACROSCOPIC PERFORMANCE: MMCs

- | | | |
|-----|--|--|
| 34. | Mode I Fatigue Cracking in a Fiber Reinforced Metal Matrix Composite | D.P. Walls
G. Bao
F.W. Zok |
| 35. | Fatigue Crack Growth in Fiber-Reinforced Metal-Matrix Composites | G. Bao
R.M. McMeeking |
| 36. | The Anisotropic Mechanical Properties of a Ti Matrix Composite Reinforced with SiC Fibers | S. Jansson
H.E. Dève
A.G. Evans |
| 37. | Models for the Creep of Ceramic Matrix Composite Materials | R.M. McMeeking |
| 38. | The Creep and Fracture Resistance of γ -TiAl Reinforced with Al_2O_3 Fibers | C.H. Weber
J. Yang
J.P.A. Löfvander
C.G. Levi
A.G. Evans |
| 39. | The Mechanical Properties of Al Alloys Reinforced with Continuous Al_2O_3 Fibers | M.-S. Hu
J. Yang
H.C. Cao
A.G. Evans
R. Mehrabian |
| 40. | The Mode I Fracture Resistance of Unidirectional Fiber-Reinforced Aluminum Matrix Composites | H.C. Cao
J. Yang
A.G. Evans |
| 41. | The Ultimate Tensile Strength of Metal and Ceramic-Matrix Composites | M.Y. He
A.G. Evans
W.A. Curtin |
| 42. | Cracking and Damage Mechanisms in Ceramic/Metal Multilayers | M.C. Shaw
D.B Marshall
M.S. Dadkhah
A.G. Evans |

- | | | |
|-----|--|--|
| 43. | The Mechanics of Crack Growth in Layered Materials | M.Y. He
F.E. Heredia
D.J. Wissuchek
M.C. Shaw
A.G. Evans |
| 44. | Small Scale Yielding at a Crack Normal to the Interface Between an Elastic and a Yielding Material | M.Y. He
R.M. McMeeking
Zhang |
| 45. | Cracking and Stress Redistribution in Ceramic Layered Composites | K.S. Chan
M.Y. He
J.W. Hutchinson |
| 46. | The Effect of Interface Diffusion and Slip on the Creep Resistance of Particulate Composite Materials | P. Sofronis
R.M. McMeeking |
| 47. | Power Law Creep of a Composite Material Containing Discontinuous Rigid Aligned Fibers | R.M. McMeeking |
| 48. | Effects of Misfit Strain and Reverse Loading on the Flow Strength of Particulate-Reinforced Al Matrix Composites | S.M. Pickard
S. Schmauder
D.B. Zahl
A.G. Evans |
| 49. | Continuum Models for Deformation: Discontinuous Reinforcements | J.W. Hutchinson
R.M. McMeeking |

EXECUTIVE SUMMARY

1. GENERAL STRATEGY

The overall program embraces property profiles, manufacturing, design and sensor development (Fig. 1) consistent with a concurrent engineering philosophy. For this purpose, the program has created networks with the other composites activities. *Manufacturing* research on MMCs is strongly coupled with the 3M Model Factory and with the DARPA consolidation team. Major links with Corning and SEP are being established for CMC manufacturing. *Design Team* activities are coordinated by exchange visits, in February/March, to Pratt and Whitney, General Electric, McDonnell Douglas and Corning. Other visits and exchanges are being discussed. These visits serve both as a critique of the research plan and as a means of disseminating the knowledge acquired in 1992.

The program strategy concerned with design attempts to provide a balance of effort between *properties* and *design* by having studies of mechanisms and property profiles, which intersect with a focused activity devoted to design problems (Fig. 2). The latter includes two foci, one on MMCs and one on CMCs. Each focus reflects differences in the property emphases required for design. The intersections with the mechanism studies ensure that commonalties in behavior continue to be identified, and also facilitate the efficient transfer of models between MMCs and CMCs.

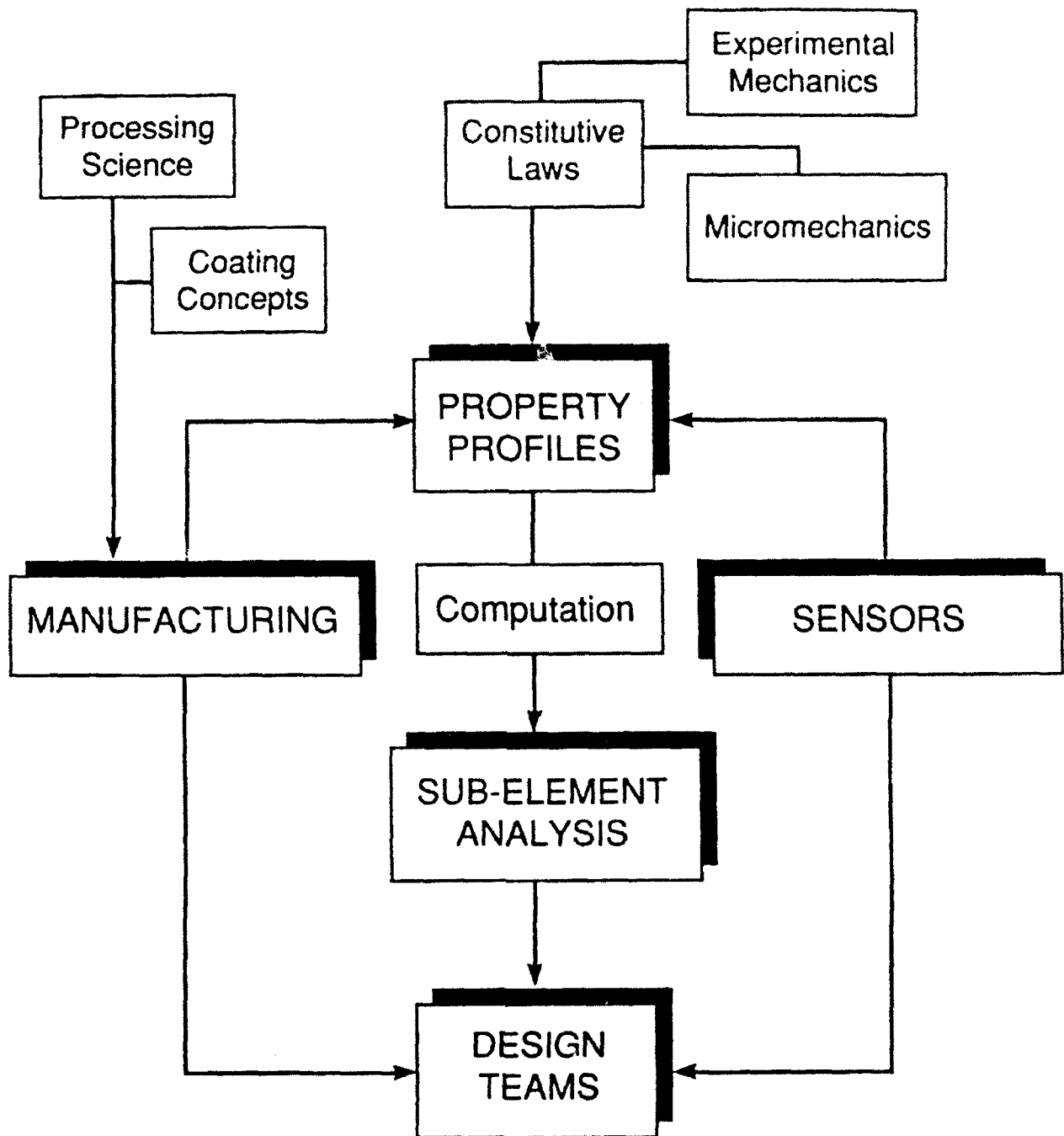


Fig. 1 The Concurrent Engineering Approach

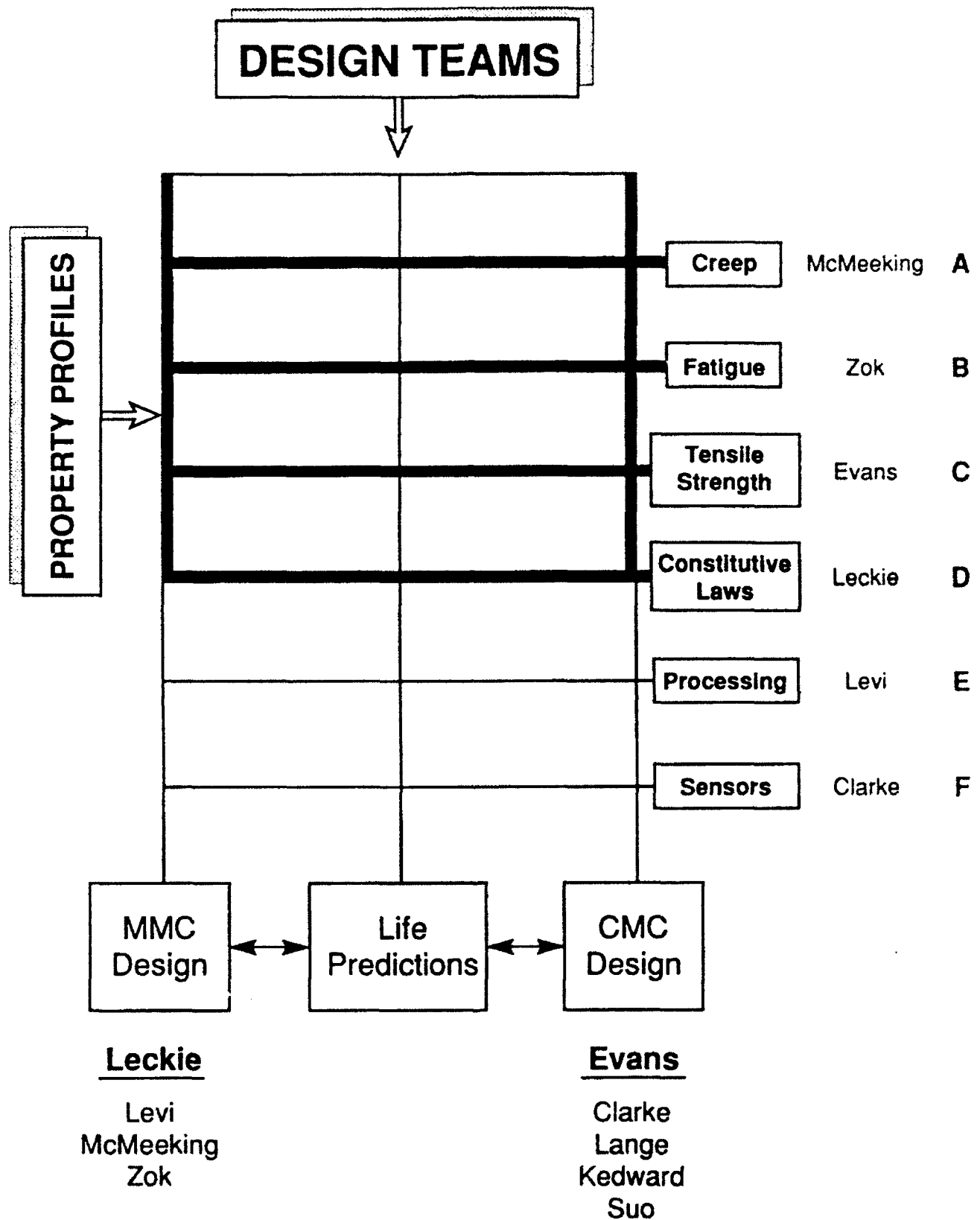


Fig. 2
Matrix Structure of Program

2. PROPERTY PROFILES

Each research activity concerned with properties begins with experiments that identify the principal property-controlling phenomena. Models are then developed that relate the physical response to constituent properties. These models, when validated, provide the constitutive laws required for calculating stress redistribution, failure and damage progression. They also provide a solid physics and mechanics understanding, which can be used to judge the effectiveness of the simplified procedures needed for design purposes.

2.1 Fatigue

Studies of the propagation of dominant mode I fatigue cracks from notches in MMCs, including the role of fiber bridging and fiber failure, have been comprehensively addressed (Zok, McMeeking). Software programs that include these effects have been developed. These are being transferred to Pratt and Whitney and KAMAN Sciences. The effects of thermal cycling on crack growth in MMCs have also been modelled (McMeeking). The results highlight the opposing effects of cycling on matrix crack growth and fiber failure (the fatigue threshold), when thermal cycles are superposed onto load cycles. Notably, matrix crack growth is enhanced by out-of-phase thermomechanical cycling, but fiber failure is suppressed (and vice versa for in-phase cycling). Experimental studies that examine these predictions are planned (Zok).

Studies have also been conducted on systems that exhibit *multiple* matrix cracking (Zok). The tensile stress-strain behavior of composites containing such cracks is analogous to the behavior of unidirectional CMCs

under monotonic tensile loading. As a result, models developed to describe the tensile response of the CMCs have found utility in describing the MMCs. However, two important differences in the two classes of composite have been identified and are presently being addressed. The first deals with the nature of the crack patterns. In the CMCs, the cracks are more or less uniformly spaced and generally span across the entire composite section. In contrast, the MMCs exhibit a broader distribution of crack sizes, many of which are short compared with the specimen dimensions. Methodologies for measurement and interpretation of crack densities in MMCs are being developed. The second problem deals with degradation in the interfacial sliding properties with cyclic sliding in the MMCs. Such degradation is presently being studied using fiber push-out tests in fatigued specimens.

Thermal fatigue studies on MMCs subject to transverse loading have been performed and have established the conditions that allow shakedown (Leckie). The shakedown range is found to be strongly influenced by the extent of matrix creep, which defines a temperature limitation on the use of the material. The eventual outcome of this activity would be the specification of parameters that ensure shakedown and avoid ratcheting.

The next challenge for MMCs concern the quantification of transitions in fatigue behavior, especially those found at higher temperatures. These include multiple matrix cracking and shear band formation. Experimental studies are in progress which will be used to establish a mechanism map. The map, when developed, would explicitly identify the transitions (Zok). The analogous behavior found in CMCs will facilitate this development. Other high temperature phenomena to be explored include changes in the interfacial sliding behavior due to both relaxations in the thermal residual stresses and the growth of reaction products near the fiber-matrix interface.

Fatigue damage studies on 2-D CMCs will focus on interface and fiber degradation phenomena, especially at elevated temperatures (Evans, Zok). Cyclic loading into the stress range at which matrix cracks exist is known to modify the interface sliding stress and may weaken the fibers. These degradation effects can be distinguished, because they change the hysteresis loop and reduce the UTS, respectively. Experiments that probe these material responses are planned. In addition, models that include the influence of cyclic fiber failure and pull-out on fatigue damage will be developed (Suo).

2.2 Matrix Cracking

Models of the plastic strain and modulus changes caused by various modes of matrix cracking have been developed. These solutions have provided a rationale for experimental studies on the tensile and shear behavior of CMCs and on the fatigue of MMCs (Hutchinson, Zok, Evans, Suo, Budiansky, McMeeking). The information has been used in two distinct ways. (i) Test methodologies have been devised that relate stress/displacement measurements to constituent properties (Table I). (ii) Stress/strain curves and matrix crack evolution have been simulated for specific combinations of constituent properties.

The development of the procedures and their implementation are still in progress. Independent solutions have been established for matrix cracks in 0° plies and 90° plies upon tensile loading. The former has been experimentally validated on 1-D materials (SiC/SiC and SiC/CAS). Measurements of plastic strain, hysteresis loops and crack densities have been checked against the models for consistency.

TABLE I**Relevant Constituent Properties and Measurement Methods**

CONSTITUENT PROPERTY	MEASUREMENT
Sliding Stress, τ	<ul style="list-style-type: none">• Pull-Out Length, \bar{h}• Saturation Crack Spacing, $\bar{\Gamma}_s$• Hysteresis Loop, $\delta \epsilon_{1/2}$• Unloading Modulus, \bar{E}_L
Characteristic Strength, S_c , m	<ul style="list-style-type: none">• Fracture Mirrors• Ultimate Strength, S
Misfit Strain, Ω (q)	<ul style="list-style-type: none">• Bilayer Distortion• Permanent Strain, ϵ_p• Residual Crack Opening
Matrix Fracture Energy, Γ_m	<ul style="list-style-type: none">• Monolithic Material• Saturation Crack Spacing, $\bar{\Gamma}_s$• Matrix Cracking Stress, $\bar{\sigma}_{mc}$
Debond Energy, Γ_l	<ul style="list-style-type: none">• Permanent Strain, ϵ_p• Residual Crack Opening

The next challenge is to couple the models together in order to simulate the evolution of matrix cracks in 2-D materials, subject to tensile loading (Hutchinson, Budiansky). Related effects on the ultimate tensile strength caused by stress concentrations in the fibers in the presence of matrix cracks, would also be evaluated. Experimental measurements of stress/strain behavior in 2-D CMCs, with concurrent observations of matrix crack evolution, would be used to guide and validate such models (Evans, Kedward).

2.3 Constitutive Equations

Constitutive equations provide the link between material behavior at the meso-scale and the performance of engineering components. The equations can be established from the results of uniaxial and transverse tensile tests together with in-plane shear loading. For a complete formulation, which describes accurately the growth of failure mechanisms and the conditions of failure at the meso-scale, it is also necessary to perform calculations which are valid at the micro-scale.

These procedures have been completed for metal-matrix composites (Jansson, Leckie), and the resulting constitutive equations are operational in the ABAQUS finite element code. The behavior of simple panels penetrated by circular holes have been studied and the results await comparison with experiments which are planned for the coming year. The constitutive equations are formulated in terms of state variables which include the hardening tensors and damage state variables which describe debonding at the interface and void growth in the matrix. The format is *sufficiently general* to allow the inclusion of failure mechanisms such as environmental attack as the appropriate understanding is available. For

example, the effect of matrix and fiber creep mechanisms (Aravas) have also been introduced into ABAQUS, and it is proposed to extend the creep conditions to include the effects of variable loading and temperature.

A similar approach has been taken towards the modulus of CMCs. In this case, efforts have been made to include the influence of matrix cracking, in-plane shearing and fiber breakage. The latter consideration is based on the global load sharing model (Hayhurst). The equations are also available in ABAQUS. At present, matrix cracking is introduced by assuming a matrix stress accompanied by an increase of strain. However, based on the more recent understanding of the growth of matrix cracks (above) it is intended to introduce these mechanisms into the constitutive equations for CMCs.

2.4 Creep

The emphases of the creep investigations have been on the anisotropic characteristics of unidirectional layers in which the fibers are elastic, but the matrix creeps. Experiments and models of the longitudinal creep properties of such materials have been initiated (McMeeking, Leckie, Evans, Zok, Aravas). The critical issues in this orientation concern the incidence of fiber failure and the subsequent sliding response of the interface. A modelling effort has established an approach that allows the stochastic evolution of fiber failure to occur as stress is transferred onto the fibers by matrix creep (McMeeking). This approach leads to creep rates with a large power law exponent. Various attempts are underway to incorporate the interface sliding initiated by fiber breaks and to introduce sliding into the creep rate formulation. Experiments being performed on unidirectional Ti matrix materials are examining the incidence of fiber failures on the creep

deformation (Evans, Leckie, Zok). These results will guide the modelling effort concerned with interface sliding effects. Insight will also be gained about fiber failure stochastics during creep, especially differences from room temperature behavior.

The transverse creep properties are expected to have direct analogies with composite deformation for a power law hardening matrix (Section 2.3). In particular, the same effects of debonding and matrix damages arise and can be incorporated in an equivalent manner (Leckie, Aravas). Testing is being performed on Ti MMCs and on SiC/CAS to validate the models.

Experiments on Ti-matrix $0^\circ/90^\circ$ cross-ply composites are planned. Creep models appropriate to cross-ply materials will be developed by combining those corresponding to the unidirectional materials in the longitudinal and transverse orientations, using a rule-of-mixtures approach. Such an approach is expected to be adequate for loadings in which the principal stresses coincide with the fiber axes. Alternate approaches will be sought to describe the material response in other orientations.

Some CMCs contain fibers that creep more extensively than the matrix. This creep deformation has been found to elevate the stress in the matrix and cause time dependent evolution of matrix cracks. This coupled process results in continuous creep deformation with relatively low creep ductility. Experiments on such materials are continuing (Evans, Leckie) and a modelling effort will be initiated (Suo). The models would include load transfer into the matrix by creeping fibers, with sliding interfaces, leading to enhanced matrix cracking.

2.5 Tensile Strength

The ultimate strength (UTS) of both CMCs and MMCs (as well as fatigue and creep thresholds) is dominated by fiber failure. With the global load sharing (GLS) concept of fiber failure now well established, the recent emphasis has been on defining the constituent properties needed to ensure GLS. The approach has been to perform local load sharing calculations and then compare experimental UTS data with the GLS predictions (Curtin, Evans, Leckie). The situation is unresolved. However, initial calculations on CMCs (Curtin) and MMCs (Evans) have provided some insight. Two key remaining issues concern the magnitude of the stress concentration in intact fibers caused by matrix cracks and the role of fiber pull-out in alleviating those stresses. Calculations of these effects are planned (Budiansky, Suo).

Degradation of the fiber strength upon either high temperature (creep) testing, atmospheric exposure, or fatigue are other topics of interest. Rupture testing performed under these conditions will be assessed in terms of degradation in fiber properties.

3. DESIGN TEAMS

3.1 The Approach

The overall philosophy of the design effort is to eventually combine *material models*, with a *materials selector*, and a *data base*, within a unified software package (Prinz). One example of a composites data base is that developed for MMCs by KAMAN Sciences, which forms the basis for a potential collaboration. The materials selector has already been developed

for monolithic materials (Ashby) and is available for purchase. This selector requires expansion to incorporate phenomena that have special significance for high temperature composites, including creep and thermal fatigue. These new features will be developed and included in the advanced selector software (Ashby).

The modelling approach is illustrated in Table II. Failure mechanisms and their effect on material behavior have been introduced into constitutive equations. The stress, strain and damage fields which develop in components during the cycles of loading and temperature can then be computed. Experiments shall be performed on simple components such as holes in plates, and comparison made with the computational predictions. Since constitutive equations are modeled using the results of coupon tests, it is likely that additional failure modes shall come to light during component testing. These mechanisms shall be studied and the appropriate mechanics developed so that their influence is correctly factored into the constitutive equations. In this way, increased confidence in the reliability of the constitutive equations can be established in a systematic way.

In practice, it is most probable that the constitutive equations are too complex for application at the creative level of the design process. It is then that simple but reliable procedures are of greater use. Some success has been achieved in this regard for MMCs subjected to cyclic mechanical and thermal loading (Jansson, Ponter, Leckie), as well as for strength calculations of CMC panels penetrated by holes (Suo) and the fatigue of MMCs (Zok, McMeeking). In all cases simplifications are introduced after a complete and reliable analysis has been completed which provides a standard against which the effects of simplification can be assessed.

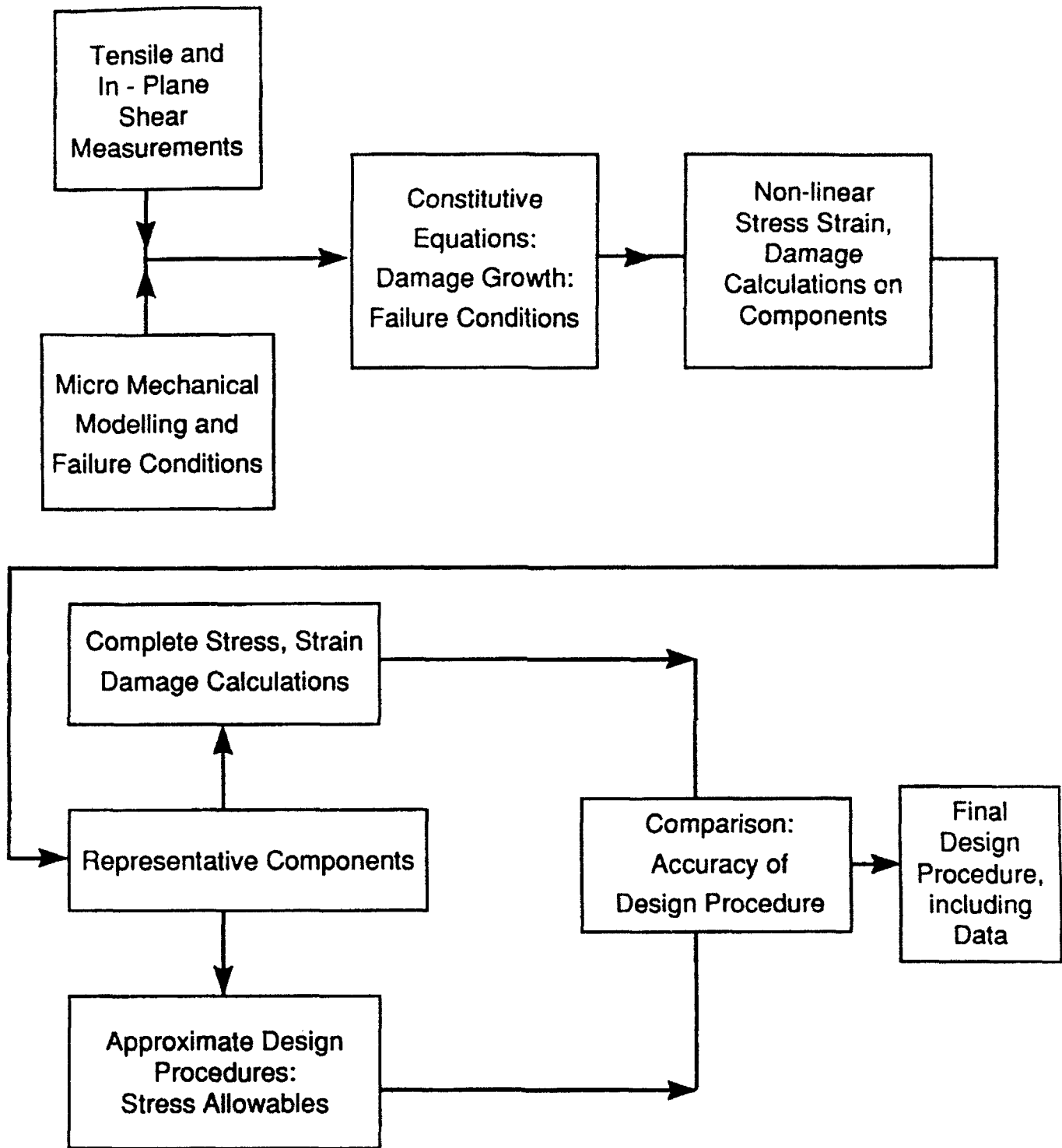


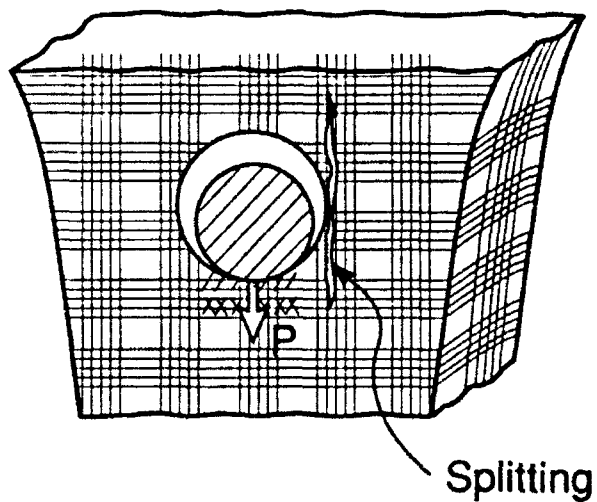
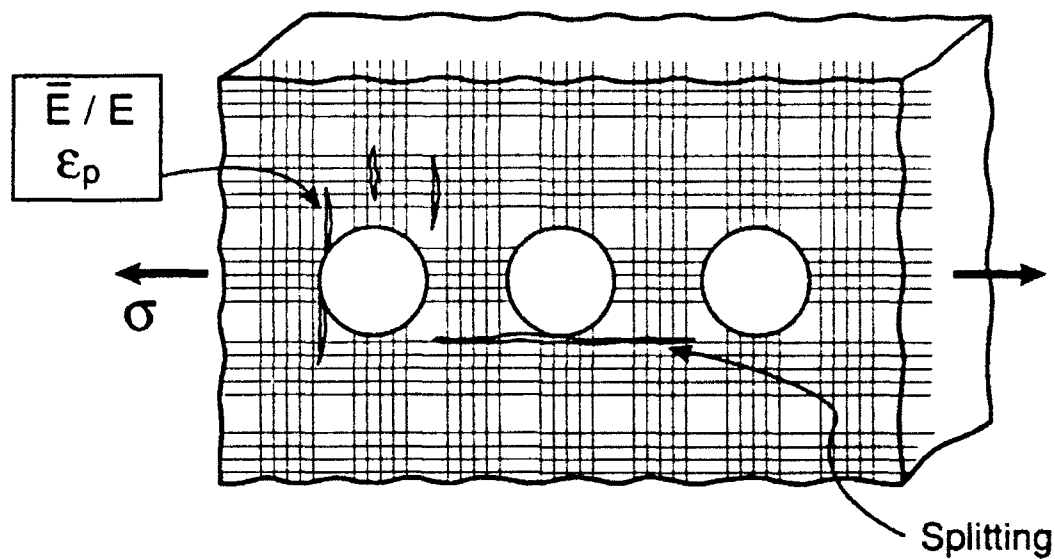
Table II
The Modelling Approach

3.2 Ceramic Matrix Composite Design

The design effort on CMCs will have its major focus on pin-loaded holes used for attachments (Fig. 3). A smaller activity, expected to expand in 1994, will address delamination cracking. The hole design includes several related topics. Each topic is concerned with aspects of constitutive law development (Table III), highlighted during the study group. Combined experimental and modelling efforts on the *tensile properties* of CMCs have established that the plastic strains are dominated by matrix cracks in the 0° plies. The matrix cracking models developed in the program demonstrate that these strains are governed by four independent constituent properties [(Table I) τ , Γ_i , Ω and Γ_m] which combine and interrelate through five non-dimensional parameters (Table IV). This modelling background suggests a concept for using model-based knowledge to develop constitutive laws. The following steps are involved (Table III). (i) A model-based methodology for inferring the constituent properties of unidirectional CMCs from macroscopic stress/strain behavior has been devised and is being experimentally tested on a range of materials (Evans). (ii) Upon validation, the models would allow stress/strain curves to be simulated (Hutchinson). This capability would facilitate a sensitivity study to be performed, in order to determine the minimum number of independent parameters that adequately represent the constitutive law. A strictly empirical law would require 3 parameters (yield strength, hardening rate and unloading modulus). Consequently, the objective might be to seek 3 combinations of the 4 constituent properties. (iii) Experiments would be performed and models developed that establish the matrix cracking sequence in 2-D materials (Hutchinson, Evans, Kedward). These would be conducted on

DESIGN PROBLEM IN CMC's

Design of Holes in Nozzles / Combustors



Issues

Tensile Rupture
Crushing
Splitting

Design Variables

Hole Size
Hole Spacing
Fiber Architecture
Material Choice
New Concepts

Fig. 3

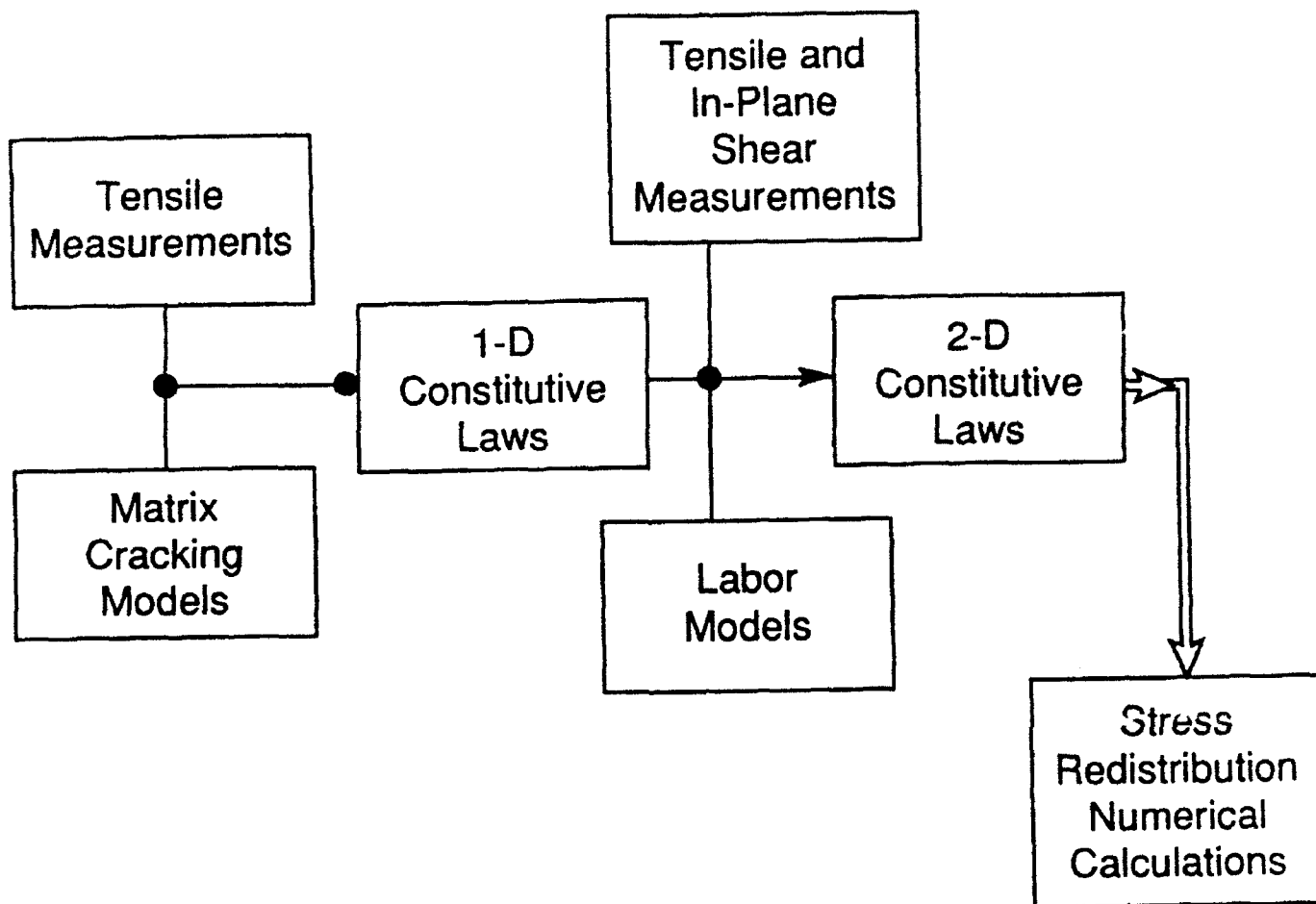


Table III
Design Strategy for CMCs

TABLE IV

Summary of Non-Dimensional Coefficients

$$\mathcal{A}_b = [f/(1-f)]^2 (E_f E_L / E_m^2) (a_o \tau / RS_u), \text{ Flaw Index for Bridging}$$

$$\mathcal{A}_p = (a_o / \bar{h}) (S_p / E_L), \text{ Flaw Index for Pull-Out}$$

$$\mathcal{D} = \Gamma_m (1-f)^2 E_f E_m / f \tau^2 E_L R, \text{ Crack Spacing Index}$$

$$\mathcal{H} = b_2 (1-a_1 f)^2 R \bar{\sigma}_p^2 / 4 \bar{d} \tau E_m f^2, \text{ Hysteresis Index}$$

$$I = \bar{\sigma}_p / E_m \Omega, \text{ Misfit Index}$$

$$\mathcal{M} = 6 \tau \Gamma_m f^2 E_f / (1-f) E_m^2 R E_L, \text{ Matrix Cracking Index}$$

$$Q = E_p f \Omega / E_L (1-\nu), \text{ Residual Stress Index}$$

$$\Delta_1 = (1/c_1 \Omega) \sqrt{\Gamma_1 / E_m R}, \text{ Debond Index}$$

CMCs with a range of different constituent properties and fiber architectures. The plastic strains would be related to constituent properties by adapting the 1-D models.

The in-plane shear behavior will be characterized by performing experiments and developing models of matrix cracking that govern the plastic *shear strain* in 2-D CMC (Evans, Hutchinson, Bao). The information will be used to establish the constitutive laws for in-plane shear, as well as interlaminar shear. For continuity of interpolation between tension and shear, the shear models will include the same constituent properties as those used to represent the tensile behavior.

The model-based constitutive laws, based on matrix damage, will be built into a CDM (continuum damage mechanics) formulation, compatible with finite element codes (Hayhurst). Computations will be performed to explore *stress redistribution* around holes and other strain concentration sites. The calculations will establish visualizations of stress evolution that can be compared with experimental measurements performed using the SPATE method, as well as by Moiré interferometry (Mackin, Evans). These experiments will be on specimens with notches and holes, loaded in tension. The comparisons between the measured and calculated stress patterns will represent the ultimate validation of the constitutive law. The composite codes, when validated, will be made available to industry.

Some preliminary experimental work will be performed on pin-loaded holes. Damage patterns will be monitored and stress redistribution effects assessed using SPATE (Kedward, Evans, Mackin). These experiments will be conducted on SiC/CAS and SiC/C. The results will provide the focus for future CDM computations, based on the constitutive law for the material.

Smaller scale activities will involve basic aspects of stress redistribution around holes caused by fatigue and creep *damage*, using the experience gained from the matrix cracking studies. Some experimental measurements of these effects will be performed using SPATE (Zok, Evans).

Some delamination crack growth measurements and calculations are also envisaged (Ashby, Kedward, Hutchinson). Cantilever beam and C-specimens will be used for this purpose (Fig. 4). During such tests, crack growth, multiple cracking and stiffness changes will be addressed. Models of bridging by inclined fibers will be developed (Ashby) and used for interpretation.

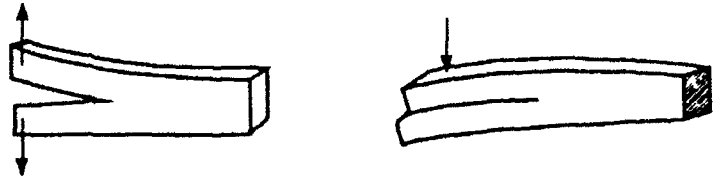
3.3 Metal Matrix Composite Design

The 3D constitutive equations for MMCs are now available for use in the ABAQUS finite element code, and the immediate task is to use these equations to predict the behavior of representative components (Leckie). One such system is a ring-type structure which is being studied together with Pratt and Whitney. Clearly no experimental verification is possible with a component of this scale, but the experience of Pratt and Whitney shall provide invaluable input on the effectiveness of the calculations. A component sufficiently simple to be tested is the panel penetrated by holes. The holes shall be both unloaded and loaded (Jansson), and it is expected to include the effects of cyclic mechanical and thermal loading.

It is proposed to develop simplified procedures which are based on shakedown procedures (Jansson, Leckie). Demonstrations have already been made of the effectiveness of the Gohfeld method (which uses only simple calculations) in representing the behavior of MMCs subjected to cyclic thermal loading.

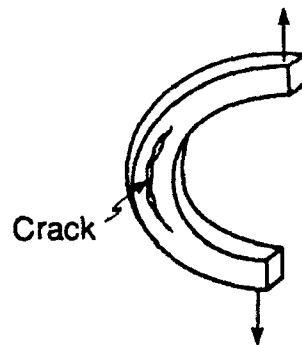
TRANSVERSE CRACKING OF CMC

CONVENTIONAL
COUPON
TESTS



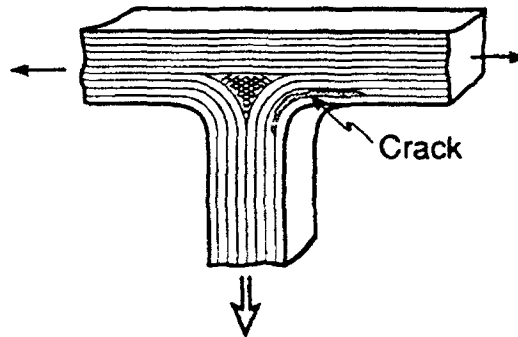
- Fiber Bridging Problem ($G \gg \Gamma_T$)

IMPROVED
TESTS

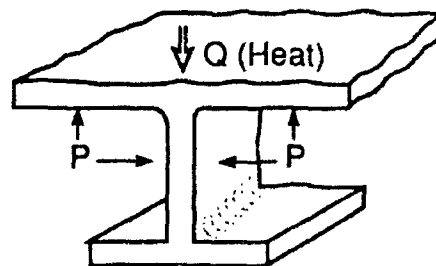


da/dN vs. G

SUB - ELEMENT
TEST



DESIGN
PROBLEM



- Thermal Conductivity
- Fiber Architecture
- Matrix Toughness

Fig. 4

During the complex histories of stress and temperature, it is known that the matrix-fiber interface properties change. Fatigue loading (Zok) is known to decrease the interface sliding stress. Transverse creep appears to cause matrix-fiber debonding (Jansson), which might result in loss of the ability to transfer stress between matrix and fiber. It is intended to study this effect of transverse creep on the integrity of the longitudinal strength of the material by performing tests on panels which shall allow rotation of the stress fields. A good understanding now exists of the fatigue properties of MMCs (Zok). It is intended to extend the ideas developed from earlier theoretical studies (McMeeking, Evans) to include cyclic thermal effects and experimental programs on holes in plates.

4. MANUFACTURING

The activities in processing and manufacturing have had the following foci:

- Matrix development to address specific requirements identified by the design problems, particularly first matrix cracking in CMCs (Lange) and creep strengthening in MMC/IMCs (Levi, Lucas).
- Hybrid architectures which offer possible solutions to environmental degradation and thermal shock problems (Evans, Lange, Leckie, Levi, Yang, Zok).
- Software development that predicts and controls fiber damage and interface properties during densification (Wadley).
- Processing techniques to generate model MMC sub-elements (Leckie, Levi, Yang).

4.1 Metal Matrix Composites

Work on MMC matrix development has focused on dispersion strengthening approaches to increase the *transverse* tensile and creep strength of 1-D and 2-D fiber architectures. The initial work has emphasized a model system, Cu/Al₂O₃, wherein dispersoids are produced by internal oxidation of a dilute Cu-Al alloy deposited by PVD onto sapphire fibers. These are subsequently consolidated by HIP'ing. Specimens with fiber volume fractions of $0.3 \leq f \leq 0.5$ and 2-3% γ -Al₂O₃ dispersoids (~ 20 nm in size) have been produced in this manner and will be tested to assess their transverse creep behavior. The new emphasis will be on higher temperature matrices based on TiB dispersoids in Ti-(Cr/Mo)-B alloys (Levi). Initial solidification studies have demonstrated the potential of these materials as *in-situ* composites. Efforts are underway to develop sputtering capabilities to implement this concept.

Fiber damage during densification of composite prepreps generated by plasma-spray (GE) and PVD (3M) have also been emphasized (Wadley). Interdiffusion studies coupled with push-out tests have been used to study the evolution of reaction layers in Ti/SiC composites and their effect on the relevant interfacial properties as a function of process parameters. Additional efforts under other programs have focused on developing predictive models for fiber breakage during densification. The interdiffusion and breakage models are being incorporated into software that predicts pressure-temperature paths, which simultaneously minimize fiber damage and control the interface properties.

The feasibility of producing MMC sub-elements consisting of fiber reinforced rings (1-D) and tubes (2-D) has been demonstrated by using

liquid metal infiltration of Al alloy matrices (Levi). These are presently undergoing testing in combined tension/torsion modes. Future efforts will be directed toward extending the technique to other shapes (e.g., plates with reinforced holes), as well as devising methods to modify the (currently strong) interfaces. The identification of methods that provide the appropriate interfacial debonding/sliding characteristics should enable the use of these composites as *model systems* for higher temperature MMCs, such as Ti.

4.2 Intermetallic Matrix Composites

The focus of the IMC processing activities has been on the synthesis of $\text{MoSi}_2/\beta\text{-SiC}_p$ composites by solidification processing. These materials are of interest as potential matrices for fiber composites. Significant progress was made in the elucidation of the relevant Mo-Si-C phase equilibria, the growth mechanisms of SiC from the melt and their impact on reinforcement morphology, as well as the orientation relationships between matrix and reinforcements, and the interfacial structure. An amorphous C layer, ≤ 5 nm thick, was found at the MoSi_2/SiC interface in the as cast condition, and persisted after 12 h heat treatments at 1500°C . This interfacial layer has been reproduced in $\alpha\text{-SiC}_p/(\text{MoSi}_2 + \text{C})$ composites produced by powder metallurgy techniques and was found to exhibit promising debonding and pull-out behavior during fracture (Levi). Future efforts are aimed at implementing this *in-situ coating* concept in $\alpha\text{-SiC}$ fiber composites.

4.3 Ceramic Matrix Composites

The processing issues for creating CMCs with high *matrix strength* continue to be explored (Lange, Evans). The basic concept is to create a strong ceramic matrix framework within a fiber preform, by means of slurry

infiltration followed by heat treatment. This strong framework would then be infiltrated by a polymer precursor and pyrolyzed to further densify the matrix. It has been demonstrated that strong matrices of Si_3N_4 can be produced using this approach (Lange). Further work will address relationships between matrix strength and microstructure (Lange, Evans).

4.4 Hybrids

These activities cover materials consisting of thin monolithic ceramic layers alternating with layers containing high strength fibers bonded by a glass or metallic binder. The primary motivation behind this concept is the potential for manufacturing shapes that have a high resistance to environmental degradation and also have good thermal shock resistance. The concept has been demonstrated using alumina plates and graphite reinforced polymer prepregs (Lange). The availability of glass-ceramic bonded SiC_f prepregs and tape-cast SiC plates has facilitated the extension of this technique to high temperature systems (Lange). Future assessment will address new crack control concepts. These concepts would prevent damage from propagating into the fiber reinforced layers, especially upon thermal loading (Zok, Lange). If successful, this concept would allow the development of hybrid CMCs which impart resistance to environmental degradation, as well as high thermal strain tolerance.

Preliminary work has been performed on laminates consisting of alumina plates and sapphire-fiber reinforced Cu monotapes (Levi). The latter are produced by deposition of Cu on individual fibers which are subsequently aligned and bonded by hot pressing between two Cu foils. After suitable surface preparation, the alumina/monotape assemblies are

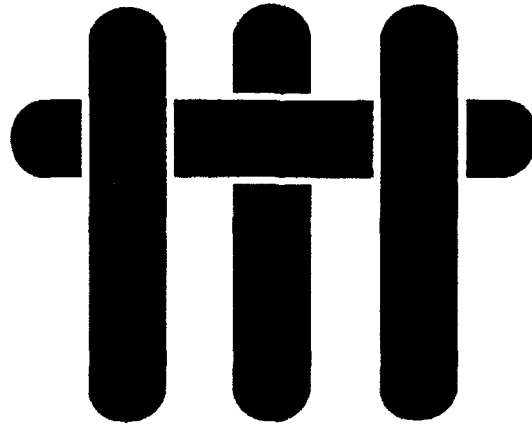
bonded by hot pressing. Future work is aimed at implementing the concept with Ni based alloys.

5. SENSORS

The principal challenge being addressed is the non-destructive and non-evasive measurement of stresses in composites (Clarke, Wadley). The motivation is to make detailed measurements of stresses in components for incorporation into evolving design models, as well as validation of the stress distributions computed by finite element methods. A major emphasis has been placed on measuring the residual stresses in sapphire fibers in various matrices, using the recently developed technique of optical fluorescence spectroscopy. These measurements have provided data on the distribution of residual thermal stresses in the fiber reinforcement, as a function of depth below the surface. This approach will be extended, in conjunction with finite element modelling (Hutchinson), to measure the stresses during the process of fiber pull-out from a variety of metal and ceramic matrices. Initial experiments indicate that such in-situ measurements are feasible.

The technique will also be applied to the measurement of the stresses in sapphire fibers located in the vicinity of pin-loaded holes in order to understand the manner in which the stresses redistribute during loading. It is anticipated that this measurement will provide information about the detailed fiber loadings and also about the stresses that cause debonding of the fibers from the matrix. Moreover, in support of the activities on thermal ratcheting, the redistribution of stresses with thermal cycling will be established. This will be accomplished by using the fluorescence technique as well as Moiré interferometry, based on lithographically defined features.

M A T E R I A L S



MODE I FATIGUE CRACKING IN A FIBER REINFORCED METAL MATRIX COMPOSITE

by

D. P. Walls[#], G. Bao^{*} and F. W. Zok

Materials Department
University of California
Santa Barbara, California 93106-5050

[#]Presently at United Technologies, Pratt and Whitney
West Palm Beach, Florida 33410-9600

^{*}Presently at Department of Mechanical Engineering
The Johns Hopkins University
Baltimore, Maryland 21218

ABSTRACT

The mode I fatigue crack growth behavior of a fiber reinforced metal matrix composite with weak interfaces is examined. In the longitudinal orientation, matrix cracks initially grow with minimal fiber failure. The tractions exerted by the intact fibers shield the crack tip from the applied stress and reduce the rate of crack growth relative to that in the unreinforced matrix alloy. In some instances, further growth is accompanied by fiber failure and a concomitant loss in crack tip shielding. The measurements are compared with model predictions, incorporating the intrinsic fatigue properties of the matrix and the shielding contributions derived from the intact fibers. The magnitude of the interface sliding stress inferred from the comparisons between experiment and theory is found to be in broad agreement with values measured using alternate techniques. The results also indicate that the interface sliding stress degrades with cyclic sliding, an effect yet to be incorporated in the model. In contrast, the transverse fatigue properties are found to be inferior to those of the monolithic matrix alloy, a consequence of the poor fatigue resistance of the fiber/matrix interface.

1. INTRODUCTION

Fiber reinforced metal matrix composites exhibit a variety of damage modes under cyclic loading conditions¹⁻⁵. In the presence of holes or notches, the damage may involve the propagation of a *single* mode I matrix crack perpendicular to the fibers¹⁻³. Provided the fiber/matrix interface is sufficiently weak, cracking initially occurs without fiber failure. The tractions exerted on the crack face by the intact fibers shield the crack tip from the remote stress and thus reduce the crack growth rate relative to that of the matrix alone. Further growth may lead to fiber failure, both in the crack wake and ahead of the crack tip, leading to an acceleration in crack growth. Alternatively, the damage may be in the form of a process zone comprised of *multiple* mode I cracks⁴. The mechanics of this process again involves issues of crack bridging and fiber failure, as well as an understanding of the role of the *interactions* between cracks. In yet other instances, failure occurs by splitting parallel to the fiber direction^{4,5}. The splitting mode is enhanced by the application of bending moments, as exemplified by tests conducted on compact tension specimens⁵.

A comprehensive understanding of the material parameters governing the various damage modes and the role of the damage in fatigue lifetime is not yet available. However, the recognition that the damage modes have close analogies in fiber reinforced *ceramic* matrix composites (CMCs) under *monotonic* loading conditions suggests that the existing mechanics (developed for CMCs) may have applicability to MMCs, provided appropriate modifications are made to account for the cyclic nature of the imposed stress. The present article examines one of these fatigue mechanisms (mode I matrix cracking), and attempts to assess the utility of the mechanics formulisms⁶⁻⁸ in describing fatigue crack growth. The study compares experimental measurements with model predictions, incorporating the effects of fiber bridging. The role of fiber failure in the fatigue cracking process is also examined.

The paper is organized in the following way. First, a summary of the mechanics of crack bridging by frictionally constrained fibers under cyclic loading is presented (Section 2). The mechanics identifies the important material properties and loading parameters governing fatigue, and provides guidance for the design and interpretation of the experiments. This is followed by a description of the materials and experimental methods employed (Section 3), and a summary of the measurements and observations, along with comparisons with model predictions (Sections 4 and 5).

2. MECHANICS OF CRACK BRIDGING

2.1 Shielding Effects

The mechanics of crack bridging by frictionally constrained fibers in brittle matrix composites under monotonic tensile loading has been well established⁹⁻¹¹. A fundamental assumption in the analysis is that the driving force for crack extension is the *crack tip* stress intensity factor, K_t , as governed by the remote stress and the tractions acting in the crack wake. Equating K_t with the composite fracture toughness (which usually scales with the fracture toughness of the matrix itself), gives the stress required for matrix cracking in terms of the component geometry and various constituent properties.

These concepts have been extended to describe matrix cracking in fiber reinforced metal matrix composites under *cyclic* loading conditions⁶⁻⁸. By analogy with the monotonic loading problem, the driving force for crack extension is taken to be the crack tip stress intensity factor *amplitude*, ΔK_t :

$$\Delta K_t = \Delta K_a + \Delta K_b \quad (1)$$

where ΔK_a is the component due to the applied stress amplitude, $\Delta \sigma_a$, and ΔK_b is the component due to the bridging tractions, $\Delta \sigma_b$, exerted by intact fibers in the crack wake. For an *infinite* center-cracked tensile panel, these components are given by¹²

$$\Delta K_a = \Delta \sigma_a \sqrt{\pi a} \quad (2)$$

and

$$\Delta K_b = -2 \sqrt{\frac{a}{\pi}} \int_{a_0}^a \frac{\Delta \sigma_b(x)}{\sqrt{a^2 - x^2}} dx \quad (3)$$

where $2a_0$ is the initial notch length, $2a$ is the current crack length and x is the distance from the crack center.

To evaluate the distribution of bridging tractions, $\Delta \sigma_b(x)$, it is first necessary to specify the contributions to the change in crack opening displacement Δu due to the applied stress Δu_a and that due to the bridging fibers Δu_b ¹²:

$$\Delta u_a = \frac{4}{\bar{E}} \Delta \sigma_a \sqrt{a^2 - x^2} \quad (4)$$

and

$$\Delta u_b = \frac{-4}{\bar{E}} \int_{a_0}^a \Delta \sigma_b(t) H(t, x, a) dt \quad (5)$$

where \bar{E} is an effective composite modulus (taking account of material orthotropy) and the Green's function H is¹²

$$H(t, x, a) = \frac{1}{\pi} \log \left| \frac{\sqrt{a^2 - x^2} + \sqrt{a^2 - t^2}}{\sqrt{a^2 - x^2} - \sqrt{a^2 - t^2}} \right| \quad (6)$$

The sum of these components,

$$\Delta u = \Delta u_a + \Delta u_b \quad (7)$$

is required to be consistent with the cyclic traction law (taking into account reverse slip during unloading)⁶:

$$\Delta u = \frac{1}{2} \lambda \Delta \sigma_b^2 \quad (8)$$

Here λ is a material parameter defined by*

$$\lambda = \frac{D(1-f)^2 E_m^2}{4E^2 E_f \tau f^2} \quad (9)$$

where D is the fiber diameter, f is the fiber volume fractions, E_m and E_f are the matrix and fiber Young's moduli and E is the longitudinal composite modulus ($= f E_f + (1-f) E_m$). Combining Eqns. 4-8 gives an integral equation of the form

$$\frac{1}{2} \lambda \Delta \sigma_b^2 = \frac{4}{E} \Delta \sigma_a \sqrt{a^2 - x^2} - \frac{4}{E} \int_{a_0}^a \Delta \sigma_b(t) H(t, x, a) dt \quad (10)$$

* The parameter λ differs from that used in Refs. 6 and 9 by a factor of $E_m(1-f)/E$. This modification provides consistency between the *steady-state* stress intensity factor and the value obtained from energy-based approaches [10]. A more detailed discussion of the origin of such effects can be found in [13].

This equation is solved numerically for $\Delta\sigma_b$ using an iterative scheme, and the result combined with Eqns. 1-3 to evaluate ΔK_t .

The effects of finite specimen width, $2w$, have also been studied through calculations based on finite element methods⁷. For specimens with a normalized notch size $a_0/w = 0.2$ (a value comparable to those used in the present experiments) and crack lengths in the range $a/w \leq 0.5$, the effects of finite width on the *crack tip* stress intensity amplitude can be approximated by the relation

$$\Delta K_t(a/w, \Delta\sigma) \cong Y(a/w) \Delta K_t(a/\infty, \Delta\sigma) \quad (11)$$

where $\Delta K_t(a/w, \Delta\sigma)$ and $\Delta K_t(a/\infty, \Delta\sigma)$ represent values for the finite and infinite specimens, respectively, and

$$Y(a/w) = \sqrt{\sec \pi a / 2w} \quad (12)$$

(the usual finite width correction used in calculating the *applied* stress intensity¹²). The error introduced by this approximation is less than ~3%. As seen later, this range of crack lengths is consistent with the majority of values measured experimentally, making the approximate width correction (Eqns. 11 and 12) suitable for subsequent calculations.

2.2 Fatigue Crack Growth

By analogy to monolithic materials, it is expected that the rate of fatigue crack growth in composites can be described in terms of ΔK_t through an empirical relation of the form

$$da/dN = \beta (\Delta K_t)^n \quad (13)$$

where N is the number of loading cycles. The parameters β and n represent the behavior of a matrix crack propagating through an array of elastic fibers and are thus properties of the *composite*. However, in view of the lack of understanding of the effects of the fibers on the processes occurring at the crack tip, it seems adequate to select values of β and n that are representative of the *monolithic matrix alloy*. With this approach, the effects of the fibers *at the crack tip* are neglected.

2.3 Fiber Failure

Once the fibers begin to fail, their contribution to crack tip shielding is reduced substantially. To incorporate such effects in the model, a deterministic criterion for fiber failure has been used⁷. The calculations are conducted by continuously adjusting the unbridged portion of the crack to maintain a stress at the tip of the unbridged segment equal to the fiber strength. Through this approach, the entire cracking history (a vs N) can be simulated.

The results of these calculations can also be used to develop a criterion for a "threshold" stress amplitude, $\Delta\sigma_{th}$, below which fiber failure does not occur for *any* crack length. Within such a regime, the crack growth rate approaches a steady-state value, with all fibers in the crack wake remaining intact. The variation in the "threshold" stress amplitude with fiber strength is plotted in Fig. 1. The maximum value of $\Delta\sigma_{th}$ occurs when there is no notch, i.e. $a_0 = 0$, whereupon

$$\Delta\sigma_{th}/f S (1 - R) = 1 \quad (14)$$

where R is the ratio of the minimum to maximum applied stress. Increasing either the notch length or interface sliding stress (or, equivalently, decreasing the fiber strength or fiber diameter) has the effect of decreasing the quantity $\Delta\sigma_{th}/(1 - R) fS$.

3. EXPERIMENTAL METHODS

3.1 Material

The material used in this study was a metastable β -titanium alloy (Ti-15V-3Cr-3Al-3Sn) reinforced with continuous, aligned SCS-6 (SiC) fibers. The fibers are 140 μm in diameter and are coated with a 3 μm graded C/Si layer. The purpose of the coating is to inhibit fiber/matrix interaction during consolidation. The composite was fabricated through a foil-fiber-foil technique, wherein Ti-alloy foils and fiber mats are alternately stacked and subsequently vacuum hot-pressed. During consolidation, a brittle reaction product consisting primarily of TiC forms at the interface between the Ti matrix and the C-rich fiber coating¹⁴. Prior studies have shown this system to exhibit the requisite properties for interface debonding and sliding to occur during matrix cracking^{2,15,16}. A transverse cross section of the composite is shown in Fig. 2.

3.2 Fatigue testing

Fatigue tests were conducted in the 0° orientation using center-notched tensile specimens. To minimize machining damage, the notches were formed using electrical discharge machining. The normalized notch lengths were in the range $0.23 \leq a_0/w \leq 0.35$. One face of each specimen was subsequently diamond polished to a 1 μm finish. Tests were conducted on a servohydraulic mechanical test system at fixed stress amplitude, $\Delta\sigma$. In all cases the stress ratio, R , was maintained at 0.1. Crack extension was monitored using two techniques: indirect potential drop (with thin foil

crack gauges mounted at the notch tips), and with a traveling stereo-microscope. The loading parameters and specimen geometry were selected to elucidate the effects of stress amplitude, $\Delta\sigma_a$, and notch size, $2a_0$. The transverse fatigue behavior was measured using compact tension specimens, in accordance with the ASTM standards¹⁷.

The extent of fiber failure during fatigue cracking was monitored using an acoustic emission (AE) system. The system consists of a 175 kHz resonant piezoelectric transducer, a variable gain amplifier, and a detector. The detector incorporates a variable threshold voltage with two counting techniques. *Ringdown* counting records each positive slope threshold crossing of a decaying acoustic signal, whereas *event* counting records the first crossing and ignores subsequent crossings within a fixed reset period (1 ms). The latter technique (employed in the present study) has the potential to resolve *individual* fiber fractures provided that three conditions are satisfied: a) the acoustic signal decays below the threshold within the reset period, b) multiple fiber failures do not occur within the reset period, and c) the system settings can be adjusted to prevent signals from alternate acoustic sources from crossing the threshold. To determine the system settings appropriate to the Ti/SiC composite, a series of preliminary tensile tests were conducted on *monofilament* composite specimens. The specimens were prepared by extracting individual SiC fibers from the composite and bonding the fibers onto aluminum strips using an epoxy adhesive. Tensile tests were conducted with the transducer attached to the aluminum strip, and the number of acoustic events associated with fiber failure recorded. The system settings were systematically varied until individual fiber failures were consistently counted as *single* acoustic events. These settings were subsequently used during fatigue testing of the composite. Furthermore, the accuracy of the acoustic emission measurements was evaluated by examining the tested specimens following matrix dissolution, as described below.

3.3 Observations

Direct observations of fiber bridging and fiber fracture were also made. For this purpose, tested specimens were sectioned along a plane $\sim 3\text{mm}$ above the matrix crack plane, and the matrix subsequently dissolved down to a depth of $\sim 6\text{mm}$. During matrix dissolution, the fractured fibers were removed, whereas the intact fibers continued to span the entire length of the specimen. A comparison of the spatial distribution of fractured fibers with the matrix crack prior to dissolution provided a direct measure of the length over which intact fibers had bridged the matrix crack. The fatigue fracture surfaces were also examined in a scanning electron microscopy (SEM).

4. LONGITUDINAL PROPERTIES

4.1 Measurements and Observations

Figures 3(a) – (c) show representative trends in the crack growth behavior, plotted as crack extension, Δa , vs. number of loading cycles, N , for tests conducted at various stress amplitudes. Here, the specimens had an initial notch size, $2a_0 = 3\text{ mm}$. The results are re-plotted as crack growth rate, da/dN , vs. applied stress intensity range, ΔK_a , in Fig. 3(d). Similarly, Figs. 4(a) – (d) show trends with notch length at a fixed stress amplitude, $\Delta\sigma_a = 400\text{ MPa}$.

In all cases, the crack growth rates initially decreased with increasing crack length, despite the corresponding increase in ΔK_a . This behavior is a manifestation of crack tip shielding by intact fibers in the crack wake. The presence of such fibers was confirmed through comparisons between the matrix cracks following fatigue testing and the distribution of underlying fibers following matrix dissolution: an example is shown in Fig. 5. For tests conducted at low stress amplitudes or with small notches, the deceleration in crack growth continued throughout the duration of the tests (Figs. 3(a),

(b) and 4(a), (b)). In contrast, tests conducted at high stress amplitudes or large notches exhibited a transition in which the growth rate accelerated rapidly with crack extension (Figs. 3(c) and 4(c)). The transition was correlated with the onset of fiber failure. The distribution of broken fibers following fatigue testing for one such test is shown in Fig. 6. (These observations correspond to the data in Fig. 3(c)). In this case, the zone of intact fibers at the end of the test was only $\sim 300 \mu\text{m}$ (or ~ 2 fiber spacings).

The evolution of fiber failure during fatigue cracking was also confirmed by the acoustic emission measurements. For tests conducted at low stress amplitudes or with short notches, the total number of acoustic events was typically ≤ 10 . These measurements correspond to the failure of fibers that were partially cut during machining of the notch, an example of which is seen in Fig. 5. In contrast, tests conducted at high stress amplitudes or with long notches exhibited extensive acoustic activity, in accord with observations of fiber failure. Figure 7 shows one example of the evolution of the number, n_f , of failed fibers with crack extension, corresponding to the test results presented in Fig. 4(c). The parameters in this figure have been normalized such that a line of slope unity represents failure of *all* the fibers in the crack wake; the region above the line corresponds to the incidence of fiber failure *ahead* of the crack tip. In this case, fiber failure began at a relatively small amount of crack extension ($\Delta a/D \approx 2-3$). Further crack growth was accompanied by increasing fiber failure and a concomitant increase in crack growth rate. The acoustic emission measurements also indicate that, beyond $\Delta a/D \approx 12$, fiber failure occurs ahead of the crack tip. This point corresponds closely to the onset of rapid crack acceleration (at $N \approx 8,000$), seen in Fig. 4(c). SEM examination of the specimen following matrix dissolution (Fig. 8) confirmed the number of failed fibers measured through acoustic emission (within $\sim 10\%$).

SEM examinations of the fracture surfaces revealed two notable features. Firstly, the amount of fiber pullout on the fatigue fracture surface was small; typically $\leq 2D$

(Fig. 9). This observation indicates that the fiber strength distribution is narrow, in accord with the reported values of Weibull modulus for the SCS-6 fibers (~ 10). Secondly, the fiber coatings exhibited extensive fragmentation following fatigue (Fig. 10(a)). In contrast, the coatings on the fibers in the fast fracture region were left intact (Fig. 10(b)). Evidently, the cyclic sliding leads to a degradation in the fiber coating.

4.2 Comparison Between Experiment and Theory

The measured crack growth curves have been compared with model predictions⁷, taking into account the effect of bridging fibers on ΔK_I . The parameters β and n in Eqn. 13 were taken to be those for the matrix alloy⁵ and are given in Table 1. The various elastic moduli¹⁴ are also given in Table 1. The material parameter that is subject to the most uncertainty is the interface sliding stress, τ . Consequently, the approach adopted here was to compare the experimental data with model predictions for a range of values of τ and then assess whether consistency is achieved over the entire range of measurements. The model predictions also accounted for fiber failure, assuming a deterministic fiber strength, S . In this regime, the calculations were based on a fixed value of τ (chosen to be consistent with the data in the regime prior to fiber failure) and comparisons made for a range of values of S . The inferred value of S was then compared with values reported elsewhere.

Figures 3 and 4 show the comparisons between experiment and theory. In the regime prior to fiber failure, all the experimental data are consistent with the model for τ in the range of 15 to 35 MPa.

The values of τ inferred from the fatigue tests have been compared with those measured on both pristine and "fatigued" fibers using single fiber pushout tests¹⁸ (Fig. 11). Specimens with "fatigued" fibers were prepared by cutting composite sections

~ 600 μm thick, adjacent to a matrix fatigue crack. The sections were then ground and polished to a final section thickness of ~ 400 μm . The pristine specimens were prepared in a similar fashion, using undeformed material. The pushout tests show that the sliding resistance of the pristine fibers is initially ~ 90 MPa, but decreases as the fiber slides out of the composite. This trend has previously been rationalized in terms of the wear of asperities on the fiber coating during sliding¹⁹. In contrast, the sliding stress for the fatigued fiber is initially only ~ 20 MPa, but subsequently *increases* with pushout distance. This behavior is consistent with the extensive fragmentation of the fiber coating following fatigue (Fig. 10). Comparisons of the data with the range of values of τ inferred from the fatigue crack growth experiments shows broad agreement, providing additional confidence in the utility of the micromechanical model. However, it must be emphasized that the fiber coatings degrade during cyclic sliding, leading to changes in the interface sliding stress. Such effects have yet to be incorporated in the model.

The model predictions in the regime following fiber failure are consistent with a fiber strength of ~ 4 GPa (Figs. 3(c) and 4(c)): a value comparable to previous measurements of the strength of pristine SCS-6 fibers^{20*}.

The present observations have also been used to assess the predictions of the "threshold" stress amplitude, described in Section 2.3. A comparison of the measurements and predictions is shown in Fig. 12. Here, the experimental data have been plotted for an average value of sliding stress, $\tau = 25$ MPa, with the error bars corresponding to the uncertainty in τ (15-35 MPa). Despite the rather broad uncertainty, the observations appear to be consistent with the predictions. Specifically,

* It is recognized that a deterministic fiber failure criterion is not, strictly speaking, applicable to ceramic fibers. However, in the present case, the range of fiber strength is narrow and thus the criterion appears to be adequate.

both the experiments and the theory indicate that a transition to the regime of fiber failure can be brought upon by increasing either $\Delta\sigma_a$ or a_0 .

5. TRANSVERSE PROPERTIES

5.1 Measurements and Observations

In contrast to the longitudinal behavior, fatigue crack growth in the transverse orientation was not accompanied by crack bridging. Indeed, the fatigue resistance of the composite in this orientation was *inferior* to that of the matrix alloy. The trends in the crack growth rate with the *applied* stress intensity amplitude are shown in Fig. 13. The behavior of the composite closely parallels that of the matrix alloy, though the growth rates are somewhat higher in the composite. SEM examinations of the fatigue fracture surface indicate that the cracks propagate along the matrix ligaments between fibers, with no evidence of fiber bridging or fiber fracture in the crack wake (Fig. 14). These observations are consistent with the static tensile properties of the composite, wherein the transverse strength is lower than that of the matrix¹⁴.

5.2 Comparison Between Experiment and Theory

An upper bound estimate of the transverse crack growth rate in the composites can be obtained by neglecting the fatigue resistance of the fiber/matrix interface. The driving force for crack extension in the composite is thus obtained through a net section correction of the form

$$\Delta K_t = \Delta K_a / A_m \quad (16)$$

where A_m is the area fraction of matrix on the fracture surface. Measurements made on the fracture surface give $A_m \approx 0.38$. This value compares favorably with one

calculated, assuming that the fibers are arranged in a square array and that the fatigue crack propagates along the narrowest matrix ligament between fibers, giving

$$A_m = 1 - (4\pi/f)^{1/2} \approx 0.33. \quad (17)$$

The model predictions based on this adjustment are shown by the dashed lines on Fig. 13. Evidently, the predictions lie above the measured data. This result suggests that either the fiber/matrix interface provides some fatigue resistance, or a closure effect arises from the presence of the debonded fibers in the crack wake. The latter effect is consistent with the thermal expansion mismatch in this composite system.

6. CONCLUDING REMARKS

The fatigue crack growth characteristics of a unidirectional, fiber reinforced metal matrix composite have been measured and the results compared with model predictions. The results indicate that the properties of the fiber/matrix interface play a central role. In the longitudinal orientation, matrix cracking initially proceeds with minimal fiber failure: the weak fiber/matrix interface allows debonding and sliding to occur, leaving the fibers intact in the crack wake. The bridging fibers provide substantial crack tip shielding during crack growth, as evidenced by the reductions in crack growth rate with increased crack extension. The measurements have been found to be consistent with the predictions of a micromechanical model in which the fibers are assumed to be frictionally coupled to the matrix, with a constant interface sliding stress. The values of the sliding stress inferred from such comparisons are in broad agreement with values measured from single fiber pushout tests on *fatigued* specimens. These values, however, are substantially lower than those measured on pristine fibers,

suggesting that the fiber coatings degrade during cyclic sliding. The role of such degradation on the cyclic traction law will be addressed elsewhere²¹. In some instances, the fibers in the crack wake fail, leading to a loss in crack tip shielding and an acceleration in crack growth. The behavior in this regime is also consistent with the model predictions, using a deterministic value for fiber strength. In the transverse orientation, the weak fiber/matrix interface results in a degradation in the fatigue resistance of the composite relative to that of the matrix alloy alone.

An important conclusion derived from both the experimental measurements and the model predictions pertains to the use of the *applied* ΔK as a loading parameter in describing fatigue crack growth in this class of composite. It is apparent that the bridging effects in the longitudinal orientation are so pronounced that ΔK_a does not generally provide even a rough estimate of the crack tip stress field. Consequently, no unique relationship exists between da/dN and ΔK_a , except in the extreme cases where the crack extension into the composite is small, i.e. less than one fiber spacing, or when all the fibers in the crack wake have failed. Similar conclusions have been reached regarding the use of the applied stress intensity factor in characterizing matrix cracking in brittle matrix composites.

ACKNOWLEDGMENTS

Funding for this work was supplied by the Defense Advanced Research Projects Agency through the University Research Initiative Program of UCSB under ONR Contract no. N-0014-86-K-0753, and the College of Engineering, UCSB.

REFERENCES

- (1) B. N. Cox and D. B. Marshall, *Fatigue Frac. Eng. Mater. Struct.*, **14** (1991), 847.
- (2) M. D. Sensmeier and P. K. Wright, in "Fundamental Relationships Between Microstructure and Mechanical Properties of Metal Matrix Composites", P. K. Liaw and M. N. Gungor (Eds.), The Minerals Metals and Materials Society, 1990, pp. 441-457.
- (3) P. K. Wright, R. Nimmer, G. Smith, M. Sensmeier and M. Brun, in "Interfaces in Metal-Ceramic Composites", R. Y. Lin, R. J. Arsenault, G. P. Martins and S. G. Fishman (Eds.), The Minerals, Metals and Materials Society, 1989, pp. 559-581.
- (4) D. M. Harmon and C. R. Saff, in "Metal Matrix Composites: Testing, Analysis and Failure Modes", ASTM STP 1032, Ed. W. S. Johnson, ASTM, Philadelphia.
- (5) P. Kantzos, J. Telesman and L. Ghosn, NASA TM-103095 (1989).
- (6) R. M. McMeeking and A. G. Evans, *Mech. Materials*, **9** (1990), 217.
- (7) G. Bao and R. M. McMeeking, to be published (1992).
- (8) B. N. Cox and C. S. Lo, *Acta Metall. Mater.*, **40** (1992), 69.
- (9) D. B. Marshall, B. N. Cox and A. G. Evans, *Acta Metall.*, **33** (1985), 2013.
- (10) B. Budiansky, J. W. Hutchinson and A. G. Evans, *J. Mech. Phys. Solids*, **34** (1986), 167.
- (11) D. B. Marshall and B. N. Cox, *Acta Metall.*, **5** (1987), 2607.

- (12) H. Tada, P. C. Paris and G. R. Irwin, "The Stress Analysis of Cracks Handbook", Del Research, St. Louis (1985).
- (13) M. D. Thouless, *Acta Metall.*, 37 (1989), 2297.
- (14) S. Jansson, H. Deve and A. G. Evans, *Metall. Trans.*, 22A (1991), 2975.
- (15) D. P. Walls, G. Bao and F. Zok, *Scripta Metall. Mater.*, 25 (1991), 911.
- (16) P. Bowen, A. R. Ibbotson and C. J. Beevers, in "Fatigue of Advanced Materials", Eds. R. O. Ritchie, R. H. Dauskardt and B. N. Cox, Materials and Component Engineering Pub. Ltd., Birmingham, pp. 379-93, 1991.
- (17) ASTM E399, Annual Book of ASTM Standards, ASTM, Philadelphia (1988).
- (18) P. D. Warren, T. J. Mackin and A. G. Evans, *Acta Metall. Mater.*, 40 (1992) 1243-49.
- (19) T. J. Mackin, P. D. Warren and A. G. Evans, *Acta Metall. Mater.*, 40 (1992) 1251-57.
- (20) K. K. Chawla, "Composite Materials Science and Engineering," Springer-Verlag, NY 1987.
- (21) D. P. Walls and F. W. Zok, to be published.
- (22) L. Cui and B. Budiansky, to be published.

FIGURES

- Fig. 1 A diagram showing the influence of notch length, $2a_0$, and material parameters (τ , D , f , S) on the applied stress $\Delta\sigma/(1-R)$ at which fiber failure is predicted to occur during fatigue cracking (adapted from Refs. 7 and 22).
- Fig. 2 A transverse section through the composite.
- Fig. 3 The influence of stress amplitude on crack growth in the longitudinal orientation, for a notch length $2a_0 = 3$ mm: (a) $\Delta\sigma = 300$ MPa, (b) 370 MPa, (c) 436 MPa. The solid lines are model predictions, assuming no fiber failure in the crack wake. The additional lines in (c) show the model predictions incorporating fiber failure, using a sliding stress, $\tau = 35$ MPa, and 3 values of fiber strength. (d) The data of (a)-(c) replotted in the conventional format.
- Fig. 4 The influence of notch length on crack growth in the longitudinal orientation, for a stress amplitude $\Delta\sigma_a = 400$ MPa ($R = 0.1$): (a) $2a_0 = 3$ mm, (b) 6 mm, (c) 9 mm. The solid lines are model predictions assuming no fiber failure. The additional lines in (c) show model predictions incorporating fiber failure, using a sliding stress $\tau = 25$ MPa, and 3 values of fiber strength. (d) The data in (a)-(c) replotted in the conventional format.
- Fig. 5 Comparison between (a) a matrix fatigue crack, as seen on the external surface, and (b) the underlying fibers following matrix dissolution. The micrographs are at the same magnification and represent the identical region of the specimen. The fatigue test was conducted at $\Delta\sigma_a = 300$ MPa, $R = 0.1$, and $2a_0 = 3$ mm.
- Fig. 6 A comparison similar to that shown in Fig. 5, for a specimen tested at $\Delta\sigma_a = 436$ MPa, $R = 0.1$ and $2a_0 = 3$ mm. Note the extent of fiber failure in the crack wake.
- Fig. 7 Evolution of fiber failure with crack extension (t is the thickness of the composite panel).
- Fig. 8 Comparison of matrix crack and underlying fibers for test conducted at $\Delta\sigma_a = 400$ MPa, $R = 0.1$ and $2a_0 = 9$ mm. Note the absence of intact fibers in the crack wake and the extent of fiber failure *ahead* of the crack tip.

- Fig. 9 SEM view of fatigue fracture surface, showing the extent of fiber pullout.
- Fig. 10 SEM observations of failed fibers in (a) the fatigue region, and (b) the fast fracture region. Note the damage on the fiber coating in (a).
- Fig. 11 Results of single fiber push out tests on pristine and fatigued fibers. Also shown is the range of τ inferred from the fatigue crack growth experiments.
- Fig. 12 A diagram showing the conditions under which fiber failure was observed during fatigue cracking. The line shows model prediction, based on the results of Fig. 3. (The parameter ξ is defined on Fig. 1).
- Fig. 13 Comparison of crack growth rates in composite in transverse orientation with that of the monolithic matrix alloy. The broken lines represent model predictions for the composite, based on a net section correction (Eqn. 16, $A_m = 0.38$).
- Fig. 14 Fatigue fracture surface of the composite in the transverse orientation.

TABLE 1 Mechanical Properties of Fiber, Matrix, and Composite

Matrix Modulus	$E_m = 115 \text{ GPa [14]}$
Fiber Modulus	$E_f = 360 \text{ GPa [14]}$
Longitudinal Composite Modulus	$E = 200 \text{ GPa [14]}$
Effective Composite Modulus	$\bar{E} = 193 \text{ GPa}^*$
Coefficient in Paris Law	$\beta = 5.5 \times 10^4 \text{ (m}^{1-n/2}\text{) [5]}$
Exponent in Paris Law	$n = 2.8 \text{ [5]}$

*Calculated in Reference [7].

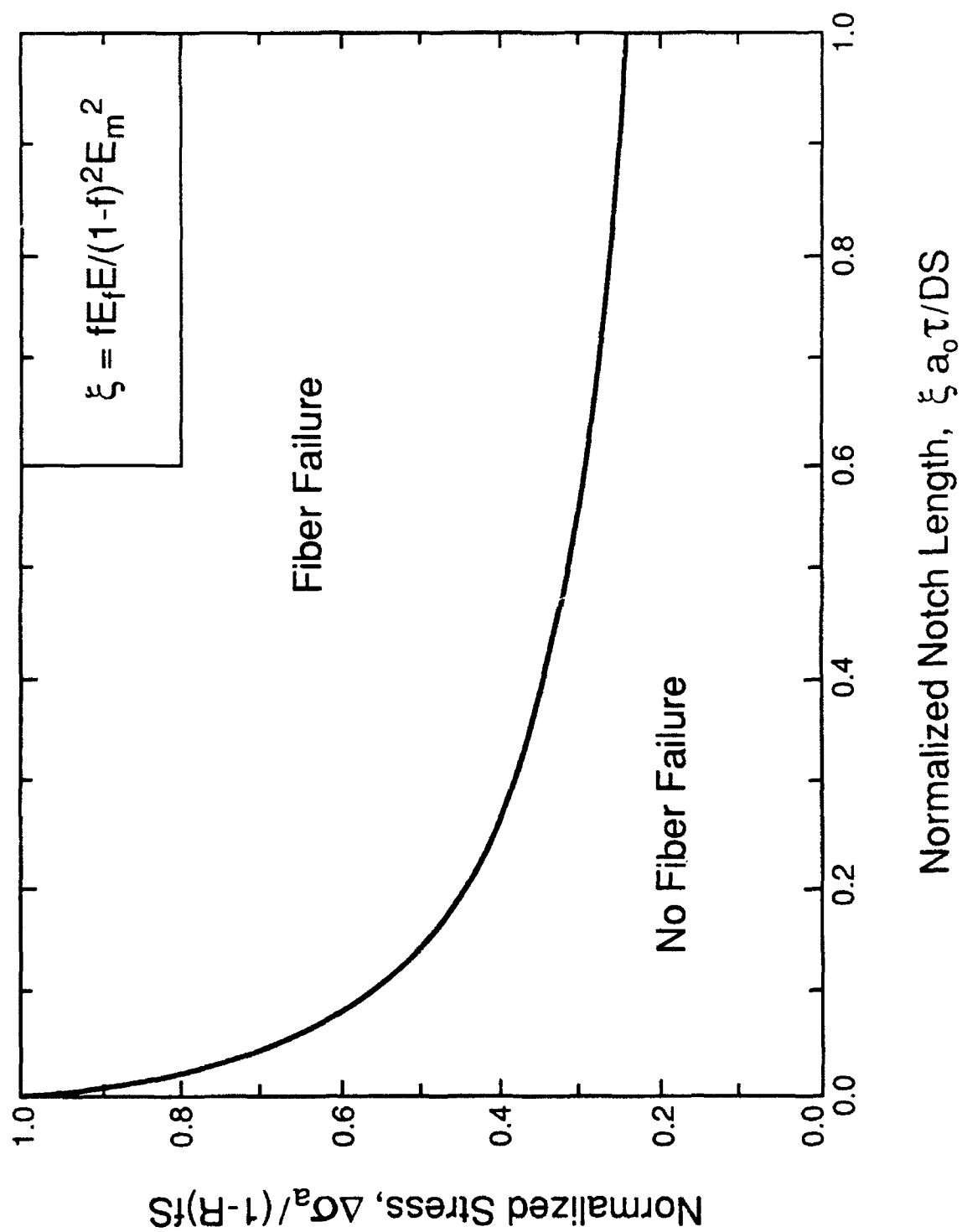


Fig. 1

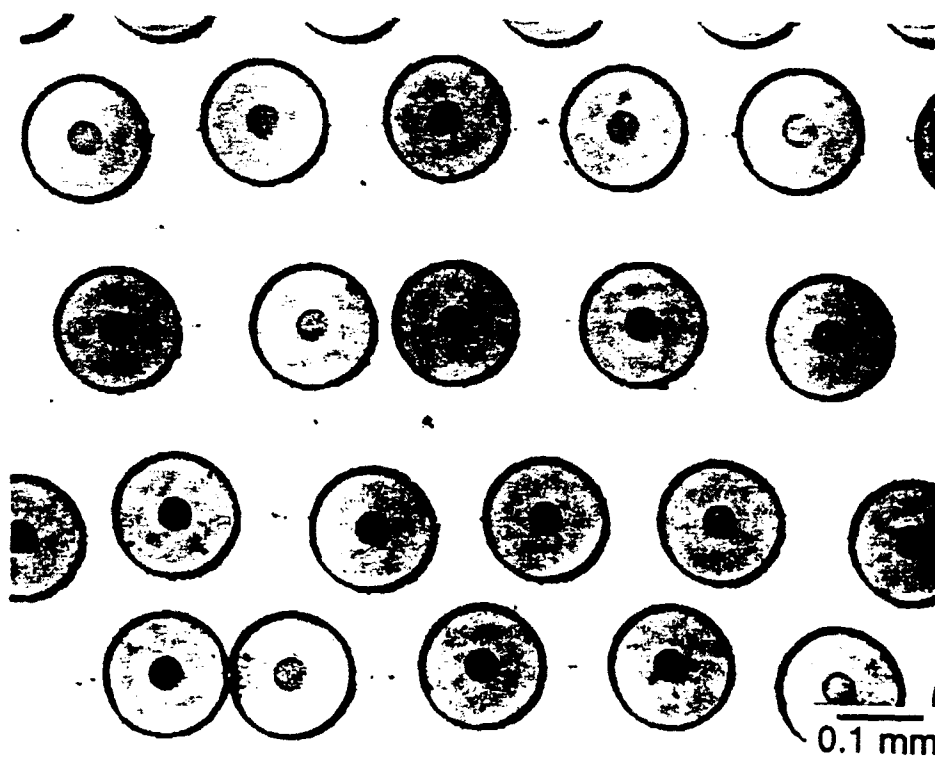


Fig. 2

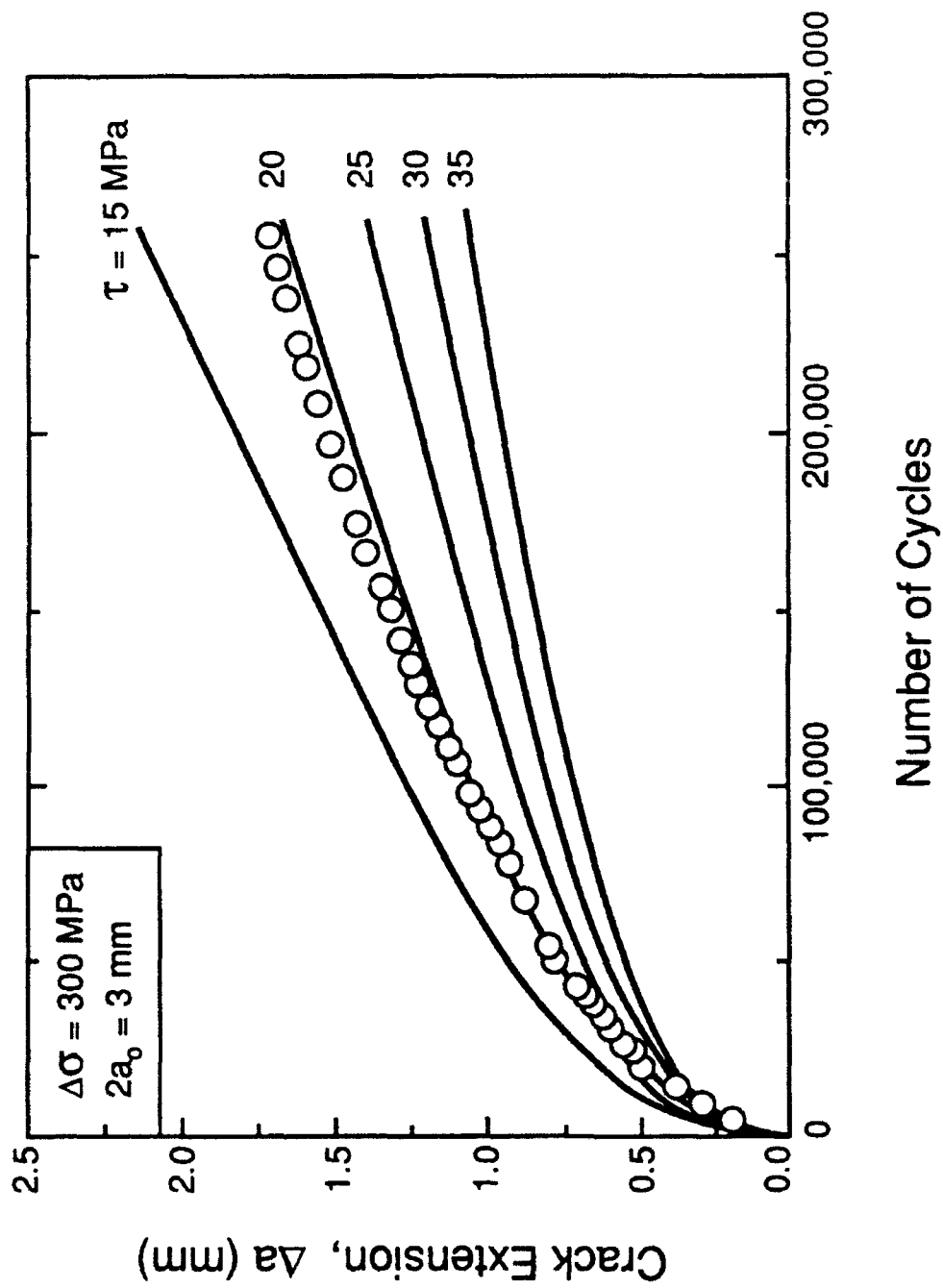


Fig. 3a

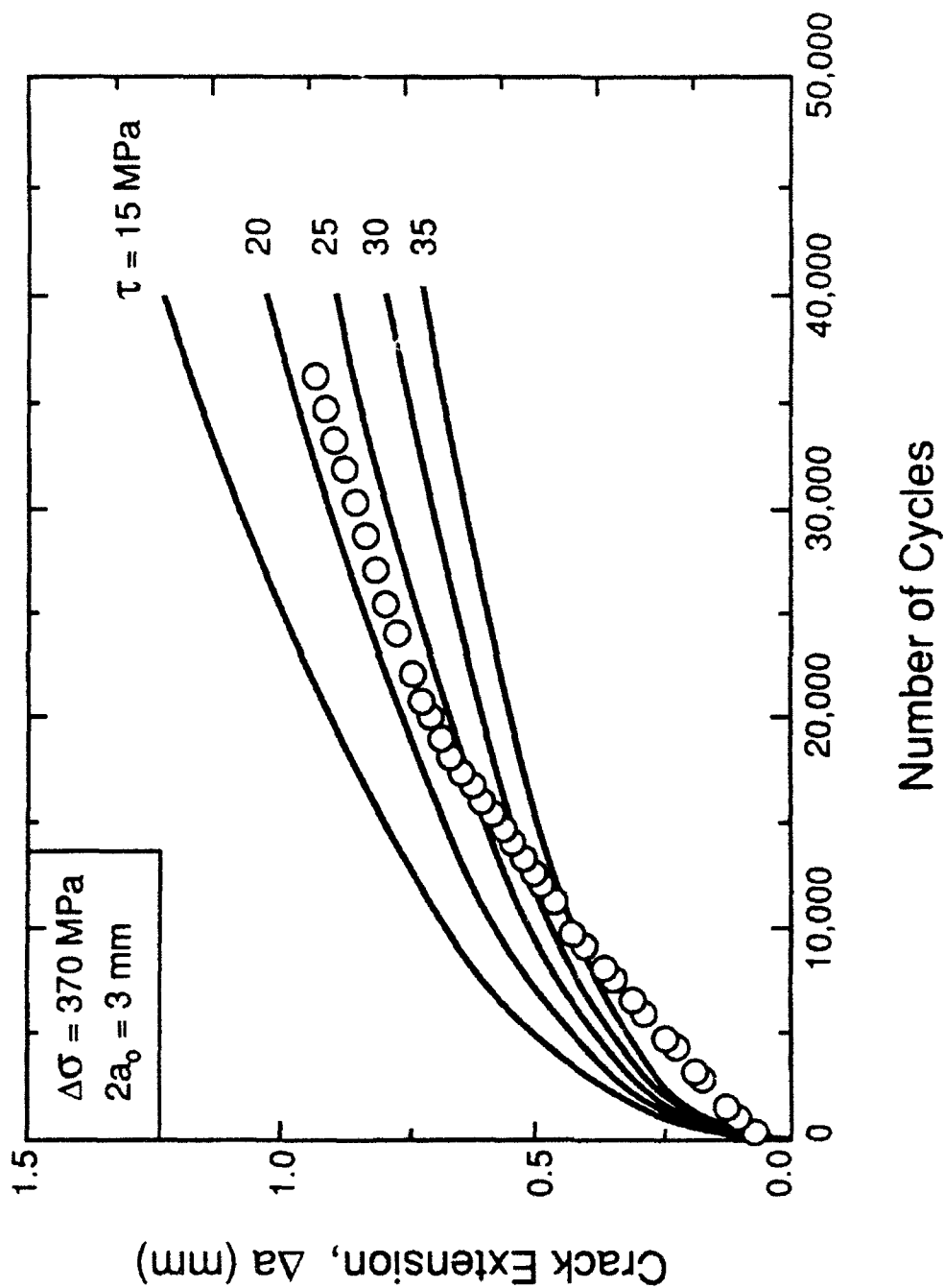


Fig. 3b

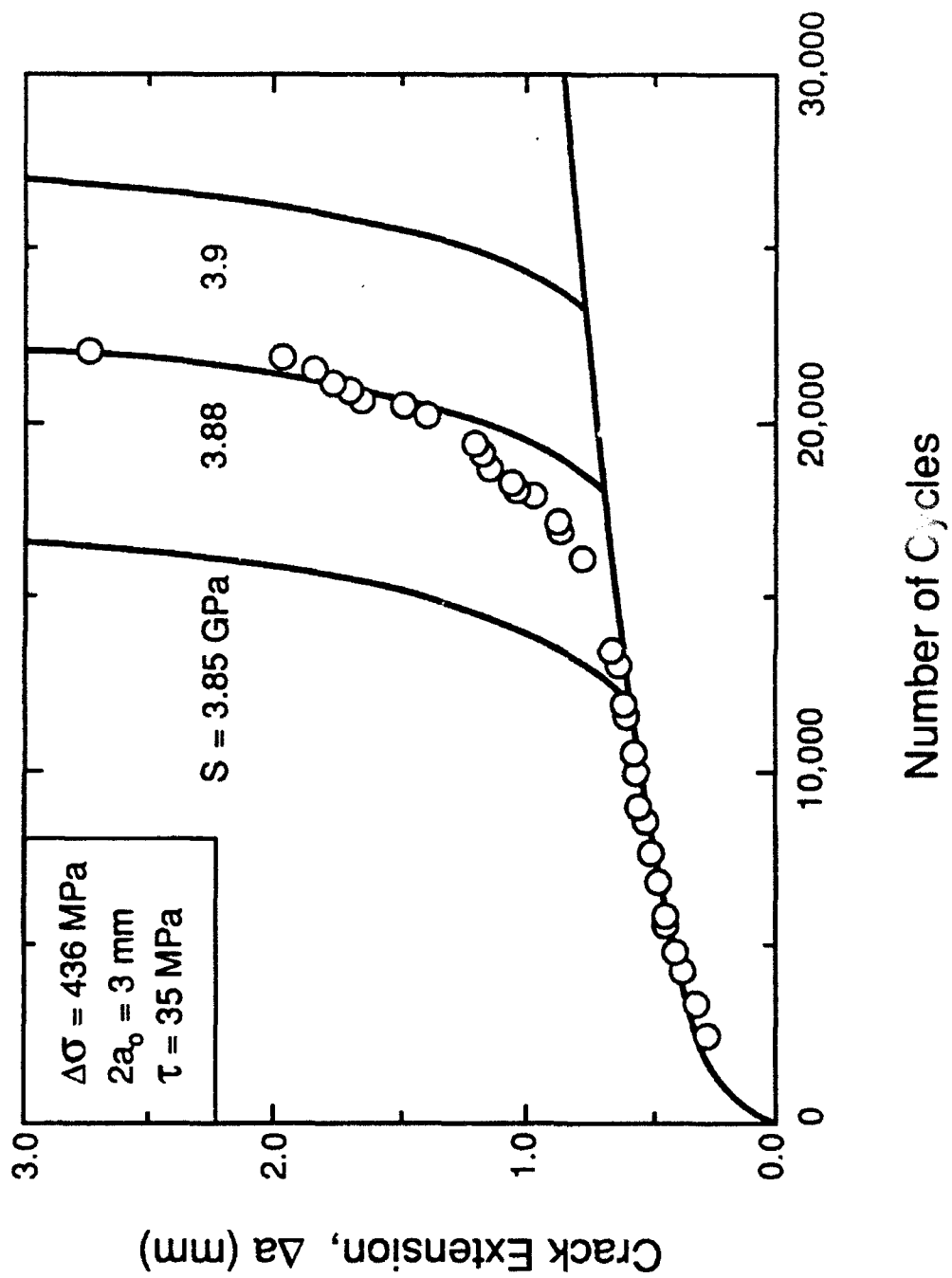


Fig. 3c

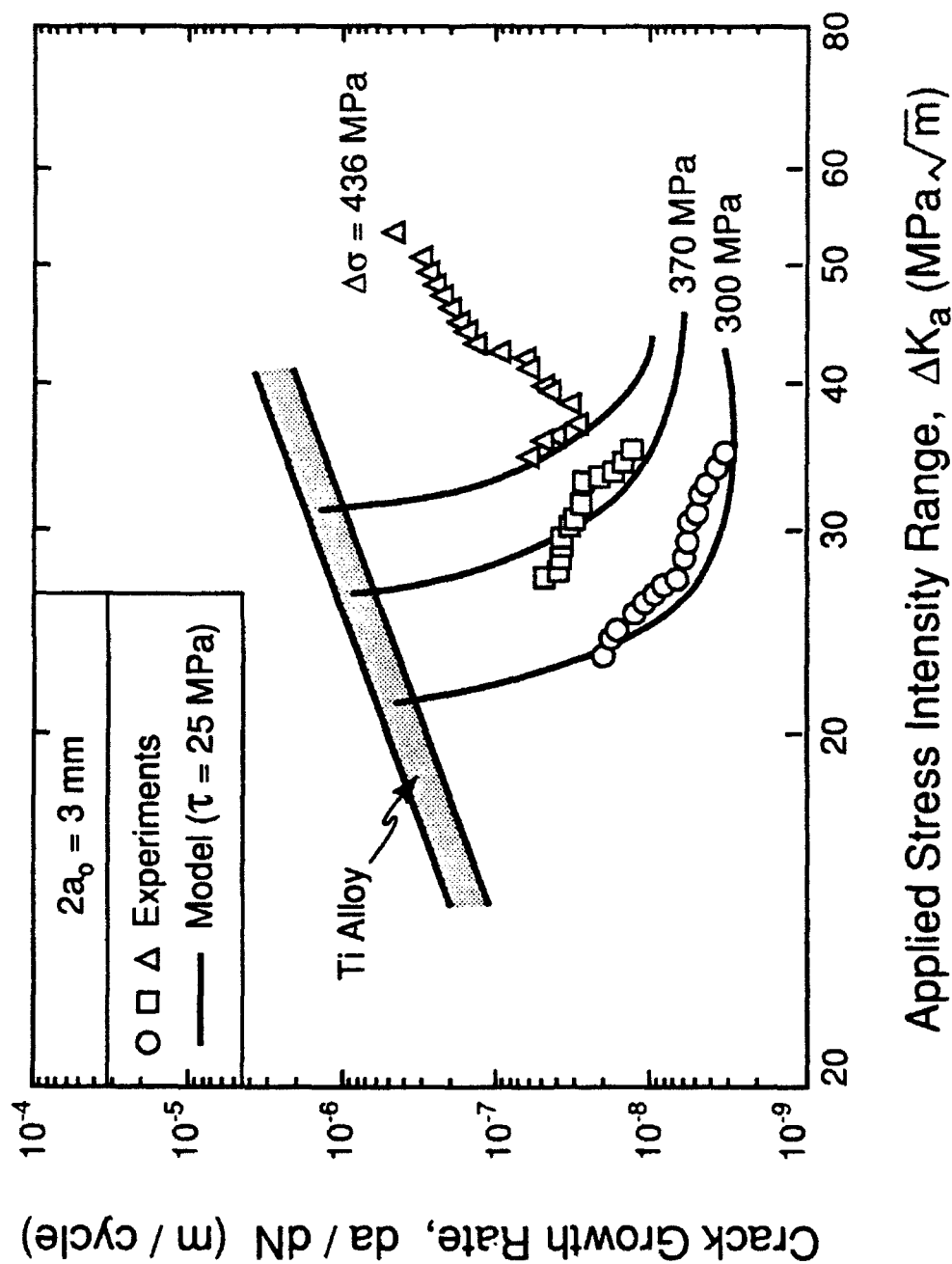


Fig. 3d

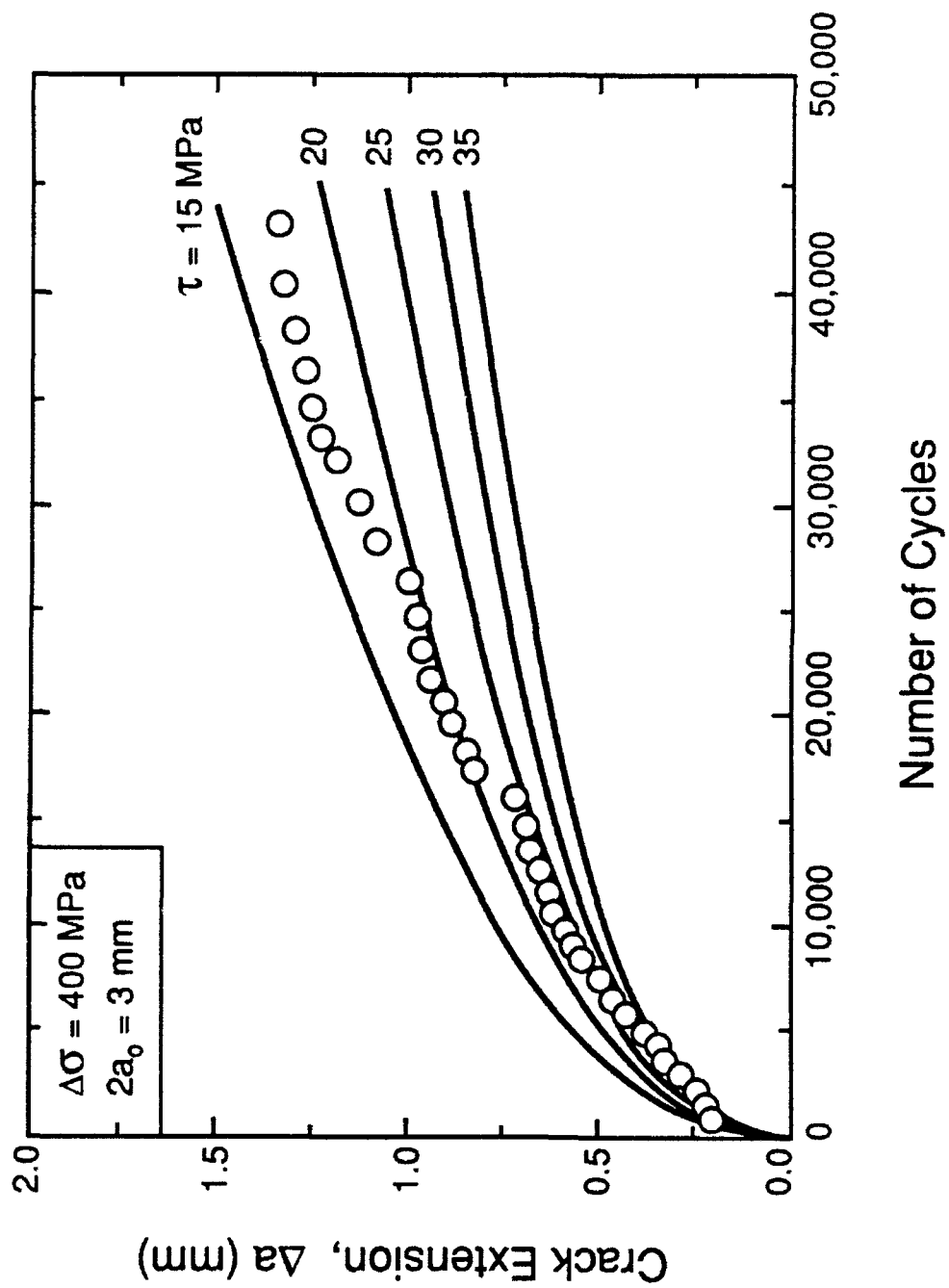


Fig. 4a

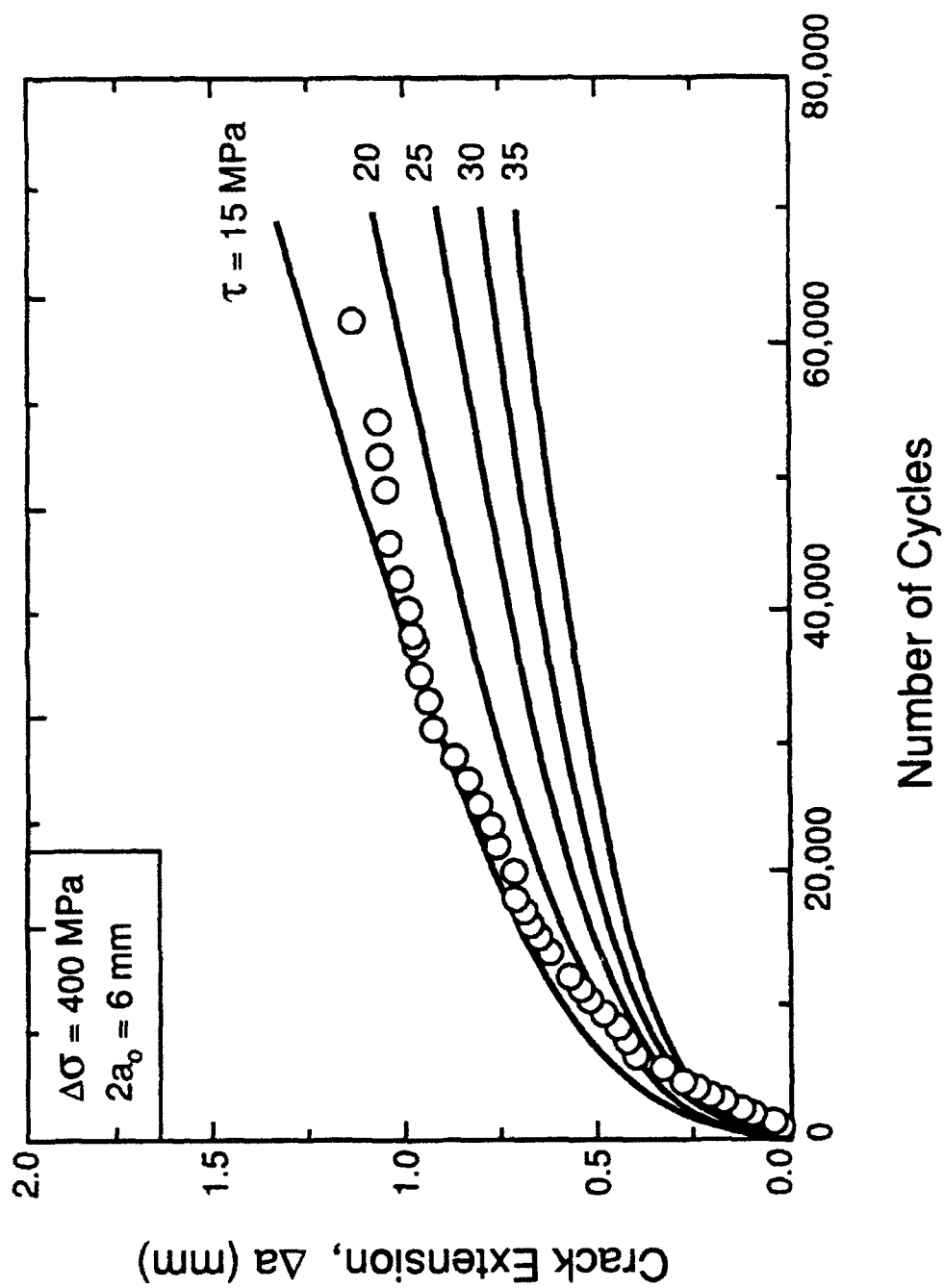


Fig. 4b

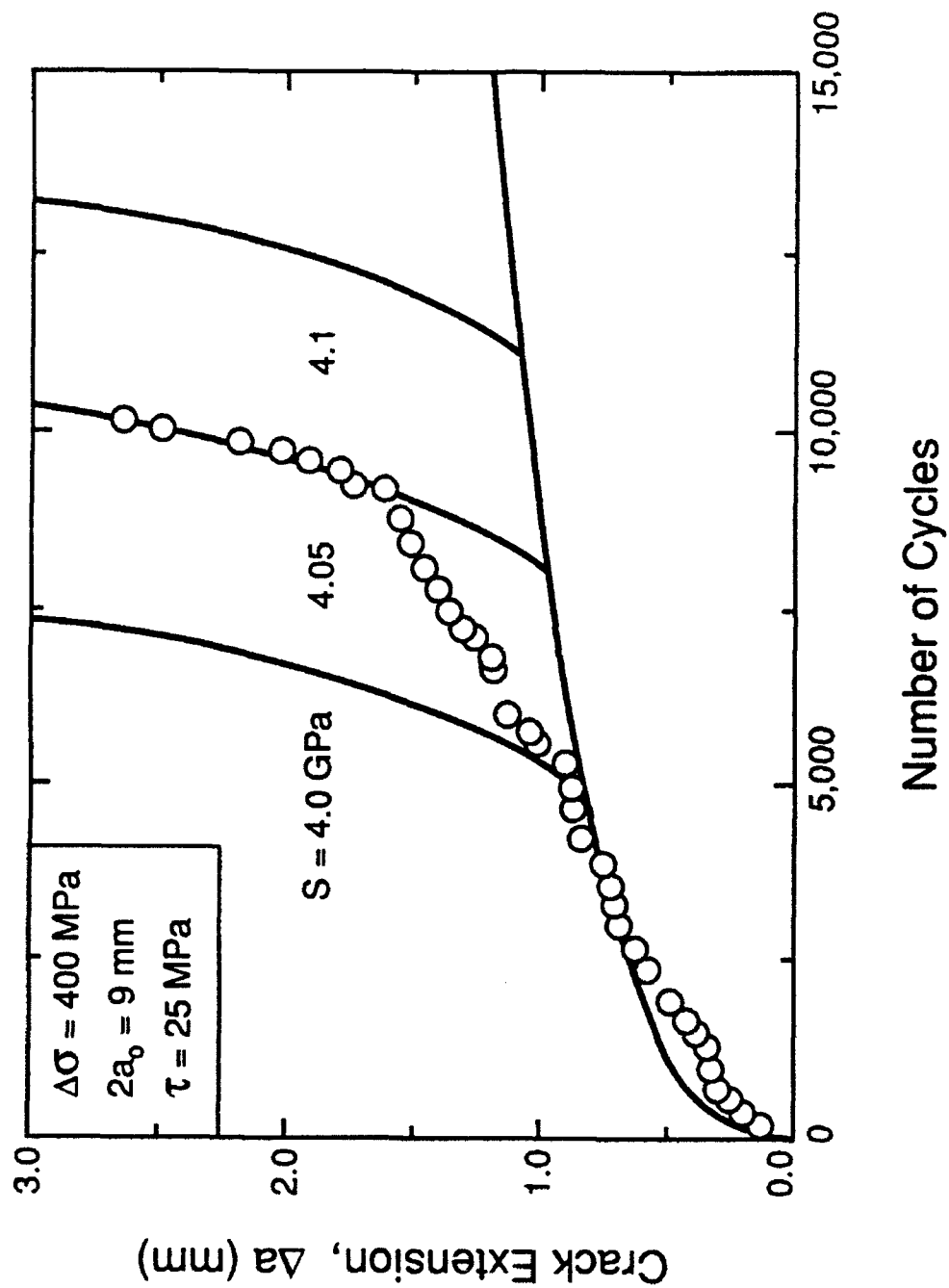


Fig. 4c

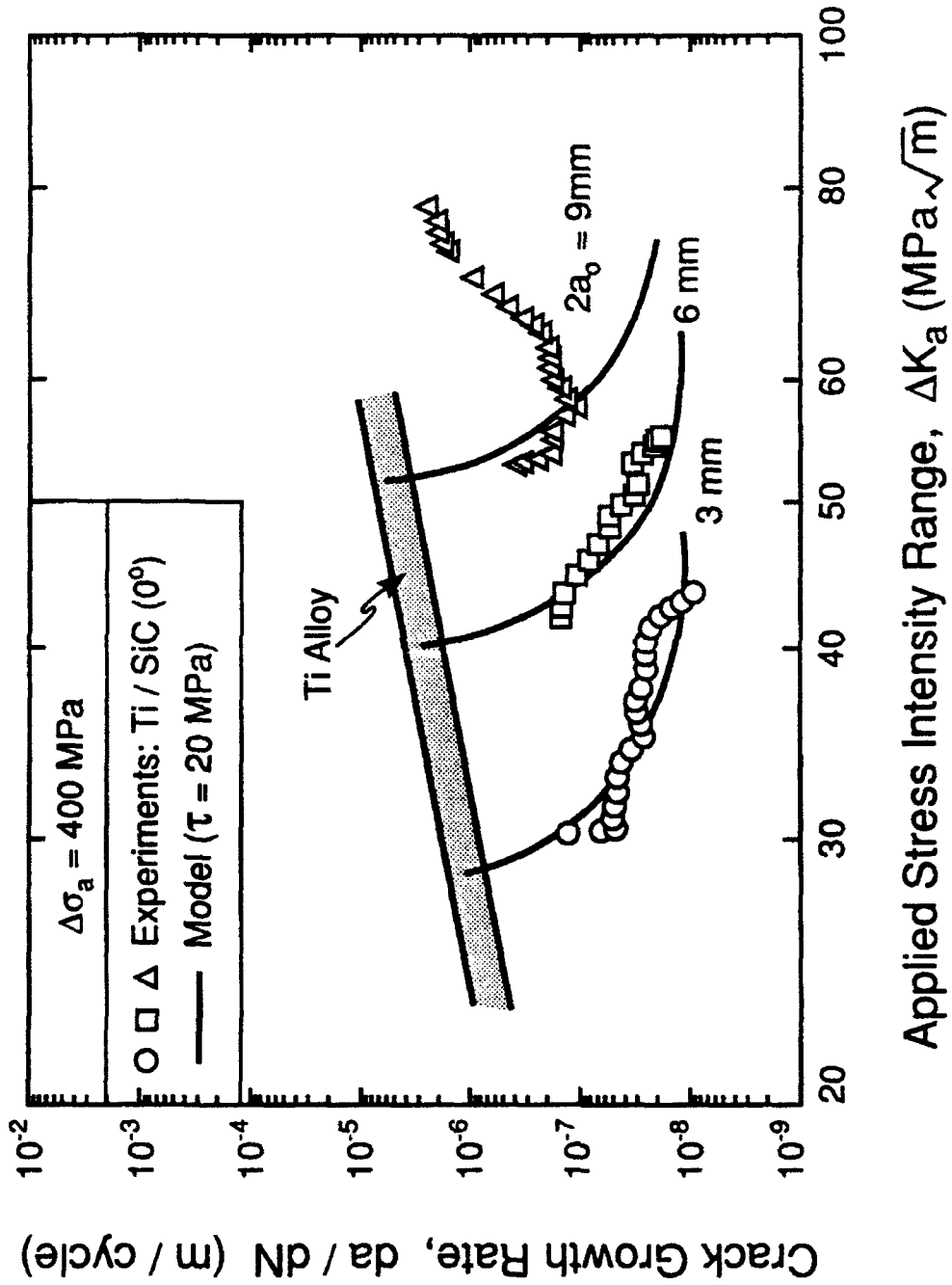


Fig. 4d

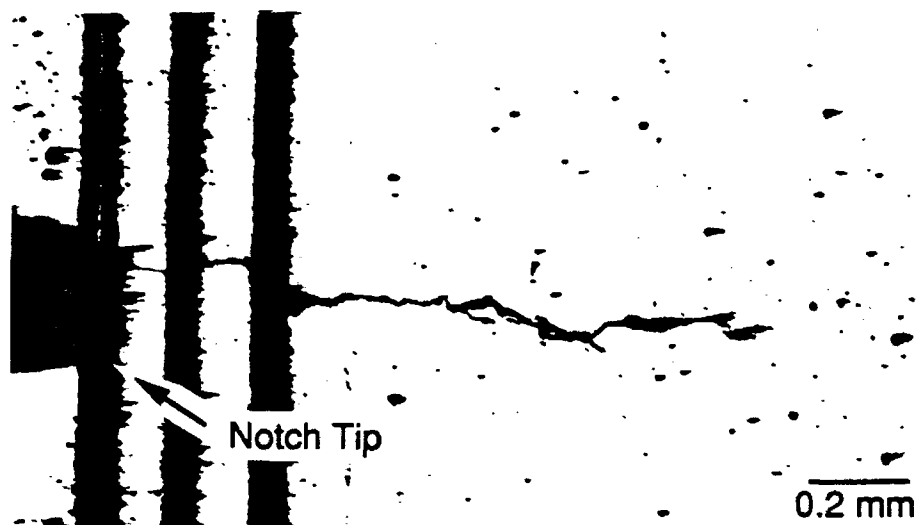


Fig. 5a

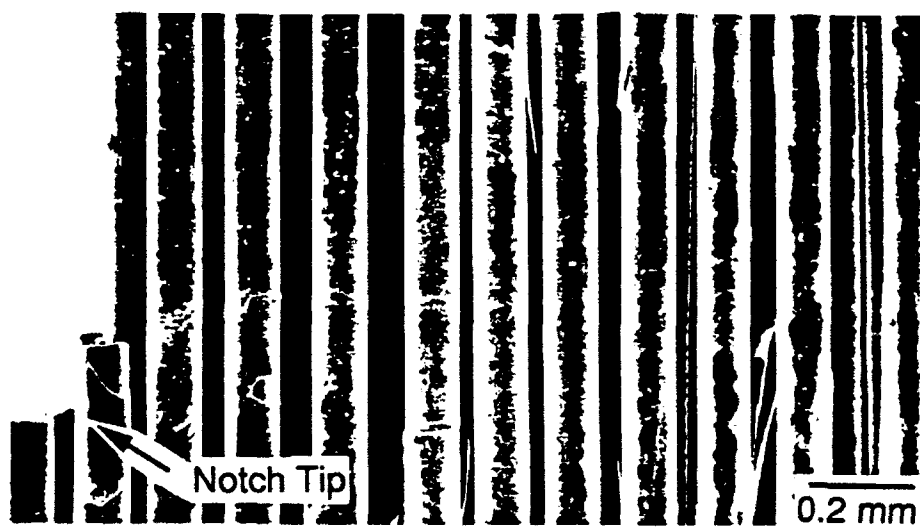


Fig. 5b

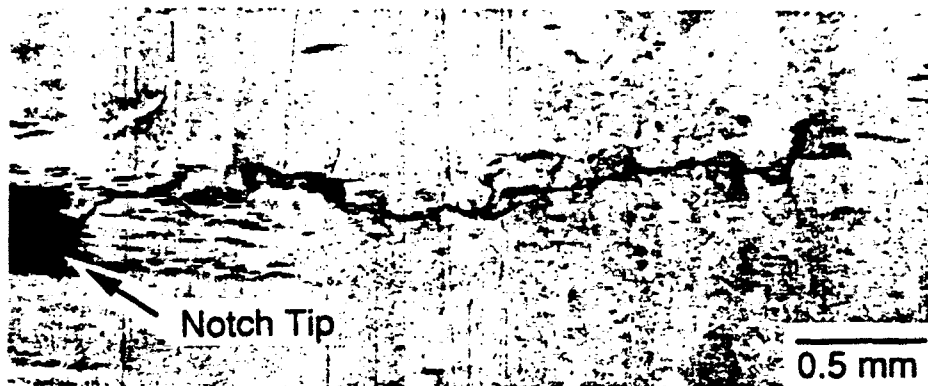


Fig. 6a

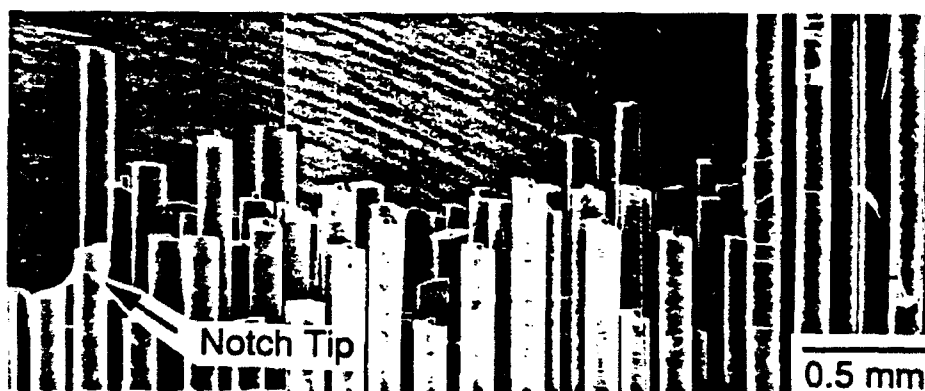


Fig. 6b

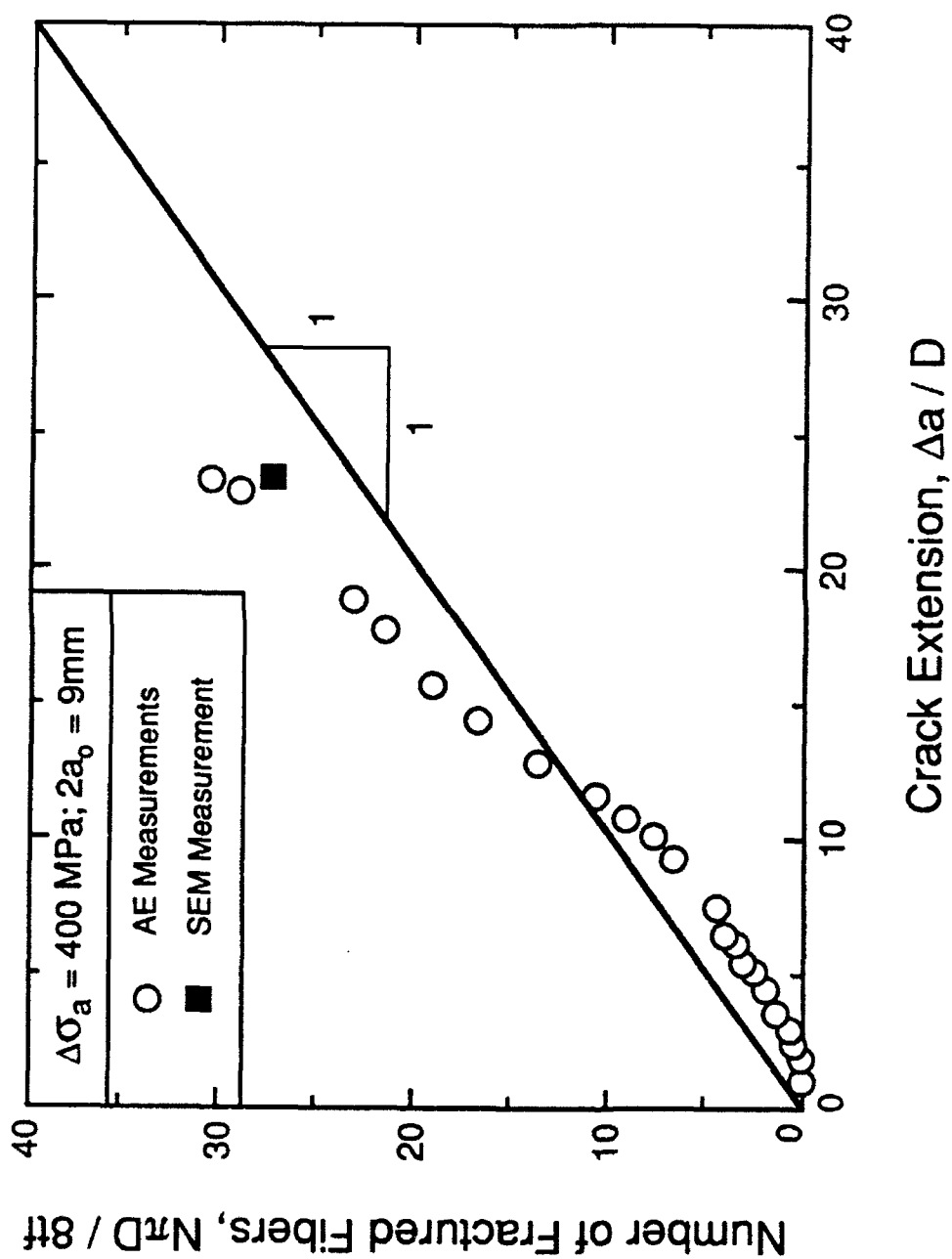


Fig. 7

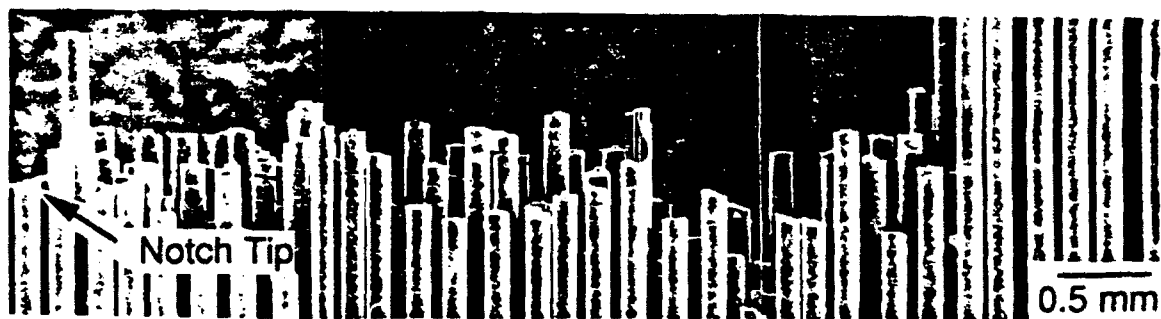
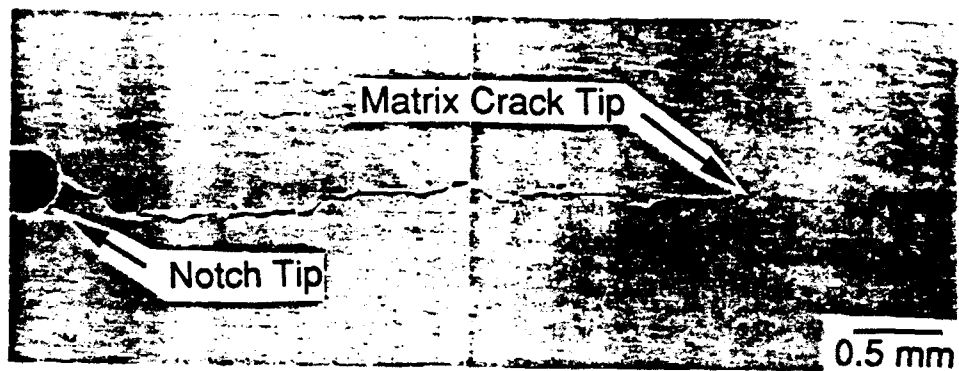


Fig. 8

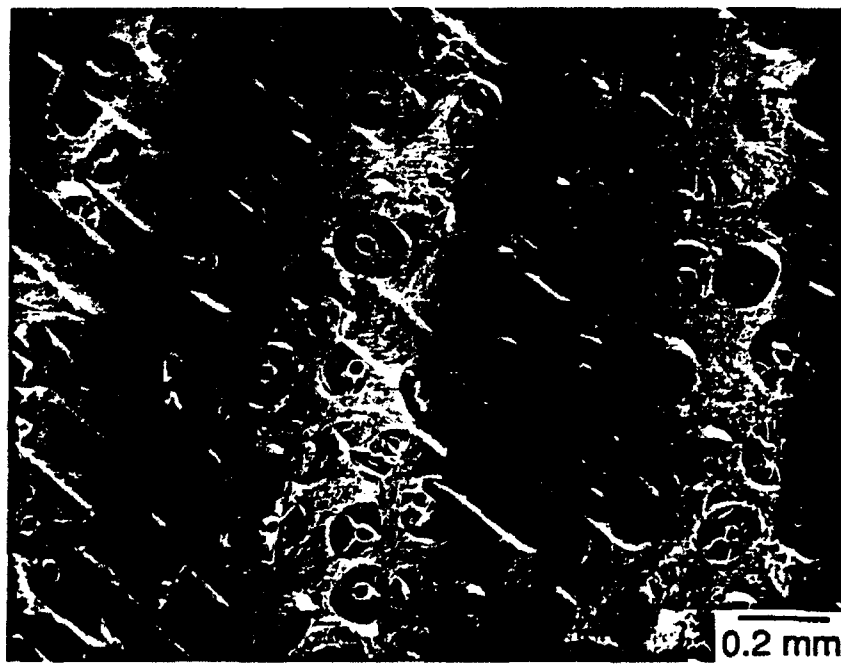


Fig. 9

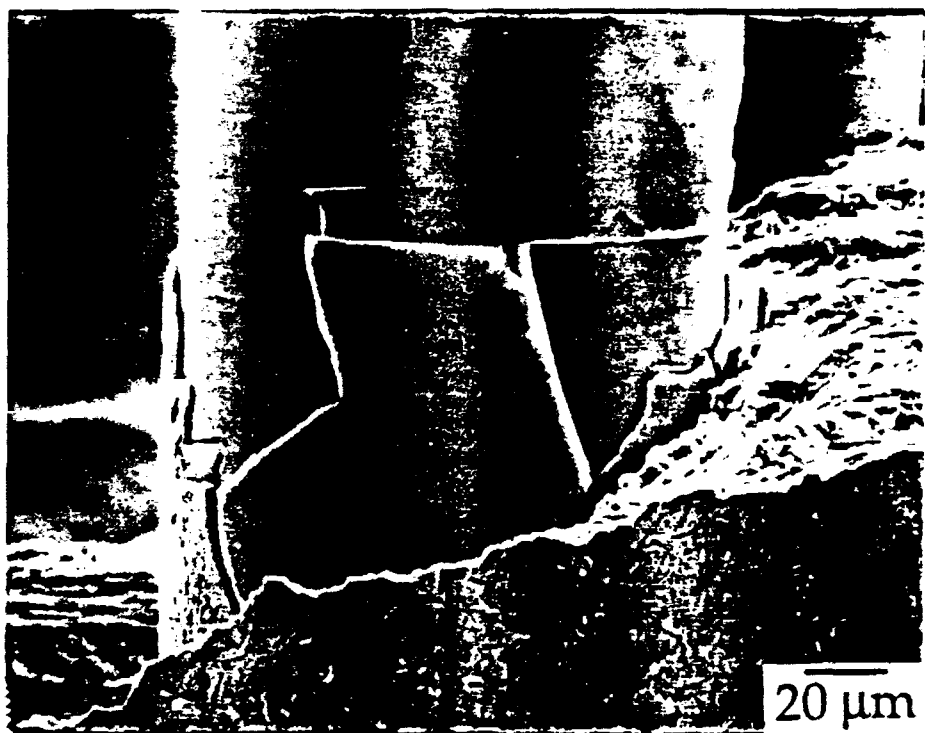


Fig. 10a

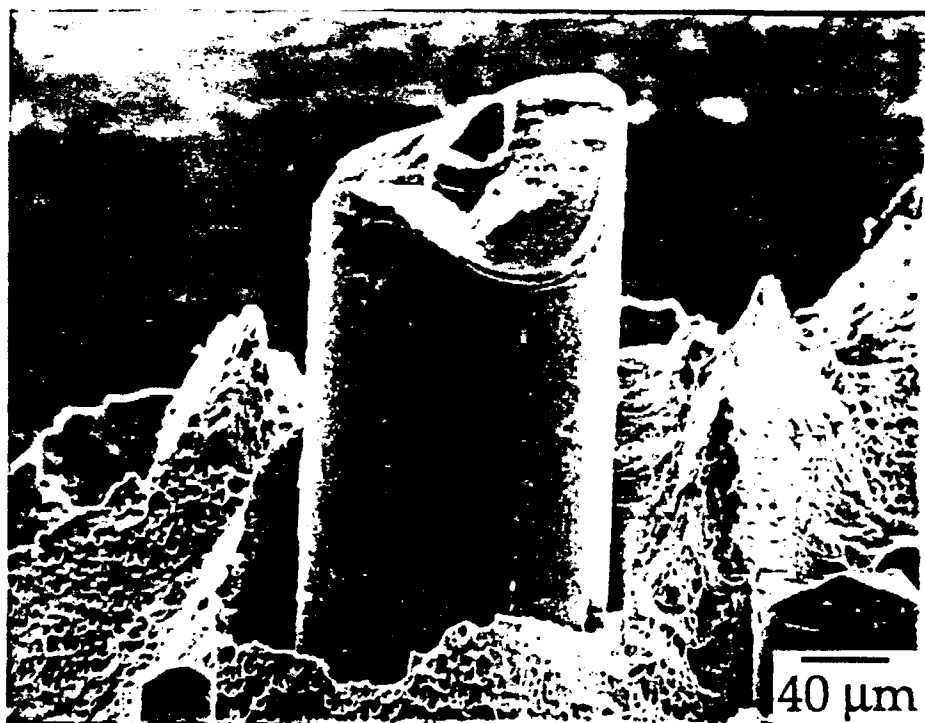


Fig. 10b

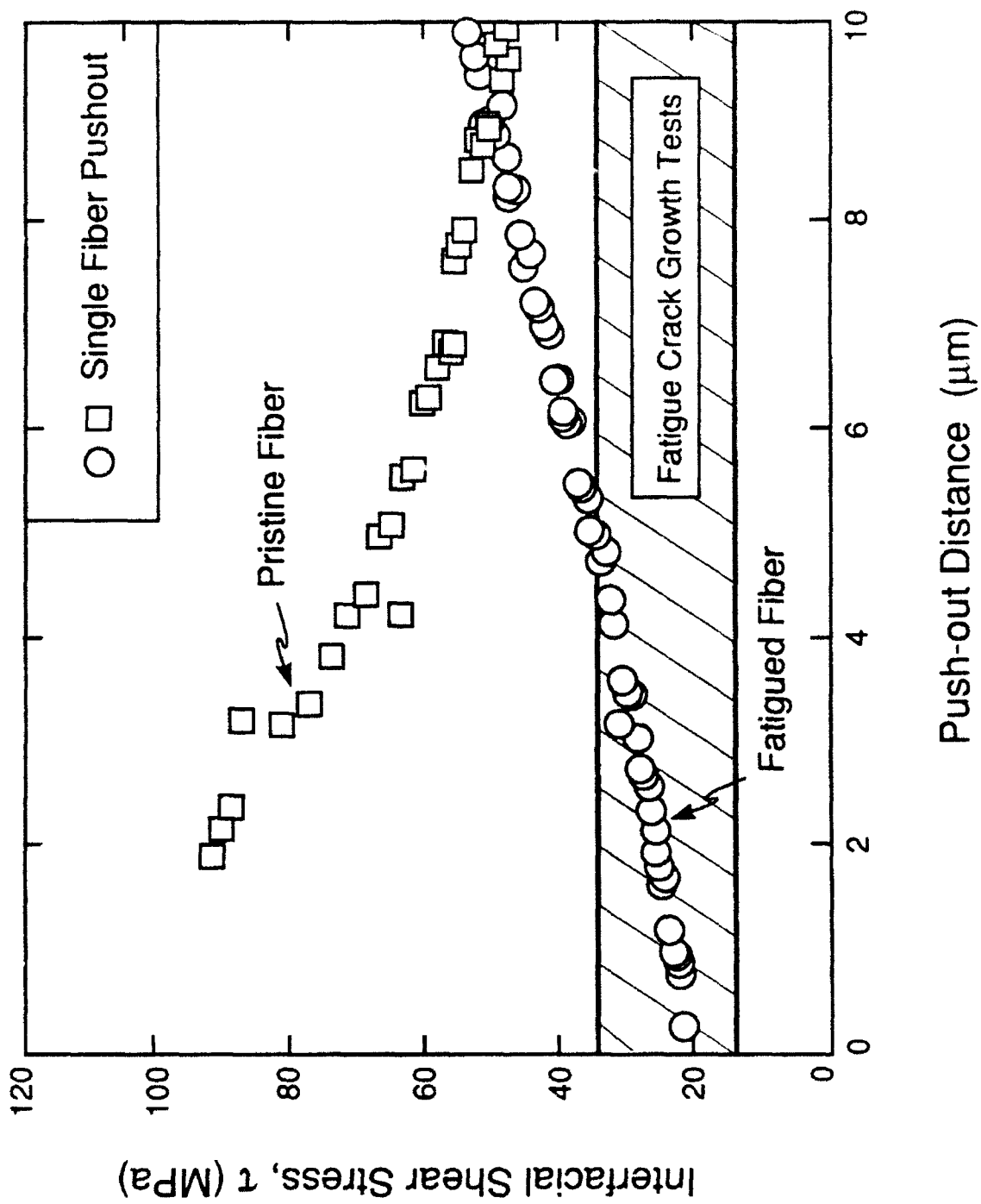


Fig. 11

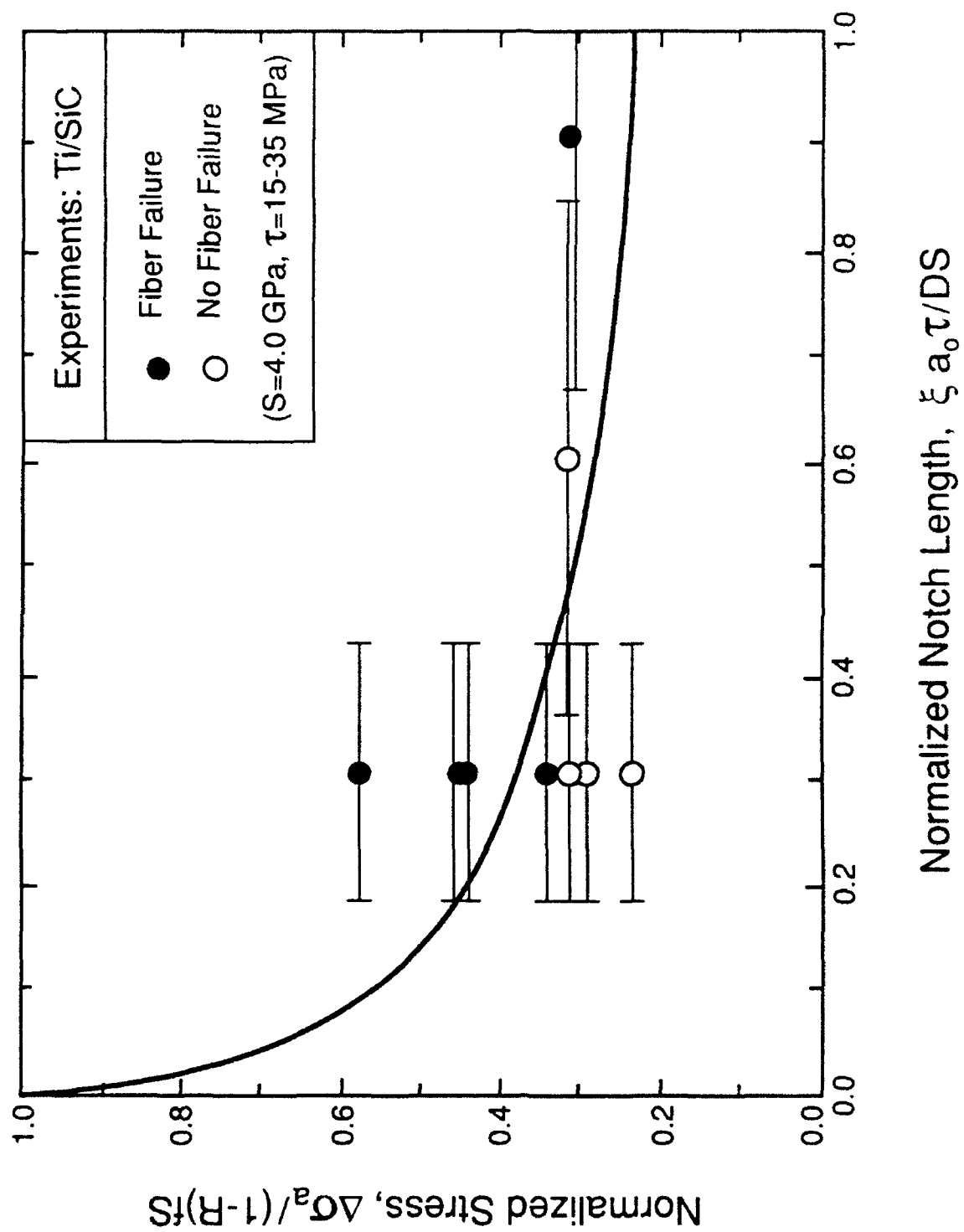


Fig. 12

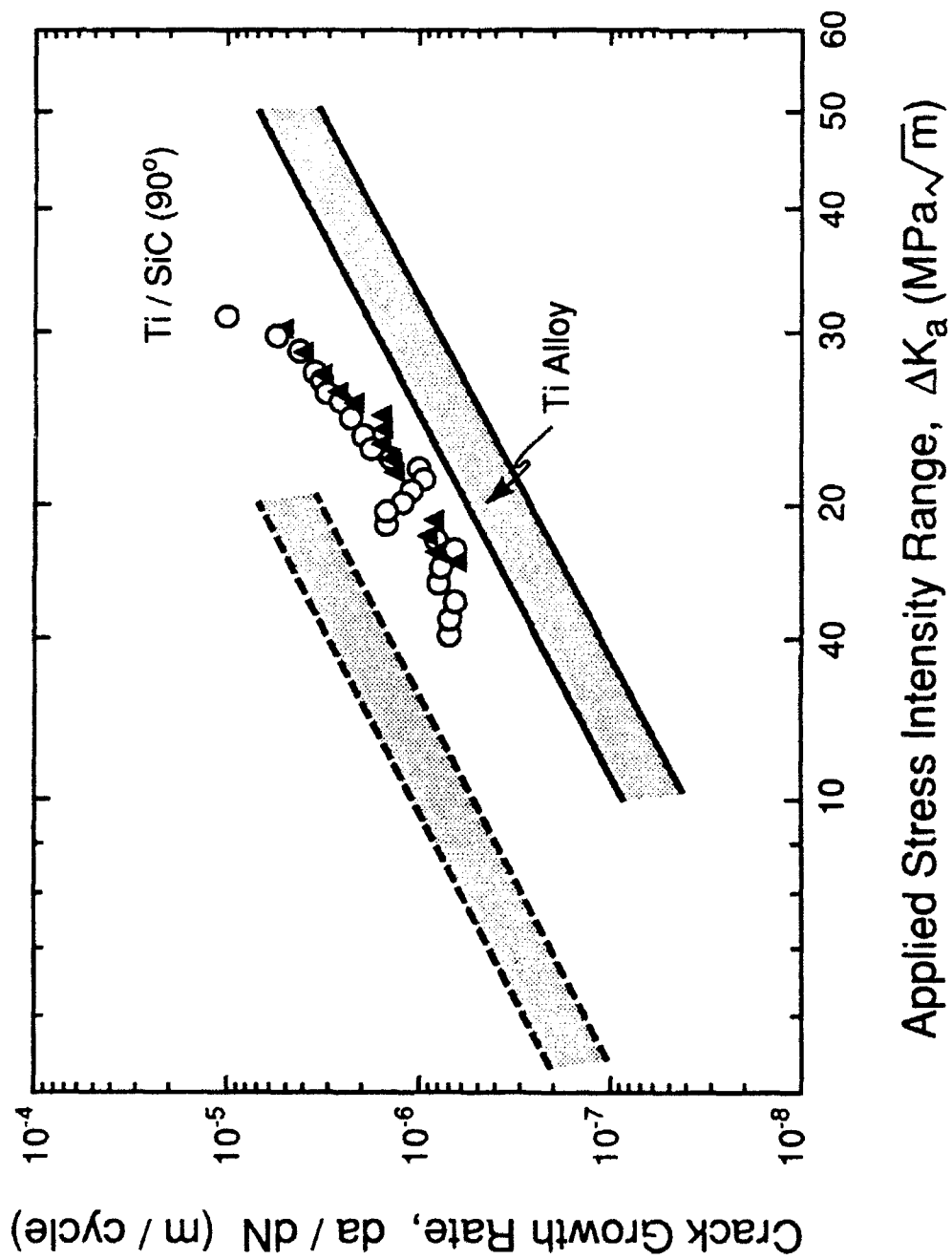


Fig. 13

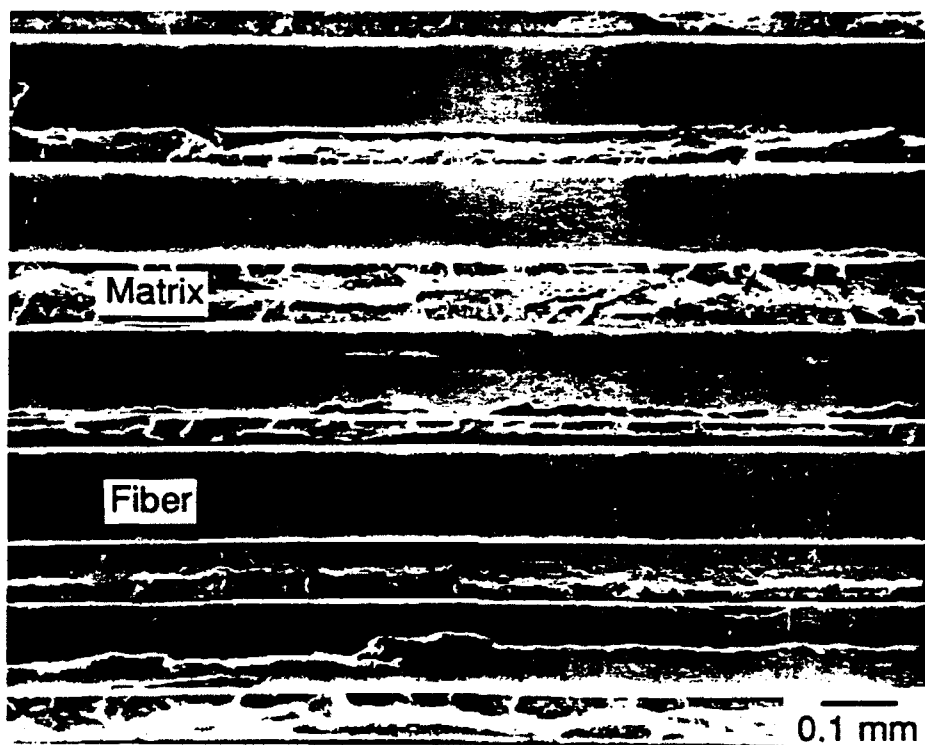


Fig. 14

FATIGUE CRACK GROWTH IN FIBER-REINFORCED METAL-MATRIX COMPOSITES

G. Bao[†] and R.M. McMeeking^{*}

[†]Department of Mechanical Engineering
The Johns Hopkins University, Baltimore, MD 21218

^{*}Department of Mechanical and Environmental Engineering
University of California, Santa Barbara, CA 93106

Submitted to Acta Metallurgica et Materialia

April, 1993

ABSTRACT

Fatigue crack growth in fiber-reinforced metal-matrix composites is modeled based on a crack tip shielding analysis. The fiber/matrix interface is assumed to be weak, allowing interfacial debonding and sliding to occur readily during matrix cracking. The presence of intact fibers in the wake of the matrix crack shields the crack tip from the applied stresses and reduces the stress intensity factors and the matrix crack growth rate. Two regimes of fatigue cracking have been simulated. The first is the case where the applied load is low, so that all the fibers between the original notch tip and the current crack tip remain intact. The crack growth rate decreases markedly with crack extension, and approaches a "steady-state". The second regime occurs if the fibers fail when the stress on them reaches a unique fiber strength. The fiber breakage reduces the shielding contribution, resulting in a significant acceleration in the crack growth rate. It is suggested that a criterion based on the onset of fiber failure may be used for a conservative lifetime prediction. The results of the calculations have been summarized in calibrated functions which represent the crack tip stress intensity factor and the applied load for fiber failure.

NOMENCLATURE

a	matrix crack half length
a_0	initial notch half length
D	fiber diameter
E	Young's modulus of composites: $f E_f + (1-f)E_m$
\bar{E}	effective composite Young's modulus considering material orthotropy
E_f	Young's modulus of fiber
E_m	Young's modulus of matrix
f	volume fraction of fibers
$F(a/w)$	shape function for stress intensity factor: $\sqrt{\sec(\pi a/2w)}$
ℓ	unbridged segment half length
n	Paris law exponent
N	number of load cycles
S	fiber strength
w	finite panel width
α	non-dimensional bridge length: $(a-\ell)/a$
β	Paris law coefficient
δ	total crack opening displacement
δ_F	crack opening displacement induced by bridging fibers
δ_A	crack opening displacement caused by applied stress
ΔK	ratio of ΔK_{tip} to ΔK_a
ΔK_A	range in applied mode I stress intensity factor
ΔK_{tip}	range in mode I crack tip stress intensity factor
$\Delta \delta$	change in crack opening
$\Delta \Sigma$	non-dimensional measure of the stress amplitude/crack length: $2\lambda \bar{E} \Delta \sigma / a$
$\Delta \Sigma_0$	non-dimensional measure of the stress amplitude/notch length: $2\lambda \bar{E} \Delta \sigma / a_0$
$\Delta \sigma$	cyclic applied stress amplitude

$\Delta\sigma_s$	cyclic bridging stress amplitude
λ	bridging law coefficient: $D(1-f)^2(E_m)^2/4f^2 E_f E^2\tau$
ν	Poisson's ratio
σ	applied stress
σ_{\max}	maximum applied stress
σ_s	bridging stress due to fibers
Σ	non-dimensional measure of the maximum applied stress: $4\lambda\bar{E}\Delta\sigma_{\max}/\ell$
τ	interface sliding stress
η	non-dimensional measure of fiber strength: $4\lambda\bar{E} f S/\ell$

INTRODUCTION

Fatigue crack growth in metal matrix composites reinforced with brittle fibers has been studied extensively (Naik and Johnson, 1991; Kantzos, Telesman and Ghosn, 1989; Sensmeier and Wright, 1990; McMeeking and Evans, 1990; Walls, Bao and Zok, 1991, 1993). Experimental results (Sensmeier and Wright, 1990; Walls, Bao and Zok, 1991, 1993) indicate the following fatigue cracking behavior. Under tensile cyclic loading of the composite in the fiber direction, the matrix undergoes mode I fatigue cracking normal to the fibers, while the fibers in the crack wake remain intact due to the frictional sliding at the fiber/matrix interface. These fibers bridge the crack and shield the crack tip from the applied stress. Consequently, a transient occurs in which the crack growth rate da/dN diminishes upon crack extension, and a steady-state regime follows in which da/dN is small. When the applied stress level is high, the stress in the fiber at the original notch tip may reach the fiber strength and then the fibers begin to fail. The crack growth thereafter accelerates again, leading to the final rupture. These features of fatigue cracking in fiber reinforced metal-matrix composites are shown in Fig. 1 in which a typical fatigue crack growth curve of a Ti matrix composite with SiC fibers is replotted from the work of Walls, Bao and Zok (1991). The composite tested contains 35% of unidirectional fibers, with fiber diameter $D = 140\mu\text{m}$ (Jansson, Deve and Evans, 1990).

In this paper, the micromechanical model of McMeeking and Evans (1990) is extended to predict the above fatigue crack growth behavior. The materials of particular interest for this model include Ti/SiC composites that have "weak" interfaces. Attention here is focused on mode I cracking that initiates from a sharp notch. Matrix fatigue cracking in metal matrix composites in the absence of a notch has been modeled recently by McMeeking and Evans (1990). The analysis of fiber stresses, interface sliding and crack bridging in their model is analogous to that conducted earlier for fiber-reinforced ceramics subject to monotonic tensile loading (Marshall, Cox and

Evans, 1985; Marshall and Cox, 1987; McCartney, 1987). Following the analysis of Marshall and Oliver (1987) and Cox (1990), McMeeking and Evans (1990) considered the effect of reversal of the fiber interface sliding direction during cyclic loading. They found that the results for bridging during monotonic loading can be scaled simply to represent the effect of bridging during fatigue loading. The model is further developed here to include the effects of an initial sharp notch which is unbridged by fibers at the outset. This analysis permits the inclusion of the effect of breaking fibers which can increase the size of the unbridged segment. The influence of finite specimen width and, of greater importance, the role of fiber failure in fatigue cracking behavior is accounted for too. Fatigue crack growth curves, both with and without fiber fracture, are predicted for given values of the relevant parameters.

Calibrated functions have been devised to represent the results. One set of functions provides values for the crack tip stress intensity factor amplitude as a function of material parameters, the applied load, the matrix crack length and the size of the unbridged segment of the crack. Another set of functions gives the applied load sufficient to fail a fiber in terms of the fiber strength, material parameters, the matrix crack length and the extent of the unbridged segment.

The results in this paper are based on individual models (for bridging fibers, for their effect on crack tip stress intensities, for the incidence of fiber failure, for cyclic loading of bridging fibers and for matrix fatigue) which, in one way or another, have been developed and used previously. In addition, the basic method of analysis employed to solve integral equations in this paper has been used widely. However, the previous applications mostly have concerned monotonic loading of brittle matrix composites and only the work of McMeeking and Evans (1990), Cox and Marshall (1991) and Cox and Lo (1992a, 1992b) addressed the question of cyclic loading. Furthermore, the earlier modelling of fatigue in fiber-reinforced metals has not fully explored the phenomena when there are notches and failing fibers. In this paper, all of

the individual model elements are brought together in a treatment of matrix fatigue crack growth in conjunction with notches and fiber failure. The models have been shown to agree well with the available data for matrix fatigue growth with and without fiber failure (Walls et al., 1993). Therefore, the comprehensive model in this paper is suitable for studying in some detail the phenomena associated with this important damage mechanism in fiber-reinforced metals to augment the insights available from experimental data. Such features that can be studied are: the deceleration of the crack growth rate as the matrix crack grows; the relative influence of notches; the interplay between applied load amplitude and the matrix crack length in controlling the crack growth rate; and the relatively sudden and dramatic transition from survival of fibers to failure of fibers leading to rapid crack growth as the load is increased or a critical matrix crack length is reached and exceeded. It is true that these features can be deduced directly or indirectly from results available in several different papers in the literature. However, we believe that it is important to bring the results and phenomena together and present them in a focused manner for the matrix fatigue crack growth problem.

The model presented in this paper is based on certain assumptions. Important ones are: the interface shear strength τ is uniform and does not degrade during fiber load cycling; the strength of the fibers is deterministic and not statistical; the matrix fatigue crack growth obeys the Paris law for fatigue crack growth in the monolithic matrix; the entire component or specimen, except for the fiber bridging, can be analyzed elastically which implies that crack tip plastic zones are small. Some assumptions are known to be inexact. For example, measurements have shown that the interface shear strength τ for a fatigued specimen with a matrix crack is lower than that for a pristine material (Warren, Mackin and Evans, 1991). This is known to influence the crack tip opening shape since the fiber constraint near the matrix crack tip on freshly exposed surfaces is relatively stronger than the fiber constraint far from the matrix crack tip on

old and therefore fatigued surfaces (Kantzos et al., 1989). In some cases this influences the fatigue crack growth rate. However, there has been significant success when the model with the fixed value for τ is compared with the data for matrix fatigue crack growth. There are some discrepancies in the transient behavior which can be attributed to the degradation of τ . However, even those discrepancies can be rationalized in terms of interpolation among models with a fixed τ (Walls et al., 1993).

The value of the interface shear strength τ which is used to compare the models to the experiments is usually chosen empirically to obtain one match to the steady state crack growth rate usually observed after some crack growth in large specimens with short cracks under modest load amplitudes. Furthermore, the fiber strength S is usually chosen empirically so that onset of fiber failure in the model agrees in one case with the initiation of fiber failure in an experiment. There is therefore an element of fitting in the model presented in this paper. However, it should be emphasized that with this minimal degree of fitting, the model is capable of capturing the rich interplay among phenomena as controlled by load amplitude, peak load level, matrix crack length and initial notch length. Furthermore, the pragmatic approach to choosing values for τ and S is made necessary by the fact that *in situ* properties are needed. In contrast to other empirical material constants such as fiber and matrix elastic moduli which are relatively unchanged *in situ*, it is well known that the interface shear strength τ and fiber strength S are sensitive to processing, treatment, handling and to fatigue cycling itself (Walls et al., 1993).

CRACK-TIP SHIELDING ANALYSIS

Consider the crack configuration depicted in Fig. 2. The center section of length ℓ is unbridged. The unbridged center section can represent the original notch of length $2a_0$ or a current unbridged segment after fiber failure. The bridged sections represent

the growing, mode I, plane strain matrix fatigue crack in the infinite body. With the possibility that fibers can break, the bridge segment can become unbridged. The current unbridged segment will then have a length $2\ell > 2a_0$. Both the fibers and the matrix are assumed to be linear elastic, with Young's modulus E_f and E_m respectively. Plasticity of the matrix is neglected in this study. The continuous reinforcing fibers are aligned normal to the plane of the matrix crack. The fracture energy of the fiber/matrix interface is assumed to be small, such that debonding and sliding occur readily during matrix cracking. The sliding behavior of the interface is characterized by a constant frictional shear stress τ , such that the bridging stress σ_s is related to the crack opening displacement δ during monotonic opening by (Aveston, Cooper and Kelly, 1971; McCartney, 1987; Hutchinson and Jensen, 1990)

$$\delta = \lambda \sigma_s^2 \quad (1)$$

where λ is a material parameter given by

$$\lambda = D (1 - f)^2 E_m^2 / 4 E^2 E_f f^2 \tau. \quad (2)$$

The bridging stress σ_s is the force per unit surface area applied by the fibers to the crack surface and the opening δ is the additional displacement of the material on one side of the crack compared to the other due to the presence of the crack and is measured on a gauge length larger than the interface slip zones on the fibers at the crack. In eq. (2), D is the fiber diameter, f the fiber volume fraction and E the composite Young's modulus. $E = f E_f + (1-f) E_m$. Upon cyclic loading, the change in crack opening displacement $\Delta\delta$ after the first peak opening is related to the change in bridging stress $\Delta\sigma_s$ in a similar fashion (McMeeking and Evans, 1990)

$$\Delta\delta = \pm \frac{1}{2}\lambda (\Delta\sigma_s)^2 \quad (3)$$

where the plus (+) and minus (-) signs correspond to the loading and unloading portions of the cycle, respectively.

The bridging law and the theory of elasticity and fracture mechanics can be used to solve the problem depicted in Fig. 2. Pertinent results are the distribution of fiber stresses within the bridged zone and the crack tip stress intensity factor. Such solutions have been obtained for both infinite and finite geometries previously by many workers (Marshall et al., 1985; Marshall and Cox, 1987; McCartney, 1987; Cox, 1990; Cox and Lo, 1992a). A summary of the analytical method is provided in the Appendix. Values for the bridging stress amplitude have been computed for the applied load range $0 \leq \Delta\Sigma \leq 20$ where the dimensionless parameter $\Delta\Sigma$ is such that

$$\Delta\Sigma = 2\lambda \bar{E} \Delta\sigma/a \quad (4)$$

with \bar{E} an effective elastic modulus for crack problems which takes the orthotropy of the material into account (see Appendix). A representative result for the bridging stress is shown in Fig. 3 where it is shown in dimensionless form as a function of position on the matrix crack. Each curve represents a result for a case with a different unbridged segment.

Two features in Fig. 3 are noteworthy. The peak stress in the bridging zone always occurs at the edge of the unbridged segment. This implies that if fiber failure occurs at a unique deterministic strength, it will always start at the original notch tip. In addition, when the crack length a becomes very large, for low values of $\Delta\sigma$ almost all the applied stress is transferred through the intact fibers (i.e., $\Delta\sigma_s \approx \Delta\sigma$), as indicated by the $\ell/a = 0$ curve. The bridging stress is then rather uniformly distributed except in the

crack tip region where $\Delta\sigma_s$ falls well below $\Delta\sigma$. At higher values of $\Delta\sigma$, the fiber stresses $\Delta\sigma_s$ are nonuniform even for long cracks and fall somewhat below $\Delta\sigma$, indicating that the shielding effect in that case is less effective.

The stress intensity factor range at the crack tip ΔK_{tip} is normalized by the stress intensity factor range which would occur in the absence of the bridging fibers. For an infinite body, this would be

$$\Delta K_A = \Delta\sigma \sqrt{\pi a}. \quad (5)$$

The resulting ratio is

$$\Delta\kappa = \frac{\Delta K_{tip}}{\Delta K_A}. \quad (6)$$

Numerical results for $\Delta\kappa$ for the problem shown in Fig. 2 are plotted in Fig. 4 against the non-dimensional bridge length $(a - \ell)/a$ for $\Delta\Sigma = 1, 2, 4, 8, 12$ and 20. For a small bridge, ΔK_{tip} is almost the same as ΔK_A , since the shielding effect is small. The stress intensity at the crack tip is reduced significantly as the crack length a is increased beyond the bridged segment to produce a large bridge. These general trends are shown clearly in Fig. 4.

For the purpose of investigating when a fiber will fail, it is of interest to determine the largest stress in the fibers in a given state of matrix crack length, unbridged segment and applied stress. The maximum fiber stress, which always occur in the fiber adjacent to the unbridged segment, is plotted in Fig. 5a against the normalized bridge length $(a - \ell)/a$. These calculations were carried out with the bridging law in eq. (1) and represent the stress in the fiber at maximum applied load. Results are presented in Fig. 5a for several values of the maximum applied load σ_{max} . The points

in Fig. 5a were obtained by numerical calculation. The full lines were obtained by fitting functions to the numerical results which will be discussed below. The results in Fig. 5a can be replotted to give the length $(a-\ell)$ of the bridge which will have a maximum fiber stress exactly equal to S as a function of the maximum applied stress σ_{\max} . This is shown in Fig. 5b. Since the unbridged segment ℓ will grow as fibers fail, the value of η (defined in (10b) below) will increase when fibers break. However, in the initial configuration with $\ell = a_0$, the curves can be used to predict when the first fiber will fail. At the beginning of fatigue crack growth, the bridge length $a-\ell$ is zero and gets bigger as fatigue cracking proceeds. Therefore, at a given maximum load, the state of the specimen starts at the bottom of the diagram and moves upwards at constant Σ (defined in (10c) below) since ℓ is fixed at a_0 . This will proceed until the curve representing the fiber strength is reached at which point the first fiber will fail. Thus, the diagram predicts directly the amount of fatigue crack growth which can occur before fiber failure will occur. Note that if the fiber strength is high enough or the maximum applied stress is low enough, fatigue crack growth will proceed without fibers ever failing.

The numerical results for the maximum fiber stress just discussed can be augmented with an exact result due to Suo, Ho and Gong (1993) for the situation where the maximum applied stress is low and the matrix crack is very long compared to the unbridged segment. In this situation, the unbridged segment will behave like an isolated crack since the stress transmitted through the bridge almost everywhere will be equal to the applied stress. Only near the tip of the matrix crack and near the edge of the unbridged segment will the bridge stress differ from the applied stress. However, the tip of the matrix crack is too far away from the unbridged segment to have any influence. Thus, the unbridged segment will behave like a finite crack in a uniform stress field. Furthermore, the smallness of the applied stress will ensure that the region of nonuniform bridge stress will be effectively small and the unbridged segment will

behave as a crack with small scale yielding. Thus, the value of the J-integral (Rice, 1968) for the tip of the unbridged segment is just that for a finite elastic crack in a uniform tensile stress. Denoting the value of the J-integral to be J , we thus have

$$J = \frac{\sigma_{\max}^2 \pi \ell}{\bar{E}} \quad (7)$$

when the maximum stress is being applied. An elementary result (Rice, 1968) given the J-integral to be the energy per unit area absorbed by the bridging process and thus

$$J = \int_0^{\delta_0} \sigma_s(\delta) d\delta = \frac{2}{3} \lambda (fS)^3 \quad (8)$$

where δ_0 is the crack opening displacement when $\sigma_s = fS$. Thus, eq. (7) & (8) can be combined to give

$$fS = \left(\frac{3\pi\sigma_{\max}^2 \ell}{2\lambda \bar{E}} \right)^{\frac{1}{3}} \quad (9)$$

$$\text{or} \quad \eta = (6\pi)^{\frac{1}{3}} \Sigma^{\frac{2}{3}} \quad (10a)$$

$$\text{where} \quad \eta = \frac{D(1-f)^2 E_m^2 \bar{E} S}{E^2 E_f f \ell \tau} \quad (10b)$$

$$\text{and} \quad \Sigma = \frac{D(1-f)^2 E_m^2 \bar{E} \sigma_{\max}}{E^2 E_f f^2 \ell \tau} \quad (10c)$$

As noted above, this result is valid for small Σ and large a/ℓ . The latter means that $(a-\ell)/a = \alpha$ in Fig. 5a is close to unity. The result for $\Sigma = 0.5$ in Fig. 5a agrees closely

with eq. (10a) but for $\Sigma = 1$ the agreement is merely good. Thus, we conclude that the asymptotic limit in eq. (10a) can be used when $\Sigma \leq 0.5$ and inspection of Fig. 5a suggests that it will be applicable for $\ell/a \leq 0.5$.

FINITE GEOMETRY

The crack tip shielding analysis performed in the previous section is based on a model geometry of a center crack in an infinite body. Clearly, fatigue tests on center-notched tensile specimens are conducted with finite widths. To justify the relevance of the model just developed for finite widths, finite element calculations have been carried out for such specimens using the ABAQUS code (Hibbitt et al., 1990). The specimen length $2h$ is much larger than the specimen width w ($h/w = 10$) and the non-dimensional original notch size, a_0/w is taken to be 0.2 for these calculations, as shown schematically inset in Fig. 6.

To simulate the intact fibers that bridge the matrix crack, non-linear springs are used, with a spring law identical to eq. (1). Crack tip stress intensity factors ΔK_{tip} are obtained through the J-integral, and normalized by the applied stress intensity, ΔK_A

$$\Delta K_A = \Delta \sigma \sqrt{\pi a} F(a/w) \quad (11a)$$

where $F(a/w)$ is given in Tada et al., (1985) to be approximately

$$F(a/w) = \sqrt{\sec \frac{\pi a}{2w}}. \quad (11b)$$

Plotted in Fig. 6 as the solid lines are finite element results for the normalized crack tip stress intensity amplitude $\Delta K_{tip}/\Delta K_A$ against the normalized crack extension

$(a - a_0)/a$ for $\Delta\Sigma_0 = 1$ and $\Delta\Sigma_0 = 2$ where $\Delta\Sigma_0$ is the value of $\Delta\Sigma$ when $a = a_0$. The corresponding results for the infinite body ($w \rightarrow \infty$) are shown as the dashed lines. Inspection of these results indicates that for $(a - a_0)/a < 0.6$, the values of $\Delta K_{tip}/\Delta K_A$ for finite width specimen are essentially the same as those given by the infinite body solution. Consequently for $(a - a_0)/a < 0.6$, the results in Fig. 4 can be used for the finite strip as long as ΔK_A is computed according to eq. (11). These findings imply that in general as long as $a/w < 0.5$, the results in Fig. 4 can be used to determine the stress intensity factor in the finite strip.

Following the argument leading to eq. (9), we infer that the maximum stress in the fiber adjacent to the unbridged segment is such that

$$fS = \left(\frac{3\pi F^2 (\ell / w) \sigma_{\max}^2 \ell}{2\lambda \bar{E}} \right)^{\frac{1}{3}} \quad (12a)$$

$$\text{or} \quad \eta = (6\pi)^{\frac{1}{3}} [F(\ell / w) \Sigma]^{\frac{2}{3}} \quad (12b)$$

when σ_{\max} is small and the matrix crack is very large compared to the unbridged segment. This result is valid for any value of ℓ/w as long as the applied stress is sufficiently low so that small scale "yielding" prevails in the bridge next to the unbridged segment (Suo et al., 1993).

CALIBRATED FUNCTIONS

It is convenient to approximate the numerical results in Fig. 4 by a set of functions. These functions can then be used to compute results without recourse to the numerical methods used to generate the curves in the first place. Calibration functions of this type were pioneered by Cox and Lo (1992b) including those for finite geometries

with center notches as in this paper and for edge notches. The functions suggested here serve the same purpose as those of Cox and Lo (1992b) and are presented as possible alternatives. We state the following expression for $\Delta\kappa = \Delta K_{\text{tip}}/\Delta K_A$:

$$\Delta\kappa(\Delta\Sigma, \alpha) = \exp \{-\sin\alpha [A(\Delta\Sigma) + B(\Delta\Sigma)\alpha + C(\Delta\Sigma)\alpha^2]/\alpha^{1/4}\}$$

where $\alpha = (a - \ell)/a$ (13)

$$A(\Delta\Sigma) = -0.049 + 3.0 / \sqrt{\Delta\Sigma} - 0.027 / \Delta\Sigma$$

$$B(\Delta\Sigma) = -0.399 + 2.504 / \sqrt{\Delta\Sigma} - 3.207 / \Delta\Sigma + 0.379 / \Delta\Sigma^{3/2}$$

$$C(\Delta\Sigma) = 0.439 - 1.784 / \sqrt{\Delta\Sigma} + 1.374 / \Delta\Sigma - 0.04 / \Delta\Sigma^{3/2}$$

This approximation is accurate to within a few percent of the numerical results depicted in Fig. 4 for the range $0.1 \leq \Delta\Sigma \leq 12$. It is similarly close to the function devised by Cox and Lo (1992b) for the case of the finite crack in tension. In addition, it should be noted that the expression in eq. (13) is valid for the finite strip with ΔK_A given by eq. (11) as long as $a/w < 0.5$.

In a similar manner, a function can be fitted to the peak fiber stresses shown in Fig. 5. This function finds its utility in predictions of fiber failure. The function is

$$\eta = \phi(\Sigma) \exp \left[-\frac{(1-\alpha)^m}{\sqrt{\alpha} \psi(\Sigma)} \right] \quad (14a)$$

where $\alpha = (a - \ell)/a$ as before,

$$\phi(\Sigma) = \sqrt{\Sigma^2 + (6\pi \Sigma^2)^{2/3}} \quad (14b)$$

$$\psi(\Sigma) = 13.1 - 2.3 \Sigma + 0.2 \Sigma^2 \quad (14c)$$

$$m(\Sigma) = 14.037 - 15.327 \Sigma + 7.237 \Sigma^2 \\ - 1.5628 \Sigma^3 + 0.1274 \Sigma^4 \quad (14d)$$

and η and Σ are given by (10b) and (10c) respectively. When $\alpha = 1$, the form given in eq. (14a) represents the relationship for an infinite body split by a bridged matrix crack with a center unbridged notch. The form given in eq. (14b) has been deduced from an expression of Cui and Budiansky (1993) and is asymptotically exact both for small and large Σ . Cui and Budiansky (1993) have shown that this expression compares well with their numerical results for Σ ranging from 0.4 to extremely large values. The function in eq. (14a) has been plotted and compared with the numerical results in Fig. 5a. It can be seen that the agreement is good. No comparison has been made between (14a) and numerical results for values of α not equal to unity for values of Σ other than those shown in Fig. 5a. Thus the accuracy of (14a) outside the range shown in Fig. 5a (apart from $\alpha = 1$) is not known.

The form in eq. (14a) is valid for the infinite body only and forms cannot as yet be given for the finite strip. However, based on the work of Suo et al. (1993), in the case of the finite strip with the matrix crack extending across the entire width so that $a = w$, the form

$$\eta^2 = \Sigma^2 / (1 - \ell/w)^2 + [6\pi F^2(\ell/w) \Sigma^2]^{2/3} \quad (15)$$

can be stated with $F(\ell/w)$ given by (11b). The form in eq. (15) is an interpolation between results for small and large Σ in the manner of Suo et al. (1992) but using the findings of Cui and Budiansky (1993) to give accuracy for small ℓ/w . For cases where the matrix extends over only a fraction of the width of the finite strip, it is possible that

eq. (14a) can be used with $\phi(\Sigma)$ given by the right hand side of eq. (15), $(1-\alpha)$ replaced by $\ell(w-a)/a(w-\ell)$ but $\sqrt{\alpha}$ retained as it is. The resulting behavior takes η from zero in the absence of bridging to the known estimate for η when the matrix crack extends over the entire width of the finite strip. However, no attempt has been made to check whether this assertion is reasonable.

MATRIX FATIGUE CRACKING

The governing equation for matrix fatigue crack growth in fiber reinforced composite is assumed to be simply the Paris law (McMeeking and Evans, 1990)

$$da/dN = \beta (\Delta K_{tip}/\bar{E}_m)^n \quad (16)$$

where β and n are material parameters for the matrix material. An underlying assumption here is that the fatigue crack growth rate in the matrix is governed by the crack tip stress intensity amplitude, ΔK_{tip} , in accord with the Paris law for the matrix alloy alone. Therefore, the intact fibers contribute to the composite fatigue behavior only through ΔK_{tip} . In the calculation of ΔK_{tip} , the composite is taken to be homogeneous and orthotropic, and the crack front is assumed to be straight. In practice, however, only the matrix is fatigue cracked when fibers remain intact, and the crack front adopts a rather complex shape. As a consequence, the local stress intensity factor amplitude will not generally be equal to the calculated ΔK_{tip} values established through idealized bridging calculations. One approximate model for the effect is that the average stress intensity factor amplitude at the matrix crack front is equal to $\Delta K_{tip}/\sqrt{(1-f)\bar{E}/E_m}$ (Budiansky Amazigo and Evans, 1988), accounting for the reduced area of material being cracked as well as the elastic inhomogeneity. To permit incorporation of this effect into the model, the modulus \bar{E}_m has been used in eq. (16)

instead of E_m . Thus, the Budiansky et al., 1988 model would be accounted for by use of $\bar{E}_m = \sqrt{(1-f) \bar{E}/E_m}$. However, in this paper, \bar{E}_m will simply be assumed to be E_m and any effect of this assumption will be compensated for in the empirical choice of a value for τ .

The fatigue crack growth law of eq. (16) was integrated with ΔK_{tip} evaluated from the expression in eq. (13) with $\Delta K_A = \Delta \sigma \sqrt{\pi a}$ as for the infinite body. The calculation was carried out for exponents $n = 2$ and 4 and for 4 values of $\Delta \Sigma_0$ in each case where $\Delta \Sigma_0 = \Delta \Sigma a/a_0$. Note that $\Delta \Sigma_0$ remains constant if $\Delta \sigma$ is held fixed during fatigue. The results for non-failing fibers are shown in Fig. 7a and 7b. The plots show that for the load amplitudes assumed, the crack does not have to extend very far compared to the original notch length for the rate of crack extension to diminish dramatically.

The theoretical predictions of fatigue crack growth in Fig. 7 have two of the features exhibited in the experimental results, i.e., a transient region in which da/dN diminishes upon crack growth, and a seemingly steady-state region in which da/dN remains almost constant. The non-dimensional parameter $\Delta \Sigma_0$ that governs the prediction is a combination of the original notch size, material properties and the fixed applied load amplitudes. Fatigue crack growth curves for situations with a varying load amplitude $\Delta \sigma$ have not been presented because there are too many possibilities. However, they can be pieced together in a rather complicated manner from the curves for constant $\Delta \Sigma_0$. The appropriate procedure can be deduced from integration of eq. (16).

It has been observed experimentally that at high values of applied stress amplitude $\Delta \sigma$, the crack growth rate decreases first due to the fiber shielding, reaches a minimum value and then increases with further crack extension, as exemplified by the crack growth curve shown in Fig. 1 (Walls et al., 1991, 1993). The acceleration in crack growth rate has been attributed to the occurrence of fiber failure, as suggested by the

direct observations of fiber bridging and fiber fracture along the length of the matrix crack (Walls et al., 1991, 1993).

In practice, there is a statistical characteristic to the fiber failure process. However, to incorporate the effects of fiber breaking into the fatigue crack growth model just developed, a deterministic approach is adopted. The fibers are assumed to have a unique strength S , such that they fail in the plane of the matrix crack when the stress on them there reaches S . Both the bridging law eq. (3) and the Paris law eq. (16) remain valid. The frictional pull-out effect of broken fibers on ΔK_{tip} is neglected since the deterministic fiber strength implies that fibers break at the matrix crack rather than inside the material. Once the fibers begin to fail, the unbridged notch length is continuously adjusted in the calculation to maintain a fiber stress at the unbridged notch tip equal to the fiber strength. The conditions giving rise to this have been presented and discussed already in connection with Fig. 5.

Of interest, however, is the relationship between the current unbridged segment length 2ℓ and the original notch length $2a_0$ for a given fatigue problem. For simplicity, attention will be confined to cases where $\Delta\sigma$ is fixed during fatigue. The function in eq. (14) can be used to predict ℓ vs. a_0 during fatiguing for given fiber strength. A particular result is shown in Fig. 8 for crack growth in an infinite body. The dashed line on the diagonal specifies $\ell = a_0$ and so depicts the relationship prior to first fiber failure. At the beginning of fatiguing, $a = a_0$ so the top right of Fig. 8 is the starting point for the process. As the fatigue crack grows at first without fiber failure, the state of the specimen will move down the dashed line on the diagonal towards the bottom as indicated by the arrow. The state departs from the dashed line when fibers begin to fail. The point of departure for several ratios of maximum applied stress to volume fraction reduced fiber strength are marked on Fig. 8. Thereafter, as the fatigue crack grows, the state of the specimen follows the relevant full line towards the top left of the diagram as

indicated by the arrow. Each full line in Fig. 8 represents the relationship for the fixed ratio of σ_{\max}/fS noted at the intersection of that full line with the diagonal dashed line.

If the fibers are weak or the maximum applied stress is high, the fibers break close to the matrix crack tip (a_0/a is close to unity) and the bridging zone is always a small fraction of the crack length (ℓ/a remains close to unity as the crack grows). This means that fibers will continuously fail close to the matrix crack tip as the matrix crack grows. In this case there will not be much shielding and the fatigue crack growth rate will be similar to what would be expected in an unreinforced matrix. If the fibers are moderately strong or the maximum applied stress is moderately high, the fibers remain intact at first and a sizable bridging zone can develop. However when the first fiber fails, say when $a_0/a = 0.5$, subsequent fiber failure occurs fairly rapidly as the crack grows. The unbridged crack length increases faster than the matrix crack length. In that case the value of ΔK_{tip} will increase quite rapidly as the matrix crack grows after the first fiber fails. That means that the matrix crack growth rate will accelerate significantly after first fiber failure. When the fibers are strong or the maximum applied stress is modest, first fiber failure is delayed. However, after it occurs, say when $a_0/a = 0.1$, many fibers fail essentially simultaneously and the unbridged length increases very rapidly. This causes ΔK_{tip} to jump to a higher value with a corresponding sudden increase in the crack growth rate. As noted previously, when the fiber strength is higher than a threshold value, they will never break and the fatigue crack growth rate will persist at the low level associated with extensively bridged cracks. The annotation on Fig. 8 makes it clear that the sensitivity to fiber strength is quite marked, with the different types of behavior outlined in the last few sentences occurs over a very narrow range of fiber strengths, or equivalently over a very narrow range of maximum applied stress.

Plotted in Fig. 9 are the fatigue crack growth curves predicted from the Paris law eq. (18) for infinitely large specimens taking fiber fracture into account. Without fibers

breaking, the fatigue crack growth curves are the same as those in Fig. 7. In the presence of fiber fracture three matrix fatigue crack growth curves are presented corresponding to three different fiber failure strengths. If fibers are relatively weak, fiber failure occurs early on, and a gradual transition is predicted. For stronger fibers, however, the transition occurs later but becomes more abrupt as can be seen in Fig. 9. This sudden increase of crack growth rate is due to the sudden lengthening of the unbridged zone after first failure of stronger fibers as depicted in Fig. 8. Once the fiber failure process starts for strong fibers, it tends to continue rapidly until most of the fibers fail in the bridging zone that has been previously built up. As a consequence the crack growth rate increases suddenly and is comparable to the fatigue crack growth rate in the unreinforced matrix. This has been observed in experiments (Walls et al., 1991, 1993).

FIBER FAILURE

The rapid growth of fatigue cracks after fibers have commenced failing, as depicted in Fig. 9, suggests that an important strategy for design and use of fiber reinforced metal components will be the avoidance of fiber failure. Once fibers begin to fail after significant crack growth, they will quickly break along the fatigue crack. In addition, further crack growth will be accompanied by more fiber failure. As a consequence, the benefits of fiber reinforcement will be partially lost and if there are many matrix fatigue cracks, fiber reinforcement may be significantly impaired. Therefore, it can be suggested that the end of useful life of the composite material can be considered to be the onset of fiber failure. It should be noted that fracture of the composite material after fatigue crack growth will depend on a combination of the matrix toughness and the fiber strength. This has been studied by Cui and Budiansky (1993). However for high toughness matrices such as titanium alloys, fracture of the

composite material after matrix fatigue and fiber failure will depend primarily on matrix toughness. A very approximate estimate for residual composite strength after fiber failure is therefore $K_{IC}/\sqrt{\pi a}$ where K_{IC} is the fracture toughness of the matrix alloy. A more exact assessment of residual strength can be carried out using the more accurate models of Cui and Budiansky (1993). However, an important point is that fiber failure is a necessary precursor before the residual strength of the composite material becomes a relevant consideration. Therefore, the life up to fiber failure is an important determinant and the time between first fiber failure and composite fracture is likely to be relatively short.

As noted previously, if the maximum applied stress is low enough, fibers will never fail during matrix fatigue crack growth. It is useful to investigate the circumstances which will ensure that fibers will remain intact throughout crack growth. As implemented by Walls et al. (1993), this can be done by plotting the ratio of the maximum applied stress to the fiber strength against the intercepts of the curves in Fig. 5a with $\alpha = 1$ (where $\ell/a \rightarrow 0$). The result, shown in Fig. 10, is a map determining when fibers will fail and when they do not. The numerical results have been shown for the infinite body in which case $a_0/w = 0$. Below the line in the diagram, no fiber failure will occur no matter how much matrix fatigue crack growth occurs. However, if a component is highly stressed so that it operates above the line in the diagram, eventually fiber failure will occur during matrix fatigue crack growth. Walls et al. (1993) have found this diagram to be effective in distinguishing the incidence of fiber failure from nonfailure in experiments.

For comparison with the numerical results, a relationship derived from eq. (15) has been plotted in Fig. 10. This is

$$\left[\frac{(1 - a_0/w) f S}{\sigma_{\max}} \right]^{\frac{4}{3}} - \left[\frac{\sigma_{\max}}{(1 - a_0/w) f S} \right]^{\frac{2}{3}} = \left[\left(1 - \frac{a_0}{w} \right)^2 F^2 \left(\frac{a_0}{w} \right) \frac{6\pi}{\eta} \right]^{\frac{2}{3}} \quad (17)$$

where η is given by eq. (10b) and $F^2(a_0/w) = \sec(\pi a_0/2w)$. It can be seen that the prediction agrees well with the numerical results. Furthermore, the form of eq. (17) indicates that the map can be generalized to the finite strip without significant alteration. In view of this, the map in Fig. 10 has been presented in a form allowing for the notch to width ratio of a finite strip.

The map in Fig. 10 can be adapted to show the extent to which crack growth can occur in an infinite body prior to fiber failure. If the loading of a very large component is such that according to Fig. 10 fiber failure will eventually occur, the matrix crack will reach the length $2a_f$ and then fibers will commence failing. The ratio of this length to the original notch length is shown in Fig. 11 for various levels of loading and original notch length taking fiber strength and volume fraction into account. For a given notch length, the contours in Fig. 11 indicate the permissible maximum stress for a given extension of the matrix crack. For example, the contour marked $a_f/a_0 = 2$ shows the relationship between maximum applied stress and notch length which will produce exactly a doubling of the flaw length before fiber failure will begin to occur. Similarly the contour for $a_f/a_0 = 20$ shows the maximum stress which will exactly cause the matrix crack to reach 20 times the length of the initial notch before fiber breakage. The line with $a_f/a_0 = \infty$ is the boundary between fiber nonfailure and failure from Fig. 10 and for a maximum stress lying on or below this contour, the matrix crack can extend to infinity without fiber failure. The plots in Fig. 7 can be used to predict how many cycles of constant load amplitude will occur before the matrix crack reaches the extent at which fiber failure will commence. Thus, for large components, Figs. 7 and 11 can be combined to provide a basis for life estimation up to fiber failure for values of $\Delta\Sigma_0$ ranging from 1 to 8.

CONCLUDING REMARKS

A model has been presented for matrix fatigue crack growth emanating from a finite notch. Predictions have been presented for the relationship between the matrix crack length and the number of load cycles of a given amplitude. In addition, the matrix crack length when fibers will begin to fail has been identified in terms of fiber strength, maximum applied stress and initial notch length. These predictions have been compared to experimental data for fatiguing of titanium/SiC fibrous composites and the model has been shown to work well (Walls et al., 1993). As mentioned in the introduction, the comparison between the model and the data has been based on a number of empirical steps. Over and above the use of empirical values for fiber and matrix elastic moduli, fiber volume fraction, fiber diameter and monolithic matrix fatigue crack growth rates, a single value for the interface shear stress τ is determined to ensure that the steady state fatigue crack growth rate in one experiment is accurately predicted. The transient prior to steady state matrix fatigue crack growth is then predicted accurately without any further empiricism. Furthermore, it is then found that when no fiber failure occurs, the model with the same value of τ can predict the results of other experiments carried out at different load amplitudes and with different notch lengths.

Fiber failure is treated in a similar way. A value of fiber strength S is determined that will cause the model to accurately predict the onset of fiber breakage in one experiment. Without further empiricism, the model then accurately predicts the rate of matrix fatigue crack growth after the initiation of fiber breakage in that experiment. In addition, without alteration to parametric values, the model accurately predicts the onset of fiber failure when different initial notch lengths and maximum applied stress magnitudes are used in the experiments. The value of τ used in the comparison of the model with experimental data is consistent with in situ measurements by push out of fibers (Warren et al., 1991) after fatigue cycling of the specimen. In addition, the fiber

strength used in the model is in good agreement with the strength of fibers tested after being removed from the composite by dissolution of the matrix. This strength is less than that for pristine fibers and the reduced value is thought to be due to processing of the composite material.

ACKNOWLEDGMENT

This work was supported in part by DARPA through the University Research Initiative at UCSB (ONR Prime Contracts N00014-86-K0753 and N-00014-93-1-0224). The work of GB was in addition supported by NSF through a Research Initiation Award MSS-9210250. Provision of the ABAQUS Finite Element Code by Hibbitt, Karlsson and Sorensen Inc. through an Academic User's License is gratefully acknowledged.

REFERENCES

- Aveston, J., Cooper, G.A. and Kelly, A., 1967, in The Properties of Fiber Composites, IPC Science and Technology Press, p. 15.
- Bao, G., Ho, S., Suo, Z. and Fan, B., 1992, *Int. J. Solids Struct.*, **29**, 1105.
- Budiansky, B., Amazigo, J. and Evans, A.G., 1988, *J. Mech. Phys. Solids*, **36**, 167.
- Cox, B.N., 1990, *Acta metall. mater.*, **38**, 2411.
- Cox, B.N. and Lo, C., 1992a, *Acta metall. mater.*, **40**, 69.
- Cox, B.N. and Lo, C., 1992b, *ibid.*, to appear.
- Cox, B.N. and Marshall, D.B., 1991, *Fatigue Fract. Engng. Mater. Struct.*, **14**, 847.
- Cui, L. and Budiansky, B., 1993, to be published.
- Evans, A.G., 1991, *Mater. Sci. Engng.*, **A143**, 63.
- Hibbitt, H.D., Karlsson, B.I. and Sorensen, E.P., 1990, *ABAQUS User's Manual Version 4.8*, Hibbitt, Karlsson and Sorensen, Inc., Providence, RI.
- Hutchinson, J.W. and Jensen, H.K., 1990, *Mech. of Materials*, **9**, 139.

- Jansson, S., Deve, H. and Evans, A.G., 1990, *Metall. Trans.*, **22A**, 2975.
- Kantzos, P., Telesman, J. and Ghosn, L., 1989, NASA TM-103095.
- Marshall, D.B. and Cox, B.N., 1987, *Acta Metall.*, **35**, 2607.
- Marshall, D.B., Cox, B.N. and Evans, A.G., 1985, *Acta Metall.*, **33**, 2013.
- Marshall, D.B. and Oliver, W.C., 1987, *J. Amer. Ceram. Soc.*, **70**, 542.
- McCartney, L.N., 1987, *Proc. Roy Soc. Lond.*, **A409**, 329.
- McMeeking, R.M. and Evans, A.G., 1990, *Mech. of Materials*, **9**, 217.
- Naik, R.A. and Johnson, W.S., 1991, Third Symposium on Composite Materials: Fatigue and Fracture, ASTM STP 1110 (edited by T.K. O'Brien), p. 753, American Society for Testing and Materials.
- Rice, J.R., 1968, *J. App. Mech.*, **35**, 379.
- Sensmeier, M.D. and Wright, P.K., 1990, in "Fundamental Relationships between Microstructure and Mechanical Properties of Metal Matrix Composites", (edited by P.K. Liaw and M.N. Gungor), p. 441, The Minerals Metals and Materials Society.
- Sih, G.C., Paris, P.C. and Irwin, G.R., 1965, *Int. J. Frac. Mech.*, **1**, 189.
- Suo, Z., Ho, S. and Gong, X., 1993, *Trans. ASME, Series H (J. Eng. Mat. Tech.)* to appear.
- Tada, H., Paris, P.C. and Irwin, G.R., 1985, The Stress Analysis of Cracks Handbook, Del Research, St. Louis.
- Thouless, M.D. and Evans, A.G., 1988, *Acta Metall.*, **36**, 517.
- Walls, D., Bao, G. and Zok, F., 1991, *Scripta Metall. Mater.*, **25**, 911.
- Walls, D., Bao, G. and Zok, F., 1993, to appear.
- Warren, P., Mackin, T. and Evans, A.G., 1991, *Acta Metall. Mater.*, **40**, 1243.

APPENDIX

GOVERNING EQUATIONS

The equation governing the stress distribution along a bridged matrix crack subject to a monotonic applied stress σ_{\max} and the bridging law eq. (1) is (Marshall and Cox, 1987)

$$\bar{\Sigma}_s^2(\bar{x})/16 + \int_{1-\alpha}^1 \bar{\Sigma}_s(\bar{x}) H(t, \bar{x}) dt = \bar{\Sigma} \sqrt{1-\bar{x}^2} \quad (\text{A1})$$

where

$$\bar{\Sigma}_s = 4 \lambda \bar{E} \sigma_s / a \quad (\text{A2})$$

and σ_s is the stress transmitted through the matrix crack by the fibers defined as a traction on the crack area. Thus σ_s is equal to the actual stress in the fibers at the matrix crack multiplied by the volume fraction of fibers. In addition, λ is given by eq. (2),

$$1 - \alpha = \ell / a \quad (\text{A3})$$

2ℓ is the length of the unbridged segment, $2a$ is the length of the matrix crack, $\bar{x} = x/a$ where x is the distance from the center of the notch,

$$H(t, \bar{x}) = \frac{1}{\pi} \log \left| \frac{\sqrt{1-\bar{x}^2} + \sqrt{1-t^2}}{\sqrt{1-\bar{x}^2} - \sqrt{1-t^2}} \right| \quad (\text{A4})$$

$$\bar{\Sigma} = 4 \lambda \bar{E} \sigma_{\max} / a = \Sigma \ell / a \quad (\text{A5})$$

with Σ given by eq. (10c) and \bar{E} is an effective elastic modulus taking the material orthotropy into account.

Consider a plane strain, center crack running in the x-direction in an infinite, orthotropic body. Results from Sih, Paris and Irwin (1965) for cracks in orthotropic bodies can be used to provide solutions for the point force on a crack surface and therefore for fully and partially bridged cracks. This justifies the use of \bar{E} in (A1). For example, when the coordinates x and y coincide with the principal axes 1 and 2 of the orthotropic material, the crack opening displacement δ_A due to the remote applied tension σ is (Bao et al., 1992)

$$\delta_A = \frac{4\sigma}{E'_2} \left[\frac{E'_2}{E'_1} \right]^{\frac{1}{4}} \sqrt{a^2 - x^2} \quad (A6)$$

provided that

$$\rho = \frac{\sqrt{E'_1 E'_2}}{2G_{12}} - (v'_{12} v'_{21})^{\frac{1}{2}} = 1 \quad (A7)$$

Consequently, the effective Young's modulus \bar{E} is given by

$$\bar{E} = E'_2 [E'_1 / E'_2]^{\frac{1}{4}} \quad (A8)$$

where

$$\begin{aligned} E'_1 &= E_1 / (1 - v_{13} v_{31}) \\ E'_2 &= E_2 / (1 - v_{23} v_{32}) \\ v'_{12} &= (v_{12} + v_{13} v_{32}) / (1 - v_{13} v_{31}) \\ v'_{21} &= (v_{21} + v_{23} v_{31}) / (1 - v_{23} v_{32}). \end{aligned} \quad (A9)$$

In the cases where ρ is close to 1, \bar{E} can be approximated by

$$\bar{E} = \left(\frac{1+\rho}{2} \right)^{\frac{1}{2}} E_2' [E_1' / E_2']^{\frac{1}{4}} \quad (\text{A10})$$

For more general situations Cui and Budiansky (1993) have provided numerical values for orthotropy factors A which can be used to determine \bar{E} . The relationship between \bar{E} and A is

$$\bar{E} = \frac{A E}{1 - \nu^2} \quad (\text{A11})$$

in which ν is the Poisson's ratio of fiber and matrix which are assumed to be the same. The orthotropic modulus \bar{E} can be used to determine the opening of the crack due to the applied load and for the effect of fibers on the crack opening (Cui and Budiansky, 1993).

For a bridged matrix crack subject to load cycling such that the amplitude of the applied load is $\Delta\sigma$ the bridging behavior is given by eq. (3) and the governing is (Marshall and Cox, 1987; McMeeking and Evans, 1990)

$$\Delta\Sigma_s^2(\bar{x})/16 + \int_{1-\alpha}^1 \Delta\Sigma_s(t) H(t, \bar{x}) dt = \Delta\Sigma \sqrt{1 - \bar{x}^2} \quad (\text{A12})$$

where $\Delta\Sigma$ is given by eq. (4) and

$$\Delta\Sigma_s = 2 \lambda \bar{E} \Delta\sigma_s / a \quad (\text{A13})$$

and $\Delta\sigma_s$ is the amplitude of the stress cycle at the matrix crack surface. Note that as shown by McMeeking and Evans (1990) $\bar{\Sigma}_s$ and $\Delta\Sigma_s$ obey exactly the same equation so that results for them can be interchanged.

The equations were solved by standard methods discussed by Marshall and Cox (1987).

FIGURE CAPTIONS

- Fig. 1 A typical fatigue crack growth curve for a Ti/SiC composite. The length Δa of the matrix fatigue crack beyond the original notch is plotted against N the number of load cycles. The actual dimensions of the specimen are shown in the insert.
- Fig. 2 Schematic of a center crack in an infinite body under remote tension, with bridging fibers in the matrix crack wake.
- Fig. 3 Distributions of the non-dimensional bridging stress for different unbridged lengths for $\Delta\Sigma = 1$.
- Fig. 4 Non-dimensional stress intensity ranges versus normalized crack extension for different applied stress amplitudes.
- Fig. 5 Plots giving the relationship among the length of the crack, a , the unbridged segment ℓ , the maximum stress in the fibers S and the maximum applied load σ_{\max} .
- Fig. 6 Full lines show the normalized stress intensity ranges versus normalized crack extension for a finite width specimen computed by finite elements. The dashed lines show the results for an infinite body computed by solution of the integral equation.
- Fig. 7 Predicted fatigue crack growth curves when fibers do not fail. The normalized crack extension is plotted versus the normalized number of load cycles. (a) Paris law exponent $n = 2$; (b) Paris law exponent $n = 4$.
- Fig. 8 Fiber breaking rate related to fiber strength, applied load and matrix crack growth rate; 2ℓ is the length of the current unbridged segment of the crack, whereas $2a_0$ is the length of the original unbridged notch.
- Fig. 9 Predicted fatigue crack growth curves in the presence of fiber failure for $n = 2$ and different values of $\Delta\Sigma_0$.

- Fig. 10 Map for fiber failure and non-failure in a finite strip with a central notch in which a matrix crack can grow by fatigue.
- Fig. 11 Relationship between applied stress, fiber strength and notch length for a specified extension of the matrix crack before fiber failure will occur.

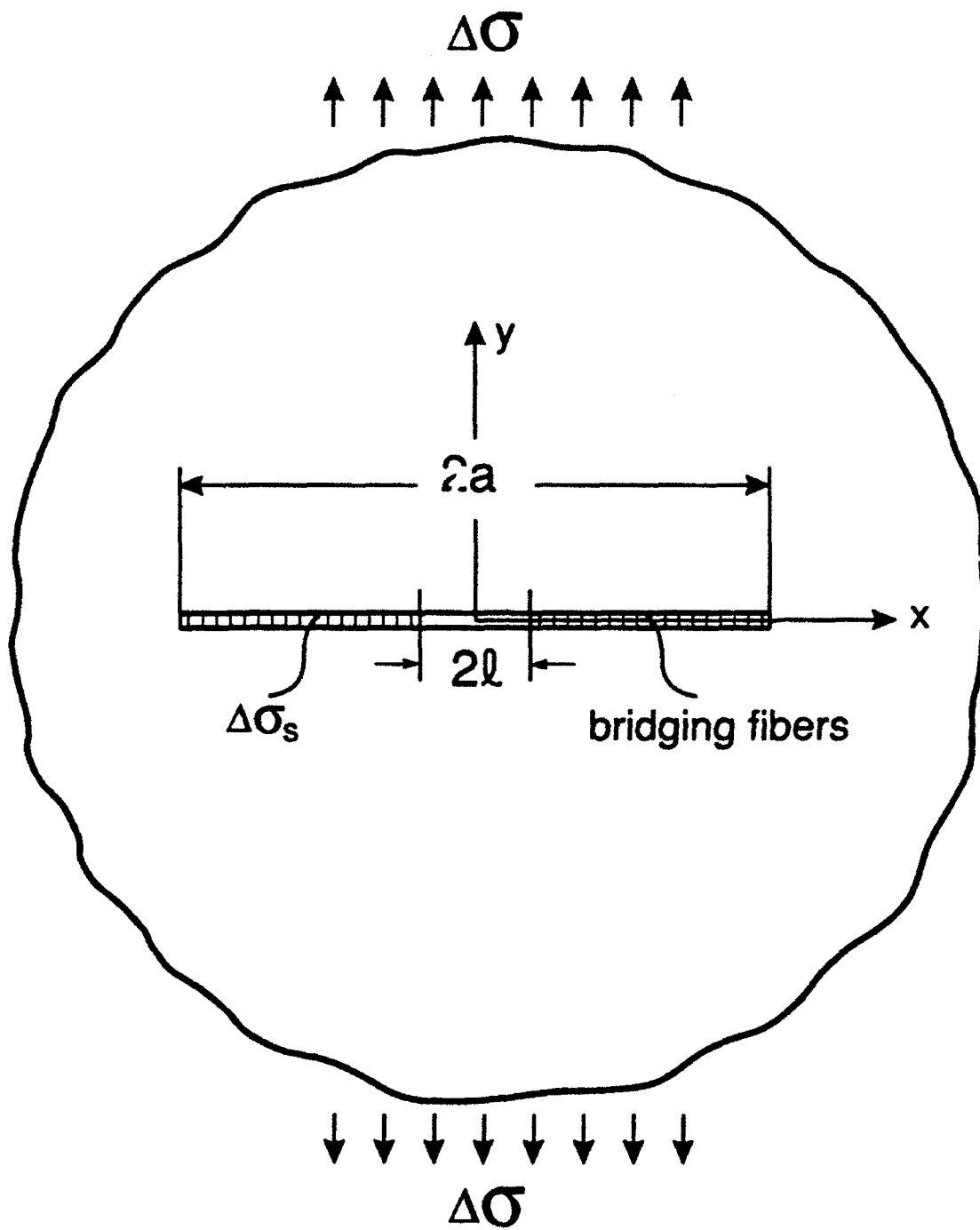


Fig. 2

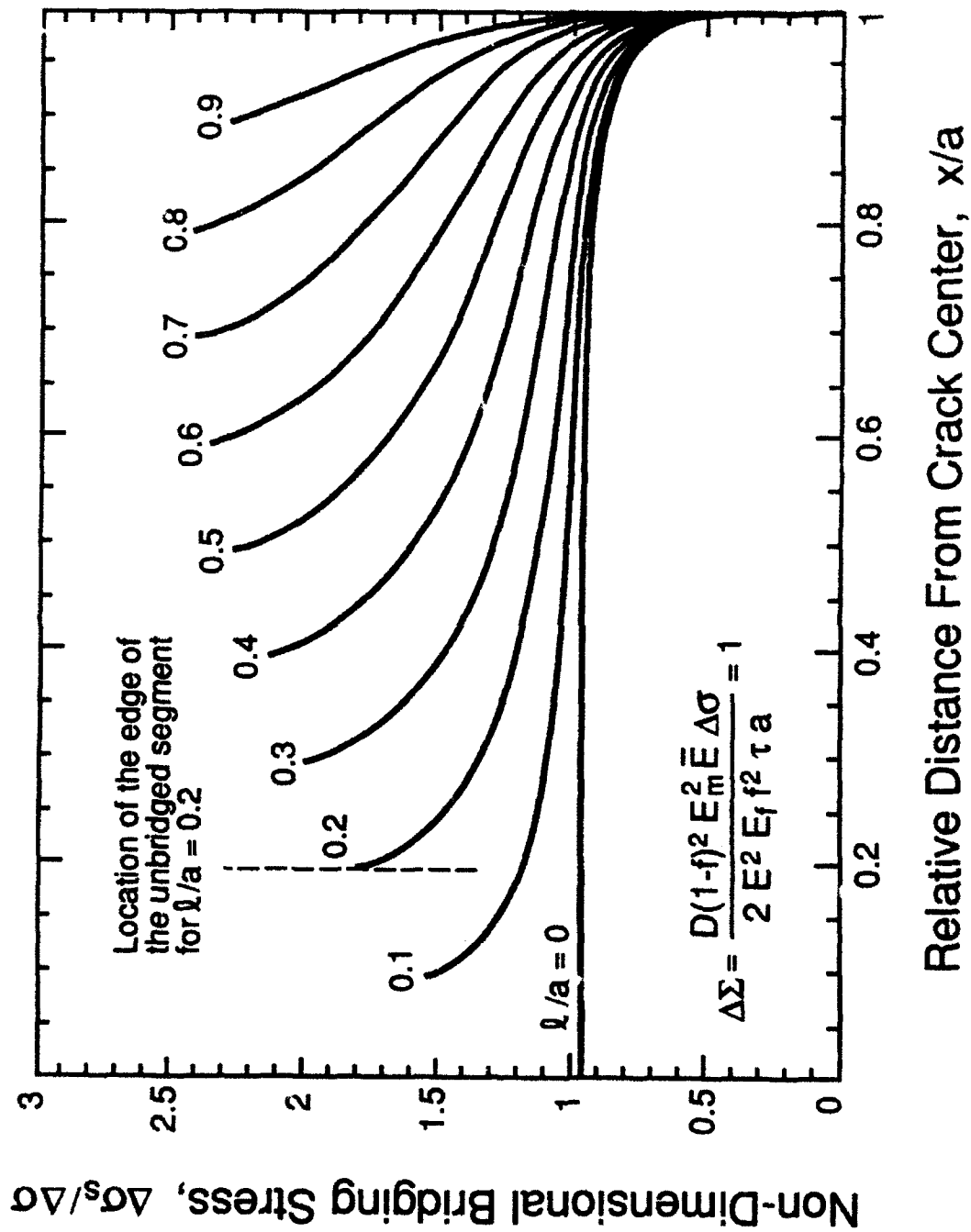


Fig. 3

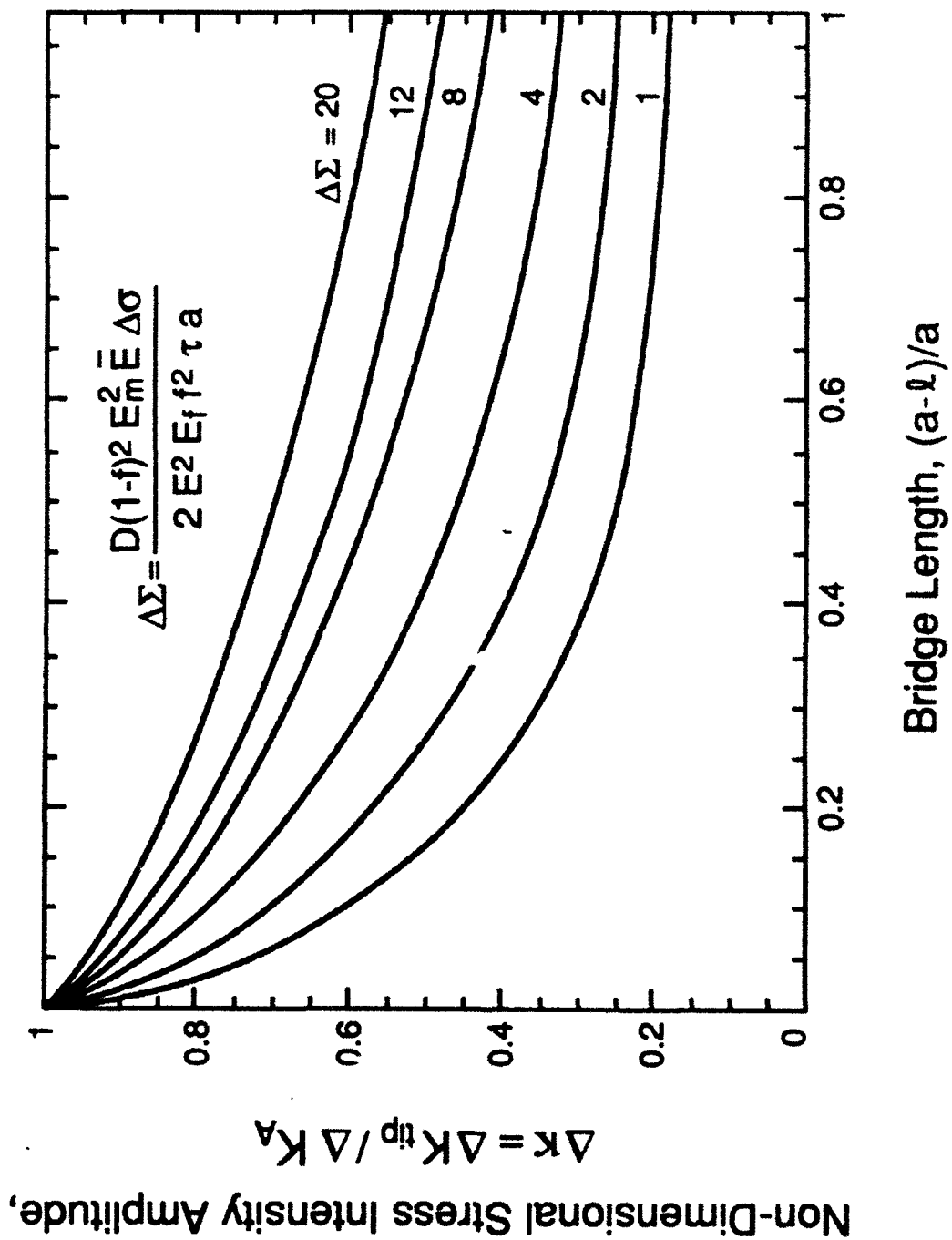


Fig. 4

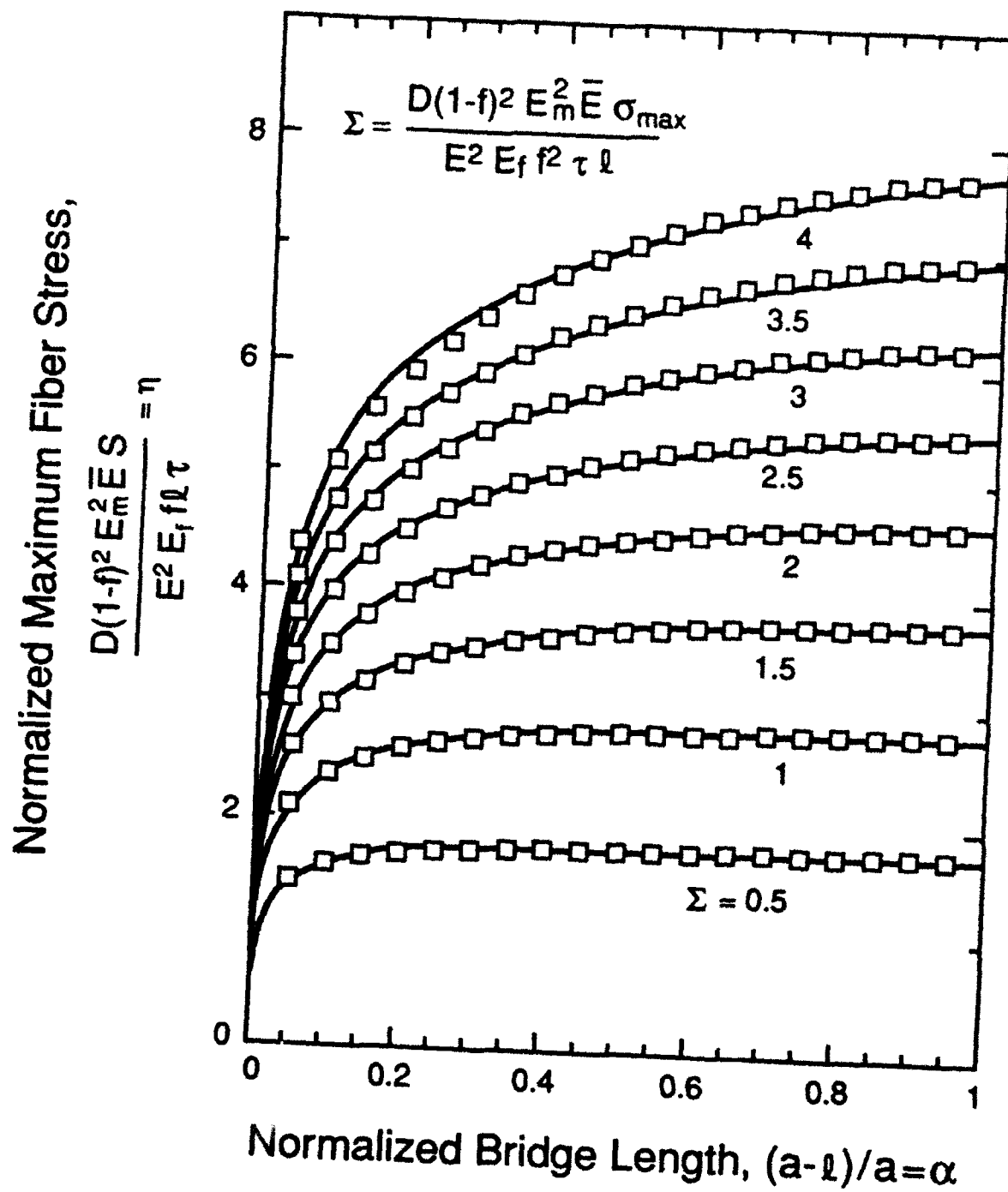


Fig. 5a

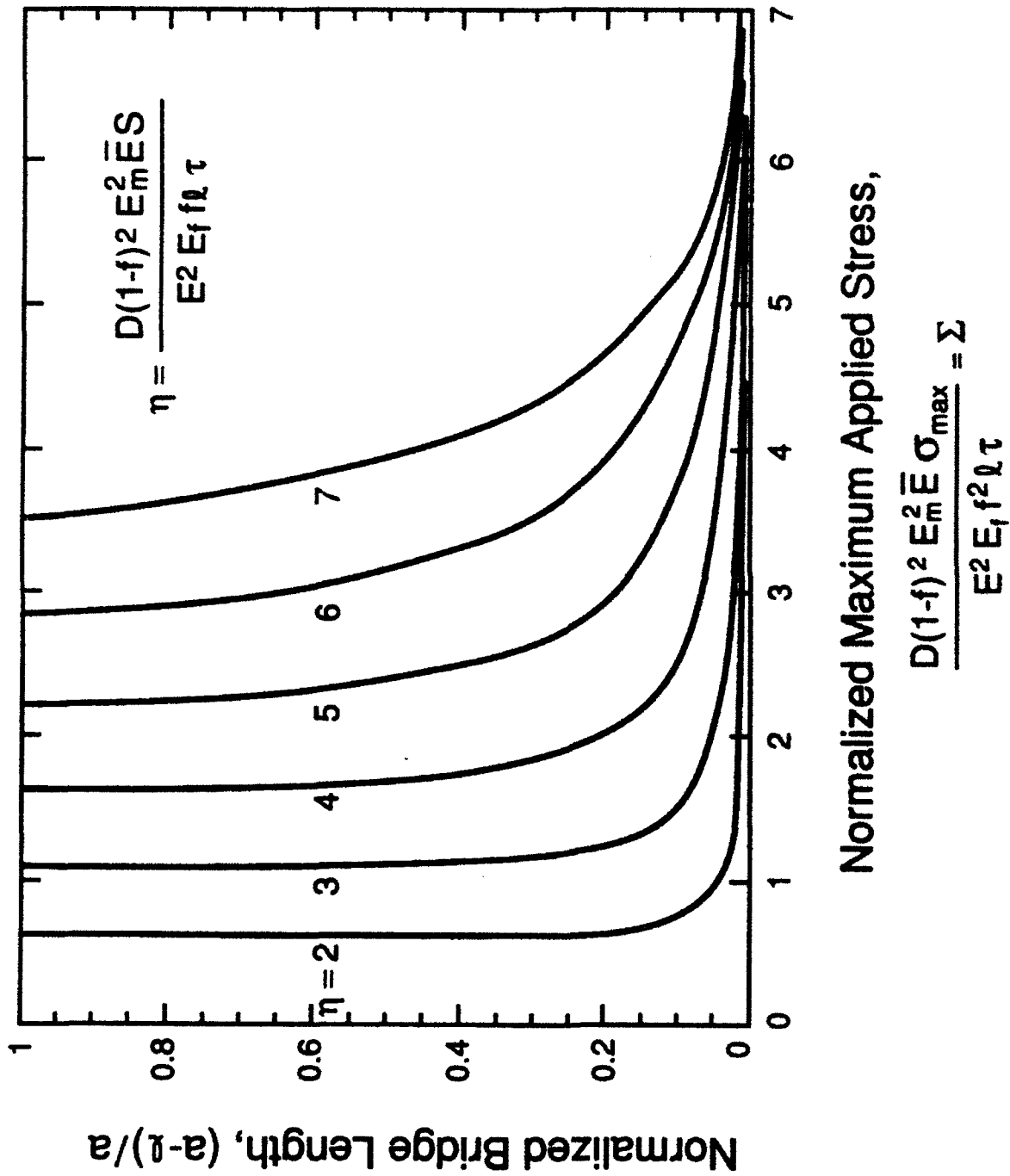


Fig. 5b

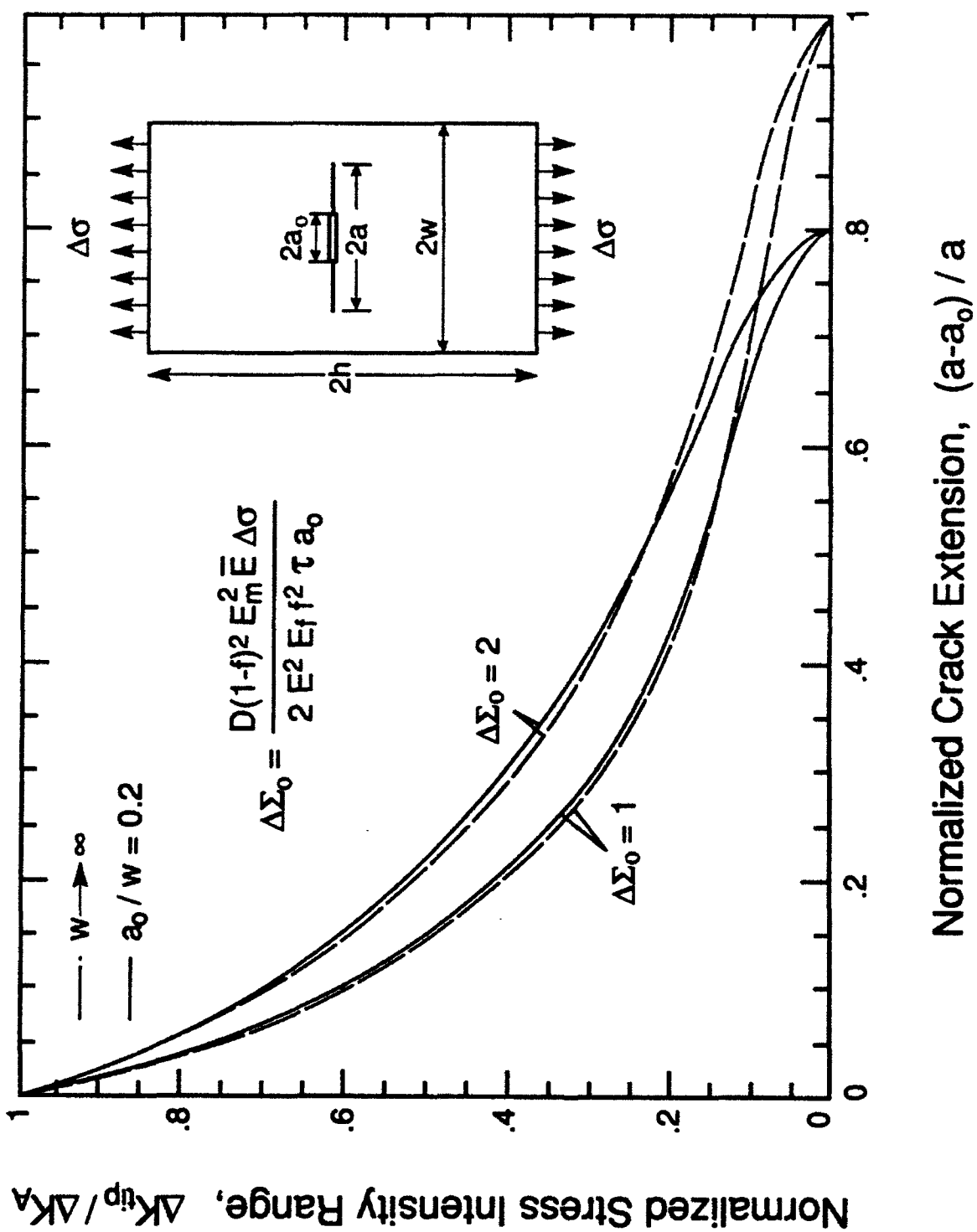


Fig. 6

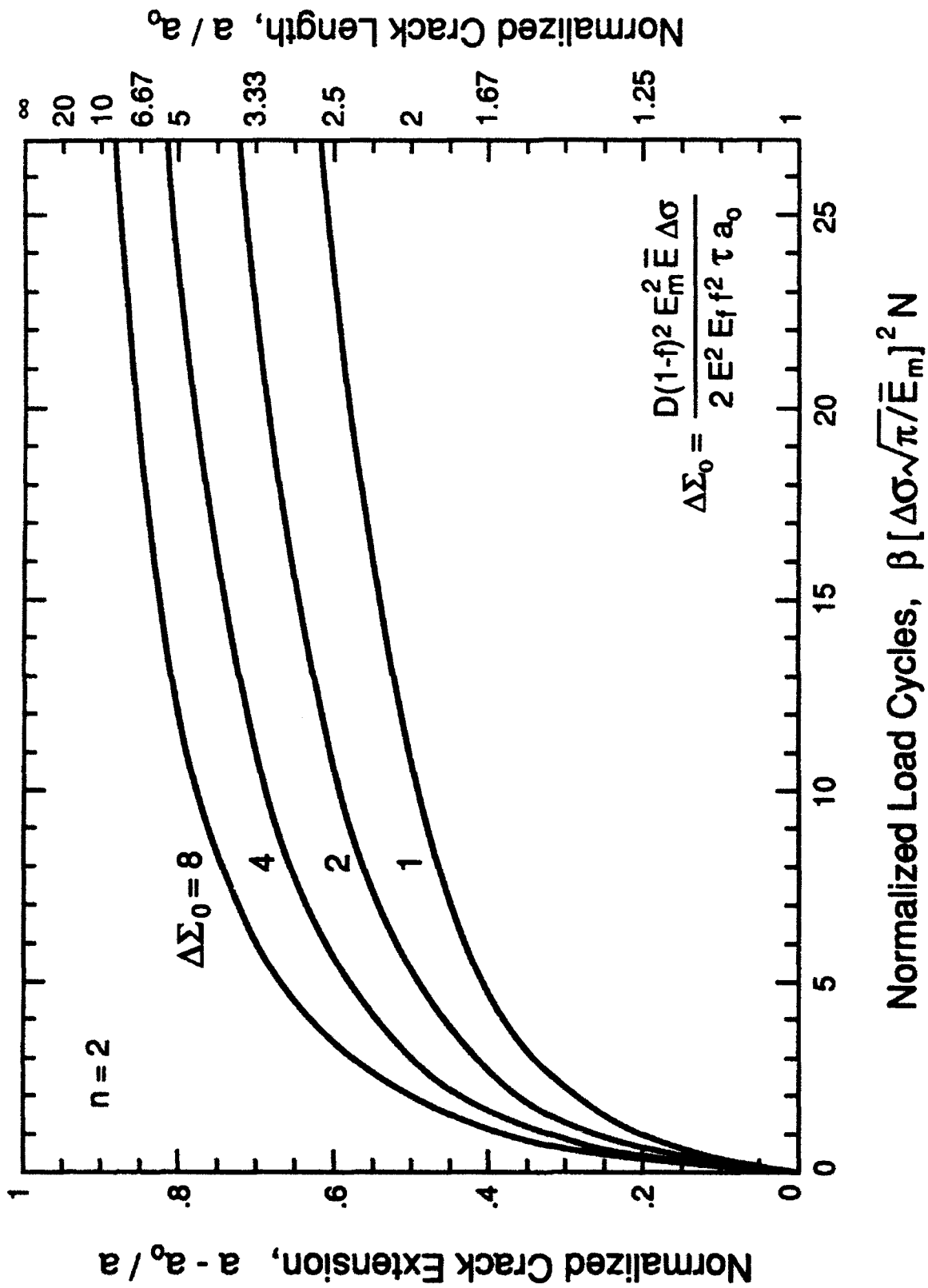


Fig. 7a

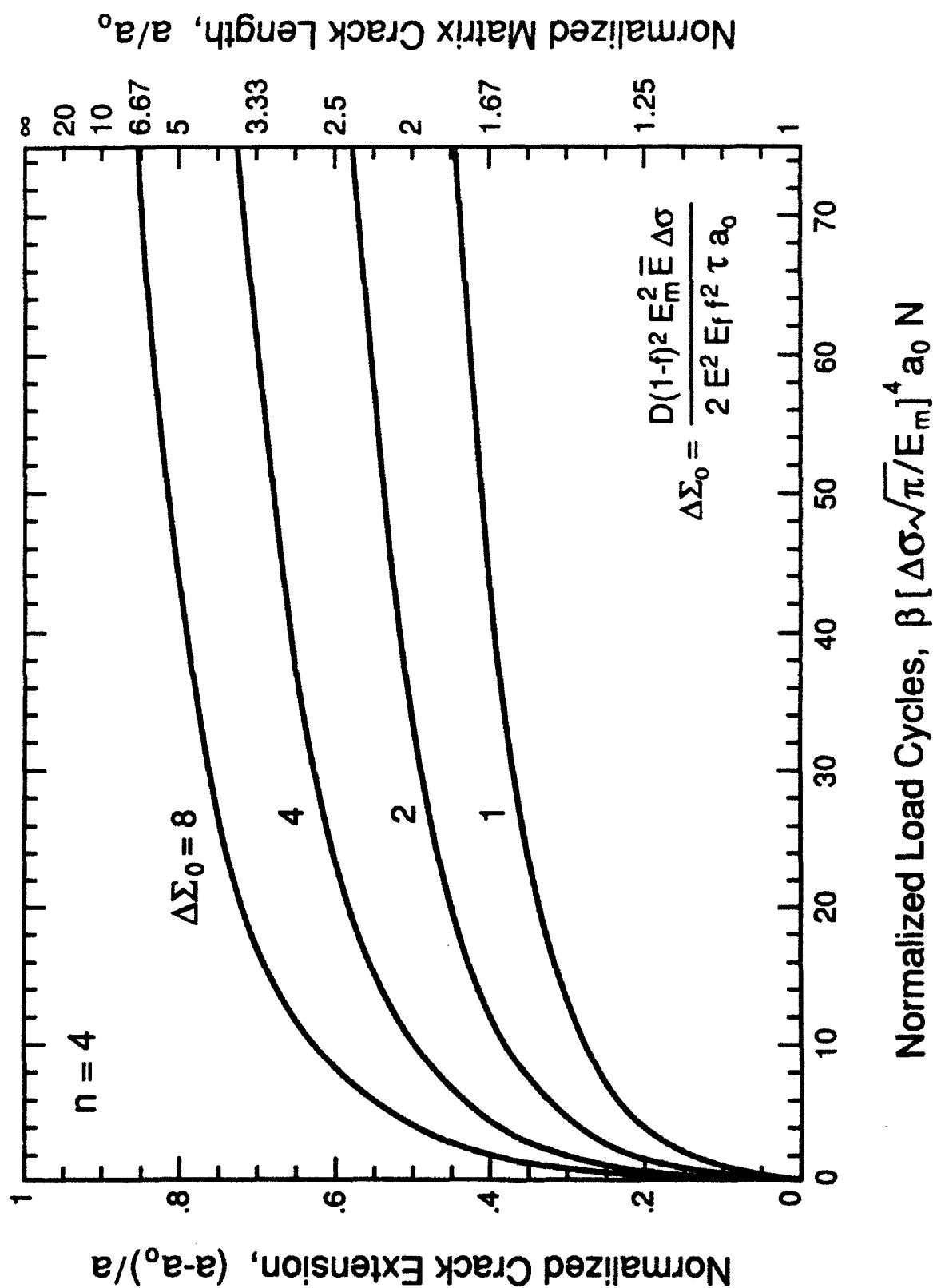


Fig. 7b

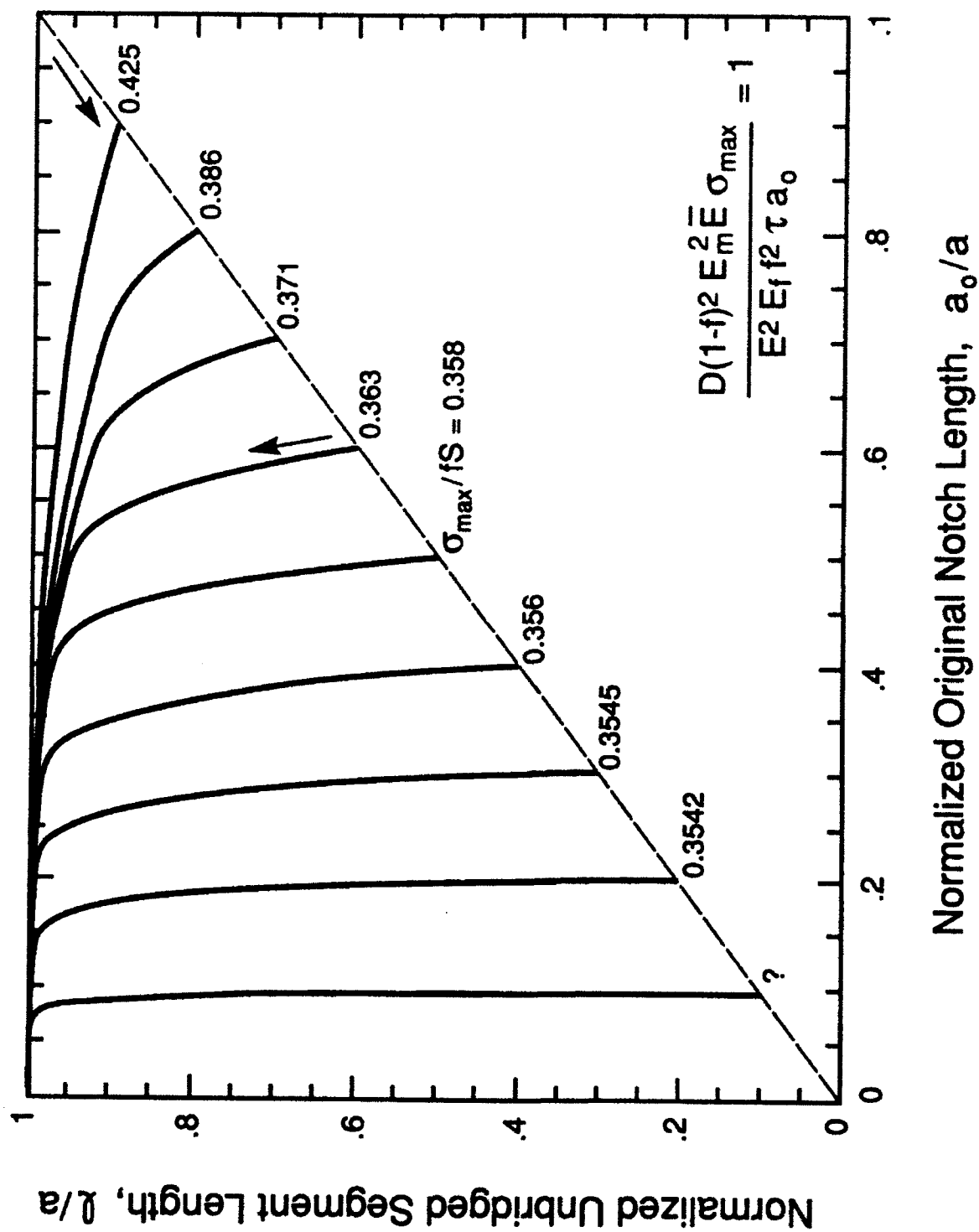


Fig. 8

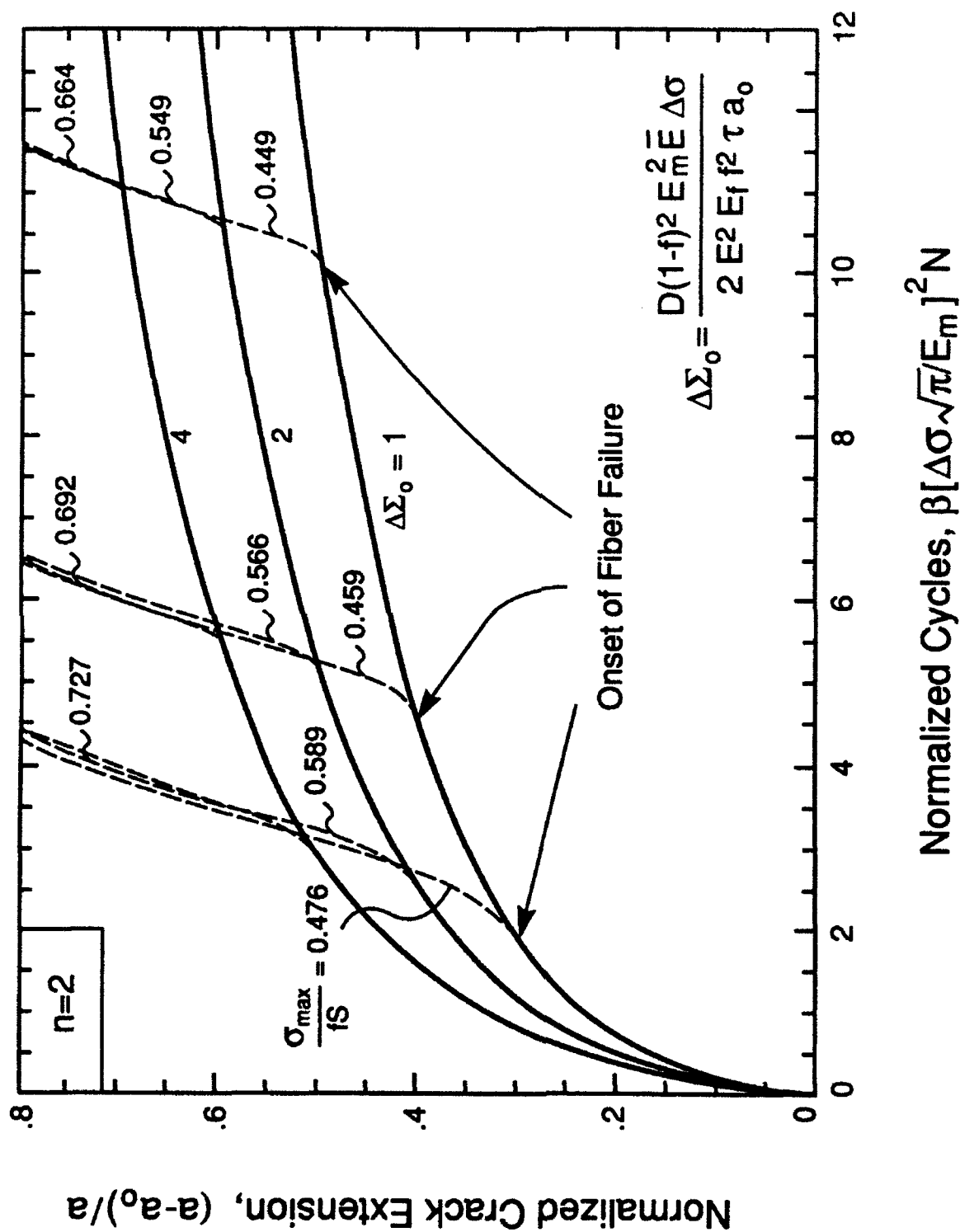


Fig. 9

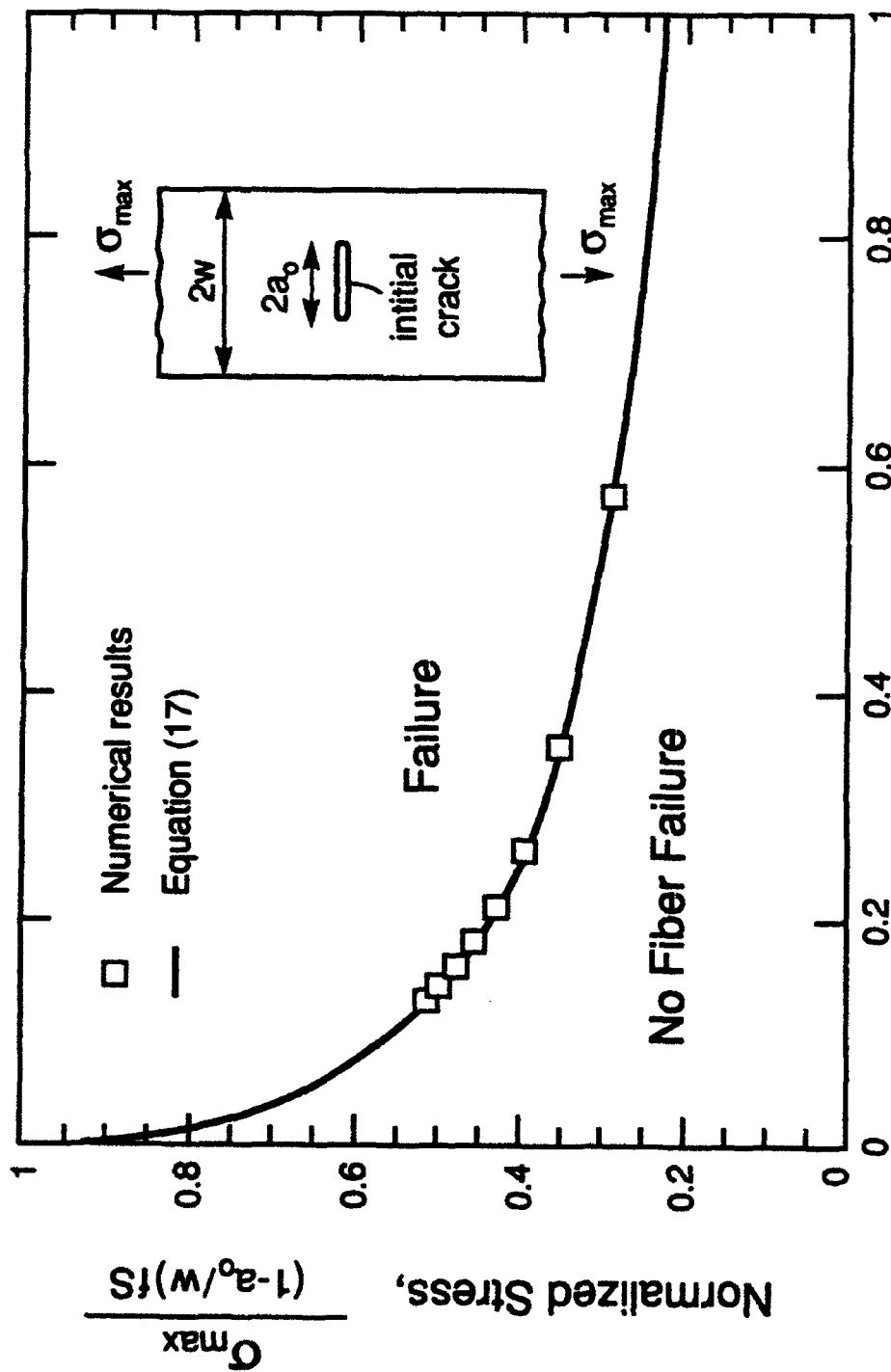


Fig. 10

Normalized Notch Length, $\frac{fE_f E^2 a_0 \tau}{D(1-f)^2 E_m^2 \bar{E} S} \left(1 - \frac{a_0}{w}\right)^2 \sec\left(\frac{\pi a_0}{2w}\right)$

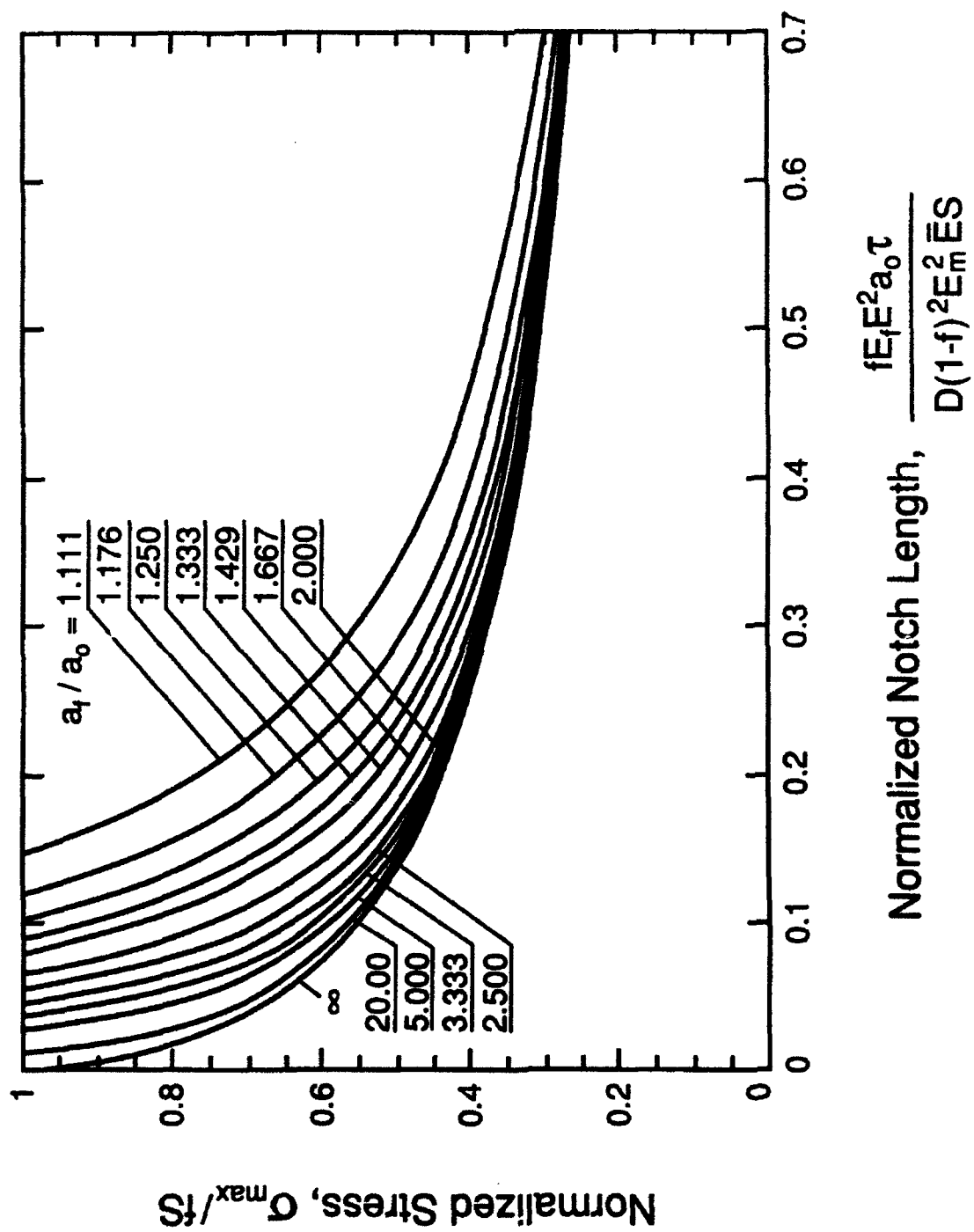


Fig. 11

The Anisotropic Mechanical Properties of a Ti Matrix Composite Reinforced with SiC Fibers

S. JANSSON, H.E. DÈVE, and A.G. EVANS

The anisotropic mechanical properties of a Ti alloy composite reinforced with SiC fibers have been investigated and rationalized using analytical models. The appropriate material model for this composite involves the following features: an interface that debonds and slides, a flaw insensitive ductile matrix, and high-strength elastic fibers subject to residual compressive stress caused by thermal expansion mismatch. This model is broadly consistent with the longitudinal, transverse, and shear properties of the composite.

I. INTRODUCTION

VARIOUS Ti matrix composites reinforced with SiC monofilaments have been subject to assessment.^[1-5] The present study describes measurements and preliminary analysis conducted on a Ti-15-3 alloy uniaxially reinforced with SiC (SCS-6) fibers. The ultimate objective is to use measurements and analysis to establish the constitutive properties of the composite, consistent with the deformation and fracture mechanisms operating in the material.

Previous research on these materials has emphasized some of the *transverse tensile* properties, particularly the influence of the residual stress and incidence of interface debonding. The higher thermal expansion coefficient of the matrix compared to the fiber causes the interface to be subject to normal compression, of order 300 MPa.^[3] Furthermore, the "interface" between the fiber and the matrix is "weakly" bonded.^[2,4] Consequently, it has been proposed that the composite exhibits elastic properties characteristic of those for bonded interfaces until the stress at the interface caused by the applied load exceeds the residual compression, at about 200 MPa.^[2,3] Thereupon, interface debonding occurs and reduces the longitudinal modulus to about one-third the initial value (Figure 1). Subsequently, general yielding at the matrix occurs, followed by fracture. This sequence of events is broadly consistent with measurements of the unloading and reloading behavior and by observations of interface debonding.^[2] Notably, subsequent to initial loading above the debond stress, bilinear reversible unloading/reloading behavior has been found, provided that the peak stress was less than about 300 MPa (Figure 1). The "knee" has been attributed to the stress at which the interface separates. Furthermore, debonding has been detected, using a replica technique, at stresses above ~200 MPa. Numerical procedures have been used to simulate this behavior for a Ti-6V-4Al matrix system by assuming that the interface has a negligible fracture energy (*i.e.*, zero mode I strength) and is subject to a friction coefficient, $\mu \approx 0.3$.^[3] The results are broadly consistent with the

experimental measurements, provided that the fibers are assumed to have anisotropic elastic properties, with a transverse modulus about 70 pct of the longitudinal modulus.

In the present study, measurements and observations are performed to extend previous work and have the objective of developing a material model that provides an overall rationale for the mechanical characteristics of these composites. For this purpose, tests are performed in both longitudinal and transverse tension, as well as in shear, accompanied by various microstructural and damage observations. In addition, various analytical solutions are used to rationalize the observations.

II. MATERIAL

The matrix is a metastable β titanium alloy: Ti-15V-3Cr-3Al-3Sn. The SCS-6 fibers consist of a C core and have a graded C:Si coating. The fiber diameter is typically 140 μm . The materials are made by hot-pressing alloy foils between fiber tapes. The fiber volume fraction in this material is $f = 0.35$. A cross-sectional view reveals several features (Figure 2(a)). The fiber lay-up is randomly distributed. There are also several reaction products formed around the fibers (Figure 2(b)). Consistent with previous studies,^[6,7] there are three noticeable layers. The two layers adjacent to the fiber are graded C:Si coatings with detectable amounts of Ti in layer B (Figure 2(b)). The outer layer is TiC. Also, in this composite, a thin TiC layer exists between many of the alloy sheets.

III. MECHANICAL MEASUREMENTS

A. Constituent Properties

A thin tensile specimen made of the matrix material was produced by delaminating a matrix layer along the TiC film, followed by grinding to produce a flat gage section, $0.1 \times 5 \times 30$ mm. The longitudinal strain was measured with a 3.2-mm strain gage. The stress-strain curve of the foil (Figure 3) indicates that Young's modulus $E = 115$ GPa, the initial yield strength $\sigma_0 \approx 750$ MPa, and the ultimate tensile strength $\sigma_{m,u} \approx 950$ MPa.

The modulus of the fibers was measured on single fibers extracted from the composite. For this purpose, a

S. JANSSON, Research Engineer, Department of Mechanical and Environmental Engineering and A.G. EVANS, Professor and Chairman, Materials Department, are with the College of Engineering, University of California, Santa Barbara, CA 93106. H.E. DÈVE, Senior Materials Scientist, is with 3M, 3M Center Building 60-EN-0, St. Paul, MN 55144-1000.

Manuscript submitted June 8, 1990.

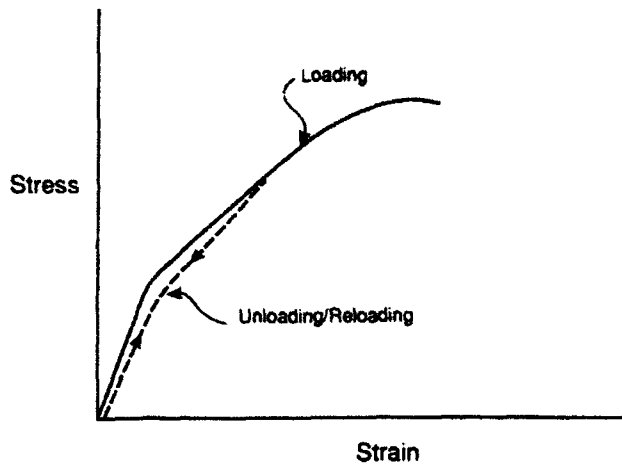


Fig. 1—A schematic of the transverse tensile characteristics of Ti matrix composites reinforced with SiC fibers.^[1,2,3]

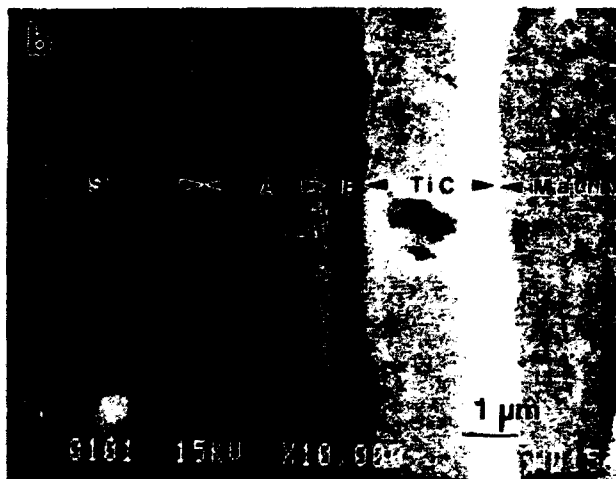
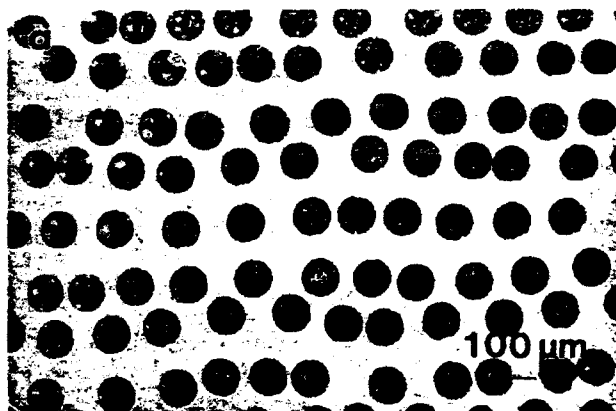


Fig. 2—SEM cross section of the composite revealing (a) the overall spatial arrangement of the fibers and (b) the reaction product layer around the fibers.

cantilever mode was used, wherein a load was imposed at the end and the deflection measured. The average Young's modulus of 50 fibers, determined by assuming elastic homogeneity, was $E_f = 360$ GPa. This value is

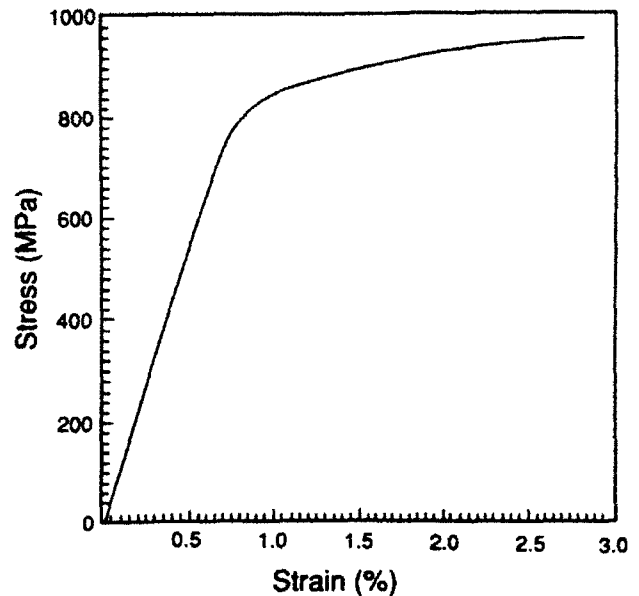


Fig. 3—Tensile stress-strain curve for the matrix.

somewhat lower than the cited axial value of 400 to 425 GPa.^[5] The low modulus is attributed to the soft carbon core and carbon surface layer. For reference purposes, it is noted that the average tensile strength of the fibers $\bar{S} \approx 4.3$ GPa for a 25-mm gage length and, by assuming a Weibull distribution, the shape parameter $m \approx 9$ ^[5] and the scale parameter $S_0 = 4.5$ GPa for a reference length $L_0 = 1$ m.

B. Test Specimens for Composites

The specimen used for both *longitudinal* and *transverse tests* has a large radius at the transition from the gripping section to the reduced gage section to minimize stress concentrations. The gage section is 1-mm wide and 6.25-mm long. The in-plane strains that develop upon testing were measured with 3.2-mm strain gages, while the strain in the thickness direction was obtained using 1.62-mm gages.

In-plane shear properties were determined with specimens of Iosipescu type⁽⁸⁾ (Figure 4). The specimen is a

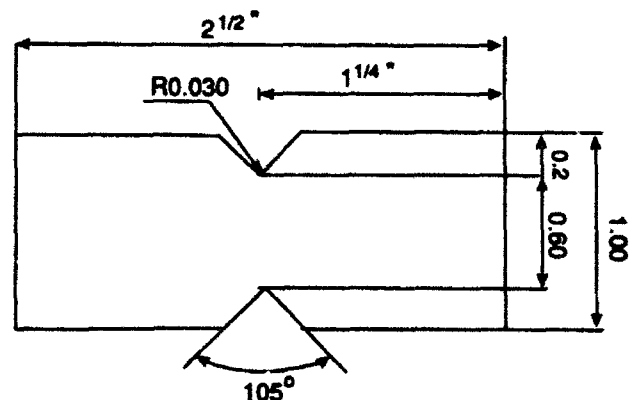


Fig. 4—A schematic of the Iosipescu specimen.

short beam in antisymmetric loading, with a symmetry line in the midspan subject to pure shear. However, the stress is singular if the notch is too sharp and parabolic if the notch is too blunt. In practice, the notch angle is selected to be slightly larger than critical (110 deg) in order to be conservative and to avoid high stress concentrations. The shear strain that developed was measured with two 1.62-mm strain gages mounted on opposite sides of the specimen in the gage section: one at +45 deg and one at -45 deg. Properties have been obtained for two fiber orientations (Figure 7): fibers oriented in the direction of the notches, with longitudinal loading, and fibers oriented perpendicular to the notches, with transverse loading. All tests were conducted at the strain rate of $\sim 10^{-5} \text{ s}^{-1}$.

The flexural properties were obtained in three-point bending. Two beam lengths have been used. A long beam (span to thickness: 8.2) provided a measure of the tensile properties and a short beam (span to thickness: 3.7) was used to measure the interlaminar shear properties.

C. Composite Properties

The measured moduli and Poisson's ratios are summarized in Table I. The *longitudinal* tensile stress-strain curve (Figure 5) indicates that the response is linear up to approximately 850 MPa, at a strain of 0.5 pct, and the ultimate strength $\sigma_u = 1800 \text{ MPa}$, occurring at a strain of 1 pct. The *transverse* tensile stress-strain curve (Figure 6(a)) indicates a deviation from linearity at 150 MPa at a strain of ~ 0.15 pct and an ultimate strength of $\sigma_{t,u} = 420 \text{ MPa}$ at a strain of 1.2 pct. The strain in the thickness direction (Figure 6(b)) exhibits an abrupt increase at the onset of nonlinearity, indicative of a volume increase. Subsequently, the slope diminishes and asymptotically approaches the initial elastic slope.

Measurements of in-plane shear properties (Figure 7) indicate that the initial elastic response for the two orientations is similar but that the flow strength is noticeably different. Such a difference has not been observed for ductile matrix systems with bonded interfaces.

The *flexural* experiments performed on long beam resulted in failure from the tensile surface. Based on a linear elastic formulation, the corresponding tensile stress at the ultimate load was 2.5 GPa. The tests on short beams resulted in nonlinearity occurring by interlaminar shear. The shear stress at the onset of flow was 260 MPa (Figure 8).

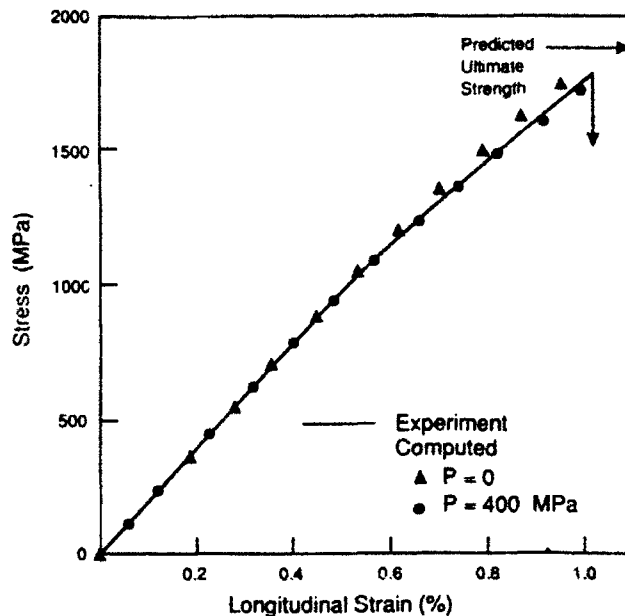


Fig. 5—The stress-strain curve in longitudinal tension. Also shown as the triangles and circles are predicted results for two levels of residual stress as well as the ultimate strength predicted using weakest link statistics.

D. In Situ Measurements

Transverse tension tests have been conducted *in situ* in a scanning electron microscope (SEM). The test specimens used in the *in situ* tests were similar to those used in the servohydraulic testing frame but with a gage section of $5 \times 1 \times 0.5 \text{ mm}$. The composites were tested in a SEM testing stage,* with the fiber axis normal to

*Instrumented JSM-840 stage, Ernest Fullam Inc., Latham, NY 12110.

the plane of observation (Figure 9). Within the accuracy of the optical measurements of the matrix-fiber separation ($\sim 0.1 \mu\text{m}$), the experiments confirm that interface separation commences at a stress of $200 \pm 10 \text{ MPa}$ (Figure 9). Furthermore, when the peak stress is below 300 MPa, the debond closes upon unloading (Figure 9), with an unloading curve of the type sketched in Figure 1. However, upon loading above 300 MPa, debond closure does not occur upon unloading (Figure 9), indicative of plastic deformation in the matrix.

Table I. Summary of Elastic Properties

		E_{11} (GPa)	ν_{12}	E_{22} (GPa)	ν_{23}	ν_{21}	G_{12} (GPa)
Experiments		196	0.25	129	0.34	0.20	62.0
Calculations	bonded interface	201	0.27	171	0.32	0.23	64.4
	sliding interface ($\tau_i = 0$)	201	—	127	—	—	29
Fiber properties: $E = 360 \text{ GPa}$ and $\nu = 0.17$.							
Matrix properties: $E = 115 \text{ GPa}$ and $\nu = 0.33$.							

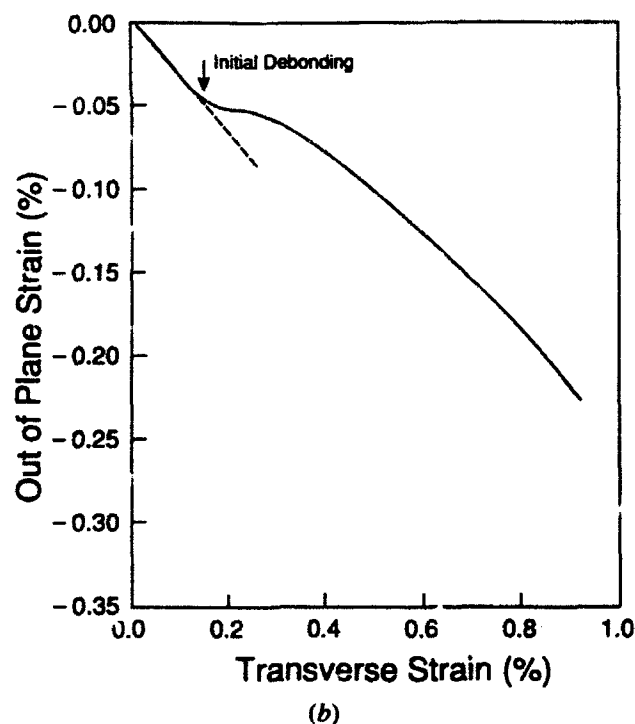
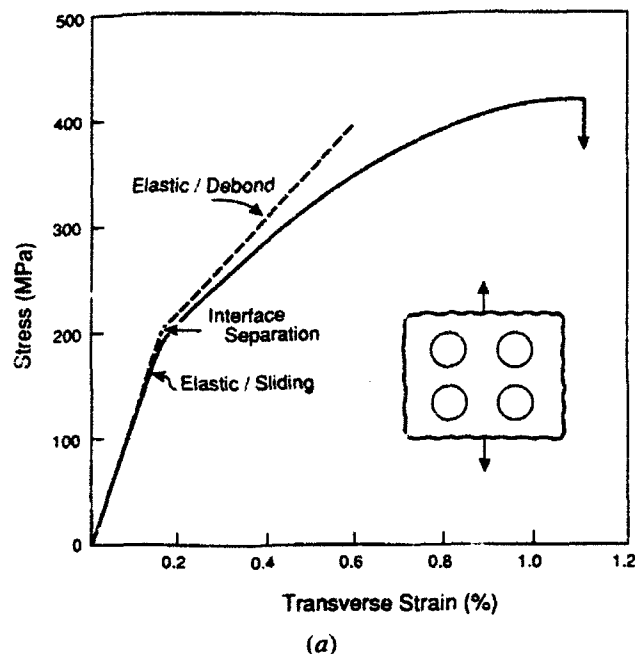


Fig. 6—(a) Stress-strain curve in transverse tension; also shown as the dotted curve is the bilinear elastic behavior predicted with interface debonding (b) The change in strain in the thickness orientation with the imposed transverse strain showing the dilatation that occurs upon debonding.

IV. CHARACTERIZATION

Specimens tested in longitudinal tension exhibit the fracture characteristics depicted in Figure 10. The two most notable features are the extensive fiber/matrix separation and the fully ductile nature of the matrix fracture.

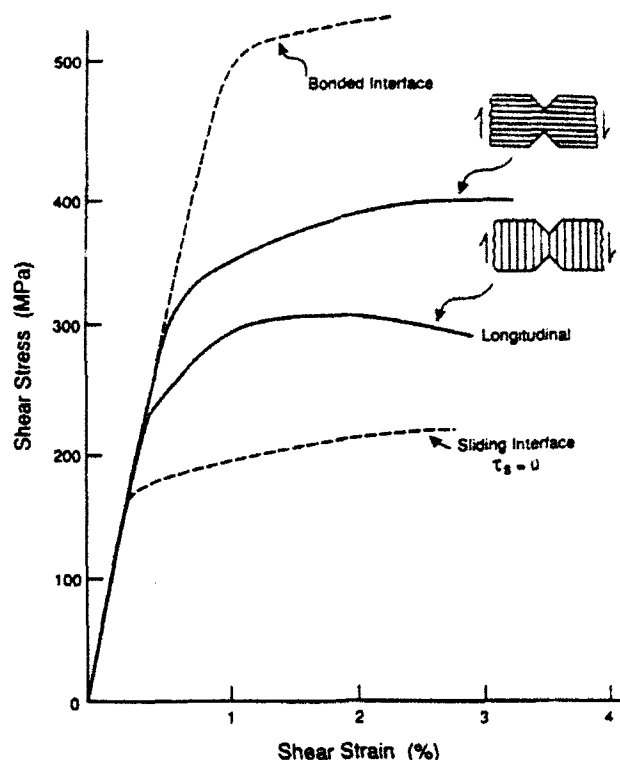


Fig. 7—The shear stress-strain curves measured for the two orientations; also shown are the predicted curves for a bonded interface and a sliding interface with $\tau_s = 0$.

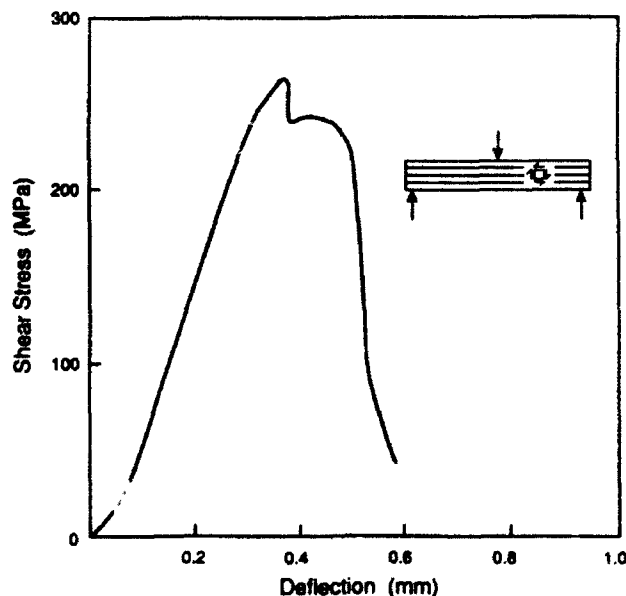


Fig. 8—The interlaminar shear-stress deflection curve obtained using a short span three-point flexure specimen.

It is also noted that the fracture plane is irregular, having height variability up to about 3 fiber diameters, and that extensive delamination occurs along the TiC planes. Close inspection of the fiber/matrix separations (Figure 10), coupled with EDAX analysis, indicates two features. The

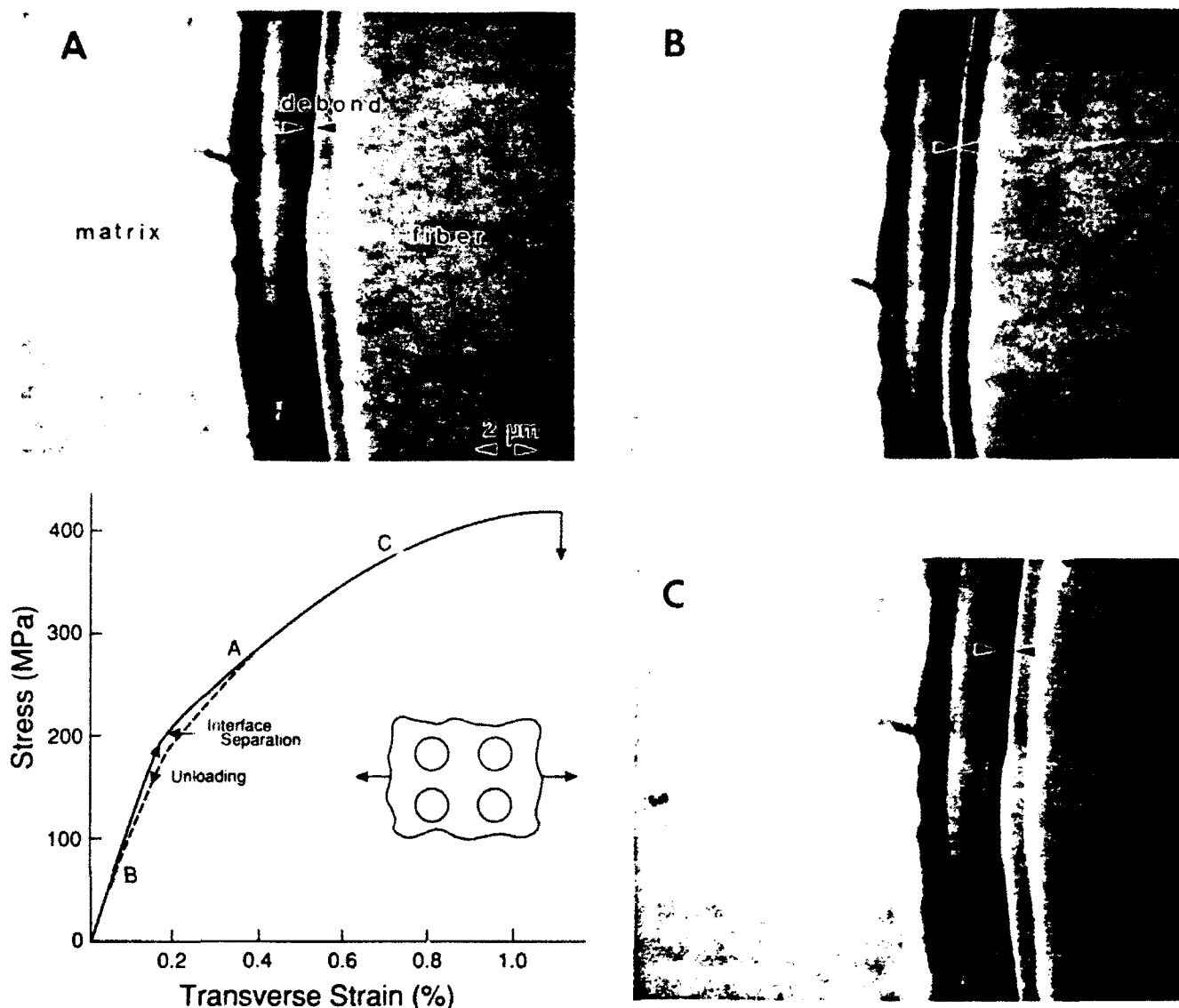


Fig. 9—*In situ* observations conducted in the SEM upon transverse loading.

debonding occurred primarily at the A/B interface (Figure 2(a)), with the outer carbon layer attached to the matrix and the inner carbon layer attached to the fibers. Furthermore, the outer C layer exhibits multiple cracking. The latter phenomenon is typical of brittle debond layers when attached to the ductile member of a composite system.^[9]

The fracture surfaces of specimens tested in transverse tension are also irregular. Inspection of side surfaces remote from the fracture surface confirms that transverse debonding propagates predominantly in the inner carbon coating in mode I debonding and along the A/B interface in mixed mode debonding (Figure 11). Additionally, the reaction product layer exhibits radial cracks normal to the transverse tension. These cracks induce shear bands in the matrix, which may contribute to the failure process (Figure 11(c)). It is also noted that the area fraction of matrix on the fracture surface $A_m = 0.4$,

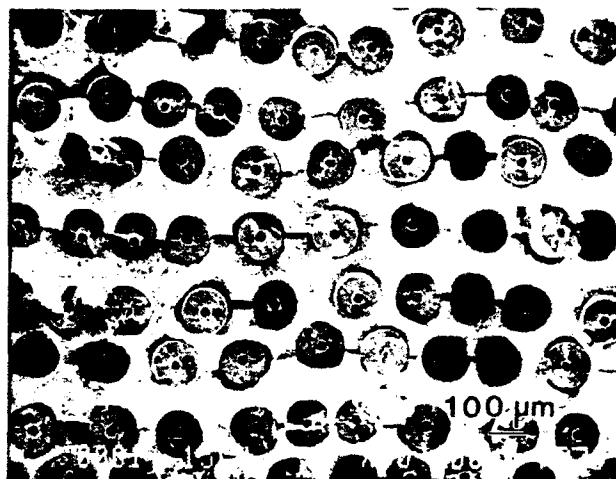
indicating that the fracture selects material planes that contain a higher than average area fraction of fibers.

The specimens tested in shear exhibit matrix features characteristic of mode II ductile fracture (Figure 12). Also, fibers are exposed by the fracture with fragments of reaction product layer attached.

V. PRELIMINARY ANALYSIS OF RESULTS

A. The Material Model

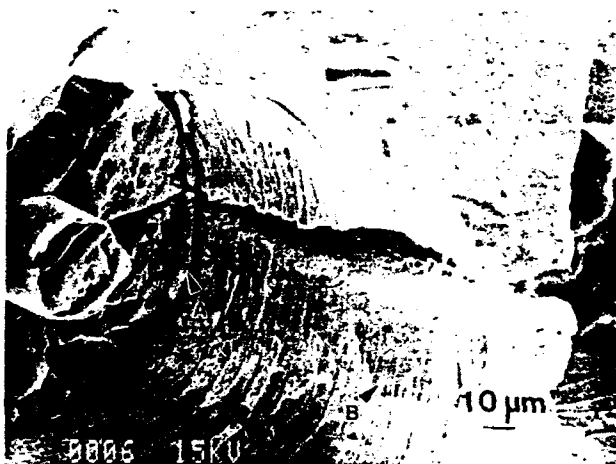
A full analysis of composite behavior would require further mechanical measurements and damage observations as well as selected numerical calculations. Instead, the intent here is to use simple analytical results in an attempt to provide a physical rationale for the observed composite characteristics and to use this information to



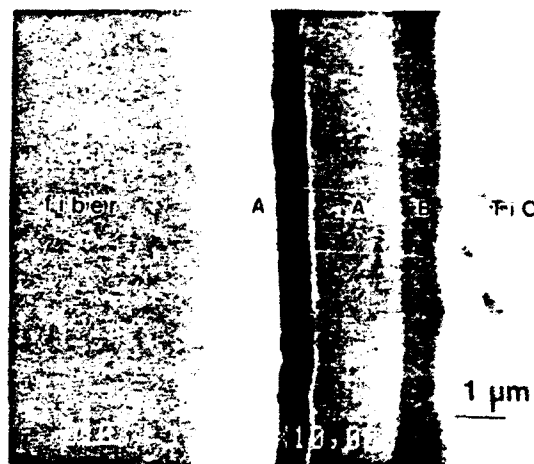
(a)



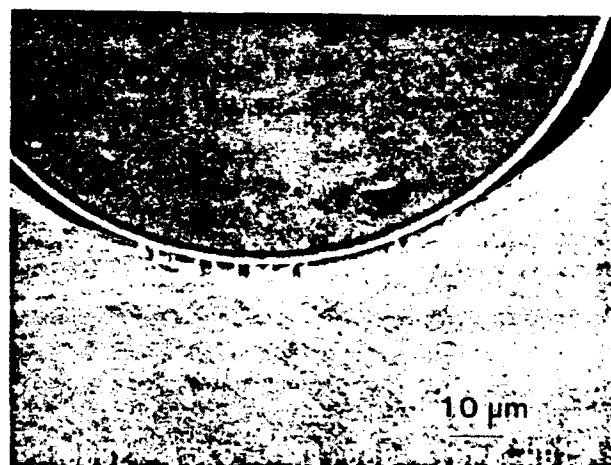
(a)



(b)



(b)



(c)

Fig. 10—The fracture surface of a specimen tested in longitudinal tension: (a) a low magnification view; and (b) a close-up of a debonded interface indicating the debond at A and the multiple cracked reaction product B.

design additional experiments as well as to motivate further numerical calculations. For this purpose, the elastic properties, the flow stress, and the ultimate strength are examined successively using a physically consistent material description. The *material model* that seemingly provides the best rationale, depicted in Figure 13, is consistent with that suggested by previous studies.^[2,3] The interphase between the fiber and matrix is characterized by a debond fracture energy Γ , that depends on the loading phase ψ (increasing as ψ increases) and by a sliding stress τ , along the *debonded interface*.^[10] The sliding stress τ , in turn, depends on the stress normal to the interface, perhaps in accordance with a Coulomb friction coefficient, μ . When the dominant debond interphase in carbon, Γ_c , appears to be small^[10] ($<1 \text{ Jm}^{-2}$), debonding occurs readily in all modes of loading and, consequently, the mechanical response of the interface is dominated by sliding.^[10,11] Since a carbon layer is retained

Fig. 11—SEM view of the side surface of a specimen tested to failure in transverse tension: (a) overview; (b) a high resolution view of the debonded interface; and (c) a high resolution view of cracks in the reaction product layer and of shear bands induced in the matrix.

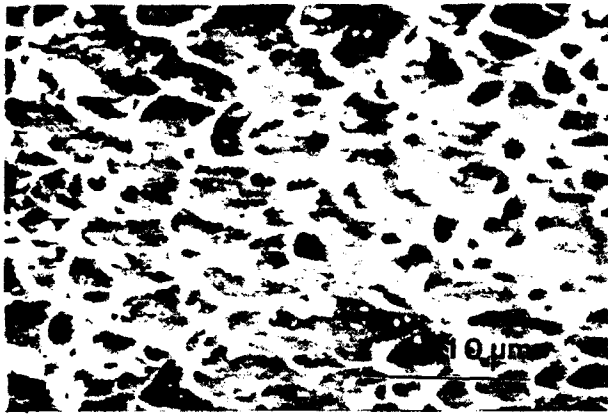


Fig. 12—A matrix region of a fracture surface of a specimen tested in shear.

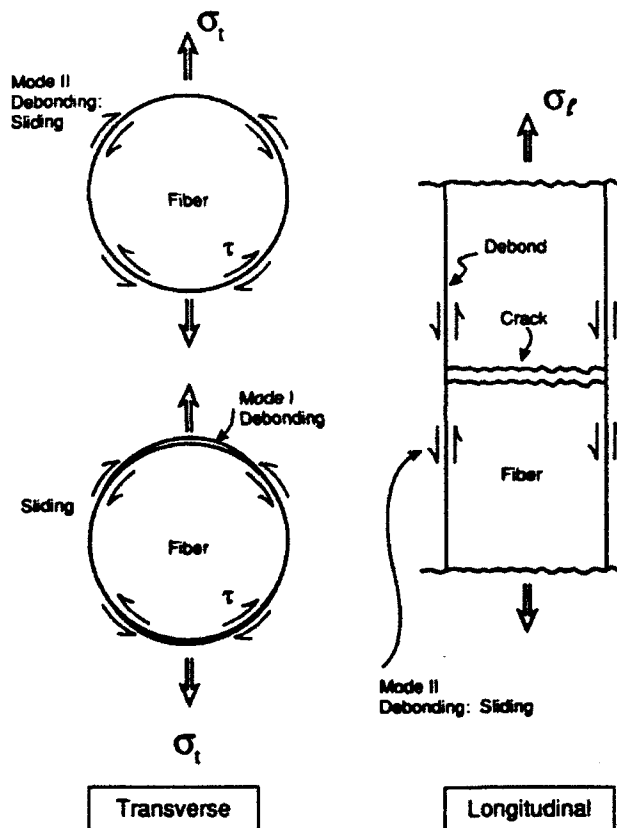


Fig. 13—The material model used to rationalize the mechanical behavior of the composite: (a) mode II debonding and sliding followed by mode I debonding in transverse tension; and (b) fiber cracking and mode II debonding and sliding in longitudinal tension.

in the present composite, a material model based on $\Gamma_t = 0$ is assumed but with frictional sliding.

Residual stress is another important feature of the model. Thermal expansion misfit between the fiber and matrix is insufficient to cause matrix yielding on cooling^[3] and, consequently, elastic solutions may be used. The longitudinal misfit dominates the axial residual stress

in the matrix, p , which is spatially quite uniform and is given for the concentric cylinder model by^[12]

$$\frac{p}{E_m} = \frac{\lambda_2}{\lambda_1} \left[\frac{E_f}{E_f} \right] \frac{f \Delta \alpha \Delta T}{(1 - \nu_m)} \quad [1]$$

where E is the longitudinal composite modulus,

$$E_f = E_m(1 - f) + E_f f \quad [2]$$

and the λ_i are given by ($\nu = \nu_f = \nu_m$)

$$\lambda_1 = \{1 - (1 - E_f/E_f)(1 - \nu)/2 - (E_f/E_f)\nu^2\}/(1 - \nu^2) \quad [3]$$

$$\lambda_2 = 1 - (1 - E_f/E_f)/2$$

For the present composite^[2] ($\Delta \alpha \approx 5 \times 10^{-6} \text{ C}^{-1}$, $\Delta T = 900 \text{ }^\circ\text{C}$), $p \approx 400 \text{ MPa}$, consistent with finite element calculations^[3] and with X-ray measurements.^[13]

The radial and tangential stresses in the matrix are spatially nonuniform, but the compressive stress q normal to the interface is given simply by^[12]

$$\frac{q}{E_m} = - \frac{(1 - f)\Delta \alpha \Delta T}{2\lambda_1(1 - \nu_m)} \quad [4]$$

which for the present composite is $q \approx -300 \text{ MPa}$.

Finally, the fibers are considered to be elastic and have strength properties governed by weakest link statistics. Furthermore, the fibers are regarded as noninteracting, because cracks in the fiber dissipate local stress concentrations by debonding and sliding along the interface.

B. Elastic Properties

The effective elastic properties for a bonded interface and elastically isotropic fibers, based on the properties of the fibers and the matrix listed in Table I, are calculated by using the homogenization method.^[14] It is apparent that the calculated and measured elastic properties are relatively close, except for an appreciable discrepancy in the transverse Young's modulus, E_{22} . This discrepancy is addressed by allowing the interface to debond in mode II and then slide at a characteristic sliding stress τ_s . For transverse tension, τ_s is expected to be small because the applied load reduces the stress normal to those segments of interface susceptible to sliding (Figure 13). In the limit $\tau_s \rightarrow 0$, numerical calculations^[14] yield a transverse modulus similar to the measured value (Table I). The sliding interface model must also be consistent with the result that the shear modulus is the same as that for a bonded interface. In the limit $\tau_s \rightarrow 0$, the calculated shear modulus is much smaller than the measured value (Table I). It is thus presumed that, in shear, the stress normal to the interface on the sliding segments is essentially unchanged such that the sliding stress τ_s has sufficient magnitude to inhibit sliding and lead to a modulus essentially the same as that for the bonded interface. As elaborated below, τ_s is inferred from the shear tests as being of order 90 MPa. Lower values have been obtained from fiber push-through tests.^[15]

C. Flow Strength

1. Longitudinal tension

The flow strength in longitudinal tension is unaffected by the interface and can be examined using a simple

parallel model, with an initial stress p in the matrix. Yielding of the matrix should initiate at an applied stress, σ_0 , given by

$$\sigma_0 = fE_f\epsilon_0 + (1-f)[\sigma_0 - p] \quad [5]$$

where ϵ_0 is the matrix yield strain. The flow stress σ at larger strains ϵ is

$$\sigma_f = fE_f\epsilon_f + (1-f)[\sigma_m - p] \quad [6]$$

where σ_m is the matrix flow strength at strain $\epsilon + p/E_m$. The stress-strain curve (σ vs ϵ) predicted using this simple formulation is plotted in Figure 5 for the cases $p = 0$ and $p = 400$ MPa. The latter agrees well with the measured curve. The influence of p on $\sigma(\epsilon)$ is small; however, by taking into account experimental scatter, the experiments consistently indicate the presence of a compressive residual stress. The effects on the transverse properties are much more important, as elaborated below.

2. Transverse tension

The transverse flow strength is sensitive to interface bonding and also depends on the spatial arrangement of the fibers. Estimates of the limit flow strength σ_t of composites with elastic reinforcements having bonded interfaces may be expressed in the form^[16,17]

$$\sigma_t = (2/\sqrt{3})\sigma_m[1 + \beta f] \quad [7]$$

where σ_m is the reference flow strength of the matrix at plastic strain ϵ_p and β is a coefficient that depends on the work-hardening coefficient, N , and may also depend on the fiber volume fraction. However, the flow strength is strongly dependent on the spatial arrangement of the fibers.^[14] For typical values of N , β is of order unity when $f = 0.35$. However, even when $\beta = 0$, corresponding to the lower bound, Eq. [7] predicts $\sigma_t \approx 940$ MPa, substantially in excess of the measured transverse flow strength. The discrepancy is attributed to interface debonding. To further address the effect of debonding, various elasticity solutions are invoked. The stress normal to the sliding interface at the interface poles σ_t is related to the applied stress σ , prior to debonding by

$$\sigma_t/\sigma_f = \frac{11 - 17\nu_m + 6\nu_f^2 + \frac{G_m}{G_f}(9 - 14\nu_f - 9\nu_m + 14\nu_m\nu_f)}{5 - 6\nu_m + \frac{G_m}{G_f}[8 - 12\nu_f - 6\nu_m + 12\nu_m\nu_f] + \left(\frac{G_m}{G_f}\right)^2(3 - 8\nu_f + 4\nu_f^2)} \quad [8]$$

Interface separation should initiate when $\sigma_t \geq q$. Thus, based on Eqs. [4] and [8], elastic separation is predicted to occur at a transverse stress, $\sigma_t \approx 200$ MPa, consistent with both the measured onset of nonlinearity (Figure 6) and with the observations of debonding. Subsequent to debonding and while the material remains predominantly elastic, the composite would develop a reduced transverse Young's modulus given approximately (for high modulus fibers and for $f \geq 0.4$) by^[19]

$$E_t \approx E_m(1 - 1.6f) \quad [9]$$

The bilinear elastic stress-strain behavior, based on the above value of the separation stress and using Eq. [9] to estimate the behavior after debonding, is plotted in Figure 6(a). This curve is comparable to the measured curve for stresses up to ~ 350 MPa. At larger stresses, the slip bands that extend from the cracks in the interfaces (Figure 11) interact and further soften the material. A model of this behavior has yet to be developed.

3. Shear

The flow strength in shear also depends on the interface response. For a bonded interface, a rigorous upper bound for the flow stress when the fibers are randomly oriented is^[21]

$$\tau = (1/\sqrt{3})(1 + 0.17f)\sigma_m \quad [10]$$

This result, plotted in Figure 7, again overestimates the measured properties. However, given the tendency for mode II interfacial debonding and sliding, one hypothesis is that the interface slides at stress τ_s . In this case, the flow strength in shear becomes

$$\tau = (1/\sqrt{3})A_m\sigma_m + \frac{\pi}{2}\tau_s(1 - A_m) \quad [11]$$

The experimental curve for the weaker orientation is consistent with Eq. [11] when a sliding stress $\tau_s \approx 90$ MPa is selected. This value is approximately twice as high as the saturated sliding stress in pushout tests.^[15]

D. Ultimate Strength

1. Longitudinal tension

The ultimate strength of the composite in longitudinal tension is dominated by the properties of the fibers. This situation arises because fiber cracks induce debonding and sliding along the A/B interface (Figure 10) and this negates the concentration of stress in neighboring fibers (Figure 13). Consequently, the fibers can be treated as a noninteracting fiber bundle having strength S_c . The composite ultimate strength σ_u is then

$$\sigma_u = fS_c + (1-f)\sigma_{m,f} \quad [12]$$

where $\sigma_{m,f}$ is now the matrix strength at the failure strain

ϵ_f . The strength of the fiber bundle in the composite, S_c , usually has some dependence on the interface sliding stress, τ_s . Such sliding allows failed fibers to sustain stresses through load transfer from the matrix. When this transfer length is small compared with the specimen gage length, L_g , multiple fiber failures are possible, leading to an ultimate tensile strength independent of L_g , with S_c given by^[22]

$$S_c = S_0 \left[\frac{2\tau_s L_0}{S_0 R(m+2)} \right]^{1/(m+1)} \left(\frac{m+1}{m+2} \right) \quad [13]$$

where S_0 and L_0 are scale parameters and m the shape parameter in the Weibull distribution. Conversely, when only partial load transfer occurs within the gage length, S_c decreases as L_c decreases in approximate accordance with the fiber bundle solution.^[20]

*Note that $S_0 = \bar{S}/\Gamma[(m+1)/m]$, where Γ is the gamma function and \bar{S} is the mean strength for fiber having length L_0 .

$$S_c = S_0(L_0/mL_c)^{1/m} \quad [14]$$

To identify the relevant composite failure mode, the transfer length on each side of a failed fiber is given by^[22]

$$l \approx R(S_f/2\tau_s) \quad [15]$$

where S_f is the nominal stress on the fibers at the ultimate strength of the composite. With $S_f = 3.5$ GPa and $\tau_s = 90$ MPa, Eq. [15] gives $l \approx 1.5$ mm. The total slip length, $2l \approx 3$ mm, is thus comparable to the specimen gage length, $L_g \approx 6.25$ mm, indicating that the fiber bundle solution (Eq. [14]) is more likely to apply. Indeed, the ultimate strength predicted from Eq. [14], $\sigma_u \approx 1870$ MPa, is similar to the measured value (Figure 5). However, it is important to appreciate that Eq. [13] is expected to become more relevant at larger L_g .

Load transfer lengths from failed fiber within the loading span used in the three-point bending tests would again be in the range indicative of a gage length dependence, qualitatively consistent with the greater strength measured in bending than in tension. Furthermore, a standard weakest link analysis predicts a ratio λ of the bending to the tensile strength given by

$$\lambda = [2(m+1)V_g/V_b]^{1/m} \quad [16]$$

where V_g and V_b are, respectively, the gage volume in tension and the volume between the loading points in bending. For the present case, $\lambda = 1.47$, compared with a measured ratio of 1.4.

Transverse tension

The ultimate strength in transverse tension is preceded by the formation of cracks in the reaction product layers (Figure 11(c)). These cracks, in turn, induce shear bands in the matrix. Such observations suggest a strength controlled by the coalescence of the cracks in the reinforcements by ductile failure of the intervening matrix. Should this hypothesis apply, the transverse strength would be influenced by the fiber diameter (the crack size), the matrix toughness, and the fiber volume fraction. However, the following simple model based only on the matrix strength apparently agrees quite well with the measured composite strength. The matrix ligament caused by debonding, subject to plane strain in the fiber direction, should fail at a stress $\sigma_{t,u}$ given by

$$\sigma_{t,u} = (2/\sqrt{3})\sigma_{m,u}A_m \quad [17]$$

where $\sigma_{m,u}$ is the ultimate strength of the matrix and A_m is the area fraction of matrix on the transverse fracture plane. Noting that $\sigma_{m,u} = 950$ MPa and $A_m = 0.4$, the transverse strength given by Eq. [17] is $\sigma_{t,u} = 430$ MPa compared with a measured value of 420 MPa. This agreement suggests that the matrix is sufficiently ductile

that the cracks in the reinforcements do not act as fracture flaws. However, further study of the transverse strength is needed to thoroughly investigate this important implication.

VI. CONCLUDING REMARKS

The longitudinal properties of a Ti-15-3 composite reinforced with SCS-6 SiC fibers are consistent with simple models in which the strength is dominated by the bundle properties of the fibers. All other properties are strongly influenced by the *fiber/matrix interface* and by the presence of residual stress. The experimental measurements are qualitatively consistent with an interface model wherein debonding occurs readily in both modes I and II and frictional sliding proceeds over the debonded surfaces. Furthermore, sliding appears to be influenced by the normal compression at the interface, suggestive of a Coulomb friction law. These interface features cause the composite flow strength in both transverse tension and shear to be appreciably lower than the matrix flow strength.

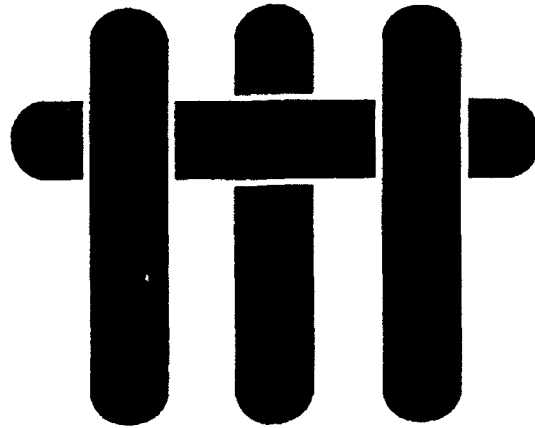
Residual stress has effects on several properties. These stresses change as the composite is subject to various thermal and mechanical loadings, causing such properties to depend on the thermomechanical history of the material. In the as-processed state, the interface is subject to normal compression. This stress suppresses initial debonding in transverse tension and inhibits sliding in shear loading. Consequently, the composite exhibits bilinear elastic behavior in transverse tension.

REFERENCES

1. W.S. Johnson, S.J. Lubowski, A.L. Highsmith, W.D. Brewer, and C.A. Hoogstraten: NASA Technical Report, NASP TM-1014, April 1988.
2. A.L. Highsmith, S.J. Lubowski, and W.S. Johnson: ASTM STP 1080, J.M. Kennedy, H.M. Moelles, and W.S. Johnson, eds., 1990, in press.
3. R.P. Nimmer, R.J. Bankert, E.S. Russell, and G.A. Smith: *ASM Materials Conf.*, Indianapolis, IN, Oct. 1989.
4. P.R. Smith and F.H. Froes: *J. Met.*, 1984, pp. 19-25.
5. M.A. Mitrnick: in *Metal Matrix Composites*, G.J. Dvorak and C. Zweben, eds., Technomic Publishing Company, Lancaster, PA, 1987.
6. J.M. Yang and S.M. Jang: *J. Met.*, 1989, vol. 41 (11), pp. 56-59.
7. C. Jones, C.J. Kiely, and S.S. Wang: *J. Mater. Res.*, 1989, vol. 4 (2), pp. 327-35.
8. S.S. Wang and A. Dasgupta: *Development of Iosipescu-Type Test for Determining In-Plane Shear Properties of Fiber Composite Materials: Critical Analysis and Experiment*, Department of Theoretical and Applied Mechanics, University of Illinois at Urbana-Champaign, UILU-ENG-86-5021, 1986.
9. H.C. Cao, B.J. Dalgleish, H.E. Dève, C. Elliott, A.G. Evans, R. Mehrabian, and G.R. Odette: *Acta Metall.*, 1989, vol. 37.
10. A.G. Evans and D.B. Marshall: *Acta Metall.*, 1989, vol. 37, p. 2567.
11. H.C. Cao, E. Bischoff, M. Rühle, D.B. Marshall, A.G. Evans, and J.J. Brennan: *J. Am. Ceram. Soc.*, 1990, vol. 73, p. 1691.
12. B. Budiansky, J.W. Hutchinson, and A.G. Evans: *Mech. Phys. Solids*, 1986, vol. 34, p. 167.
13. K.M. Brown, R.W. Hendrick, and W.D. Brewer: *TMS Fall Meeting*, Detroit, MI, 1989.

14. S. Jansson: *Homogenized Nonlinear Constitutive Properties and Local Stress Concentrations for Co-Posites with Periodical Internal Structure*, UCSB, Mechanical Engineering, 1990.
15. P. Warren, T.J. Mackin, and A.G. Evans: *J. Am. Ceram. Soc.*, 1990, in press.
16. G. Bao, J.W. Hutchinson, and R.M. McMeeking: *Acta Metall.*, in press.
17. J.M. Duva: *J. Eng. Mater. Technol.*, 1984, vol. 100, p. 317.
18. N.I. Muskhelishvili: *Some Basic Problems of the Mathematical Theory of Elasticity*, Nordhoff, pp. 221-22.
19. K. Takahashi and T.-W. Chou: *Metall. Trans. A*, 1988, vol. 19A, pp. 129-35.
20. B.D. Coleman: *Mech. Phys. Solids*, 1958, vol. 7, p. 60.
21. S. Jansson: UCSB, Mechanical Engineering, current research, 1991.
22. W. Curtin: *Appl. Phys. Lett.*, in press.

M A T E R I A L S



**MODELS FOR THE CREEP OF CERAMIC
MATRIX COMPOSITE MATERIALS**

Robert M. McMeeking

**Department of Mechanical and Environmental Engineering
University of California
Santa Barbara, California 93106**

September 1992

Introduction

This review is intended to focus on ceramic matrix composite materials. However, the creep models which exist and which will be discussed are generic in the sense that they can apply to materials with polymer, metal or ceramic matrices. Only a case by case distinction between linear and nonlinear behavior separates the materials into classes of response. The temperature dependent issue of whether the fibers creep or do not creep permits further classification. Therefore, in the review of the models, it is more attractive to use a classification scheme which accords with the nature of the material response rather than one which identifies the materials per se. Thus, this review could apply to polymer, metal or ceramic matrix materials equally well.

Only fiber and whisker reinforced materials will be considered. The fibers and whiskers will be identified as ceramics but with different characteristics from the matrix. As noted above, at certain temperatures, the reinforcement phase will not be creeping and then it will be treated as elastic or rigid as appropriate to the model. At higher temperatures, the reinforcement phase will creep, and that must be allowed for in the appropriate model. On the other hand, the case of creeping fibers in an elastic matrix will not be considered, although certain of the models have a symmetry between fiber and matrix which permits such an interpretation. The models reviewed will be for materials with long fibers, broken long fibers and short fibers or whiskers. Aligned fibers and two and three dimensional reinforcement by long fibers will be discussed. However, general laminate behavior will not be a subject of this review.

The material behaviors considered will include linear elasticity plus linear or nonlinear creep behavior. The nonlinear case will be restricted to power law rheologies. In some cases the elasticity will be idealized as rigid. In ceramics, it is commonly the case that creep occurs by mass transport on the grain boundaries¹. This usually leads to a linear rheology. In the models considered, this behavior will be represented by a continuum creep model with a fixed viscosity. That is, the viscosity is strain rate

independent, although it will in general be temperature dependent. Thus, the mass transport per se will not be explicit in the models. In some situations, even though the mechanism is mass transport, the creep behavior involves a power law response with a low exponent. Such a case is polycrystalline alumina at certain temperatures¹. This explains the inclusion of power law models in this review. An additional constitutive feature considered in this review is mass transport on the interface between the fiber and the matrix. This path can be a faster route for diffusion than the grain boundaries within the matrix. Therefore it merits a separate treatment as a mechanism for creep. A rudimentary model for the progressive breaking of reinforcements will be discussed. Creep void growth and other types of rupture damage in the matrix and the fiber will, however, be excluded from consideration.

Because the creep behavior of a ceramic composite often has a linear rheology, the behavior of the composite usually can be represented by an anisotropic viscoelastic constitutive law. Thus, a rather general model for such composites involves hereditary integrals with time dependent creep or relaxation moduli^{2,3} with a general anisotropy. the parameters for the law can be determined through creep and relaxation tests, but a multiplicity of experiments are required to evaluate all the functions appearing in a general anisotropic law. As a consequence, some guidance from micromechanics is essential for the generalization of the results. In this review, the focus will be on the micromechanics based models and the hereditary integral methods will not be considered. However, the micromechanics models can, if desired, be recast in the classical viscoelastic form. It should be noted that there exists a vast literature on the linear elastic properties of reinforced materials. These elasticity models can be converted into creep models by use of standard methods of linear viscoelasticity². This approach will be avoided in this review even though it can provide effective creep models for ceramic matrix composites. Instead, the focus in this chapter will be on models which involve nonlinearities or have features such as interface diffusion which

are not accounted for when linear elastic models are converted to linear viscoelastic constitutive laws.

Material Models

All phases of the composite material will be assumed to be isotropic. The creep behavior of a ceramic will be represented by the law

$$\dot{\epsilon}_{ij} = \frac{1}{2G} \dot{S}_{ij} + \frac{1}{9K} \delta_{ij} \dot{\sigma}_{kk} + \frac{3}{2} B \bar{\sigma}^{n-1} S_{ij} + \alpha \delta_{ij} \dot{T} \quad (1)$$

where $\dot{\epsilon}$ is the strain rate, $\underline{\sigma}$ is the stress, $\dot{\underline{\sigma}}$ is the stress rate, G is the elastic shear modulus, K is the elastic bulk modulus, δ_{ij} is the Kronecker delta, B is the creep rheology parameter, n is the creep index, \underline{S} is the deviatoric stress and the effective stress $\bar{\sigma}$ is defined by

$$\bar{\sigma} = \sqrt{\frac{3}{2} S_{ij} S_{ij}}, \quad (2)$$

α is the coefficient of thermal expansion and \dot{T} is the rate of change of temperature. In all expressions the Einstein repeated index summation convention is used. x_1 , x_2 and x_3 will be taken to be synonymous with x , y and z so that $\sigma_{11} = \sigma_{xx}$ etc.. The parameter B will be temperature dependent through an activation energy expression and can be related to microstructural parameters such as grain size, diffusion coefficients etc. on a case by case basis depending on the mechanism of creep involved¹. In addition, the index will depend on the mechanism which is active. In the linear case, $n = 1$ and B is equal to $1/3\eta$ where η is the linear shear viscosity of the material. Stresses, strains and material parameters for the fibers will be denoted with a subscript or superscript f and for the matrix with a subscript or superscript m .

Various models will be used for the interface between the fiber and the matrix. For bonded interfaces, complete continuity of all components of the velocity will be invoked. The simplest model for a weak interface is that a shear drag equal to τ opposes the relative shear velocity jump across the interface. The direction of the shear drag is determined by the direction of the relative velocity. However, the magnitude of τ is independent of the velocities. This model is assumed to represent friction occurring mainly because of roughness of the surfaces or due to a superposed large normal pressure on the interface. Creep can, of course, relax the superposed normal stress over time, but on a short time scale the parameter τ can be assumed to be relatively invariant. No attempt will be made to account for Coulomb friction associated with local normal pressures on the interface.

On the other hand, a model for the viscous flow of creeping material along a fiber surface is exploited in some of the cases covered. This model is thought to represent the movement of material in steady state along a rough fiber surface and is given by (McMeeking, to be published)

$$\underline{v}_i^{\text{Rel}} = \bar{B} \bar{\sigma}^{n-1} n_j \sigma_{jk} (\delta_{ki} - n_k n_i) \quad (3)$$

where $\underline{v}^{\text{Rel}}$ is the relative velocity of the matrix material with respect to the fiber, \bar{B} is a rheology parameter proportional to B but dependent also on roughness parameters for the fiber, \underline{n} is the unit outward normal to the fiber surface and the stress is that prevailing in the creeping matrix material. The law simply says that the velocity is in the direction of the shear stress on the interface but is controlled by power law creep.

When there is mass transport by diffusion taking place in the interface between the fiber and the matrix, the relative velocity is given by¹

$$\underline{v}^{\text{Rel}} = -\underline{n} (\underline{\nabla} \cdot \underline{j}) \quad (4)$$

where \underline{j} is the mass flux of material in the plane of the interface and $\underline{\nabla}$ is the divergence operator in 2-dimensions also in the plane of the interface. The mass flux in the interface is measured as the mass per unit time passing across a line element of unit length in the interface. The flux is proportional to the stress gradient so that

$$\underline{j} = \mathcal{D} \underline{\nabla} \sigma_{nn} \quad (5)$$

where \mathcal{D} is an effective diffusion coefficient and

$$\sigma_{nn} = \underline{n} \cdot \underline{\sigma} \cdot \underline{n} \quad (6)$$

is the normal stress at the interface. Combination of eq. (4 & 5) for a homogeneous interface gives

$$\underline{v}^{Rel} = -\underline{n} \mathcal{D} \nabla^2 \sigma_{nn}. \quad (7)$$

The diffusion parameter \mathcal{D} controls mass transport in a thin layer at the interface and so its relation to other parameters can be stated as¹

$$\mathcal{D} = \frac{\delta D_b \Omega}{kT} \quad (8)$$

where δ is the thickness of the thin layer in which diffusion is occurring, D_b is the diffusion coefficient in the material near or at the interface, Ω is the atomic volume, k is Boltzmann's constant and T is the absolute temperature. The diffusion could occur in the matrix material, in the fiber or in both. The relevant diffusion parameters for the matrix, the fiber or some weighted average would be used respectively.

It is worth noting that the "rule of mixtures" for stress, stress rate, strain and strain rate is always an exact result in terms of the averages over the phases⁴. That is

$$\sigma_{ij} = f \sigma_{ij}^f + (1 - f) \sigma_{ij}^m \quad (9)$$

$$\epsilon_{ij} = f \epsilon_{ij}^f + (1 - f) \epsilon_{ij}^m \quad (10)$$

etc. where the unsuperscripted tensor variables are the averages over the composite material and the superscripted variables are the averages over the fibers (f) and the matrix (m) respectively. The volume fraction of the fibrous phase is f. The result applies irrespective of the configuration of the composite material, e.g. unidirectional or multidirectional reinforcement. However, an allowance must be made for the contribution arising from gaps which can appear such as at the ends of fibers. The difficulty in the use of the rule of mixtures is the requirement that the average values in the fibers and in the matrix must be known somehow.

Materials with Long Intact Fibers

Creep laws for materials with long intact fibers are relevant to cases where the fibers are unbroken at the outset, and never fracture during life. As a model, it also applies to cases where some but not all of the fibers are broken so that some fibers remain intact during service. Obviously these situations would occur only when the manufacturing procedure can produce composites with many or all of the fibers intact.

In the problem of the creep of materials with intact unidirectional fibers, as shown in Fig. 1, most of the insights arise from the compatibility of the strain rates in the fibers and in the matrix. When a stress σ_{zz} is applied to the composite parallel to

the fibers, the strains and strain rates of the fibers and the matrix in the z-direction must be all the same⁵. This gives rise to a creep law of the form

$$\dot{\epsilon}_{zz} = \frac{\dot{\sigma}_{zz}}{E_L} + \dot{\epsilon}_{zz}^c + \alpha_L \dot{T} \quad (11)$$

and

$$\dot{\epsilon}_{xx} = \dot{\epsilon}_{yy} = -\frac{\nu_L \dot{\sigma}_{zz}}{E_L} + \dot{\epsilon}_{xx}^c + \alpha_T \dot{T} \quad (12)$$

where E_L is the longitudinal composite modulus, $\dot{\epsilon}_{zz}^c$ is the longitudinal creep strain rate, α_L is the longitudinal coefficient of thermal expansion, ν_L is the Poisson's ratio for the composite relating transverse elastic strain to longitudinal stress, $\dot{\epsilon}_{xx}^c$ is the transverse creep strain rate and α_T is the transverse coefficient of thermal expansion. The temperature is taken to be uniform throughout the composite material. Evolution laws for the creep rates are required and these laws involve the stress levels in the matrix and fibers. Thus, in turn, evolution laws are required for the matrix and fiber stresses.

The exact laws based on continuum analysis of the fibers and the matrix would be very complicated. The analysis would involve equilibrium of stresses around and in the fibers and compatibility of matrix deformation with the fiber strains. Furthermore, end and edge effects near the free surfaces of the composite material would introduce complications. However, a simplified model can be developed for the interior of the composite material based on the notion that the fibers and the matrix interact only by having to experience the same longitudinal strain. Otherwise, the phases behave as two uniaxially stressed materials. McLean⁵ introduced such a model for materials with elastic fibers and he notes that McDanel, Signorelli and Weeton⁶ developed the model

for the case where both the fibrous and the matrix phase are creeping. In both cases, the longitudinal parameters are the same, namely

$$E_L = f E_f + (1 - f) E_m \quad (13)$$

$$\alpha_L = [f E_f \alpha_f + (1 - f) E_m \alpha_m] / E_L \quad (14)$$

$$\dot{\epsilon}_{zz}^c = [f E_f B_f \sigma_f^{nf} + (1 - f) E_m B_m \sigma_m^{nm}] / E_L. \quad (15)$$

When the fibers do not creep, B_f is simply set to zero. The longitudinal stress σ_{zz} in the fibers and the matrix are denoted σ_f and σ_m respectively. To accompany eq. (13-15), evolution laws for the fiber and the matrix stresses are required. These are

$$\dot{\sigma}_f = E_f (\dot{\epsilon}_{zz} - B_f \sigma_f^{nf} - \alpha_f \dot{T}) \quad (16)$$

and

$$\dot{\sigma}_m = E_m (\dot{\epsilon}_{zz} - B_m \sigma_m^{nm} - \alpha_m \dot{T}). \quad (17)$$

Indeed, combining these by the rule of mixtures, eq. (9), leads to eq. (13) to (15).

Since the fibers and the matrix do not interact transversely, the model implies that no transverse stresses develop in the matrix or the fibers. The rule of mixtures, eq. (10), then leads to

$$v_{\perp} = f v_f + (1 - f) v_m \quad (18)$$

$$\alpha_T = f \alpha_f + (1 - f) \alpha_m + f(1 - f) (\alpha_f - \alpha_m) (v_f E_m - v_m E_f) / E_L \quad (19)$$

and

$$\begin{aligned} \dot{\epsilon}_{xx}^c = & -\frac{1}{2} (1-f) B_m \sigma_m^{n_m} - \frac{1}{2} f B_f \sigma_f^{n_f} \\ & + f (1-f) (B_m \sigma_m^{n_m} - B_f \sigma_f^{n_f}) (v_f E_m - v_m E_f) / E_L. \end{aligned} \quad (20)$$

The data suggest that the elastic parameters in this model are reasonably good to first order⁷ and experience with plasticity calculations^{8,9,10} indicates that there is little plastic constraint between fibers and matrices at low volume fractions. Thus, the model should work reasonably well for any creep exponents at low volume fractions of fibers.

Indeed, McLean⁵ has used the isothermal version of the model successfully to explain longitudinal creep data for materials with non-creeping fibers.

Of interest, is the prediction of the uniaxial stress model when the applied stress and the temperature are held constant. The governing equations (19), (16) & (17) then have the feature that as time passes the solution always tends towards asymptotic values for stress in the fibers and the matrix. The evolution of the matrix stress occurs according to

$$\left[\frac{1}{E_m} + \frac{1-f}{f E_f} \right] \dot{\sigma}_m = B_m \sigma_m^{n_m} - B_f \left[\frac{\sigma - (1-f) \sigma_m}{f} \right]^{n_f} \quad (21)$$

and it can be shown that for any initial value of matrix stress, the matrix stress rate tends to zero. Therefore, the matrix stress tends toward the value which makes the right hand side of eq. (21) equal to zero. This can be solved easily for four common ceramic cases. One is when both matrix and fibers creep with a linear rheology so that both creep indices are equal to one. In that case the stresses tend towards the state in which

$$\sigma_m = \frac{B_f \sigma}{f B_m + (1-f) B_f} \quad (22)$$

and

$$\sigma_f = \frac{B_m \sigma}{f B_m + (1-f) B_f} \quad (23)$$

Another case is when the fibers creep linearly and the matrix creeps with an index of 2. Then the matrix tends towards a stress

$$\sigma_m = \left(\frac{B_f}{B_m} \right) \left[\sqrt{\left(\frac{B_m}{B_f} \right) \frac{\sigma}{f} + \frac{(1-f)^2}{4f^2}} - \frac{1-f}{2f} \right] \quad (24)$$

and of course $\sigma_m = [\sigma - (1-f) \sigma_m]/f$. The opposite case of a linear matrix and quadratic fibers is such that the fibers tend towards the stress

$$\sigma_f = \left(\frac{B_m}{B_f} \right) \left[\sqrt{\left(\frac{B_f}{B_m} \right) \frac{\sigma}{1-f} + \frac{f^2}{4(1-f)^2}} - \frac{f}{2(1-f)} \right] \quad (25)$$

and $\sigma_m = [\sigma - f \sigma_f]/(1-f)$. Finally, when the fibers do not creep, the matrix stress tends towards zero and the fiber stresses approach $\sigma/(1-f)$.

In the latter case, the transient stress can be stated as well. The isothermal result for constant σ is⁵

$$\sigma_m(t) = \left\{ \frac{(n-1)f E_f E_m B t}{E_L} + \frac{1}{[\sigma_m(0)]^{n-1}} \right\}^{1-n} \quad (26)$$

when $n \neq 1$ and

$$\sigma_m(t) = \sigma_m(0) \exp(-f E_f E_m B t/E_L) \quad (27)$$

when $n = 1$. The subscript on the creep rheology parameter for the matrix has been dropped and the unsubscripted B refers to the matrix henceforth. In both cases $\sigma_f = [\sigma - (1 - f) \sigma_m]/f$ and the composite strain is σ_f/E_f . The stress at time zero would be computed from the prior history with $t = 0$ being the time when both the temperature and the applied stress become constant. For example if the temperature is held constant at creep levels until equilibrium is achieved and then the load is suddenly applied, $\sigma_m(0) = \sigma E_m/E_L$. To the extent that there are any thermal residual stresses at $t = 0$, they will contribute to $\sigma_m(0)$. However, eq. (26) & (27) make it clear that thermal residual stresses will be relaxed away by creep.

Steady Transverse Creep with Well-Bonded Elastic Fibers The previous paragraph has made it clear that if there are elastic fibers and a constant macroscopic stress is applied, the longitudinal creep rate will eventually fall to zero. With constant transverse stresses applied as well, the process of transient creep will be much more complicated than that associated with eq. (27) and (28). However, it can be deduced that the longitudinal creep rate will still fall to zero eventually. Furthermore, any transverse steady creep rate must occur in a plane strain mode. During such steady creep, the fiber does not deform further because the stress in the fiber is constant. In addition, any debonding which might tend to occur would have achieved a steady level because the stresses are fixed.

For materials with a strong bond between the matrix and the fiber, models for steady transverse creep are available. The case of a linear matrix is represented exactly

by the effect of rigid fibers in an incompressible linear elastic matrix and is covered in texts on elastic materials^{7,11,12}. For example, the transverse shear modulus, and therefore the shear viscosity, of a material containing up to about 60% rigid fibers in a square array is approximated well by¹¹

$$G_T = \frac{1+2f}{1-f} G_m. \quad (28)$$

It follows that in the coordinates of Fig. 1, steady transverse creep with well bonded fibers obeys

$$\dot{\epsilon}_{yy} = -\dot{\epsilon}_{xx} = \frac{3B}{4} \left(\frac{1-f}{1+2f} \right) (\sigma_{yy} - \sigma_{xx}) \quad (29)$$

and

$$\dot{\epsilon}_{xy} = \frac{3B}{2} \left(\frac{1-f}{1+2f} \right) \sigma_{xy} \quad (30)$$

with $\dot{\epsilon}_{zz} = 0$. A material with fibers in a hexagonal array will creep slightly faster than this. Similarly, creep in longitudinal shear with fibers in a square array can be approximated well by

$$\dot{\epsilon}_{xz} = \frac{3B}{2} \left(\frac{1-f}{1+f} \right) \sigma_{xz} \quad (31)$$

and

$$\dot{\epsilon}_{yz} = \frac{3B}{2} \left(\frac{1-f}{1+f} \right) \sigma_{yz}. \quad (32)$$

There are few comprehensive results for power law matrices. Results given by Schmauder and McMeeking¹¹ for up to 60% by volume of fibers in a square array with a creep index of 5 can be represented approximately by

$$\dot{\epsilon}_{xx} = -\dot{\epsilon}_{yy} = 0.42 B |\sigma_{xx} - \sigma_{yy}|^4 (\sigma_{xx} - \sigma_{yy})/S^5 \quad (33)$$

where $\dot{\epsilon}_{zz} = \dot{\epsilon}_{xy} = \sigma_{xy} = 0$

$$S = (1 + f^2)/(1 - f) \quad (34)$$

is the creep strength, defined to be the stress required for the composite at a given strain rate divided by the stress required for the matrix alone at the same strain rate. The expression in eq. (34) is only suitable for $n = 5$. The result in eq. (33) when $f = 0$ is the plane strain creep rate for the matrix alone. Results for $\sigma_{xy} \neq 0$ are not given because of the relative anisotropy of the composite with a square array of fibers. Relevant results for other power law indices and other fiber arrangements are not available in sufficient quantity to allow representative expressions to be developed for them.

Three-Dimensional Continuous Reinforcement This configuration of reinforcement can be achieved by the use of a woven fiber reinforcement or interpenetrating networks of the two phases. Another possibility is that random orientation of whiskers produces a percolating network and even if the whiskers are not bonded together, this network effectively forms a mechanically continuous phase. In the case of woven reinforcements, there may be some freedom for the woven network to reconfigure itself by the straightening of fibers in the weave or because of void space in the matrix. Such effects will be ignored and it will be assumed that the fibers are relatively straight and that there is little or no void space in the matrix. A straightforward model for these

materials is that the strain rate is homogeneous throughout the composite. The response is then given by

$$\begin{aligned} \dot{\sigma}_{ij} = & 2 \bar{G} \dot{\epsilon}_{ij} + (\bar{K} - \frac{2}{3} \bar{G}) \delta_{ij} \dot{\epsilon}_{kk} - 3 \bar{K} \bar{\alpha} \dot{T} \delta_{ij} \\ & - 3 f G_f B_f \bar{\sigma}_f^{n_f-1} S_{ij}^f - 3 (1-f) G_m B_m \bar{\sigma}_m^{n_m-1} S_{ij}^m \end{aligned} \quad (35)$$

where

$$\bar{G} = f G_f + (1-f) G_m \quad (36)$$

$$\bar{K} = f K_f + (1-f) K_m \quad (37)$$

and

$$\bar{\alpha} = f \alpha_f K_f + (1-f) \alpha_m K_m. \quad (38)$$

The evolution of the fiber and matrix average stresses appearing in the last two terms in eq. (35) is given by eq. (35) with $f = 1$ and $f = 0$ respectively. It is of interest that the constitutive law in eq. (35) is independent of the configuration of the reinforcements and the matrix. As a consequence, the law is fully isotropic and therefore may be unsuitable for woven reinforcements with unequal numbers of fibers in the principal directions. In addition, the fully isotropic law may not truly represent materials in which the fibers are woven in 3 orthogonal directions. Perhaps these deficiencies could be remedied by replacing the thermoelastic part of the law with an appropriate anisotropic model. A similar alteration to the creep part may be necessary but no micromechanical guidance is available at this stage.

If the composite strain rate is known, the composite stress during steady state isothermal creep can be computed from the rule of mixtures for the stress, eq. (9). This gives

$$S_{ij} = \frac{2}{3} \left[\frac{f}{B_f} \left(\frac{\dot{\epsilon}}{B_f} \right)^{\frac{1-n_f}{n_f}} + \frac{1-f}{B_m} \left(\frac{\dot{\epsilon}}{B_m} \right)^{\frac{1-n_m}{n_m}} \right] \dot{\epsilon}_{ij} \quad (39)$$

where $\dot{\epsilon}$ must be deviatoric (i.e. $\dot{\epsilon}_{kk} = 0$) and

$$\dot{\epsilon} = \sqrt{\frac{2}{3} \dot{\epsilon}_{ij} \dot{\epsilon}_{ij}} \quad (40)$$

A hydrostatic stress can be superposed, but it is caused only by elastic volumetric strain of the composite. The result in eq. (39) is, perhaps, not very useful since it is rare that a steady strain rate will be kinematically imposed. When both fiber and matrix creep, the steady solutions for a fixed stress in isothermal states are quite complex but can be computed by numerical inversion of eq. (39). The solution can however be given for the isothermal case where the fibers do not creep. (For non-fiber composites, this should be interpreted to mean that one of the network phases creeps while the other does not.)

The matrix deviatoric stress is then given by

$$S_{ij}^m(t) = \frac{S_{ij}^m(0)}{\bar{\sigma}_m(0)} \left[3(n-1)f G_f G_m B t / \bar{G} + (\bar{\sigma}_m(0))^{1-n} \right]^{\frac{1}{1-n}} \quad (41)$$

when $n \neq 1$ and for $n = 1$

$$S_{ij}^m(t) = S_{ij}^m(0) \exp(-3 f G_f G_m B t / \bar{G}). \quad (42)$$

The subscripts on B and n have been dropped since only the matrix creeps. The interpretation of time and the initial conditions for eq. (41) & (42) are the same as for eq. (26) & (27). The fiber deviatoric stresses are given by

$$S_{ij}^f = [S_{ij} - (1 - f) S_{ij}^m]/f \quad (43)$$

and the composite deviatoric strain e_{ij} is therefore

$$e_{ij} = S_{ij}^f / 2 G_f. \quad (44)$$

The volumetric strains are invariant and given by

$$\epsilon_{kk} = \sigma_{kk} / 3 \bar{K}. \quad (45)$$

As expected, the matrix deviatoric stresses will be relaxed away completely. Thereafter, the "fiber" phase sustains the entire deviatoric stress. As a consequence, in the asymptotic state

$$S_{ij}^f = S_{ij} / f \quad (46)$$

and the composite strain will be given by (44) to (46) as

$$\epsilon_{ij} = \frac{\sigma_{ij}}{2fG_f} + \left(\frac{1}{3\bar{K}} - \frac{1}{2fG_f} \right) \frac{1}{3} \sigma_{kk} \delta_{ij}. \quad (47)$$

It follows that in uniaxial stress, with $\sigma_{zz} = \sigma$ and $\epsilon_{zz} = \epsilon$, the asymptotic result will be

$$\varepsilon = \left[\frac{1}{3fG_f} + \frac{1}{9\bar{K}} \right] \sigma. \quad (48)$$

This result indicates that the composite will have an asymptotic modulus slightly stiffer than $f E_f$ because the matrix phase is capable of sustaining a hydrostatic stress.

Two-Dimensional Continuous Reinforcement This configuration of reinforcement occurs when fibers are woven into a mat. It could also represent whisker reinforced materials in which the whiskers are randomly oriented in the plane, especially if uniaxial pressing has been used to consolidate the composite material. In the case of the whisker reinforced material, it is to be assumed that their volume fraction is so high that they touch each other. The whiskers have either been bonded together, say by diffusion, or the contact between the whiskers acts, as is likely, as a bond even if there is no interdiffusion.

In a simple model for this case, which as in the 3-d case ignores fiber straightening and anisotropy of the fibrous network, a plane stress version of eq. (35) can be developed. As such, it can only be used for plane stress states. Consider the x-y plane to be that in which the fibers are woven or the whiskers are lying. The strain rates in this plane are taken to be homogeneous throughout the composite material and σ_{zz} , σ_{xz} and σ_{yz} are taken to be zero. The resulting law is

$$\begin{aligned} \dot{\sigma}_{\alpha\beta} = & 2\bar{G} \left[\dot{\varepsilon}_{\alpha\beta} + \frac{\bar{v}}{1-\bar{v}} \delta_{\alpha\beta} \dot{\varepsilon}_{\gamma\gamma} - \frac{1+\bar{v}}{1-\bar{v}} \dot{\alpha} \dot{T} \delta_{\alpha\beta} \right] \\ & - 3f G_f B_f \bar{\sigma}_f^{n_f-1} \left[S_{\alpha\beta}^f + \frac{v_f}{(1-v_f)} \delta_{\alpha\beta} S_{\gamma\gamma}^f \right] \\ & - 3(1-f) G_m B_m \bar{\sigma}_m^{n_m-1} \left[S_{\alpha\beta}^m + \frac{v_m}{(1-v_m)} \delta_{\alpha\beta} S_{\gamma\gamma}^m \right] \end{aligned} \quad (49)$$

where Greek subscripts range over 1 & 2 and where

$$\frac{\bar{v}}{1-\bar{v}} = \left[f G_f \frac{v_f}{1-v_f} + (1-f) G_m \frac{v_m}{1-v_m} \right] / \bar{G} \quad (50)$$

and

$$\hat{\alpha} = \left[f \alpha_f G_f \frac{1+v_f}{1-v_f} + (1-f) \alpha_m G_m \frac{1+v_m}{1-v_m} \right] / \left(\frac{1+\bar{v}}{1-\bar{v}} \bar{G} \right). \quad (51)$$

The fiber and matrix evolution laws for stress are identical to eq. (49) with $f = 0$ and $f = 1$ respectively. Being isotropic in the plane, this law suffers from the same deficiencies as the 3-d version regarding the orthotropy of the woven mat and any inequality between the warp and the woof. As before, this could be remedied with an anisotropic version of the law.

In steady state isothermal creep, the relationship between in plane components of stress and in plane components of strain rate are given by

$$\sigma_{\alpha\beta} = \frac{2}{3} \left[\frac{f}{B_f} \left(\frac{\dot{\epsilon}}{B_f} \right)^{\frac{1-n_f}{n_f}} + \frac{1-f}{B_m} \left(\frac{\dot{\epsilon}}{B_m} \right)^{\frac{1-n_m}{n_m}} \right] (\dot{\epsilon}_{\alpha\beta} + \dot{\epsilon}_{\gamma\gamma} \delta_{\alpha\beta}) \quad (52)$$

with $\sigma_{xz} = \sigma_{yz} = \sigma_{zz} = 0$ and with $\dot{\epsilon}$ given by eq. (40) but with $\dot{\epsilon}_{xz} = \dot{\epsilon}_{yz} = 0$. As in the 3-d case, this must be inverted numerically to establish a steady state isothermal creep rate for a given imposed stress.

When the fibers are elastic and non-creeping, the isothermal behavior at fixed applied plane stress is given in terms of the deviatoric stress by eq. (41) or (42) and

eq. (43). The expression for the deviatoric composite strain, eq. (44), still applies.

However, the composite strain obeys

$$\dot{\epsilon}_{\gamma\gamma} = \frac{3}{2}(1-f) \frac{G_m}{G} B \bar{\sigma}_m^{n-1} \frac{(1+\nu_m)(1-\bar{\nu})}{(1+\bar{\nu})(1-\nu_m)} S_{\gamma\gamma}^m \quad (53)$$

and

$$\dot{\epsilon}_{zz} = - \left[f \frac{\nu_f}{1-\nu_f} + (1-f) \frac{\nu_m}{1-\nu_m} \right] \dot{\epsilon}_{\gamma\gamma} - \frac{3}{2}(1-f) \frac{(1-2\nu_m)}{(1-\nu_m)} B \bar{\sigma}_m^{n-1} S_{\gamma\gamma}^m. \quad (54)$$

The latter result indicates that the volumetric strains can be relaxed to some extent by matrix creep. This contrasts with the 3-d case where complete compatibility of strains precludes such relaxation. The extent to which the relaxation occurs has not yet been calculated. However, if it is assumed that the relaxation can be complete so that the matrix volumetric strain is zero, then the fiber stress tends towards $\sigma_{\alpha\beta}/f$ and therefore the composite strain approaches

$$\epsilon_{ij} = \frac{1+\nu_f}{f E_f} \sigma_{ij} - \frac{\nu_f}{f E_f} \delta_{ij} \sigma_{\gamma\gamma} \quad (55)$$

which, of course, is restricted to plane stress. It can be seen that in uniaxial stress, the effective asymptotic modulus would now equal $f E_f$. A properly calculated solution for $\epsilon_{kk}(t)$ is required to investigate whether this result holds true.

Uniaxial Reinforcement with Long Brittle Fibers

The reinforcement configuration of interest now is once more that depicted in Fig. 1 and the loading will be restricted to a longitudinal steady stress σ_{zz} . The possibility will be taken into account that the fibers might be overstressed and therefore could fail. Only elastic fibers which break in a brittle manner will be considered, although ceramic fibers are also known to creep and possibly rupture due to grain boundary damage. Frictionally constrained fibers only will be considered since well bonded fibers will fail upon matrix cracking and vice versa. The case where the fibers have a deterministic strength S can be considered. In that situation, the fibers will remain intact when the fiber stress is below the deterministic strength level and they will break when the fiber stress exceeds the strength. The fracturing of the fibers could occur during the initial application of the load, in which case elastic analysis is appropriate. If the fibers survive the initial application of the load, then subsequent failure can occur as the matrix relaxes according to eq. (26) or (27) and the fiber stress increases. Thus the time elapsed before first fiber failure can be estimated based on eq. (26) or (27) by setting the fiber stress equal to the deterministic strength. This predicts that failure of a fiber will occur when

$$\sigma_m = [\sigma - f S]/(1 - f) \quad (56)$$

from which the time to failure can be computed through eq. (26) or (27). The failure of one fiber in a homogeneous stress state will cause a neighboring fiber to fail nearby because of the fiber/matrix shear stress interaction and the resulting localized load sharing around the broken fiber. Thus a single fiber failure will tend to cause a spreading of damage in the form of fiber breaks near a single plane across the section. This will lead to localized rapid creep and elastic strains in the matrix near the breaks perhaps giving rise to matrix failure. It follows therefore that tertiary failure of the

composite will tend to occur soon after the occurrence of one fiber failure when the fiber strength is deterministic.

Tertiary failure processes akin to this have been modelled by Phoenix and coworkers¹³⁻¹⁵ in the context of epoxy matrix composites. Indeed, they show that such tertiary failures can occur even when the fiber strength is statistical in nature. This mechanism will not be pursued further in this paper but some other basic results considered on the assumption that when there is a sufficient spread in fiber strengths such tertiary failures can be postponed well beyond the occurrence of first fiber failure or indeed eliminated completely. Thus, attention will be focused on fibers which obey the classical Weibull model that the probability of survival of a fiber of length L stressed to a level σ_f is given by

$$P_s = \exp \left[- \frac{L}{L_g} \left(\frac{\sigma_f}{S} \right)^m \right] \quad (57)$$

where L_g is a datum gauge length, S is a datum strength and m is the Weibull modulus. Clearly the results given below can be generalized to account for variations on the statistical form which differ from eq. (57). However, the basic ideas will remain the same.

Long Term Creep Threshold Consider a specimen of length L_s containing a very large number of wholly intact fibers. A stress σ is suddenly applied to the specimen parallel to the fibers. The temperature has been raised to the creep level already and is now held fixed. Upon first application of the load, some of the fibers will break. The sudden application of the load means that the initial response is elastic. This elastic behavior has been modelled by Curtin¹⁶ among others but details will not be given here. If the applied stress exceeds the ultimate strength of the composite in this elastic mode of

response, then the composite will fail and long term creep is obviously not an issue. However, it will be assumed that the applied stress is below the elastic ultimate strength and therefore creep can commence. It should be noted, however, that matrix cracking can occur in the ceramic matrix and the characteristics of creep relaxation would depend on the degree of matrix cracking. However, this aspect of the problem will not be considered in detail. For cases where there is matrix cracking and for which the specimen length L_s is sufficiently long, Curtin¹⁶ has given the theoretical prediction that the ultimate elastic strength is

$$S_u = f [4 L_g S^m \tau / D (m + 2)]^{1/(m+1)} (m + 1)/(m + 2) \quad (58)$$

where τ is the interface shear strength between the fiber and the matrix and D is the diameter of the fibers. The interface shear strength is usually controlled by friction. For specimens shorter than δ_c , the ultimate brittle strength exceeds S_u where δ_c is given by¹⁶

$$\delta_c = [S L_g^{1/m} D/2 \tau]^{m/(m+1)}. \quad (59)$$

This critical length is usually somewhat less than the datum gauge length.

When the applied stress σ is less than S_u , creep of the matrix will commence after application of the load. During this creep, the matrix will relax and the stress on the fibers will increase. Therefore, further fiber failure will occur. In addition, the process of matrix creep will depend on the extent of prior fiber failure and, as mentioned previously, on the amount of matrix cracking. The details will be rather complicated. However, the question of whether steady state creep or, perhaps, rupture will occur or whether sufficient fibers will survive to provide an intact elastic specimen can be answered by consideration of the stress in the fibers after the matrix has been assumed

to relax completely. Clearly, when the matrix carries no stress, the fibers will at least fail to the extent they do in a dry bundle. It is possible that a greater degree of fiber failure will be caused by the transient stresses during creep relaxation, but this effect has not yet been modelled. Instead, the dry bundle behavior will be used to provide an initial estimate of fiber failure in these circumstances.

Given eq. (57), the elastic stress strain curve for a fiber bundle is

$$\sigma = f E_f \epsilon \exp \left[-\frac{L_s}{L_g} \left(\frac{E_f \epsilon}{S} \right)^m \right]. \quad (60)$$

Thus when a stress σ is applied to the composite, creep will occur until the strain has the value consistent with eq. (60). Numerical inversion of eq. (60) can be used to establish this strain. The stress-strain curve in eq. (60) has a stress maximum when

$$\epsilon = \frac{S}{E_f} \left(\frac{L_g}{m L_s} \right)^{\frac{1}{m}} \quad (61)$$

with a corresponding stress level given by

$$\sigma_c = f S \left(\frac{L_g}{m L_s} \right)^{\frac{1}{m}} \exp(-1/m). \quad (62)$$

This result is plotted as a function of m in Fig. 2. If $\sigma < \sigma_c$ the composite will creep until the strain is consistent with eq. (60) and thereafter no further creep strain will occur. Of course, the non creeping state will be approached asymptotically. (It should be noted that due to possible fiber failure during the creep transient, the true value for σ_c may lie below the result given in eq. (62).) For an applied composite stress equal to

or exceeding σ_c , creep will not disappear with time because all of the fibers will eventually fail and the strain will continue to accumulate.

The critical threshold stress for ongoing creep given by eq. (62) is specimen length dependent. For very long specimens, the threshold stress is low whereas short specimens will require a high stress for ongoing creep to continue without limit. On the other hand, the ultimate brittle strength as given by eq. (58) for a composite specimen longer than δ_c is specimen length independent. Thus there are always specimens long enough so that σ_c is less than S_u . This means that the specimen can be loaded without failure initially and if σ exceeds σ_c , the specimen will go into a process of long term creep. (It should be remembered, however, that this model is based on the assumption that tertiary failure is delayed and does not occur until a substantial amount of matrix creep has occurred.) For shorter specimens, the relationship between σ_c and S_u depends on the material parameters appearing in eq. (58) and (62). However, for typical values of the parameters, σ_c is less than S_u so that there is usually a window of stress capable of giving rise to long term creep without specimen failure when the specimen length exceeds δ_c . Typical values for the parameters are given by, among others, Hild et al.¹⁷. From these parameters, predictions for σ_c can be made. For example, a LAS matrix composite containing 46% of SiC (Nicalon) fibers (m equals 3 or 4) is predicted to have a value for σ_c between 400 MPa and 440 MPa for a specimen length of 25 mm whereas its measured ultimate brittle strength is between 660 MPa and 760 MPa. At 250 mm specimen length, the long term creep threshold σ_c is predicted to fall to the range 185 MPa to 250 MPa. Similarly, a CAS matrix composite with 37% SiC (Nicalon) fibers (m equals 3.6) in a specimen length of 25 mm is predicted to suffer long term creep if the stress exceeds 160 MPa whereas the measured ultimate brittle strength is 430 MPa. For a 250 mm specimen length, this creep threshold is predicted to fall to 85 MPa. Thus it is clear that in some practical cases, applied stresses which are modest fractions of the elastic ultimate strength will cause long term creep.

Steady State Creep For specimens which have (i) previously experienced an applied stress exceeding the long term creep threshold or (ii) which had every fiber broken prior to testing or service (e.g. during processing) or (iii) which had few fibers intact to begin with so that initially the long term creep threshold is much lower than σ_c as predicted by eq. (62), a prediction of the long term creep behavior can be made. Prior to this state, there will, of course, be a transient which involves matrix creep and, perhaps, the fragmentation of fibers. This transient has not been fully modelled. Only a rudimentary assessment of the creep behavior has been made revealing the following features.

For those composites initially having some of the fibers intact, there will always be some which must be stretched elastically. This will require a stress which will tend towards the value given by eq. (60) with f replaced by f_i , the volume fraction of fibers initially intact. If a relaxation test were carried out, the stress would asymptote to the level predicted by eq. (60). The remaining broken fibers will interact with the matrix in a complex way, but at a given strain and strain rate, a characteristic stress contribution can be identified in principle. Details have not been worked out. However, the total stress would be the sum of the contribution from the broken and unbroken fibers. If the transient behavior is ignored (i.e. assumed to die away relatively fast compared to the strain rate) a basic model can be constructed.

Steady State Creep with Broken Fibers First, consider a composite with a volume fraction f of fibers, all of which are broken. There are two possible models for the steady state creep behavior of such a material. In one, favored by Mileiko¹⁸ and Lilholt¹⁹ among others, the matrix serves simply to transmit shear stress from one fiber to another and the longitudinal stress in the matrix is negligible. The kinematics of this model requires void space to increase in volume at the ends of the fibers. However,

with broken fibers there is no inherent constraint on this occurring. Furthermore, if matrix cracking has occurred, the matrix will not be able to sustain large amounts of longitudinal tension and its main role will be to transmit shear from fiber to fiber. Indeed, matrix cracking will probably promote this mode of matrix flow since there will be no driving stress for other mechanisms of straining. The other model, favored by McLean²⁰ and developed by Kelly and Street²¹ involves a stretching flow of the matrix between fibers at a rate equal to the macroscopic strain rate of the composite material. This requires substantial axial stress in the matrix. In addition, volume is preserved by the flow and there is no need for space to develop at the end of the fiber. The model requires a considerable matrix flow to occur transporting material from the side of a given fiber to its end and the injection of matrix in between adjacent ends of the broken fibers. There is good reason to believe that the Mileiko¹⁸ pattern of flow prevails when there are broken fibers.

In a version of the Mileiko¹⁸ model in which it is assumed that each of six neighboring fibers has a break somewhere within the span of the length of a given fiber but that the location of those breaks is random within the span, the relationship between the steady state creep rate and the composite stress is (McMeeking, unpublished work)

$$\dot{\epsilon} = g(n, f) (D/L)^{n+1} B \sigma^n \quad (63)$$

where L is the average length of the broken fiber segments and

$$g(n, f) = 2\sqrt{3} \left[\frac{\sqrt{3}(2n+1)}{2nf} \right]^n \left(\frac{1 - f^{\frac{n-1}{2}}}{(n-1)} \right) \quad (64)$$

when $n \neq 1$ and

$$g(1, f) = (9/f) \ln(1/\sqrt{f}). \quad (65)$$

These functions have been computed for uniform fiber length and based on a hexagonal shape for the fiber even though interpreted to be circular. That explains why creep strength goes to infinity at $f = 0$ rather than at f less than 1. In this creep model, the influence of both volume fraction and the aspect ratio L/D on the strain rate is clear with both having a strong effect. As noted, this model could serve as a constitutive law for the creep of a material in which all of the fibers are broken to fragments of average length L . In addition, it could be used for short fiber composites which have weak bonds between the fiber end and the matrix so that debonding can readily occur and void space can develop as a result. However, the aspect ratio L/D should be large so that the Mileiko¹⁸ flow pattern will occur and end effects can be neglected when the composite creep law is computed.

The shear stress transmitted to a fiber is limited to the shear strength τ . As a result, the formula given in eq. (63) is valid only up to a composite macroscopic stress of

$$\sigma = \frac{2nf}{2n+1} \left(\frac{L}{D} \right) \tau \quad (66)$$

for both the linear and nonlinear cases. According to the model, at this level of applied stress, the shear stress on the fiber interface will start to exceed τ . Therefore, at stresses higher than the value given in eq. (66), the strain rate will exceed the level predicted in eq. (63). This situation will persist in the presence of matrix cracks up to a composite macroscopic stress of

$$\sigma_{\text{LIM}} = f \tau L/D \quad (67)$$

at which stress the entire fiber surface is subject to a shear stress equal in magnitude to τ . Then, the mechanism represented by eq. (63) provides an indeterminate strain rate as in rate independent plasticity. Thus σ_{LIM} can be thought of as a yield stress. This concept is probably satisfactory for materials with many matrix cracks so that there is no constraint on stretching the matrix. However, when there are no matrix cracks, the strain rate is probably controlled by the mechanism which generates void space at the fiber ends. This has been considered to require negligible stress in the version of the model leading to eq. (63). For a proper consideration of the limit behavior, the contribution to the stress arising from void development at the fiber ends should be taken into account.

The Effect of Fiber Fracture If the stress applied to the composite is increased, the stress sustained by fibers will increase also. When the probability of survival of fibers obeys the statistical relationship given by eq. (57), the effect of a raised stress will be to fracture more fibers, with a preference for breaking long fibers. This will have the effect of reducing the average fiber length L and therefore raising the strain rate at a given applied stress as can be deduced from eq. (63). Therefore, the composite will no longer have a simple power law behavior in steady state creep since the fiber fragment length will depend on the largest stress which the composite material has previously experienced. In this regard, the elastic transients will play an important role in determining the fiber fragment length. However, the average fragment length in steady state creep will generally be smaller than the average fragment length arising during initial elastic response. Therefore, some guidance can be obtained from a model designed to predict the steady state creep response only.

For the Mileiko¹⁸ model of composite creep leading to the steady state creep rate for fixed fiber length given in eq. (63), a rudimentary fiber fragment length model gives (McMeeking, unpublished work)

$$L = (m+1) \left[\frac{(n+1) f S}{(2n+1) \sigma} \right]^m L_g \quad (68)$$

subject to L being less than the specimen length. When a stress σ is applied to the composite material and steady state is allowed to develop, the average length for the fiber fragments is predicted by eq. (68). This model is by no means precise, based as it is on some approximations in the calculations as well as the notion that all fibers can be treated as if they had the same length. However, the model conveys the important notion that the fiber fragment length will fall as the applied stress is increased.

The fiber fragment average length during steady state creep can be substituted into eq. (63) from which results

$$\dot{\epsilon} = h(n, f, D/L_g, m, S) B \sigma^{n+m+nm} \quad (69)$$

where h is a rather complicated function of its arguments and can readily be calculated. A significant conclusion is that the creep index for the composite is no longer just n but is $n+m+nm$. Thus a ceramic matrix material with a creep index for the matrix of 1 will have composite creep index of $2m+1$. In the case of a fiber with a Weibull modulus of $m=4$, the composite creep index will be 9. Similar effects will be apparent in composites with a nonlinearly creeping ceramic matrix, say with $n=2$. It has been observed that *metal* matrix composites with noncreeping reinforcements often have a creep index which differs from that of the matrix^{5,22} and the effect is usually attributed

to damage of the fibers or of the interface. It can be expected that ceramic matrix composites will exhibit a similar behavior.

It should be noted that the model leading to eq. (69) is incomplete since the stress required to cause the enlargement of void space at the fiber breaks is omitted from consideration. At high strain rates this contribution to stress can be expected to dominate other contributions. Therefore at high stress or strain, the creep behavior will diverge from eq. (69) and perhaps exhibit the n th power dependence on stress as controlled by the matrix. The creep rate at these high stresses can be expected to *exceed* the creep rate of the matrix at the same applied stress since the void space at the fiber ends is a form of damage.

Creep of an Initially Undamaged Composite The issue to be addressed in this section is the long term behavior of a composite stressed above the threshold σ_c given by eq. (62) which means that the specimen will creep continuously. As in the immediately preceding sections, elastic transient effects will be omitted from the model of long term creep of the initially undamaged composite. No model exists as yet for the transient behavior, but there is little doubt that the transient behavior is important. Many composite materials in service at creep temperatures will probably always respond in the transient stage since the time for that to die away will typically be rather long. However, a quasi-steady state model, as before, will give some insight into the state towards which the transients will be taking the material. However, the model presented below is rather selective, since it includes some elastic effects and ignores others. It is not known how deficient this feature of the model is. Perhaps the material state will evolve rather rapidly towards the state predicted below and therefore the model may have some merit.

The specimen is composed of a mixture of matrix, unbroken fibers and broken fibers. The volume fraction of intact fibers is given by eq. (57) with $L = L_s$, the specimen length. To the neglect of transients, the macroscopic stress supported by these intact fibers is given by eq. (60). The strain will now exceed the level of eq. (61) associated with the ultimate strength of the fiber bundle. Therefore the stress supported by the intact fibers will be less than σ_c which is the ultimate strength of the fiber bundle without matrix. The applied stress exceeds σ_c and the balance in excess of the amount borne by the intact fibers will cause the composite material to creep.

The steady state result given in eq. (69) will be taken to express the creep behavior controlled by the broken fibers. The volume fraction of broken fibers is

$$f_b = 1 - \exp \left[-\frac{L_s}{L_g} \left(\frac{E_f \epsilon}{S} \right)^m \right] \quad (70)$$

and a material with this volume fraction of broken fibers creeping at a rate $\dot{\epsilon}$ will support a stress

$$\sigma_b = [\dot{\epsilon}/B \ h(n, f_b, D/L_g, m, S)]^{1/p} \quad (71)$$

where

$$p = n + m + nm \quad (72)$$

which comes directly from eq. (69). The total stress sustained by the composite material is therefore

$$\sigma = f_b \sigma_b + \sigma_u \quad (73)$$

where σ_u is the contribution due to unbroken fibers. This leads to

$$\sigma = f_b [\dot{\epsilon} / B h(f_b)]^{1/p} + f E_f \epsilon \exp \left[-\frac{L_s}{L_g} \left(\frac{E_f \epsilon}{S} \right)^m \right] \quad (74)$$

which can be seen to be a rather nonlinear Kelvin-Voigt material in which the stress is the sum of a viscous element and an elastic element both of which are nonlinear. As the strain increases, the second term on the right hand side of eq. (74) (i.e. the term due to the intact fibers) will diminish and become rather small when only a few unbroken fibers are left. At the same time, f_b will approach f and so the strain rate will approach the steady state rate for a material in which all of the fibers are broken. However, as long as a few fibers remain intact, the creep behavior will not precisely duplicate that for the fully broken material. This transient effect will be compounded by the redistribution of stress from the matrix to the fibers which will occur both after the first application of load to the composite material and after each fracture of a fiber, both effects having been omitted from this version of the model.

Creep of Materials with Strong Interfaces

It seems unlikely that long fiber ceramic matrix composites with strong bonds will find application because of their low temperature brittleness. However, for completeness, a model which applies to the creep of such materials can be stated. It is that due to Kelly and Street²¹. It is possible also that the model applies to aligned whisker reinforced composites since they may have strong bonds. In addition, the model has a wide currency since it is believed to apply to weakly bonded composites as

well. However, the Mileiko¹⁸ model predicts a lower creep strength for weakly bonded or unbonded composites and therefore is considered to apply in that case.

The Kelly and Street²¹ model uses the notion that creep of the composite material can be modelled by the behavior of a unit cell. Each unit cell contains one fiber plus matrix around it so that the volume of the fiber divided by the volume of the unit cell equals the fiber volume fraction of the composite material. The perimeter of the unit cell is assumed to be deforming at a rate consistent with the macroscopic strain rate of the composite material. (It can be observed at this stage that this notion is inconsistent with the presence of transverse matrix cracks which would make it impossible to sustain the longitudinal stress necessary to stretch the matrix. This is an additional reason why the Kelly and Street²¹ model is not likely to be applicable to unbonded ceramic matrix materials which are likely to have matrix cracks.) Only steady state creep of materials with aligned reinforcements which are shorter than the specimen is considered. The unit cell is assumed to conserve volume. This means that material originally adjacent to the reinforcement must flow around the fiber and finish up at its end. This phenomenon has to occur when the end of the fiber or whisker is strongly bonded to the matrix. For this reason, the Kelly and Street²¹ model is considered to be relevant to materials with strong bonds.

Kelly and Street²¹ analyzed this model but their deductions were not consistent with the mechanics. McMeeking²³ has remedied this deficiency for nonlinear materials. His results for $n = 2$ are relevant to composite materials with nonlinearly creeping ceramic matrices which tend to have low creep indices. In that case, the steady state creep rate is given by eq. (63) with $n = 2$ and

$$g(2, f) = \frac{75\sqrt{3}}{8f^2} \left(\frac{1}{2} - \frac{8}{5}\sqrt{f} + \frac{3}{2}f - \frac{1}{2}f^2 + \frac{1}{10}f^3 \right) \quad (75)$$

which is invalid for $f = 0$. When f is close to zero a different form should be used which accounts for the matrix stress so that the matrix creep law is recovered smoothly as the volume fraction of fiber disappears. This result is developed below and is given in eq. (77). Comparison of eq. (75) with eq. (64) for $n = 2$ will show that the model of Kelly and Street²¹ creeps more slowly than the Mileiko¹⁸ law confirming that the Mileiko model is the preferred one when it is kinematically admissible.

It is thought that at higher temperatures, the interface between the fiber and the matrix becomes weak and sliding occurs according to the constitutive law given in eq. (3). In that case, creep of a composite with a well bonded interface obeys eq. (63) with $n = 2$ and²³

$$g(2, f) = \frac{25\sqrt{3}}{8f^2} \left[3 \left(\frac{1}{2} - \frac{8}{5}\sqrt{f} + \frac{3}{2}f - \frac{1}{2}f^2 + \frac{1}{10}f^3 \right) + \frac{(1-f)^3 \bar{B}}{2DB} \right] \quad (76)$$

This form for g is identical with that in eq. (75) when $\bar{B} = 0$. Thus, sliding at the interface increases the creep rate at a given stress. If \bar{B}/BD is very large, signifying a very weak interface, then the interface term will dominate the matrix term in eq. (76). It should be noted that there is a relative size effect, with large diameter fibers making sliding less important.

At large strain rates, stretching of the matrix as it slides past the matrix will contribute to the creep strength. Under those circumstances, the term $g(2, f)$ in eq. (63) should be replaced by²³

$$\bar{g}(2, f) = \left[1/\sqrt{g(2, f)} + (1-f) \left(\frac{D}{L} \right)^{1.5} \right]^{-2} \quad (77)$$

where, in eq. (77), $g(2, f)$ is to be calculated according to eq. (76). Note that as $g(2, f)$ becomes large (i.e., the composite strain rate is large because either f is small or \bar{B} is large), the composite strain rate will approach

$$\dot{\epsilon} = \bar{B} [\sigma / (1 - f)]^2 \quad (78)$$

which is the rate that would prevail if the fibers were replaced by long cylindrical holes.

Creep of Materials with a Linear Rheology The equivalent correction to the Kelly and Street²¹ model for cases where the matrix creep obeys a linear rheology ($n = 1$) was not given by McMeeking²³. However, consideration of this case can be included in a model with accounts for the ability of a well bonded interface between the fiber and the matrix to sustain sliding according to eq. (3) and in which mass transport may cause the effect described by eq. (4). In unpublished work, McMeeking has given the steady state creep law for the composite material in these circumstances to be

$$\sigma = \frac{\dot{\epsilon}}{\bar{B}} \left[h(f) \left(\frac{L}{D} \right)^2 + 1 - f \right] \quad (79)$$

where

$$\begin{aligned} 1/h(f) = & \frac{9}{8f} \left[4 \ln(1/\sqrt{f}) - 3 + 4f - f^2 \right] \\ & + \frac{3 \bar{B} (1-f)^2}{f \bar{B} D} + \frac{48 f \mathcal{D}}{\bar{B} D^3} \end{aligned} \quad (80)$$

Recall that if sliding between the fiber and the matrix occurs readily, \bar{B} will be large and also rapid mass transport is associated with a large value of \mathcal{D} .

It is thought that as the temperature is increased, the relative importance of sliding and mass transport is enhanced. Thus at low creep temperatures, $\bar{B}/B D$ and $\mathcal{D}/B D^3$ would be small. Then only the first term on the right hand side of eq. (80) will be important and when L/D is large, as required by this asymptotic model, the creep strength will be high. As the temperature is increased, either $\bar{B}/B D$ or $\mathcal{D}/B D^3$ or both will increase in magnitude. When they become large, $h(f)$ will become small and the creep strength of the composite will fall, as can be seen in eq. (79). However, if $h(f)$ becomes negligible, the steady state creep law for the composite will be approximately

$$\dot{\epsilon} = B \sigma / (1 - f). \quad (81)$$

As in the case of the quadratic matrix rheology, the creep behavior when sliding dominates (or as in this new case mass transport is significant) is the same as for a material containing cylindrical holes instead of fibers even if the interface is nominally well bonded. This behavior will occur when $h(f)$ is much smaller than $(D/L)^2$ so that the relevant term containing $h(f)$ in eq. (79) is negligible.

It should be noted that the creep behavior is affected in the way predicted by eq. (79) and (80) whether interface sliding occurs readily or mass transport occurs rapidly at the interface between the fiber and the matrix. It follows that rapid sliding by itself is sufficient to diminish the creep strength of the composite material and long range mass transport at the interface is not necessary. Note also that if the matrix does not creep (i.e. $B = 0$) neither sliding nor mass transport will have any effect on creep and the composite will be rigid. This feature arises because the matrix must deform when any sliding or mass transport occurs at the interface.

An additional feature is a size effect in the creep law when sliding or mass transport at the interface are significant enough to affect the composite behavior. A small diameter fiber (i.e. small D) will tend to enhance the effect of sliding or mass

transport on the creep rate of the composite and the composite will creep faster. Similarly, a large diameter fiber will tend to suppress the effect of sliding or mass transport and the creep strength of the composite will correspondingly be increased. Similar effects tied to grain size are known to occur in the creep of ceramics and metals controlled by mass transport on the grain boundaries¹. Note that the mass transport term in eq. (80) is much more sensitive to fiber diameter than the sliding term. The cubic dependence on fiber diameter in the mass transport controlled term will cause it to disappear rapidly as D is increased. However, if both \mathcal{D} and \bar{B} are substantial, the creep strength of a composite will not be improved substantially by increase of fiber diameter until both the effects of sliding and mass transport are suppressed. It seems likely that in practice this will mean that mass transport will be relatively easy to eliminate as a contributor to rapid creep strain of the composite by increase of the fiber diameter, whereas the effect of sliding at a given temperature will be more persistent. Furthermore, there is also an interplay with volume fraction, with the importance of interface sliding being greater at low volume fractions of fibers and mass transport being more significant at higher volume fractions.

Discussion

As previously noted, this chapter has been concerned mainly with those models for the creep of ceramic matrix composite materials which feature some novelty which cannot be represented simply by taking models for the linear elastic properties of a composite and, through transformation, turning the model into a linear viscoelastic one. If this were done, the coverage of models would be much more comprehensive since elastic models for composites abound. Instead, it was decided to concentrate mainly on phenomena which cannot be treated in this manner. However, it was necessary to introduce a few models for materials with linear matrices which could have been

developed by the transformation route. Otherwise, the discussion of some novel aspects such as fiber brittle failure or the comparison of nonlinear materials with linear ones would have been incomprehensible. To summarize those models which could have been introduced by the transformation route, it can be stated that the inverse of the composite linear elastic modulus can be used to represent a linear steady state creep coefficient when the kinematics are switched from strain to strain rate in the relevant model.

No attempt has been made to discuss in a comprehensive manner models which are based on finite element calculations or other numerical analyses. Only some results of Schmauder and McMeeking¹⁰ for transverse creep of power law materials were discussed. The main reason that such analyses were in general omitted is that they tend to be in the literature for a small number of specific problems and little has been done to provide comprehensive results for the range of parameters which would be technologically interesting - i.e. volume fractions of reinforcements from zero to 60%, reinforcement aspect ratios from 1 to 10^6 , etc.. Attention was restricted in this chapter to cases where comprehensive results could be stated. In almost all cases, this means that only approximate models were available for use. Furthermore, numerical analyses for creep in the literature tend to be for metal matrix composites and so use creep indices which are rather high for ceramic matrices. Indeed, this latter fault applies to the finite element calculations so far performed by Schmauder and McMeeking¹⁰ even though there was an attempt to be comprehensive. Those finite element results which are available in the literature such as the work by Dragone and Nix²⁴ are very valuable and provide accurate results for a number of specific cases against which the more approximate models discussed in this chapter can be checked. A limited amount of this checking for a single model has been done by McMeeking²³ in comparison with the Dragone and Nix²⁴ calculations. The results show that the approximate model is reasonably accurate. However, more extensive checking of the approximate models is

required and to do this in many cases it will be necessary to create the finite element analyses.

Also omitted from this chapter was any attempt to compare the models with experiments. This would require a lengthy chapter by itself and some comparisons are given elsewhere in this book. In addition, limited data are available for such comparisons in general. For metals, there are some successful comparisons⁵ and some unsuccessful ones²². It seems that when there is good knowledge of the material properties and the operating mechanisms, the right model can be chosen, but lack of such knowledge makes it virtually impossible to identify which features must be present in the model. Thus, multidisciplinary work is necessary to understand the microstructure, to identify the mechanisms and to select and develop the appropriate model. An example of such an effort, although for the closely related subject of the plastic yielding of a metal matrix composite, is the work of Evans, Hutchinson and McMeeking²⁵, where careful control of the metallurgy and the experiments was used to confirm the validity of the models.

Acknowledgment

This research was performed while the author was supported by the DARPA University Research Initiative at the University of California, Santa Barbara contract ONR N00014-86-K0753.

References

- ¹ M. F. Ashby and H. Frost, Deformation Maps, Pergamon Press, Oxford (1982).

- 2 R. M. Christensen, Theory of Viscoelasticity: An Introduction, Academic Press, New York (1982).
- 3 R. A. Schapery, "On the Characterization of Nonlinear Viscoelastic Materials," *Polymer Engineering and Science*, **9**, 295-310 (1969).
- 4 R. Hill, "Elastic Properties of Reinforced Solids: Some Theoretical Principles," *J. Mech. Phys. Solids*, **11**, 357-72 (1963).
- 5 M. McLean, "Creep Deformation of Metal-Matrix Composites," *Composites Science and Technology*, **23**, 37-52 (1985).
- 6 D. McDanel, R. A. Signorelli and J. W. Weeton, NASA Report No. TND-4173, NASA Lewis Research Center, Cleveland, Ohio (1967).
- 7 R. M. Christensen, Mechanics of Composite Materials, Wiley-Interscience, New York (1979).
- 8 S. Jansson and F. A. Leckie, "Mechanical Behavior of a Continuous Fiber-Reinforced Aluminum Matrix Composite Subjected to Transverse and Thermal Loading," *Journal of the Mechanics and Physics of Solids*, **40**, 593-612 (1992).
- 9 G. Bao, J. W. Hutchinson and R. M. McMeeking, "Particle Reinforcement of Ductile Matrices against Plastic Flow and Creep," *Acta Metallurgica et Materialia*, **39**, 1871-1882 (1991).
- 10 S. Schmauder and R. M. McMeeking, unpublished work (1992).
- 11 J. E. Ashton, J. C. Halpin and P. H. Petit, Primer on Composite Materials Analysis, Technomic Publishing, Stanford, CT (1969).
- 12 J. M. Whitney and R. L. McCullough, Micromechanical Materials Modeling, (Delaware Composites Design Encyclopedia, Vol. 2), Technomic Publishing, Lancaster, PA (1989).

- 13 S. L. Phoenix, P. Schwartz and H. H. Robinson IV, "Statistics for the Strength and Lifetime in Creep-Rupture of Model Carbon/Epoxy Composites," *Composites Science and Technology*, **32**, 81-120 (1988).
- 14 D. C. Lagoudas, C.-Y. Hui and S. L. Phoenix, "Time Evolution of Overstress Profiles Near Broken Fibers in a Composite with a Viscoelastic Matrix," *International Journal of Solids and Structures*, **25** 45-66 (1989).
- 15 H. Otani, S. L. Phoenix and P. Petrina, "Matrix Effects on Lifetime Statistics for Carbon Fibre-Epoxy Microcomposites in Creep Rupture," *Journal of Materials Science*, **26**, 1955-1970 (1991).
- 16 W. A. Curtin, "Theory of Mechanical Properties of Ceramic Matrix Composites," *Journal of the American Ceramic Society*, **74**, 2837-2845 (1991).
- 17 F. Hild, J.-M. Domergue, F. A. Leckie and A. G. Evans, "Tensile and Flexural Ultimate Strength of Fiber-Reinforced Ceramic-Matrix Composites," to be published (1992).
- 18 S. T. Mileiko, "Steady State Creep of a Composite Material with Short Fibres," *Journal of Materials Science*, **5**, 254-261 (1970).
- 19 H. Lilholt, "Creep of Fibrous Composite Materials," *Composites Science and Technology*, **22**, 277-294 (1985).
- 20 D. McLean, "Viscous Flow of Aligned Composites," *Journal of Materials Science*, **7**, 98-104 (1972).
- 21 A. Kelly and K. N. Street, "Creep of Discontinuous Fibre Composites II, Theory for the Steady State," *Proceedings of the Royal Society, London*, **A328**, 283-293 (1972).
- 22 T. G. Nieh, "Creep Rupture of a Silicon Carbide Reinforced Aluminum Composite," *Metallurgical Transactions A*, **15A**, 139-146 (1984).

- 23 R. M. McMeeking, "Power Law Creep of a Composite Material Containing Discontinuous Rigid Aligned Fibers," to appear in *International Journal of Solids and Structures* (1992).
- 24 T. L. Dragone and W. D. Nix, "Geometric Factors Affecting the Internal Stress Distribution and High Temperature Creep Rate of Discontinuous Fiber Reinforced Metals," *Acta Metallurgica et Materialia*, **38**, 1941-1953 (1990).
- 25 A. G. Evans, J. W. Hutchinson and R. M. McMeeking, "Stress-Strain Behavior of Metal Matrix Composites with Discontinuous Reinforcements," *Scripta Metallurgica et Materialia*, **25**, 3-8 (1991).

Figure Captions

Fig. 1 A uniaxially reinforced fiber composite.

Fig. 2 Threshold for long term creep of a uniaxially reinforced composite as a function of Weibull modulus for the fiber strength distribution.

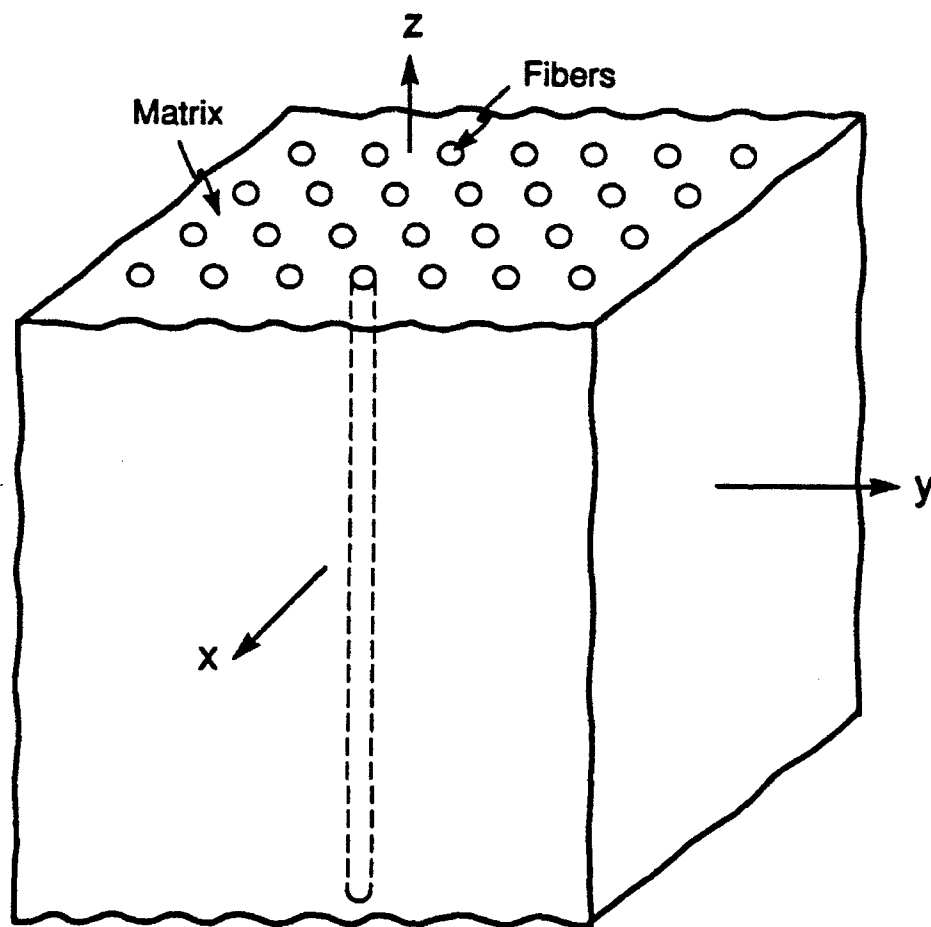


Fig. 1

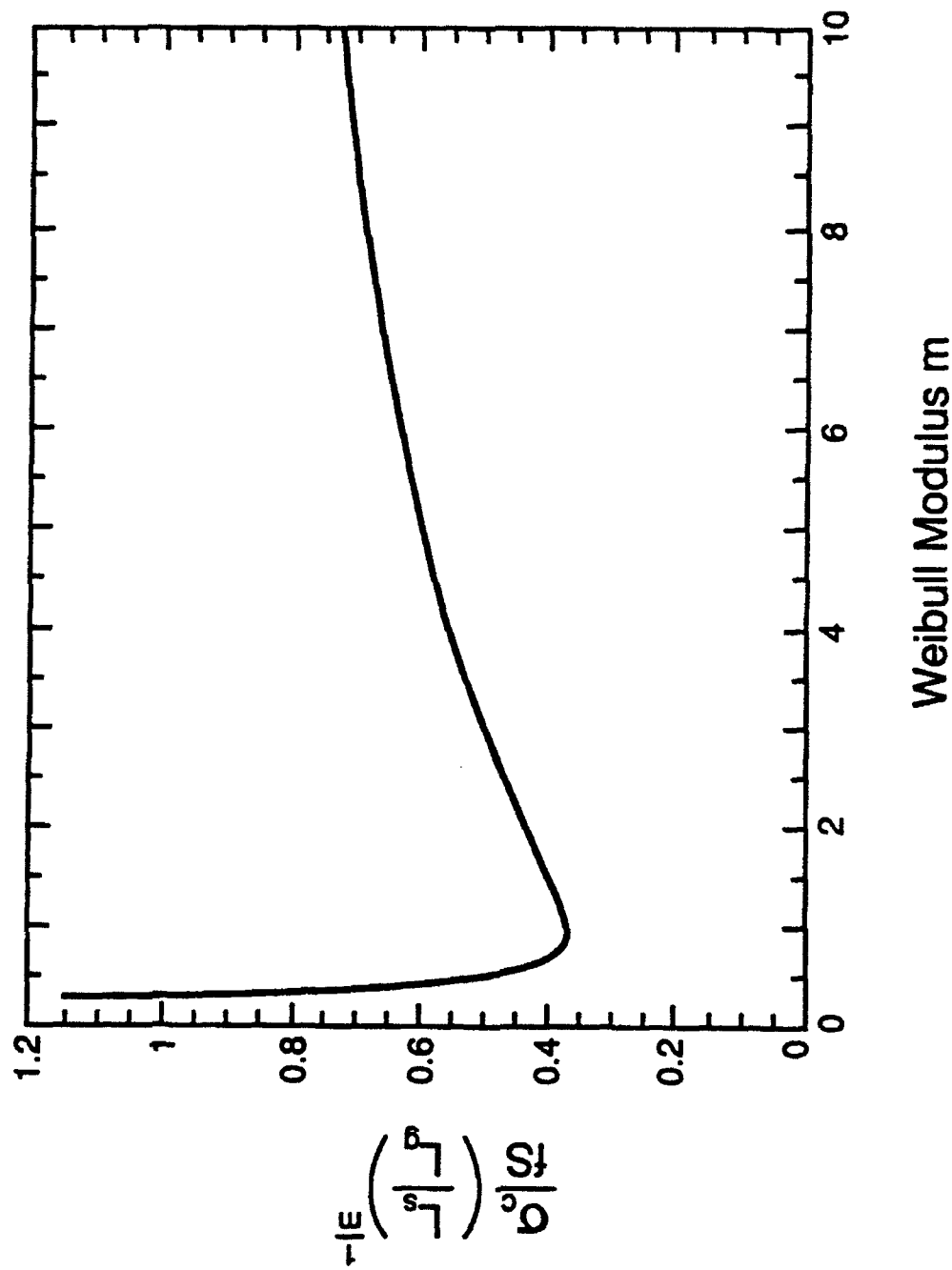
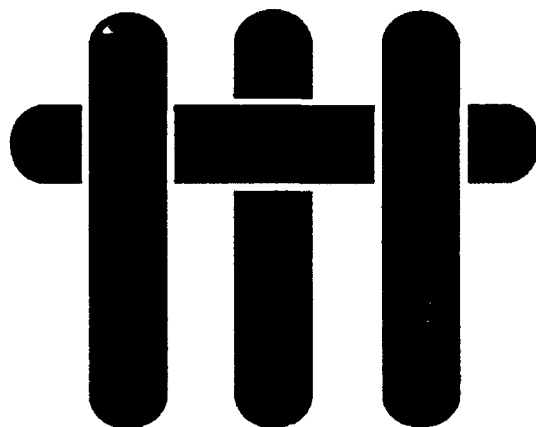


Fig. 2

M A T E R I A L S



THE CREEP AND FRACTURE RESISTANCE OF γ -TiAl REINFORCED WITH Al_2O_3 FIBERS

(Accepted for publication in Acta. Metall. et Mater., Mar. '93)

by

C.H. Weber, J.Y. Yang, J.P.A. Löfvander,
C.G. Levi and A.G. Evans

Materials Department
College of Engineering
University of California
Santa Barbara, California 93106-5050

ABSTRACT

The creep properties and microstructures of γ -TiAl reinforced with continuous Al_2O_3 fibers have been investigated. Novel fiber coating concepts have been used to create "weak" fiber/matrix interfaces that allow the fibers to impart enhanced creep and fracture resistance, simultaneously. Several major facets of the creep behavior were identified. Under conditions of limited fiber fracture, creep-resistant sapphire fibers were found to limit *longitudinal* creep to a short transient strain, consistent with model predictions. At the same time, the interlaminar *shear* creep properties were found to be insensitive to fiber reinforcement, again consistent with predictions. It was also demonstrated that the "weak" interfaces were maintained after creep and resulted in significant levels of toughening.

1. INTRODUCTION

Titanium-aluminides have potential as high-temperature structural materials for aerospace applications. Compared to Ti-based alloys, these materials have superior elastic moduli and high-temperature strength, as well as improved oxidation and creep resistance.^{1, 2} These factors also give γ -TiAl an advantage over α_2 -Ti₃Al for high temperature applications. Two key problems with γ -TiAl are its low toughness and ductility below 700°C, as well as inadequate creep strength for a number of proposed applications. There have been several successful demonstrations of improved toughness³⁻⁶ but more limited assessment of the approaches for enhancing creep strength. Attempts to improve the creep resistance by solid-solution and particulate strengthening have only had limited success.⁷⁻⁹ A potentially more powerful approach involves reinforcing with unidirectional continuous fibers. Such fibers are also capable of enhancing strength and toughness if the appropriate fiber coating is used.¹⁰

An appreciable literature exists concerning models of the effect of fibers on the longitudinal¹¹⁻¹⁷ and transverse¹⁸ creep characteristics of unidirectional composites. However, there have been few experimental studies on systems having practical utility at elevated temperatures. The principal intent of this study is to quantify the effect of fibers, and fiber/matrix interface characteristics, on the longitudinal creep of γ -TiAl, and to provide a comparison with models.

In one limit, the models suggest that composites with continuous elastic fibers demonstrate *transient* creep, with a creep strain limited by the elastic deformation of the fibers.¹² When the fibers also creep, the composite will usually be expected to exhibit steady-state behavior, following an initial transient, subject to a 'rule-of-mixtures' creep rate.¹² However, these expectations are modified by fiber failures,^{13,17} which initiate tertiary creep and may lead to creep brittleness. In some cases, the presence of a "weak" fiber/matrix interface may further obviate creep strength by allowing debonding and

relative sliding between fiber and matrix, either at free surfaces or at prematurely failed fibers.¹⁹

These concepts may be assessed by using two types of alumina fiber reinforcements. (i) *Sapphire fibers*, which are expected to be essentially elastic up to $\sim 1600^{\circ}\text{C}$, when loaded parallel to the c-axis,²⁰ are used to evaluate the elastic fiber concept. Novel fiber coating procedures are used to explore the effect of weak fiber/matrix interfaces on the composite creep rate.^{10,21} (ii) Fibers consisting of *fine grained polycrystalline Al_2O_3* , which should creep noticeably at $\sim 1000^{\circ}\text{C}$,²² provide information about composite behavior in the presence of creeping fibers.

2. EXPERIMENTAL

2.1 Materials and Processing

The matrix used in the present study is a γ -TiAl alloy (Ti-48 Al-2.5 Nb-0.3 Ta at %), supplied by Pratt and Whitney as rapidly solidified powder having an average particle diameter of $\sim 120\text{ }\mu\text{m}$. The polycrystalline Al_2O_3 fibers, produced by a sol-gel process, supplied by 3M, had a diameter of $\sim 15\text{ }\mu\text{m}$ and a submicron grain size. The sapphire reinforcements, produced by the EFG (edge-defined film-fed growth) process at Saphikon, Inc.[†], had a nominal c-axis orientation and a diameter of $\sim 130\text{ }\mu\text{m}$.

Samples with strong interfaces resulted when no coating was applied to the fibers. Composites with "weak" fiber/matrix interfaces were obtained when the fibers were suitably coated.²¹ For the present specimens, the sapphire fibers were coated with colloidal graphite. Thus, to prevent dissolution of the graphite into the TiAl matrix, the fibers were provided with an outer coating of Al_2O_3 . Densification of the Al_2O_3 coating was achieved during a 1300°C vacuum heat treatment, prior to composite consolidation.

[†] Milford, NH.

Composites with fiber coatings were produced by mechanically blending the fibers and the TiAl powders, and then densifying by hot isostatic pressing (HIP) at 276 MPa and 1100°C for 2 h. For the *sapphire* fiber composites, this was achieved using a slurry prepared with TiAl powders and deionized water, and by utilising the rigidity of the fibers to facilitate the mixing process. To remove the bulk of the water from the slurry, the can was first heated to 60°C in air for 48 h. To remove residual moisture, the cans were evacuated at 350°C for 1.5 h, and then sealed by crimping and welding. The composites containing *polycrystalline fibers* were manually fabricated by first stacking equal-length bundles into Ti cans (sealed at one end) having inner diameter 12 mm and length 55 mm. Dry TiAl powder was mixed with the fibers in the can. Mechanical agitation of the can during mixing facilitated powder dispersion. Residual moisture was again removed under vacuum. Unreinforced TiAl was also produced by HIPing, in order to provide a reference against which the properties of the composite could be compared. Fiber volume fractions, f , = 0.15 - 0.25, were achieved for the *sapphire* fiber composite after consolidation, (Fig. 1). For the *polycrystalline fiber* composite, a fiber volume fraction f = 0.07 was measured after HIPing. Higher fiber volume fractions were precluded in this material by the occurrence of uneven fiber distributions in the densified composite.

The composites reinforced with polycrystalline Al_2O_3 fibers were shaped into test specimens by electro-discharge machining. Rectangular test bars of the sapphire-reinforced material were produced by a cutting and surface grinding process, using diamond impregnated wheels. These samples were ground to a 400 grit surface finish. Beams with reduced central sections were also utilised, (Fig. 2). These specimens were machined by using a high speed diamond core drill, with a 200 grit size. In the composites with sapphire fibers, brittle fiber fractures were observed occasionally, attributed to machining damage. In one case, when the tensile surface was profiled with the 200 grit diamond core drill (rather than the 400 grit wheel used on rectangular

beams), substantial fiber fracture occurred, consistent with the deeper scoring resulting from the larger grit size.

2.2 Creep Measurements

Creep tests were performed in argon (≈ 0.1 MPa) using a hydraulic testing machine with a 2200 °C temperature capability. The composites were tested in four-point flexure, with an inner/outer span ratio of 1/2. Initial tests were conducted on rectangular beams, with cross-section 3x3.5mm. However, large levels of shear deformation in the outer span led to discontinuities in the curvature of the beam at the inner loading points, resulting in premature fiber fracture. Enhancing the thickness of the outer-span (Fig. 2) ameliorated this problem, by reducing the outer span shear stresses.

Measurements of the axial creep properties were carried out by using a device which directly and continuously evaluated the (constant) curvature over the inner span (which experiences a constant moment) by measurement of the displacement Δ (Fig. 3). The maximum tensile creep strain $\dot{\epsilon}$ is then given rigorously by,²⁴

$$\epsilon = h\Delta / (\Delta^2 + s^2) \quad (1)$$

where h is the beam thickness and s the span (Fig. 3). The device allows strain measurements accurate to within $\pm 0.01\%$, and a resolution of $\pm 0.0005\%$. Subsequent numerical treatment of the data then yields the corresponding strain rate behavior. The corresponding shear strain rate $\dot{\gamma}$ in the outer span, when the reinforcing fibers are elastic (Fig. 4), is^a

^a Eqn. 2 is applied to the shear deformation of both rectangular beams, as well as the profiled beams (Fig. 2). For the latter, the variation in height of the beam in the transition region outside the inner loading point may lead to a small additional error.

$$\dot{\gamma} = 2\dot{\Delta}_p / (L - \ell) \quad (2)$$

where $\dot{\Delta}_p$ is the load-point displacement-rate, L is the outer span and ℓ the inner span.

The stresses that develop in the composite relate to the applied moment through the longitudinal constitutive properties of the composite. Determining precise values for the axial and shear stresses during flexural creep is quite straightforward when the fibers do not creep, and the stresses are substantially below the fiber bundle strength. The procedures are more involved when the fibers are subject to creep, as summarised in the Appendices.

Tests on the TiAl matrix were also conducted in uniaxial compression. These tests were performed in argon, on samples measuring approximately 6 mm in diameter and 12 mm long.

2.3 Fracture Resistance

Fracture resistance measurements were performed, following creep, by using a chevron-notch, three-point bend technique. Testing was conducted in a hydraulic testing machine, at room temperature, at a cross-head displacement rate of $\sim 100 \mu\text{m/s}$. A stiff loading frame guaranteed stable crack propagation, following initial pop-in. Fiber push-out tests have also been conducted, before and after creep testing, in order to evaluate the interfacial sliding stress, τ , as described elsewhere.^{21,23}

2.4 Characterization

Various microstructural and microchemical characteristics of the composites have been established, by using conventional and analytical transmission electron microscopy (TEM). These studies were conducted in a JEOL 2000 FX instrument,

equipped with a LINK eXL energy dispersive X-ray spectroscopy (EDS) system with a high take-off angle detector. Indexing of electron diffraction patterns was conducted using Desktop Microscopist Software. Thin specimens suitable for TEM were prepared both by mechanical dimpling followed by either ion beam thinning (5kV/13°) or twin jet polishing. The latter was carried out in a Fishione Model 110/130 by using 4% Sulfuric acid/Methanol solution at -15°C and 95 mA. Specimens were also examined by scanning electron microscopy (SEM), before and after mechanical testing. These studies were conducted with a JEOL SM840 equipped with a Tracor Northern EDS system.

3. MICROSTRUCTURES

3.1 As-Processed

Microstructural analysis of the TiAl/Al₂O₃ composites conducted by using TEM revealed a γ -TiAl matrix with a $\approx 5\ \mu\text{m}$ grain size, insensitive to both the volume fraction and type of reinforcement. Intragranular carbides (resulting from carbon contamination during the TiAl powder atomization process) were identified by selected area diffraction (SAD), as Ti₂AlC. These were present in small quantities (volume fraction, $f < 0.02$), but with a wide size distribution (ranging from < 0.1 to $\sim 1\ \mu\text{m}$) (Fig. 5). There were no indications of α_2 -Ti₃Al. The grain size of the polycrystalline Al₂O₃ fibers was $\sim 0.2\ \mu\text{m}$ (Fig. 6a). The sapphire fibers were largely devoid of both grain boundaries and dislocations (Fig. 6b). In the absence of coatings, bonding between the matrix and the fibers appeared intimate, with no evidence of reaction zones (Fig. 6a, b). However, limited interdiffusion occurred. In the polycrystalline fibers, Ti was evident to a depth of $\sim 0.8\ \mu\text{m}$. The extent of the interdiffusion zone was substantially less for the sapphire fibers ($\sim 0.2\ \mu\text{m}$).

In the composites incorporating fiber coatings, a continuous graphitic structure was evident, with the layers displaying a wavy morphology parallel to the surface of the fibers. This arrangement, also evident after creep (Fig. 7b), provided a "weak" interface and low interfacial sliding stresses.^{10,21} Surrounding the graphite was a continuous, fine grained ($\approx 0.1 \mu\text{m}$) Al_2O_3 coating, $0.2 - 5 \mu\text{m}$ thick, again, also evident after creep (Fig. 7a), containing a small amount of residual porosity. No interface reactions were found. Nor was there evidence of significant levels of interdiffusion between the fiber, matrix and coating.

3.2 After Creep

The polycrystalline Al_2O_3 coatings on the fibers were found to be effective in preventing the migration of the graphite into the TiAl during creep. This protection is evident both from the retention of the 200-500 nm graphite layer (even after more than 50 h at 982°C (1800°F)) and the spatial uniformity of the matrix carbide concentration in the TiAl (Fig. 7a).

However, following creep, several changes in microstructure were evident. Locally enhanced matrix creep at the fiber breaks in the sapphire fibers produced by machining resulted in separation of the fiber ends, (Fig. 8b). In the matrix adjacent to a fiber failure, extensive creep damage was often evident. Such damage provides a mechanism for creep rupture in the composite. In composites containing polycrystalline fibers, fiber fractures occurred at regular spacings after a creep strain of $\sim 2\%$ (Fig. 8a). The maximum value of the ratio of crack spacing, l , to crack radius, R , was $l/R \sim 10$. This spacing occurred close to the tensile surface. The maximum fiber cracking depth was $\sim h/3$ from the tensile surface. No fiber fractures were found on the compression side. Cracking appeared to be caused by creep damage coalescence within the fibers (Fig. 9), similar to that observed for other aluminas.²⁵

Significant levels of dislocation activity were observed in the γ -TiAl, with some dislocation pinning evident at the intragranular carbides (Fig. 10). Few dislocations were evident in either the polycrystalline Al_2O_3 or the sapphire fibers.

4. CREEP STRENGTHS

4.1 Axial Creep

Measurements of axial creep at 982°C (1800°F) revealed substantial differences between the various materials (Figs. 11,14). i) The matrix-only material exhibited steady-state deformation after a short transient, (Fig. 11), with a power-law exponent, $n = 2.6$ (Fig. 12). ii) The material with the polycrystalline fibers exhibited primary and steady-state creep, (Fig. 11), with a creep-rate somewhat less than that for the matrix, (at the same nominal stress). iii) The composites with sapphire fibers exhibited *transient creep* (creep-rate diminishing with strain) and a total creep strain $\sim 0.15\%$, (Figs. 11,13). Unloading at the end of the creep test, while maintaining the temperature, resulted in *reverse creep* . These behaviors were similar for both the coated and uncoated fibers, in the absence of significant fiber fracture. However, when premature fiber fracture occurred as a result of machining damage, an acceleration in creep was evident, (Fig. 14).

The axial creep-rate of a composite containing intact continuous, elastic fibers, is predicted to be transient¹² and, when the matrix experiences power law creep (equation A2), is given by,

$$\dot{\epsilon} = \alpha \dot{\epsilon}_m \left[1 - (f E_f / \sigma) \epsilon \right]^n \quad (3)$$

where E_f is Young's modulus for the fiber, $\dot{\epsilon}_m$ is the matrix creep-rate at the same applied stress and α is a coefficient that depends on f , E_f/E_m and n , given by¹²

$$\alpha = \left[\frac{E_m(1-f)}{E_f f + E_m(1-f)} \right] (1-f)^{-n} \quad (4)$$

For the present composites, ($f = 0.15-0.25$, $n = 2.6$, $E_f/E_m = 2.8$), $\alpha \approx 1.1$. Integration of equation (3) then gives the strain history,

$$\epsilon = \epsilon_c - (\epsilon_c - \epsilon_0) \left[1 + (1 - \epsilon_0 / \epsilon_c)^{n-1} \left\{ \frac{(n-1)\alpha \dot{\epsilon}_m t}{\epsilon_c} \right\} \right]^{-1/(n-1)} \quad (5)$$

where ϵ_c is the strain at which creep stops, given by

$$\epsilon_c = \sigma / f E_f \quad (6)$$

A comparison with these predictions of the creep rates measured on the composites containing *coated* sapphire fibers (Fig. 13), indicates a slighter higher than expected creep rate after the first few hours but good agreement, within the accuracy of the data, after about 15 h. In particular, the limiting creep strain appears well represented by equation (6). The discrepancy during the early stages is probably caused by transient stress redistribution effects within the beam, not accounted for in equation (5). Similar agreement obtains from the initial creep of the composite with *uncoated* fibers, prior to fiber failure. This result is of significance because it emphasises that the presence of a "weak" fiber/matrix interface does not degrade the axial creep properties of the composite.

When polycrystalline fiber reinforcements are used, the lower creep strengths, as well as the attainment of a steady-state deformation, involve both fiber creep and fragmentation of the fibers. The occurrence of creep in the fibers is consistent with the extremely fine grain size²² ($\leq 200\text{nm}$). However, there is insufficient information to compare explicitly with models.

4.2 Interlaminar Creep

In the composites reinforced with sapphire fibers, steady-state interlaminar shear creep is found to occur in the outer span, after a brief initial transient. The shear deformation of the composite may be compared with that for the unreinforced matrix by using the equivalent stress and strain as comparators (Appendix II). This comparison demonstrates that the shear creep rate of the composite and of the unreinforced matrix are similar (Fig. 12). Consequently, the reinforcing fibers are found to have little effect on the shear creep response, consistent with theoretical predictions (Appendix III, Fig. C2).

5. FRACTURE RESISTANCE

Fracture resistance measurements conducted on the material with *coated* sapphire fibers, after creep (Fig. 15), were initially characterised by pop-in, due to unstable crack propagation from the notch. However, bridging fibers were found to cause crack arrest, with subsequent pull-out, (Fig. 16b), resulting in significant enhancement of the fracture resistance. The pull-out contribution to the work-of-rupture is estimated from the area under the tail of the load-displacement curve as, $\Delta\Gamma_p \approx 2.1 \text{ kJm}^{-2}$. The fiber pull-out lengths ranged between about 20 - 225 μm , with an average value, $\bar{h} \approx 105 \mu\text{m}$. In contrast, the composite with *uncoated* sapphire fibers exhibited unstable crack growth, with no pull-out (Fig. 16a). The frictional sliding stress, characterizing pull-out of the

coated sapphire fibers, obtained using fiber push-out tests²¹ was $\tau = 40\text{--}50$ MPa. The toughening, $\Delta\Gamma_p$, caused by fiber pull-out is predicted to be²⁶

$$\Delta\Gamma_p = \tau f \bar{h}^2 / R \quad (7)$$

where R is the fiber radius, and $\bar{h} = \sqrt{\pi R^2 \sum_i^m h_i^2 / f}$, with m being the number of fibers per unit area. Using the parameters summarised in Table I, the magnitude predicted by equation (7) is found to be $\approx 40\%$ lower than the toughening value determined experimentally. This discrepancy may be partly due to the bending stresses that occur in the fibers bridging the crack during pull-out, resulting in additional fiber failure and, thus, to an underestimation of the true average pull-out length. In addition, bending may lead to an increase in the effective sliding stress by causing additional compressive forces normal to the fiber/matrix interface.

6. CONCLUSIONS

The present study has demonstrated *for the first time* that continuous ceramic fibers can substantially enhance the longitudinal creep properties of intermetallic matrices, in the presence of weak fiber/matrix interfaces, provided that the fibers are strong and resistant to both creep and creep rupture. In addition, the comparatively high fracture resistance of γ -TiAl reinforced with coated sapphire fibers critically demonstrates the feasibility of using continuous fiber reinforcement with weak fiber/matrix interfaces to *simultaneously* achieve high uniaxial creep and fracture resistance.

The importance of fiber coatings for *both* fracture resistance and creep strength has been vividly demonstrated. Fiber pull-out and toughening have been demonstrated when coatings are used. It is also shown that double coating techniques can be used to protect debond coatings during creep.

The creep properties under shear loading were found to be insensitive to unidirectional fiber reinforcement, in accordance with predictions, indicating the need for multidirectional reinforcement under more complex loading conditions.

ACKNOWLEDGEMENTS

This work was sponsored by the Defense Advanced Research Projects Agency under University Research Initiative Grant No. N00014-86-K-0753 and contract MDA972-90-K-0001, supervised by Dr. W. Coblenz and monitored by Dr. S.G. Fishman of the Office of Naval Research. Thanks are expressed to Dr. D.G. Backman at General Electric for supplying the sapphire fibers, to Mr. J. Sorensen at 3M for supplying the alumina fibers, and to Dr. M.L. Emiliani at Pratt and Whitney Laboratories for providing the TiAl powders.

APPENDIX I

Axial Stress Redistribution in a Creeping Beam

For a beam subject to elastic bending, the maximum tensile and compressive stresses, σ_e , are

$$\sigma_e = (3/2) \{P(L - \ell)/bh^2\} \quad (A1)$$

where L and ℓ are the length of the outer span and inner span, respectively, P the load and b the beam width. When the *entire body* is subject to power law, steady-state creep, with the strain-rate, $\dot{\epsilon}$ characterized by,

$$\dot{\epsilon} = \dot{\epsilon}_0 (\sigma/\sigma_0)^n \quad (A2)$$

where σ_0 is a reference stress, $\dot{\epsilon}_0$ a reference strain-rate and n the power law exponent, the maximum stress $\hat{\sigma}$ in the flexural specimen is²⁷

$$\hat{\sigma}/\sigma_e = (2n + 1)/3n \quad (A3)$$

The corresponding stress distribution is

$$\frac{\sigma(y)}{\sigma_e} = \left(\frac{2n + 1}{3n} \right) \left(\frac{2y}{h} \right)^{1/n} \quad (A4)$$

where y is the distance from the neutral axis

For matrices reinforced by *creeping* fibers account must be taken of the redistribution in moment from the matrix to the fibers. This results in a stress distribution that is a function of both the fiber volume fraction and the applied load.²⁴

For the TiAl/*polycrystalline* Al_2O_3 fiber composite, the fiber volume fraction is low and the fibers appear to creep with rates similar to the matrix. In this limiting case, equation (A3) provides a sufficiently accurate representation of the composite stress distribution. Another limiting case occurs when the fibers are elastic, and not subject to significant fragmentation. Then, the composite stress during creep is given by equation (A1). These two well known bounds are used in this study to gain understanding of the influence of the fibers on creep behavior.

An interesting situation arises when the composite is reinforced with *elastic* fibers. Then, following an initial transient, all axial load is carried by the fibers, resulting in a linear stress distribution across the beam. Consequently the shear stress distribution is the same as that for the elastic case.

To compare the composite shear behavior with the matrix creep behavior obtained in flexure, the stresses and strains are expressed in terms of the equivalent values σ' and strains ϵ' , by using

$$\sigma' = \left(\frac{1}{\sqrt{2}} \right) \left[(\sigma_{11} - \sigma_{22})^2 + (\sigma_{33} - \sigma_{22})^2 + (\sigma_{11} - \sigma_{33})^2 + 6(\sigma_{12}^2 + \sigma_{23}^2 + \sigma_{13}^2) \right]^{1/2} \quad (B4)$$

and

$$\epsilon' = \left(\frac{\sqrt{2}}{3} \right) \left[(\epsilon_{11} - \epsilon_{22})^2 + (\epsilon_{33} - \epsilon_{22})^2 + (\epsilon_{11} - \epsilon_{33})^2 + 6(\epsilon_{12}^2 + \epsilon_{23}^2 + \epsilon_{13}^2) \right]^{1/2} \quad (B5)$$

where σ_{kk} and ϵ_{kk} refer to the normal stresses and strains, respectively. In shear, $\sigma' = \sqrt{3} \tau$ and $\epsilon' = \gamma / \sqrt{3}$, whereas, in flexure, $\sigma' = \sigma$ and $\epsilon' = 2\epsilon/3$.

APPENDIX II

Shear Stress Redistribution in a Creeping Beam

The maximum shear stress τ in four-point flexure occurs at the mid-beam height in the *outer-span* region. For a monolithic elastic beam in four-point flexure, this stress is²⁸

$$\tau = 3P/4bh \quad (B1)$$

where P is the applied load, and b and h are the beam width and height, respectively.

When creep occurs according to equation (A2) there is a redistribution in shear stress across the height of the beam. The magnitude of the shear stress can be determined from equilibrium, by integrating the imbalance in axial stress, $\Delta\sigma$, across an element of width dx , over the height of the beam,

$$\tau = \frac{\int_0^y \Delta\sigma dy}{dx} \quad (B2)$$

For non-linear creep, $\Delta\sigma$ is found from the axial stress distribution given by equation (A4). The maximum shear stress normalised by the corresponding elastic stress, τ_e , is then

$$\frac{\tau}{\tau_e} = \left(\frac{4n+2}{3n+3} \right) \quad (B3)$$

This result shows that non-linear creep results in a magnification of the maximum shear stresses.

$$\tau_c / \tau_m = \xi^{(1-n)/n} \int_0^1 \left\{ \xi - \sqrt{1 - \bar{x}^2} \right\}^{-1/n} d\bar{x} + (1 - 1/\xi) \quad (C4)$$

The results of the numerical integration of equation (C4) for different values of the matrix creep exponent, n , (Fig. C2) indicate that, for materials characterised by a high creep exponents, the fibers have little effect on the creep behavior when the volume fraction, $f \leq 0.4$. These predictions are consistent with the shear creep behavior of the TiAl/sapphire composite ($f = 0.15 - 0.25$ and $n = 2.6$), Fig. (C2).

REFERENCES

- [1] H.A. Lipsitt, *MRS Symposium Proceedings*, **39**, 351 (1985).
- [2] Young-Won Kim, *Journal of Metals*, **41**, 24 (1989).
- [3] C.K. Elliot, G.R. Odette, G.E. Lucas and J.W. Sheckard, *MRS Symposium Proceedings*, **120**, 695 (1988).
- [4] L. Christodoulou, P.A. Parrish and C.R. Crowe, *MRS Symposium Proceedings*, **120**, 29 (1988).
- [5] H.E. Dève and A.G. Evans, *Acta Metall. Mater.*, **39**, 1171 (1991).
- [6] H.E. Dève, A.G. Evans and D.S. Shih, *Acta Metall. Mater.*, **40**, 1259 (1992).
- [7] P.L. Martin, D.H. Carter, R.M. Aiken, Sr., R.M. Aiken, Jr. and L. Christodoulou, "Creep and Fracture of Engineering Materials and Structures," Conf. Proc., Inst. of Metals, Swansea (1990) 265.
- [8] J. Rösler, J.J. Valencia, C.G. Levi, A.G. Evans and R. Mehrabian, *MRS Symposium Proceedings*, **194**, 241 (1990).
- [9] J. Rösler, G. Bao and A.G. Evans, *Acta Metall. Mater.*, **39**, 2733 (1991).
- [10] A.G. Evans, F.W. Zok and J.B. Davis, *Composites Science and Technology*, **42**, 369 (1991).
- [11] A. Kelly and K.N. Street, *Proc. Roy. Soc. Lond. A.*, **328**, 283 (1972).
- [12] M. McLean, *Comp. Sci. and Tech.*, **23**, 37 (1985).
- [13] M. McLean, *MRS Symposium Proceedings*, **120**, 67 (1988).
- [14] S. Goto and M. McLean, *Acta Metall. Mater.*, **39**, 153 (1991).
- [15] S.T. Mileiko, *J. Mat. Sci.*, **5**, 277 (1970).
- [16] G. Bao, J.W. Hutchinson and R.M. McMeeking, *Acta Metall. Mater.*, **39**, 1871 (1991).
- [17] R.M. McMeeking, to appear in *Elevated Temperature Mechanical Behavior of Ceramic Matrix Composites* (S.V. Nair and K. Jakus, eds.), Butterworth-Heinemann, Stoneham, Mass., 1992.
- [18] M.-Y. He, *MRS Symposium Proceedings*, **194**, 15 (1990).
- [19] N. Masaki, K. Wakashima and J. Unekawa, *J. Mat. Sci.*, **20**, 4123 (1985).

- [20] J.B. Wachtman, Jr., and L.H. Maxwell, *J. Am. Ceram. Soc.*, **40**, 377 (1957).
- [21] T.J. Mackin, J. Yang, C.G. Levi and A.G. Evans, *Mat. Sci. and Eng.*, in press.
- [22] R.M. Cannon, A.H. Heuer and W. Rhodes, *J. Am. Ceram. Soc.*, **63**, 46 (1980).
- [23] T.J. Mackin, P. Warren and A.G. Evans, *Acta Metall. Mater.*, **40**, 1251 (1992).
- [24] C.H. Weber, J.P.A. Löfvander and A.G. Evans, *submitted to J. Am. Ceram. Soc.*.
- [25] E. Slamovitch, B.J. Dalgleish and A.G. Evans, *J. Am. Ceram. Soc.*, **68**, 575 (1985).
- [26] M.D. Thouless and A.G. Evans, *Acta Metall.*, **36**, 517 (1988).
- [27] S. Timoshenko, *Strength of Materials, Part II, 3d ed.*, Van Nostrand, Princeton, (1956) 527.
- [28] J.M. Gere & S.P. Timoshenko, *Mechanics of Materials*, Brooks/Cole, (1984) 226.

FIGURE CAPTIONS

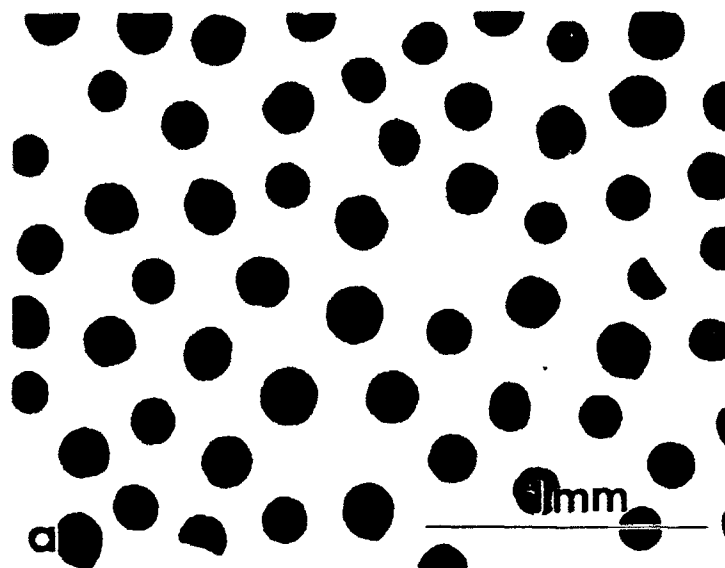
- Fig. 1. Scanning electron micrographs of the γ -TiAl/sapphire composite: transverse section.
- Fig. 2. Modified four-point flexure sample, with reduced center section to minimise fiber damage.
- Fig. 3. Schematic of the method used to measure bending deflections during creep.
- Fig. 4. Schematic of interlaminar shear creep during flexure.
- Fig. 5. Transmission electron micrograph of the matrix in as-processed γ -TiAl, indicating the Ti_2AlC precipitates.
- Fig. 6. TEM micrograph of the fiber (f)/matrix (m) interface region (shown arrowed) in γ -TiAl reinforced with a) polycrystalline Al_2O_3 b) sapphire.
- Fig. 7. TEM micrograph of the fiber/matrix interface region in γ -TiAl reinforced with coated sapphire fibers after creep at 982°C (1800°F) for 50 h, a) overview, b) detail of region outlined in (a). Diffraction pattern shows the TiAl [011] zone axis, recorded next to the interface. (M, matrix: S, sapphire fiber: A, Al_2O_3 coating: C, carbon coating)
- Fig. 8. TEM micrographs of γ -TiAl matrices with Al_2O_3 fibers a) multiple cracking in polycrystalline fibers, b) fracture in sapphire fiber (arrowed).
- Fig. 9. Evidence for creep crack growth in polycrystalline Al_2O_3 fibers.
- Fig. 10. Transmission electron micrographs of unreinforced γ -TiAl after creep, a) bright-field and b) weak beam dark-field.
- Fig. 11. Comparison of the creep behavior between matrix and composites.
- Fig. 12. Steady-state composite creep under interlaminar loading in TiAl/sapphire at 982°C (1800°F) plotted as equivalent stresses and strain-rates. Also shown are compression (c) and flexural (f) creep rates for the matrix.

- Fig. 13. Comparison of TiAl/sapphire creep data with model at 982°C (1800°F) and a nominal applied stress of 75 MPa.
- Fig. 14. Transition to 'steady-state' creep after onset of fiber fracture in TiAl/sapphire, containing uncoated damaged fibers.
- Fig. 15. Work-of-fracture data for TiAl/sapphire after creep.
- Fig. 16. a) No fiber pull-out in TiAl/sapphire for strongly bonded interfaces.
b) Weakened interfaces result in substantial levels of pull-out.
- Fig. C1. Unit-cell model for the interlaminar shear creep behavior of continuous fiber composites.
- Fig. C2. Comparison of shear creep behavior of TiAl/sapphire with model at 982°C (1800°F) for effective stresses of 7-12 MPa.

Table I

Constitutional Properties For TiAl/Sapphire

Pull-Out Length, \bar{h} (μm)	105
Fiber Radius, R (μm)	65
Fiber Volume Fraction, f	0.15
Sliding Stress τ (MPa)	40-50



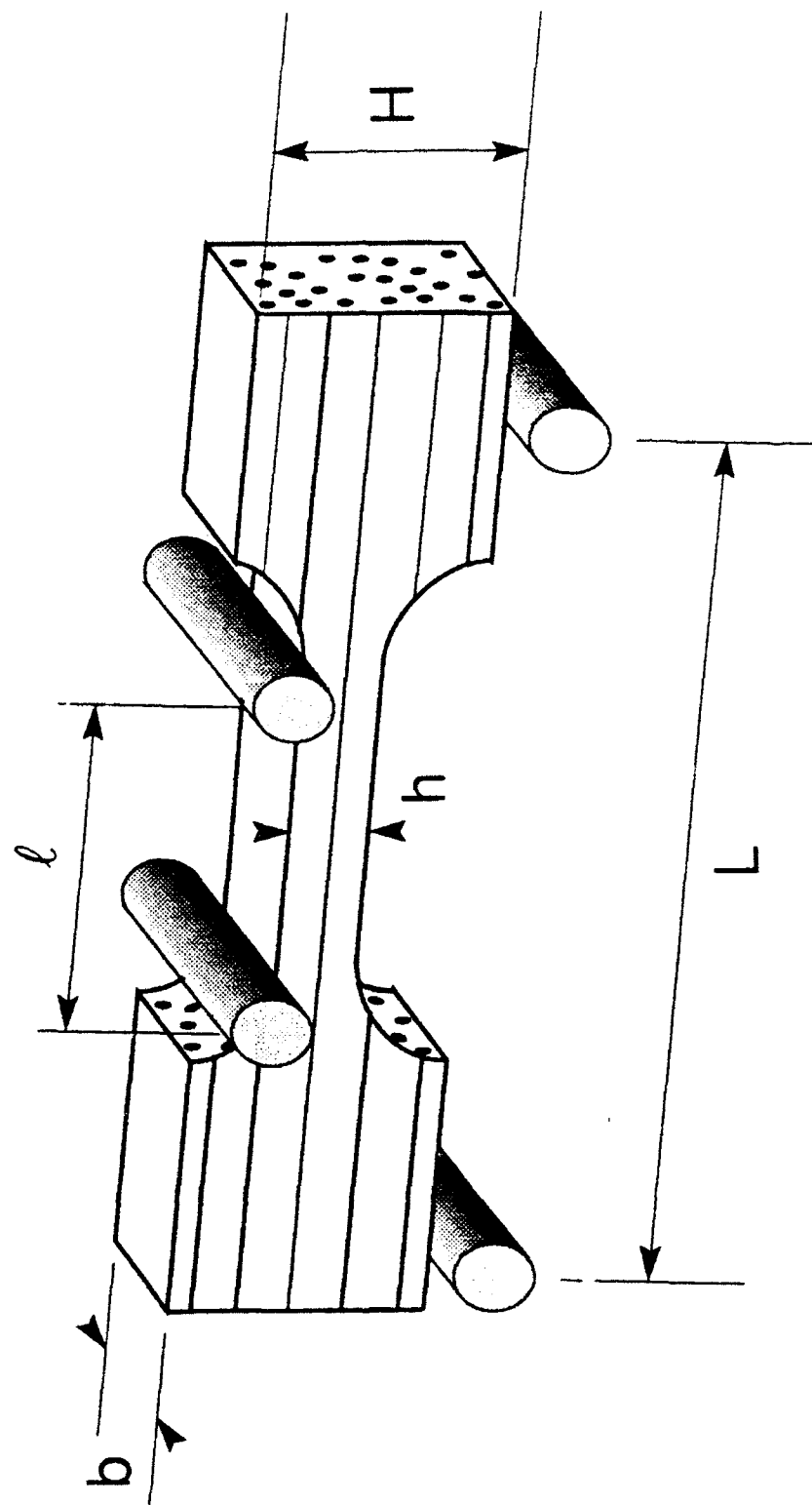


Fig. 2

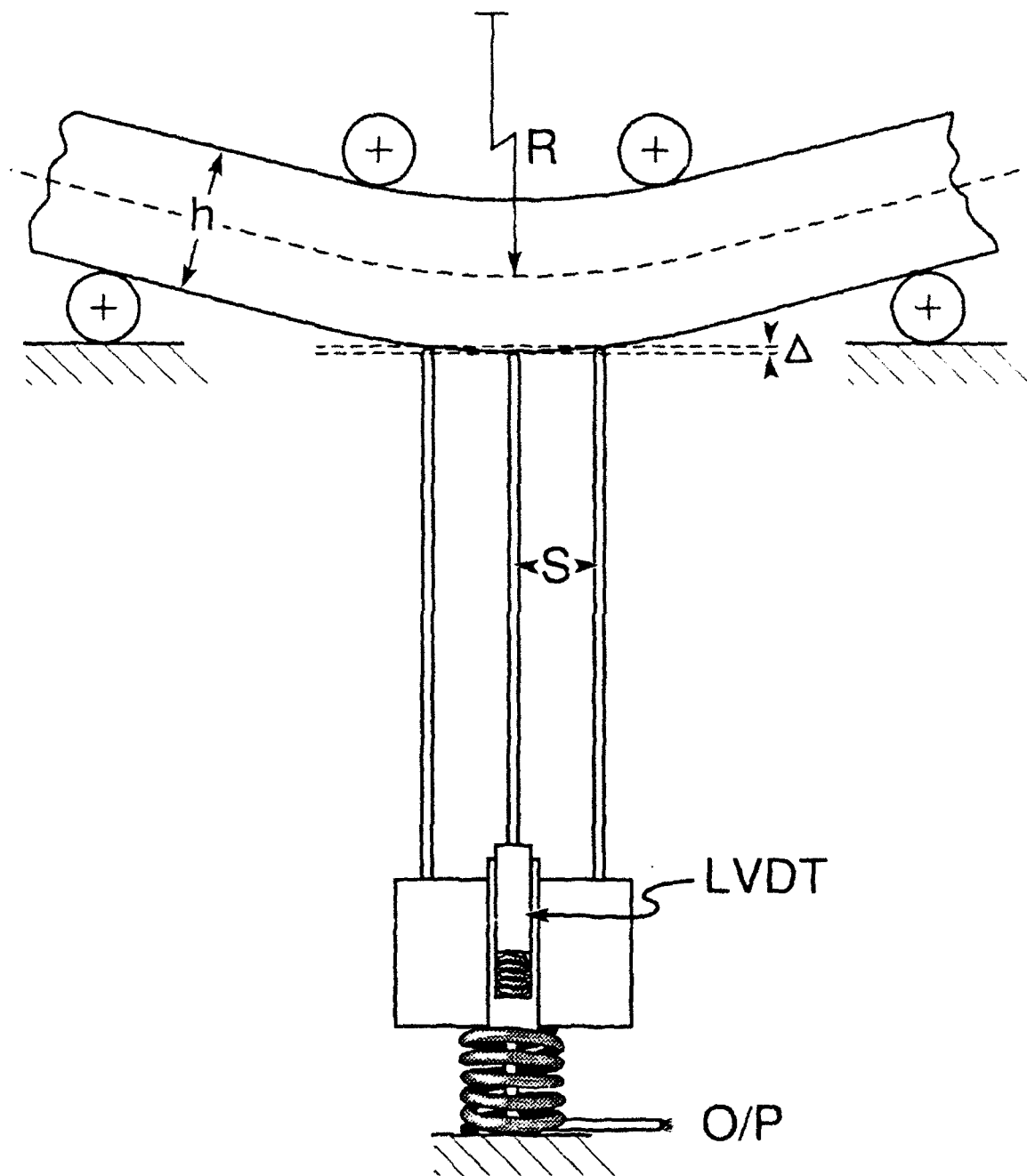
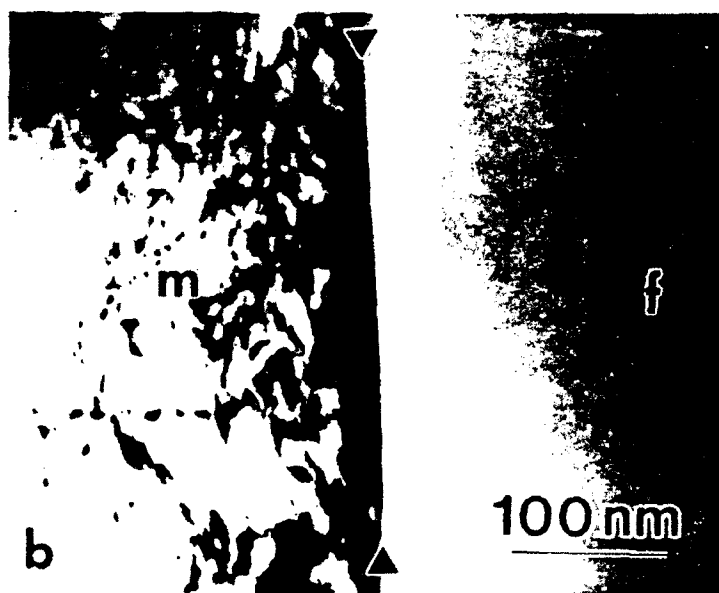
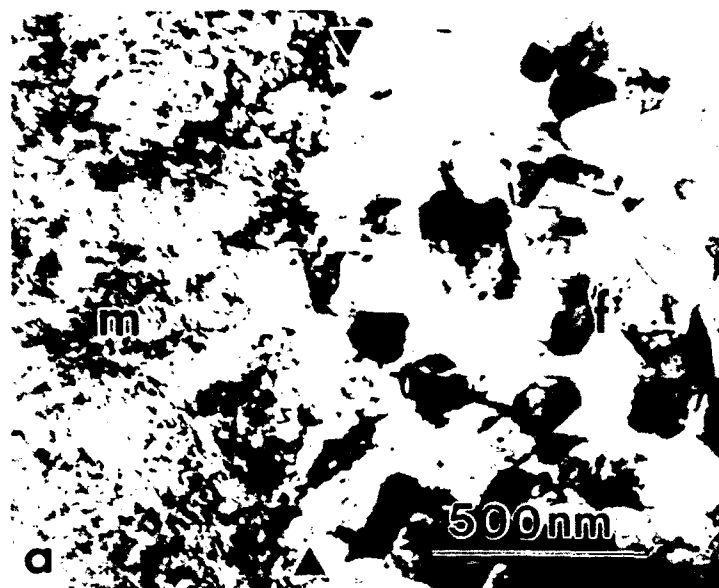


Fig. 3









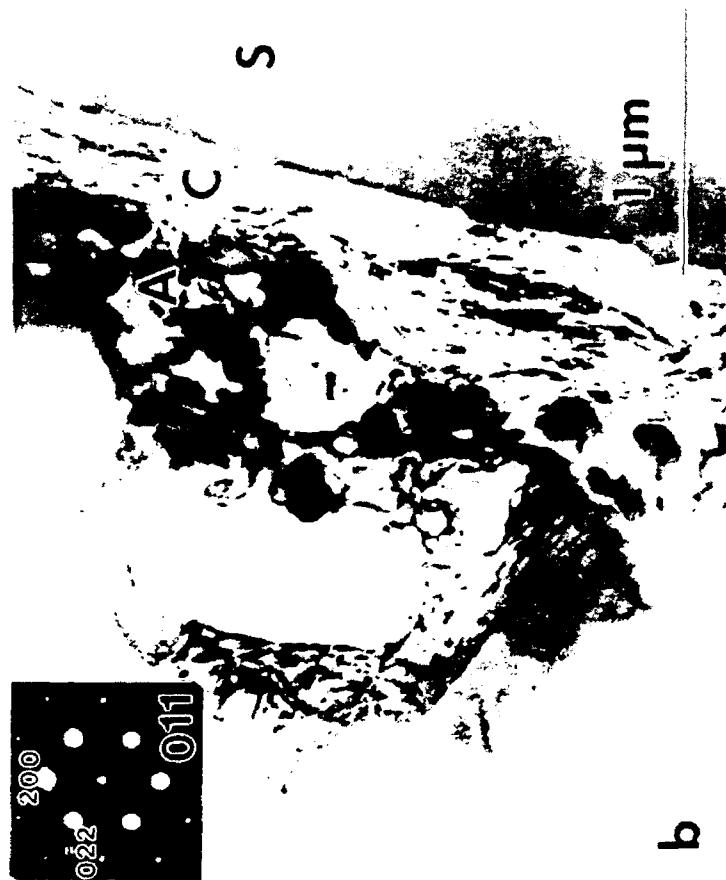
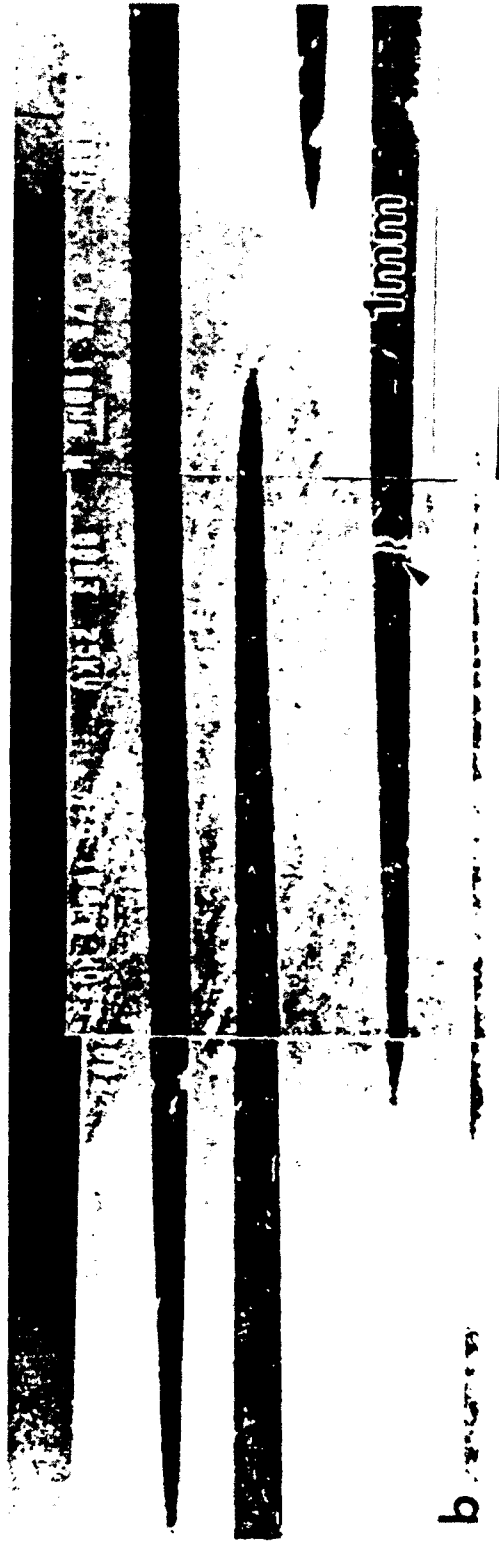
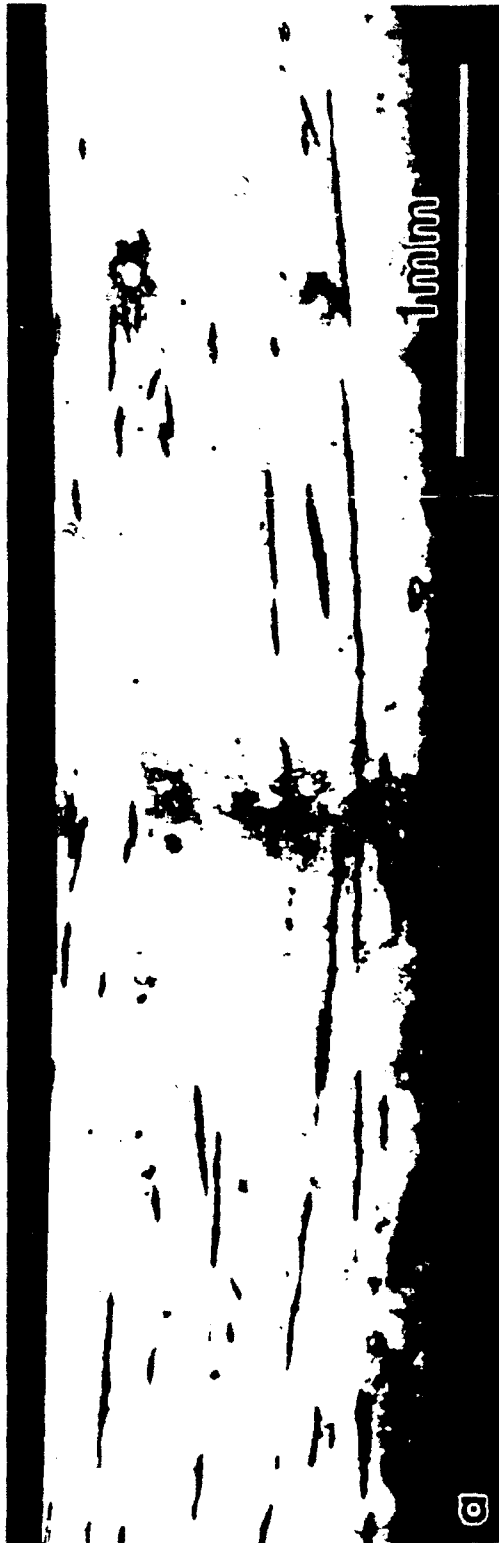


Fig. 7b



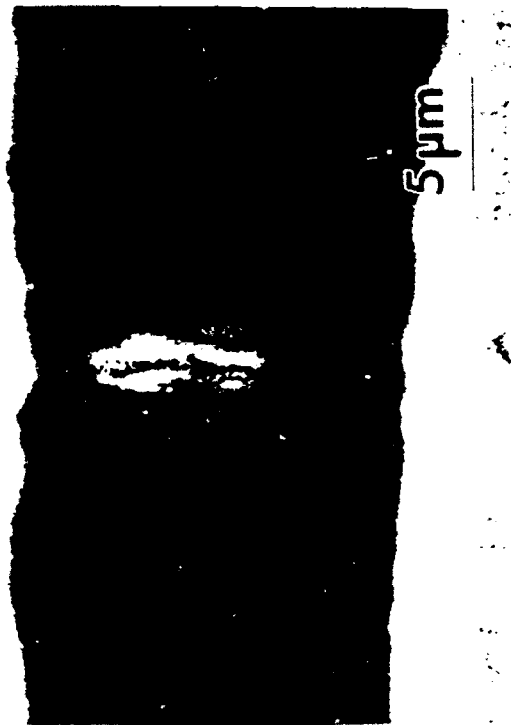
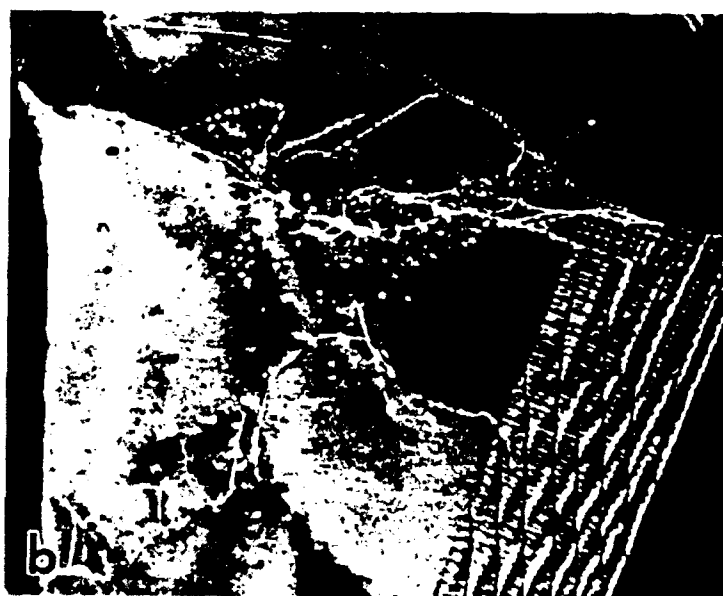


Fig. 9



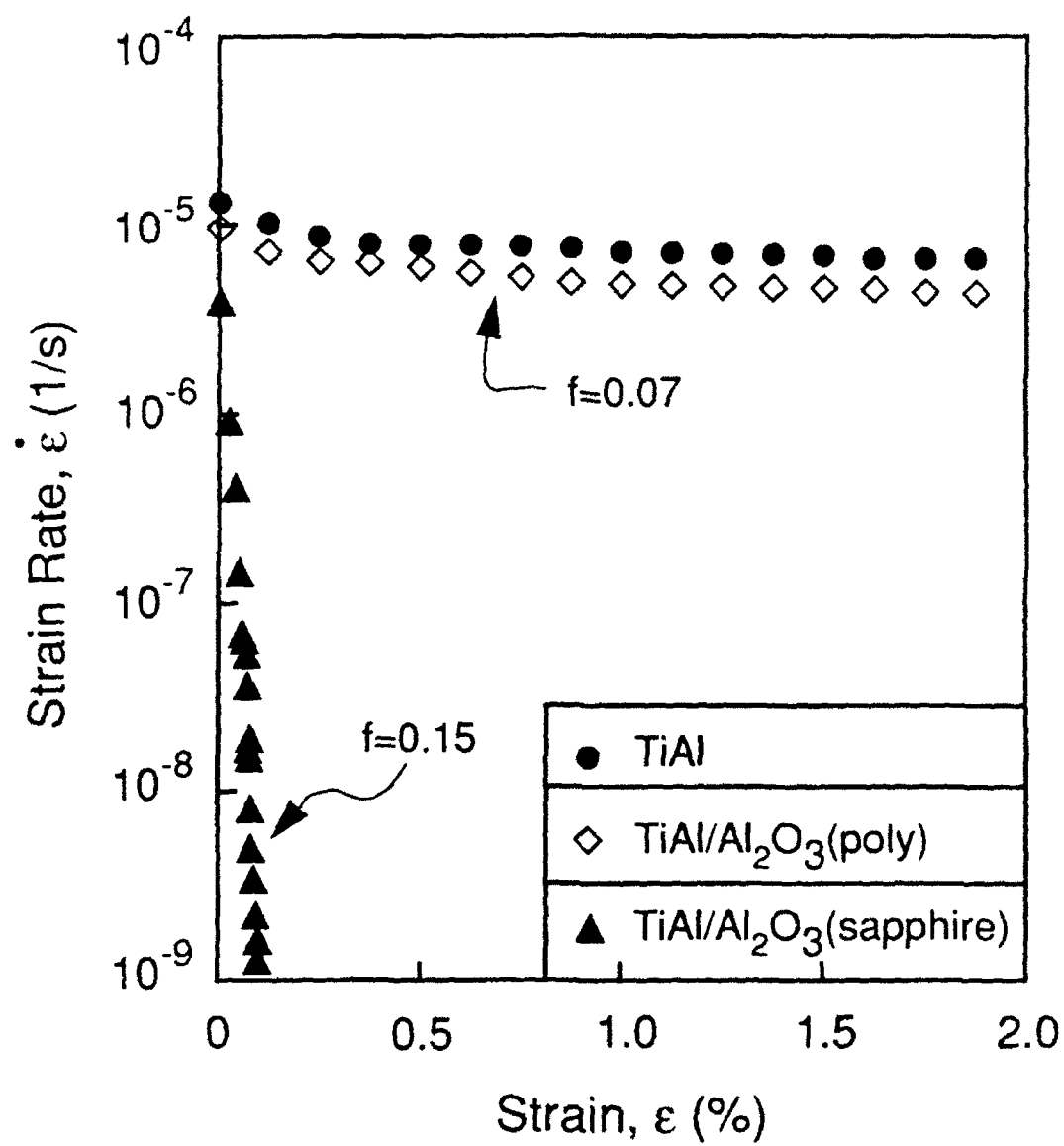


Fig. 11

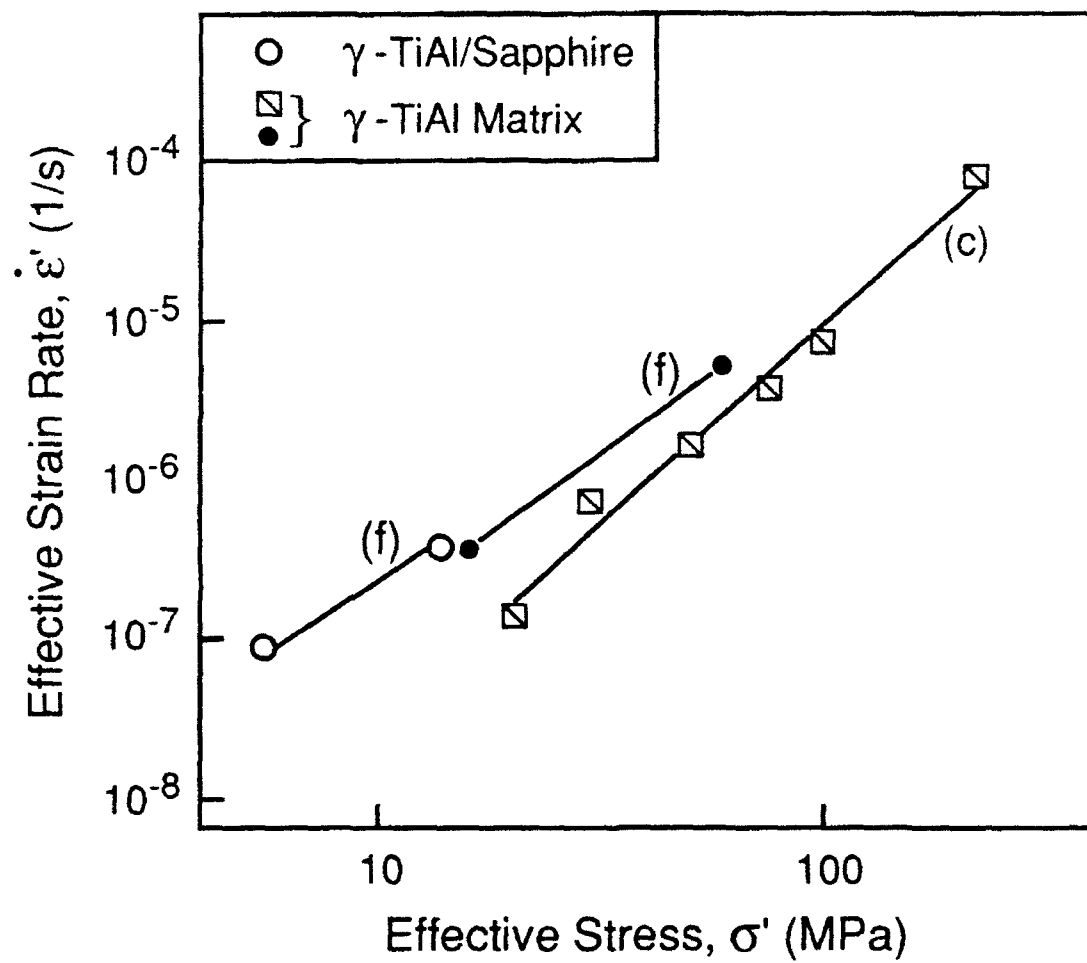
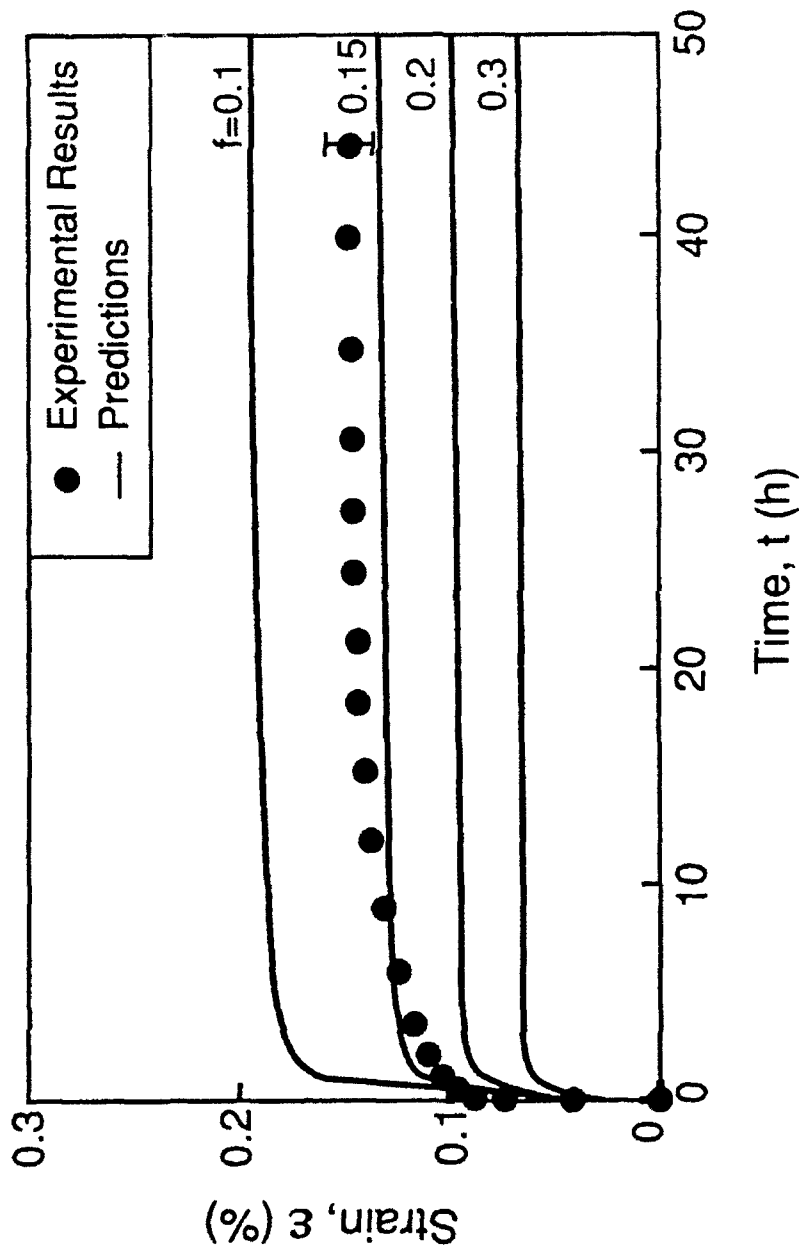


Fig. 12



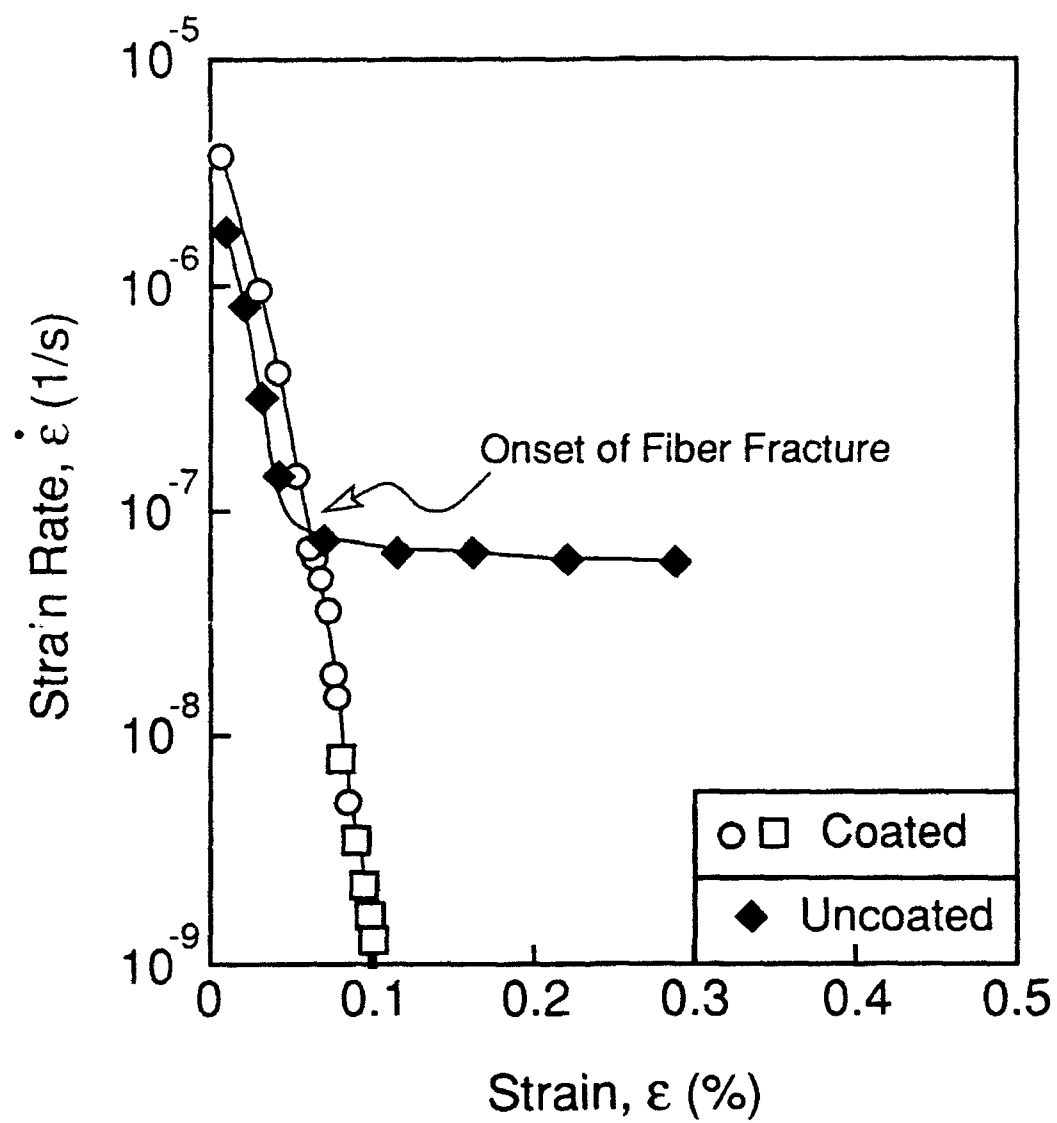
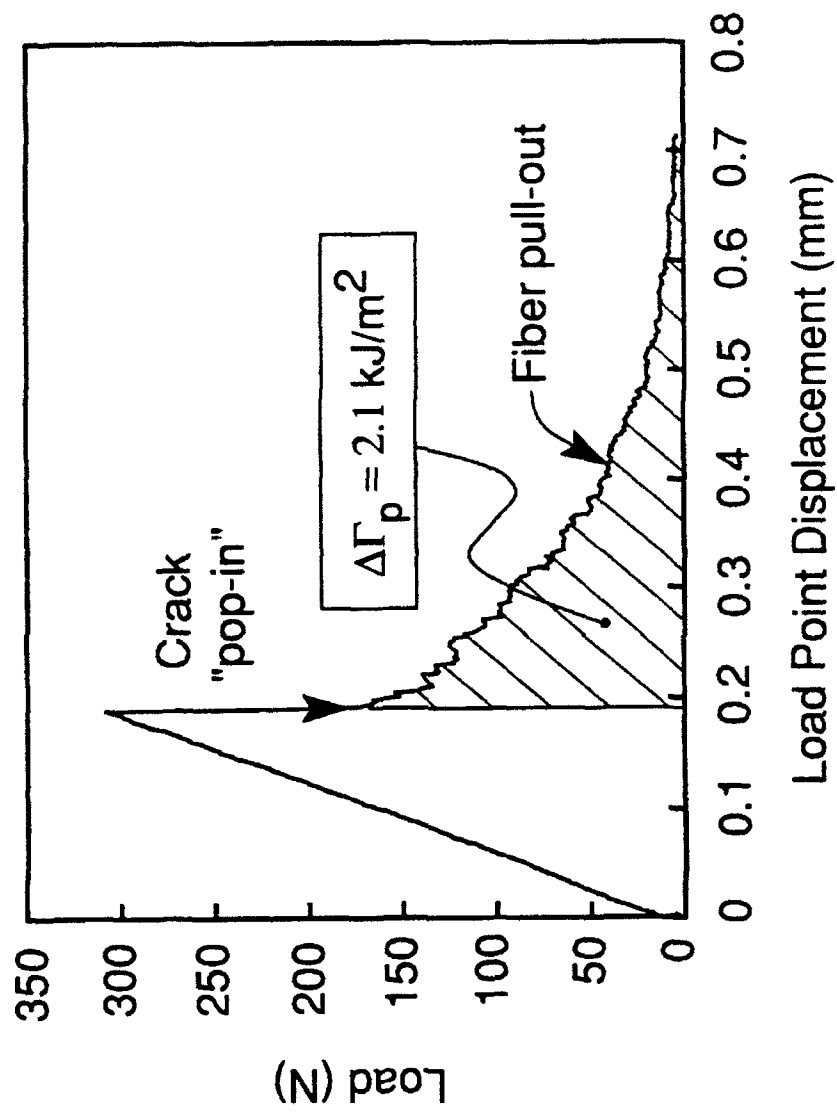


Fig. 14



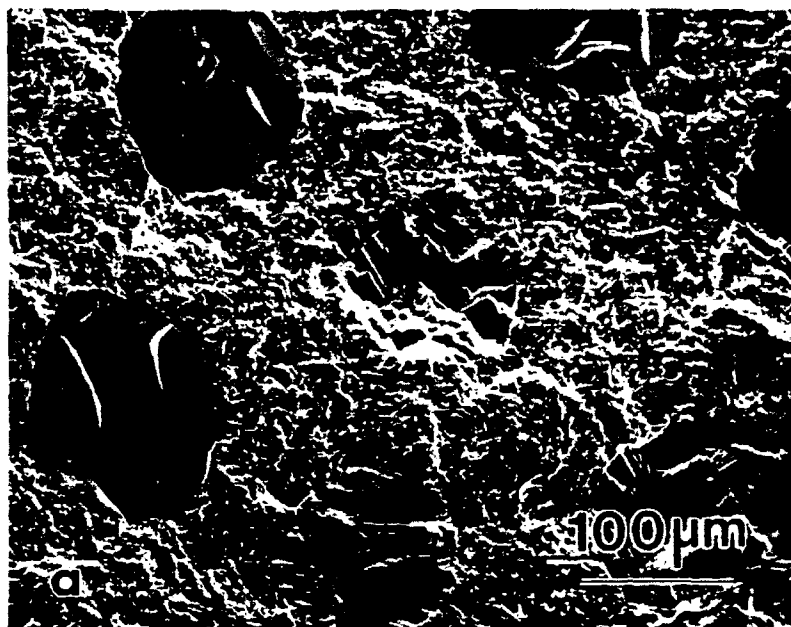
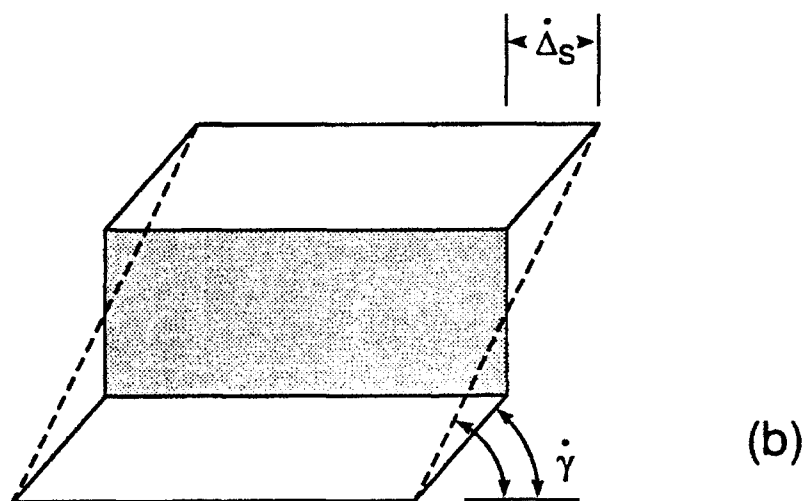
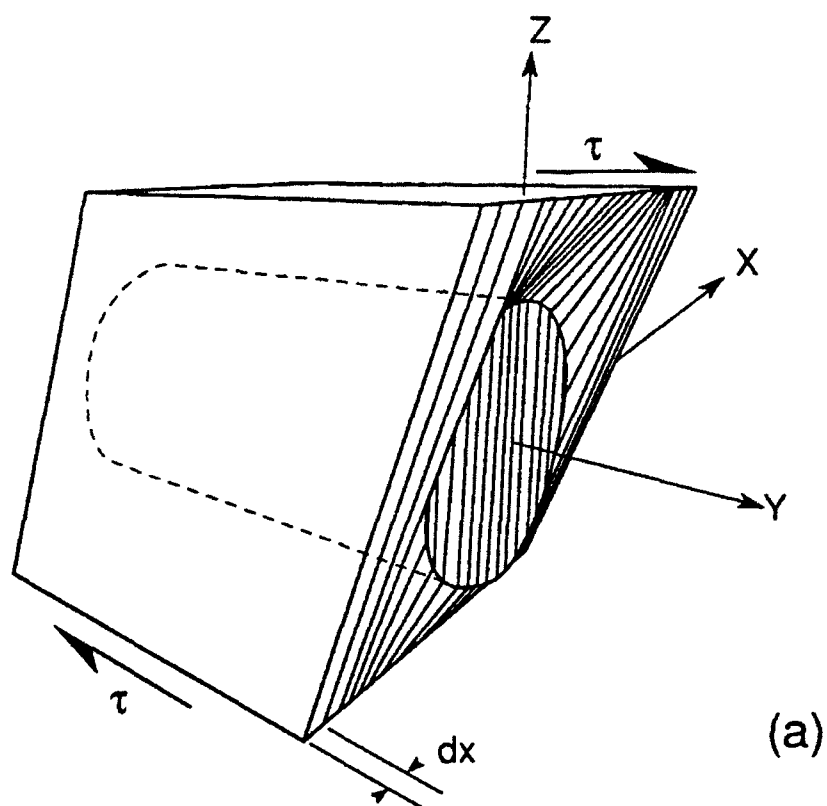


Fig. 16at



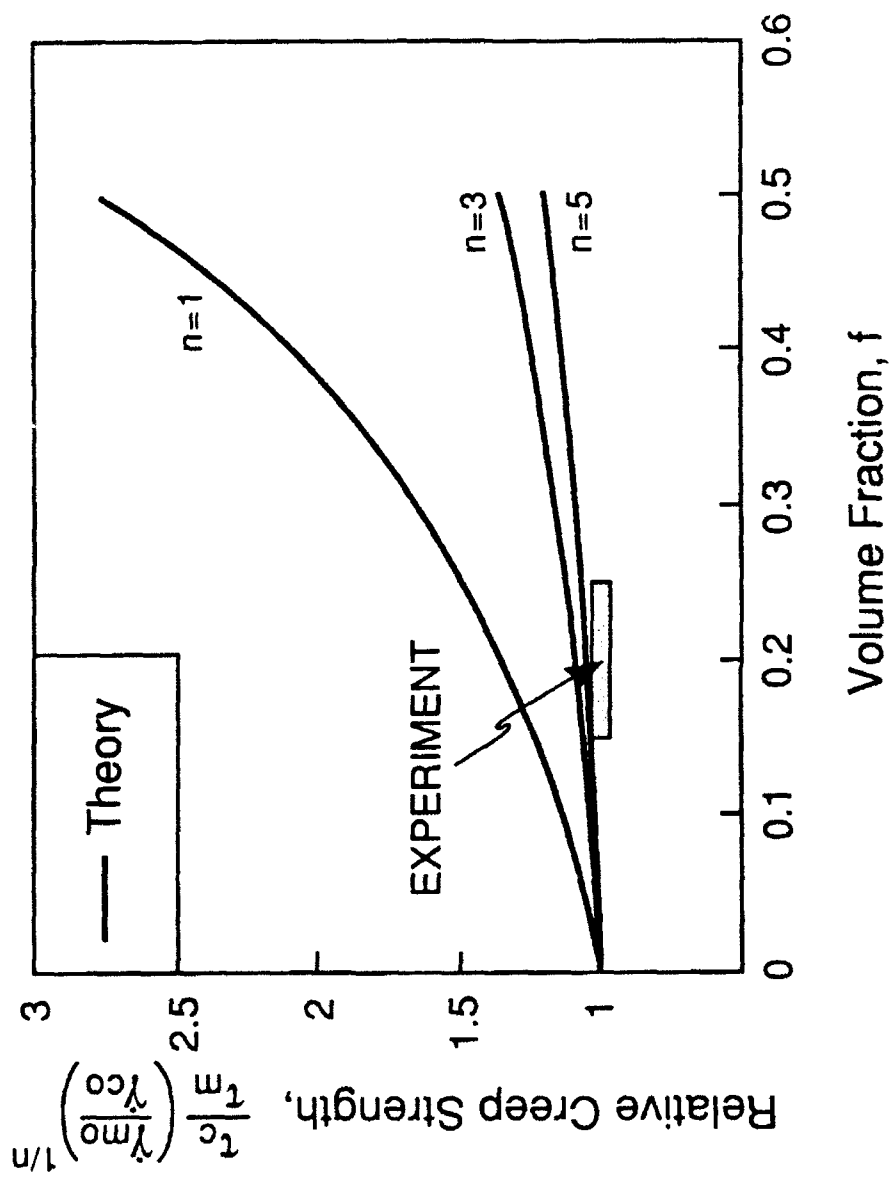


Fig. 2

THE MECHANICAL PROPERTIES OF Al ALLOYS REINFORCED WITH CONTINUOUS Al_2O_3 FIBERS

ML-S. HU¹, J. YANG¹, H. C. CAO¹, A. G. EVANS¹ and R. MEHRABIAN²

¹Materials Department, College of Engineering, University of California, Santa Barbara, CA 93106 and

²Carnegie Mellon University, Pittsburgh, PA 15213, U.S.A.

(Received 16 December 1991)

Abstract—The mechanical properties of aluminum matrix composites unidirectionally reinforced with Al_2O_3 fibers have been measured and characterized in longitudinal and transverse tension, as well as in shear. The flow strengths in transverse tension and shear are found to exceed those of the matrices, although the ductilities are lower. The strengthening is generally consistent with the development of plastic constraint in the matrix around well-bonded fibers, subject to the *in situ* properties of the matrix being known from independent measurements. The properties in longitudinal tension are found to involve interactions between fibers, such that fiber bundle strengths are not achieved, even when a low strength, pure Al matrix is used. Instead, the strengths are consistent with a crack growth controlled failure mechanism, wherein the strength is governed by the resistance of the material to crack extension from failed fibers.

Résumé—Les propriétés mécaniques de compositions à matrice d'aluminium renforcées unidirectionnellement avec des fibres de Al_2O_3 ont été mesurées et caractérisées en tractions longitudinale et transversale, ainsi qu'en cisaillement. Les résistances à l'écoulement en traction transversale et en cisaillement sont supérieures à celles de la matrice, bien que les ductilités soient moindres. En général, le durcissement est consistant avec le développement d'une contrainte plastique dans la matrice autour des fibres bien liées, pourvu que les propriétés *in situ* de la matrice soient déterminées à partir de mesures indépendantes. Les propriétés en traction longitudinale mettent en jeu des interactions entre les fibres, de sorte que l'on n'atteint pas les résistances d'un faisceau de fibres, même quand on utilise une matrice d'aluminium pur à faible résistance mécanique. Par contre, les résistances mécaniques sont compatibles avec un mécanisme de rupture contrôlé par la croissance des fissures, si bien que la résistance est gouvernée par la résistance du matériau au développement des fissures à partir des fibres endommagées.

Zusammenfassung—Die mechanischen Eigenschaften von Verbundwerkstoffen mit Al-Matrix, die gerichtet verstärkt sind mit Al_2O_3 -Fasern, werden gemessen und in longitudinalen und transversalen Zugversuchen und in Scherung charakterisiert. Die Fließfestigkeit in transversalem Zug und in Scherung überschreitet die der Matrix, wenn auch die Duktilität geringer ist. Die Härtung ist im allgemeinen verträglich mit der Entwicklung von plastischen Zwangsvorgängen in der Matrix um die gut gebundenen Fasern herum, die den von unabhängigen Messungen her bekannten Eigenschaften der Matrix unterworfen sind. Die Eigenschaften bei longitudinalem Zug umfassen Wechselwirkungen zwischen den Fasern in der Art, daß die Festigkeit von Faserbündeln nicht erreicht wird, auch wenn eine Matrix, wie reines Al, mit niedriger Festigkeit benutzt wird. Stattdessen sind die Festigkeiten verträglich mit einem durch Rißwachstum gesteuerten Bruchmechanismus, wobei die Festigkeit vom Widerstand des Materials gegenüber der Rißausbreitung von gebrochenen Fasern aus bestimmt wird.

1. INTRODUCTION

A basic understanding of the longitudinal, transverse and shear properties of fiber-reinforced metal matrix composites requires that these properties be expressed in terms of the constituent and interface properties [1–7]. Such relationships are the basis for designing and producing components with well-defined structural characteristics. A central issue concerns the fiber/matrix interface, which may be classified as either “strong” or “weak” [5]. The former is exemplified by Al alloys reinforced with Al_2O_3 [8, 9], while the latter is typified by Ti alloys reinforced with coated SiC fibers [7, 10–11]. The present study is concerned with the systems having “strong” interfaces.

Investigation of Ti matrix composites with coated SiC fibers have indicated the advantages and disadvantages of “weak” interfaces [5, 7, 10–11]. The *longitudinal* tensile properties approach those expected from a *rule-of-mixtures*. Furthermore, the strain to failure is essentially the failure strain of the fibers. Such behavior arises because debonding and sliding at the interface occurs in response to fiber fractures which eliminates stress concentrations in neighboring fibers. However, the *transverse* tensile properties are *diminished* by having a “weak” interface, such that the ultimate strength is appreciably less than the *matrix yield strength*. The transverse tensile modulus is also reduced at stresses above that at which the interface separates.

Metal matrix composites with a "strong" interface are expected to exhibit less anisotropy. Stress concentrations around cracked fibers would not normally be fully relaxed and the ultimate strain in longitudinal tension would be less than the fiber failure

strain [3]. However, the transverse tensile strength should be relatively large, because plastic constraint elevates the flow strength above that of the matrix [12, 13]. One intent of the present study is to relate the longitudinal and transverse properties of such a

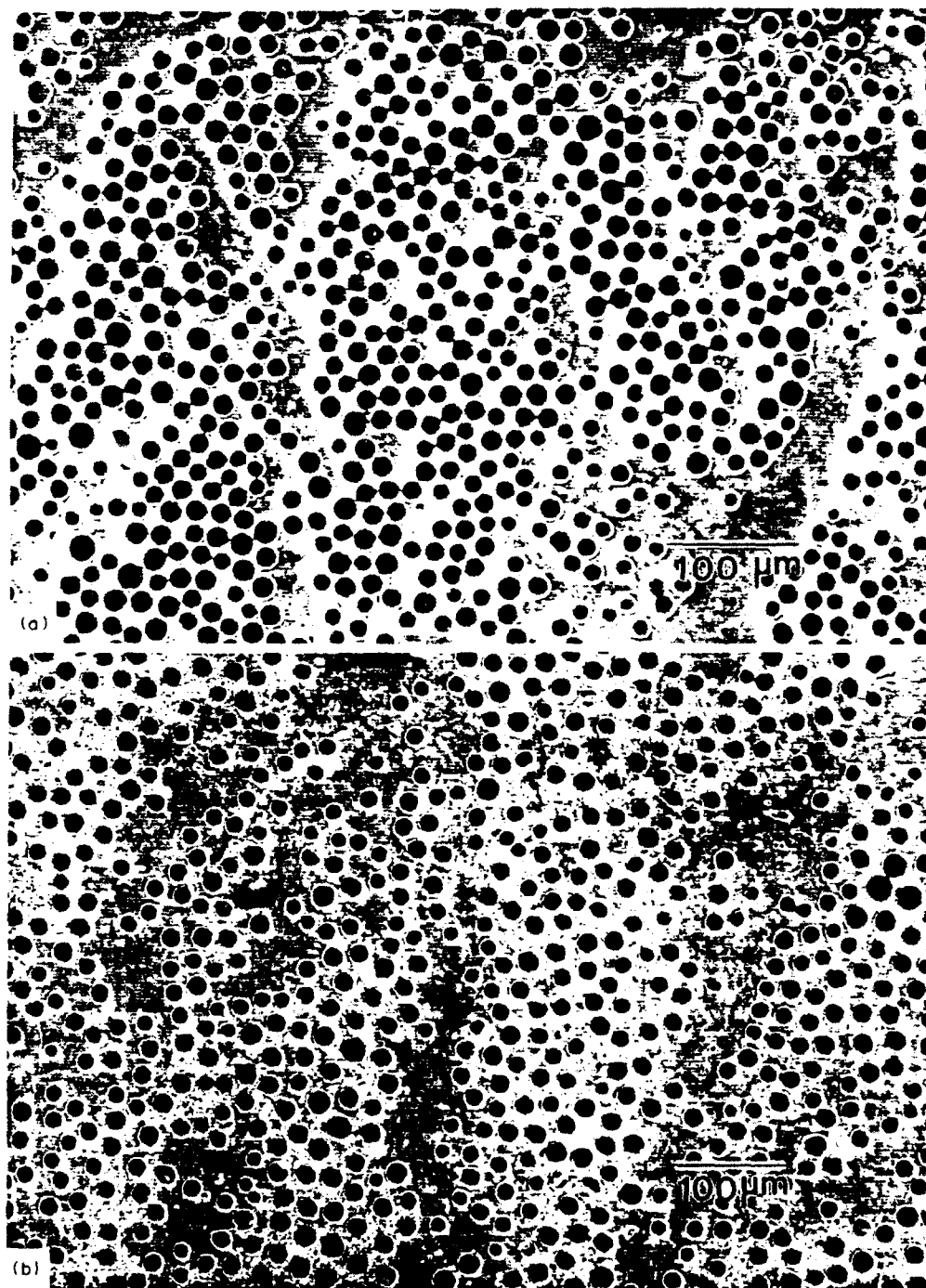


Fig. 1 SEM cross sections of several of the composites processed by squeeze casting. (a) Conventional casting. (b) casting into a fiber perform with SiC particulates on the fibers revealing superior fiber homogeneity.

composite to the properties of the fibers, the matrix and the interface. For this purpose composites consisting of Al_2O_3 fibers in Al alloy matrix have been produced and tested. An understanding of the behavior of such composites is dominated by three factors: (i) The *in situ* flow strength of the matrix, (ii) the *in situ* fiber strength and (iii) the strain concentration transmitted from a failed fiber to the neighboring fibers.

2. MATERIALS

Appreciable prior experience with Al matrix composites produced by squeeze casting has been used to identify systems that have supposedly well-characterized matrix and fiber properties [8, 14–16]. A solution strengthened matrix of Al 4 wt % Mg has the attributes that composites can be produced by squeeze casting without extensive Mg segregation to the interface [8]. This leads to a matrix with a relatively well-defined strength and good ductility. To provide contrasts in matrix properties, pure Al and a 2124 alloy were also used. The fibers used were FP- Al_2O_3 provided by DuPont.

Preliminary composite processing studies revealed that squeeze casting resulted in an inhomogeneous fiber distribution [Fig. 1(a)]. Superior homogeneity was achieved by first drawing the fibers through a slurry containing fine particulates of either Al_2O_3 or SiC. The attached particulates inhibit fiber contact during subsequent processing and allow materials to be processed with superior spatial homogeneity and having fiber volume fractions between 0.3 and 0.5 [Fig. 1(b)]. Most of the mechanical property investigations have been on materials processed in this manner. The two materials subject to comprehensive testing have the microstructural and constituent characteristics summarized in Table 1.

3. TEST PROCEDURES

Mechanical measurements have been made in tension, flexure and shear. Comprehensive studies were conducted in flexure on beams with faces carefully polished to minimize surface damage from machining. In these studies, strain-gauges were bonded to the tensile and compressive faces, as needed to measure both the longitudinal and transverse strains. The tension tests were performed on specimens with a reduced area in the gauge section produced by diamond machining followed by polishing. A strain

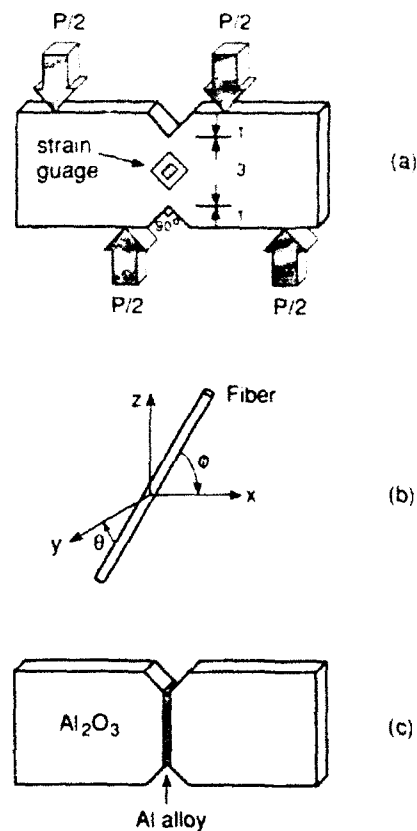


Fig. 2. Specimens used for shear testing (dimensions are in mm). (a) A notched beam under asymmetric 4-point flexure. (b) angles used to define fiber orientation and (c) a diffusion bonded shear specimen.

gauge was used to measure the strain in the gauge section.

The shear properties of the composites are assessed by using a notch shear specimen adapted from the Iosipescu test [17, 18]. This test concentrates the shear deformation in the reduced section between the notches and allows approximate determination of the shear flow strength from the load and the cross section. The dimensions of the specimen and loading configuration are given in Fig. 2(a). A strain gauge (gauge length, 0.6 mm) was attached to the reduced section, with an angle of 45° to the loading direction. Tests have been conducted with fibers aligned both parallel and normal to the notches, herein referred to as transverse shear ($\phi = 90^\circ$, $\theta = 0^\circ$ or 90°) and longitudinal shear ($\phi = 0^\circ$, $\theta = 90^\circ$), respectively, as defined in Fig. 2(b).

Information regarding the shear strength of the Al matrix has been obtained by devising the shear test depicted in Fig. 2(c). In order to perform this test, thin strips of the alloy used to prepare the composite matrix were solid-state diffusion bonded between plates of high-purity sintered Al_2O_3 . This resulted in a body consisting of a thin layer of matrix ($\sim 50 \mu\text{m}$) between Al_2O_3 , similar in characteristics to the

Table 1. Properties of constituents

<i>Fibers</i>	
	$E_f = 340 \text{ GPa}$
	$m = 6.5$
	$S_f = 1.7 \text{ GPa for } L_f = 0.025 \text{ m}$
<i>Matrices</i>	
Al-4% Mg	$E_m = 70 \text{ GPa}$
Al	$E_m = 70 \text{ GPa}$
Al (2124)	$E_m = 70 \text{ GPa}$

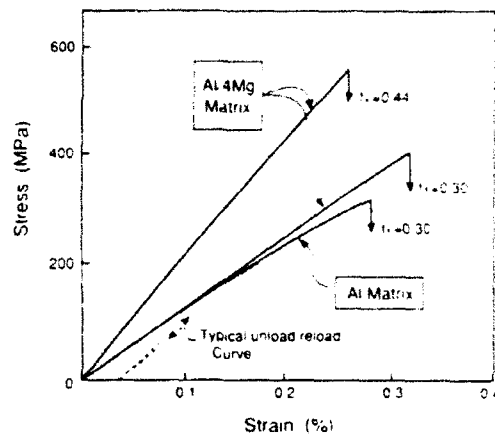


Fig. 3. Tensile stress-strain curves obtained in longitudinal tension.

matrix between the fibers in the composite. The bonded system was tested in shear with the shear displacement monitored using a displacement gauge located adjacent to the bond plane.

Observations of the materials have been made using optical and scanning electron (SEM) microscopes, both *in situ* and after testing, with the objective of identifying the damage processes and the failure sequence.

4. MEASUREMENT AND OBSERVATIONS

4.1. Longitudinal properties

Typical stress-strain curves obtained in longitudinal tension are summarized in Fig. 3. Trends in longitudinal elastic modulus with fiber volume fraction are plotted on Fig. 4. The ultimate strengths are found to be sensitive to flaws introduced during specimen preparation. Only data for nominally flaw-free material have been presented in Fig. 3. There are several noteworthy features. The curves exhibit only slight non-linearity prior to failure. Larger strengths are obtained with the Al-4 Mg alloy matrix com-

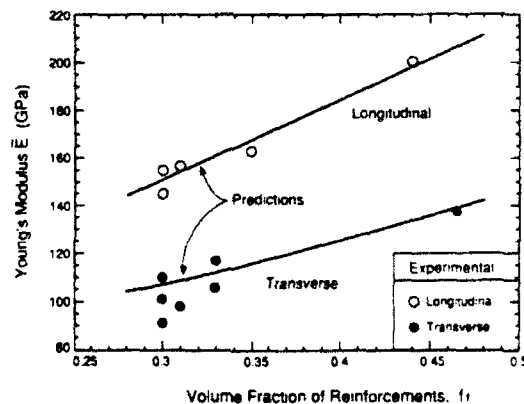


Fig. 4. Trends in Young's modulus with fiber volume fraction. Also shown are predicted lines for $E_f = 340$ GPa.

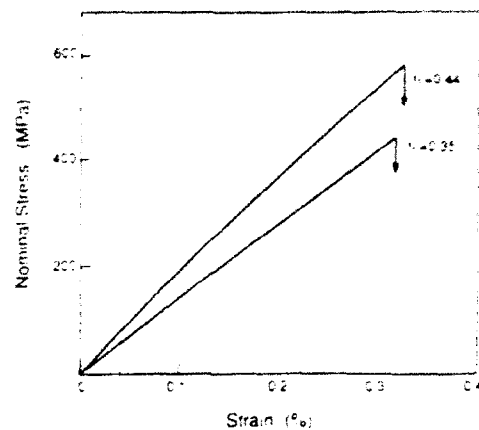


Fig. 5. Longitudinal stress-strain curves measured in four-point flexure. The stresses were calculated from elastic beam theory.

pared with the pure Al matrix. These are significant effects of fiber volume fraction.

The two matrices gave very different characteristics in flexure. Materials with the Al 4 wt % Mg matrix exhibited slight non-linearity up to the ultimate load, with failure initiating by fracture from the tensile face of the specimen (Fig. 5). Conversely, materials with a pure Al matrix exhibited extreme non-linearity, with extensive matrix deformation occurring by shear between the inner and outer loading points. No attempt was made to interpret the information obtained from the latter.

The dominant influence of the fibers on the longitudinal properties suggests that it would be insightful to make comparisons with the stress normalized by

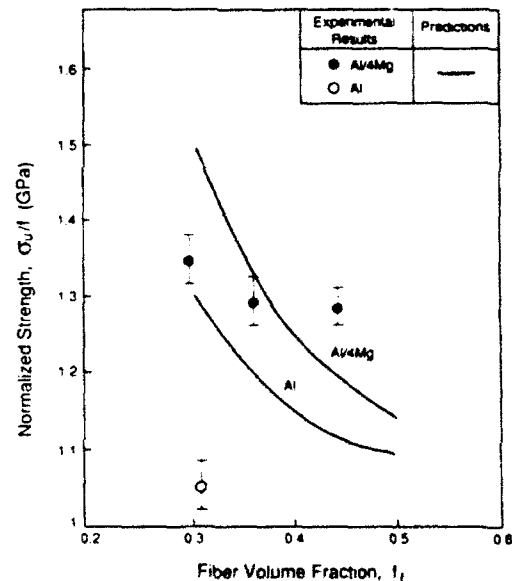


Fig. 6. Normalized ultimate tensile strength as a function of fiber volume fraction. Also shown are curves predicted using fracture mechanics model [equation 11(b)].

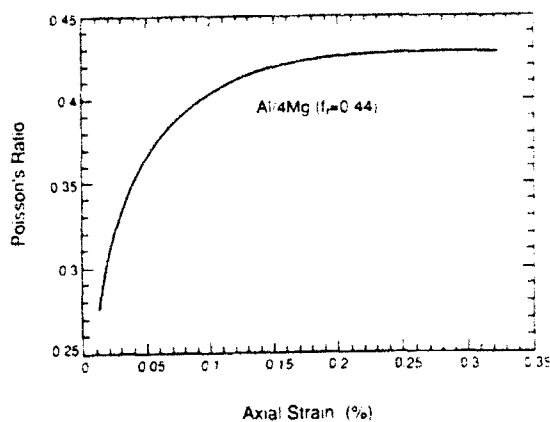


Fig. 7. Relationship between transverse and axial strains (Poisson's ratio) measured upon tensile testing of longitudinal specimens.

the fiber volume fraction, f . Accordingly, the normalized strength σ_u/f is found to be insensitive to fiber volume fraction (Fig. 6), but appreciably larger for composites with Al-4 Mg than Al matrices.

Simultaneous measurements of the longitudinal ϵ_{11} and transverse ϵ_{22} strains subject to longitudinal loading revealed that the Poisson's ratio, $\nu_{12} = -\epsilon_{22}/\epsilon_{11}$, varied monotonically from an initial value $\nu_{12} \approx 0.25$ to a final value at the ultimate strain, $\nu_{12} = 0.4$ (Fig. 7). Such characteristics are in accordance with the trend expected when there is no significant dilatation caused by reinforcement cracking.[†]

Observations of fracture surfaces indicate planar regions with intervening steps (Fig. 8). The planar regions appears to relate to fiber bundles having locally high fiber concentration. The plastic stretch of the intervening matrix [Fig. 9(a)] is about equal to the intrabundle fiber spacing. In circumventing regions nearly devoid of fibers, debonding occurs at the bundle perimeter, leading to a substantially larger plastic stretch [Fig. 9(b)]. These locations coincide with the steps, evident in Fig. 8, manifest as changes in the level of the fracture plane by several fiber diameters. In those materials processed with particulates, plastic failure of the matrix involves hole nucleation and growth from the particulates [Fig. 9(c)]. In consequence, the plastic stretch of the matrix is reduced and, on average, is about half that for the materials without particulates.

4.2. Transverse and shear properties

The transverse properties measured in tension are summarized in Fig. 10. Also shown for reference are the properties of particulate reinforced Al and Al/4 Mg matrices [14-16]. Trends in transverse elastic

modulus with fiber volume fraction are plotted on Fig. 4. The transverse flow strength increases with increase in matrix strength in the order Al \rightarrow Al-4 Mg \rightarrow 2124. There also appear to be significant effects of fiber volume fraction. The ductilities are relatively low in all cases, but largest for the composites with the Al matrix. The addition of particulates gives slightly greater strength, but lower ductility. Furthermore, SEM observations of the fracture surfaces (Fig. 11) confirm that transverse fracture is ductile and apparently occurs by the nucleation of holes, both at the fiber interface and from particles in the matrix (when present). The density of holes is larger in composites having higher particulate content [Fig. 11(b)]. The fracture plane is parallel to the fibers and inclined at 45° to the loading direction, suggesting that transverse failure is dominated by shear localization.

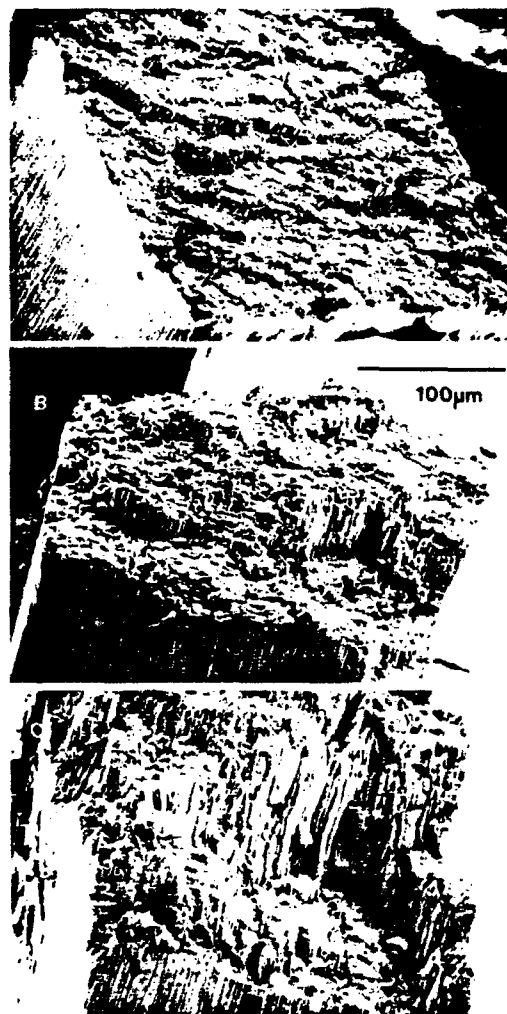


Fig. 8. SEM micrographs showing the roughness of tensile fracture surfaces of (A) Al 4 Mg, $f = 0.44$, (B) Al 4 Mg, $f = 0.3$, (C) Al, $f = 0.3$.

[†]Such behavior contrasts with the substantial dilatation that occurs in certain Al alloy matrix materials with discontinuous reinforcements [14, 15].

Stress-strain curves obtained on notched shear specimens (Fig. 12) indicate the same trends revealed in the transverse tension tests, with strength increasing in the order Al → Al-4Mg → 2124. There are significant differences between the two fiber orientations, with the longitudinal shear orientations being the strongest. On fracture surfaces associated with the longitudinal shear specimen, fiber splitting and bending [indicated by arrows in Fig. 13(A)] occur adjacent to areas having low fiber content. For the transverse shear specimen, failure occurs by shear localization in the matrix between fibers [Fig. 13(B)].

4.3. Matrix properties

The shear tests conducted on specimens diffusion bonded with Al [Fig. 2(c)] gave the shear stress-strain curve indicated on Fig. 14. The non-linear

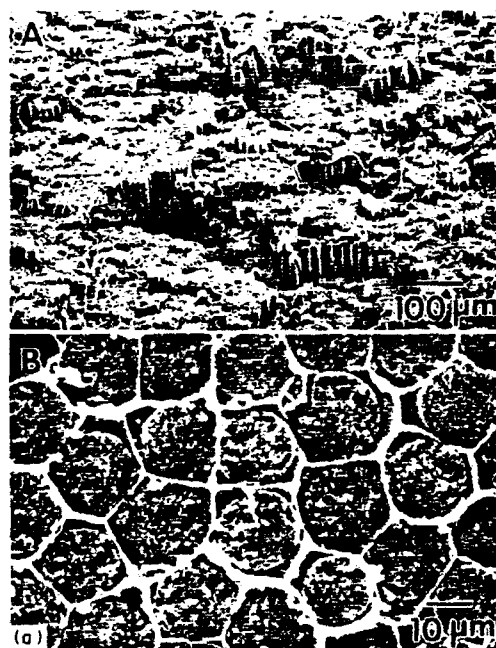


Fig. 9(a).

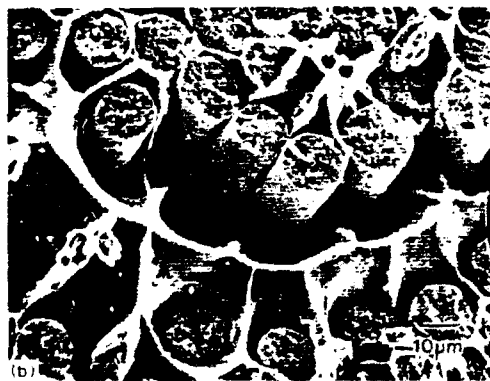


Fig. 9(b).

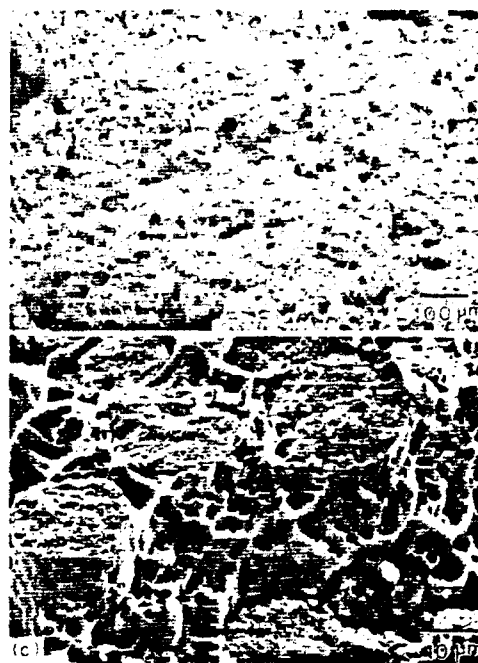


Fig. 9(c).

Fig. 9. SEM views of the fracture surface of specimens tested in longitudinal tension. (a) Material without particulates in a region having a high-fiber concentration revealing the plastic stretch of the matrix and the good interface bonding. (b) Same material as (a) but in a region with low fiber concentration, indicating the greater plastic stretch of the matrix and some debonding. (c) Material containing SiC particulates indicating good interface bonding and holes in the matrix caused by the particulates that reduce the plastic stretch.

deformation was localized to the thin metal layers and failure occurred by ductile hole nucleation and growth from the interfaces.

Microhardness tests conducted on the composites with indentations introduced into matrix regions devoid of fibers, gave Vickers hardnesses, H_v , of 760 ± 20 , 530 ± 30 and 175 ± 30 MPa for matrices of the 2124 alloy, Al-4Mg and Al, respectively. Estimates of the matrix flow strength, $\bar{\sigma}$ (at a strain of $\sim 7\%$) may be made using, $\bar{\sigma} \approx H_v^{3/2}$ (see Fig. 16).

5. SOME RELATED MECHANICS AND STATISTICS

5.1. Transverse flow strength

Continuum plasticity calculations provide a means of simulating the plane strain transverse deformation of unidirectional composites [12, 13]. Such calculations predict a substantial influence of the spatial arrangement of fibers on the flow strength. Results obtained using two different methods are summarized on Fig. 15(a), wherein the strength, $\bar{\sigma}(c)$, is normalized by the flow strength of the matrix $\bar{\sigma}(c)$ at the

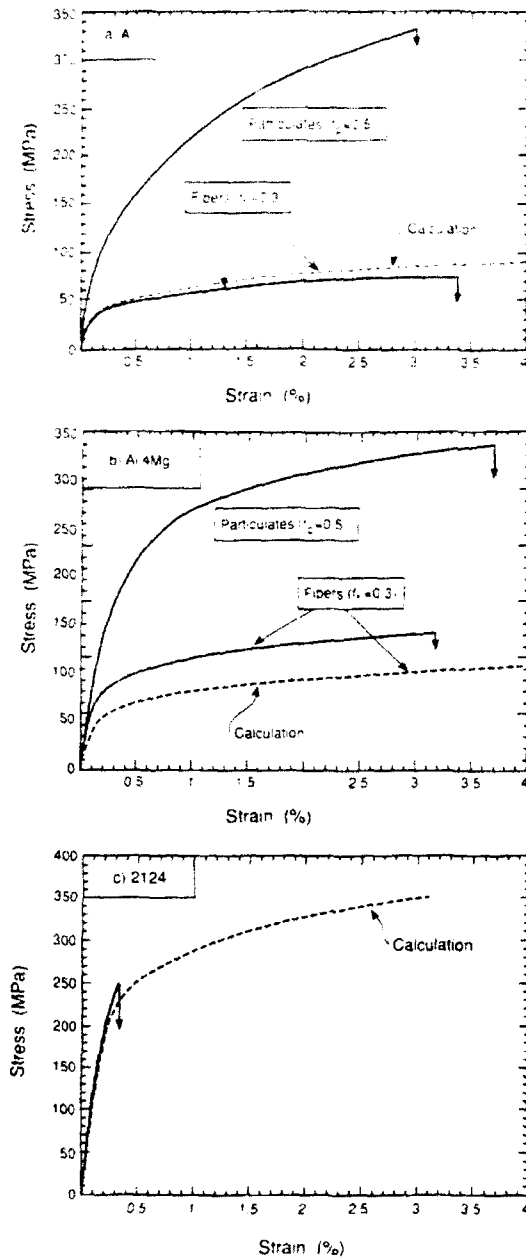


Fig. 10 (a, b, c) Transverse tensile stress-strain curves compared with curves for the same matrices reinforced with 9 μ m SiC particulates. Also shown are transverse flow curves calculated as described in the text.

equivalent strain. Corresponding stress-strain curves are plotted on Fig. 15(b). The numerical calculations have been conducted with periodic boundary conditions using a Ramberg-Osgood power hardening constitutive law for the matrix [20]

$$\epsilon = \sigma_0 E + \alpha \epsilon_0 (\sigma / \sigma_0)^n \quad (1)$$

where σ_0 is yield strength, ϵ_0 is the yield strain, n is the hardening coefficient and $\alpha \approx 3.7$. Also shown

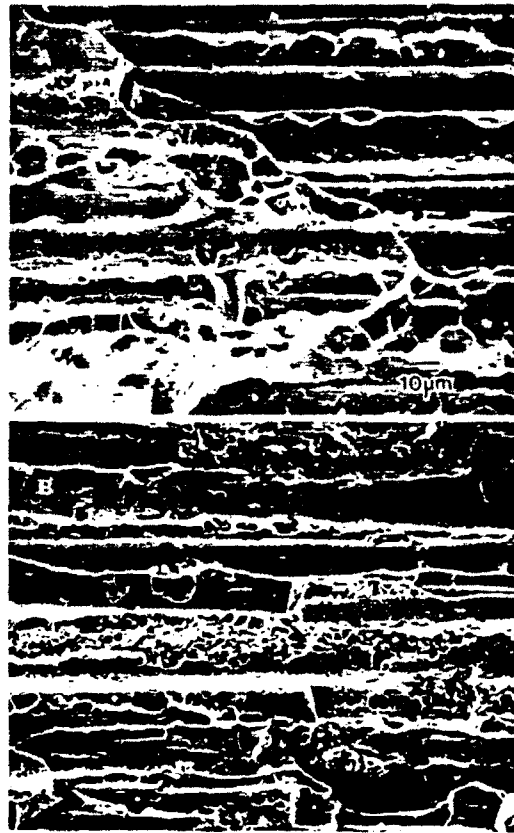


Fig. 11. SEM views of fracture surface associated with transverse tensile testing (A) Low particulate content (B) High particulate content

are predictions based on self-consistent method [21]. Both methods appear to yield similar strengths. Other fiber arrangements give lower strengthening factors [12]. Comparisons with experimental measurements, described below, provide insight about the spatial arrangement having the most practical relevance. To facilitate interpretation, it is noted that for the particulate reinforced composite $\bar{\sigma}(\bar{\epsilon})$ can also be

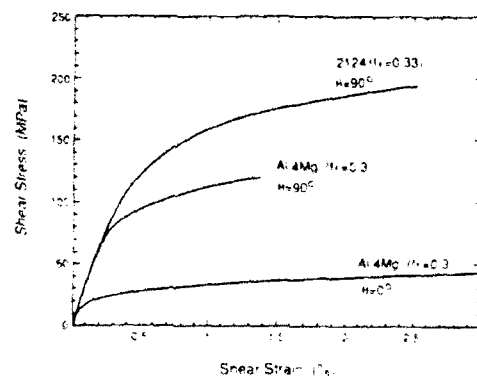


Fig. 12 Shear stress-strain curves obtained using notched specimens



Fig. 13. SEM views of fracture surface associated with the asymmetric 4-point flexure. (A) Longitudinal shear ($\Phi = 0^\circ$, $q = 90^\circ$). (B) Transverse shear ($\Phi = 90^\circ$, $\theta = 0^\circ$). The loading direction is the same in both cases.

approximately expressed in Ramberg-Osgood form [13]

$$\bar{\epsilon} = \bar{\sigma} \bar{E} + \alpha \bar{\sigma}_N (\bar{\sigma} / \bar{\sigma}_N)^n \quad (2)$$

where \bar{E} is the elastic modulus of the composite and $\bar{\sigma}_N$ is the reference strength, which depends on n , f and spatial arrangement.

5.2. Longitudinal strengths

For composites with interfaces that resist debonding (typical of the materials tested in this study), the longitudinal strength is dominated by the behavior around cracked fibers. When the fibers are either relatively closely spaced or the matrix has a high yield strength, an appreciable stress concentration for a failed fiber is transmitted to its neighbors [3]. This leads to coordinated fiber fracture and an ultimate strength controlled by *crack extension*. Conversely, when either the fiber spacing is large or the matrix yield strength is low, such that the stress concentration is dissipated by matrix slip, the fibers may be treated as statistically independent entities, leading to an ultimate strength governed by *probabilistic considerations* [1-6].

[†]The slip length, is given by $l = R(S_f / 2\tau)$, where S_f is the stress on the fibers at the composite ultimate strength [6]. For this composite, l is found to be $\approx 100 \mu\text{m}$, which is small compared with the gauge length ($L_g \approx 6 \text{ mm}$).

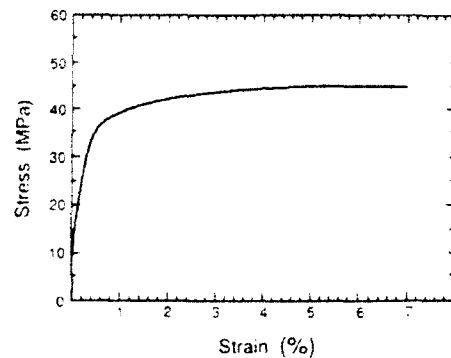


Fig. 14. Shear stress strain curve obtained on an Al diffusion bonded specimen

For conditions wherein the stochastic model applies, multiple cracking of the fibers is possible whenever the slip length l^\dagger is small compared with the specimen gauge length L_g , because shear load transfer occurs from the matrix around fiber fracture sites [6]. The associated shear resistance τ is governed by the matrix shear strength, $\tau = \sigma_0 / \sqrt{3}$. For this case, the ultimate strength σ_u can be related to the fiber strength S_f , as dictated by the underlying statistical properties of the fibers, in accordance with

$$\sigma_u = f_f S_f + (1 - f_f) \sigma_0 \quad (3)$$

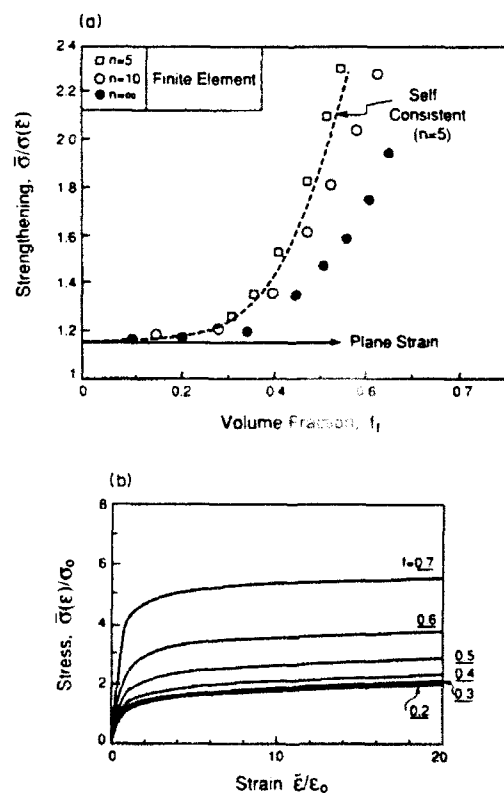


Fig. 15. (a) Calculated transverse flow strengths as a function of fiber volume fraction. (b) Calculated transverse stress-strain curves (normalized by the matrix yield stress and strain).

with S_i are given by [6]

$$S_i = S_0 \left[\frac{2\tau L_i}{RS_0(m+2)} \right]^{m+1} \left(\frac{m+1}{m+2} \right) \quad (4)$$

where S_0 and L_0 are scale parameters and m is the shape parameter associated with the fiber strength distribution (Table 1) and R is the fiber radius. Note that, in this limit, S_i is independent of gauge length.

When fiber fracture involves stress concentration effects from neighboring failed fibers, analysis of the ultimate strength requires a stress concentration model, as well as a composite fracture criterion. Such analyses have previously used a numerical simulation to evaluate the fiber failure probabilities [3]. Their general implication is that a transition in ultimate strength occurs, such that fracture mechanics considerations become increasingly important at larger values of τ and f . Consequently, an approach based on fracture mechanics, suggested by a companion study [22], is used to provide useful insight when composite failure involves the coplanar failure of fibers (Fig. 8). The crack growth resistance K_R of the material for relatively small crack extensions, L , is given by [22]

$$K_R \approx K_0 + 2\sqrt{\frac{2}{\pi}} \chi \sigma_0 (1 - f_f) \sqrt{L} \quad (5)$$

where χ is a constraint factor (of order 2.5) and K_0 is the fracture resistance of the fibers, ($K_0 \approx 3 \text{ MPa} \sqrt{\text{m}}$). The stress intensity factor, K , for a circular crack large compared with the fiber diameter is

$$K = \frac{2}{\sqrt{\pi}} \sigma \sqrt{a} \quad (6)$$

when a is the crack radius and σ is the imposed stress. For a small crack *within* a single fiber, the elevation of the stress caused by the high modulus of the fiber is important, such that

$$K \approx \frac{2}{\sqrt{\pi}} \sigma \sqrt{a} (E_f/E) \quad (7)$$

For a crack growing out of a single fiber, radius R , interpolation between equations (6) and (7) gives

$$K = \frac{2\sigma}{\sqrt{\pi}} \{ \sqrt{L+R} + \lambda \sqrt{R} \} \quad (8)$$

where $a \equiv L + R$ and λ is a coefficient that reflects stress elevation effects given by,

$$\lambda = (E_f - E)/E.$$

Equating K to K_R for crack growth gives

$$\Sigma = \frac{\sqrt{\pi/2} + \sqrt{2\Sigma_0}\sqrt{l}}{\sqrt{1+l+\lambda}} \quad (9)$$

where

$$\Sigma = \sigma \sqrt{R}/K_0, \quad \Sigma_0 = \chi \sigma_0 \sqrt{R} (1 - f_f)/K_0$$

and $l = L/R$. The fracture instability is given by the criterion

$$\frac{dK_R}{dL} = \frac{dK}{dL} \quad (10)$$

subject to $K_R = K$. Differentiating equations (5) and (8) and equating [with Σ given by equation (9)] leads to a solution for the ultimate strength, which occurs at a crack extension

$$l_* = \frac{L_*}{R} = \frac{B + \sqrt{B^2 - AC}}{A} \quad (11a)$$

where

$$B = \lambda^2 (1 - \lambda^2) + \frac{\pi}{8\Sigma_0^2} (1 + \lambda^2)$$

$$A = \left(\frac{\pi}{8\Sigma_0^2} - \lambda^2 \right)^2$$

$$C = (\lambda^2 - 1)^2.$$

The ultimate strength is then given by substituting l_* into equation (9)

$$\sigma_u = \frac{K_0}{\sqrt{R}} \Sigma(l_*) \quad (11b)$$

6. PROPERTY ANALYSIS

6.1. Elastic properties

The expected *longitudinal* elastic properties of the composite, $\bar{E} = f_f E_f + (1 - f_f) E_m$, based on the reported properties of the fibers and the matrix (Table 1) do not agree with the present experimental measurements. The most feasible interpretation of the discrepancy is that the fibers have a lower modulus than expected. The inferred fiber modulus is $E_f = 340 \text{ GPa}$ (Fig. 4). Using this value for E_f , the *transverse* elastic modulus, E_T , is predicted using [23]

$$\frac{E_T}{E_m} = \frac{1 + \zeta \eta f_f}{1 - \eta f_f} \quad (12)$$

where

$$\eta = \left(\frac{E_f}{E_m} - 1 \right) / \left(\frac{E_f}{E_m} + \zeta \right)$$

and ζ is a parameter dependent on the geometry and spatial arrangement of the reinforcements. Agreement between measurements and predictions (Fig. 4) requires that $\zeta \approx 2$; the value associated with a square array of continuous fibers [23]. A similar conclusion regarding the relevant spatial arrangement of fibers is reached when the transverse flow properties are addressed, as elaborated below.

6.2. Transverse and shear properties

The transverse and shear stress-strain curves for the three different matrices, as well as the curves for

the particulate reinforced materials, are qualitatively consistent with the continuum calculations. Notably, the composite strength increases as both the matrix strength and the reinforcement volume fraction increase. Additionally, the transverse and shear properties are consistently related to each other by a factor, $\sqrt{3}$, in good accordance with the Mises criterion. However, more detailed analysis reveals discrepancies. For rational assessment of these discrepancies, further diagnosis of the material properties reflects the concern that the matrix properties in the composite often differ from those associated within the monolithic matrix. Consistency is thus sought between the properties of the composites (particulate and fiber-reinforced), and the *in situ* matrix properties assessed from the hardness.

For the Al and Al 4 Mg systems, the experimental curves for the particulate composites [15, 16] are first fitted to equation (2) to evaluate the hardening exponent, n , and the composite reference strength $\bar{\sigma}_0$. Then, $\bar{\sigma}_0$ is used to determine the matrix reference strength, σ_0 , using a procedure described elsewhere [13], leading to the calculated matrix strengths plotted on Fig. 16.[†] (Note that the Al matrices exhibit the largest work hardening but the lowest yield strength.) Thereafter, the matrix properties (determined in this manner) are used to predict the transverse properties of the fiber composites, using the *maximum strengthening ratio* predicted from either finite element or self-consistent calculations (Fig. 15).

Inspection of the results (Figs 10 and 16) establishes the following factors for the three respective matrices. (i) The Al matrix composites exhibit complete consistency between the flow properties of the two composites as well as the matrix properties determined either by hardness measurements or by shear tests. However, the *matrix flow strength* is larger than that usually attributed to bulk Al [Fig. 16(a)]. (ii) For Al 4 Mg matrix composites, the matrix flow properties ascertained from the particulate composite and from hardness measurements are similar to the properties of the bulk alloy (Fig. 16). However, the *transverse properties* measured on the fiber composites are appreciably larger than the predictions. (iii) Materials with 2124 matrices exhibit consistency between hardness measurements and the bulk matrix properties, as well as the calculated transverse flow strength.

Two principal discrepancies emerge from the above analysis. (i) The matrix in the Al alloy composite is anomalously strong. (ii) The transverse strength of the Al Mg composite is anomalously high. These

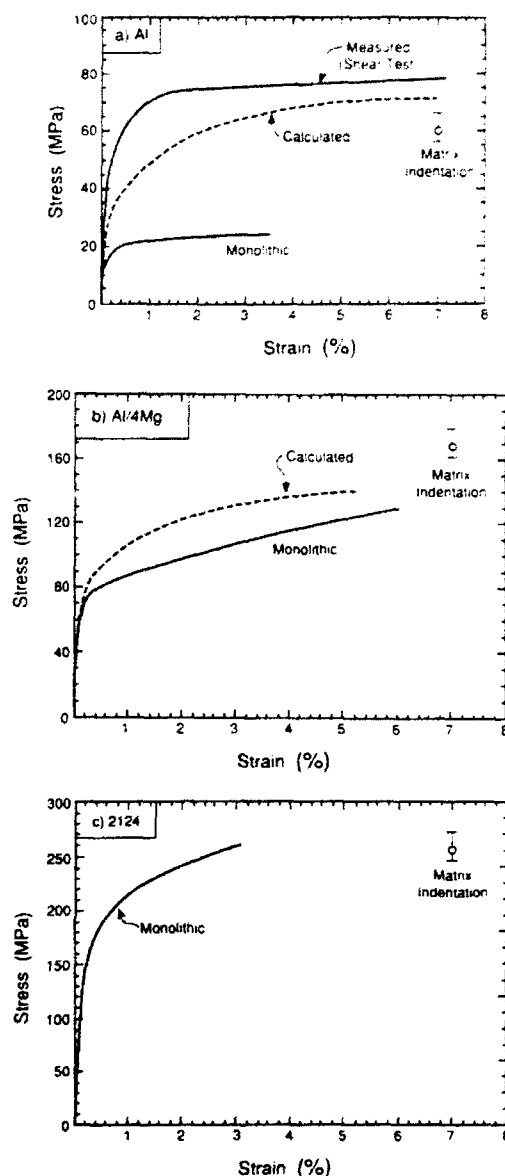


Fig. 16. Comparison of measured and calculated matrix stress-strain curves. Also shown are stress-strain curves for the bulk matrices as well as the matrix flow strength inferred from hardness measurements.

discrepancies may be addressed through the following considerations. Composite matrices can be strengthened in two ways.[‡] Firstly, reaction with the reinforcements plus contamination may lead to either solute or precipitation hardening. Secondly, grain and dislocation cell evolution during processing may involve interactions with the reinforcements, resulting in Hall-Petch strengthening. Related studies [25] suggest the latter.

It is concluded that the spatial distributions of fibers giving the *highest transverse and shear strengthening levels* appear to be most applicable to these composites, as also found above, for the transverse

[†]For the 2124 matrix composites, since particulate composite data were not available, the flow strength of the monolithic matrix was used to calculate the composite transverse strength.

[‡]Contrary to some previous assertions, residual stress effects caused by thermal expansion mismatch cannot account for the observed behavior because such effects are eliminated at strains, $\epsilon \approx 3-5\epsilon_0$ [24].

elastic properties. The absence of preferred shear planes that might cause diminished levels of strengthening [12] is inferred, even though transverse failure involves shear localization. A further implication is that cell calculations based on regular arrangements of fibers provide a reasonable simulation of the behavior found in actual composites.

6.3. Longitudinal strength

One of the difficulties in the analysis of the longitudinal properties concerns the *in situ* strength of the fibers. Fracture mirror measurements (which can be used for this purpose [26]) have not been successful for FP-Al₂O₃ fibers. Consequently, literature data [27] are used to estimate the fiber properties (Table 1). On this basis, the *probabilistic failure* model for non-interacting fibers [equation (3)] predicts ultimate strengths $\sigma_u f \approx 2$ –2.5, appreciably in excess of measured values (Fig. 6). The invalidity of the model is consistent with the co-ordinated nature of the fiber failures as manifest in the relatively planar intrabundle failure (Fig. 8). Accordingly, the predictions based on a *crack extension mechanism* [equation (11)] obtained by assuming that a *single fiber* acts as the initial flaw (Fig. 6), are appreciably closer to the measured values. However, the corresponding extent of crack growth prior to failure is only, $L_* \approx 0.5R$. A more complete attempt at predicting the longitudinal strength, using more information about intrabundle fiber spacing, is made in a companion paper [22]. However, a rigorous model may require statistical consideration of the cracking of the *nearest neighbor fibers*, including the explicit of matrix deformation around a failed fiber.

7. CONCLUDING REMARKS

The results of the preceding study have provided a comprehensive comparison between experiment and theory on the mechanical properties of unidirectional metal matrix composites with well-bonded fibers. In general, the transverse and shear properties are in good accordance with elastic and elastic/plastic strengthening levels predicted from cell calculations, provided that consistent values of the *in situ* properties of the matrix and fibers are used. In some cases, the *in situ* properties differ from those of the constituent materials *ex situ*, because of various effects that occur during processing. Consequently, the use of *ex situ* properties typically lead to erroneous conclusions about the comparisons between theory and experiment.

The ultimate strengths and ductilities in transverse tension have not been explicitly addressed. The observations have revealed that fracture occurs by ductile mechanisms operating in the matrix, with voids being nucleated at both of the fiber interface and at particulates in the matrix. A strength and ductility

model would involve analysis of the nucleation and coalescence of these voids within the relatively large hydrostatic tensile field that develops in the matrix and, indeed causes the transverse strengthening [13].

Analysis of the longitudinal properties has established that fiber interactions are involved in the failure process, leading to an ultimate strength governed by flaw propagation within fiber bundles. Consequently, the strengths are sensitive to fiber damage that occurs during processing and machining. Effects of fiber volume fraction and matrix flow strength are broadly consistent with a simplified model based on the crack extension instability.

Some general results applicable to metal matrix composites with a relatively large volume fraction of well-bonded fibers emerge from the preceding discussion. Well-bonded fibers in ductile matrix composites lead to high stiffness and *flow strength*, relative to the matrix, in longitudinal and transverse tension, as well as in shear. The *longitudinal failure* properties involve flaw propagation within fiber bundles, leading to relatively low failure strains, which are also sensitive to processing and machining damage. *Transverse failure* involves ductile fracture in the matrix, but also occurs at relatively low strains because of high hydrostatic stress in the matrix coupled with void nucleation at the fiber matrix interface.

REFERENCES

1. C. Zweben, *AIAA JI* **6**, 2325 (1968).
2. J. M. Hedgepeth and P. van Dyke, *J. Comp. Mater.* **1**, 294 (1967).
3. S. Ochiai and K. Osamura, *Metall. Trans.* **21A**, 971 (1991).
4. B. D. Coleman, *J. Mech. Phys. Solids* **7**, 60 (1958).
5. A. G. Evans, *Mater. Sci. Engng.*, in press.
6. W. A. Curtin, *J. Am. Ceram. Soc.* **74**, 2837 (1991).
7. S. Jansson, H. E. Deve and A. G. Evans, *Metall. Trans.* **22A**, 2975 (1991).
8. Y. L. Klipfel, M. Y. He, R. M. McMeeking, A. G. Evans and R. Mehrabian, *Acta metall.* **38**, 1063 (1990).
9. B. J. Dalgleish, K. P. Trumble and A. G. Evans, *Acta metall.* **37**, 1923 (1989).
10. R. P. Nimmer, R. J. Bankert, E. S. Russel and G. A. Smith, *ASM Materials Conference*, Indianapolis, Oct. (1989).
11. A. L. Highsmith, S. J. Lubowski and W. S. Johnson, *ASTM STP 1080* (edited by Kennedy, Moelles and Johnson) (1990).
12. J. R. Brockenbrough, S. Suresh, H. A. Winecke, *Acta metall. mater.* **39**, 735 (1991).
13. G. Bao, J. W. Hutchinson and R. M. McMeeking, *Acta metall. mater.* **39**, 1871 (1991).
14. J. Yang, C. Cady, M. S. Hu, F. W. Zok, R. Mehrabian and A. G. Evans, *Acta metall. mater.* **38**, 2613 (1990).
15. J. Yang, S. M. Pickard, R. Mehrabian and A. G. Evans, *Acta metall. mater.* **39**, 1863 (1991).
16. M. S. Hu, *Scripta metall. mater.* **25**, 695 (1991).
17. N. Iosipescu, *J. Mater.* **2**, 537 (1967).
18. D. E. Walrath and D. F. Adams, *Exp. Mech.* **23**, 105 (1983).
19. D. Tabor, *Hardness of Metals*, Clarendon Press, Oxford, U.K. (1951).

20. S. Schmauder and R. M. McMeeking, to be published.
21. W. Huang, *J. Composite Mater.* **5**, 320 (1971).
22. H. C. Cao, J. Yang and A. G. Evans, to be published.
23. J. C. Halpin and S. W. Tsai, *Air Force Materials Laboratory Tech. Report* 67-423. Also discussed in *Primer on Composite Materials Analysis*, by J. E. Ashton, J. C. Halpin and P. H. Petit, Technomic, Stamford CN (1969).
24. D. Zahn and R. M. McMeeking, *Acta metall. mater.* **39**, 1117 (1991).
25. S. M. Pickard, S. Schmauder, D. B. Zahl, J. Yang and A. G. Evans, to be published.
26. H. C. Cao, E. Bischoff, O. Sbaizero, M. Ruhle, A. G. Evans, D. B. Marshall and J. J. Brennan, *J. Am. Ceram. Soc.* **73**, 1691 (1990).
27. J. Nunes, Army Materials and Mechanics Research Center, AMMRC TR 82-61.

THE MODE I FRACTURE RESISTANCE OF UNIDIRECTIONAL FIBER-REINFORCED ALUMINUM MATRIX COMPOSITES

H. C. CAO, J. YANG and A. G. EVANS

Materials Department, College of Engineering, University of California,
Santa Barbara, CA 93106-5050, U.S.A.

(Received 16 December 1991)

Abstract—The mode I fracture resistance has been measured for Al and Al-4 Mg matrix composites, unidirectionally reinforced with ceramic fibers, prepared using a squeeze casting technique. Effects of SiC particle additions have also been investigated. The Al-4 Mg system had a high toughness, whereas the Al matrix system had a relatively low fracture resistance. In all cases, the addition of particulates slightly decreased the resistance to crack growth. The fracture resistance was simulated by a ductile bridging model with plastic dissipation occurring within a zone governed by the fiber spacing. The tensile strength of these composites has been estimated, based on the resistance behavior and microstructure.

Résumé—La résistance à la rupture du mode I a été mesurée pour des composites à matrice d'aluminium et à matrice d'aluminium-4% magnésium, renforcés dans une direction avec des fibres céramiques et élaborés à partir d'une technique de coulée sous pression. On a étudié également l'effet d'additions de particules de SiC. Le système Al-4 Mg présente une résistance élevée, alors que le système à matrice Al présente une résistance à la rupture relativement faible. Dans tous les cas, l'addition de particules abaisse un peu la résistance à la croissance des fissures. On a simulé la résistance à la rupture à l'aide d'un modèle de pont ductile avec dissipation plastique, actif à l'intérieur d'une zone régie par l'espacement des fibres. On a estimé la résistance à la traction de ces composites en se basant sur la résistance à la rupture et sur la microstructure.

Zusammenfassung—Der Widerstand für Mode-I-Bruch wird an Verbundwerkstoffen mit Matrix Al oder Al-4 Mg, gerichtet verstärkt mit keramischen Fasern und hergestellt mit dem Quetsch-Guß-Verfahren, gemessen. Außerdem wird der Einfluß von SiC-Zugaben untersucht. Das System mit Al-4 Mg wies eine hohe Härte auf, dagegen hatte das System mit Al-Matrix einen vergleichsweise geringen Bruchwiderstand. In sämtlichen Fällen verringerte die Zugabe von Teilchen ein wenig den Rißausbreitungswiderstand. Der Bruchwiderstand wird simuliert mit einem duktilen Überbrückungsmodell, bei dem innerhalb einer vom Faserabstand bestimmten Zone plastische Dissipation auftritt. Die Zugfestigkeit dieser Verbundwerkstoffe wird abgeschätzt auf der Grundlage des Widerstandsverhaltens und der Mikrostruktur.

1. INTRODUCTION

The fracture resistance of composites that consist of one brittle and one ductile constituent has been the subject of extensive recent research [1-6]. The systems investigated include ceramics and intermetallics reinforced with metals and alloys [1-5], as well as layered materials [5-7] and metal matrix composites [8, 9]. Various cracking behaviors have been identified [10]. The present article provides a contribution to this topic by investigating the mode I fracture resistance of metal matrix composites (MMC) consisting of Al alloy matrices reinforced with continuous Al_2O_3 fibers [11, 12]. This system typifies an MMC with a well-bonded interface [10, 13].

The mode I fracture behavior of materials with one brittle and one ductile constituent is seemingly insensitive to the morphology of the constituents. The interpretation and prediction of the fracture resistance is essentially the same for brittle matrices reinforced with metals [1-5], layered materials [5-7] and metal matrices reinforced with brittle fibers. Notably,

the fracture resistance in excess of that for the brittle constituent derives almost entirely from plastic dissipation in the metal. The dissipation is found to be reflected in the magnitude of a parameter, $f_m \sigma_m u$ [1, 2, 14], where σ_m is the flow strength of the metal, f_m its volume fraction and u the plastic stretch between the crack faces. The plastic stretch is, in turn, strongly influenced by the ductility of the metal, as well as debonding tendencies at the interface [2, 6]. For systems involving combinations of Al with Al_2O_3 , which exhibit good bonding and high metal ductility [11, 13], it has been found that the stretch may be adequately related to the stress on the metal ligaments by a linear softening law [14]

$$\sigma \approx \sigma_c (1 - u/u_c) \quad (1)$$

where u_c is the rupture stretch and σ_c is the constrained flow strength of the metal. In turn, σ_c is a multiple χ of the uniaxial flow strength, σ_0 [1, 2, 14]

$$\sigma_c = \chi \sigma_0 \quad (2)$$

Table 1. Summary of composite properties

Materials	Matrix	Reinforcements		E^* (GPa)	σ (MPa)
		f	f_p		
A	Al 4 Mg	0.47	0	210	120
B		0.44	0.03	180	120
C		0.3	0.15	160	120
D	Al	0.3	0	150	60
E		0.31	0.02	155	60
F		0.30	0.15	160	60

*Ref. [12]

For a bonded interface, γ depends on the work hardening coefficient for the metal, N (for Al alloys with $N \approx 5$, $\gamma \approx 2.5$) [1, 2]. Subject to equations (1) and (2), calculations of the plastic dissipation upon crack extension Δa [14] predict that the crack growth resistance, $\Delta \mathcal{G}_R$, increases as the crack extends in accordance with the non-dimensional relation†

$$\Delta \mathcal{G}_R / \gamma \sigma_m u_c f_m = 1.6l - 0.09l^2 - 0.53l^3 \quad (3)$$

$$\equiv g(l)$$

where $l = \Delta a / L_s$, with L_s being the crack length at which steady-state toughening commences, defined as [14]

$$L_s = 0.37 E u_c (1 - \nu^2) \sigma_m \quad (4)$$

where E is the longitudinal Young's modulus of the composite.

The increase in resistance superposes on an initiation resistance \mathcal{G}_0 . The magnitude of \mathcal{G}_0 is also known to reflect plastic dissipation, through crack tip blunting, and may be appreciably larger than the intrinsic fracture energy of the brittle material, Γ_0 [7]. The full fracture resistance of the composite is

$$\mathcal{G}_R = \mathcal{G}_0 + \Delta \mathcal{G}_R$$

$$\equiv K_R^2 / E \quad (5)$$

where K is the stress intensity factor.

The application of the above concepts to MMCs is addressed in this article. It involves measurements of the resistance $K_R(\Delta a)$, the critical stretch u_c , the metal volume fraction, f_m , and the *in situ* flow strength of the matrix σ_m . This information is obtained for a combination of tests described both in the present article and in a companion study [12].

2. MATERIALS

All materials examined in this study have been processed using a squeeze casting approach [11, 12]. Two matrices have been used: a high purity Al, as well as an Al 4% Mg alloy having the characteristics described elsewhere [12]. The reinforcements are FP Al_2O_3 fibers. Two approaches have been used to produce the fiber-reinforced materials. In one case, the fiber strands were drawn through a slurry

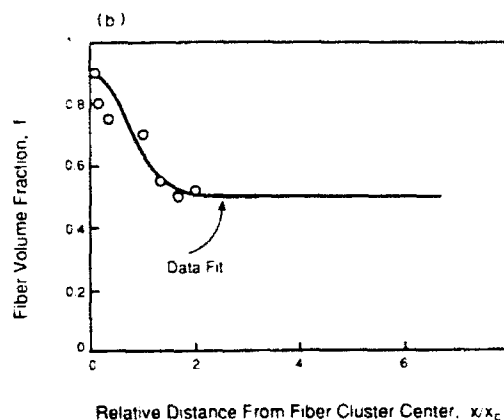
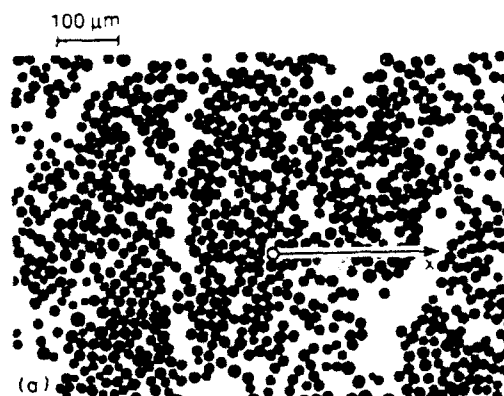


Fig. 1. (a) Digital image of a cross sectional SEM view of a Al 4 Mg FP fiber composite [12] ($f_c = 0.47$). (b) Volume fraction of ceramic fiber as a function of the area measured from a cluster center

of particles of either Al_2O_3 or SiC, causing the particles to adhere to the fibers. The particles separate the fibers and maintain fiber separation during the squeeze casting operation. These composites have a fiber volume fraction in the range $f_f = 0.3$ – 0.45 . The resultant composite contains SiC particulates with volume fraction f_p in the range, 0.03–0.15. Composites produced without such particles have fibers configured within bundles having high local volume fraction [12], $f_l \approx 0.7$ – 0.8 and a similar overall fiber fraction, $f_f \approx 0.3$ – 0.5 . A summary of the materials produced and of the associated reinforcement characteristics is presented in Table 1.

In both materials, some clustering is evident, with an average cluster diameter of $\sim 500 \mu\text{m}$. The fiber volume fraction is highest at the center of the cluster and lowest at a cluster junction. The fiber spatial distribution, taking the center of a cluster as the origin, can be approximately represented by (Fig. 1)

$$\bar{f}(x, x_c) = f_m + A \exp[-(x/x_c)^n] \quad (6)$$

where \bar{f} is the mean fiber volume fraction within an area of radius x , x_c is the cluster dimension and A and

†This polynomial form has been obtained by fitting to the numerical result from Bao and Hui [14].

Table 2. Fiber distribution parameters.

Mean ceramic fraction, ϕ	Cluster size, λ (mm)	β	ρ
0.47	400	0.4	2

Typical values for present composite

β are fitting parameters having typical values indicated on Table 2. At the center of each cluster, the fibers are nearly close packed.

3. PRELIMINARY OBSERVATIONS AND TEST PROCEDURES

Observations of the mode I crack extension process have indicated the existence of a fracture process zone (Fig. 2). Within this zone, the ceramic reinforcements are cracked. The cracks are essentially coplanar, although multiple cracking is apparent in some cases. The intervening matrix is intact within a bridging zone and subject to plastic stretching. The leading edge of the bridging zone is defined as the crack tip [1, 5, 9]. This convention is useful for relating the resultant fracture resistance to microstructure, but places an onus on the techniques needed to observe and monitor the crack tip.*

The selection of test specimens to measure the fracture resistance reflects the influence of the bridging zone [15] and also addresses plane strain requirements. Preliminary tests were conducted using single edge notched beams subject to three point flexure. From these tests, an initial estimate of the initiation fracture resistance was obtained as, $K_{I0} = 10\text{--}15 \text{ MPa}\sqrt{\text{m}}$. Based on this estimate and on the matrix flow strength,† the size requirement (crack length and specimen width) for valid plane strain toughness testing according to ASTM E399 is 70 mm for Al and 17 mm for Al-4 Mg matrix materials. These values should be considered as an upper bound because the yield strengths of the associated composites are significantly raised by the incorporation of the ceramic fibers. More precise estimates of the slip zone size (Appendix A) give specimen size requirements of 24 and 6 mm for Al and Al-4 Mg matrix composites, respectively. Consequently, compact tension specimens were chosen for most tests, with a width $w = 25.4 \text{ mm}$ and thickness $b \approx 5 \text{ mm}$. For such specimens, stable crack growth could be achieved using a servo-controlled testing machine. Precracks were not essential because fiber fractures occurred readily at the notch root to create a sharp crack.

All compact tension measurements were made with extensometers attached to the specimens to allow control of the crack opening displacements experienced by the specimen. Crack length measurements

were made *in situ* on the surface by using an optical telescope and by polishing the side surfaces prior to testing. Partial unloading after each crack increment provided a check on the crack length, reflected by compliance changes.

In a few cases, transverse sections were prepared at various stages of crack extension to establish that the cracking features in the specimen interior were comparable to measurements performed on the surface. In other cases, crack extension was monitored *in situ* in the scanning electron microscope [6].

4. EXPERIMENTAL RESULTS

4.1. Fracture resistance measurements

A typical load displacement (P, δ) curve obtained for a compact tension specimen is presented in Fig. 3. A summary of fracture resistance curves is presented in Figs 4 and 5. The major characteristics of these curves are as follows. The initiation resistance K_{I0} appears to be relatively insensitive to the matrix characteristics within the range encompassed by the present group of materials (Fig. 4). However, there are appreciable variations in the subsequent propagation resistance $K_{IR} > K_{I0}$. Also, large-scale bridging effects [15] occur in some cases, as indicated on the figures (labelled LSB). The steady-state fracture resistance K_{Is} is substantially larger for composites having an Al-4% Mg matrix than for those with a pure Al matrix (Fig. 5(a)). Furthermore, particles in the matrix tend to reduce K_{Is} for otherwise comparable materials, but cause a slightly steeper rise in the initial resistance [Fig. 5(b)]. There are relatively minor effects of notch depth [Fig. 5(c)]. In materials with an Al matrix, crack path instability is observed in some specimens, wherein a crack deflects onto planes parallel to the fiber orientation. Consequently, the results are not regarded as strictly valid and, in the analysis that follows, the more reliable results obtained on Al-4 Mg matrix composites are emphasized.

4.2. Observations and measurements

In situ observations such as that presented in Fig. 2 have established the following sequence of events during fracture (Fig. 6). (i) Crack extension initiates when the tip communicates a brittle crack into the next reinforcing element, accompanied by the formation of a crack tip plastic zone. (ii) When the crack grows, intact matrix remains in a bridging zone and experiences appreciable plastic deformation. (iii) The matrix fails by ductile rupture at the trailing edge of the bridging zone, when the crack attains steady-state. Fracture surface observations provide further information (Fig. 7). Systems without particulates exhibit ductile matrix rupture by necking to a ridge between the fibers [Fig. 7(a)]. The plastic stretch of the matrix is found to increase with increase in the fiber spacing, but on average is, $u_s \approx 10 \mu\text{m}$. In materials containing particulates used to separate the fibers, the particles act as void nuclei and limit the

*For this reason, previous work on resistance behavior has often defined the crack tip as being located at the trailing edge of the bridging zone.

† $\sigma_y = 60 \text{ MPa}$ for Al matrix materials and 120 MPa for Al-4 Mg matrix materials [12].

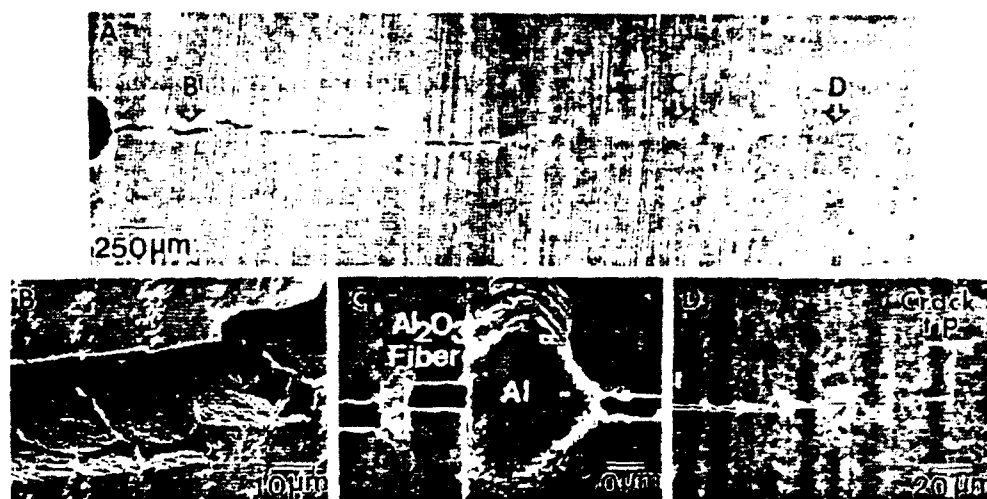


Fig. 2 SEM micrographs of a mode I crack. The top micrograph is an overview. The lower three are local regions revealing cracked fibers and intact matrix at the locations B, C, D indicated on the top figure.

plastic stretch of the matrix ligaments [Fig. 7(b)] to $u_c \approx 6 \mu\text{m}$.

5. INTERPRETATION

5.1. Fracture resistance

An approach for interpreting the separate contributions to the fracture resistance from initiation and growth recognizes the superior understanding associated with the latter. Consequently, by using the material parameters listed in Table 1 (assuming that $\gamma = 2.5$, as appropriate to a bonded interface), the resistance is predicted from equations (3) and (4) by regarding K_{Ic} as an unknown.

The comparison with experimental results is good (Fig. 8) and infers that $K_{Ic} \approx 13 \text{ MPa}\sqrt{\text{m}}$. The rising resistance thus appears to be rigorously predicted by ductile ligament bridging concepts, previously used to interpret fracture in brittle matrix composites containing ductile reinforcements [1, 2, 6, 14]. The most significant variable influencing the resistance is the

matrix yield strength, σ_y , provided that the matrix remains ductile. Notably, a soft matrix *reduces* the fracture resistance. This behavior arises because the width of the plastic dissipation zone in the bridging region is governed by the fiber spacing [1, 2] and consequently, the plastic dissipation diminishes as σ_y decreases. Such behavior is opposite to that usually associated with the *unreinforced* matrix. However, it is important to emphasize that any changes in matrix microstructure used to increase strength *that might also diminish ductility* would cause the composite fracture resistance to decrease through a reduced plastic stretch, u_c .

The initiation resistance has not been as extensively investigated. One fracture hypothesis, analogous to the RKR criterion for carbide cracking in steels [17], is presented in Appendix A. This *stress-based* criterion predicts, $K_{Ic} \approx 13 \text{ MPa}\sqrt{\text{m}}$. While this prediction is similar to the value inferred from fitting the experimental results, it is not felt that such reasonable agreement validates the RKR criterion, because of

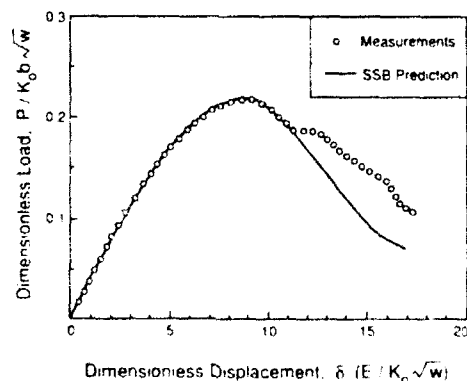


Fig. 3. A load (P), displacement (δ) curve obtained on a compact tension specimen (material-A). Also shown is a predicted curve for small-scale bridging, SSB.

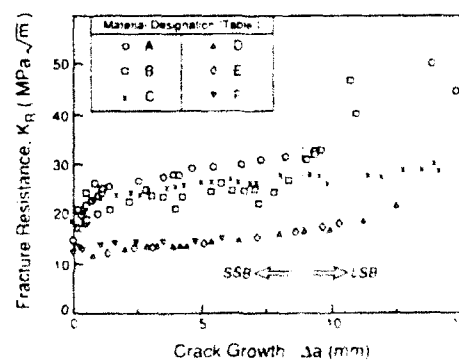
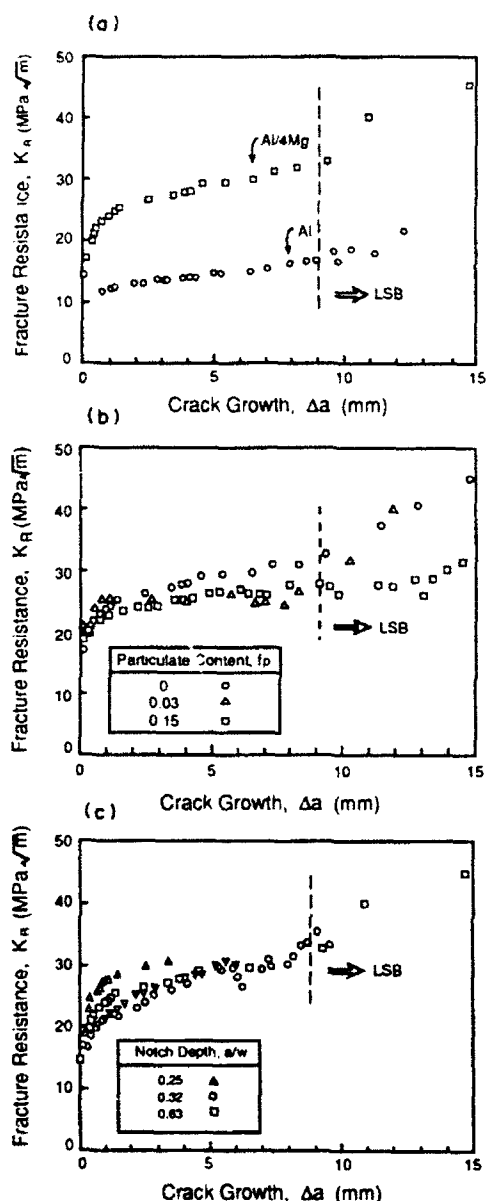


Fig. 4. Fracture resistance curves obtained for each of the materials indicated in Table 1 with notch depth $a_0/w = 0.3$. LSB refers to large-scale bridging and SSB to small-scale bridging.



considerable uncertainty in the material parameters that govern K_0 . This is an area that merits appreciable further study.

Finally, the crack bridging formulae [equations (1)–(4)] may be used to predict the load/displacement curve $P(\delta)$. A preliminary attempt is reported for small-scale bridging (Appendix B). A predicted $P(\delta)$ curve is superimposed onto that determined experimentally (Fig. 3). The correlation is good for the initial portion of crack propagation. The discrepancy at larger crack extension is associated with large-scale

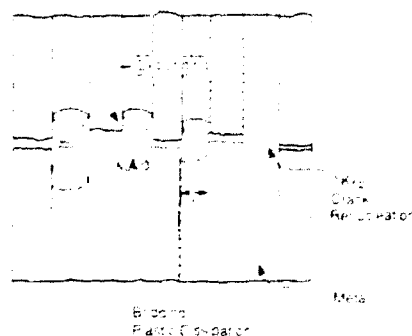


Fig. 6 A schematic of mode I crack extension in composites with one brittle and one ductile constituent

bridging (LSB). A numerical procedure would be needed to extend the analysis into the LSB range.

5.2. Longitudinal tensile strength

Upon obtaining the complete fracture resistance curve, it is possible to predict the fracture strength of the composite, based on independent information concerning the flaw population. Failure begins with the breakage of individual fibers having the lowest fracture strain. However, subsequent events depend largely on the matrix ductility and the interface properties between the matrix and the fibers. When the interface is strong, as in the present composite, if the matrix has a relatively high flow strength and the

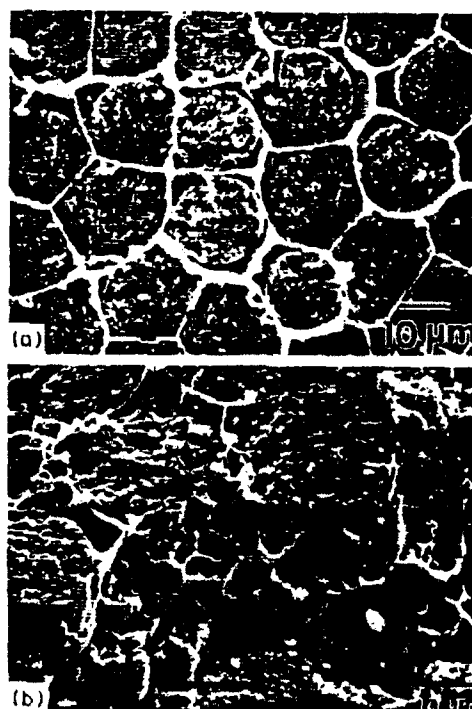


Fig. 7. Scanning electron micrographs of fracture surface of the reinforced materials. (a) Necking to a ridge in materials without particulates, (b) matrix rupture by hole nucleation and growth from particulates.

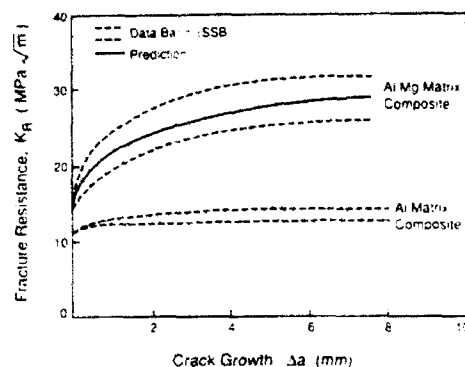


Fig. 8. Predicted resistance curves compared with the SSB data bands obtained from Fig. 4 (all t_c and a_c) for both the Al-4 Mg and Al matrix composites

fibers are closely packed, the initially failed fibers communicate with the neighboring material and elevate the stress in the surrounding fibers. The subsequent interactions lead to the formation of a macroscopic crack, which causes final rupture of the composite. The present observations suggest that the localized fiber clusters (Fig. 1) are the failure initiating entities. A tensile strength is thus predicted by assuming the presence of flaws having size comparable to the cluster dimension in the composite and then using a fracture mechanics approach, incorporating the fracture resistance curve.

For a composite with nonuniform fiber distribution, given by equation (6), the resistance curve can be obtained from equation (3) as

$$\mathcal{G}_R = \mathcal{G}_0 + [1 - \bar{f}(a/x_c)]\lambda\sigma_0 u_c g \quad (7)$$

where a is the crack length and \bar{f} is given by equation (6) with $x = a$. The driving force for a penny-shaped flaw subject to stress σ is given by [12]

$$\mathcal{G} = 4\sigma^2 a_0 (\lambda + \sqrt{a/a_0})^2 / \pi E \quad (8)$$

where a_0 is the initial crack length and $\lambda = E_f/E$ is the Young's modulus ratio of the fiber to that of the composite. Equating equations (7) and (8), the non-

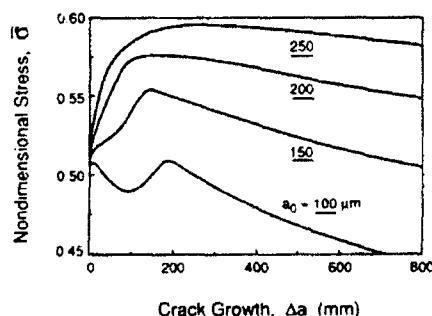


Fig. 9. Non-dimensional crack extension stress as a function of crack length for different initial flaw size (Al-4 Mg composite) obtained using the parameters from Tables 1 and 2.

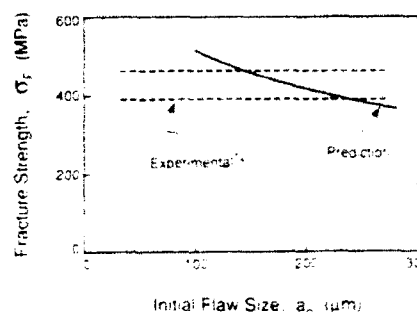


Fig. 10. Dependence of predicted fracture strength from Fig. 9 on initial flaw size and comparison with the experimental measurements [12] (Al-4 Mg matrix composites)

dimensional stress $\bar{\sigma}$ sustained by the composite as the crack extends can be derived as

$$\begin{aligned} \bar{\sigma} &\equiv 2\sigma(a_0/\pi\mathcal{G}_0 E)^{1/2} \\ &= \frac{[1 + [1 - \bar{f}(a/x_c)]\lambda\sigma_0 u_c/g]^{1/2}}{\lambda + \sqrt{a/a_0}} \quad (9) \end{aligned}$$

This non-dimensional stress (Fig. 9) exhibits a maximum that represents the fracture strength, σ_f . This strength shows a weak dependence on initial flaw size (Fig. 10), provided that a_0 is smaller than the cluster size. Agreement with the experimentally measured strengths [12] is quite good for Al-4 Mg matrix composites (Fig. 10). Similar comparisons for the Al matrix composites have not been attempted, because of the uncertainties concerning the resistance curve, noted above.

The preceding analysis implicitly assumes small-scale bridging dominance. When the crack extension before the final failure is appreciably greater than the initial flaw size, large-scale bridging would have to be taken into account.

6. CONCLUSIONS

The fracture resistances of ceramic fiber reinforced Al alloy matrix composites have been measured. The initial fracture resistance at zero crack extension has been shown to be insensitive to matrix characteristics. Conversely, the subsequent crack growth resistance is strongly influenced by matrix properties. The crack growth resistance has been attributed to plastic dissipation through ductile bridging, modelled using a softening traction law. The dissipation is limited to a material volume that scales with the fiber spacing. Consequently, high toughness is encouraged by a high yield strength matrix and large diameter fibers. Occasional debonding at concentrated metal phases expands the plastic zone and further enhances the local crack growth resistance. The addition of a particulate phase tends to reduce the steady-state toughness, but leads to an enhanced tearing modulus, an important property when the flaw size in the material is small.

The longitudinal tensile strength has been predicted using the resistance curve and a flaw size estimate. Failure initiation is considered to begin with random failure of individual fibers closely packed within a cluster, which then coalesce into a macroscopic crack. This prediction correlates well with experimental results for Al-4Mg matrix materials.

REFERENCES

1. L. S. Sigl, P. A. Mataga, B. J. Dalgleish, R. M. McMeeking and A. G. Evans, *Acta metall.* **34**, 2435 (1986).
2. M. F. Ashby, F. J. Blunt and M. Bannister, *Acta metall.* **37**, 1847 (1989).
3. B. V. Velamakanni, I. F. Lange and A. G. Evans, *J. Am. Ceram. Soc.* **73**, 388 (1990).
4. P. R. Subramanian, M. G. Mendiratta, D. B. Miracle and D. M. Dimduk, *Intermetallic Matrix Composites*, MRS Proceedings (edited by D. L. Anton *et al.*) **194**, 147 (1990).
5. G. R. Odette and W. Sheppard, to be published.
6. H. E. Deve, G. R. Odette, A. G. Evans and R. Mehrabian, *Acta metall.* **38**, 1491 (1990).
7. H. C. Cao and A. G. Evans, *Acta metall. mater.* **39**, 2997 (1991).
8. Y. T. Low and R. J. Arsenault, *Acta metall.* **37**, 2413 (1989).
9. F. W. Zok, S. Jansson, A. G. Evans and V. Nardonne, *Metall. Trans.* **22A**, 1991 (1991).
10. A. G. Evans, *Mater. Sci. Engng.*, in press.
11. Y. L. Klipfel, J. Yang, M. Y. He, R. Mehrabian and A. G. Evans, *Acta metall.* **38**, 1063 (1990).
12. M. Hu, J. Yang, H. C. Cao and A. G. Evans, *Acta metall. mater.* **40**, 2315 (1992).
13. B. J. Dalgleish, K. P. Trumble and A. G. Evans, *Acta metall.* **37**, 1923 (1989).
14. G. Bao and C. Y. Hui, *Int. J. Solids Struct.* **26**, 631 (1990).
15. F. W. Zok and C. L. Hom, *Acta metall.* **38**, 1895 (1990).
16. M. Shaw, D. B. Marshall, W. Morris and A. G. Evans, *Advanced Composite Materials* (edited by M. Sacks), Orlando, Florida (1991).
17. R. O. Ritchie, J. F. Knott and J. R. Rice, *J. Mech. Phys. Solids* **21**, 395 (1973).
18. J. Nunes, *Army Materials and Mechanics Research Center, AMMRC, TR82-61* (1990).
19. H. C. Cao, *Advanced Composite Materials* (edited by M. Sacks), pp. 485-492 (1991).
20. H. Tada, P. C. Paris and G. R. Irwin, *The Stress Analysis of Cracks Handbook*, Del Research Corporation (1973).
21. V. Kumar, M. D. German and C. F. Shih, *An Engineering Approach for Elastic-Plastic Fracture Analysis*, Electric Power Research Institute (1981).

APPENDIX A

Estimation of the Initiation Resistance

In order to estimate σ_c , a criterion for crack growth is needed. One criterion, analogous to that used to predict

cracking of carbide particles in steels [17] is that the stress on the fiber ahead of the crack tip reaches the fiber strength, S . This criterion gives [7]

$$\sigma_c \approx 2.5 \sigma_c f \quad (A1)$$

where h is the space between fibers. In order to apply this result, the relevant magnitudes of the fiber strength S and spacing h need to be deduced. Standard weakest link statistics dictate that the relevant fiber strength S has the form [18]

$$S = S_0 (\lambda/l)^m \quad (A2)$$

where S_0 is the fiber strength at the reference gauge length l , m is the shape parameter and λ is the slip dimension that governs the region subject to the concentrated crack tip stress field. This dimension is given by [19]

$$\lambda \approx 0.3(E\sigma_c/\sigma_c^2) \quad (A3)$$

Using magnitudes of S_0 and m from the literature [18], equations (A2) and (A3) give $\lambda = 120 \mu\text{m}$ and $S = 3.7 \text{ GPa}$. The fiber spacing h is not a well-delineated entity. An average value [12] is $h = 2 \mu\text{m}$. Inserting S and h into equation (A1) gives $\sigma_c \approx 955 \text{ Jm}^{-1/2}$, such that $K \approx 13 \text{ MPa}\sqrt{\text{m}}$.

APPENDIX B

Estimation of $P(\delta)$ in Small-Scale Bridging

For a linear elastic material, the crack mouth opening displacement δ_c is related to the applied load P and the crack size, a , through

$$\delta_c = (P/Eh)U(a/w) \quad (B1)$$

where $E = E/(1-\nu^2)$, h is the specimen thickness, w the specimen width and U is a function given by Tada [20]. For elastic plastic materials, the crack opening displacement consists of an elastic contribution, given by equation (B1), and a plastic contribution δ_p . For materials obeying power law hardening with yield strain ϵ_0 and strain hardening index n ($n = 1-N$), δ_p is given by

$$\delta_p = (3/7)(P/P_0)^{1/n} H(a/w, n) \epsilon_0 a \quad (B2)$$

where P_0 is the limit load, given by

$$P_0 = 1.455\eta(w-a)\sigma_c$$

with

$$\eta = \left[\left(\frac{2a}{w-a} \right)^2 + 2 \left(\frac{2a}{w-a} \right) + 2 \right]^{1/2} - \left[\frac{2a}{w-a} + 1 \right]$$

and H is a numerical function, tabulated by Shih [21] for different values of η and a/w . Furthermore, the fracture resistance is related to the applied load by

$$K = (P/bw^{3/2})T(a/w) \quad (B3)$$

where T is a numerical function given by Tada [20]. Equating K to K_R , the $P(\delta)$ relation can be obtained after eliminating a . K_R is ascertained from equations (1)-(4) with $K_0 = 13 \text{ MPa}\sqrt{\text{m}}$, $u_0 = 10 \mu\text{m}$, $f = 0.44$, $\gamma = 2.5$, $\sigma_c = 120 \text{ MPa}$, $w = 25.4 \text{ mm}$ and an initial crack length, $a_0 = 8 \text{ mm}$.

THE ULTIMATE TENSILE STRENGTH OF METAL AND CERAMIC-MATRIX COMPOSITES

M. Y. HE,¹ A. G. EVANS¹ and W. A. CURTIN²

¹Materials Department, College of Engineering, University of California, Santa Barbara, CA 93106-5050
 and ²B.P. America, Warrensville, OH 44128, U.S.A.

(Received 3 July 1992)

Abstract—The tensile strength of ceramic and metal matrix composites is subject to an important role of the fiber matrix interface. The mechanical properties of this interface dictate the stress concentration that develops in fibers that surround a failed fiber. An analysis of this phenomenon is used to illustrate interface conditions that sufficiently diminish the stress concentration that a global load sharing criterion may be used to prescribe the contribution of the fibers to the composite strength. This, in turn, leads to a criterion for the transition to failure by local load sharing.

1. INTRODUCTION

Continuous fiber-reinforced composites exhibit tensile properties sensitive to a major mechanism transition between *global* and *local* load sharing. The existence of this transition has been identified for ceramic-matrix (CMC) and metal-matrix (MMC) composites [1-9]. The transition, when it occurs, leads to a substantial tensile strength discontinuity, involving a major *decrease* in ultimate strength when local load sharing conditions arise [3, 4, 6]. For constituent characteristics that provide global load sharing, fiber fractures that occur prior to composite failure (for statistical reasons) do not lead to a significant stress concentration on the intact *nearest neighbor* fibers [5, 10, 11]. Instead, the load is borne, almost equally, by all the intact fibers. In this case, whenever the gauge length, L , exceeds the load transfer length, d_c , multiple fiber failures are expected within the gauge, L , prior to composite failure. The load transfer length thus becomes an important composite characteristic. It is defined as the length over which the fiber displaces, relative to the matrix, upon failure of a fiber [5, 11] (Fig. 1). For simplicity, it is generally assumed that sliding occurs in accordance with a constant shear stress, τ , interface sliding law [12-14]. This shear resistance is related either to debonding and frictional sliding of the fiber coating, or to shear yielding of the matrix. For this case, d_c is given by [5]

$$d_c = \sigma_f R / 2\tau \quad (1)$$

where σ_f is the remote stress on the fiber and R the fiber radius (Fig. 1). More complex sliding laws can be used, as appropriate [14].

For CMCs, composite failure subject to global load sharing is preceded by multiple matrix cracks [5]. Hence, the matrix does not contribute *directly* to composite failure. However, there is a vitally important *indirect* influence, associated with the load

transfer *along the fiber*, via the interface sliding stress, τ [5]. The essential phenomenon concerns the influence of load transfer on the stochastics of fiber failure, whereby the nominal fiber gauge length becomes dependent on d_c . The consequence is a gauge length independent tensile strength (when $d_c \leq L$), given by [5]

$$S_u = f_f S_0 [2/(m+2)]^{1/(m+1)} [(m+1)/(m+2)] \quad (2)$$

where f_f is the volume fraction of fibers along the loading axis; m is the shape parameter (Weibull modulus) and S_0 the scale parameter representing the fiber strength; L_0 is a normalizing length (usually taken to be 1 m). For shorter gauge lengths ($L < d_c$), the tensile strength s_u exceeds S_u [7, 11].

For MMCs subject to global load sharing, the contribution of the *fibers* to the tensile strength is still given by equation (1), with the appropriate, τ [7, 8]. However, in this case, the matrix also carries some load, governed by its yield strength, σ_0 . Consequently, the tensile strength (when $d_c \leq L$) becomes

$$\sigma_u = S_u + f_m \sigma_0 \quad (3)$$

where f_m is the volume fraction of matrix. This result is independent of both the misfit strain (residual stress) and the gauge length [7].

When a transition to local load sharing occurs, composite failure involves the progressive evolution of a dominant (mode I) crack, from a region containing failed fibers [4, 6]. In this case, two composite characteristics have major importance. (i) The localized spatial distributions of fibers, which influence the stress concentration transmitted to nearest neighbor fibers [1, 2]. (ii) The short crack crack-growth resistance of the composite, which dictates crack evolution within local regions [5, 6]. It is *not* the intention of this article to derive failure models when local load sharing conditions obtain [1, 2, 4]. Rather, derivation

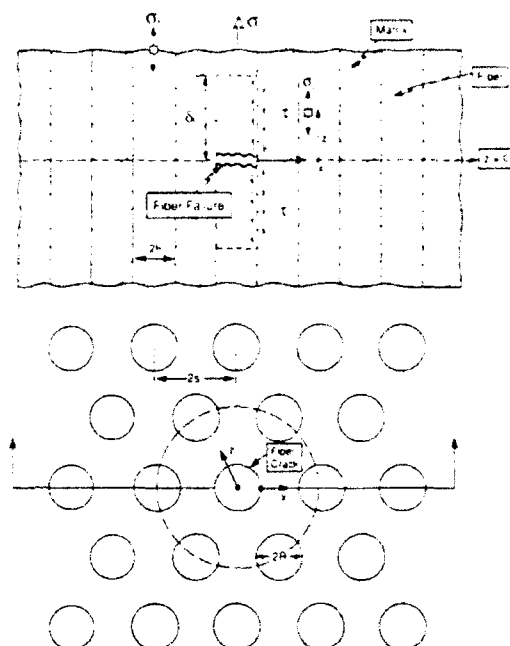


Fig. 1. Schematic indicating the fiber arrangements and the interface characteristics used in the analysis.

of a physically-based criterion for the *avoidance* of local load sharing is addressed.

The basic *mechanics* underlying the transition from global to local load sharing has the following features. When a fiber fails and sliding occurs along the interface (Fig. 1), stress concentrations σ_z develop in the nearest and next-nearest fibers. It is expected that the magnitude of the stress concentration be sensitive to three principal variables; the interface sliding stress, τ , the fiber volume fraction and the fiber/matrix stiffness ratio. Calculation of the stress distributions around a failed fiber, subject to the above variables, thus provides essential background.

The stress information must be combined with *stochastics* to provide a transition criterion. The approach adopted here involves comparison of the *survival probabilities* Φ_i of successive fiber "annuli" within the array depicted in Fig. 1: nearest neighbors, next-nearest neighbors, etc. A conservative condition for ensuring global load sharing is used to provide preliminary results, based on Φ_i for the nearest neighbor and next-nearest neighbor fibers.

2. GEOMETRIC AND STOCHASTIC CONSIDERATIONS

Statistical considerations dictate that some fibers in the composite fail at moderate loads. Such failures induce a *stress concentration* in the neighboring fibers. The magnitude of the stress depends on the *material variables* noted above, as well as the *geometric arrangement* of the fibers. In turn, the stress at the

neighboring fibers governs the probability of survival, through the *statistical properties* of the fibers. In this section, some of the underlying geometric and statistical phenomena are presented, with the objective of specifying levels of stress concentration relevant to global and local load sharing. Then, the mechanics that relate the stress concentration to material properties are presented in the following section.

The close-packed arrangement of fibers shown in Fig. 1 is used, since this is the preferred fiber geometry for the avoidance of fiber damage during processing. Each fiber has 6 nearest neighbors located at $r = 2s$. Then, there are 6-12 next-nearest neighbors located between $r = 2\sqrt{3}s$ and $4s$. For the composites of primary interest, the interface sliding stress τ is small compared with the bundle strength of the fiber, S_b . The load transfer length is thus large relative to the fiber spacing. Furthermore, gradients in stress along the fiber axis, z , are small compared with those in-plane ($z = 0$). Consequently, the σ_z stresses along r , at $z = 0$, are most relevant to the evolution of fiber failures in the composite.

A *preliminary* assessment of composite behavior may be obtained by evaluating the relative survival probabilities of the nearest Φ_N^N and next-nearest, Φ_{NN}^{NN} neighbor fibers, subject to the stress $\sigma_z(r)$. The development of a well-defined crack from an initial fiber failure *cannot occur*, whenever $\Phi_N^N < \Phi_{NN}^{NN}$, *because there is no mechanism for systematically concentrating the $\sigma_z(r)$ stress at the periphery of the damage zone of failed fibers*. Consequently, this inequality *ensures* that the composite will exhibit global load sharing.

The survival probability of a row of N fibers that fracture in accordance with a two-parameter Weibull distribution, subject to a uniform stress σ_z , over a length δ_c , is given by [5, 11]

$$-\ln \Phi_i = N[\sigma_z/S_0]^m (\delta_c/L_0). \quad (4)$$

Consequently, for $\delta_c \gg s$ (Fig. 1), the condition for GLS depends on the stress ratio

$$\lambda = \sigma_z^N / \sigma_z^{NN}$$

and is given as

$$\lambda < (N^{NN}/N^N)^{1/m}. \quad (5)$$

The *stress ratio* λ in the nearest and next-nearest neighbor fiber "annuli" thus provides a preliminary measure of the importance of the stress concentration for the operative load sharing mechanism. The locations of neighboring fibers is related to the fiber radius, R , through the fiber volume fraction f , in accordance with

$$f \approx 2\pi/[\sqrt{3}(2s/R)^2]. \quad (6)$$

Consequently, for some typical values, $N^N = 6$, $N^{NN} = 9$ and $m = 10$, a coefficient, $\lambda \leq 1.04$ appears to be required for GLS to be assured. However,

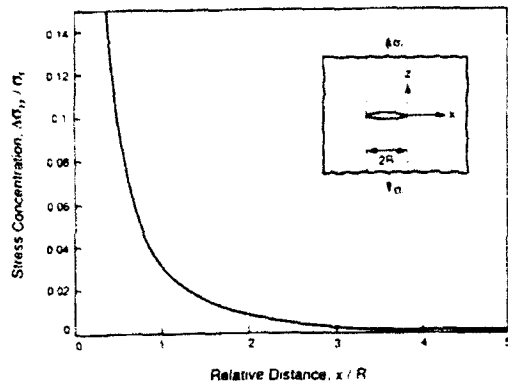


Fig. 2. The stress concentration along the crack plane $\Delta\sigma_{zz}$, for an elastically isotropic system with $\tau = \infty$.

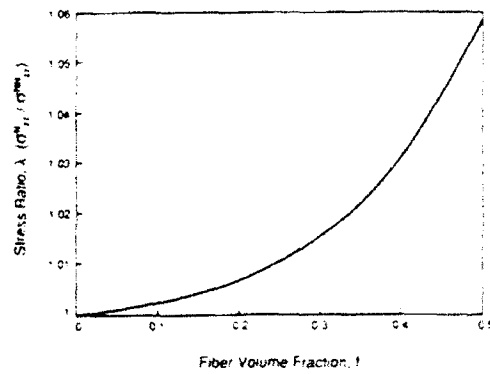


Fig. 3. The stress ratio, λ , for $\tau = \infty$, as a function of fiber volume fraction.

larger values of λ may still allow GLS, especially when m is small. These results provide a *perspective* for assessing the mechanics.

3. MECHANICS SOLUTIONS

The mechanics problem represented by Fig. 1 is addressed at three levels. (i) Some basic analytical solutions for elastically homogeneous materials are used both to provide perspective and to establish various bounds. (ii) Numerical results are derived for elastically homogeneous material, in order to establish a detailed understanding of the role of the interface sliding stress, τ . (iii) Numerical results with different stiffness ratios are derived in order to examine the influence of matrix properties.

3.1. Basic analytical results

Two analytical results provide important insight. (i) The field around a penny-shaped crack, which provides the solution for an elastically homogeneous system, as $\tau \rightarrow \infty$. (ii) The stress ahead of a crack subject to slip on a plane normal to the crack, occurring at constant sliding stress, τ .

The full-field solution for a penny crack in an isotropic elastic solid (Fig. 2), yields information about the local stress elevation $\Delta\sigma_{zz}$ caused by the crack

$$\Delta\sigma_{zz} = \sigma_{zz}(x) - \sigma. \quad (7)$$

Features relevant to load sharing are based on the stresses that arise at nearest and next-nearest neighbor fiber locations. The stresses in the nearest neighbor fibers are non-uniform. However, based on maximum values in the fibers, the stress ratio $\sigma_{zz}^N / \sigma_{zz}^N$ (Fig. 3) exceeds the levels required for GLS, at fiber volume fractions $f \geq 0.4$.

The solution for the semi-infinite crack with a constant τ sliding plane at the tip (Fig. 4) indicates two key influences of sliding [15]. (i) Sliding causes the σ_{zz} stress ahead of the crack to increase when the sliding distance δ_c is small. (ii) The stress concentration decreases toward zero as $\tau \rightarrow 0$. The transition

to the latter stress reduction regime is governed by a non-dimensional parameter

$$\Omega = x(\tau/K)^2 \quad (8)$$

where K is the mode I stress intensity factor. Notably, reduced σ_{zz} stresses caused by sliding arise when

$$\Omega \leq 0.02. \quad (9)$$

Connection to the present problem is made by noting that K , for a failed fiber in an elastically homogeneous system is: $K \approx (2/\sqrt{\pi})\sigma_f\sqrt{R}$. Consequently

$$\Omega = (\pi/4)(x/R)(\tau/\sigma_f)^2. \quad (10)$$

By equating x to s and relating s/R to f by equation (6), the slip calculations (Fig. 4) establish that reductions in the stresses on neighboring fibers caused by interface sliding are only expected (for typical f) when τ is small, of order, $\tau/\sigma_f \leq 0.1$. Furthermore, the requirement for small values of τ/σ_f is most important when the failure probability of the nearest neighbor fibers approaches unity. This occurs when $\sigma_f \rightarrow S_b$, the fiber bundle strength. This perspective facilitates the choices of τ suitable for the numerical calculations performed in the following section.

3.2. Numerical results

The variables in the analysis are the interface sliding stress, the applied stress, the fiber volume

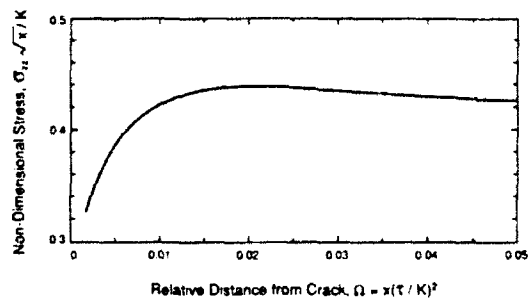


Fig. 4. The effects of a sliding plane on the crack tip field for a semi-infinite crack. The sliding length δ is given by: $\delta = 0.05 (K/\tau)^2$; x is the distance from the crack tip.

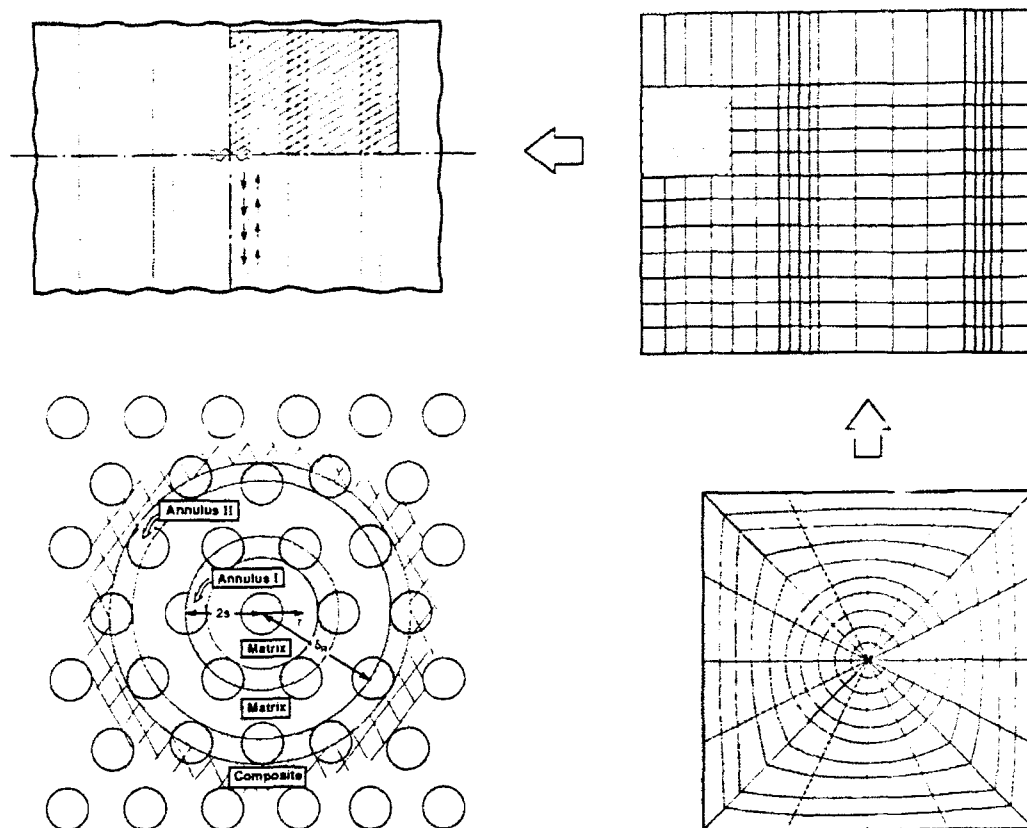
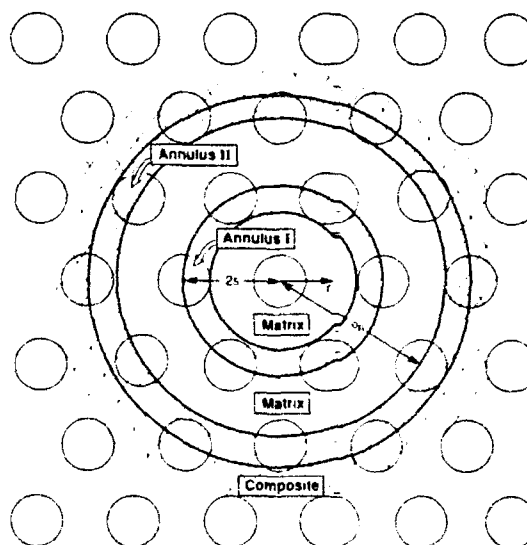


Fig. 5. A finite element mesh in the vicinity of the failed fiber.

fraction and the Young's modulus of the fiber and matrix, E_f and E_m , respectively[†]. The matrix is considered to remain elastic. A finite element method is used for the calculations. The calculations are conducted with the load transfer length *prescribed* by equation (1) and by using sliding elements introduced at the interface that satisfy $\sigma_{rz} = \tau$, when $z \leq \delta_c$. The calculations are axisymmetric, with the mesh shown in Fig. 5. Emphasis is given to the $\sigma_{zz}(x)$ stress on the crack plane, $z = 0$. However, σ_{rz} is also calculated at the interface of nearest neighbor fibers and compared with τ . This comparison addresses the incidence of sliding at those interfaces. In some cases, $\sigma_{zz}(z)$ is calculated at nearest neighbor fiber locations.

For elastically homogeneous systems, the calculations explicitly refer to the hexagonal fiber arrangement shown in Fig. 1. These results are presented first. However, when $E_f \neq E_m$, the annular configuration depicted in Fig. 6 is used. The nearest and next-nearest neighbor fibers are considered to be located within annuli having the fiber modulus for that location. Outside the second annulus, the material is considered to be homogeneous and have the actual composite modulus.

The salient trends in σ_{zz} for the *elastically homogeneous* system are summarized in Figs 7-11. The $\Delta\sigma_{zz}$ stress concentration on the crack plane diminishes as τ/σ_f decreases (Fig. 7), such that the largest

Fig. 6. The configuration of annuli used for numerical analysis, with $E_f > E_m$.

[†]Poisson's ratio is assumed to be the same for both.

$\Delta\sigma_{zz}$ (which occurs at $x=0$) is only $1.03\sigma_f$ when $\tau/\sigma_f=0.01$. This stress concentration is below the level at which local load sharing mechanisms are expected to operate. Consequently, smaller values of τ/σ_f are not considered. The effects of τ on the $\Delta\sigma_{zz}$ stress at the mid-point of the nearest neighbor fibers (Fig. 8) indicate the same characteristics found in the asymptotic solutions (Figs 2, 4): (i) $\Delta\sigma_{zz} \rightarrow 0$ as $\tau \rightarrow 0$. (ii) a peak in $\Delta\sigma_{zz}$ occurs in the range $\tau/\sigma_f=0.1-0.2$ for typical f . (iii) at large sliding stresses, $\Delta\sigma_{zz}$ asymptotically approaches the penny-shaped crack solution.

Evaluation of σ_{xz} at the interface of the nearest neighbor fibers indicates that, in all cases (Fig. 9) within the range, $0.01 < \tau/\sigma_f < 1$, σ_{xz} is smaller than τ . Sliding of these interfaces can thus be neglected for the sliding law assumed in this study. A typical variation in $\Delta\sigma_{zz}$ along a nearest neighbor fiber (Fig. 10) indicates an essentially linear decrease.

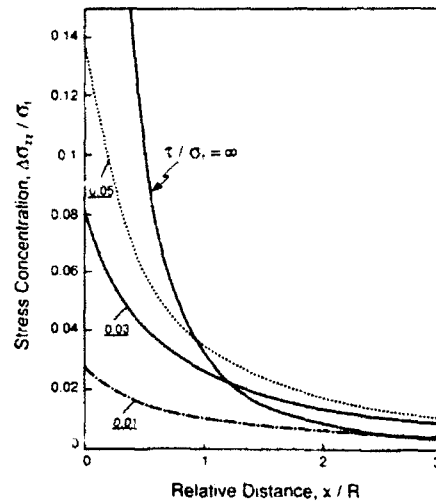


Fig. 7. Effect of τ/σ_f on the stress concentration, $\Delta\sigma_{zz}(r)$, at $z=0$.

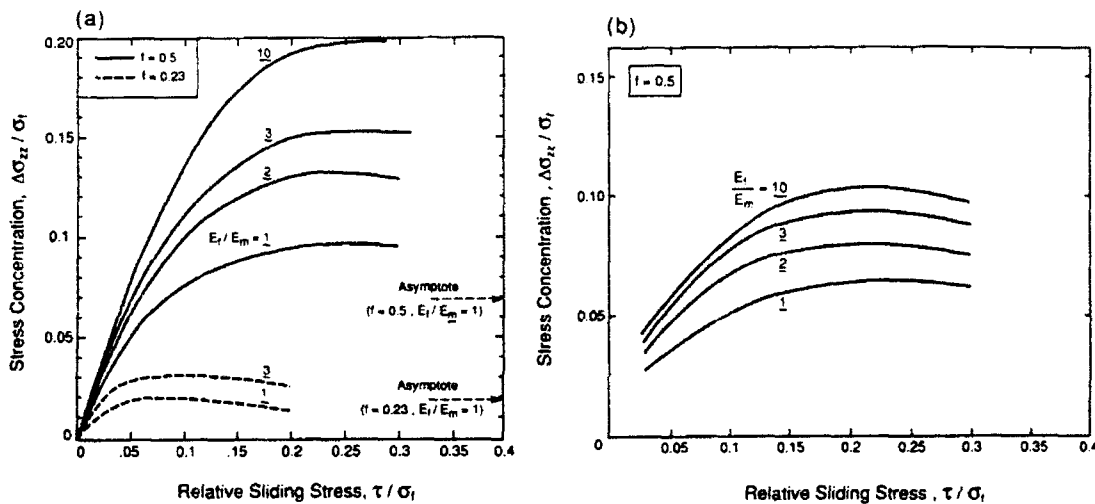


Fig. 8. Variation in the stress concentration at the nearest neighbor fibers with sliding stress for typical fiber volume fractions, at several stiffness ratios: (a) maximum stress in the fiber, (b) average stress in the fiber.

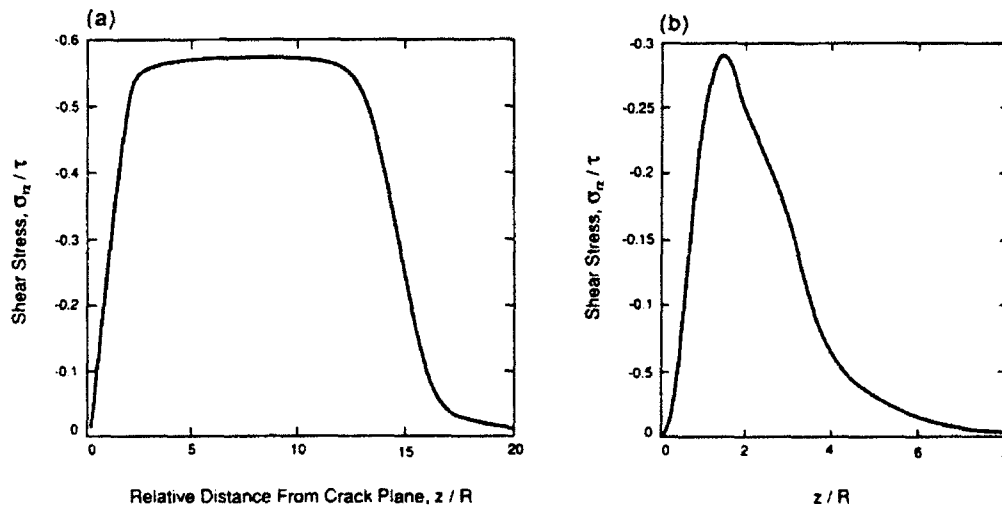


Fig. 9. Interface shear stress, σ_{xz} , in nearest neighbor fibers, (a) $\tau/\sigma_f=0.03$, $f=0.5$, (b) $\tau/\sigma_f=0.2$, $f=0.5$.

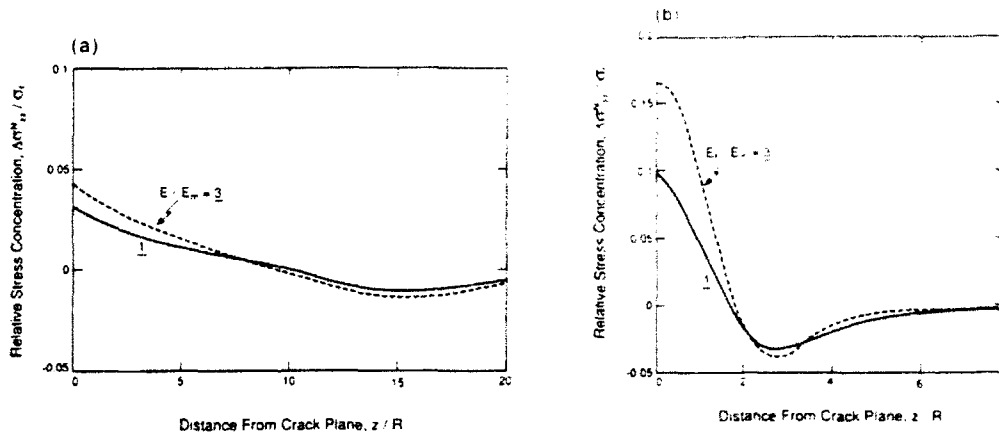


Fig. 10. Axial stress, $\sigma_{zz}(z)$, in nearest neighbor fibers. (a) $\tau/\sigma_f = 0.03$, $f = 0.5$. (b) $\tau/\sigma_f = 0.2$, $f = 0.5$.

between the maximum value at the crack plane ($z = 0$) and zero at $z \approx \delta_c$.

A comparison of the stress concentrations in the nearest and next-nearest fibers (Figs 11 and 12) as a function of volume fraction gives an indication of how reduction in f influences the stress concentration ratio, as well as the pronounced effect of τ/σ_f for values ≤ 0.05 .

Calculations conducted with elastic mismatch ($E_f/E_m > 1$), summarized in Figs 8, 11 and 12 demonstrate that a reduced matrix stiffness invariably increases the stress concentration in neighboring fibers. The effects are substantial, even at small mismatches ($E_f/E_m \approx 3$), indicating the importance of matrix stiffness loss on the GLS \rightarrow LLS transition. Such stiffness loss may arise either because of macrocracking in CMCs [16, 17] or plasticity in MMCs [6, 8]. However, even when $E_f/E_m = 10$, and $f = 0.5$, the average stress [Fig. 8(b)] does not achieve the level expected when all of the load from the failed fiber is transferred onto its nearest neighbor, $\Delta\sigma_{zz}/\sigma_f = 0.16$.

One calculation is conducted with plasticity allowed in the matrix. The calculations are for a

non-hardening matrix, with a Mises yield criterion, subject to the uniaxial yield strength, σ_u , and isotropic elastic properties. The results (Fig. 13) indicate that yielding increases the stress concentration on neighboring fibers, consistent with the influence of a reduced matrix modulus. Further calculations with plasticity would be needed to explore these effects in detail.

4. THE MECHANISM TRANSITION

The preceding mechanics motivate estimates of survival probabilities that relate to the GLS \rightarrow LLS mechanism transition. A recent bundle model [7] has introduced some physically attractive concepts, especially the number of fibers, N_f , that participate in the composite failure process, when GLS is violated. However, for this concept to be used, a "uniformly-stressed" zone, around a failed fiber, that embraces N_f fibers needs to be identified. Such a zone is not yet evident from the present solutions. Consequently, the approach suggested earlier, based on the sequential failure of fiber rows, is further explored in order to provide additional perspective.

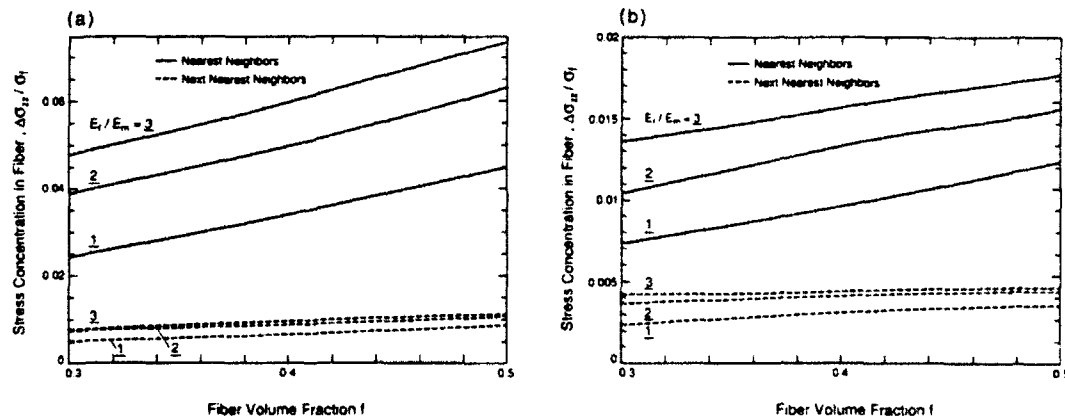


Fig. 11. The nearest and next-nearest neighbor fiber stress concentrations as a function of volume fraction (a) $\tau/\sigma_f = 0.05$, (b) $\tau/\sigma_f = 0.01$.

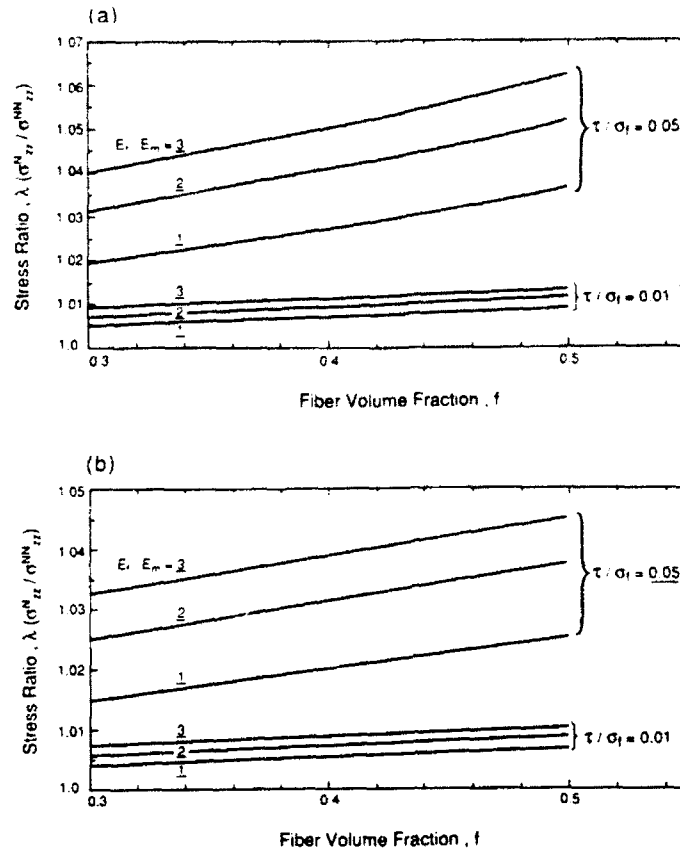


Fig. 12. Stress ratio in nearest and next nearest neighbor fibers as a function of volume fraction, (a) maximum stress, (b) average stress.

The concept is as follows. If the *failure probability* of the nearest neighbor fibers adjacent to the crack plane is high relative to that of the fibers elsewhere in the composite, then a self-organized criticality would be anticipated, whereby "coplanar" crack would evolve out of a single failed fiber. Then, a local load sharing mechanism of composite failure would obtain, perhaps characterized by a resistance curve [6]. Conversely, if the survival *probability* of the nearest neighbors exceeds that of a surrounding zone of significant size, a criticality is unlikely and a global load sharing failure mechanism would apply.

In order to apply this concept, two length scales must be considered: (i) the dimension normal to the crack (z axis) wherein the stress within the nearest neighbor fiber exceeds the applied stress, σ_f . (ii) The radius of the radial zone that experiences a significant stress concentration, designated δ_R . The hypothesis used here is that, at the small levels of τ/σ_f relevant to the mechanism transition, since $\delta_c \gg s$, stress gradients in z are small† (Fig. 10). Consequently, the stress on the crack plane ($z = 0$) is used for analysis of the

relative survival probabilities of fiber rows within δ_R . The definition of δ_R is critical. The following rationalization is used; with reference to Fig. 6. If the outer "annulus" of next-nearest neighbor fibers, width δ_R , exhibits a higher failure probability than the inner annulus of nearest neighbor fibers, width $2s$, then a well-defined crack-like criticality cannot develop.

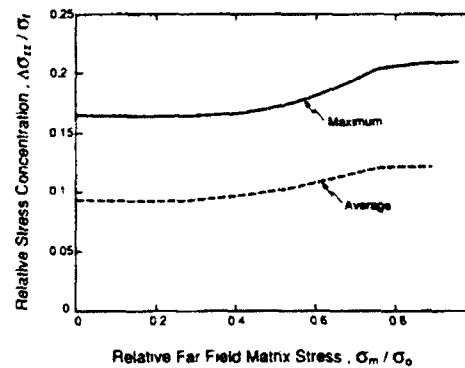


Fig. 13. Effect of matrix yielding on the stress concentration in the nearest neighbor fibers ($E_f/E_m = 3$, $f = 0.5$, $\tau/\sigma_f = 0.2$). σ_0 is the uniaxial yield strength of the matrix and σ_m is the far field stress on the matrix.

†Hence, the mechanism transition is not explicitly affected by δ_c .

Instead, fiber failures are more likely to occur in other regions of the composite in which long lengths of fiber are subject to a uniform stress, σ_f . For this case, composite failure is likely to proceed by global load sharing. Consequently, the stress concentrations from Fig. 11 may be inserted into equation (5) to provide an assessment of the interface, fiber and matrix properties needed to assure GLS.

5. CONCLUSIONS

An analysis of the effect of interface sliding on the stress concentration around failed fibers within a composite has been conducted. The analysis is used to compare the stress ratio, λ , in nearest and next-nearest fiber "annuli" as a function of the ratio of the imposed stress σ_f to the interface sliding stress, τ , the fiber volume fraction, f , and the fiber/matrix stiffness ratio. A preliminary stochastic criterion has been used to demonstrate global load sharing (GLS) when λ is smaller than a "critical" value that depends on the shape parameter, m , that characterizes the fiber strength distribution. The results highlight the importance of the ratio τ/σ_f . Notably, this ratio needs to be small (<0.1) to assure GLS at typical fiber volume fraction. Furthermore, there is an appreciable effect of the matrix stiffness on the stress concentration. The trend is to cause an increase in stress when the matrix stiffness decreases. Low matrix stiffnesses arise when a low modulus matrix is used and when either matrix microcracking or yielding occur. In this case, correspondingly smaller values of the interface sliding stress, τ/σ_f , are needed to ensure that GLS obtains in the composite. Further analysis

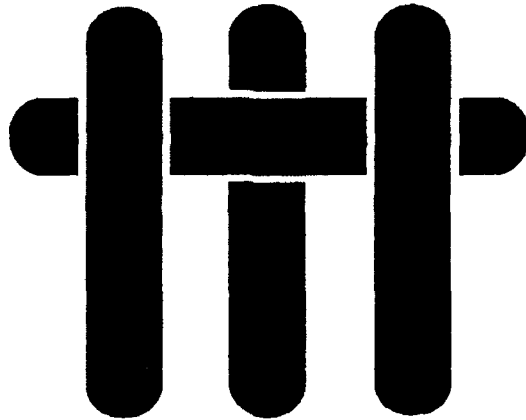
of low stiffness matrices caused by non-linearities is in progress.

Acknowledgements—This work was supported by the Office of Naval Research through contract N00014-90-J-13000. Provision of the ABAQUS finite element code by Hibbitt, Karlsson and Sorensen, Inc. of Providence, Rhode Island is gratefully acknowledged.

REFERENCES

1. C. Zweben, *Engng Fract. Mech.* **4**, 189 (1972).
2. P. van Dyke and J. M. Hedgepeth, *Text. Res. J.* **37**, 618 (1969).
3. F. E. Heredia, S. M. Spearing, A. G. Evans, W. A. Curtin and P. Mosher, *J. Am. Ceram. Soc.*, in press.
4. S. Ochiai and K. Osanuru, *Metall. Trans.* **21A**, 971 (1991).
5. W. A. Curtin, *J. Am. Ceram. Soc.* **74**, 2837 (1991).
6. M. S. Hu, J. Yang, H.-C. Cao, A. G. Evans and R. Mehrabian, *Acta metall. mater.* **40**, 2315 (1992).
7. W. A. Curtin, *Acta metall. mater.*, in press.
8. S. Jansson, H. E. Dève and A. G. Evans, *Metall. Trans.* **22A**, 2975 (1991).
9. H. R. Schweitert and P. S. Steif, *Int. J. Solids Struct.* **28**, 283 (1991).
10. S. L. Phoenix and R. L. Smith, *Int. J. Solids Struct.* **19**, 479 (1983).
11. F. Hild, J. M. Domergue, F. A. Leckie and A. G. Evans, *Int. J. Solids Struct.*, to be published.
12. P. Warren, T. J. Mackin and A. G. Evans, *Acta metall. mater.* **40**, 1243 (1992).
13. A. G. Evans, J. B. Davis and F. W. Zok, *Compos. Sci. Technol.* **42**, 3 (1991).
14. J. W. Hutchinson and H. Jensen, *Mech. Mater.* **9**, 83 (1990).
15. K. F. Chan, M. Y. He and J. W. Hutchinson, *Mater. Sci. Engng* to be published.
16. A. Pryce and P. Smith, *J. Mater. Sci.*, in press.
17. D. Beyerle, S. M. Spearing and A. G. Evans, *J. Am. Ceram. Soc.*, in press.

M A T E R I A L S



CRACKING AND DAMAGE MECHANISMS IN CERAMIC/METAL MULTILAYERS

by

M.C. Shaw,^{†*} D.B. Marshall,* M.S. Dadkhah* and A.G. Evans[†]

[†] Materials Department
College of Engineering
University of California
Santa Barbara, California 93106-5050

* Rockwell International Science Center
1049 Camino Dos Rios
Thousand Oaks, California 91360

ABSTRACT

Investigations of cracking in multilayered ceramic/metal composites are presented. Two aspects are considered: crack renucleation across intact single metal layers and subsequent crack extension. Crack renucleation criteria are determined and compared with predictions. High-resolution strain-mapping techniques are employed to determine the surface strain fields surrounding cracks. Good agreement is found between these experimental measurements and the predictions of a small-scale yielding model. Subsequent crack progression occurs either by the extension of a dominant, nearly planar crack or by the formation of a zone of periodically spaced cracks. Both patterns are analyzed. The dominant cracking behavior is found to depend on the volume fraction and yield strength of the metal.

1. INTRODUCTION

The macroscopic mechanical properties of layered metal/ceramic composites are governed by the mechanisms of deformation and damage that occur upon loading.¹⁻⁶ Especially important is the manner in which cracks that first form in a brittle layer communicate further damage to the neighboring layers. Two limiting responses have been identified: global and local load sharing.¹ When global load sharing applies, the stress redistribution caused by a crack results in a uniformly increased stress in all of the remaining uncracked layers. Consequently, a straightforward stochastic approach can be used to characterize the mechanical properties, leading to a damage mechanics representation. Conversely, local load sharing results in a stress concentration around an initial crack formed within one layer, which causes damage to progress laterally, often as a dominant mode I crack. In this case, large-scale bridging mechanics is appropriate. As yet, there is no fundamental understanding of the properties of the layers and of the interfaces that govern the occurrence of these extreme behaviors (or of intermediate mechanisms). The present article addresses the criterion that governs this fracture mechanism transition.

A previous study provided some understanding of the stress fields around a crack within a ductile-brittle layered composite.² For a crack located in a brittle layer with its tip incident upon a ductile layer (as illustrated in Fig. 1), two limits were identified: i) a small-scale yielding (SSY) limit, wherein the plastic zone in the ductile layer is small compared with the size of the crack in the brittle layer and ii) a large-scale yielding (LSY), or shear lag (SL) limit, characterized by a relatively large plastic zone. The SSY limit exhibits relatively large stress concentrations and is expected to result in local load sharing. The LSY limit is typified by much smaller stress concentrations and may allow global load sharing. Therefore, investigation of these stress fields (including their relationship with the cracking sequence) might provide insight into the transition in

mechanism. The present study describes experimental approaches for measuring the stress and displacement fields around such cracks, and compares the results with calculated stress fields.

2. EXPERIMENTAL

2.1 Materials

Metal/ceramic multilayers were produced by vacuum diffusion bonding precleaned metal and ceramic sheets. Bonding was conducted at homologous temperatures for the metal, $T/T_m \sim 0.9$, for ~ 24 h, with an applied compression ~ 2 MPa, in a vacuum $\sim 10^{-6}$ Torr. The composites were prepared from two grades of aluminum oxide,* one of higher strength than the other, bonded to high purity aluminum or copper. These systems have strongly bonded interfaces.³ The properties of the constituents are summarized in Table I. The thicknesses of the layers, as well as the ratios of the metal thickness, h_m , to the ceramic thickness, h_c , were varied, but in all cases, a total multilayer thickness of 4–8 mm was used. The range of systems and diffusion bonding conditions are summarized in Table II. Some specimens with relatively thick (2 mm) Al_2O_3 outer layers were used in order to establish a well-developed crack prior to testing (Fig. 2(a)).

2.2 Measurements

In situ observations of crack growth in the multilayered composites were obtained on beam specimens with notches cut to a depth of $\sim 50\%$ of the thickness of the outer ceramic layer with a diamond saw. The specimens were polished optically flat on one face to allow observations of crack growth. Cracks were initiated from the root of the

* Coors ADS-995, which is relatively pure and has high flexural strength, and Coors ADS-96, which is less pure and has lower strength.

notch and then extended stably to the interface using a loading fixture attached to the stage of an optical microscope (Fig. 2(a)). Most tests were done in ambient air. However, to examine environmental susceptibility, a few tests on the $\text{Al}_2\text{O}_3/\text{Al}$ materials were done in dry N_2 . High magnification micrographs were obtained from the crack tip region during loading. In all cases, cracks were oriented with the crack plane perpendicular to the layers (Figs. 1, 2) and the loads were applied in four-point flexure. Typical specimen dimensions were $1 \times 8 \times 30$ mm, with the inner and outer loading point separations being 10 and 25 mm, respectively. The nominal mode I stress intensity factors K_I were evaluated from the measured loads, crack lengths and specimen dimensions by using the calibration for an elastically homogeneous beam (Section 3.1).⁷

Optical micrographs of the crack tip region were analyzed to determine the opening displacement, δ_o , of the cracked ceramic layer adjacent to the metal, the strain, ϵ_{yy} , in the neighboring ceramic layer, and the plastic zone size, l_p (Fig. 1). This was achieved by measuring *differential* displacements of corresponding image features in pairs of micrographs: one taken at zero load (the reference) and the other obtained under load. Two image analysis techniques were used: stereo viewing of pairs of micrographs⁸ and a computerized image comparison procedure⁹ (HASMMap-High Accuracy Strain MAPing). The latter technique determines full-field maps of in-plane displacements, which can be differentiated to produce the in-plane strain fields. Since both methods measure differential displacements, their sensitivity is much greater than the point-to-point resolution of the micrographs.[‡]

Strain distributions were also measured using high-resolution moiré interferometry. The procedure involved depositing a diffraction grating on the specimen surface and forming a moiré interference pattern between the specimen grating and a fixed reference grating during loading of the specimen.^{10,11} The moiré

[‡] Displacement resolution of 10 nm is achieved from optical micrographs.

image consists of fringes which define contours of constant displacement, with the increment between fringes being equal to one-half of the grating period. A fringe multiplication technique was used¹¹ to increase the differential displacement resolution to 36 nm/fringe. Interferographs were obtained in two orthogonal directions, x or y (Fig. 1), by using two interpenetrating diffraction gratings oriented at 90°. The ϵ_{yy} strains were determined by measuring fringe spacings in the y direction, along a line within the ceramic layer, 5 μm from the interface. The $\sigma_{yy}(y)$ stress was then estimated by using the plane stress relation,¹²

$$(1 - \nu^2)\sigma_{yy}(y) = E[\epsilon_{yy}(y) + \nu\epsilon_{xx}(y)] \quad (1)$$

where ν is Poisson's ratio and E is Young's modulus of the Al_2O_3 . For the present estimate, it was assumed that $\epsilon_{xx}(y) \approx 0$.

In materials with relatively thick Al_2O_3 layers ($> 480 \mu\text{m}$), average strains, $\bar{\epsilon}_{yy}$, were measured with strain gauges, over an area $\approx 0.6 \times 0.25 \text{ mm}$.

The strength distribution of the higher strength alumina was measured using four-point flexural loading of specimens cut from as-received plates (680 μm thick) and from plates that had been surface-ground to reduce their thickness to 450 μm . The strength distribution of the lower strength alumina was also measured using four-point flexural loading of specimens cut from as-received plates (2 mm thick). The cumulative probability of failure, $\Phi(S)$, was determined (using order statistics) as a function of the nominal strength, S , for both types of alumina, by using the volume flaw solution (see Section 3),¹³

$$-\ln[1 - \Phi(S)] = (S/S_0)^m (Lhw/V_0)(m+2)/4(m+1)^2 \quad (2)$$

where L is the test span, w the specimen width and h the plate thickness, with V_0 being a reference volume (taken to be 1 m^3) and S_0 and m the reference strength and shape parameters, respectively.

3. RESULTS

3.1 Crack Growth

In multilayered composites with low volume fractions of metal ($f_m < 0.3$), a single crack formed in each ceramic layer ahead of the notch during fracture of precracked beams (Fig. 2(b)). No interfacial debonding occurred in any of the composites, during either crack renucleation or subsequent fracture, despite extensive plastic stretching of the metal layers (Fig. 3). Furthermore, the cracks renucleated sequentially in adjoining layers on nearly the same plane as the precrack. The damage is thus viewed as a dominant mode I crack, with the crack tip taken to be the edge of the cracked ceramic layer furthest from the precrack. A nominal stress intensity factor K_I can then be defined as the loading parameter.

The growth of mode I cracks in systems containing ceramic layers of thickness ($h_c = 450\text{--}680 \text{ }\mu\text{m}$) greater than that of the metal layers ($h_m = 8\text{--}250 \text{ }\mu\text{m}$) may be represented by resistance curves (Fig. 4). Two values of the stress intensity factor characterize crack growth: (i) that needed for initial crack renucleation across intact metal layers, K_N , and (ii) that needed for subsequent crack growth, K_R . Initial crack growth is controlled by crack renucleation in the ceramic layer ahead of the crack tip, whereas K_R increases during subsequent crack growth because of the bridging effect of intact metal layers in the crack wake. For a given material combination and environment (Fig. 5), the renucleation resistance increased with the thickness of the metal layers. The values of K_N ranged between 5 and $17 \text{ MPa}\sqrt{\text{m}}$, in all cases, higher than the fracture toughness of alumina¹⁴ ($K_{I0} \sim 3.5$ to $4 \text{ MPa}\sqrt{\text{m}}$) (Fig. 5(a)). The values

of K_N were also systematically higher in Cu/Al₂O₃ composites containing the higher strength Al₂O₃ than in equivalent composites with the lower strength Al₂O₃ (Fig. 5(b)). Testing of the Al/Al₂O₃ composites in air resulted in lower values of K_N than testing in dry N₂, implying a sensitivity of crack renucleation to moisture (Fig. 5(c)).

Finally, the locations at which the cracks renucleated were usually offset from the crack plane in the last cracked Al₂O₃ layer. The offset distances, Δ , measured for composites with metal layers of various thicknesses are shown in Fig. 6 as a single probability distribution, plotted as a function of Δ normalized by the thickness, h_m , of the metal layers. The results indicate that Δ scales with h_m .

3.2 Crack Tip Opening Displacements

The stationary crack tip opening displacements, δ_o , were determined by stereoscopy from in situ optical micrographs obtained before cracks renucleated in the ceramic layer ahead of the precrack. For each specimen, δ_o was found to increase with increasing K_I , following the proportionality, $\delta_o \propto K_I^2$ (Fig. 7(a)). This proportionality suggests that the data may be compared with the solution for a homogeneous metal in the small-scale yielding limit, given by,^{15,16}

$$\delta_o \equiv \frac{HK_I^2}{E_m \sigma_o}, \quad (3)$$

where E_m and σ_o are the Young's modulus and uniaxial yield strength of the metal and H is a non-dimensional parameter. For homogeneous metals, H depends only on the work hardening coefficient, and typically has values of 0.48 for aluminum and 0.18 for copper.^{16,17} It is apparent from Fig. 7(b) that smaller values of H obtain for all of the layered materials. Moreover, the magnitude of H decreases with decreasing metal layer thickness (Fig. 7(b)) and, at given layer thickness, is lower for the multilayers containing

copper than for those containing aluminum, consistent with the trend in H for the homogeneous metals.

3.3 Strain Measurements

The average strains, ϵ_{yy} , measured using strain gauges in the Al_2O_3 layers directly opposite the precrack increased with increasing K_I (Fig. 8). Both the magnitude of the strain and the rate of increase in strain, at given K_I , increased with decreasing metal layer thickness.

A moiré interference micrograph showing fringes of constant displacement in the vertical (y) direction, obtained from the region surrounding a crack tip in a multilayered $\text{Cu}/\text{Al}_2\text{O}_3$ composite, is shown in Fig. 9. The stresses, σ_{yy} , along the edge of the Al_2O_3 layer ahead of the crack tip, evaluated from the micrographs (by using Eqn. (1)) are plotted in Fig. 10, along with theoretical predictions to be discussed in the following section. The data obtained at each of three values of the applied stress intensity factor indicate that local stress concentrations exist ahead of the crack tip, with peaks offset symmetrically by approximately $50\text{ }\mu\text{m}$ from the crack plane. The magnitude of the peak stress increases linearly with K_I . The strains, ϵ_{yy} , in the metal layer displayed a similar distribution as those in the intact ceramic layer, but were much larger in magnitude with a plastic zone that extended beyond the field of view ($\pm 350\text{ }\mu\text{m}$).

The distribution of shear strains (as determined by HASMAP) around a crack in another $\text{Cu}/\text{Al}_2\text{O}_3$ multilayered composite with thicker copper layers ($130\text{ }\mu\text{m}$) is shown in Fig. 11. A zone of localized plastic strain within the copper layer ahead of the crack tip is evident. The zone extends to the side of the crack to a distance approximately 7 times the metal layer thickness ($l_p = 1\text{ mm}$).

3.4 Multiple Cracking

In composites with larger volume fractions of metal ($f_m > 0.7$), multiple cracks formed within the Al_2O_3 layers (Figs. 2(c), 2(d)) after initial renucleation from the precrack. Furthermore, in multilayers with the highest metal volume fraction ($f_m = 0.85$, Fig. 2(d)), lateral spreading of multiple cracks within the same brittle layer often occurred in *preference* to forward progression of the main crack. In all cases, the cracking eventually saturated within a damage zone ~ 2 mm in total width (approximately twice the width of the region of the specimen containing the thin ceramic layers, Fig. 2(a)), with the distribution, Φ_m , of crack spacings shown in Fig. 12. It is evident that the median crack spacing at saturation, l_s , increases as the alumina layer thickness increases.

3.5 Alumina Strengths

The strength distributions measured on the as-sintered and surface-ground specimens of the higher strength Al_2O_3 were indistinguishable (Fig. 13(a)), suggesting that the strength is controlled by volume flaws.[†] The data from both types of specimens were combined, and the magnitudes of the shape parameter, m , and the reference strength, S_0 , were ascertained by fitting Eqn. (2) to the data, giving $S_0 (V_0)^{1/m} = 37 \text{ MPa} \cdot \text{m}^{3/m}$. The corresponding median strength is, $S_m = 460 \text{ MPa}$. For the lower strength Al_2O_3 (as-sintered), $S_0 (V_0)^{1/m} = 20 \text{ MPa} \cdot \text{m}^{3/m}$ and the median strength is, $S_m = 380 \text{ MPa}$ (Fig. 13(b)).

[†] Although it is possible that the surface flaw distributions were the same within the measurement accuracy, it is considered unlikely.

4. COMPARISON WITH MODELS

4.1 Crack Tip Stresses

Two limiting solutions have been identified for the stresses, $\sigma_{yy}(x, y)$, within intact brittle layers ahead of the crack tip in layered metal/ceramic composites. In the small-scale yielding (SSY) limit, the stresses along the crack plane closely approximate the elastic solution,¹

$$\sigma_{yy}(x, 0) \approx K_I / \sqrt{2\pi x} \quad (x \geq h_m) \quad (4)$$

where K_I is computed for an elastically homogeneous medium. This result holds even when the plastic zone extends both through the metal layer and laterally up to a distance several times the metal layer thickness. The corresponding stresses in the intact ceramic layer alongside the metal/ceramic interface ($x = h_m$) are given by,¹⁸

$$\begin{aligned} \sigma_{yy}(r, \theta) &= \frac{K_I}{\sqrt{2\pi r}} \left(\cos\left(\frac{\theta}{2}\right) \left[1 + \sin\left(\frac{\theta}{2}\right) \sin\left(\frac{3\theta}{2}\right) \right] \right) \\ &\equiv \frac{K_I}{\sqrt{2\pi r}} f(\theta) \end{aligned} \quad (5)$$

where r and θ are the radial and angular coordinates from the crack tip (Fig. 1),

$$\begin{aligned} r &= \sqrt{h_m^2 + y^2} \\ \theta &= \arctan\left(\frac{y}{h_m}\right) \end{aligned} \quad (6)$$

An estimate of the size of the slip zone, obtained by equating σ_{xy} to the shear yield strength of the metal (with $K_I = \sigma_\infty \sqrt{\pi a_0}$ in Eqn. (5)), is,²

$$\ell_p/a_o = 0.61(\sigma_-/\sigma_o)^2 \quad (7)$$

where σ_o is the applied tensile stress and a_o is the length of the precrack. For larger slip lengths, corresponding to large-scale yielding (LSY), a finite element analysis has been used to evaluate the stresses.² The peak stress in the ceramic layer is,²

$$\sigma_{yy}(h_m, 0) = \sigma_- \left[1 + \frac{5.8}{\ln(\ell_p/h_m)} \right] \quad (8)$$

The distribution of σ_{yy} stresses in the intact ceramic layer for $0.05 \geq (y/\ell_p) \geq 1$ is,²

$$\sigma_{yy}(h_m, y) = \sigma_- \left[1 - 5.8 \left(\frac{a_o}{w} \right) Q \frac{\ln(y/\ell_p)}{\ln(\ell_p/h_m)} \right] \quad (9)$$

where Q is a dimensionless parameter and w is the specimen width.² The corresponding slip length is,

$$\ell_p/a_o = \sqrt{3} \sigma_-/\sigma_o \quad (10)$$

The predicted stresses, given by Eqns. (5) and (9), are compared with the moiré interferometry data in Fig. 10. The SSY predictions agree reasonably well with the experimental results, including the locations of the peak stress which are offset from the crack plane. Conversely, the LSY solution substantially underestimates the magnitudes of the stresses and fails to predict the location of maximum stress. Additionally, the SSY predictions are compared with the strain gauge measurements, made over a range of loads (Fig. 8; Appendix A). Again, the SSY predictions agree reasonably well with the data.

The stress distributions at $x = h_m$ in the ceramic layer ahead of the crack tip can be used in conjunction with the measured strength of the ceramic to predict failure of the ceramic layer and thus, the renucleation stress intensity factor, K_N . A simple estimate is obtained by equating the stress (at $x = h_m, y = 0$) from Eqn. (5) to the median strength, S_m , of the Al_2O_3 layers.† For small-scale yielding, this gives,

$$K_N = S_m \sqrt{2\pi h_m} \quad (11)$$

The prediction of Eqn. (11), with $S_m = 460$ MPa (from Fig. 13), agrees reasonably well with measured values of K_N for materials with metal layers of various thicknesses (Fig. 5(a)). Furthermore, the decrease in K_N in multilayers fabricated from the lower strength alumina (Fig. 5(b)) also is consistent with the predicted decrease in K_N resulting from a lower S_m . These correlations with the SSY predictions apply even though the normalized plastic zone size extends up to $l_p/a_0 = 2$ (Fig. 11). Consequently, the SSY stresses seemingly apply over a wider range of plastic zone sizes than had been expected,² although these findings are consistent with recent calculations.¹⁹

4.2 Multiple Cracking

4.2.1 Transition From Single to Multiple Cracking

The criterion for the transition from single to multiple cracking is a key design parameter for this class of multilayered composites. Since the present experiments indicate that SSY conditions dominate, this transition does not appear to be related to the onset of LSY conditions. Instead, it is suggested that the transition occurs when new

† A more rigorous analysis would entail statistical analysis of fracture, using the measured strength distribution of the Al_2O_3 layers and the nonuniform stress field of Eqn. (5). Preliminary calculations indicate that the present simplification does not result in significant error.

cracks are formed in the Al_2O_3 layers in the crack wake. For wake cracking to occur preferentially, the local stresses in the wake must exceed those ahead of the crack, as well as reach the fracture strength of the ceramic layer. These stresses are influenced by two contributions: the K-field of the main crack tip and the bridging tractions exerted by the intact, but plastically stretched, metal layers. The stresses associated with the K-field are always smaller in the wake than ahead of the crack tip. However, the contribution from the bridging tractions can be sufficient to make the wake stress larger than the tip stress. This contribution depends on the magnitude of the bridging tractions, T , the relative area over which the tractions are applied (the volume fraction of the metal) and the absolute thicknesses of the individual layers. The magnitude of T is known to depend on the metal yield strength and the local crack opening.^{20,21}

A simple model for wake cracking, involving a primary crack traversing three ceramic layers and partially bridged by two intact metal layers, is analyzed in Appendix B (Fig. B1). Approximate analytical solutions for the wake stresses as a function of distance from the crack plane, for this particular geometry (Fig. B2), indicate that the stress increases from zero at the crack faces to a maximum at a characteristic distance from the crack plane, and then decreases. The characteristic distance could dictate the crack spacing within the zone of multiple cracking. The analysis reveals that as the volume fraction of metal increases, the location of the larger peak stress changes from the brittle layer ahead of the crack tip to the crack wake, provided that the metal flow strength is sufficiently high (Fig. B2). This trend is qualitatively consistent with the observations in Section 3.

4.2.2 Multiple Crack Density

An important measure of the extent of crack damage relevant to a damage mechanics formulation is the crack density, ρ . No attempt is made here to understand the evolution of ρ . However, some appreciation for the applicability of damage

mechanics may be gained by comparing the measured crack spacings with values predicted by fragment length analysis.¹ Stochastic analysis of multiple cracking in bimaterial systems with sliding interfaces¹ indicates that the crack density saturates and that the saturation density, ρ_s , is related to the interfacial shear stress, τ , as well as a characteristic ceramic layer strength, S_c , through the relationship,

$$\rho_s = \lambda(m) \tau / (h_c S_c) \quad (12)$$

where λ is a dimensionless coefficient of order unity,¹ and, for a well-bonded interface, τ is the shear flow strength of the metal ($\tau \approx \sigma_0 / \sqrt{3}$). The characteristic strength, S_c (Appendix C), is,¹

$$S_c = (\lambda \tau V_o S_o^m / h_c^2 w)^{1/(m-1)} \quad (13)$$

Therefore, Eqn. (12) can be written,

$$\rho_s = \left(\frac{\lambda^m \tau^m h_c^{(1-m)} w}{V_o S_o^m} \right)^{1/(m-1)} \quad (14)$$

With the relevant parameters for the $\text{Al}_2\text{O}_3/\text{Al}$ system ($S_o V_o^{1/m} = 37 \text{ MPa} \cdot \text{m}^{3/m}$, $\tau = 30 \text{ MPa}$, $\lambda (m = 8) \approx 1.6$), the saturation crack spacings for multilayered specimens with $45 \mu\text{m}$ and $125 \mu\text{m}$ thickness alumina layers are predicted from Eqn. (14) to be $\sim 0.7 \text{ mm}$ and $\sim 1.6 \text{ mm}$, respectively. Although these are larger than the measured spacings, they are in the same range and they scale correctly (Fig. 12). A damage approach based on the stochastics of the brittle layers, coupled with interfacial slip, thus appears to be a potentially viable procedure for characterizing the properties associated with multiple cracking.

5. CONCLUSIONS

Crack growth and damage accumulation in strongly bonded ceramic/metal multilayers have been investigated, with particular emphasis on the criterion for crack advance, as well as on crack extension patterns. Crack renucleation beyond intervening metal layers is found to be governed by the small-scale yielding stress field. Plastic flow within the metal layers exerts a minimal influence, despite clear evidence of plasticity in the metal layers prior to crack renucleation. The metal layers therefore act simply to separate the intact ceramic layer from the crack tip by a distance corresponding to the metal layer thickness. This behavior leads to a simple inverse-square root dependence of the crack renucleation resistance, K_N , on the metal layer thickness, h_m . These conclusions establish that crack renucleation results from a significant stress concentration associated with cracks in adjacent brittle layers.

Damage develops either as a dominant crack, or as periodic cracks, depending on the volume fraction, layer thickness and yield strength of the metal. As the volume fraction of metal increases, at constant ceramic layer thickness, the stresses in the crack wake increase, whereas the stresses in the intact layer ahead of the crack tip decrease. This trend in stress leads to a transition in cracking mechanism with increasing volume fraction of metal, whenever the metal layers have sufficiently high yield strength. Specifically, for low metal volume fractions, mode I extension of a primary crack occurs, whereas for high metal volume fractions, periodic multiple cracking occurs.

When multiple cracking dominates, a damage mechanics approach for characterizing properties appears to be viable. To assess the validity of such an approach, a simple model has been used to relate the saturation crack density, ρ_s , to the intrinsic flow properties of the metal, the strength characteristics of the brittle layers and

the geometry of the multilayers. The predictions of the model are qualitatively consistent with the measured trends.

ACKNOWLEDGEMENT

The authors wish to gratefully acknowledge the assistance of Dr. B.J. Dalgleish in preparation of the copper/alumina multilayers, and for many valuable discussions. This work was supported by Rockwell International Independent Research and Development funding and by the Office of Naval Research, Contract No. N00014-90-J-1300.

TABLE I

Properties of Constituents

Constituent	Thermal Expansion Coefficient α ($\times 10^{-6} \text{C}^{-1}$)	Young's Modulus E (GPa)	Uniaxial Yield Strength σ_0 (MPa)	Work Hardening Coefficient n
Al ₂ O ₃	8	380	—	—
Al	25	70	50	0.2
Cu	17	120	70	0.3

TABLE II

Summary of Diffusion Bonding Conditions

Multilayer	Bonding Temperature (°C)	Bonding Pressure (MPa)	Bonding Time (h)	Al₂O₃ Thickness (μm)	Metal Thickness (μm)
Al/Al₂O₃	620	1.5	20	45	250
				680	8, 25, 50, 100, 250
	655	2.6	20	125	250
				680	8, 25, 100, 250
Cu/Al₂O₃	940	1	24	480	25, 130

APPENDIX A

Comparison of Predicted Stresses with Strain Gauge Measurements

The strain gauge data provide a measure of the average stress, $\bar{\sigma}_{yy}$, within the region bounded by the strain gauge, i.e., $h_m < x < h_m + d$, where d is the width of the strain gauge. For the stress field given by the small-scale yielding limit,²

$$\bar{\sigma}_{yy} = \frac{1}{d} \int_{h_m}^{h_m+d} \frac{K}{\sqrt{2\pi x}} dx, \quad (A1)$$

Integration gives,

$$\bar{\sigma}_{yy} = \sqrt{\frac{2}{\pi}} \frac{K}{\sqrt{d}} \left(\sqrt{\frac{h_m}{d} + 1} - \sqrt{\frac{h_m}{d}} \right) \equiv \frac{K}{\sqrt{2\pi \bar{d}}} \quad (A2)$$

where

$$\bar{d} = \left[\frac{d}{2[\sqrt{h_m + d} - \sqrt{h_m}]} \right]^2 \quad (A3)$$

Equation (A2) is compared with measurements for materials with aluminum layers of different thickness in Fig. 8.

APPENDIX B

Multiple Cracking Analysis

The mode of damage evolution (single or multiple cracking) depends on the relative magnitudes of the stresses in the ceramic layers ahead of and behind the crack tip. These depend, in turn, on the thicknesses of the metal and ceramic layers, the crack length, the strength distribution of the ceramic, and the flow properties of the metal. To assess the effect of changing the volume fraction of metal, these stresses are estimated for the specific composite geometry shown in Fig. B1.

The stresses were estimated by regarding the effect of the intact metal bridging ligaments as crack closure tractions, T , acting on the crack faces (Fig. B1). In general, the magnitude of T depends on the local crack opening, the flow properties of the metal and interfacial debonding. However, for the purpose of illustrating the transition in behavior, T is taken to be a constant ($T = 1.5 \sigma_{\infty}$) in the present analysis. Assuming that the stress concentration due to the crack tip is given by a K field, and assuming elastic homogeneity, the crack tip stresses are,¹⁸

$$\sigma_{tip} = \frac{K_{tip}}{\sqrt{2\pi r}} f(\theta) \quad (B1)$$

where K_{tip} is the local stress intensity factor given by,²⁰

$$K_{tip} = 2\sqrt{\frac{a}{\pi}} \int_0^1 \frac{(\sigma_{\infty} - T(X)) dX}{\sqrt{1-X^2}} \quad (B2)$$

where $X = 1 + x/a$ (Fig. B1). The stresses in the crack wake along the line, $x = -(h_m + h_c)$, are given by the superposition of two components, one due to the crack tip stress concentration, Eqn. (B1), and the other due to the traction T :^{18,22}

$$\sigma_{\text{wake}} = \frac{K_{\text{tip}}}{\sqrt{2\pi r}} f(\theta) + g(f_m, y/h_m, \theta, T) \quad (\text{B3})$$

where $f(\theta)$ is given by Eqn. (5) and the function $g(f_m, y/h_m, \theta, T)$ accounts for the wake stresses arising from the crack bridging tractions applied to the surface of an elastic half space over the intervals, $-2(h_c + h_m) < x < -(2h_c + h_m)$, and $-(h_c + h_m) < x < -h_c$,²²

$$g(f_m, r, \theta, T) = T(\alpha_1 + \alpha_2 + \sin\alpha_1 + \sin\alpha_2)/\pi \quad (\text{B4})$$

with,

$$\begin{aligned} \alpha_1 &= \arctan\left(\frac{h_m}{y}\right) \\ \alpha_2 &= \arctan\left(\frac{h_m + h_c}{y}\right) - \arctan\left(\frac{h_c}{y}\right) \end{aligned}$$

with h_m , h_c , and y defined in Fig. 1.

The stresses in the ceramic layers ahead of the crack tip (σ_A) and in the crack wake (σ_B) are plotted as a function of distance from the crack plane in Fig. B2 for various values of f_m . The stress distributions at both locations pass through a maximum at a distance from the crack plane of several times h_c . At small values of f_m , the maximum stress is larger ahead of the crack than in the wake, thus favoring growth of a single crack. Conversely, at large f_m , the maximum stress is larger in the wake, leading to

multiple cracking. The transition occurs at $f_m \approx 0.6$, for the particular value of T and the crack and layer geometries chosen here, for illustrative purposes.

APPENDIX C

Characteristic Ceramic Layer Strength

For a power law strength distribution in the brittle layers, the fraction, P , of flaws that can cause failure at stress S in a volume V is given by,

$$P(V, S) = \frac{V}{V_o} (S/S_o)^m \quad (C1)$$

At the point of crack saturation,¹ $S = S_c$

$$P(V_s, S_c) = \frac{V_s}{V_o} (S_c/S_o)^m \equiv 1 \quad (C2)$$

where V_s is the volume of material between the cracks. Using Eqn. (12), V_s can be re-expressed as,

$$V_s = \frac{h_c^2 S_c w}{\lambda \tau} \quad (C3)$$

Combining Eqns. (C2) and C3) yields,

$$S_c = \left(\frac{\lambda \tau V_o S_o^m}{h_c^2 w} \right)^{\frac{1}{m+1}} \quad (C4)$$

REFERENCES

- [1] W.A. Curtin, "Exact Theory of Fiber Fragmentation in a Single-Filament Composite," *J. Mater. Sci.*, **26** (1991) 5239-53.
- [2] H.C. Cao and A.G. Evans, "On Crack Extension in Ductile/Brittle Laminates," *Acta Metall. Mater.*, **39** [12] 2997-3005 (1991).
- [3] B.J. Dalgleish, K.P. Trumble and A.G. Evans, "The Strength and Fracture of Alumina Bonded with Aluminum alloys," *Acta Metall.*, **37** [7] 1923-31 (1989).
- [4] M.S. Hu and A.G. Evans, "The Cracking and Decohesion of Thin Films on Ductile Substrates," *Acta Metall.*, **37** [3] 917-25 (1989).
- [5] D.C. Agrawal and R. Raj, "Measurement of the Ultimate Shear Strength of a Metal-Ceramic Interface," *Acta Metall.*, **37** [4] 1265-70 (1989).
- [6] F.S. Shieu, R. Raj and S.L. Sass, "Control of the Mechanical Properties of Metal-Ceramic Interfaces Through Interfacial Reactions," *Acta Metall.*, **38** [11] 2215-24 (1990).
- [7] H. Tada, P.C. Paris and G.R. Irwin, *The Stress Analysis of Cracks Handbook*, Paris Productions, Inc., St. Louis, Missouri, 1985.
- [8] D.R. Williams, D.L. Davidson and J. Lankford, "Fatigue-Crack-Tip Plastic Strains by the Stereoimaging Technique," *Exp. Mech.*, **4**, 1980.
- [9] M.R. James, W.L. Morris and B.N. Cox, "A High Accuracy Automated Strain Field Mapper," *Exp. Mech.*, **30**, 60-68 (1990).
- [10] D. Post, "Moiré Interferometry," *Handbook of Experimental Mechanics*, ed. A.S. Kobayashi, Prentice Hall, NJ (1987).
- [11] M.S. Dadkhah, B. Han and M.C. Shaw, to be published.
- [12] S.P. Timoshenko and J.N. Goodier, *Theory of Elasticity*, McGraw-Hill, 1934.
- [13] N.A. Weil and I.M. Daniel, "Analysis of Fracture Probabilities In Nonuniformly Stressed Brittle Materials," *J. Am. Ceram. Soc.*, (1964) **47** [6], 268-74.
- [14] L.A. Simpson and G.J. Merrett, "The Effect of Annealing on the Fracture Toughness, Strength and Microstructure of Hot-Pressed Alumina," *J. Mater. Sci. Letters*, **9** (1974) 685-88.
- [15] J.R. Rice and M.A. Johnson, "The Role of Large Crack Tip Geometry Changes in Plane Strain Fracture," *Inelastic Behavior of Solids*, pp. 641-72, 1969 McGraw-Hill, eds. M.F. Kanninen, W.F. Adler, A.R. Rosenfield and W.F. Jaffee.

- [16] J.W. Hutchinson, "Nonlinear Fracture Mechanics," Dept. Solid Mechanics, Technical University of Denmark, 1979.
- [17] R.A. Hertzberg, *Deformation and Fracture Mechanics of Engineering Materials*, J. Wiley (1983).
- [18] B.R. Lawn and T. Wilshaw, *Fracture of Brittle Solids*, Cambridge University Press (1975).
- [19] K.S. Chan, M.Y. He and J.W. Hutchinson, to be published.
- [20] D.B. Marshall, B.N. Cox and A.G. Evans, "The Mechanics of Matrix Cracking in Brittle-Matrix Fiber Composites," *Acta Metall.*, 33 [11] 2013-21, 1985.
- [21] A.G. Evans and R.M. McMeeking, "On the Toughening of Ceramics by Strong Reinforcements," *Acta Metall.*, 34 [12] 2435-41, 1986.
- [22] T.J. Roark, *Formulas for Stress and Strain*, McGraw-Hill (1954).

FIGURE CAPTIONS

- Fig. 1. Schematic illustrating the crack geometry and the parameters measured in the experiments.
- Fig. 2. a) Schematic illustrating the typical specimen and loading geometry. b), c) and d) Cracking patterns determined by optical microscopy: b) single crack in a system with Al/480 μm Al₂O₃, c) multiple cracking in composites with Al/125 μm Al₂O₃ and d) Al/45 μm Al₂O₃. Arrows indicate the crack locations. All three composites contained 250 μm thick Al layers.
- Fig. 3. Scanning electron micrographs of fracture surfaces of Al/Al₂O₃ multilayers, showing a single aluminum layer sandwiched between two alumina layers.
- Fig. 4. Measured crack growth resistance, K_R , as a function of crack extension, Δa , for several multilayered composites.
- Fig. 5. a) Crack renucleation stress intensity factor, K_N , as a function of metal layer thickness, h_m , for a) composites fabricated from the higher strength alumina and tested in an air environment. Also shown is the SSY prediction for a median ceramic strength, $S_m = 460$ MPa. b) K_N for copper/alumina composites fabricated from *either* the higher strength or lower strength alumina and tested in an air environment. Also shown are the SSY predictions for K_N for median ceramic strengths of, $S_m = 460$ MPa and $S_m = 380$ MPa. c) K_N for aluminum/alumina multilayers fabricated from the higher strength alumina tested in air and dry nitrogen.
- Fig. 6. Cumulative distribution, Φ_d , of the offset, Δ , in crack renucleation location normalized by the metal layer thickness, h_m , for multilayers with a range of metal layer thicknesses.
- Fig. 7. a) Crack tip opening displacements, δ_o , as a function of the square of the applied stress intensity factor, K_I^2 , for several multilayer systems. Also shown is the prediction (Eqn. 3) b). The non-dimensional parameter, $H = \delta_o E_m \sigma_o / K_I^2$ as a function of inverse metal layer thickness for several different multilayer systems.

- Fig. 8. Average stresses, $\bar{\sigma}_{yy}$, in ceramic layers directly opposite the crack determined with a strain gauge, for several multilayers. Also shown are the predictions for $\bar{\sigma}_{yy}$ from Eqn. (A2).
- Fig. 9. High-resolution moiré interferograph of the crack tip region in a Cu/Al₂O₃ multilayer when subjected to an applied stress intensity factor of $K_I = 7.7 \text{ MPa}\sqrt{\text{m}}$. Each fringe represents a contour of constant differential displacement of 36 nm in the vertical direction (y-direction).
- Fig. 10. Stress distributions, $\sigma_{yy}(y)$, obtained by moiré interferometry at three loads ($K_I = 5.1, 6.4$ and $7.7 \text{ MPa}\sqrt{\text{m}}$). Comparisons with SSY and LSY predictions are also shown.
- Fig. 11. Contour map of the in-plane shear strain distribution, ϵ_{xy} , measured by HASMAP just before crack renucleation in a copper/alumina multilayer. The contour intervals represent a strain of 6×10^{-4} .
- Fig. 12. Distribution, Φ_m , of crack spacings, at saturation, from several multiply cracked aluminum/alumina specimens containing 45 μm and 125 μm thick alumina layers with 250 μm thick aluminum layers.
- Fig. 13. Cumulative failure probabilities a) for plates of the higher strength Al₂O₃ in the as-received and machined conditions, and b) plates of the lower strength alumina in the as-received condition.
- Fig. B1. Schematic of the crack configuration analyzed in Appendix B.
- Fig. B2. Approximate analytical solutions for crack tip and crack wake stresses for the crack geometry shown in Fig. B1 with various volume fractions of metal, f_m , and with bridging tractions taken to be $T = 1.5 \sigma_\infty$.

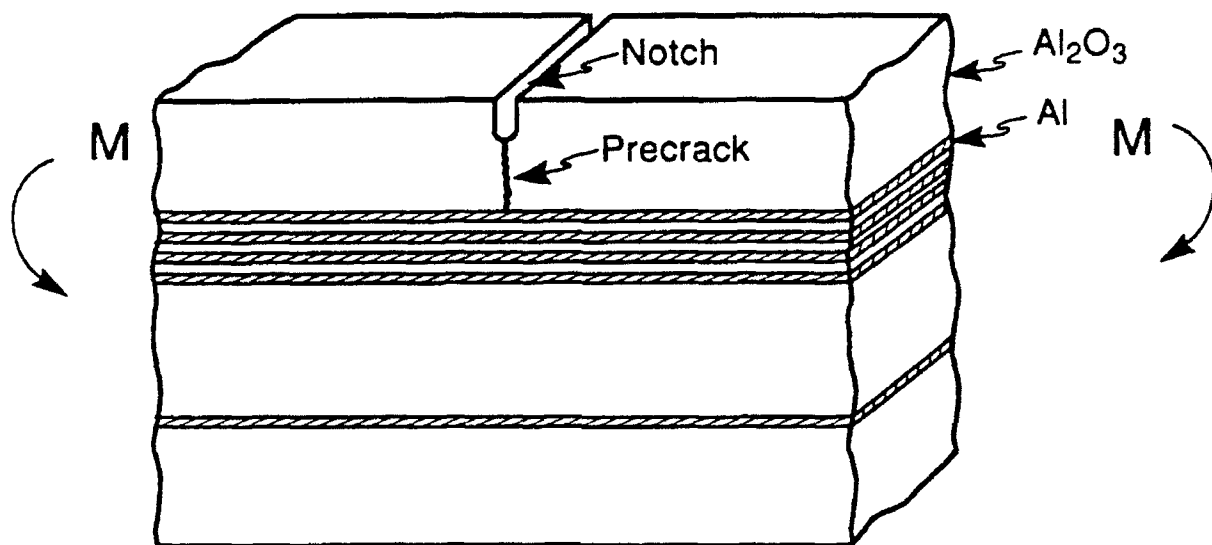


Fig. 2(a)

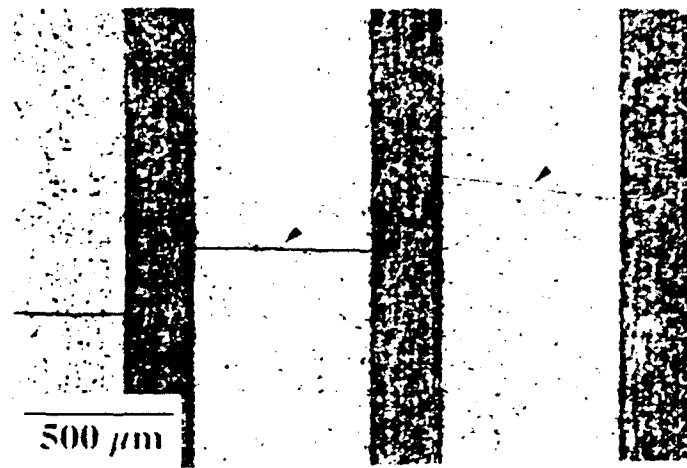


Fig. 2(b)



Fig. 2(c)

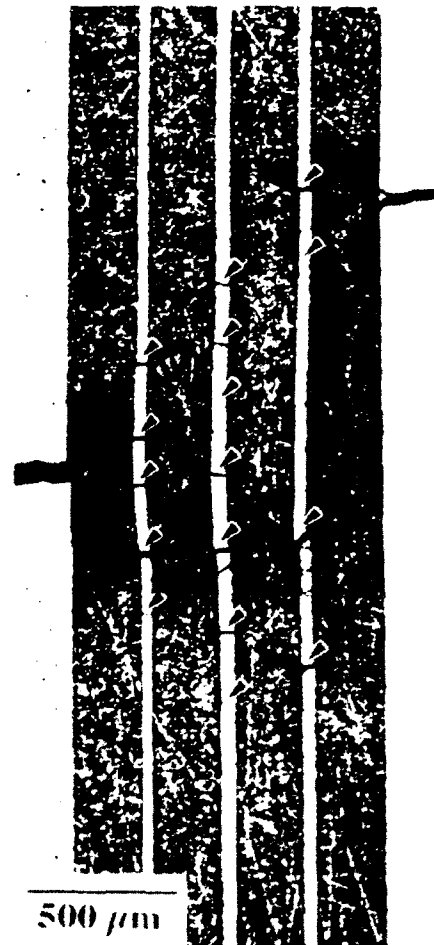


Fig. 2(d)

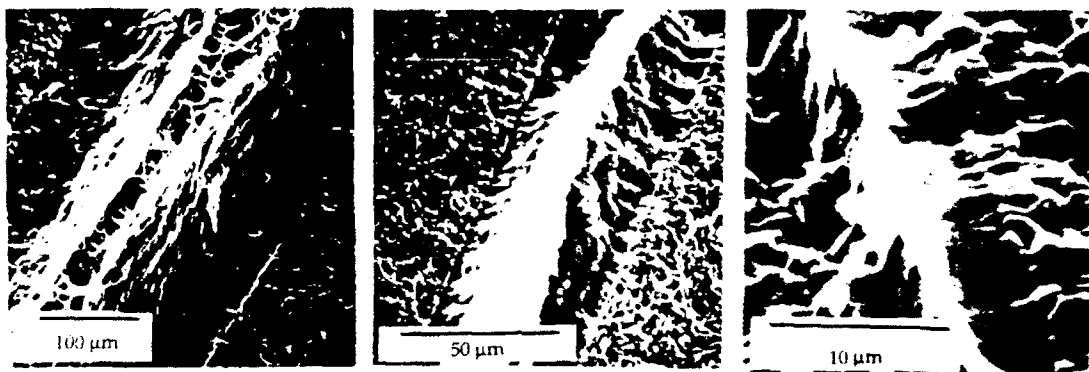


Fig. 3

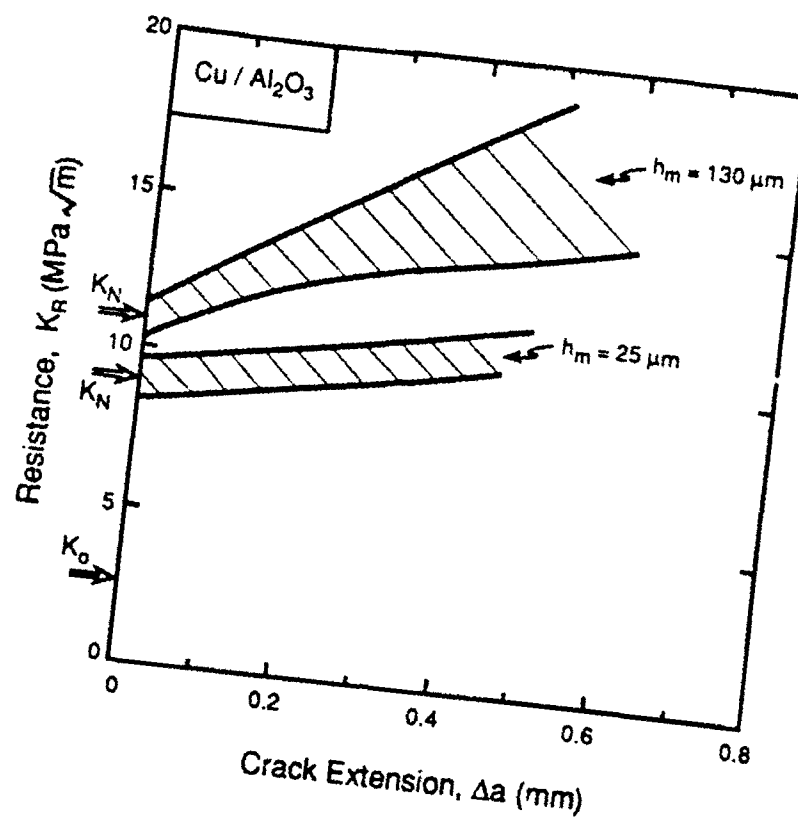
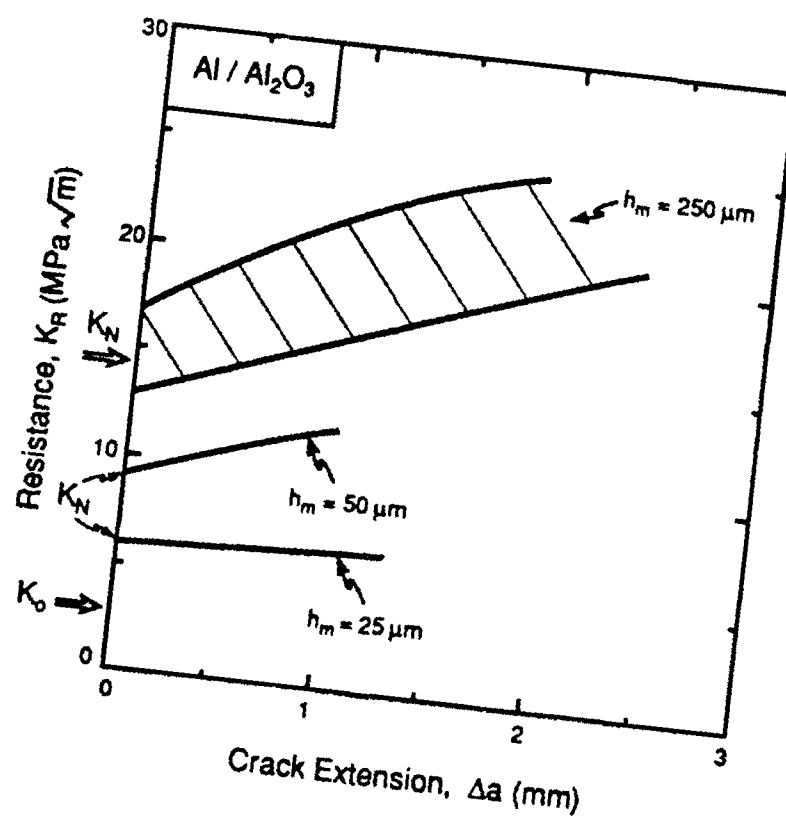


Fig. 4



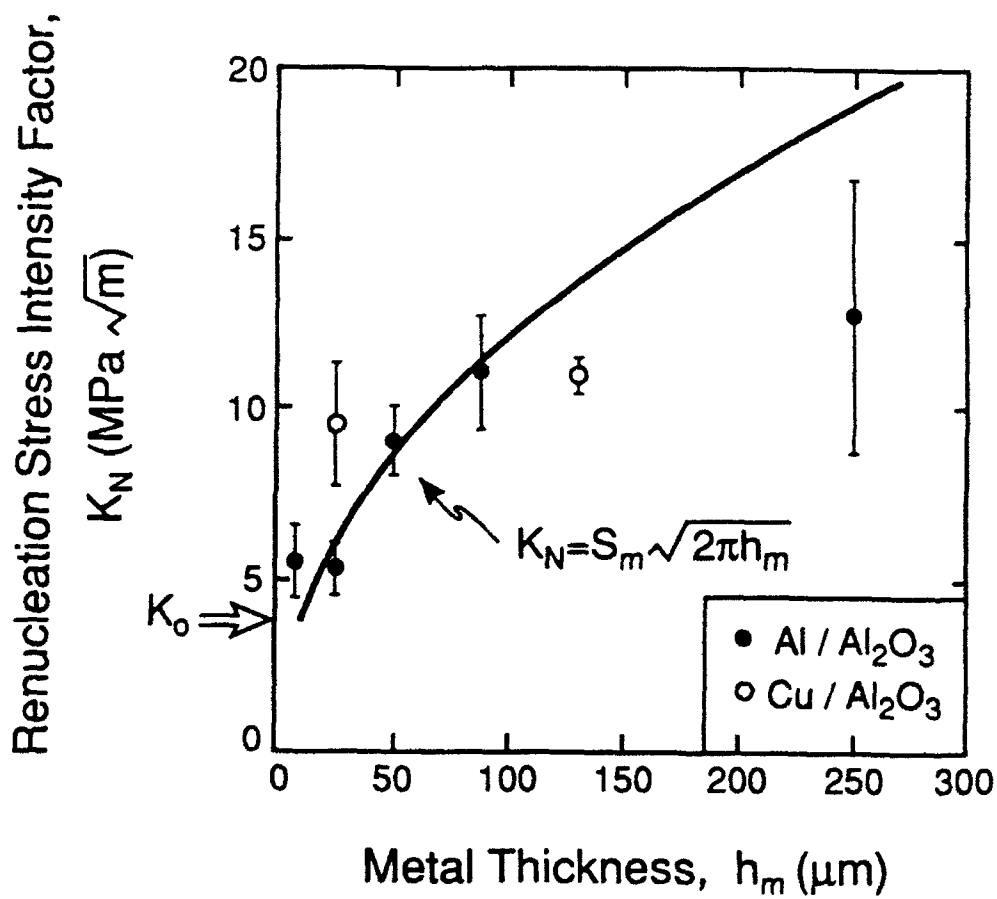


Fig. 5(a)

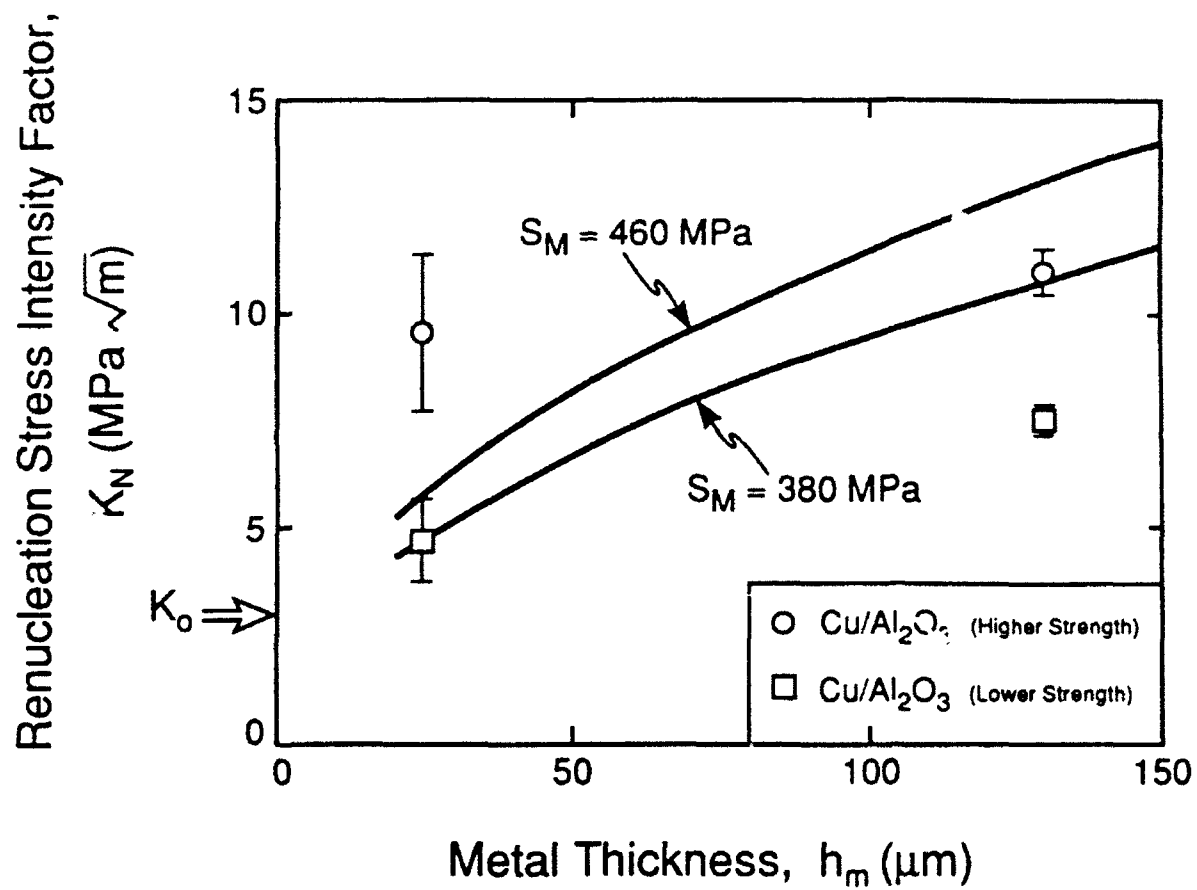


Fig. 5(b)

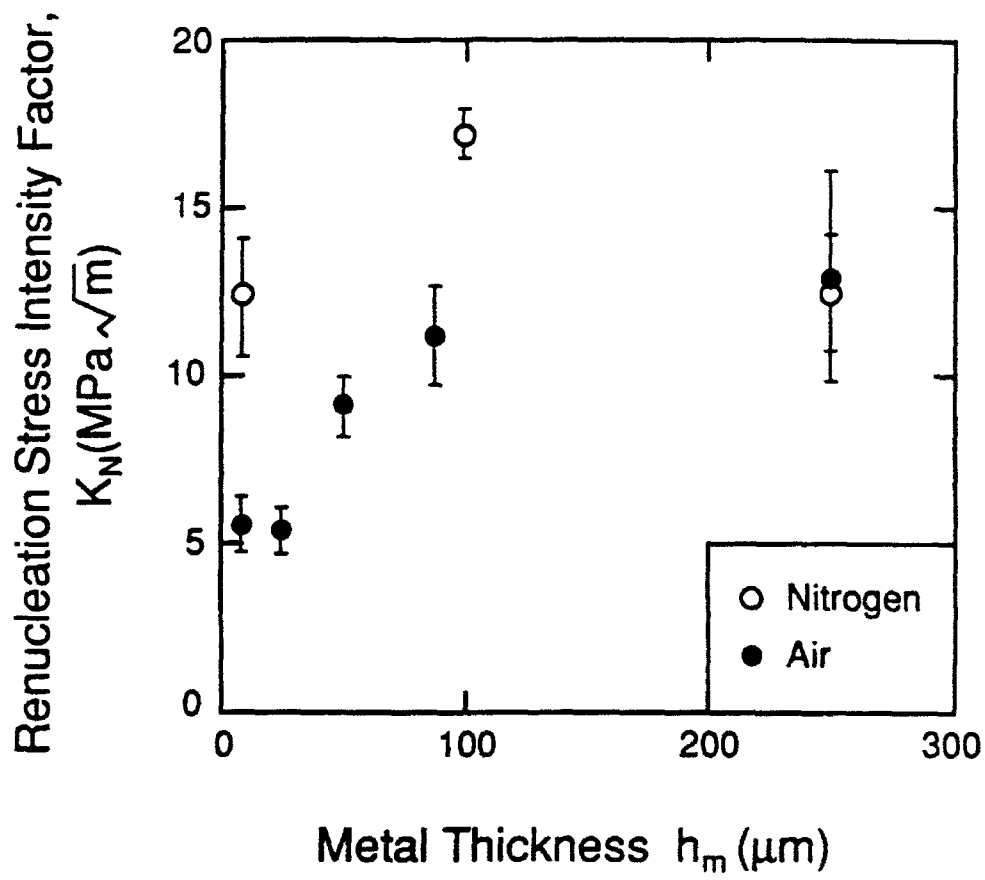


Fig. 5(c)

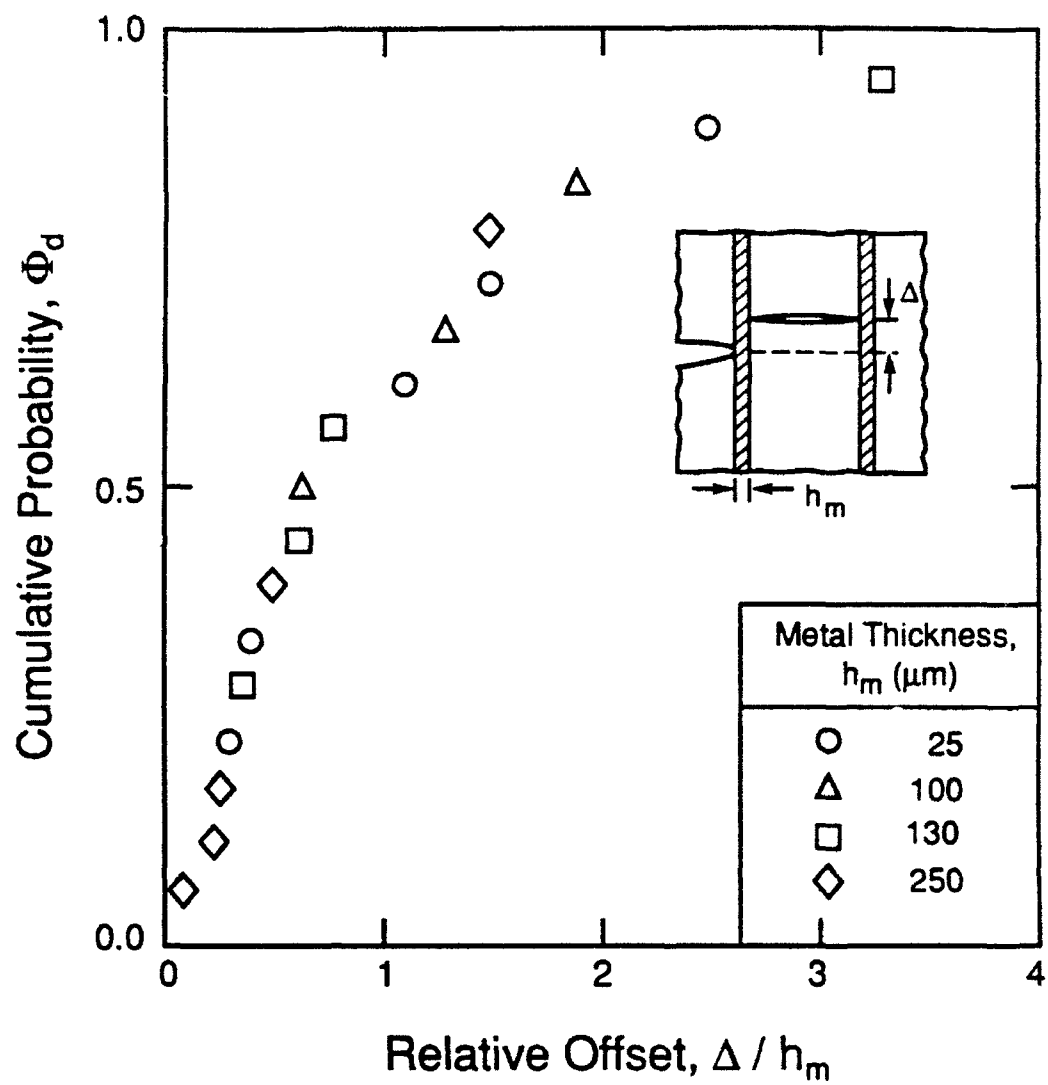


Fig. 6

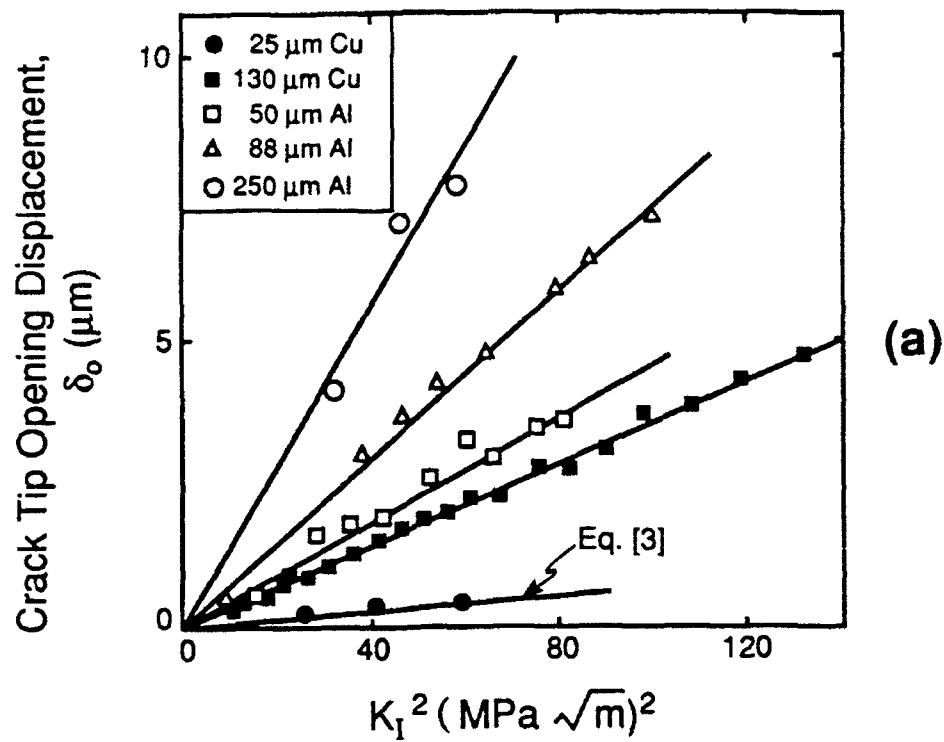
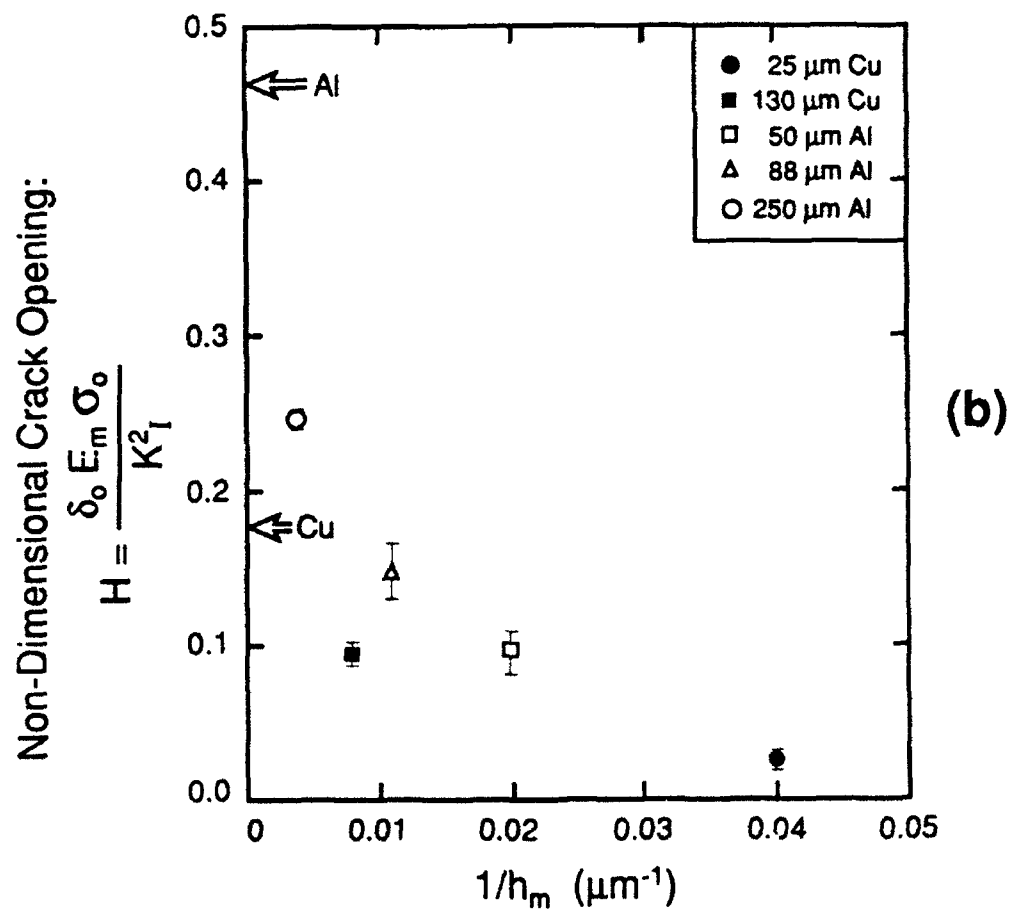


Fig. 7



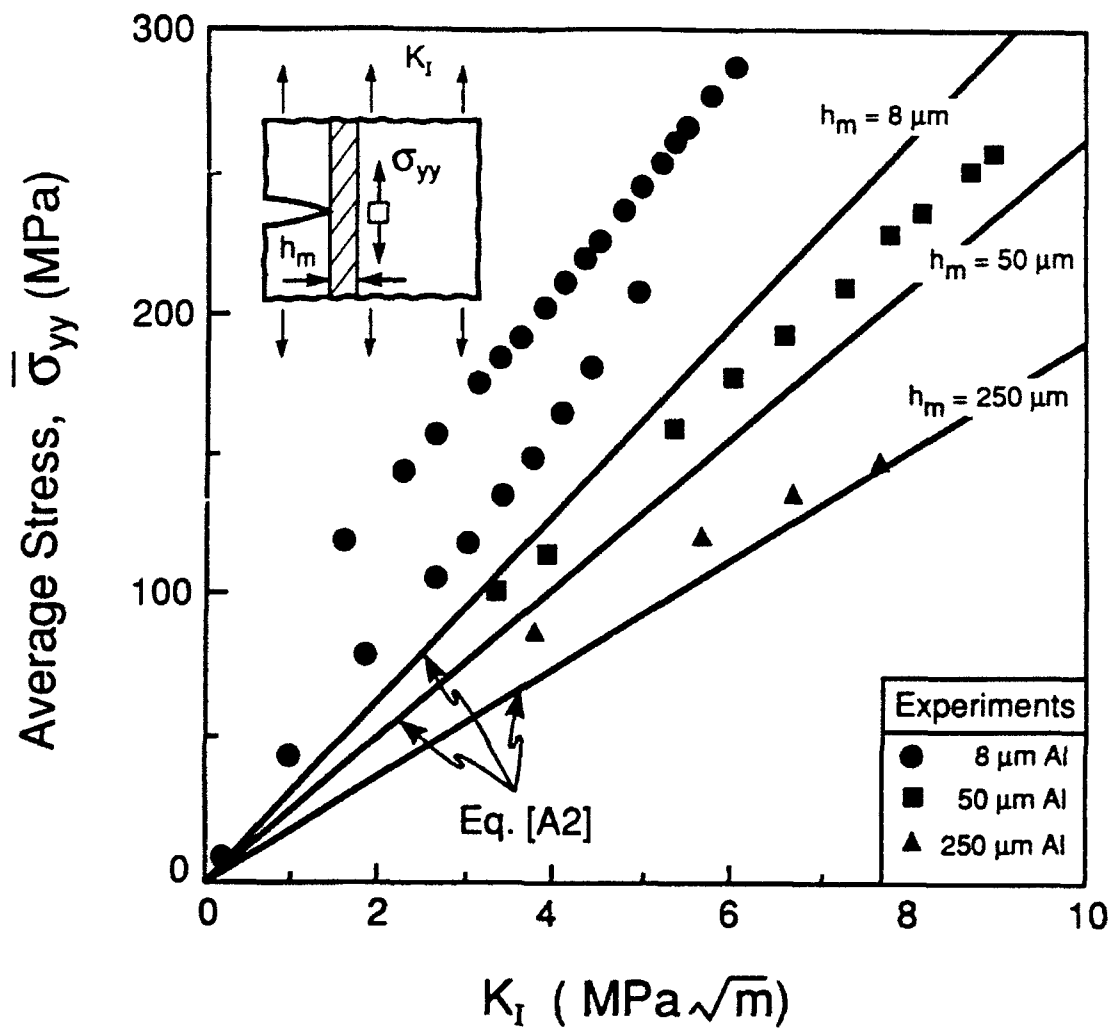


Fig. 8

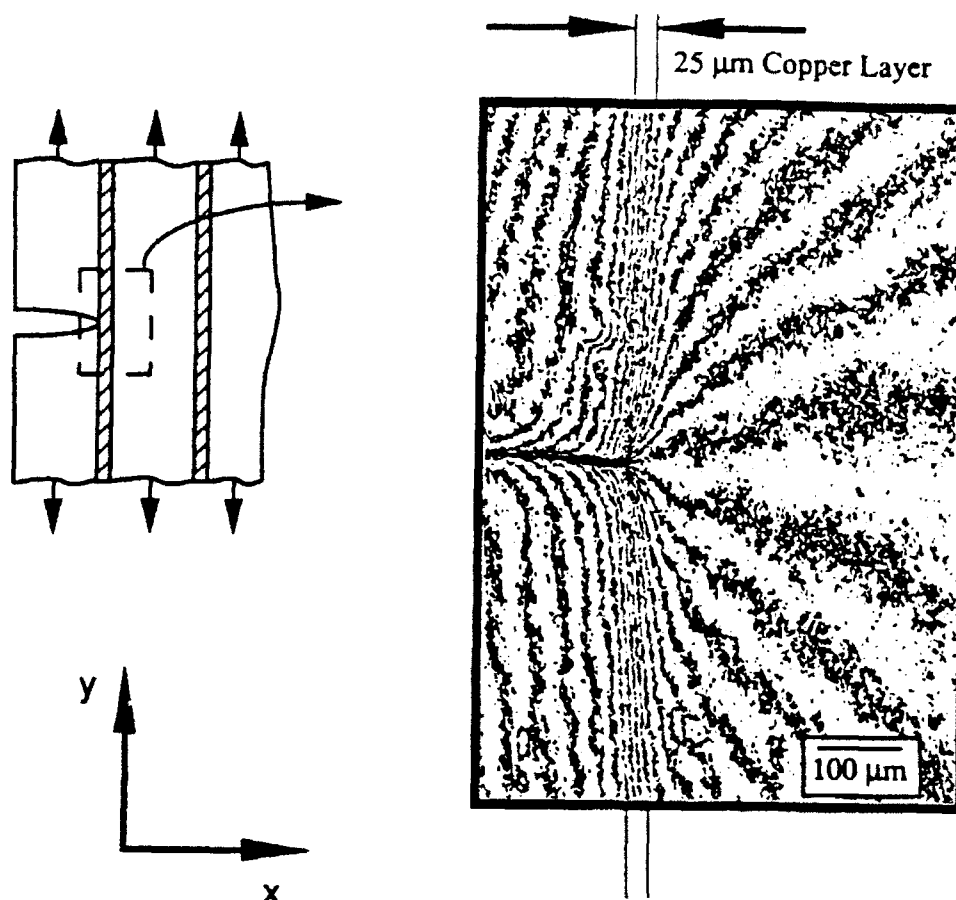


Fig. 9

Predictions	Experiments
	K_I (MPa \sqrt{m})
— S.S.Y	■ 5.1
	● 6.4
--- S.L.	▲ 7.7

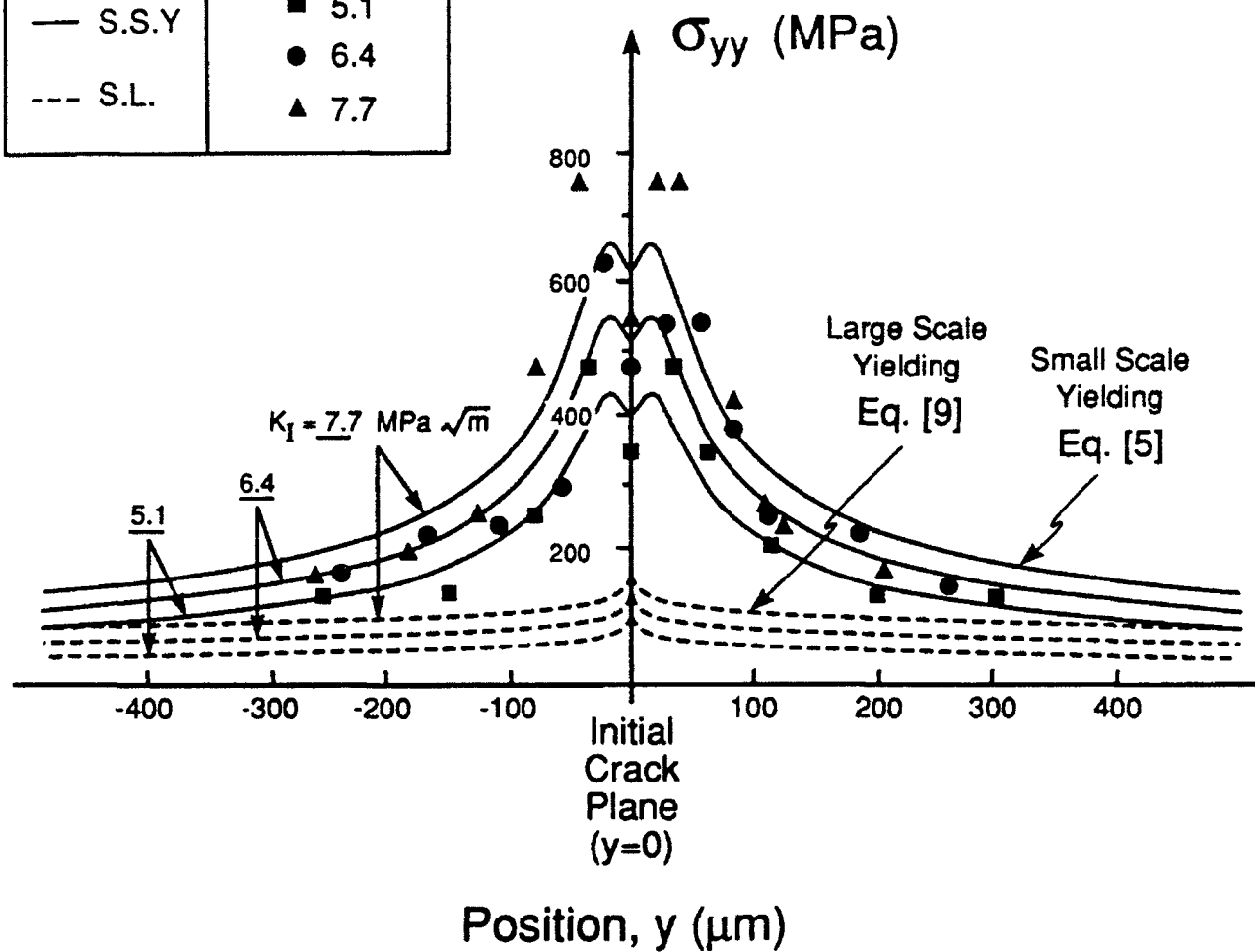


Fig. 10

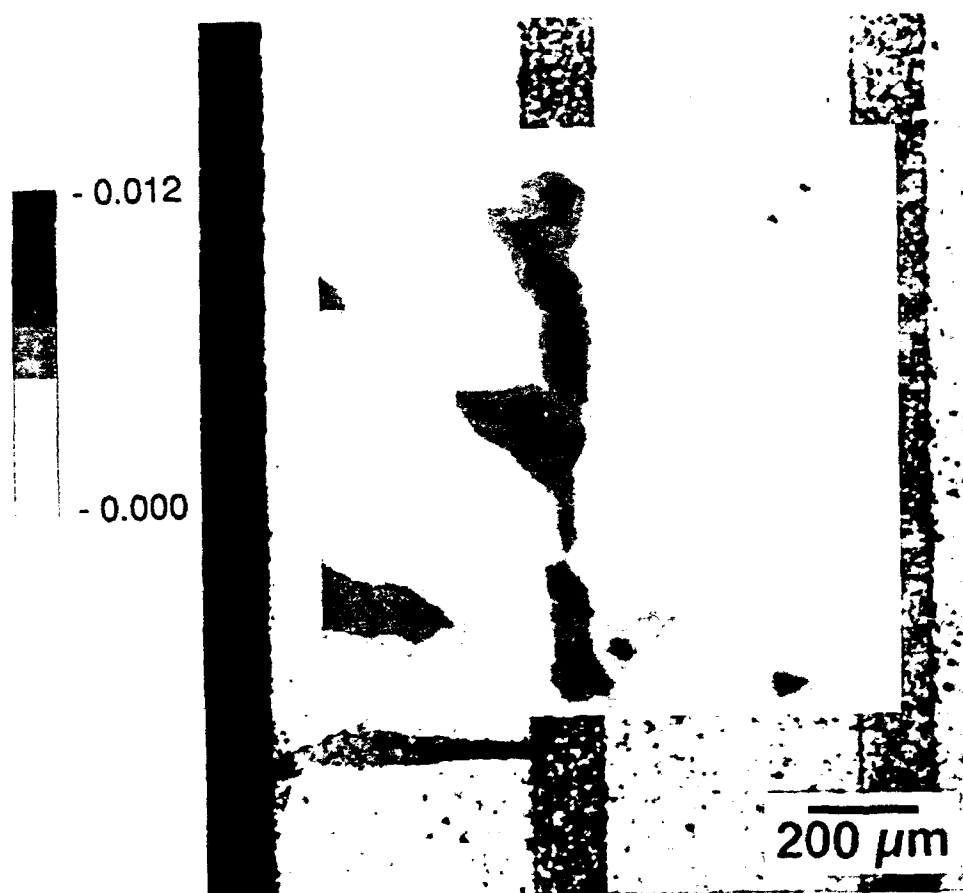


Fig. 11

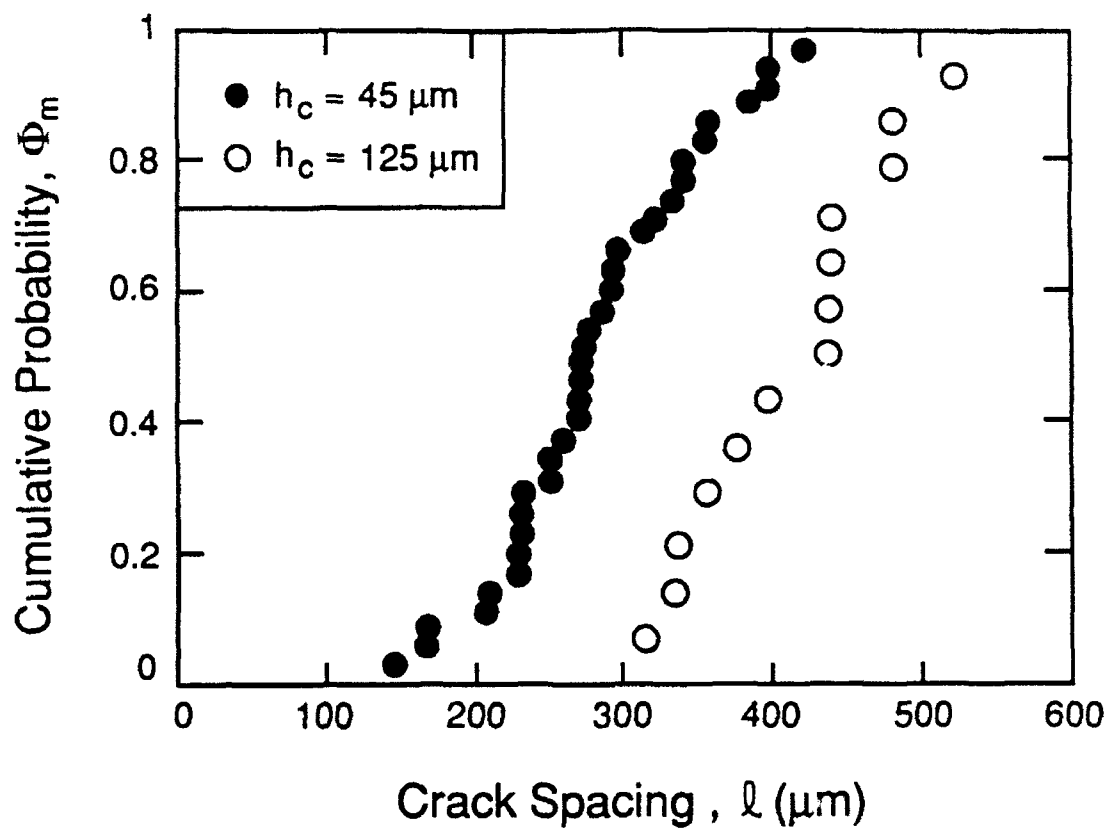


Fig. 12

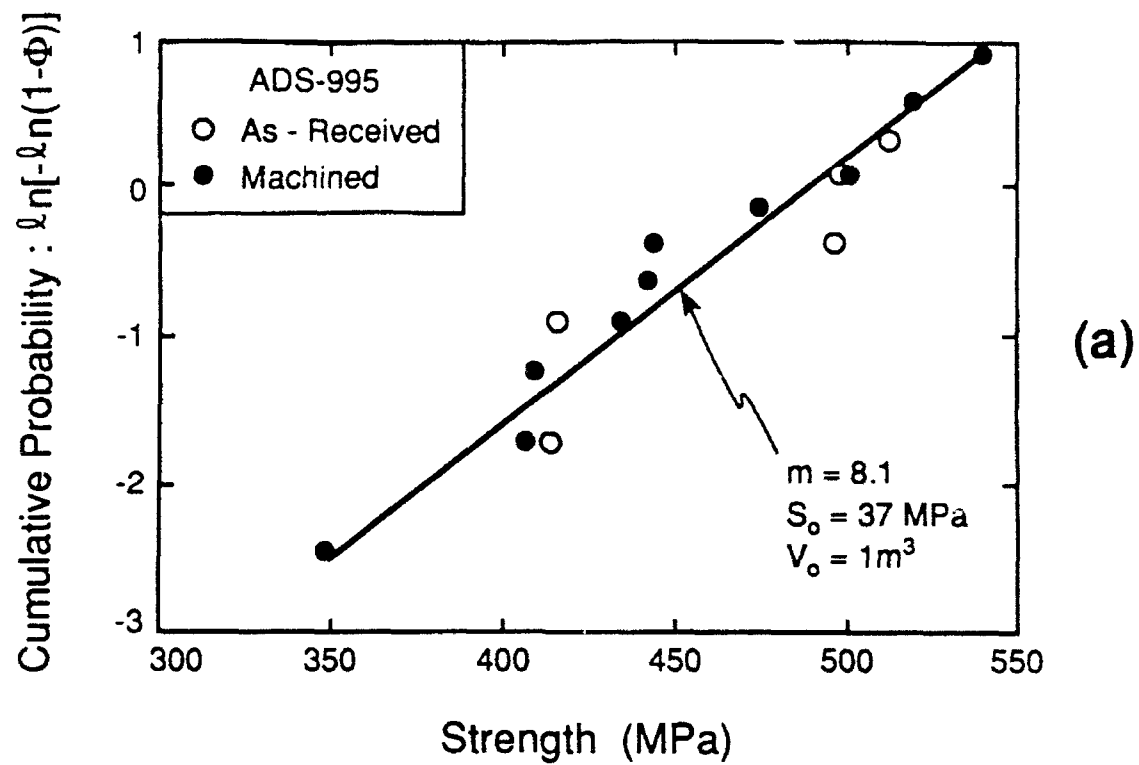
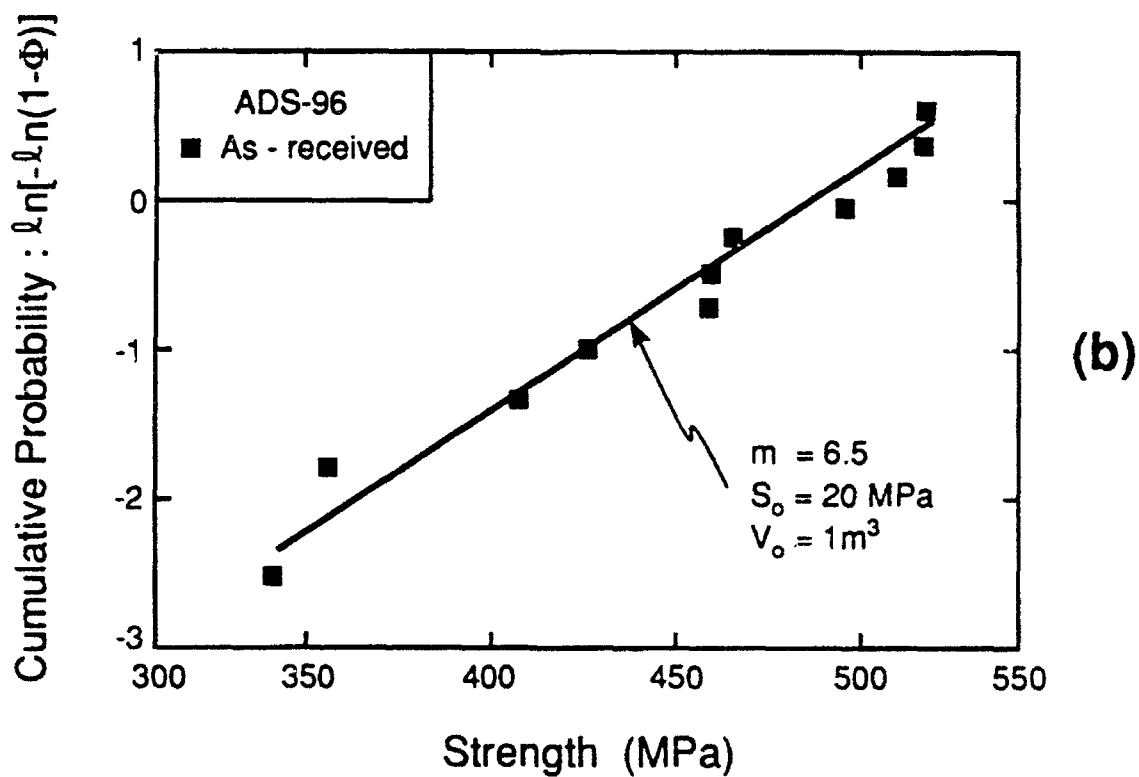


Fig. 13



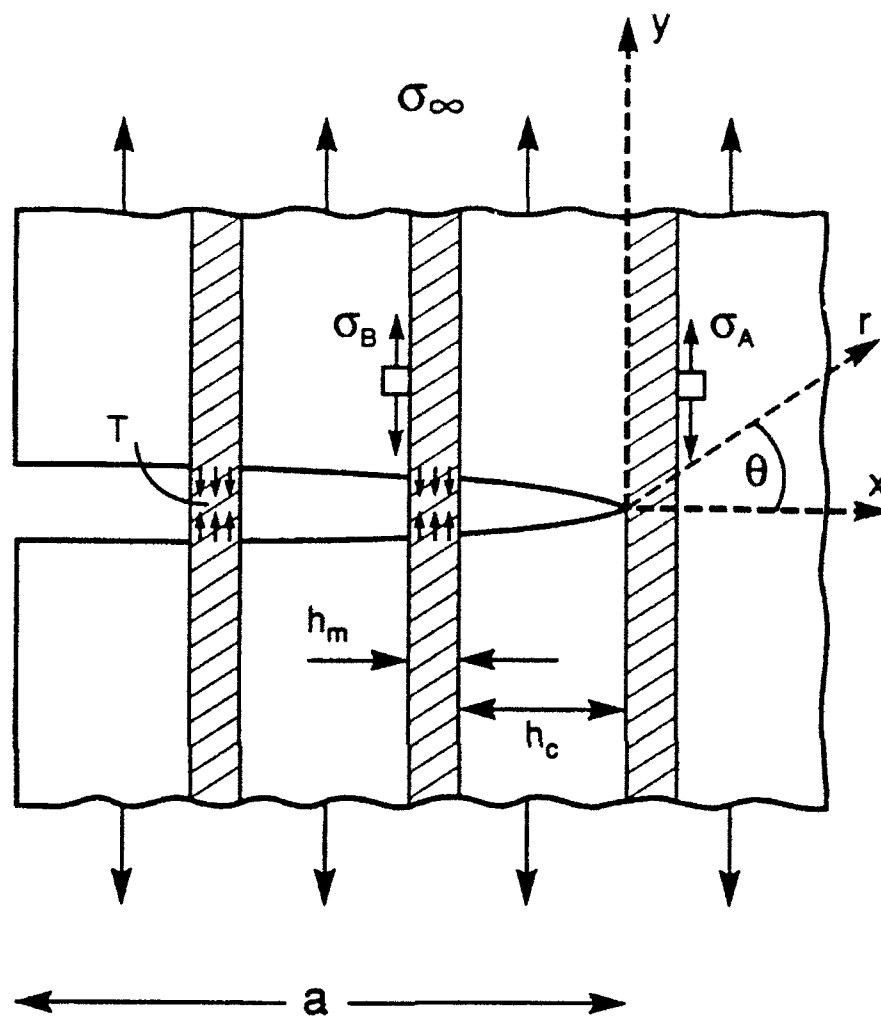


Fig. B1

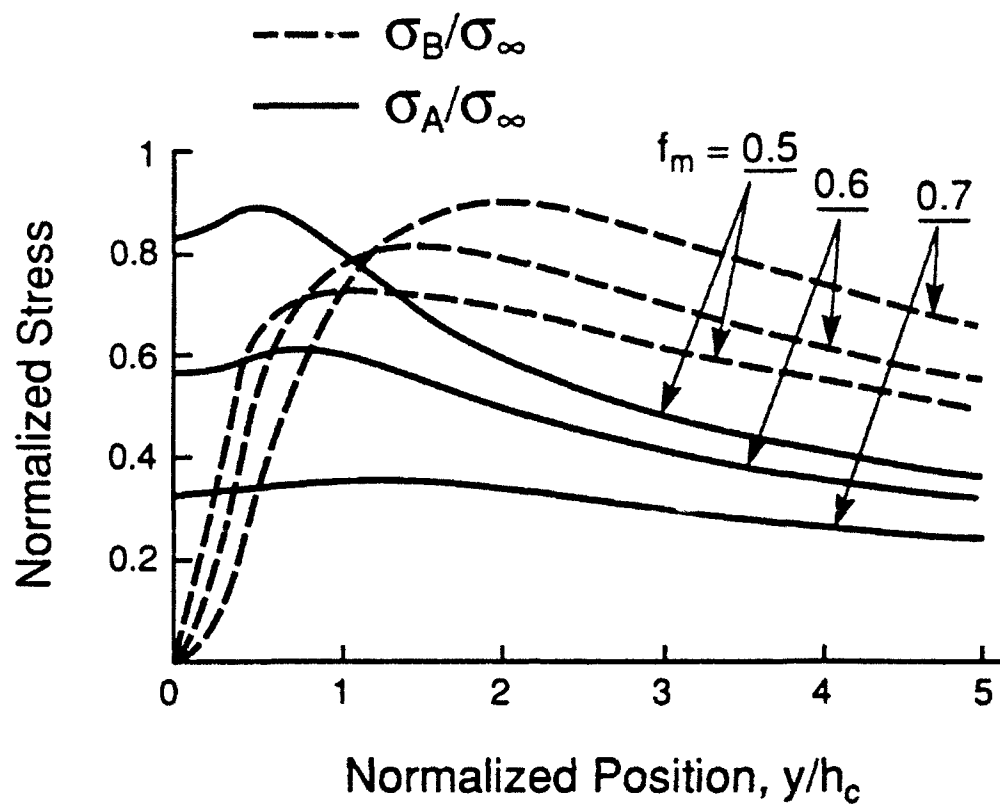
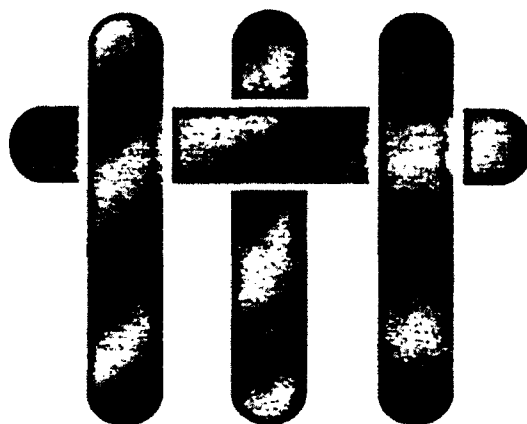


Fig. B2

M A T E R I A L S



**THE MECHANICS OF CRACK GROWTH IN
LAYERED MATERIALS**

by

M.Y. He, F.E. Heredia, D.J. Wissuchek, M.C. Shaw and A.G. Evans

Materials Department
College of Engineering
University of California
Santa Barbara, California 93106-5050

June 1992

Submitted to *Acta Metallurgica et Materialia*

ABSTRACT

Layered materials comprised of one brittle and one ductile constituent exhibit crack growth characteristics that depend on the sequential renucleation of cracks in each brittle layer. An analysis of the problem is presented with two different interface responses. One for a well-bonded, slipping interface and the other for an interface that debonds. It is shown that either slip or debonding enhance the fracture resistance, with debonding being the more effective. The analysis is compared with experimental results for several layered systems.

1. INTRODUCTION

Nanoscale and microscale layered materials can exhibit unprecedented mechanical property profiles: stiffness, tensile strength, notch strength, creep strength, fatigue resistance, etc. Furthermore, possibilities for spatial tailoring exist, especially when the materials are produced by vapor deposition. Alternating layers of brittle and ductile materials have particular interest, because the disparate properties of the constituents provide the ideal opportunity for achieving novel property profiles. Among this group are metal/ceramic and metal/intermetallic systems. Such materials provide a focus for the present article.

A substantial theoretical and experimental background relevant to layered systems of this type exists in the following fields i) pearlite,¹ ii) ceramic fiber-reinforced metals,^{2,3} iii) metal-toughened ceramics^{4,5} and intermetallics.⁶⁻⁹ However, some unique crack growth features expected in layered systems are emphasized in this study. The objective is to provide a *mechanics framework* for predicting the crack growth resistance of ductile/brittle layered materials, in terms of constituent material properties (including the interfaces), as well as the layer thicknesses. Two predominant interface responses are considered. a) A well-bonded interface subject to slip by plastic flow in the metal. b) An interface that debonds and splits in a controlled manner.

2. EXPERIMENTAL BACKGROUND

Experimental results on crack growth have been presented for layered metal/ceramic and metal intermetallic systems produced using a variety of processing techniques: diffusion bonding (DB),^{10,11} directional solidification (DS),¹² thermal processing (TP)¹³ and physical vapor deposition (PVD).¹⁴ However, different length scales are involved. Diffusion bonded systems have layer thickness, $h \gtrsim 20 \mu\text{m}$; DS

materials have $h = 1 \mu\text{m}$, TP materials have $h = 0.1 \mu\text{m}$ and PVD materials have $h = 0.01 - 1 \mu\text{m}$. Experimental studies conducted on these systems have identified the existence of a major fracture mechanism transition. The two fracture mechanisms are:¹⁰ i) Class I behavior dominated by a single crack, ii) Class II behavior involving multiple microcracking. The conditions that dictate the transition between these mechanisms have not yet been explicitly delineated. Nevertheless, it is apparent from the experiments that Class I behavior is most likely when both the metal content is relatively low and the layers are relatively thick.¹⁰ This behavior is emphasized in the present article (Fig. 1).

When the metal layers retain good ductility through processing, plastic stretch of the metal layers accompanies crack growth, resulting in a fracture surface morphology having the characteristics depicted in Fig. 2. Notably, the metal layers rupture along a ridge.¹⁰ When this occurs, without interface debonding, crack growth is subject to a resistance curve having the characteristics indicated on Fig. 3: i) An initiation resistance, K_{N_i} , exceeding that of the brittle layer, K_B , followed by a rising resistance. ii) When the metal layers are thin ($h_m < 1 \mu\text{m}$, where h_m is the metal layer thickness), a *steady-state fracture resistance*, K_s , is reached. iii) Thicker metal layers ($h_m > 10 \mu\text{m}$) may result in a continuously rising resistance caused by large-scale bridging (LSB).¹⁵⁻¹⁷ Generally, both K_{N_i} and K_s increase as h_m increases (Fig. 4).¹⁰ K_s also increases as the metal yield strength σ_0 and the metal volume fraction, f_m , increase.

Interface *debonding* and/or misaligned layers result in resistance curves having the same qualitative features, but subject to quantitative differences. Usually, *interface decohesion elevates* both K_{N_i} and K_s , but the fracture morphology is more intricate¹² (Fig. 5). *Misalignment* introduces an additional level of complexity though effects on crack path, on crack trapping, ligament formation, etc.^{13,18,19} (Fig. 6). Notably, a crack may extend along a low fracture energy plane, within a colony, having layers oriented *normal* to the loading axis. It then encounters a colony with obliquely oriented layer

planes. At this encounter, the crack is arrested and induces a series of decohesion and deformation events that dictate the subsequent behavior.^{13,18,19}

3. THE MECHANICS OF LAYERED MATERIALS

Some basic, analytical results for cracks normal to the interfaces in elastically homogeneous bodies are reviewed, before presenting numerical results that address specific issues. Asymptotic solutions for semi-infinite cracks arrested at an interface provide the information summarized in Fig. 7.²⁰ The normal stresses, σ^* , in the brittle layers *ahead* of the crack front are important, since these layers are susceptible to the events that result in macroscopic crack growth. The calculations show that yielding in the metal layer at the crack front has minimal effect on σ^* , except for very low values of yield strength, σ_0 (Fig. 7a). The essential non-dimensional parameter is

$$\Omega = h_m (\sigma_0 / K)^2 \quad (1)$$

where K is the stress intensity factor. Notably, reduced values of σ^* only arise when $\Omega < 0.02$; moreover, when Ω is small, the following limit must obtain: $\sigma^* \rightarrow 0$ as $\sigma_0 \rightarrow 0$.

When the *interfaces* decohere, the normal stress, σ^* ahead of the crack can be dramatically *reduced*²⁰ (Fig. 7b). In particular, there is a strong influence of the decohesion length L on σ^* , when L/h_m exceeds ~ 3 . Indeed, when $L/h_m = 10$, σ^* is about half the value that obtains without splitting. Furthermore, $\sigma^* \rightarrow 0$ when $L/h \rightarrow \infty$, and is negligibly small, (< 0.01) when $L/h_m > 30$. Consequently, splitting has a considerably larger effect on σ^* than slip.

To address effects of *crack size* on crack growth, numerical results for both splitting and slip have been obtained using finite element procedures with elastic homogeneity assumed. The finite element mesh is depicted in Fig. 8. For calculations with splitting,

the split length L is prescribed. When slip occurs, the shear stress σ_{xy} on the interface is not allowed to exceed the shear strength, $\tau = \sigma_0/\sqrt{3}$. This model approximates the effect of yielding in the metal layers. The numerical results obtained for both mechanisms (Fig. 9) reveal appreciable effects of crack size. The trend is for σ^* to increase as the crack size *decreases*.

In some cases, the crack does not extend. Instead, splitting occurs *ahead of the crack* (Fig. 6), resulting in ligament formation. This process is governed by the σ_{xx} stress. Variations in this stress with distance from the crack front (Fig. 10) indicate a maximum. This maximum occurs at a distance ahead of the crack $\approx 2L$.

4. CRACK GROWTH PREDICTION

The preceding mechanics must be coupled with a crack growth criterion in order to predict the crack growth resistance. It has been proposed that the RKR criterion²¹ is most appropriate when layer cracking is the operative mechanism. This criterion states that fracture proceeds when σ^* attains the fracture strength S of the brittle layers.[†] The magnitude of the tensile stress at which cracking occurs in the brittle layer is subject to a *mechanism transition*. When the layers are sufficiently *thick* that the fracture flaws are smaller than the layer thickness, the layer strength, S , is *flaw controlled*.¹⁰ In this case, S is related to the tensile strength of the material (as qualified by statistical issues associated with the stress gradient and the layer thickness). When the layers are *thin*, relative to the flaw size, the layer strength is controlled by *tunnel cracking*.²² For this cracking mode, the *fracture toughness* and the *layer thickness* have a dominant influence on S (Fig. 11). The strength controlled by tunnel cracking is given by,

[†] Consistent with the behaviors found for Fe/Fe₃C materials.^{1,21}

$$S = \Sigma(K_{IC}/\sqrt{h_b}) \quad (2)$$

where h_b is the thickness of the brittle material and Σ is a non-dimensional parameter of order unity that depends in the extent of debonding and sliding.²³

5. COMPARISON WITH EXPERIMENTS

The preceding calculations can be compared with experiments in which explicit measurements have been made of the toughness of the brittle constituents and the initiation toughness of the layered system. Such results exist for the three systems summarized in Table I, as illustrated in Fig. 3. In other layered materials, inelastic behavior in the more brittle constituent (e.g., twinning in TiAl)^{13,24} invalidates direct comparison with the present calculations.

Inspection of the results reveals that the initiation toughness K_{IC} is relatively larger for systems that exhibit interface splitting (NiAl and TiAl), in qualitative accordance with the calculations. Furthermore, explicit comparisons can be made for each material.

i) In Al_2O_3/Al and Al_2O_3/Cu , there is no interface debonding^{10,25} (Fig. 2). Moreover, for the systems tested, the Al_2O_3 layers are relatively thick and have fracture properties in the flaw controlled regime. Using independently measured value of the ceramic tensile strength,¹⁰ S , and metal yield strength, σ_0 , a comparison of the predicted and measured values of initiation toughness is shown in Fig. 4, for a range of metal thicknesses and volume fractions.¹⁰ The good correlation validates the strength-based (RKR) approach,²¹ at least when the interface is strongly bonded. ii) The NiAl/Cr(Mo) system exhibits profuse interface splitting (Fig. 5).¹² However, not all interfaces are susceptible to splitting. When splitting occurs, the split lengths are appreciably larger than the layer thickness ($L/h \approx 10$). Moreover, the thin intermetallic layer thickness dictates that fracture proceed by *tunnel cracking*, such that (Eqn. 2) applies. Predictions

are made both with and without splitting, as indicated on Fig. 12. The correlation with experiment is indicative of a predominant role of split interfaces. iii) For the TiAl-Nb system, the TiAl is relatively thick and is expected to be in the *flaw controlled* regime.^{6,17} Interface splitting is also evident in this system ($L/h = 2$). However, independent measurements of tensile strength for TiAl are not available.

The calculations assist in the interpretation of a splitting phenomenon found in TiAl/Ti₃Al with a lamellar or layered colony microstructure^{13,15,19} (Fig. 6). In this material, periodic splits occur where the crack encounters a colony with the layers oriented normal to the crack plane. There is no coplanar cracking of the TiAl layers. The splitting is attributed to the σ_{xx} stress and indeed, occurs where this stress has a maximum, at $x/L \approx 2$ (Fig. 10). However, a criterion for predicting the onset of periodic split cracking would require an in-plane strength property for the TiAl layers (or the TiAl/Ti₃Al interface), yet to be identified.

6. IMPLICATIONS

The above connections between experimental results and the analysis allow some implications to be made about crack growth in layered materials. The first important result is that materials with *thin layers* and *well-bonded* interfaces have an initiation toughness exceeding that of the brittle constituent, but only by, $\sqrt{2\pi f_m}/(1-f_m)$. Substantially higher values of initiation toughness require either *thicker layers* or interfaces that exhibit extensive *debonding* and/or *sliding*. Control of the interface has greater appeal, because the advantages of thick layers are only manifest at thicknesses in the 10–100 μm range. Interface debonding is not yet predictable from fundamental principles, but some empirical guidelines exist that provide useful insight.²⁶

While interface slip is not as effective as debonding in enhancing toughness (Fig. 7), slip may still be more attractive, when reasonable transverse properties are required. An

interesting option in this regard is suggested by an experimental observation that a ductile interface layer can lead to high toughness.¹⁷ Notably, a thin *interface layer* with *low yield strength* should provide high initiation toughness, by enabling the slip length to become large compared with the layer thickness. Such a thin layer should not degrade the propagation toughness associated with ductile phase bridging.

7. CONCLUSION

An analysis has been presented that predicts the initiation toughness for layered materials with one brittle constituent. The analysis appears to be consistent with experimental results for several ceramic/metal and intermetallic/metal systems produced by either diffusion bonding or directional solidification. Two important implications have been addressed. i) Thin layer bimaterial systems with well-bonded interfaces *are not* conducive to substantial toughening. ii) Higher initiation toughness can be achieved with thick layers. But, a more attractive approach is to introduce thin *interface layers* that allow extensive (but controlled) inelastic deformation, either by slip or debonding. Among these two options, slipping interfaces are preferred (where possible), because they provide superior transverse cracking resistance. These layers can be produced either by reaction between the bimaterial constituents or by using physical vapor deposition to produce the multilayers.

The analysis may also be used to rationalize behaviors found in lamellar microstructures, such as periodic splitting. These splitting effects are, in turn, fundamental to the high toughness exhibited by these materials. Further study of such phenomena may lead to a fundamental understanding of the fracture properties of lamellar systems.

Finally, it is recognized that new effects may emerge in nanoscale systems, wherein the deformation of the metal layers is governed by the threading of individual

dislocations. However, the expectation is that the associated enhancement in the resistance to plastic flow would lead to *lower* levels of initiation toughness than those addressed by the present analysis.

ACKNOWLEDGEMENT

The authors wish to thank Dr. D.B. Marshall for his technical support and for valuable discussions. This work was supported by the Office of Naval Research through contract N00014-90-J-1300. Provision of the ABAQUS finite element code by Hibbitt, Karlsson and Sorensen, Inc. of Providence, Rhode Island is gratefully acknowledged.

TABLE I

Material Systems Investigated

SYSTEM	LAYER THICKNESS (μm)		$K_B(\text{MPa}\sqrt{\text{m}})$
	BRITTLE	DUCTILE	
$\text{Al}_2\text{O}_3/\text{Al}$	45-680	8-250	3.5
$\text{NiAl}/\text{Cr}(\text{Mo})$	0.75	0.35	5
TiAl/Nb	100-200	50	6-8

REFERENCES

- [1] J.J. Lewandowski and J.W. Thompson, *Met. Trans.*, **17A** (1986) 1769.
- [2] S. Ochiani and K. Osanuru, *Met. Trans.*, **21A** (1991) 971.
- [3] M.S. Hu, H.-C. Cao, J. Yang and A.G. Evans, *Acta Metall. Mater.*, in press.
- [4] L.S. Sigl, P.A. Mataga, B.J. Dalgleish, R.M. McMeeking and A.G. Evans, *Acta Metall.*, **36** (1988) 945.
- [5] B.D. Flinn, C. Lo, F.W. Zok and A.G. Evans, *J. Am. Ceram. Soc.*, in press.
- [6] C.K. Elliott, G.R. Odette, G.E. Lucas and J.W. Sheckard, *Mater. Res. Soc. Proc.*, **120** (1988) 95.
- [7] P.R. Subramanian, M.G. Mendiratta, P.B. Miracle and D.M. Dimiduk, *MRS Symp. Proc.*, **194** (1990) 147.
- [8] M.F. Ashby, F.J. Blunt and M.K. Bannister, *Acta Metall.*, **37** (1989) 1947.
- [9] M.K. Bannister and M.F. Ashby, *Acta Metall. Mater.*, **39** (1991) 2575.
- [10] M.C. Shaw, D.B. Marshall, M.S. Dadkhah and A.G. Evans, *J. Am. Ceram. Soc.*, to be published.
- [11] H.-C. Cao and A.G. Evans, *Acta Metall. Mater.*, **39** (1991) 2997.
- [12] F.E. Heredia, M.Y. He, G.E. Lucas, A.G. Evans, H.E. Dève and D. Konitzer, *Acta Metall. Mater.*, to be published.
- [13] H.E. Dève, A.G. Evans and D.S. Shih, *Acta Metall. Mater.*, in press.
- [14] G.R. Rowe, *Mat. Res. Soc. Proc.*, **273** (1992) in press.
- [15] F.W. Zok and C. Hom, *Acta Metall. Mater.*, **38** (1990) 1895.
- [16] B.N. Cox and C.S. Lo, *Acta Metall. Mater.*, **40** (1992) 69.
- [17] G.R. Odette, B.L. Chao, J.W. Sheckard and G.E. Lucas, *Acta Metall. Mater.*, in press.
- [18] D.J. Wissuchek and G.E. Lucas, to be published.
- [19] K.S. Chan, *Met. Trans.*, **A22** (1992) 2021.
- [20] K.S. Chan, M.Y. He and J.W. Hutchinson, to be published.
- [21] R.O. Ritchie, J. Knott and J.R. Rice, *J. Mech. Phys. Solids*, **21** (1973) 395.

- [22] J.W. Hutchinson and Z. Suo, *Advances in Appl. Mech.*, **29** (1992) 63.
- [23] T. Ye, Z. Suo and A.G. Evans, *Intl. Jnl. Solids Structures*, in press.
- [24] H.E. Dève and A.G. Evans, *Acta Metall. Mater.*, **39** (1991) 1171.
- [25] B.J. Dalgleish, K.P. Trumble, and A.G. Evans, *Acta Metall.*, **37** (1989) 1923.
- [26] A.G. Evans and B.J. Dalgleish, *Acta Metall. Mater.*, in press.

FIGURE CAPTIONS

- Fig. 1. A schematic of crack growth in a layered material with associated resistance curve.
- Fig. 2. A scanning electron fractograph of a diffusion-bonded $\text{Al}_2\text{O}_3/\text{Al}$ material indicating plastic stretch of the Al to a ridge.
- Fig. 3. Resistance curves for three layered materials a) $\text{Al}_2\text{O}_3/\text{Al}$ with $h_m \approx 100 \mu\text{m}$, b) $\text{NiAl}/\text{Cr}(\text{Mo})$ with $h_m = 1 \mu\text{m}$, c) TiAl/Nb with $h_m \approx 50 \mu\text{m}$.
- Fig. 4. Measurements of K_N as a function of metal layer thickness for the $\text{Al}_2\text{O}_3/\text{Al}$ and $\text{Al}_2\text{O}_3/\text{Cu}$ systems. The predictions are also shown.
- Fig. 5. The fracture surface for a $\text{NiAl}/\text{Cr}(\text{Mo})$ layered material indicating splitting, as well as plastic distortion.
- Fig. 6. A crack within a layered, colony structure exhibited by the system, $\text{TiAl}/\text{Ti}_3\text{Al}$.
- Fig. 7. Asymptotic solutions for the effects of slip and splitting on the stress, σ^* .
a) The normal stress ahead of the crack as a function of relative distance from the crack with a slip.
b) The normal stress ahead of the crack as a function of the relative slip or splitting length.
- Fig. 8. Finite element mesh used to evaluate effects of slip and splitting.
- Fig. 9. Effect of crack size on the stress ahead of a crack subject to a) splitting or b) slip.
- Fig. 10. The in-plane, σ_{xx} stress ahead of a crack with a split.
- Fig. 11. A schematic of the trend in strength with brittle layer thickness.
- Fig. 12. Predictions of initiation toughness for weakly bonded layered systems with and without splitting and comparison with results for $\text{NiAl}/\text{Cr}(\text{Mo})$.

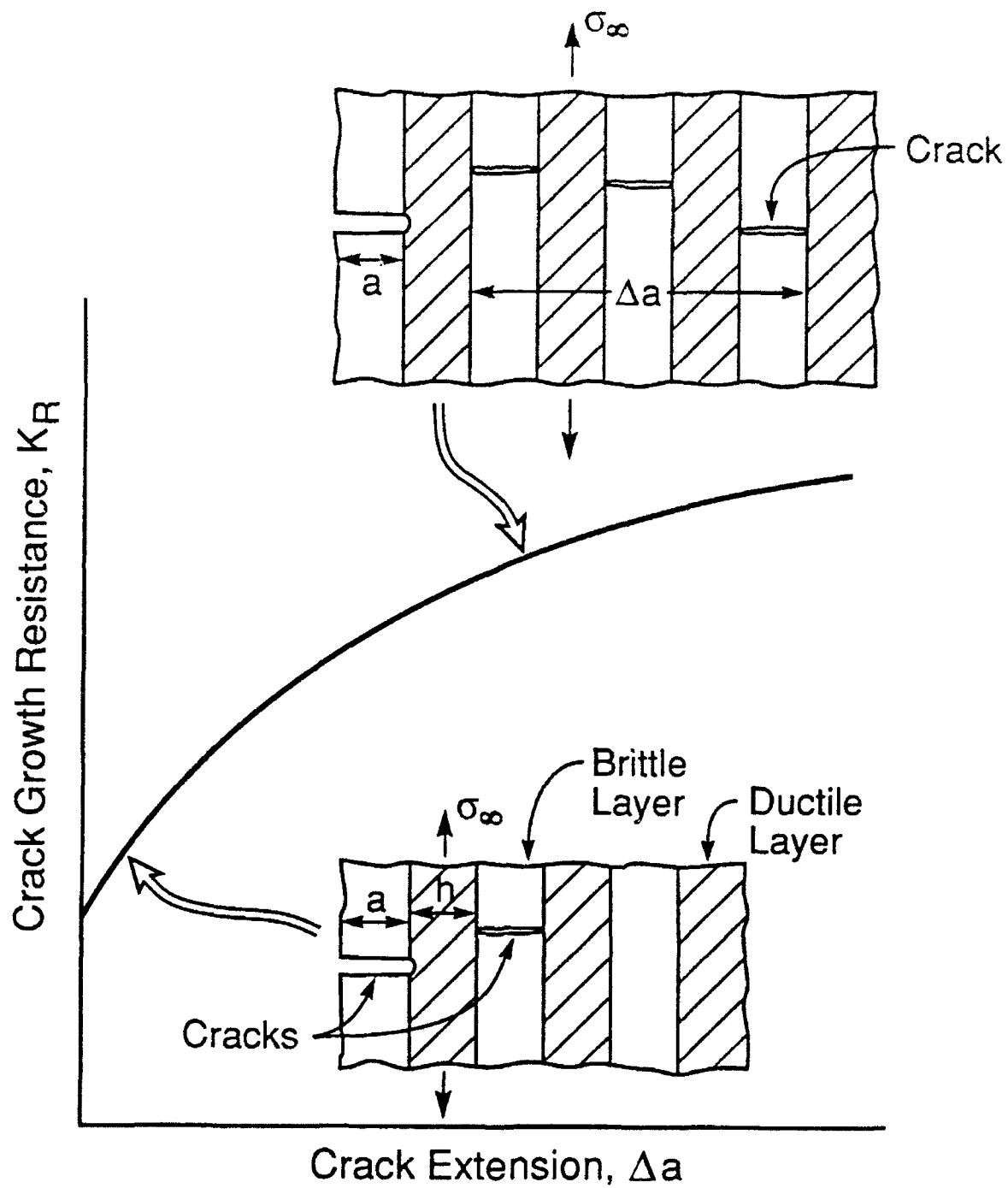
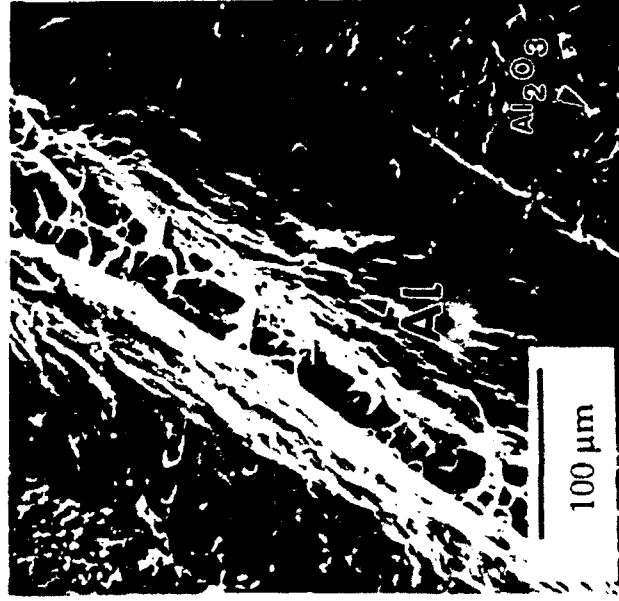
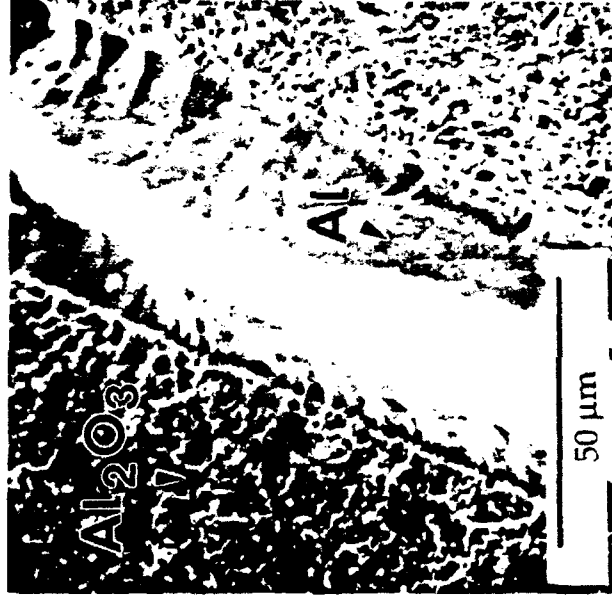


Figure 1

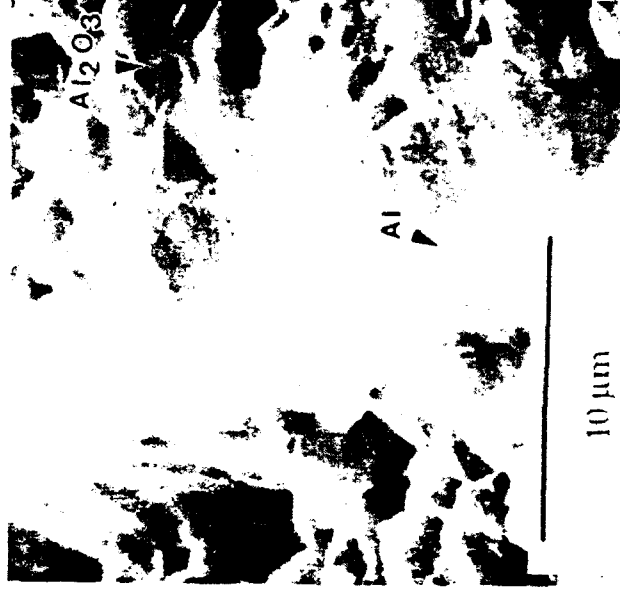
Al/Al₂O₃



$h_m = 250\ \mu\text{m}$



$h_m = 50\ \mu\text{m}$



$h_m = 8\ \mu\text{m}$

Fig. 2

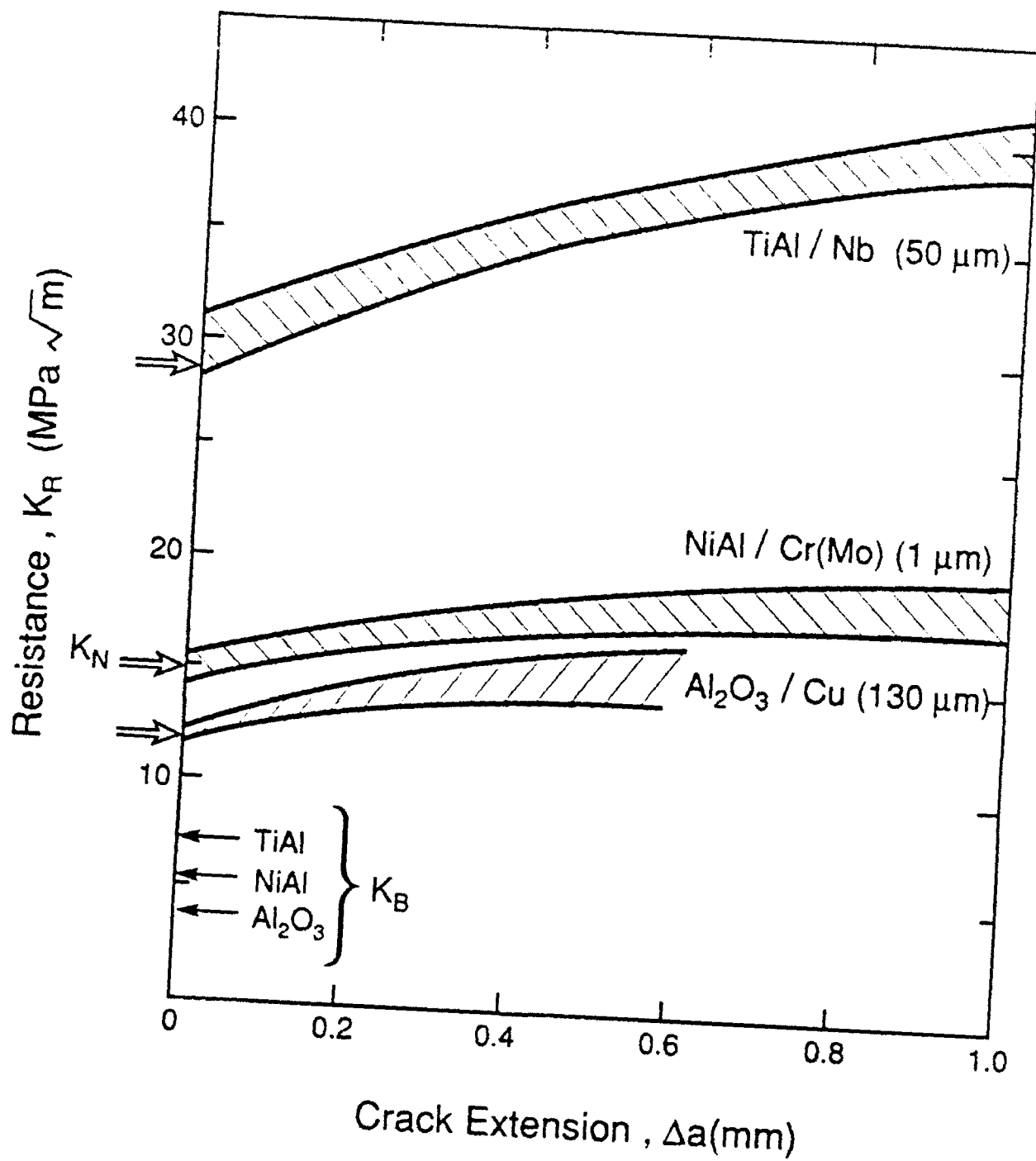


Figure 3

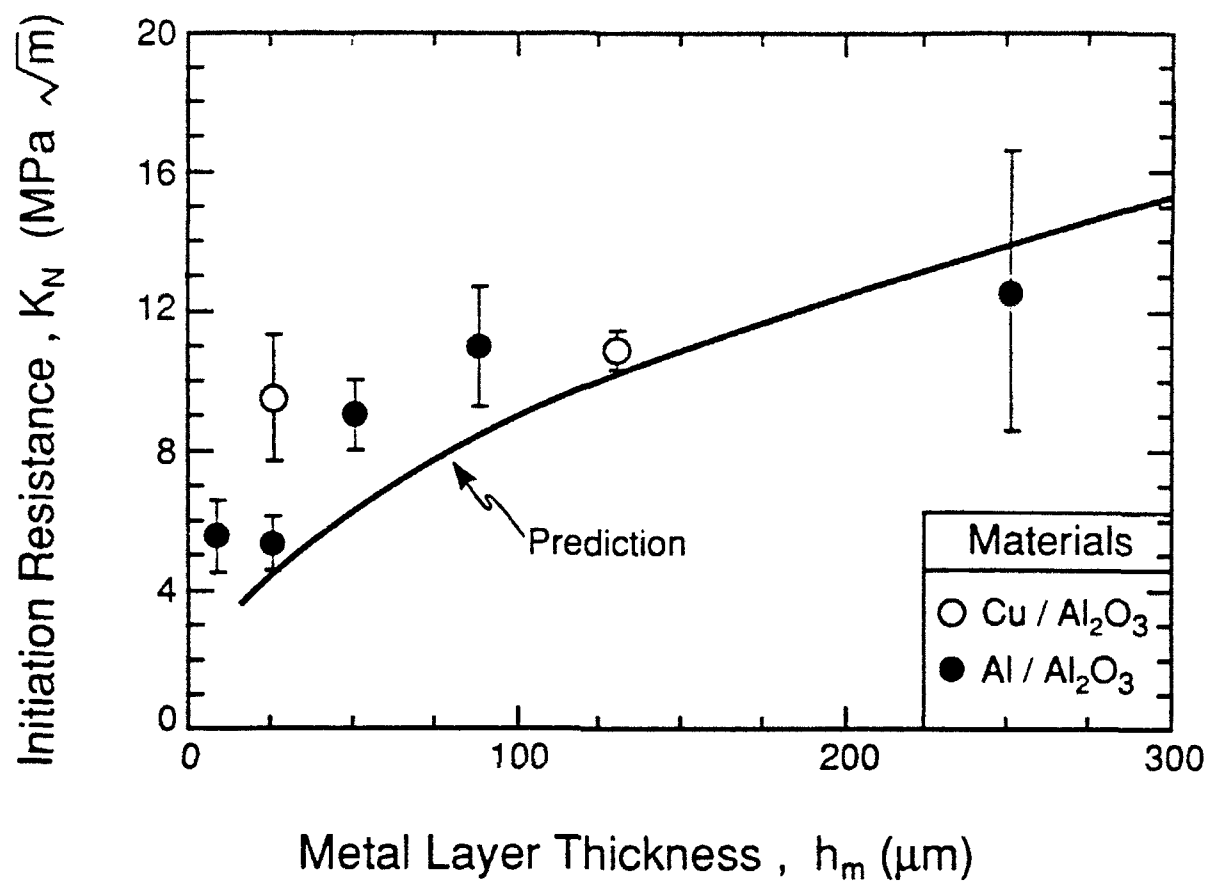


Figure 4

NiAl/Cr(Mo)



Fig.5

TiAl/Ti₃Al

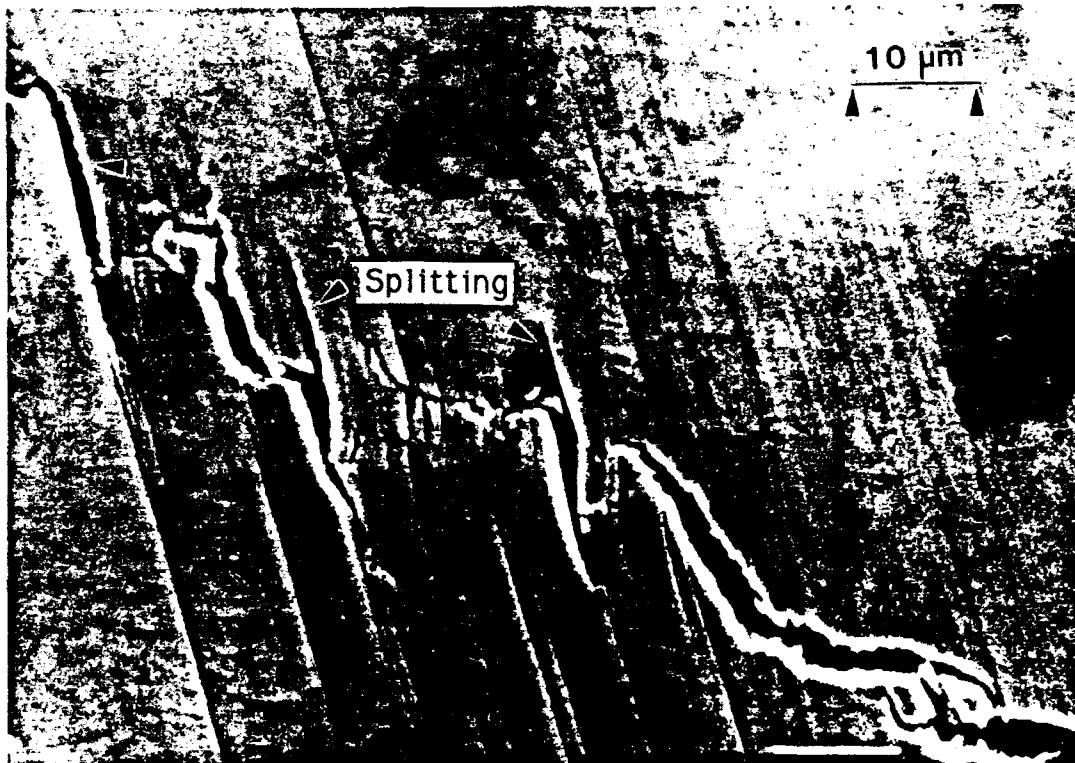
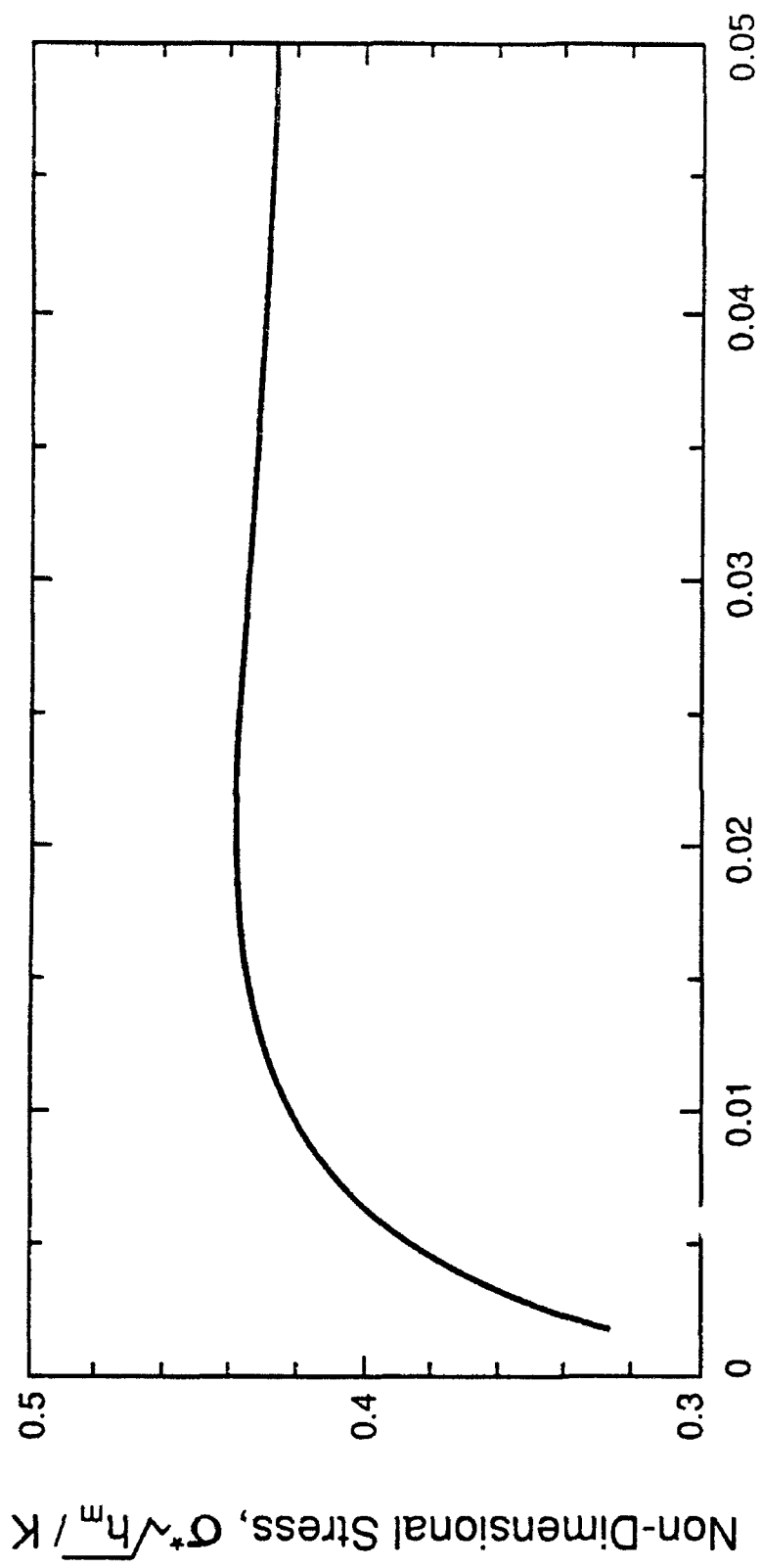


Fig. 6



Relative Distance from Crack, $\Omega = h_m(\tau / K)^2$

Figure 7a

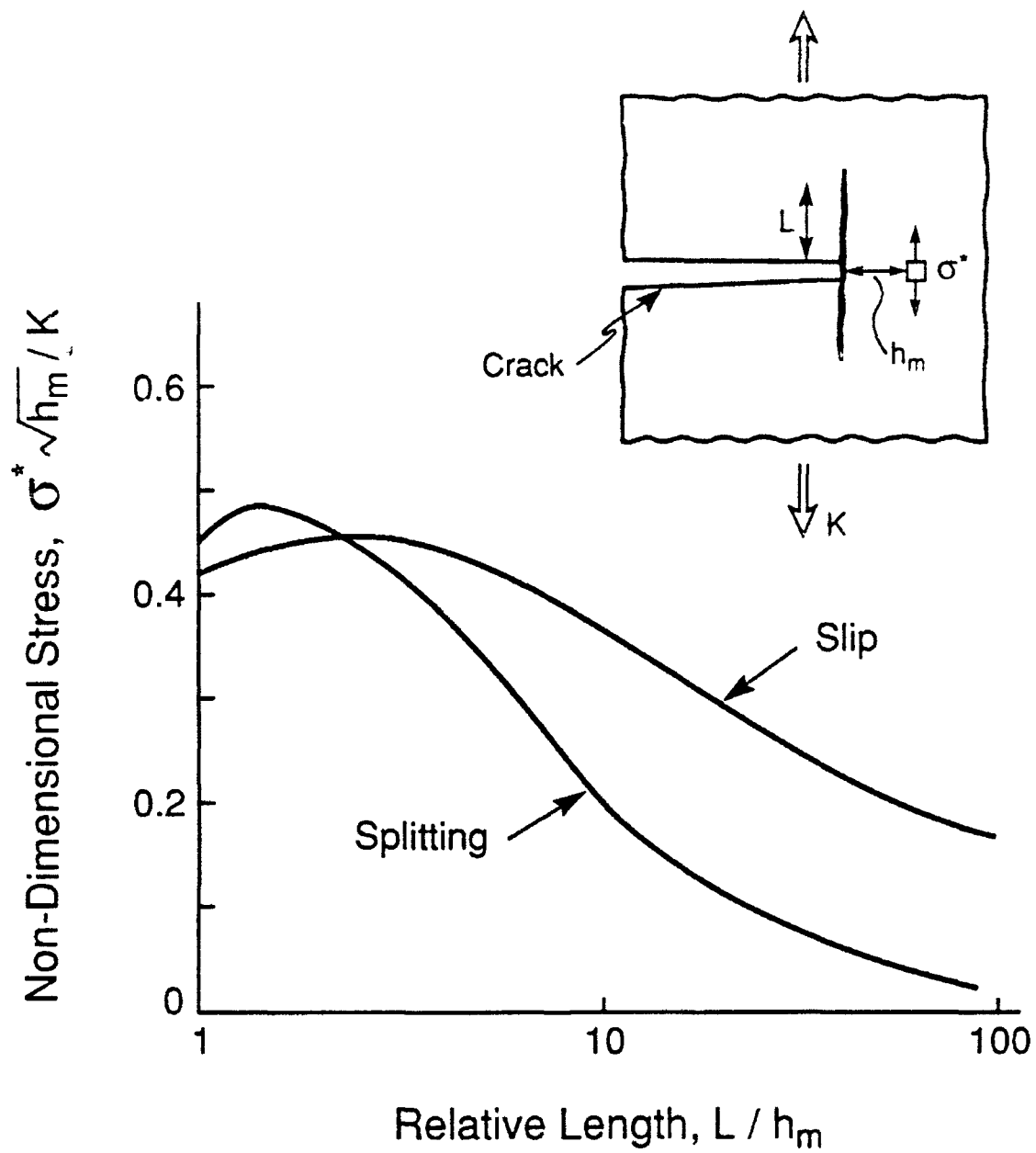


Figure 7b

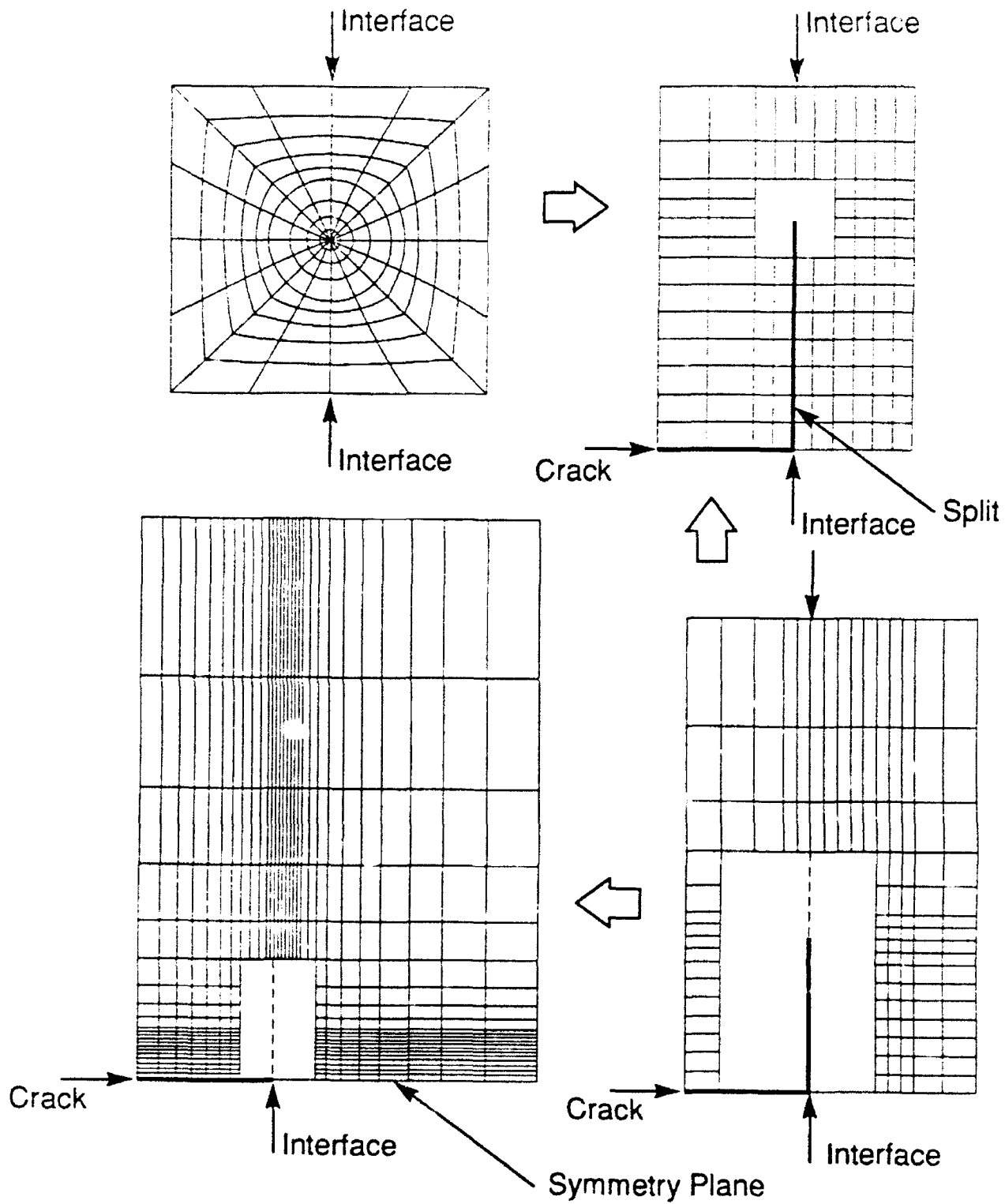


Figure 8

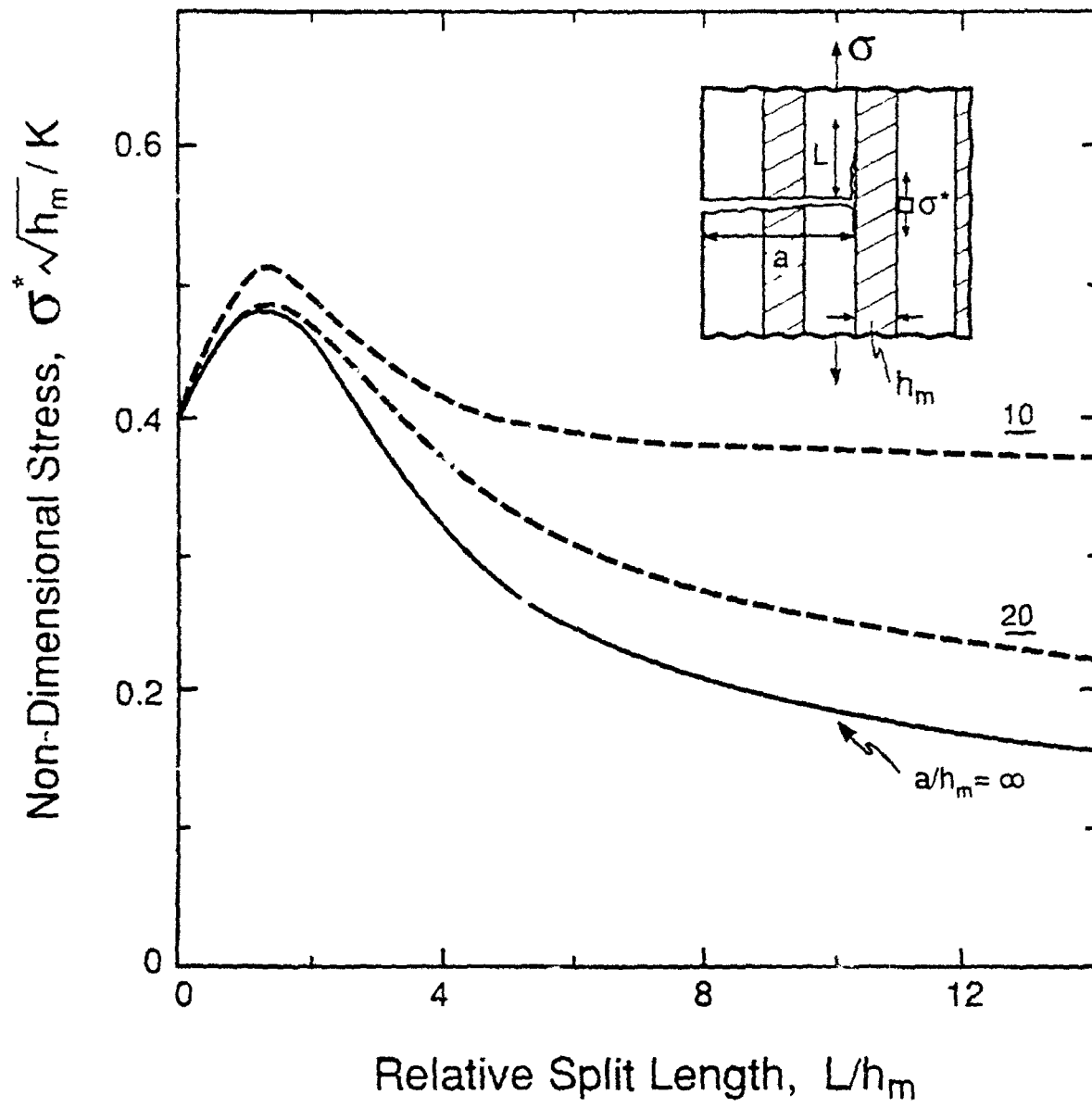


Figure 9a

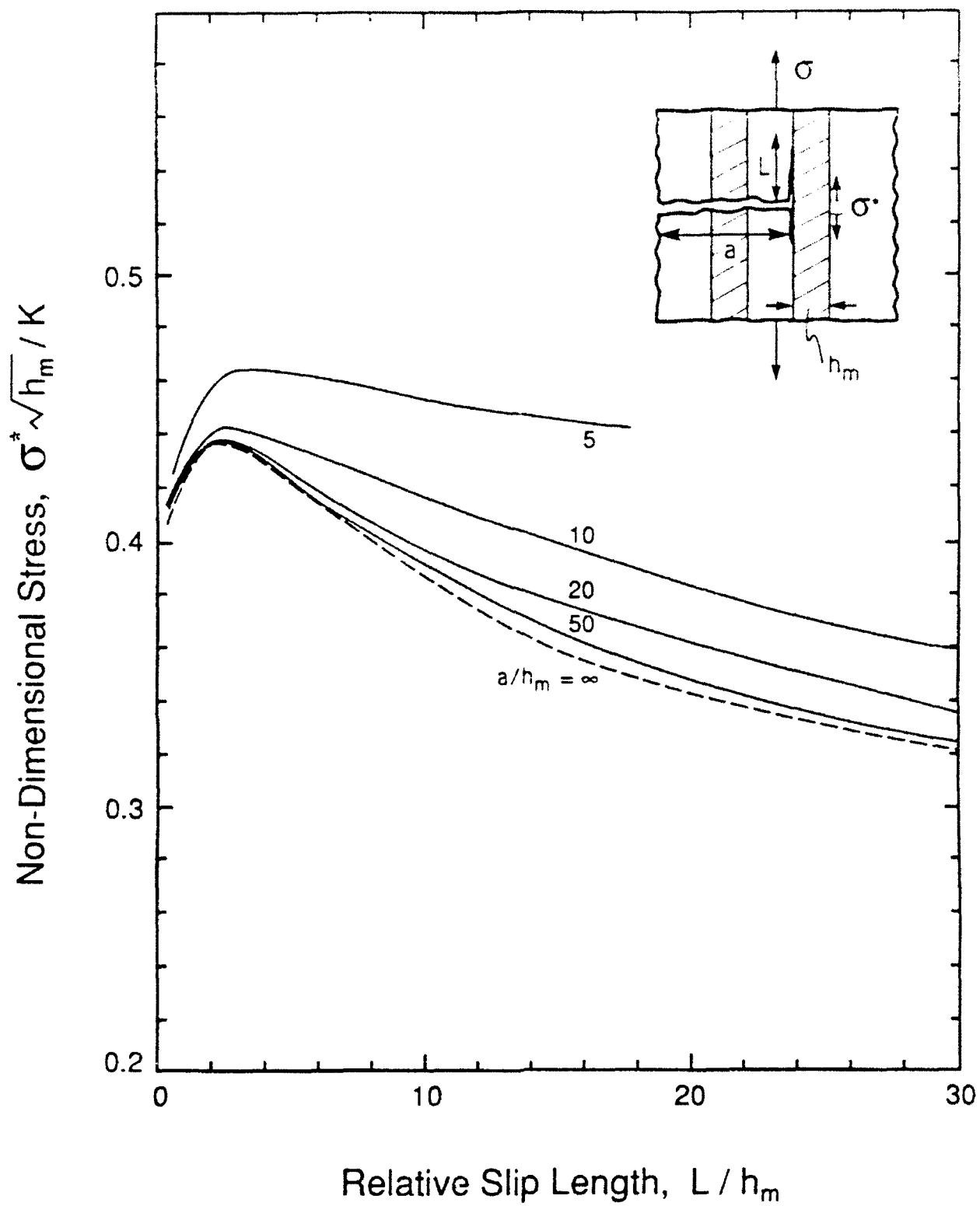


Figure 9b

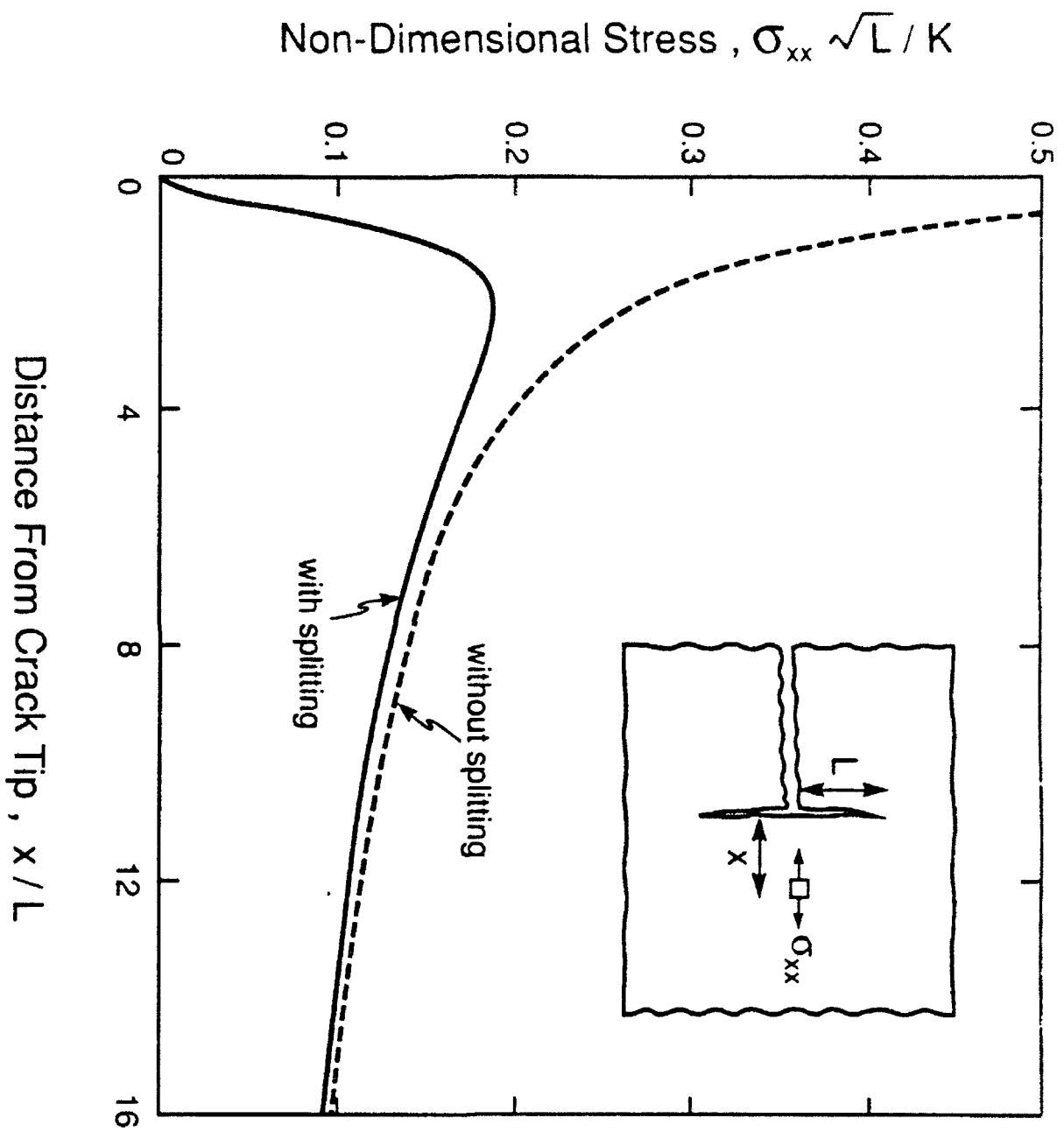


Figure 10

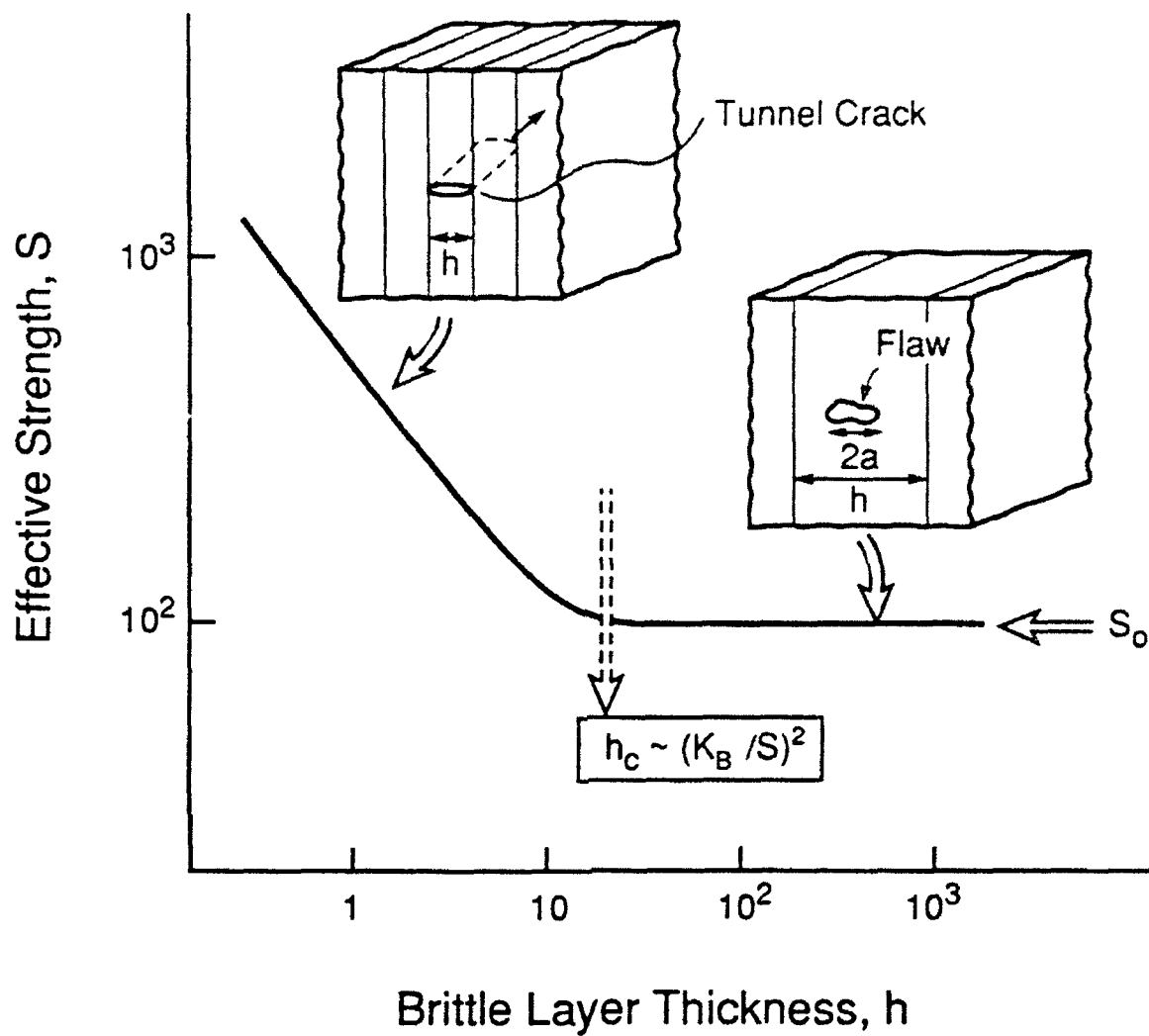


Figure 11

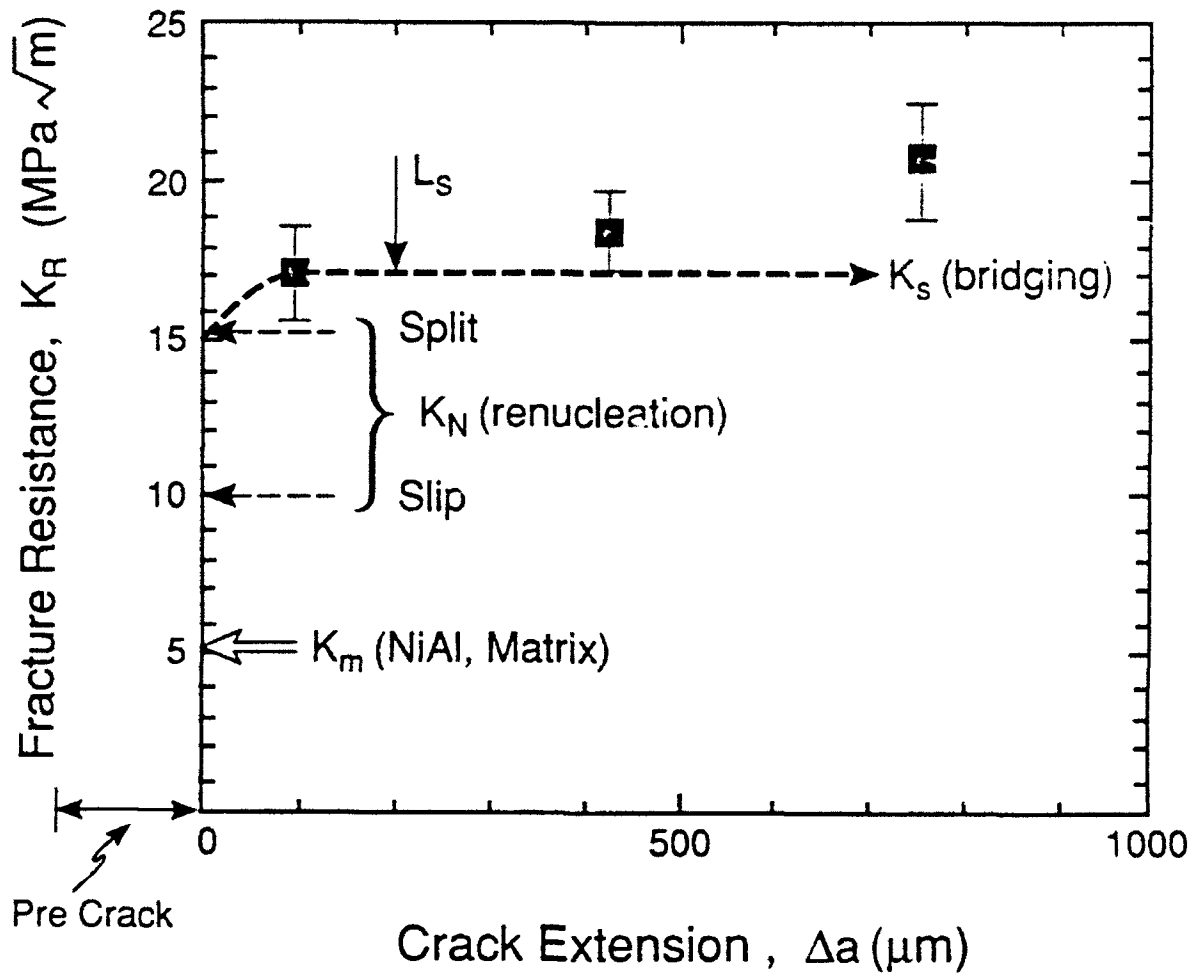


Figure 12

SMALL SCALE YIELDING AT A CRACK NORMAL TO THE INTERFACE BETWEEN AN ELASTIC AND A YIELDING MATERIAL

Ming Y. He, R. M. McMeeking and Ning T. Zhang

Materials Department & Mechanical Engineering Department, College of Engineering
University of California, Santa Barbara, CA 93106

ABSTRACT

By using the elastic singular field as a prescribed loading condition, small scale yielding solutions are obtained for a crack normal to the interface between a brittle and a ductile material. Results for both a crack in the brittle material and one in the ductile material are obtained by finite element analysis. The crack tip fields obtained by the finite element analysis are compared with the asymptotic solutions. It is found that near the tip the stress fields approach the asymptotic solutions. If the crack is in the brittle material, the high triaxial stresses are developed near the interface ahead of the crack tip.

1. INTRODUCTION

Thin films of metals, ceramics and polymers bonded to substrates are typically subject to appreciable residual stress, which can cause cracking of the films. Many analytical, numerical and experimental investigations have been conducted recently. However, comprehensive elastic-plastic analyses for cracks in films are not available. One purpose of our study is to provide one specific solution. The problem analyzed in this paper is shown in Figure 1. A perpendicular crack meets an interface between two dissimilar materials. Loads are applied which tend to open the crack (mode I loading). The tip is at the interface. One material is purely elastic and the other is elastic-perfectly plastic. By using the elastic singular field as a prescribed boundary condition, small scale yielding solutions are obtained by finite element analysis and compared with the asymptotic fields.

2. ASYMPTOTIC FIELDS

The plane strain asymptotic stress fields for a crack normal to the interface between an elastic and an elastic-perfectly plastic material when the crack tip is at the interface have been given by [1]. The results are quoted here as follows:

Problem A: If the crack is in the yielded material as in Figure 1a, the asymptotic solutions for the stresses in the perfectly plastic material are given in polar coordinates by [2]

$$\left. \begin{aligned} \sigma_{\theta} &= k \left(1 + \frac{3\pi}{2} - 2\theta \right) \\ \sigma_r &= k \left(1 + \frac{3\pi}{2} - 2\theta \right) \\ \sigma_{\theta\theta} &= k \end{aligned} \right\} \quad \frac{\pi}{2} \leq \theta \leq \frac{3\pi}{4} \quad (1)$$

and

$$\left. \begin{aligned} \sigma_\theta &= k(1 + \cos 2\theta) \\ \sigma_r &= k(1 - \cos 2\theta) \\ \sigma_{r\theta} &= -k \sin 2\theta \end{aligned} \right\} \quad \frac{3\pi}{4} \leq \theta \leq \pi \quad (2)$$

The asymptotic solutions for stresses in the elastic material are given by

$$\left. \begin{aligned} \sigma_\theta &= -\frac{4k \cos \theta}{\pi} \left[\cos \theta \left(\log \frac{r}{r_0} + \frac{1}{2} \right) - \theta \sin \theta \right] + \left(1 + \frac{\pi}{2} \right) k \sin^2 \theta \\ \sigma_r &= \frac{2k}{\pi} \left[-2 \sin^2 \theta \log \frac{r}{r_0} + \cos^2 \theta - \theta \sin 2\theta \right] + \left(1 + \frac{\pi}{2} \right) k \cos^2 \theta \\ \sigma_{r\theta} &= -\frac{2k}{\pi} \left[\sin 2\theta \left(\log \frac{r}{r_0} + \frac{1}{2} \right) + \theta \cos 2\theta \right] - \left(1 + \frac{\pi}{2} \right) k \sin \theta \cos \theta \end{aligned} \right\} \quad -\frac{\pi}{2} \leq \theta \leq \frac{\pi}{2} \quad (3)$$

where r_0 is an undetermined constant which has been determined by the finite element analysis [1].

Problem B, If the crack is in the elastic material, consistent with Figure 1b, the expressions for the asymptotic stress fields in the perfectly plastic region are given by:

$$\left. \begin{aligned} \sigma_\theta &= T + \frac{k\pi}{2} + k \cos 2\theta \\ \sigma_r &= T + \frac{k\pi}{2} - k \cos 2\theta \\ \sigma_{r\theta} &= k \sin 2\theta \end{aligned} \right\} \quad -\frac{\pi}{4} \leq \theta \leq \frac{\pi}{4} \quad (4)$$

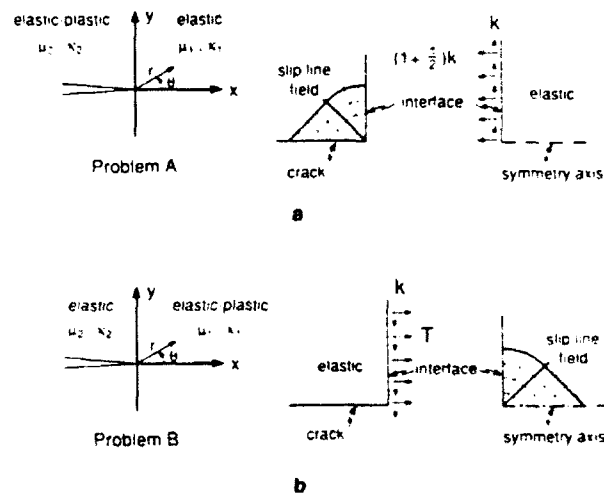


Fig. 1 Crack geometry

and

$$\left. \begin{aligned} \sigma_{\theta} &= T - 2k \left(\theta - \frac{\pi}{2} \right) \\ \sigma_r &= T - 2k \left(\theta - \frac{\pi}{2} \right) \\ \sigma_{r\theta} &= k \end{aligned} \right\} \quad \frac{\pi}{4} \leq \theta \leq \frac{\pi}{2} \quad (5)$$

The solution in the elastic region is

$$\left. \begin{aligned} \sigma_{\theta} &= \frac{T}{2}(1 - \cos 2\theta) + \frac{\pi k}{4}(3 + \cos 2\theta) - k\theta + \frac{k}{2} \sin 2\theta \\ \sigma_r &= \frac{T}{2}(1 + \cos 2\theta) + \frac{\pi k}{4}(3 - \cos 2\theta) - k\theta - \frac{k}{2} \sin 2\theta \\ \sigma_{r\theta} &= -\frac{k}{2}(\cos 2\theta - 1) - \frac{1}{2} \left(T - \frac{\pi}{2} k \right) \sin 2\theta \end{aligned} \right\} \quad \frac{\pi}{2} \leq \theta \leq \pi \quad (6)$$

3. FINITE ELEMENT ANALYSIS

The displacements of the singular elastic solution [1,2], are used as boundary conditions on the outer perimeter of a finite element mesh used to calculate plane strain small scale yielding solutions. A general purpose finite element code, ABAQUS was used. A typical finite element mesh contains 720 eight node isoparametric elements and 2358 nodes.

In order to deal with most materials combinations, we took different values of α within the range $-0.5 \leq \alpha \leq 0.75$ for $\beta = \alpha/4$, where α and β are the Dundurs parameters [4]

$$\alpha = (\mu_1(1 - \nu_2) - \mu_2(1 - \nu_1)) / (\mu_1(1 - \nu_2) + \mu_2(1 - \nu_1)) \quad (7)$$

$$\beta = (\mu_1(1 - 2\nu_2) - \mu_2(1 - 2\nu_1)) / (\mu_1(1 - \nu_2) + \mu_2(1 - \nu_1)) \quad (8)$$

μ and ν are shear modulus and Poisson's ratio of the material respectively and the subscripts $i=1$ and 2 correspond to the arrangement shown in Fig.1.

Problem A: The crack is in the elastic-perfectly plastic material and the other material is elastic. The small scale yielding solutions obtained by the finite element analysis shows that near the crack tip the stress fields are quite similar to the asymptotic fields given by (1)-(3). The stress fields shift toward the asymptotic angular distribution in the near tip region. As an example the angular distributions of the stresses at a fixed relative distance are shown in Figure 2, for $\alpha=0.5$ and $r=6\delta$, where δ , is the crack tip opening displacement and σ_y is the yield stress in tension of the plastic material. The stresses along the interface in the elastic perfectly plastic material, ($\theta=\pi/2^+$) are plotted as functions of normalized radial distance from the crack tip for $\alpha=0.25$ in Figure 3a. The counterparts for stresses along the interface in the elastic material, ($\theta=\pi/2^-$) are plotted in Figure 3b. The plots indicate that the size of the domain dominated by the

asymptotic field is very small compared to the size of the plastic zone.

Problem B: The crack is in the elastic material and the other material is elastic-perfectly plastic. The angular distributions of the stresses at a fixed relative distance are shown in Figure 4, for $\alpha=0.5$, and $r=6.318$. The results obtained by the finite element analysis are shown by solid lines. The asymptotic solutions given by (6) in the elastic side and (4) and (5) in the plastic side are also included in the Figures as dashed lines. It is clear from

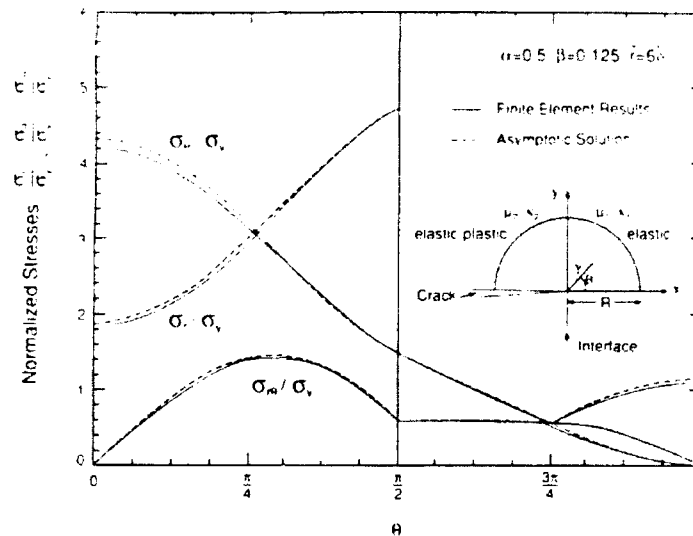


Fig. 2 θ -variation of stresses very near the crack tip for problem A: The crack is in the elastic-perfectly plastic material and the other material is elastic. $\alpha = 0.5, \bar{r} = 6.318$

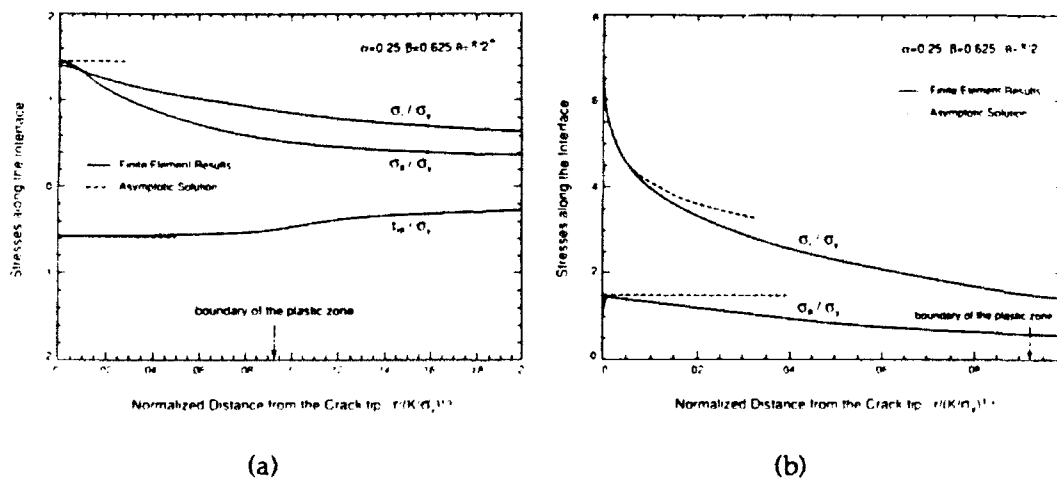


Fig. 3 Stresses along the interface as a function of normalized radial distance from the crack tip for problem A and $\alpha=0.25$ (a) Stresses in the elastic perfectly plastic material. (b) Stresses in the elastic material.

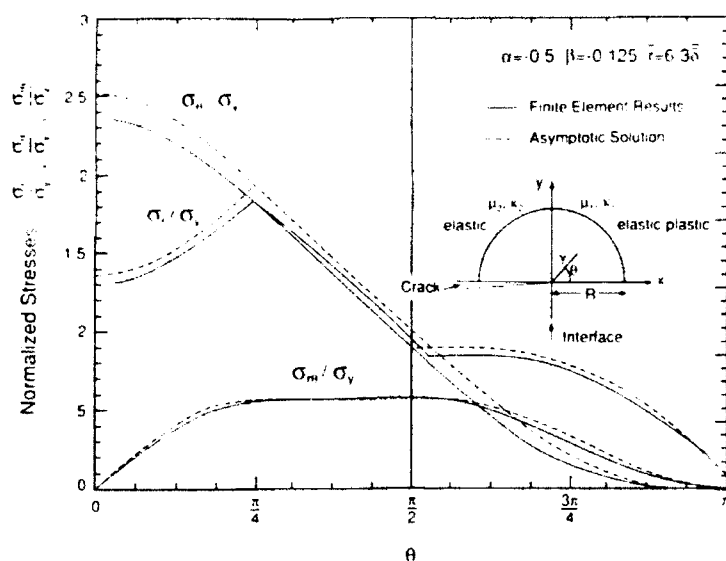


Fig. 4 θ -variation of stresses very near the crack tip for problem B: the crack is in the elastic material and the other material is perfectly plastic. $\alpha = -0.5, \bar{r} = 6.318$

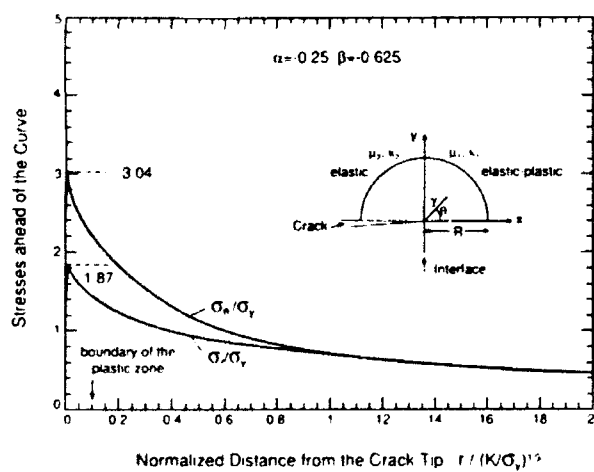


Fig. 5 Stresses ahead of the crack as a function of normalized distance for problem B. The dashed lines are the asymptotic limits and $\alpha = 0.25$.

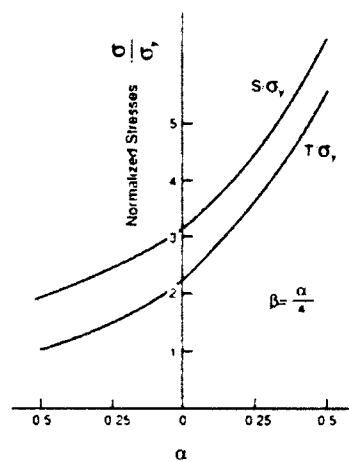


Fig. 6 Hydrostatic stress S and stress T ahead of the crack tip as a function of α

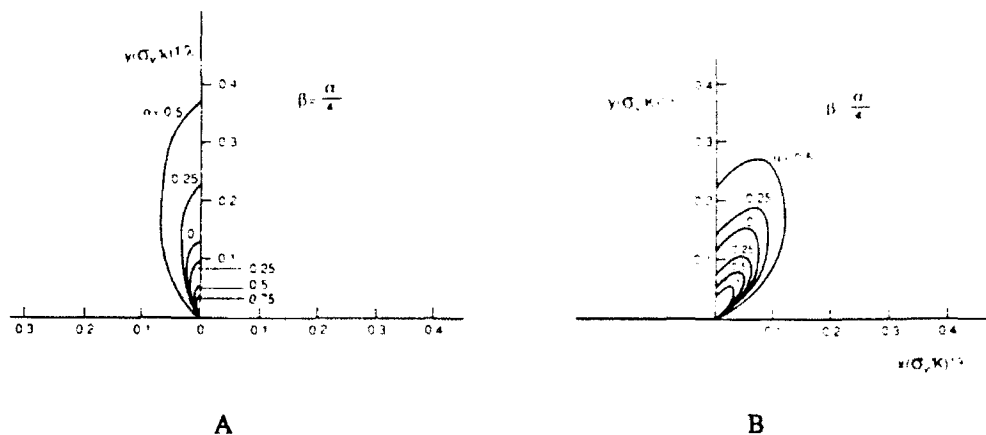


Fig. 7 Location of elastic/plastic boundary for problem A and problem B.

these plots that the fields obtained by the finite element analysis are quite similar to the asymptotic fields. The stress fields shift toward the asymptotic angular distribution as the radial distance approaches to zero. The angular distribution of the stresses determined by the finite element calculation at a very small radial distance are in very good agreement with the asymptotic solution. The stresses ahead of the crack are plotted as functions of normalized distance for $\alpha = -0.5$ in Figure 5. These plots indicate the size of the domain dominated by the asymptotic field are very small compared with the size of the plastic zone. As a function of α , Fig. 6 gives T deduced from the finite element analysis. The plot for the asymptotic values of the hydrostatic stress $S = (\sigma_\theta + \sigma_r)/2$ ahead of the crack in the plastic material is also included in Figure 6, which shows both T and S increases very rapidly with α . The results show that high triaxial stresses are developed near the interface ahead of the crack tip. For example, even for $\alpha = 0$ (i. e. one brittle and one ductile material, with the same elastic modulus and Poisson's ratio, are bonded together), the triaxial tensile stress S ahead of the crack in the ductile material will be 33% higher than in the homogeneous case. The presence of large hydrostatic stresses ahead of a crack is clearly important for the promotion of ductile fracture mechanisms involving the growth and coalescence of voids. Figures 7 show the location of the elastic/plastic boundary for problem A and B respectively. It is demonstrated that the elastic/plastic boundary depends strongly on α .

REFERENCES

1. Ming Y. He, R. M. McMeeking and Ning T. Zhang, "Asymptotic Fields and Small Scale Yielding at a Crack Perpendicular to the Interface between a Brittle and a Ductile Material," to be published.
2. J. R. Rice, "A Path independent integral and the approximate analysis of strain concentrations by notches and cracks," *J. Appl. Mech.* 35, 379-386 (1968).
3. A. R. Zak and M. L. Williams, "Crack Point Singularities at a Bi-material Interface," *J. Appl. Mech.* 30, 142-143 (1963).
4. J. Dundurs, "Edge-bonded dissimilar Orthogonal Elastic Wedges," *J. Appl. Mech.* 36, 650-652 (1969).



MECH-201

CRACKING AND STRESS REDISTRIBUTION IN CERAMIC LAYERED COMPOSITES

K. S. Chan
Southwest Research Institute
San Antonio, TX 78238-5100

M. Y. He
Materials Department
University of California, Santa Barbara
Santa Barbara, CA 93106

and

J. W. Hutchinson
Division of Applied Sciences
Harvard University
Cambridge, MA 02138

Division of Applied Sciences
HARVARD UNIVERSITY
Cambridge, Massachusetts 02138

November 1992

CRACKING AND STRESS REDISTRIBUTION IN CERAMIC LAYERED COMPOSITES

K. S. Chan
Southwest Research Institute
San Antonio, TX 78238-5100

M. Y. He
Materials Department
University of California, Santa Barbara
Santa Barbara, CA 93106

and

J. W. Hutchinson
Division of Applied Sciences
Harvard University
Cambridge, MA 02138

Abstract

Several problems are analyzed that have bearing on cracking and survivability in the presence of cracking of layered composite materials comprised of brittle layers joined either by a weak interface or by a thin layer of a well-bonded ductile metal. The problems concern a crack in one brittle layer impinging on the interface with the neighboring brittle layer and either branching, if the interface is weak, or inducing plastic yielding, if a ductile bonding agent is present. For the case of a weak interface, the effect of debonding along the interface is analyzed and results for the stress redistribution in the uncracked layer directly ahead of the crack tip are presented. Debonding lowers the high stress concentration just across the interface, but causes a small increase in the tensile stresses further ahead of the tip in the uncracked layer. A similar stress redistribution occurs when the layers are joined by a very thin ductile layer that undergoes yielding above and below the crack tip, allowing the cracked layer to redistribute its load to the neighboring uncracked layer. The role of debonding and yielding of the interface on 3D tunnel cracking through an individual layer is also discussed and analyzed. Residual stress in the layers is included in the analysis.

1. Introduction

When layered, thin sheets of a brittle material may have toughness and strength properties which are far superior to those of the material in bulk form [1-6]. To achieve good strength and toughness, the interface between adjoining layers must stymie the stress concentration effect of any crack that occurs in an individual layer, reducing the likelihood that it will propagate into the next layer. Depending on the nature of the interface, this may occur by debonding, when the interface is brittle and relatively weak, or by yielding and sliding for systems comprised of brittle layers alternating with thin ductile adhesive layers. The latter category is represented by sheets of Al_2O_3 joined by thin layers of aluminum [2] and by the model system with sheets of Al_2O_3 bonded by epoxy [3]. Some of the issues related to the design of layered brittle materials are similar to those encountered in the design of fiber-reinforced brittle matrix composites, such as the selection of interface toughness to prevent matrix cracks from penetrating the fibers. Other issues are unique to the layered geometry, and this paper addresses a few of them. In particular, the role of yielding or debonding of the interface in defeating cracks in individual layers is analyzed by considering the stress redistribution in the adjoining uncracked layer that accompanies these processes. Results will also be given for the energy release rate of 3D cracks tunneling through an individual layer. This release rate, which is influenced by interface yielding or debonding, provides the essential information needed to predict the onset of widespread layer cracking in terms of the thickness of the brittle layer material and its toughness.

The geometries of the problems to be studied are laid out in Fig. 1. Fig. 1a shows a cracked layer of width $2w$ with zones of either yielding or debonding in the interface extending a distance d above and below the crack tips. The interface is taken to be either a very thin ductile layer of an elastic-perfectly plastic material with shear flow stress, τ , or a weak plane that debonds and slips under conditions such that the layers remain in contact and exert a friction stress τ on each other. The ductile adhesive layer allows slipping of the layers it joins relative to one another by plastic yielding, but it is assumed that debonding does not occur. In this case, the condition $K_2 = 0$ must be enforced, leading to well-behaved shear stresses at the end of the yielding zone and establishing the zone length d . In the case where the interface debonds, the interface crack is fully closed for $d/w > 0.71$ [7]. The mode 2 stress intensity factor K_2 at the end of the slipped zone will be nonzero and must attain the mode 2 toughness of the interface for the debond to spread. Results for K_2 will be given.

Cracks in individual layers spread as 3D tunnel cracks propagating through the layer as depicted in Fig. 2. Once the crack has spread a distance of at least several layer thicknesses in the z -direction it approaches a steady-state wherein the behavior at the propagating crack front becomes independent of the length of the crack in the z -direction. Under these steady-state conditions, the

energy release rate of the propagating front can be computed using the plane strain solution associated with the geometry of Fig. 1a (other examples of tunnel cracks are given in the review article [8]). The steady-state energy release rate can be computed in terms of the average of the opening $\delta(x)$ of the plane strain crack. The zone of yielding or debonding increases the tunneling energy release rate, thereby lowering the overall stress at which widespread layer cracking can occur. Results for the tunneling energy release rate will be given. The role of residual stresses in the layers are readily accounted for, as will be discussed in the final section.

When the interface is weak and debonding occurs, the interface crack is fully open with mixed mode intensity factors when $d/w < 0.24$ [7]. This case can be well approximated by the asymptotic problem for a semi-infinite crack impinging the interface where the remote field is the K-field associated with the problem in Fig. 1a with $d=0$. The stress redistribution in the next layer ahead of the impinging crack tip will be given, along with a correction of previous results for the energy release rate for the doubly-deflected interface crack of [9]. When plastic yielding of a ductile adhesive layer occurs, another asymptotic problem applies when σ is sufficiently small compared to τ . Then, the asymptotic problem is that shown in Fig. 1b for a semi-infinite crack loaded remotely by the same K-field. In this case as well, emphasis will be placed on the effect of yielding in the thin adhesive layer on the stress distribution ahead of the crack tip in the uncracked layer.

2. Effect of Plastic Yielding on Stress Redistribution.

As discussed above, the thin ductile adhesive layers in Fig. 1a are assumed to be elastic-perfectly plastic with a yield stress in shear of τ and are modeled as having zero thickness. The plane strain problem is considered where the central cracked layer has the same elastic properties (E, ν) as the semi-infinite blocks adjoining across the interfaces. Under monotonic increase of the applied remote stress, σ , the zones of yielding of half-height d spread allowing slip in the form of a tangential displacement discontinuity across the interface in the yielded region. The condition $\sigma_{xy} = \pm \tau$ is enforced within the yielded zones of the interface. The Dugdale-like condition, $K_2 = 0$, at the ends of the yielded zones ensures that the shear stress on the interface falls off continuously just outside the yielded zone, and it determines the relation of d/w to σ/τ under the monotonic loading considered. Integral equation methods are employed to solve this problem, as well as the others posed below; a brief outline of the methods used are discussed in the Appendix.

The two most important functional relations needed to solve the 3D tunneling crack problem discussed below are shown in Figures 3 and 4. In Fig. 4, $\bar{\delta}$ is the average crack opening displacement defined by

$$\bar{\delta} = \frac{1}{2w} \int_{-w}^w \delta(\xi) d\xi \quad (1)$$

The elastic value of $\bar{\delta}$, valid when there is no yielding ($\tau \rightarrow \infty$), is $\bar{\delta}_0 = \pi(1-\nu^2)\sigma w/E$. Yielding of the adhesive layers begins to make a significant contribution to the average crack opening displacement when σ/τ exceeds unity. The redistribution of normal stress, $\sigma_{yy}(x,0)$, in the block of material across the interface is shown in Fig. 5 for three levels of σ/τ . The curve shown for $\sigma/\tau=1.5$ is only very slightly reduced below the elastic distribution ($\sigma_{yy}(x,0)=(x+1)/(x^2+2x)^{1/2}$) for $x/w > 0.05$. Reduction of stress ahead of the crack tip begins to be appreciable when $\sigma/\tau=2.7$, and is quite significant when $\sigma/\tau=6.4$. The drop in stress just across the interface is offset by a slight increase in stress relative to the elastic distribution further away from the interface. This is a feature seen in all the stress redistribution results.

Stress redistribution can be presented in another way when d/w is sufficiently small using the asymptotic problem depicted in Fig. 1b. As long as d/w is sufficiently small, the yielding behavior is small scale yielding with the elastic stress intensity factor K as the controlling load parameter. The remote field imposed on the semi-infinite crack is the elastic K -field. This asymptotic problem has also been solved with integral equation techniques. The extent of the yield zone in the asymptotic problem is

$$d = 0.052 \left(\frac{K}{\tau} \right)^2 \quad (2)$$

Fig. 6 displays the normal stress directly ahead of the crack tip in the adjoining block normalized by the elastic stress field for the limit $\tau = \infty$. The stress ratio in Fig. 6 depends on x/d but is otherwise independent of K in the asymptotic problem. Yielding reduces the stress below the elastic level over a region ahead of the crack tip which is a little larger than $d/10$. Beyond that region the stresses are slightly elevated above the elastic levels and approach the elastic distribution as x/d becomes large. The stress redistribution due to debonding which is also presented in Fig. 6 is more dramatic, as will be discussed later in the paper.

3. Effect of Plastic Yielding on Tunnel Cracking

As stated earlier, the steady-state energy release rate for a 3D tunneling crack can be computed using the plane strain solution. For the geometry and loading shown in Figs. 1a and 2, the leading edge of the tunneling crack propagating in the z -direction experiences mode I conditions. Let G_{ss} denote the energy release rate averaged over the propagating crack front. An energy balance accounting for the release of energy per unit advance of the tunnel crack under steady-state conditions gives that $2wG_{ss}$ is the work done by the tractions acting across the plane

of the layer crack in the plane strain problem as those tractions are reduced to zero from σ . For the present problems, this is the same as

$$G_{ss} = \int_0^\sigma \bar{\delta}(\sigma') d\sigma' \quad (3)$$

where $\bar{\delta}$ is the average crack opening displacement for the traction-free plane strain crack under monotonically increased remote σ . The elastic result for $d=0$ (i.e., $\tau=\infty$) is

$$G_{ss}^0 = \frac{\pi(1-\nu^2)\sigma^2 w}{2E} \quad (4)$$

The ratio of G_{ss} to G_{ss}^0 can be computed from the data in Fig. 4 using simple numerical integration. The result is plotted in Fig. 7. Increases of the steady-state release rate above the elastic value become important when σ/τ exceeds unity.

4. Effect of Debonding and Frictionless Slipping on Stress Redistribution

A review of the plane strain interface debonding problem for the geometry of Fig. 1a is as follows for the case where no frictional resistance is exerted across the debonded interfaces (i.e., $\tau=0$). According to [7], the debonded interface will be fully open when $d/w < 0.24$, and the interface crack tip at the end of the debond is subject to mixed mode conditions, as will be discussed further for the asymptotic problem below. For $0.24 < d/w < 0.71$, the debond crack tip is closed and therefore in a state of pure mode 2, but a portion of the interface near the main layer crack is still open. For $d/w > 0.71$, the interface is fully closed and the interface crack tip is in mode 2. The top curve for the normalized mode 2 stress intensity factor in Fig. 8 applies to the frictionless case. It was computed using the integral equation methods outlined in the Appendix under the constraint that the interface remains closed. The results are strictly correct only for $d/w > 0.71$ (and are in agreement with the results of [7]), but are only slightly in error for smaller d/w . The average crack opening displacement, $\bar{\delta}$, needed for the tunnel crack calculations is shown in Fig. 9 where the top curve again applies to the frictionless case.

The role of debonding on stress redistribution is seen in Fig. 10, where curves of the stress ahead of the right-hand layer crack tip (normalized by the remote applied stress σ) are plotted for various levels of debonding, all for the closed interface with $\tau=0$. Debonding clearly has a significant effect on lowering the stress on the adjoining material just across the interface, more so than for plastic yielding of a thin ductile layer discussed in connection with Fig. 5. For sufficiently small d/w , the debonded interface is fully open and, moreover, the asymptotic problem for a semi-infinite crack impinging on the interface applies, as depicted in the insert of Fig. 6. The stress redistribution is plotted in Fig. 6, which shows that the stress ahead of the layer crack tip is

reduced below the level in the absence of debonding over a distance from the interface equal to one-half of the debond length d . This figure also makes clear that debonding appears to be more effective in protecting the uncracked layer across the interface than plastic yielding of a thin ductile adhesive layer.

As a digression, we record the mode 1 and 2 stress intensity factors for the open interface crack tip for the asymptotic problem of Fig. 6:

$$\frac{K_1}{K} = 0.399 \quad \text{and} \quad \frac{K_2}{K} = 0.322 \quad (5)$$

The associated ratio of the energy release rate of the interface crack tip to that of a mode I crack penetrating straight through the interface without debonding is 0.263 when both the deflected tips and the penetrating tip emerge from the main crack tip at the same applied K . These results correct results given in [9] which were in error for the case of the doubly-deflected interface crack. A complete set of corrections of this energy release rate ratio for this case over the full range of elastic mismatch across the interface will be included in an upcoming paper [10].

5. The Effect of Frictional Slipping on Debonding and Tunnel Cracking

Figs. 8 and 9 contain curves for the normalized mode 2 stress intensity factor and the average crack opening displacement, respectively, in the plane strain problem for several levels of a constant friction stress τ relative to σ acting over the bonded interface. A constant friction stress, as opposed, for example, to a Coulomb friction stress, has been used by a number of workers to represent the frictional forces exerted across slipping interfaces in composites. The purpose of the present limited study is to illustrate the effect of friction in establishing the extent of debonding and its associated influence on the 3D tunneling energy release rate. Almost certainly, additional studies will be required before a good understanding is in hand, including studies with other friction laws. Some results for the effect of Coulomb friction on the mode 2 interface stress intensity factor have been presented in [11].

Let K_c denote the mode 2 toughness of the interface. Attention will be concentrated on the behavior following initiation of interface debonding when the debond length, d , is sufficiently large (i.e., greater than about $w/4$) such that the debond interface crack tip is in mode 2. Impose the debonding condition, $K_2=K_c$, on the solution presented in Figs. 8 and 9. The relationships that result between the applied stress and the debonding length and the average crack opening displacement are plotted in Figs. 11 and 12. The two nondimensional stress parameters in these figures are the applied stress parameter, $(\sigma\sqrt{w})/K_c$, and the constant friction stress parameter, $(\tau\sqrt{w})/K_c$. (Note that it is necessary to interpolate values between the curves of Figs. 8 and 9 to

arrive at the plots in Figs. 11 and 12, since a constant value of $(\tau\sqrt{w})/K_c$ does not correspond to a constant value of τ/σ .) In the range of d less than about $w/4$, the predictions are not expected to be correct since the interface undergoes mixed mode debonding and not mode 2 debonding. Thus, the details in the vicinity of the initiation of debonding are not correct. In particular, the value of $(\sigma\sqrt{w})/K_c$ at which $\bar{\delta}$ begins to depart from $\bar{\delta}_0$ (see Fig. 12) would depend on the mixed mode condition for debond initiation. But once debonding has progressed to the point that the interface crack tip is closed, the mode 2 criterion is appropriate and the curves are accurate.

In the absence of friction the debonding process is unstable, since for a fixed σ , K_2 has a maximum when $d \equiv w$ and then drops slightly to an asymptote as d increases further. Under a prescribed σ , the mode 2 debond would advance dynamically after it is initiated. In this sense, the curves shown in Figs. 11 and 12 for $\tau=0$ represent unstable debonding behavior. Friction stabilizes the debonding process giving rise to a monotonically increasing debond length and average crack opening displacement as the applied stress increases. A nondimensional friction stress on the order of $(\tau\sqrt{w})/K_c=1/8$ or more is required if friction is to be important.

The steady-state energy release rate for tunnel cracking can be computed from the curves in Fig. 12 using (3). The results of this calculation are plotted in Fig. 13. As before, G_{ss} is normalized by the value for a layer crack with no debonding given in (4). The remarks made above with respect to accuracy in the vicinity of debond initiation apply to these curves as well. It can be seen from Fig. 13 that debonding can indeed significantly promote tunneling cracking when the nondimensional friction stress is less than about $(\tau\sqrt{w})/K_c=1/2$.

6. Accounting for Residual Stress in the Cracked Layer

The role of an uniform residual tension, $\sigma_{yy}=\sigma_R$, pre-existing in the layer that subsequently undergoes tunnel cracking can be readily taken into account in the various results presented above. For the purpose of discussion, now let $\sigma_{yy}=\sigma_A$ be the applied stress, replacing the notation for σ in the earlier sections. The results in Figs. 3-4, 7-9 and 11-13 apply as they stand if σ in those figures is identified with $\sigma_A+\sigma_R$. The results for stress redistribution shown in Figs. 5 and 10 can also be used with the following modifications. With σ identified with $\sigma_A+\sigma_R$, the results in Figs. 5 and 10 are correct for the *change* in σ_{yy} in the layer ahead of the tip due to cracking if the numerical value of the ordinate is reduced by 1. To obtain the total stress σ_{yy} in the layer in question, one must then add together the *change* and the stress σ_{yy} existing in the layer prior to the cracking event.

Acknowledgment

The work of KSC was supported by the Internal Research Program, Southwest Research Institute, San Antonio, Texas. The work of M-YH was supported by the DARPA URI at the University of California, Santa Barbara (ONR Contract N00014-86-K-0753). The work of JWH was supported in part by the DARPA URI (Subagreement P.O.#VB38639-0 with the University of California, Santa Barbara, ONR Prime Contract N00014-86-K-0753) and by the Division of Applied Sciences, Harvard University.

References

1. D.B. Marshall and J.J. Ratto, *J. Am. Ceram. Soc.* 74 (1991) 2979-2987.
2. H.C. Cao and A.G. Evans, *Acta Metall. Mater.*, 39 (1991) 2997.
3. C.A. Folsom, F.W. Zok, F.F. Lange and D.B. Marshall, "The mechanical behavior of a laminar ceramic composite", to be published in *J. Am. Ceram. Soc.*
4. B.J. Dalgleish, K.P. Trumble and A.G. Evans, *Acta Metall. Mater.*, 37 (1989) 1923-1931.
5. M.C. Shaw, D.B. Marshall, M.S. Dadkhah and A.G. Evans, "Cracking and damage mechanisms in ceramic/metal multilayers, to be published in *J. Am. Ceram. Soc.*
6. M.Y. He, F.E. Heredia, D.J. Wissuchek, M.C. Shaw and A.G. Evans, "The mechanics of crack growth in layered materials" to be published in *Acta Metall. Mater.*
7. A. Dollar and P.S. Steif, *J. Appl. Mech.*, 58 (1991) 584-586.
8. J.W. Hutchinson and Z. Suo, "Mixed mode cracking in layered materials", in *Adv. Appl. Mech.*, 29 (1991) 63-191.
9. M.Y. He and J.W. Hutchinson, *Int. J. Solids Structures*, 25 (1989) 1053-1067.
10. M.Y. He and J.W. Hutchinson, "The effect of residual stress on the competition between crack deflection and penetration at an interface", to be published.
11. A. Dollar and P.S. Steif, "Interface blunting of matrix cracks in fiber-reinforced ceramics", to be published in *J. Appl. Mech.*

Appendix: Numerical Approaches

Two integral equation formulations were used in the solution of the problems discussed. Both methods have been used by various authors to solve related plane strain problems and, for this reason, details of the methods will not be given. In some cases, results were generated using both schemes as a check. The methods used for the problems for the closed interface cracks at the ends of the finite length layer crack (see Fig. 1a) will be discussed first.

The integral equations in method 1 are formed by representing both the layer crack and the mode 2 interface cracks by distributions of dislocations. With reference to Fig. 1a, let $b_0(x) = -d\delta_y/dx$ denote the amplitude of the dislocation opening distribution extending from 0 to w along $y=0$, and let $b_s(y) = -d\delta_y/dy$ denote the amplitude of the dislocation shearing distribution along $x=w$ extending from 0 to d . The condition that $\sigma_{yy}=0$ along $y=0$ for $-w < x < w$ can be written as

$$\int_0^w H_1(x, x') b_0(x') dx' + \int_0^d H_2(x, y) b_s(y) dy = -\sigma \quad (A1)$$

where $H_1(x, x')$ denotes the stress $\sigma_{yy}(x)$ along $y=0$ due to $b_0(x')$, with due regard for the symmetry of this distribution with respect to $x=0$, and $H_2(x, y)$ denotes $\sigma_{yy}(x)$ due to $b_s(y)$, with the appropriate four-fold symmetry on this distribution imposed. Similarly, the condition that $\sigma_{xy} = -\tau$ along $x=w$ between 0 and d (with the corresponding shear conditions met along the other three legs of the H-crack) is

$$\int_0^w H_3(y, x') b_0(x') dx' + \int_0^d H_4(y, y') b_s(y') dy' = -\tau \quad (A2)$$

where $H_3(y, x')$ is $\sigma_{xy}(y)$ along $x=w$ due to $b_0(x')$ and $H_4(y, y')$ is $\sigma_{xy}(y)$ due to $b_s(y')$.

Method 2 makes use of the solution for the problem of four symmetrically placed dislocations interacting with a traction free crack extending along the x -axis from $-w$ to w . With $H(y, y')$ denoting the shear stress $\sigma_{xy}(y)$ along $x=w$ between 0 and d due to $b_s(y')$, with due regard for the other three symmetrically placed dislocations, the single integral equation for b_s is

$$\int_0^d H(y, y') b_s(y') dy' = -\sigma_{xy}^0(y) - \tau \quad (A3)$$

where $\sigma_{xy}^0(y)$ is the shear stress along $x=w$ due to the remote stress acting on the layer crack in the absence of the interface cracks.

The kernels of the integrals above have Cauchy singularities. The dislocation distributions can be obtained using several well known numerical techniques. Once the distributions are known in either method, they may be used with other integral expressions to compute the stress components at any point in the plane and the mode 2 stress intensity factor at the end of the interface crack. For the cases in which K_2 is nonzero, the distribution $b_s(y)$ has an inverse square root singularity at $y=d$, while it diminishes with the square root of the distance from $y=d$ for the plastic yielding problems with $K_2=0$. The solutions are not overly sensitive to having a precise incorporation of the correct behavior of the dislocation distributions at the corner point at $x=w$ on $y=0$. A number of choices were made, including representations which built-in the correct lowest order functional behavior near this point.

The asymptotic problem for the semi-infinite layer crack and the mode 2 interface cracks (see Fig.1b) was solved using method 2. Now, $H(y,y')$ is the shear stress along $x=0$ between 0 and d due to just two symmetrically placed dislocations on $x=0$ at $\pm y'$ interacting with a traction-free semi-infinite crack, and $\sigma_{xy}^0(y)$ is the shear stress on $x=0$ due to the K-field in the absence of the interface cracks. The second asymptotic problem discussed in connection with Fig. 6 in which the interface crack opens is also solved using method 2, but here both shear dislocations and opening dislocations must be used and the problem becomes a set of dual integral equations. In all the cases involving method 2, the kernel functions H can be obtained in closed form using complex variable methods of elasticity.

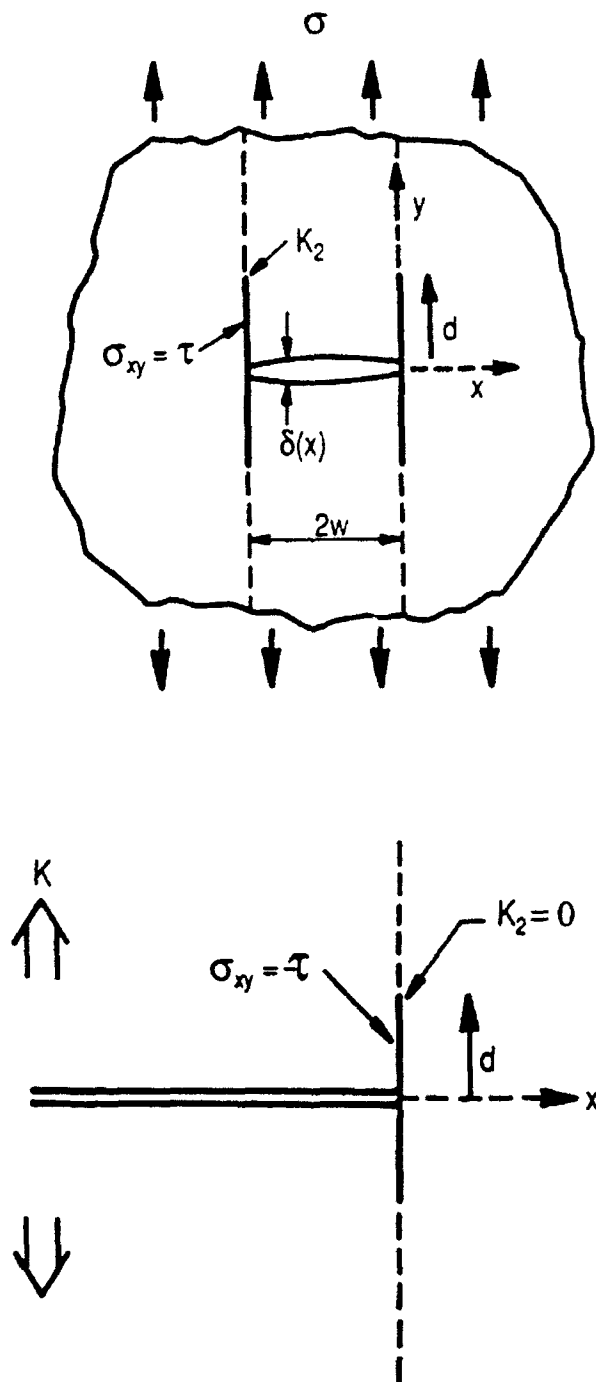


Fig.1 Specification of the plane strain problems. a) Finite layer crack. b) Asymptotic problem.

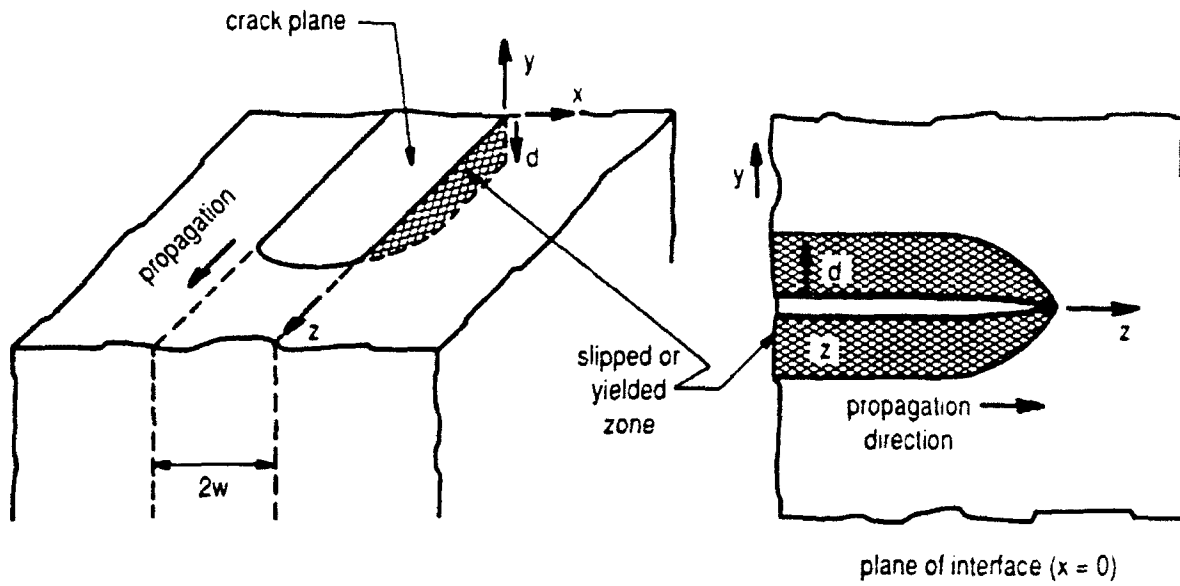


Fig.2 Specification of the 3D tunneling crack problem.

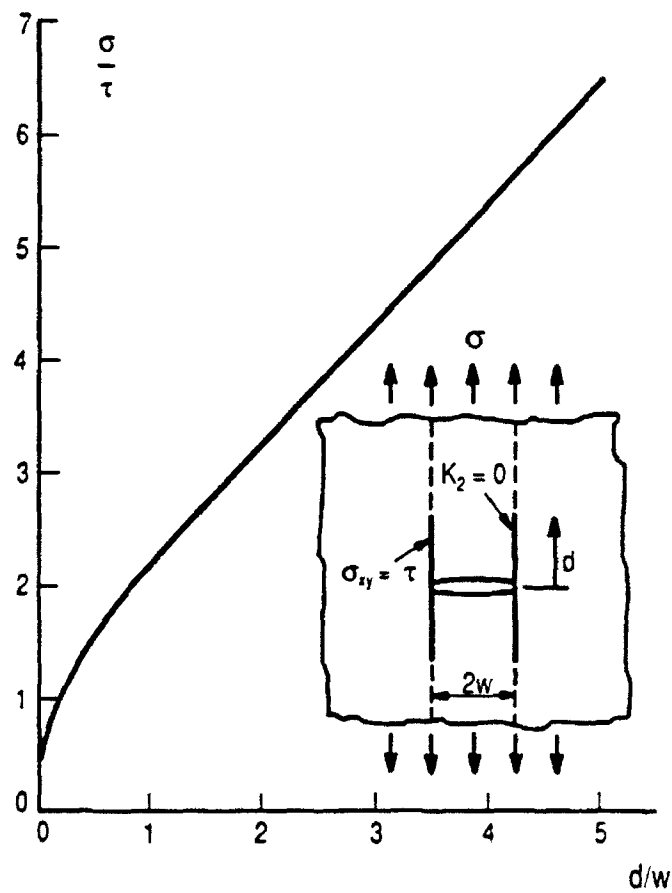


Fig.3 Relation between applied stress and height of the yielding zone in a thin ductile adhesive layer.

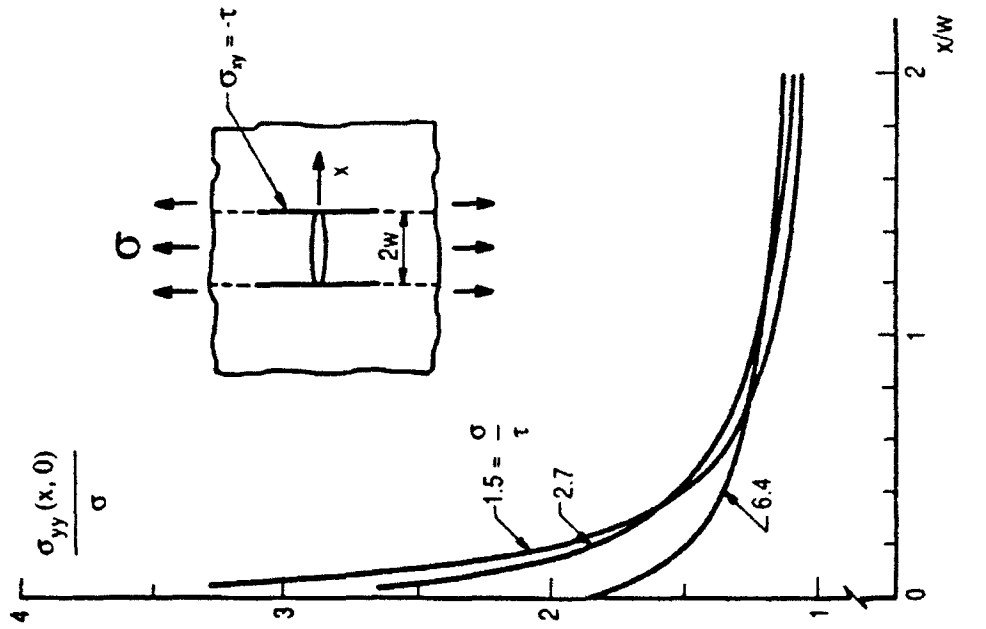


Fig.5 Stress distribution ahead of the crack tip in the uncracked layer at several levels of applied stress to shear yield stress of the thin adhesive layer.

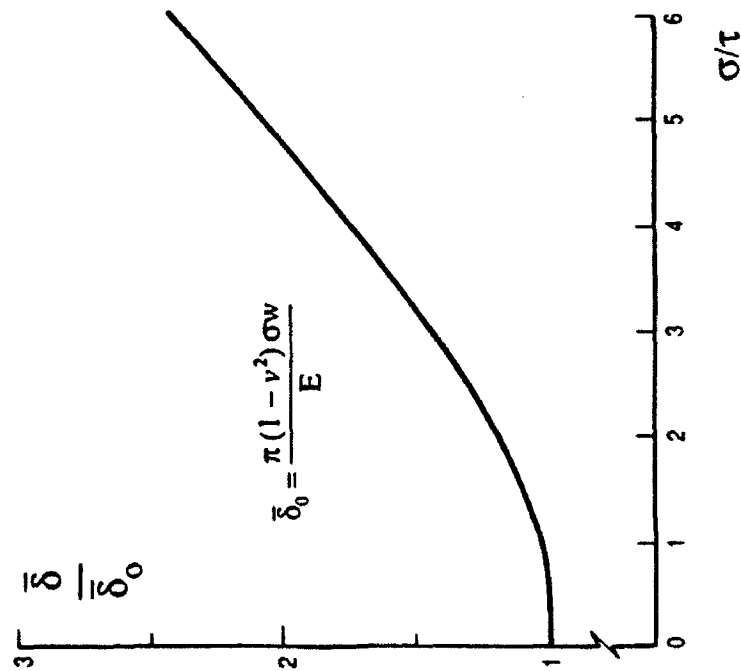


Fig.4 Average crack opening displacement as a function of the ratio of applied stress to shear yield stress of the thin ductile adhesive layer.

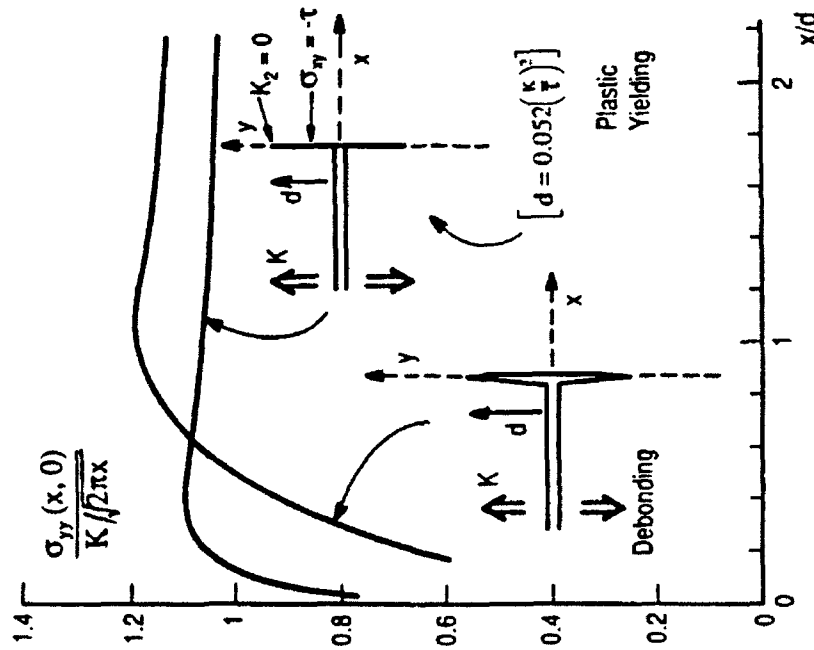


Fig.6 Stress redistribution ahead of the crack tip in the layer across the interface for the two asymptotic problems ($d < w$).

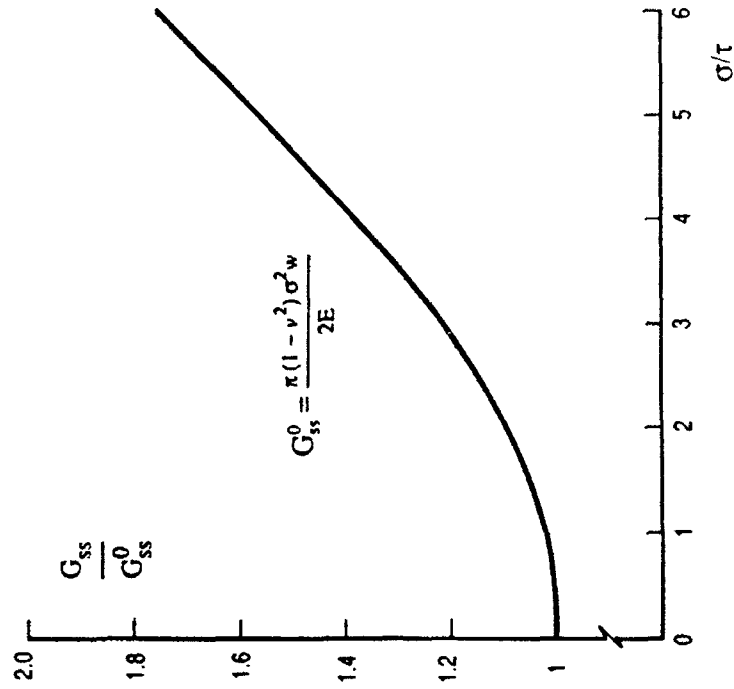


Fig.7 Normalized steady-state energy release rate for the tunneling crack for the case of thin ductile adhesive layers with shear yield stress τ .

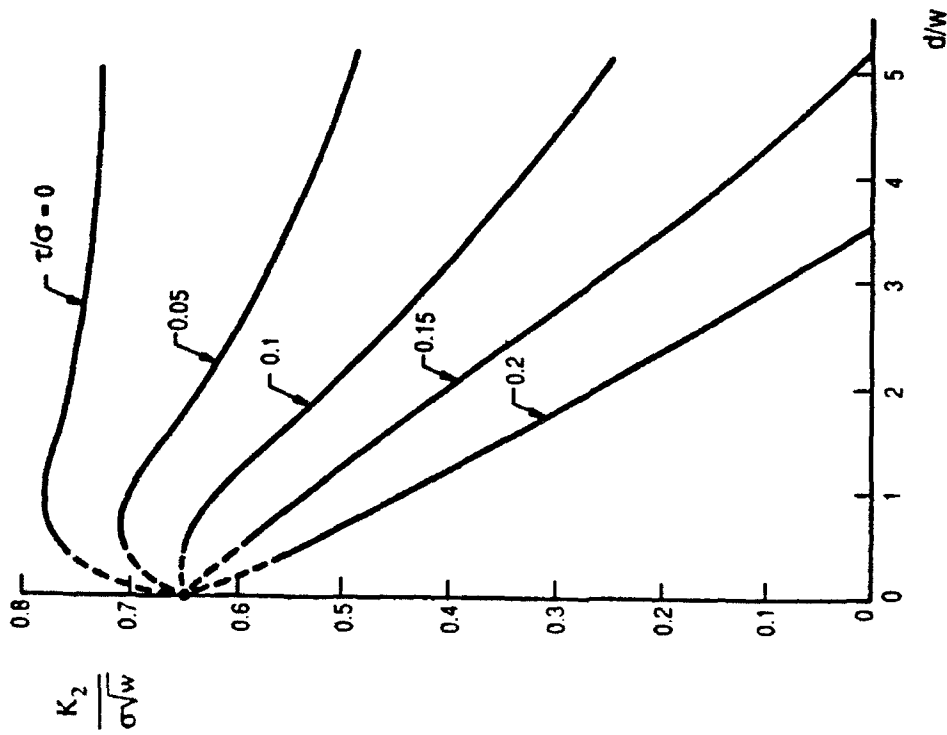


Fig.8 Normalized mode 2 stress intensity factor for the debonding interface crack at several levels of interface friction stress to applied stress.

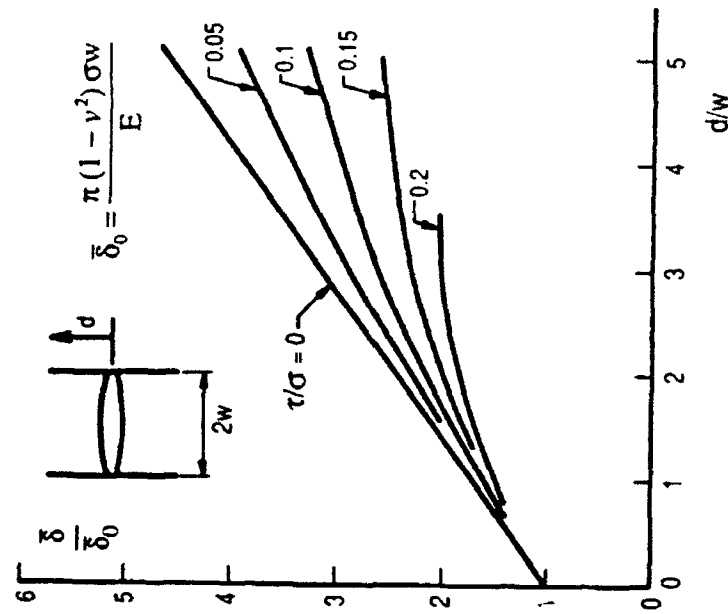


Fig.9 Average crack opening displacement as a function of debond length at several levels of interface friction stress to applied stress.

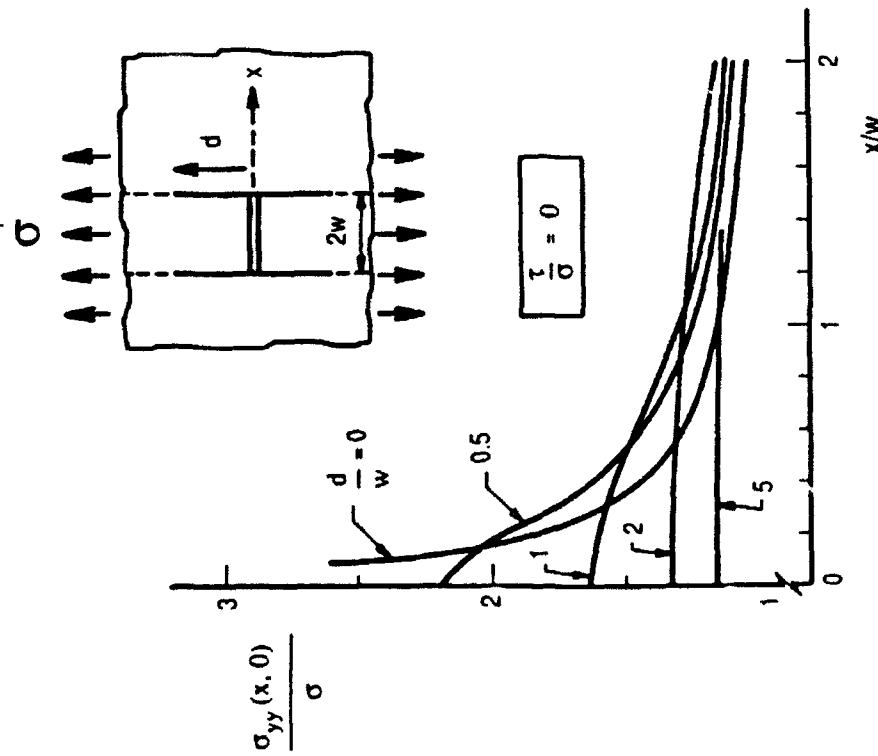


Fig. 10 Stress distribution ahead of the crack tip in the uncracked layer across the interface for the case of no interface friction.

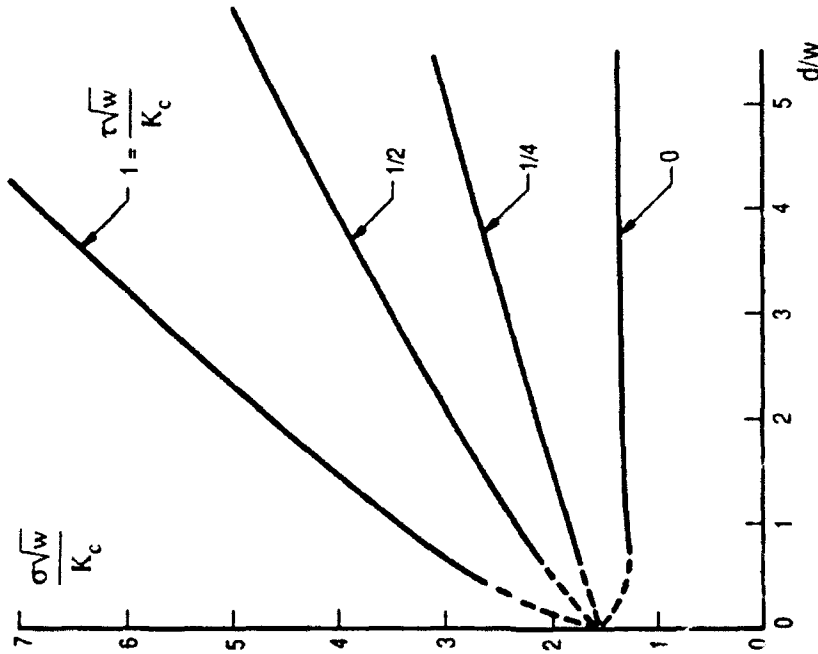


Fig. 11 Relation between normalized applied stress and debond height at several levels of the non-dimensional interface friction stress. The condition $K_2 = K_c$ is imposed where K_c is the mode 2 interface toughness.

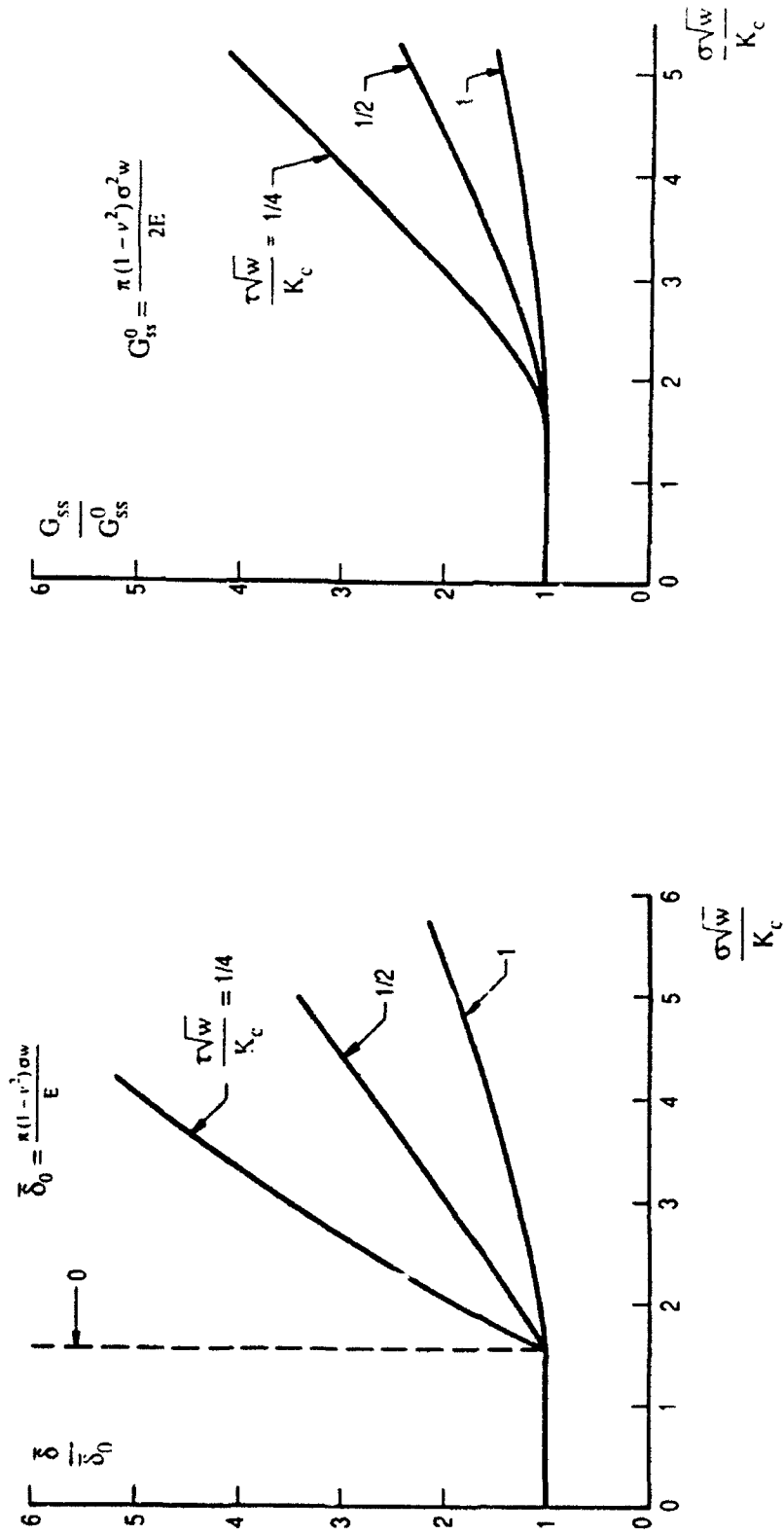


Fig. 12 Relation between the average crack opening displacement and normalized applied stress at several levels of the nondimensional interface friction stress. The condition $K_2=K_c$ has been imposed where K_c is the mode 2 interface toughness.

Fig. 13 Steady-state energy release rate for the tunneling crack. The condition $K_2=K_c$ has been imposed where K_c is the mode 2 interface toughness.

THE EFFECT OF INTERFACE DIFFUSION AND SLIP ON THE CREEP RESISTANCE OF PARTICULATE COMPOSITE MATERIALS

P. Sofronis* and R. M. McMeeking

Department of Materials and Department
of Mechanical Engineering
University of California, Santa Barbara
California 93106

December 1991

*current address: Department of Theoretical and Applied Mechanics,
University of Illinois at Urbana-Champaign,
Urbana, Illinois 61801

ABSTRACT

Reinforcements are known to increase the creep resistance of metal and intermetallic matrix composite materials. Experimental measurements at modest temperatures indicate that under a given applied strain rate the composite strength is higher than that of the matrix alone. However, at temperatures higher than approximately half of the melting temperature of the matrix, the composite strength is limited and in some cases the strengthening imparted by the reinforcements is completely lost. Diffusional relaxation and slip on the reinforcement-matrix interface are suggested as mechanisms responsible for the loss of strengthening. According to the proposed model, stress gradients caused by plastic constraint induce diffusional flow along the interface accompanied by slip of the matrix over the reinforcement. As a result the constraint tends to be relaxed and strengthening can be eliminated. The composite behavior is investigated by coupling the diffusion and slip along the interface with deformation of the matrix in the power law creep regime. A unit cell model is used in axial symmetry and the relevant boundary value problem is solved by the finite element method. Numerical results indicate that either diffusional relaxation or slip may knock down the creep resistance of the composite to levels even below the matrix strength.

INTRODUCTION

The creep strength of metal and intermetallic matrix composite materials reinforced with large rigid particles has been of interest recently for application in high temperature, high strength components. It is believed that strengthening in those materials can be understood on a continuum basis if the reinforcements are at least micron-sized, so that they are larger than the

dislocation structures (cell size, travel distance etc.). Then the underlying principle is that strengthening develops from the constraint of the reinforcement on the matrix. Consequently, creep strength at high temperature will persist only if the constraint is maintained. Conditions of slip or mass transport at the matrix-reinforcement interface can reduce the constraint and relax the matrix stresses. Rosler et al. (1990) investigated this situation in the mechanical behavior of γ -TiAl reinforced with Ti_2AlC platelets in the temperature range 293K to 1255K. At temperatures up to 1000K, the creep strength of the composite material at a given strain rate was found to be higher than that of the matrix alone. Such a temperature corresponds to half of the melting temperature of the matrix. As the temperature increases beyond 1000K, the relative composite strength reduces and at about 1250K falls below that of the matrix (see Figure 1). Rosler, Bao and Evans (1991) proposed an explanation of the diminishing relative strength at higher temperatures by means of a diffusional relaxation mechanism. Matter transported from the side to the top of long reinforcements provides additional strain of the composite material above and beyond that due to matrix flow. However, their model assumed free slip at the interface and gave no indication of the relative importance of slip versus mass transport.

In this article, the resistance of a power law creeping matrix reinforced by spherical rigid particles is addressed with theoretical models. At low and modest temperatures the interface is considered to be non-slipping and without significant mass transport. The strengthening imparted by the reinforcements is quantified under those conditions. At temperatures higher than approximately half of the melting temperature of the matrix, interface slip and diffusional relaxation are investigated as potential mechanisms

responsible for the loss of strengthening. In the analysis, the deformation of the creeping matrix is coupled with slip of the matrix on the reinforcement or diffusional mass transport along the matrix-reinforcement interface. The finite element method is used to solve the relevant boundary value problems. Interface slip or diffusional relaxation are found to knock down the creep strength of the composite. An important point is that this effect can occur due to slip alone. Furthermore, a size effect is introduced by diffusion and slip and an assessment of the dependence of the creep strength on the reinforcement size is made.

It is suggested that the net composite strength is controlled by the nature of the matrix-reinforcement interface. The following cases are probable (see Figure 2). (a) The interface is perfectly bonded and no slip or mass transport occurs; the full reinforcement constraint is imposed on the matrix and λ is greater than unity where λ is the ratio of the strength of the composite material at a given strain rate divided by the strength of the matrix material alone at the same strain rate. (b) Slip of the matrix relative to the rigid reinforcement along the particle-matrix interface can occur; the constraint of the reinforcement on the matrix is relaxed to some extent, and the relative strength λ is diminished. (c) Long range diffusional mass transport along the interface occurs; the constraint of the reinforcement on the matrix is relaxed even further, and the composite strength is less than the matrix strength.

Slip on the matrix-reinforcement interface may be possible because of the presence of an interface with a rheology different from both the matrix and the reinforcement. This situation is depicted in Figure (3b) where a thin weaker layer is interposed between the matrix and the reinforcement. The low viscosity of the layer permits a relatively high shear strain rate there.

Because of the minimal thickness of the interphase, the behavior is effectively represented as a tangential velocity parallel to the interface controlled by the shear stress (see Figure 3b). Thus

$$v_s = h \dot{\gamma} = \frac{h \tau_s}{\eta} \quad (1)$$

where v_s is the matrix velocity parallel to the interface, h is the interphase thickness, $\dot{\gamma}$ is the shear strain rate in the thin layer, τ_s is the shear stress at the interface and η is the viscosity of the interphase material. The viscosity could be stress dependent as in power law creep, but in this paper linear rheology only will be considered so that η is a constant. The quotient η/h can be combined into a slip parameter μ giving the slip velocity

$$v_s = \frac{\tau_s}{\mu} \quad (2)$$

The temperature dependence of the viscosity of the interphase material may differ from the temperature dependence of the rheology of the matrix material. Thus, at low creep temperatures, the viscosity of the interphase may be high enough to enforce a no-slip or near no-slip condition between the matrix and the reinforcement. However, at higher creep temperatures the interphase could soften relative to the matrix, initiating slip at the interface. Of course, the opposite could be true if, as the temperature rises the matrix softens relative to the interface.

An alternative possible mechanism for slip arises from short range mass transport by diffusion on the interface. Asperities on the reinforcement surface give rise to tension and compression (see Figure 3c) which produces chemical potential gradients. Diffusive fluxes occur due to these gradients and, biased by the shear stress, the mass transport augments the matrix creep

rate. As a result, the matrix velocity in the direction of the shear stress is higher than it would be due to matrix creep without mass transport. The additional velocity is proportional to the diffusion rate on the interface and inversely proportional to the square of the size scale of the roughness. The diffusion rate is controlled by the stress levels on the asperities and thus by the shear stress in the matrix. Consequently, the additional slip velocity is given by eq. (2), but in this case with μ being

$$\mu = \frac{l^2}{\mathcal{D}} \quad (3)$$

where l is an effective length scale for the asperities and \mathcal{D} is an interface diffusion constant defined fully below. The form in eq. (3) is similar to that found by Raj and Ashby (1971) for grain boundary sliding, except in that case the roughness retards the slippage rather than enhances it. The diffusion parameter \mathcal{D} is temperature dependent so that this slip mechanism may operate at high temperature but be inactive at low creep temperatures. At very high temperatures, \mathcal{D} is very large and thus μ is very small. This means that the interface can sustain only very low shear stress at very high temperature. In addition, long range mass transport by diffusion on the scale of the reinforcement size becomes significant at very high temperature. Thus, the long range diffusion regime is characterized by near zero shear drag on the interface.

CELL MODEL

The composite material behavior is modeled by the response of an axisymmetric cell. This approach has been used widely; see, for example, Bao, Hutchinson and McMeeking (1991). The unit cell is shown in Figure 2. The uniaxial stress is $\bar{\sigma}$ and in response, the axial strain rate is $\dot{\bar{\epsilon}}$. The unit cell is

constrained to remain cylindrical with zero average transverse stress and the end surfaces are required to remain planar during deformation. Both lateral and end surfaces are free of shear traction. The reinforcement in the center of the cylinder is rigid. The matrix material is incompressible and has a uniaxial stress-strain rate behavior given by

$$\frac{\dot{\epsilon}}{\dot{\epsilon}_0} = \left(\frac{\sigma}{\sigma_0} \right)^n \quad (4)$$

where $\dot{\epsilon}_0$ and σ_0 are material constants and n is the creep exponent. Under triaxial stress situations the creep law becomes

$$\sigma'_{ij} = \frac{\partial \phi}{\partial \dot{\epsilon}_{ij}} \quad (5)$$

where σ' is the deviatoric stress tensor, $\dot{\epsilon}$ is the strain rate tensor, ϕ is a creep potential such that

$$\phi = \frac{n \sigma_0 \dot{\epsilon}_0}{n+1} \left(\frac{\dot{\epsilon}_e}{\dot{\epsilon}_0} \right)^{\frac{n+1}{n}} \quad (6)$$

and $\dot{\epsilon}_e$ is the effective strain rate

$$\dot{\epsilon}_e = \sqrt{\frac{2}{3} \dot{\epsilon}_{ij} \dot{\epsilon}_{ij}} \quad (7)$$

The creep strength of the composite material is assessed through the relative strength λ defined as

$$\lambda = \frac{\bar{\sigma}(\dot{\bar{\epsilon}})}{\sigma(\dot{\bar{\epsilon}})} \quad (8)$$

where $\bar{\sigma}(\dot{\bar{\epsilon}})$ is the strength of the composite at a given axial strain rate $\dot{\bar{\epsilon}}$ (see Figure 2) and $\sigma(\dot{\bar{\epsilon}})$ is the strength of the matrix material alone at the same

axial strain rate $\dot{\bar{\epsilon}}$. Thus strengthening is characterized by $\lambda > 1$, as shown in Figure 1.

PERFECT INTERFACE

In uniaxial tension, the creep strength $\bar{\sigma}$ of the composite material at a given axial strain rate $\dot{\bar{\epsilon}}$ is given by

$$\frac{\dot{\bar{\epsilon}}}{\dot{\bar{\epsilon}}_0} = \left(\frac{\bar{\sigma}}{\bar{\sigma}_0} \right)^n \quad (9)$$

where $\bar{\sigma}_0$ is the composite reference stress. The parameter $\bar{\sigma}_0$ depends on the volume fraction V_f and the aspect ratio of the reinforcement (Bao et al. (1991)). Using eqs. (4), (8) and (9), one finds that

$$\lambda = \frac{\bar{\sigma}_0}{\sigma_0} \quad (10)$$

Hence, the reference stress $\bar{\sigma}_0$ characterizes both the strength $\bar{\sigma}$ and the relative strength λ of the composite material

By symmetry, the solution in the first quadrant of the unit cell only is required. In Figure 4, this situation is depicted with a rigid spherical reinforcement of radius R within a cylinder of the matrix material. The cylinder's height is equal to its width, $2b$. The interface is modeled by imposing both zero normal and tangential velocities v_n and v_s at any point on the interface (i.e. Figure 4 with $\mu = \infty$). The cell is stretched in the z direction with a uniform end velocity $v_z = \dot{\bar{\epsilon}} b$. Macroscopic incompressibility of the cell implies that the cylindrical surface at $r = b$ moves in radially with velocity $v_r = -b\dot{\bar{\epsilon}}/2$. On the surfaces at $r = b$ and $z = b$, the shear stress $\sigma_{rz} = 0$. By symmetry σ_{rz} and the normal velocities are also zero on $z = 0$

and $r=0$. The zero average stress condition on the cylindrical surface

requires that $\int_0^b \sigma_r dz = 0$.

The boundary value problem for the deformation of the matrix material in V is solved for velocities by minimization of the convex functional

$$U[\underline{v}] = \int_V \left[\varphi + \frac{1}{2} K \dot{\epsilon}_{kk}^2 \right] dV \quad (11)$$

where K is a large penalty function chosen to keep $\dot{\epsilon}_{kk}$ very close to zero, effectively imposing incompressibility. Solutions were found by the finite element method. Further details of the treatment of the material nonlinearity and incompressibility are described by Sofronis and McMeeking (1991).

Finite element solutions were obtained in a range of strain rates $\dot{\bar{\epsilon}}/\dot{\epsilon}_0$ from 0 to 20 and found to agree precisely with eq. (9). The composite strength $\bar{\sigma}_0$ is dependent on n and the volume fraction of reinforcements, V_f . The results for $\bar{\sigma}_0$ obtained for $n=5$ and $n=10$ when $V_f = 0.2$ agree with values obtained by Bao et al. (1991). For $n=10$, $\lambda = 1.16$, for $n=5$, $\lambda = 1.23$ and for $n=1$, $\lambda = 2.02$. These results confirm that the finite element program used for the matrix creep analysis is accurate and reliable. Furthermore, the results of Bao et al. (1991) predict well the experimental strength of composites with undamaged reinforcements and interfaces (Evans, Hutchinson and McMeeking, (1991)), confirming that the unit cell approach is realistic.

INTERFACE SLIP

In order to assess the effect of interface slip, the boundary value problem for the unit cell (see Figure 4) was solved with a different boundary

condition at the matrix-reinforcement interface. Otherwise, the boundary conditions for the problem are those described in the previous section. On the interface, slip of the matrix material over the reinforcement is modeled by requiring that $v_n = 0$ and that the shear stress τ_s is related to the tangential velocity through eq. (2). Such conditions have been used in other treatments of similar problems, especially the linear case, e. g. self consistent treatments (Mura (1982)). The boundary value problem is solved for velocities by minimization of the functional

$$U[\underline{v}] = \int_V \left[\phi + \frac{1}{2} K \dot{\epsilon}_{kk}^2 \right] dV + U_s[\underline{v}] \quad (12)$$

where

$$U_s[\underline{v}] = \int_{S_r} \frac{1}{2} \mu v_s^2 dS \quad (13)$$

and S_r is the matrix-reinforcement interface. The first variation of the functional U_s gives the virtual energy dissipation rate on the interface due to slip (Needleman and Rice (1980)). The functional U_s is convex and hence U is too, ensuring favorable convergence properties for the finite element method used for the problem.

The interface slip effect was studied by means of the dimensionless parameter ξ such that

$$\xi = \frac{\sigma_o}{\mu R \dot{\epsilon}_o} \quad (14)$$

The slip resistance of the interface drops with increasing ξ . Slip occurs freely as $\xi \rightarrow \infty$. For $\xi = 0$, that is for $v_s = 0$, the no slip condition prevails. Solutions by the finite element method were obtained for values of ξ varying from 0 to 10^5 . No significant difference in the numerical results was found for

ξ greater than 100. This indicates that for ξ greater than 100 slip is effectively free. In Figure 5 the relative strength of the composite is shown as a function of ξ for a reinforcement volume fraction $V_f = 0.2$ at applied strain rates $\dot{\epsilon}/\dot{\epsilon}_0$ equal to 0.2, 2, 20 and 50.

For the linearly viscous matrix material with $n=1$, the relative strength λ is independent of strain rate. This occurs because the slip rheology at the interface is linear too. As mentioned previously, the value of λ for $n=1$ is 2.02 when the interface is non-slipping e.g. $\xi = 0$. As ξ increases the relative strength drops rapidly and at about $\xi = 10$, it has reached an essentially asymptotic value of 1.27. Thus, slip decreases the composite relative strength by as much as 37% compared to the material with the non-slipping interface. Notice, though, that the composite remains stronger than the unreinforced matrix even when there is no shear drag at the interface.

In the case of the nonlinear matrix material, the effect of slip has been computed for $n=5$ and $n=10$ (see Figure 5). As noted previously, when $\xi = 0$ the relative strength is 1.23 and 1.16 respectively, but when slip is permitted, the relative strength decreases with ξ . Except for the high strain rate case, for large ξ the strength asymptotes to a value which is just below 1. Thus in many cases the strength of the material with a freely slipping interface is lower than the matrix. Contrary to the linear matrix case, the strain rate affects the relative decrease of strength and therefore the value of ξ at which the relative strength has effectively reached its asymptotic value. The table inset in Figure 5 shows the values of ξ for each strain rate at which the composite strength equals the matrix strength. Note also that the decrease in the composite relative strength occurs more rapidly in terms of ξ when the strain rate is low and, to a small extent, when the creep exponent is high.

The observed effect is similar to the behavior of a stressed, one dimensional system with a linear material in series with a nonlinear one. This gives a total strain rate of

$$\dot{\epsilon} = \dot{\epsilon}_0 \left(\frac{\sigma}{\sigma_0} \right)^n + \frac{\sigma}{\mu} \quad (15)$$

At high strain rates, the nonlinear material dominates the behavior because the strain rate due to that material grows rapidly with stress. Consequently, the composite material strength is similar to that of the purely nonlinear material. At low strain rates, the linear material determines the strain rate because the contribution from the nonlinear material diminishes rapidly with stress. Thus for low strain rates the composite material strength will be similar to that for the linear material alone. If that strength is low compared to the nonlinear material, the result for the composite system is a diminished strength. At intermediate strain rates there will be a transition from a strength characteristic of the nonlinear material to the strength characterizing the linear material. The behavior at constant ξ in Figure 5 is broadly in accord with this concept, although obviously somewhat more complicated. The behavior at constant strain rate in Figure 5 is consistent with the simple uniaxial model, but with a finite asymptote as $\xi \rightarrow \infty$. Perhaps a more complicated model with parallel and series elements could be constructed to exhibit the observed behavior, e.g. possibly a nonlinear material in parallel with an element consisting of a linear material in series with a nonlinear one. However, the point is clear that a high strain rate induces behavior dominated more by the nonlinear matrix whereas a low strain rate permits the linear interface properties to have more influence.

In Figure 6 the relaxation of the constraint associated with the freedom to slip at the interface is illustrated. In Figure 6a, contours of equal hydrostatic stress constraint, $\sigma_{kk}/3\sigma_o$, are shown for the case of a non-slipping interface in a composite material with $V_f = 0.2$ and a matrix creep exponent $n=10$. The strain rate is $\dot{\bar{\epsilon}}/\dot{\epsilon}_o = 20$. In this case $\bar{\sigma}(\dot{\bar{\epsilon}})/\sigma_o = 1.57$. The maximum hydrostatic constraint is 2.5 and is close to the pole of the reinforcement. The matrix also undergoes intense shear along the interface. The interface is under tension around the pole and under compression around the equator. The maximum compressive hydrostatic constraint is -0.9. In contrast with the non-slipping case, Figure 6b demonstrates that hydrostatic stress relaxation occurs when the matrix slips freely on the interface. In this example $\xi = 10^5$, so that there is essentially no shear drag at the interface. Now $\bar{\sigma}(\dot{\bar{\epsilon}})/\sigma_o = 1.28$. Clearly the maximum hydrostatic stress in terms of $\sigma_{kk}/3\sigma_o$ has dropped to 1.1 from the previous value of 2.5. Moreover, there are no longer regions under compression along the equator of the particle. Because there is no drag, intense shearing deformation along the interface is not present.

LONG RANGE INTERFACE DIFFUSION

Figure 6b shows that even when the matrix slips freely without drag over the reinforcement, a gradient in the normal stress on the interface exists. At high temperatures, this normal stress gradient motivates diffusional mass transport from the sides to the poles of the reinforcement as is shown schematically in Figure 7. In this section, the deformation of the matrix is analyzed coupled with interface diffusion and free slip.

The chemical potential per atom along the interface is (Herring, (1950))

$$\mu = -\sigma_n \Omega \quad (16)$$

where σ_n is the normal stress and Ω is the atomic volume. Strain energy terms have been taken to be negligible (Needleman and Rice (1980)). The volumetric flux \underline{j} crossing unit length in the interface is given by

$$\underline{j} = -\frac{D_b \delta_b}{KT} \underline{\nabla} \mu \quad (17)$$

where D_b is the interface diffusion coefficient, δ_b is an effective interface thickness, $\underline{\nabla}$ is the two dimensional gradient operator on the interface surface, K is Boltzmann's constant and T the absolute temperature. Substituting eq. (16) into eq. (17), one finds

$$\underline{j} = \mathcal{D} \underline{\nabla} \sigma_n \quad (18)$$

where

$$\mathcal{D} = \frac{D_b \delta_b \Omega}{KT} \quad (19)$$

is an interface diffusion constant whose dimensions are volume divided by stress. The dimensions of \underline{j} are area over time. Matter conservation along the interface requires

$$\underline{\nabla} \cdot \underline{j} + v_n = 0 \quad (20)$$

where v_n is the separation velocity between the matrix and the interface. For the case of a spherical surface with radius R , eqs. (18) and (20) are written as

$$j(s) = \mathcal{D} \frac{d\sigma_n(s)}{ds} \quad (21)$$

$$\frac{1}{\sin\left(\frac{s}{R}\right)} \frac{d}{ds} \left(j \sin\left(\frac{s}{R}\right) \right) + v_n = 0 \quad (22)$$

where the scalar j is the flux in the circumferential direction on the sphere and s is the arc length distance measured from pole of the reinforcement. Because of symmetry

$$j(0) = j(s_f) = 0 \quad (23)$$

where $s_f = \pi R/2$.

The unit cell boundary value problem in which the creep deformation of the matrix is coupled with interface diffusion and free interface slip is summarized in Figure 8. The condition for free slip implies that the tangential stress τ_s on the interface is zero. Eqs. (21) and (22) specify the boundary condition imposed on the normal velocity v_n to the interface. The rest of the boundary conditions are exactly the same as for the previous two boundary value problems. The solution is obtained for velocities by minimization of the functional

$$U[\underline{v}] = \int_V \left[\phi + \frac{1}{2} K \dot{\epsilon}_{kk}^2 \right] dV + U_d[\underline{v}] \quad (24)$$

where

$$U_d[\underline{v}] = \int_{S_f} \frac{j^2}{2\mathcal{D}} dS \quad (25)$$

where j is regarded as a functional of the velocity \underline{v} through eq. (21). Eq. (25) indicates that U_d is convex and consequently so is U . In Appendix A, it is shown that the energy dissipation rate due to diffusion over the interface S_f equals the variation to first order of U_d in \underline{v} . Solutions to the minimization of $U[\underline{v}]$ were obtained by the finite element method. The numerical treatment of the functional U_d of eq. (25) is given in Appendix B.

The diffusion effect was investigated through the dimensionless parameter

$$\chi = \frac{\mathcal{D} \sigma_o}{R^3 \dot{\epsilon}_o} \quad (26)$$

which had values ranging from 0 to 10^5 . Strain rates $\dot{\epsilon}/\dot{\epsilon}_o$ equal to 0.2 and 20 were used, with a particle volume fraction of $V_f = 0.2$. In Figure 9 the composite relative strength is plotted against χ . Figure 9 has been drawn to the same ordinate scale as Figure 5 to facilitate comparison. As before, the relative strength λ of the linear material is independent of the applied strain rate. At $\chi = 0$ the parameter λ for $n=1$ equals 1.27 which is the relative strength of the composite when interface slip is free but there is no diffusion, e. g., when $\chi = 0$ but ξ is very large. As χ increases, the composite strength decreases with λ becoming less than unity at $\chi = 0.06$. Thus the composite is weaker than the matrix alone for χ values greater than 0.06. For χ greater than 4, an asymptotic value of $\lambda = 0.75$ is essentially attained, i.e. the composite strength is 75% of the matrix strength. This level corresponds to 60% of the strength prevailing in the free slip situation with no diffusion. Compared to the no slip, no diffusion case, the strength is 37%.

In the case of the nonlinear material with strain rate $\dot{\epsilon}/\dot{\epsilon}_o = 20$, free slip but no diffusion ($\chi = 0$), the composite strength is such that $\lambda = 0.97$ and 0.95 for $n=5$ and $n=10$ respectively. For χ greater than 90, the asymptotic value of $\lambda = 0.75$ is essentially reached for both $n=5$ and $n=10$, which amount to 77% and 79%, respectively, of the strength with free slip and no diffusion; i.e. 61% and 65% respectively of the composite strength with no slip and no diffusion. Figure 9 shows clearly that the strength drops very gradually with χ when the strain rate is $\dot{\epsilon}/\dot{\epsilon}_o = 20$. In Figure 9 the behavior is also shown for a strain rate of $\dot{\epsilon}/\dot{\epsilon}_o = 0.2$ when the stress exponent is $n=5$. Then at $\chi = 0$ with free slip, the relative strength parameter λ equals 0.97. As

χ increases, the relative strength for the case with the strain rate $\dot{\bar{\epsilon}}/\dot{\epsilon}_o = 0.2$ drops faster than that of the higher strain rate case ($\dot{\bar{\epsilon}}/\dot{\epsilon}_o = 20$, see Figure 9). For χ greater than 1 in the low strain rate case, the relative strength essentially asymptotes to the value of $\lambda = 0.75$. This corresponds to 77% of the strength with free slip but no diffusion when $n=5$ and to 61% of the strength with no slip and no diffusion.

It is notable that in all cases ($n=5$ & 10 ; $\dot{\bar{\epsilon}}/\dot{\epsilon}_o = 0.2$ & 20) the asymptotic strength with very fast diffusion and free slip ($\xi = \infty$; $\chi = \infty$) is 75% of the matrix strength. Thus, the asymptotic behavior in this extreme seems to be independent of the matrix creep properties. Otherwise, the transition from no diffusion to very fast diffusion seems to follow the pattern found in the transition from no slip to free slip. That is, higher strain rates induce higher strengths in the nonlinear material while the distinctions between the $n=5$ and $n=10$ cases are not substantial. Thus a similar concept involving linear and nonlinear elements in series and perhaps a further nonlinear element in parallel provides a simple very approximate model for what is observed.

In Figure 6c the relaxation of the hydrostatic stress constraint $\sigma_{kk}/3\sigma_o$ due to diffusional mass transport on the interface is shown at $\dot{\bar{\epsilon}}/\dot{\epsilon}_o = 20$, $n=10$, $\xi = \infty$ and $\chi = 1$. In this case $\bar{\sigma}(\dot{\bar{\epsilon}})/\sigma_o = 1.24$. Long range diffusion relaxes the matrix constraint somewhat below the levels associated with free slip but no diffusion (see Figure 6b). The effect is most marked at the pole of the reinforcement. When material is deposited by diffusion extremely rapidly at the pole, i.e., at very large χ , the region above the pole is actually compressed by the inserted material (see Figure 6d for $\chi=1000$ where $\bar{\sigma}(\dot{\bar{\epsilon}})/\sigma_o = 1.01$). This phenomenon limits the reduction in strength of the

composite, because the compressive stresses retard further diffusional mass transport to the pole.

DISCUSSION

It has been shown that the loss of strength due to interface slip and mass transport depends on the dimensionless groups ξ and χ defined by eqs. (14) and (26) respectively. The composite relative strength decreases monotonically with increasing ξ or χ . An asymptotic strength, often less than that of the matrix material alone, is found for the composite when either ξ alone or both ξ and χ become infinitely large. If slip is controlled by short range diffusion, ξ is inversely proportional to the square of an interface roughness scale length l and the size R of the reinforcement. On the other hand, the long range diffusion group χ is inversely proportional to the volume of the reinforcement, i. e. R^3 . Therefore, if slip is controlled by short range diffusion, ξ is typically very much larger than χ since the roughness is almost always tiny compared to the particle size. Consequently, if diffusional mass transport is enhanced at high temperature, slip will be the phenomenon which shows up first as the temperature is raised. Depending upon the degree of material nonlinearity and the resistance to shear at the interface, slip alone may knock down the relative strength of the composite to approximately the strength of the matrix material alone. Additional long range diffusive relaxation can, in the extreme, bring the relative strength down to 75% of the matrix strength.

A reinforcement size effect is introduced to the composite creep behavior by both interface diffusive slip and mass transport. This can be assessed through the parameters ξ and χ . The larger the reinforcement, the lower ξ and χ are and thereby, the stronger the composite is. Note that the

reinforcement size has a much stronger effect through long range mass transport ($1/R^3$ in χ) than through slip ($1/R$ in ξ). However, in the case of both mechanisms, small reinforcements are undesirable if strength is imparted by continuum constraint and if slip or interface diffusion are active. On the other hand, large reinforcements are susceptible to cracking which would tend to counter the advantage of size in retarding slip and diffusive relaxation. Hence, a coupled analysis of slip and diffusion along with particle cracking is needed in order to address the net effects of reinforcement size.

The temperature dependence of the composite strength depends on the parameters μ , \mathcal{D} and $B = \dot{\epsilon}_0 / \sigma_0^n$. All three are characterized typically by an exponential dependence on an activation energy Q divided by KT (Frost and Ashby, (1982)). Ratios like \mathcal{D}/B depend exponentially on temperature through $\Delta Q/KT$ where ΔQ is the difference in activation energies for the two mechanisms associated with the parameters in the ratio. As a result, the difference ΔQ determines whether \mathcal{D}/B is an increasing or decreasing function of temperature. Thus eqs. (14) and (26) provide the temperature dependences of ξ and χ via μ/B and \mathcal{D}/B . Consequently the composite relative strength may increase or decrease with temperature. In order to estimate qualitatively the effects of temperature in a specific system one needs precise information on the magnitude and temperature dependence of \mathcal{D} and μ along the interface. Such information can only be obtained experimentally and few data are available.

CLOSURE

A model has been developed that shows that interface slip and long range interface diffusion can eliminate the constraint strengthening that rigid particulate reinforcements impart to composite materials with creeping

matrices. Two dimensionless groups have been introduced to characterize the strength degrading mechanisms. Both groups can depend on interface diffusion if slip is controlled by short range mass transport. Consequently, both can depend on the interface diffusion constant \mathcal{D} . The relative creep resistance decreases monotonically with increasing values of the dimensionless parameters and thus with \mathcal{D} . Large reinforcements provide stronger resistance to creep flow than small particles if slip or diffusive mass transport occur at the interface, because the dimensionless parameters depend inversely on particle size

APPENDIX A: POWER DISSIPATED IN DIFFUSION

The work rate that the normal interface stress σ_n does on a virtual variation δv_n of the separation velocity v_n along the interface is

$$P = \int_{S_i} \sigma_n \delta v_n dS \quad (A1)$$

Using eq. (22) to describe the variation δv_n in terms of the variation δj and substituting into eq. (A1), one finds for the spherical particle of Figure 8

$$\begin{aligned} P &= - \int_0^{s_f} \sigma_n \frac{1}{\sin\left(\frac{s}{R}\right)} \frac{d}{ds} \left(\delta j \sin\left(\frac{s}{R}\right) \right) 2\pi R \sin\left(\frac{s}{R}\right) ds = \\ &= -2\pi R \int_0^{s_f} \sigma_n d \left(\delta j \sin\left(\frac{s}{R}\right) \right) = \\ &= -2\pi R \sigma_n \delta j \sin\left(\frac{s}{R}\right) \Big|_0^{s_f} + 2\pi R \int_0^{s_f} \delta j \sin\left(\frac{s}{R}\right) \frac{d\sigma_n}{ds} ds \end{aligned} \quad (A2)$$

where $s_f = \pi R/2$. Eq. (23) dictates that $\delta j(0) = \delta j(s_f) = 0$. Then with use of eq.

(21) one may recast eq. (A2) as follows

$$\begin{aligned} P &= 2\pi R \int_0^{s_f} \delta j \frac{1}{\mathcal{D}} j \sin\left(\frac{s}{R}\right) ds \\ &= \int_{S_i} \delta j \frac{1}{\mathcal{D}} j dS \\ &= \delta U_d[\underline{v}] \end{aligned} \quad (A3)$$

by means of eq.(25).

APPENDIX B: DIFFUSIONAL TERMS AND THE FINITE ELEMENT METHOD

Integrating eq. (22), one finds with use of eq. (23)

$$j(s) = -\frac{g(s)}{\sin\left(\frac{s}{R}\right)} \quad (\text{B1})$$

where

$$g(s) = \int_0^s v_n(s') \sin\left(\frac{s'}{R}\right) ds' \quad (\text{B2})$$

At the pole of the particle, $s = J$, j is zero because for any value of $v_n(s)$ the numerator $g(s)$ in eq. (B1) goes to zero faster than the denominator $\sin\left(\frac{s}{R}\right)$. Therefore, with $j(s)$ given by eqs. (B1) and (B2), condition (23) may be restated as

$$g(s_f) = 0 \quad (\text{B3})$$

The normal velocity v_n along the interface is given as

$$v_n = v_r \sin\left(\frac{s}{R}\right) + v_z \cos\left(\frac{s}{R}\right) \quad (\text{B4})$$

where v_r and v_z are the velocity components in the r and z directions (see Figure 8). Following Needleman and Rice (1980), let us consider the finite element interpolation scheme for the velocity

$$\begin{aligned} v_r &= \sum_{i=1}^N \phi_i(s) v_i^r \\ v_z &= \sum_{i=1}^N \phi_i(s) v_i^z \end{aligned} \quad (\text{B5})$$

where v_i^r and v_i^z are the nodal velocity components of node i on the interface, N is the total number of interface nodes and $\phi_i(s)$ is the standard linear interpolation function along the element side on the interface such that

$$\phi_i(s) = \begin{cases} \frac{s - s_{i-1}}{s_i - s_{i-1}} & \text{for } s_{i-1} \leq s \leq s_i \\ \frac{s_{i+1} - s}{s_{i+1} - s_i} & \text{for } s_i \leq s \leq s_{i+1} \\ 0 & \text{for } s < s_{i-1} \quad \text{or} \quad s > s_{i+1} \end{cases} \quad (\text{B6})$$

Function $\phi_i(s)$ describes a linear interpolation along the interface side of the 8-noded quadratic isoparametric element that was used to model the creep deformation of the matrix. The node at s_i represents the middle node whereas those at s_{i-1} and s_{i+1} represent the two corner nodes of the element. For compatible deformation, velocity of the middle node is required to be the mean of the two corner node velocities. The function $g(s)$ can be expressed in terms of nodal velocities by means of eqs. (B4) and (B5)

$$g(s) = \sum_{i=1}^N (g_i^r(s) v_i^r(s) + g_i^z(s) v_i^z(s)) \quad (\text{B7})$$

where

$$g_i^r(s) = \int_0^s \phi_i(s') \sin^2\left(\frac{s'}{R}\right) ds' \quad (\text{B8})$$

$$g_i^z(s) = \int_0^s \phi_i(s') \sin\left(\frac{s'}{R}\right) \cos\left(\frac{s'}{R}\right) ds' \quad (\text{B9})$$

The functions $g_i^r(s)$ and $g_i^z(s)$ are computed analytically by using eq. (B6). Generalizing eq. (B7), one writes eq. (B1) as follows

$$j(s) = \frac{1}{\sin\left(\frac{s}{R}\right)} \sum_{i=1}^{2N} g_i(s) v_i(s) \quad (\text{B10})$$

where $g_i(s)$ is either of $g_i^r(s)$ or $g_i^z(s)$, and $v_i(s)$ is either of $v_i^r(s)$ or $v_i^z(s)$. Substituting eq. (B10) into eq. (25), one finds the finite element method expression for functional $U_d[\underline{v}]$ which is

$$U_d[\underline{v}] = v_i K_{ij}^d v_j \quad (\text{B11})$$

where

$$K_{ij}^d = \frac{\pi R}{\mathcal{D}} \int_0^{s_r} \frac{g_i(s) g_j(s)}{\sin\left(\frac{s}{R}\right)} ds \quad (\text{B12})$$

Summation from 1 to $2N$ is implied over a repeated index. Matrix K^d is symmetric but not banded. However, it is constant, independent of the velocity \underline{v} , and as such it is only computed once for any given \mathcal{D} and particle shape. The matrix K^d is added to the other finite element stiffness contributions arising from eq. (24).

ACKNOWLEDGMENT

This research was supported by the DARPA University Research Initiative at the University of California, Santa Barbara (ONR Contract N00014-86-K0753). The calculations on an FPS 500EA were made possible by FPS Computing through the UCSB Industrial Liaison Program.

REFERENCES

- Bao, G., Hutchinson, J. W. and McMeeking, R. M. (1991), "Particle reinforcement of ductile matrices against plastic flow and creep," *Acta Metall.* 39, 1871-1882.
- Evans, A. G., Hutchinson, J. W. and McMeeking, R. M. (1991), "Stress-strain behavior of metal matrix composites with discontinuous reinforcements," *Script. Met.* 25, 3-8.
- Frost, H. J. and Ashby, M. F. (1982), Deformation Mechanism Maps, Pergamon Press, Oxford.
- Herring, C. (1950), "Diffusional viscosity of a polycrystalline solid," *J. Appl. Phys.* 21, 437-447.
- Mura, T. (1982), Micromechanics of Defects in Solids, M. Nijhoff, The Hague.
- Needleman, A. and Rice, J. R. (1980), "Plastic creep flow effects in the diffusive cavitation of grain boundaries," *Acta Metall.* 28, 1315-1332.
- Raj, R. and Ashby, M. F. (1971), "On grain boundary sliding and diffusional creep," *Met. Trans.* 2, 1113-1127.
- Rosler, J., Bao, G. and Evans, A. G. (1991), "The effects of diffusional relaxation on the creep strength of composites," *Acta Metall.* 39, 2733-2738.

Rosler, J., Valencia, J. J., Levi, C. G., Evans, A. G. and Mehrabian, R. (1990), "The high temperature behavior of TiAl containing carbide reinforcements," *Mat. Res. Soc. Proc.* 194, 241-248.

Sofronis, P. and McMeeking, R. M. (1991), "Creep of a power law material containing spherical voids," To appear in *J. Appl. Mech.*

FIGURE CAPTIONS

1. Experimentally measured relative strength λ of γ -TiAl matrix composite reinforced with Ti_2AlC platelets as a function of temperature (Rosler et al. (1990)). The parameter λ gives the composite strength $\bar{\sigma}$ normalized by the matrix strength σ at the same strain rate.
2. The axisymmetric cylindrical unit cell loaded with an average axial stress $\bar{\sigma}$ and experiencing a strain rate $\dot{\bar{\epsilon}}$ in uniaxial tension.
3. Models for interface slip. An applied shear stress τ_s causes a sliding velocity v_s ; i) no slip interface; ii) interface slip as a result of a thin layer of weak material; iii) interface slip due to short range diffusion.
4. Summary of the boundary value problem with the no slip condition ($\mu = \infty$) or the linear slip rheology.
5. Composite relative strength $\lambda = \bar{\sigma}(\dot{\bar{\epsilon}}) / \sigma(\dot{\bar{\epsilon}})$ as a function of the dimensionless slip parameter ξ . When $\xi = 0$, there is no slip whereas when $\xi = \infty$ there is no interface shear drag.
6. Contours of normalized hydrostatic stress $\sigma_{kk} / 3\sigma_o$ for the same strain rate and matrix material; a) when the interface has no slip or diffusive mass transport; b) when the interface slips freely but there is no mass transport; c) when the interface slips freely and there is interface mass transport by diffusion; d) when the interface slips freely and mass transport by diffusion is very fast.

7. Long range mass transport at the interface by diffusion
8. Summary of the boundary value problem with free slip and long range diffusion at the interface
9. Composite relative strength $\lambda = \overline{\sigma}(\dot{\tilde{\epsilon}}) / \sigma(\dot{\tilde{\epsilon}})$ as a function of the dimensionless long range diffusion parameter χ . When $\chi = 0$, there is no interface mass transport. When χ is large, mass transport on the interface is very fast.

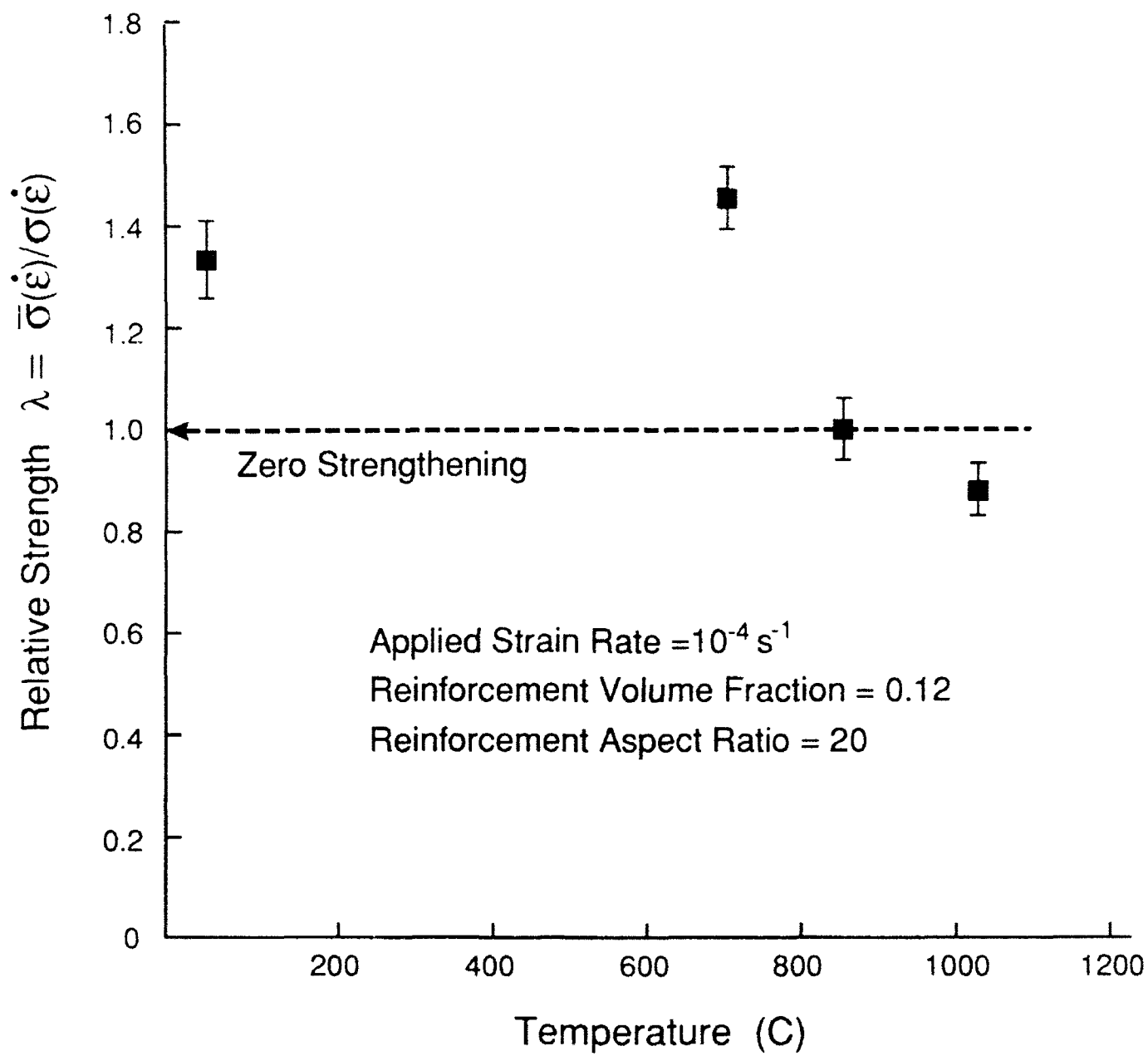


Figure 1

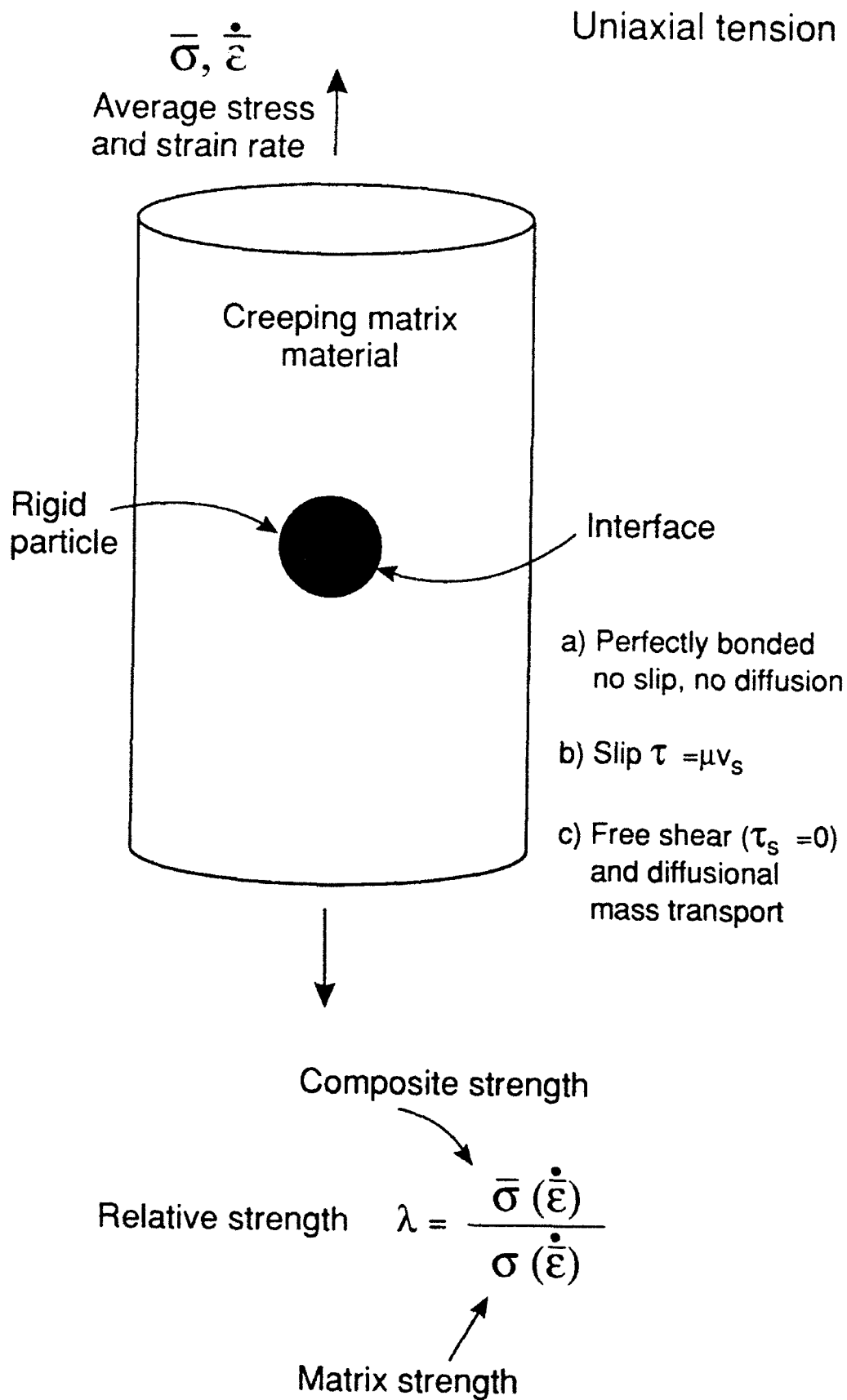


Figure 2

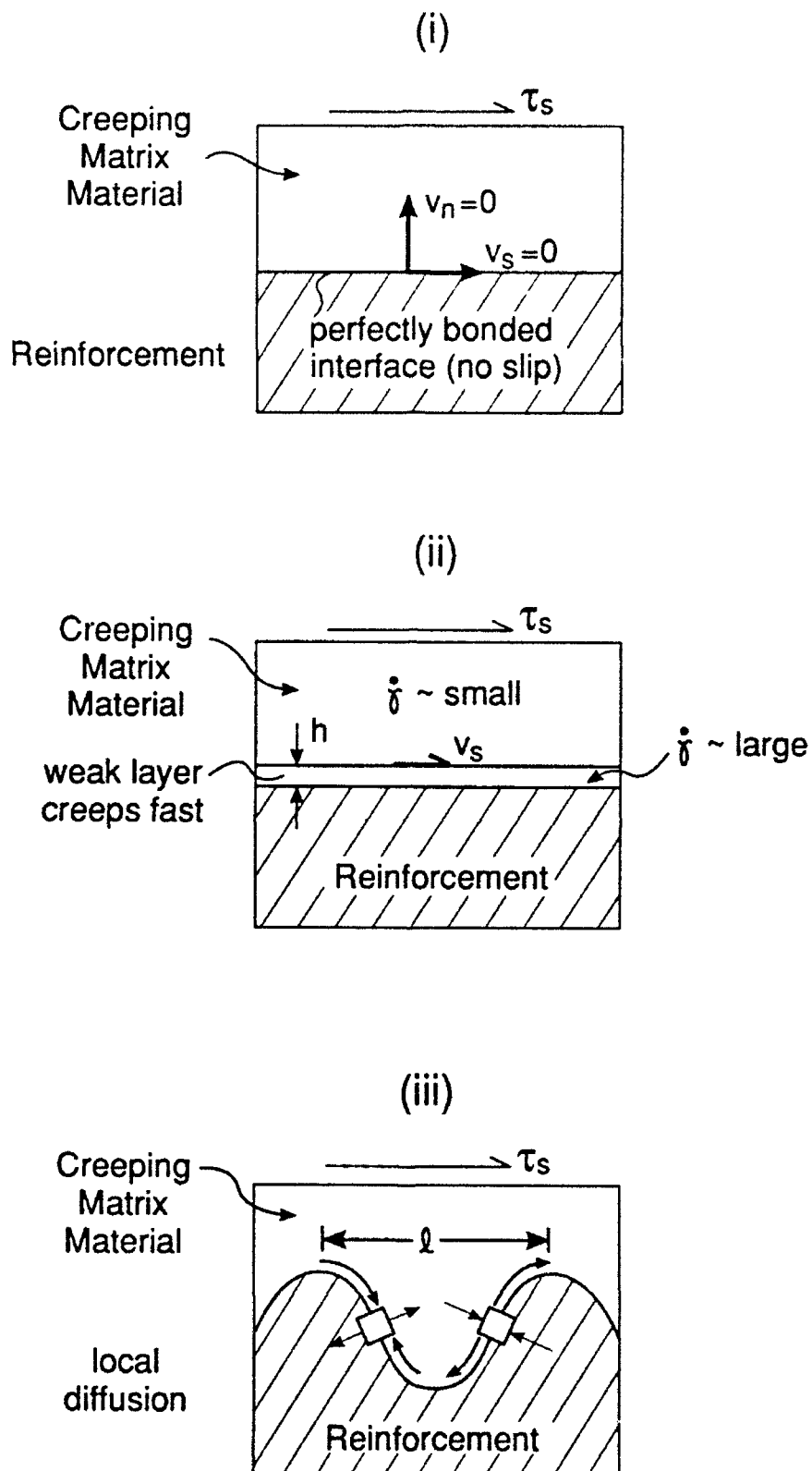


Figure 3

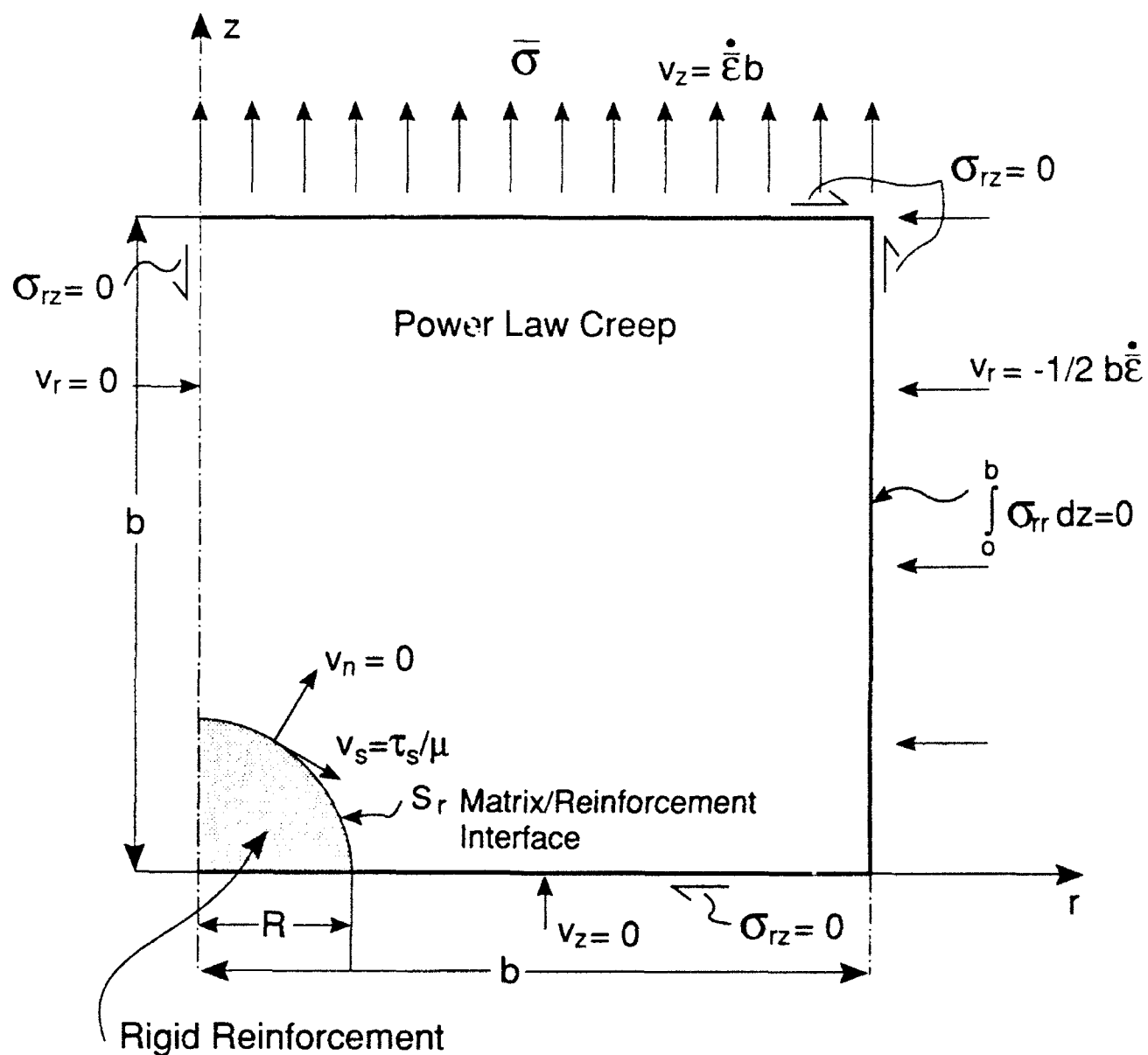


Figure 4

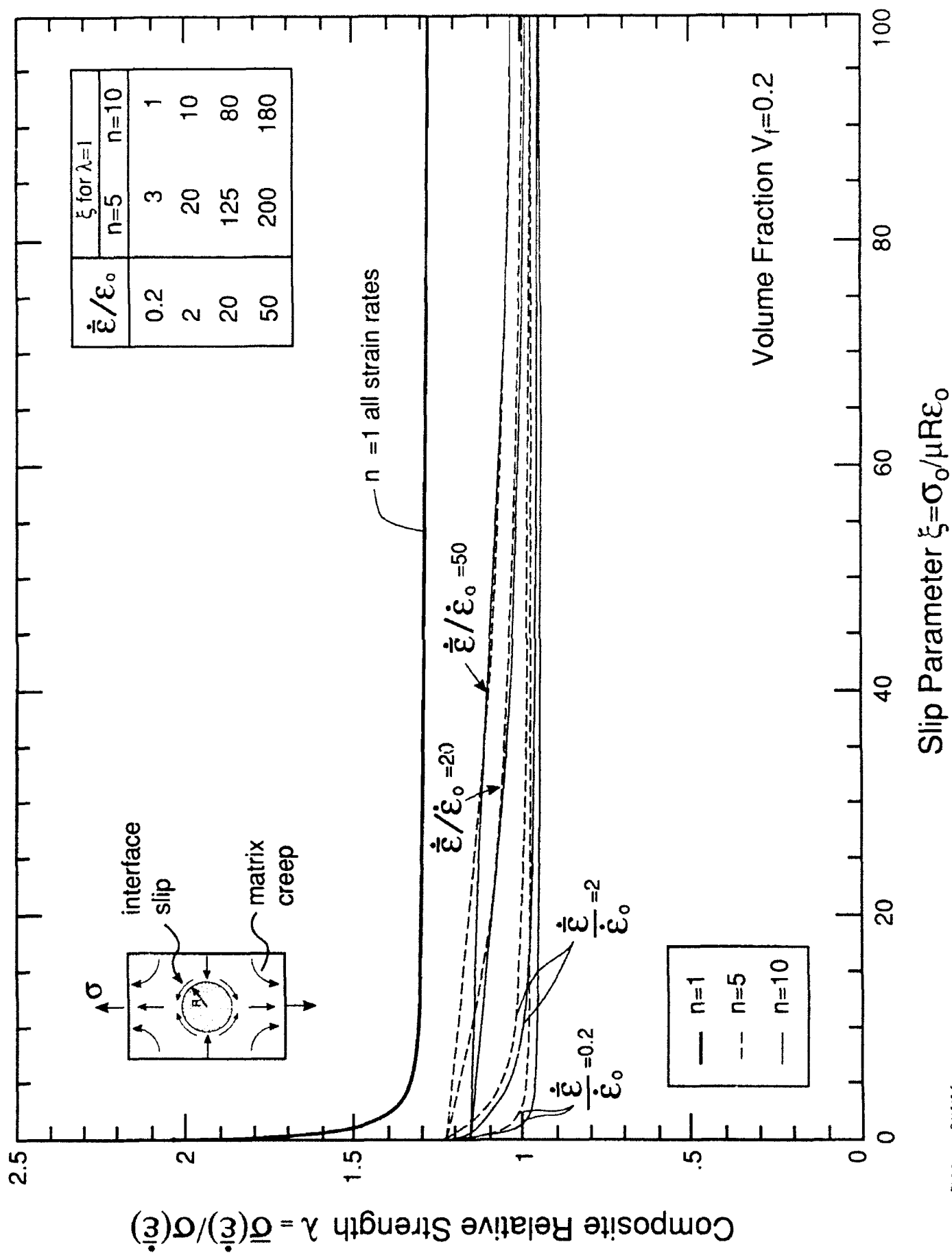
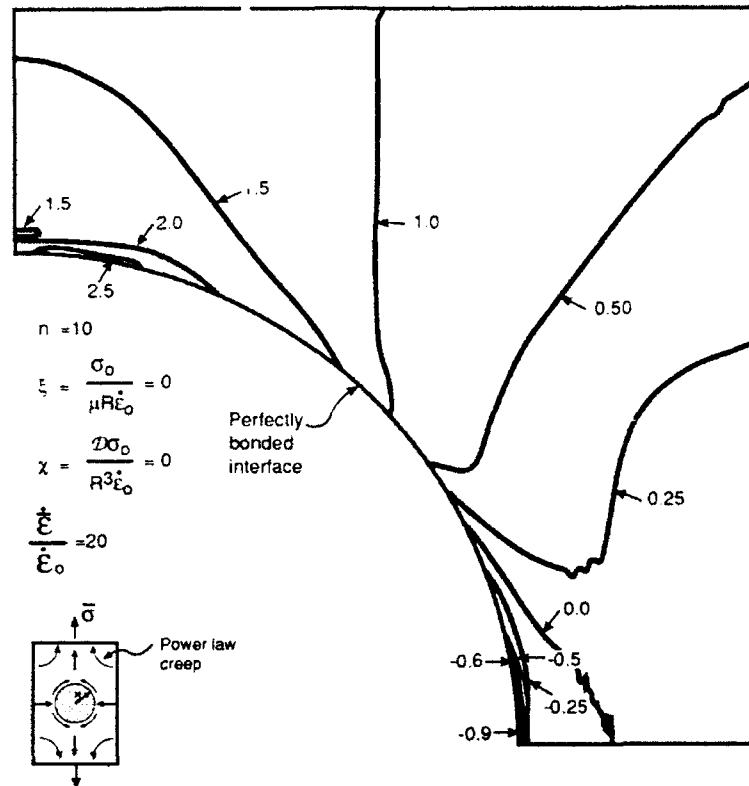


Figure 5

a



b

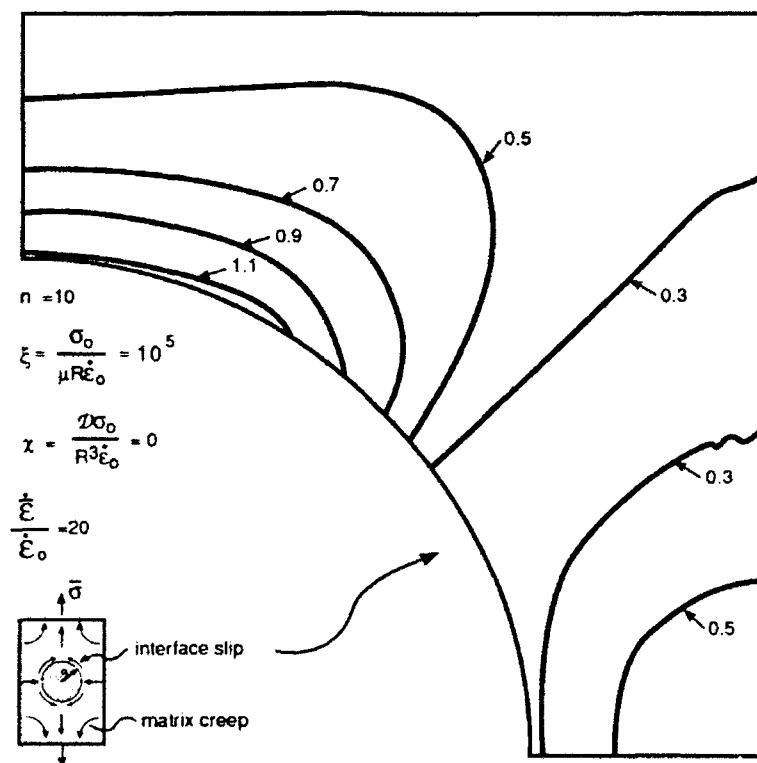
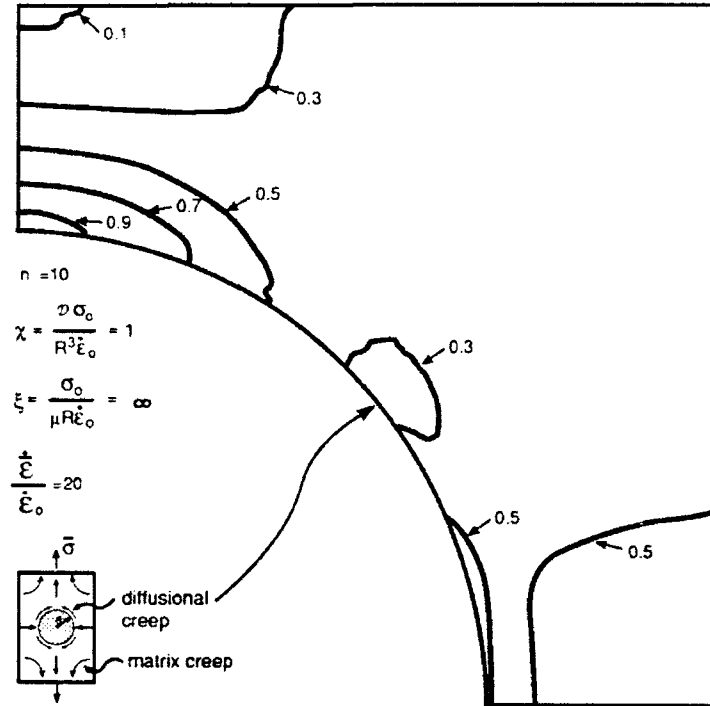


Figure 6

c



d

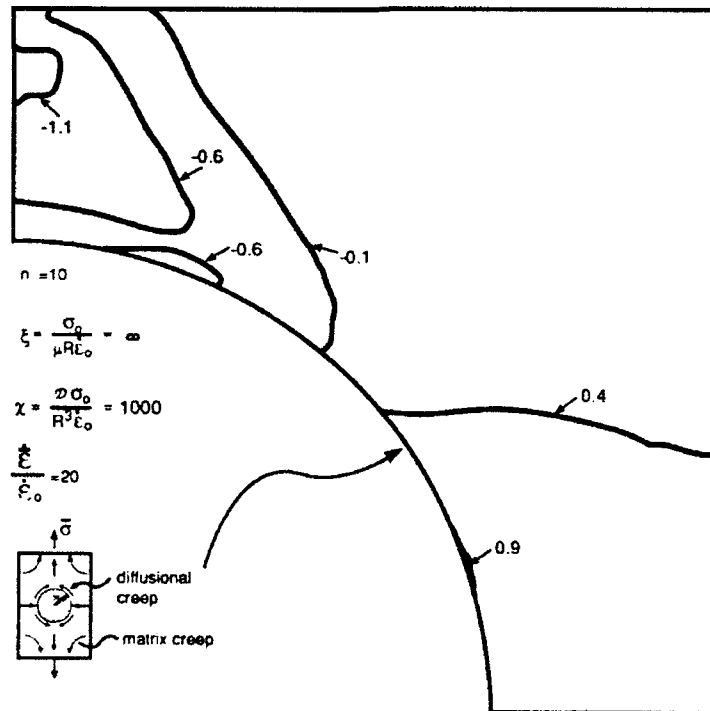


Figure 6

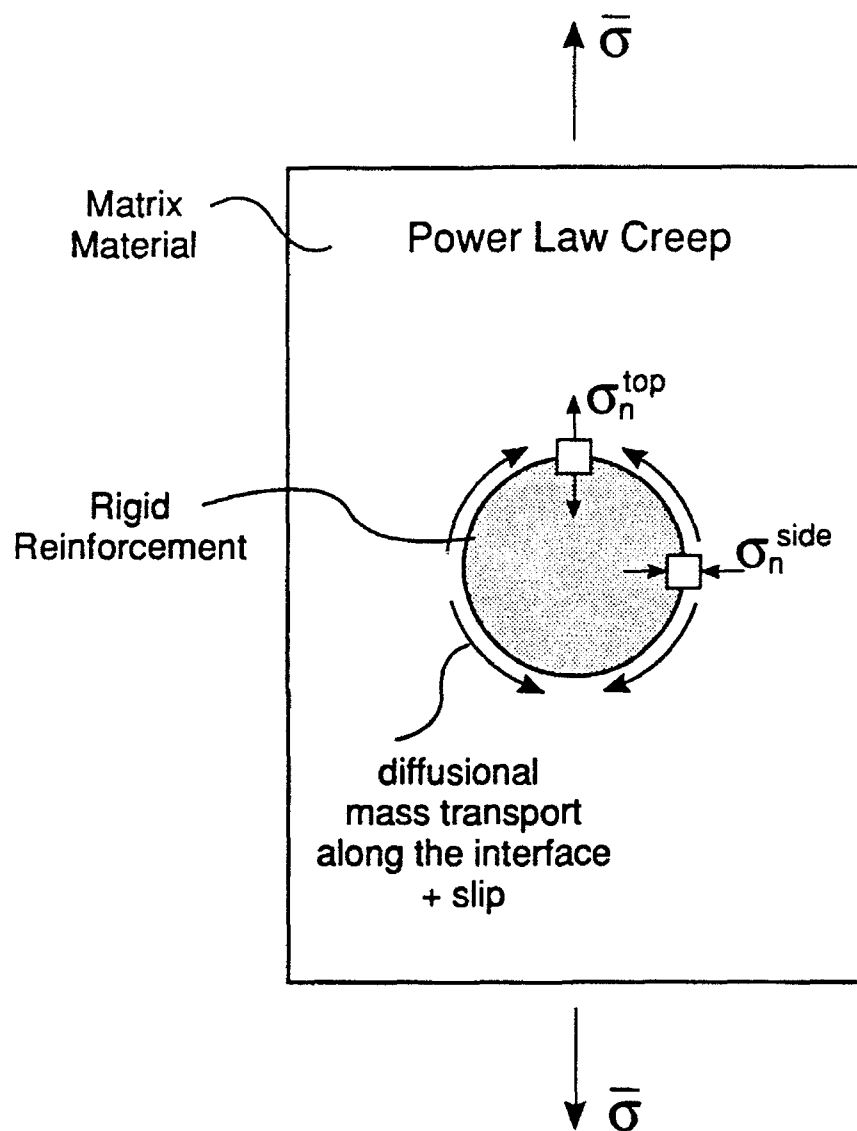


Figure 7

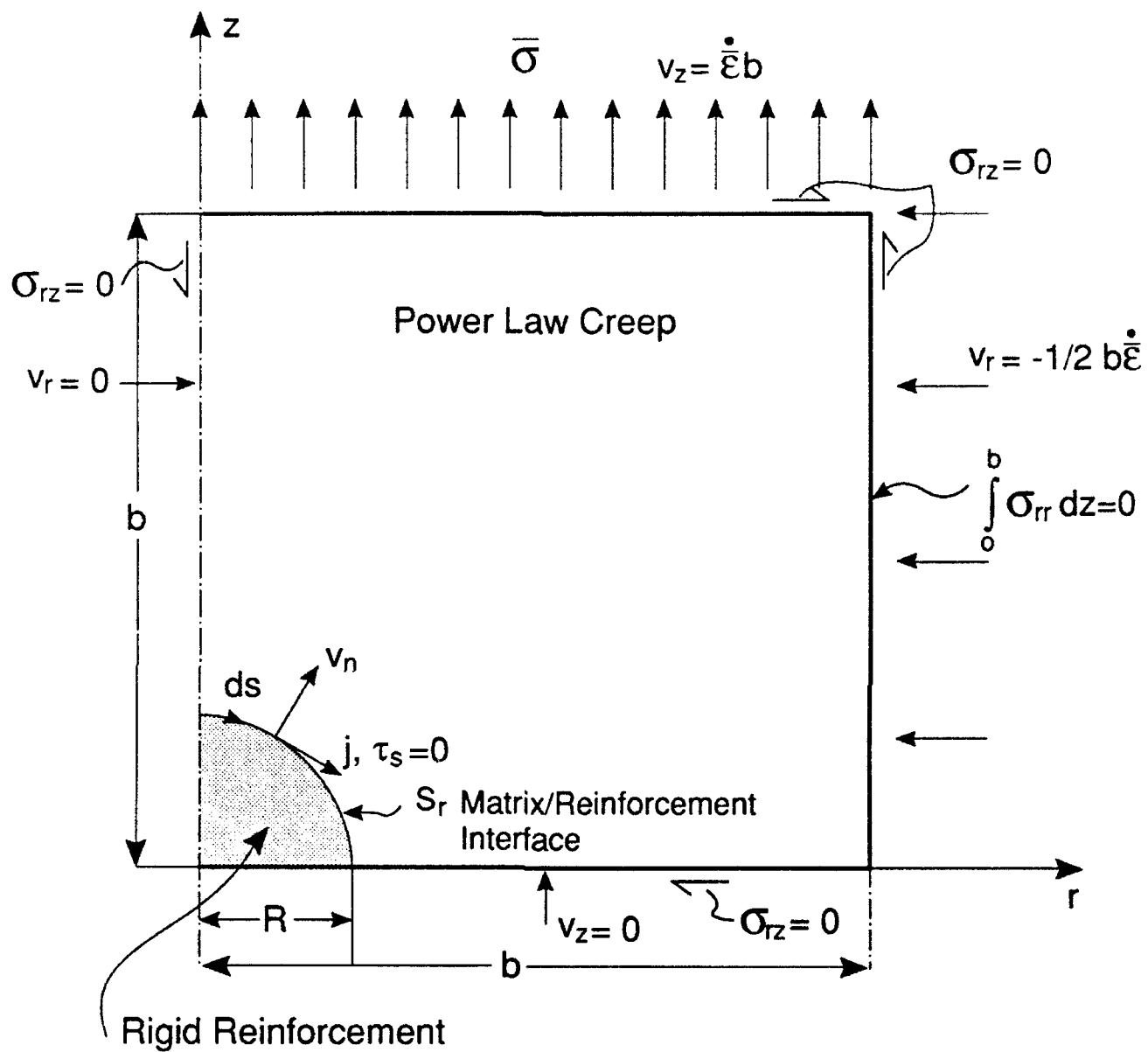


Figure 8

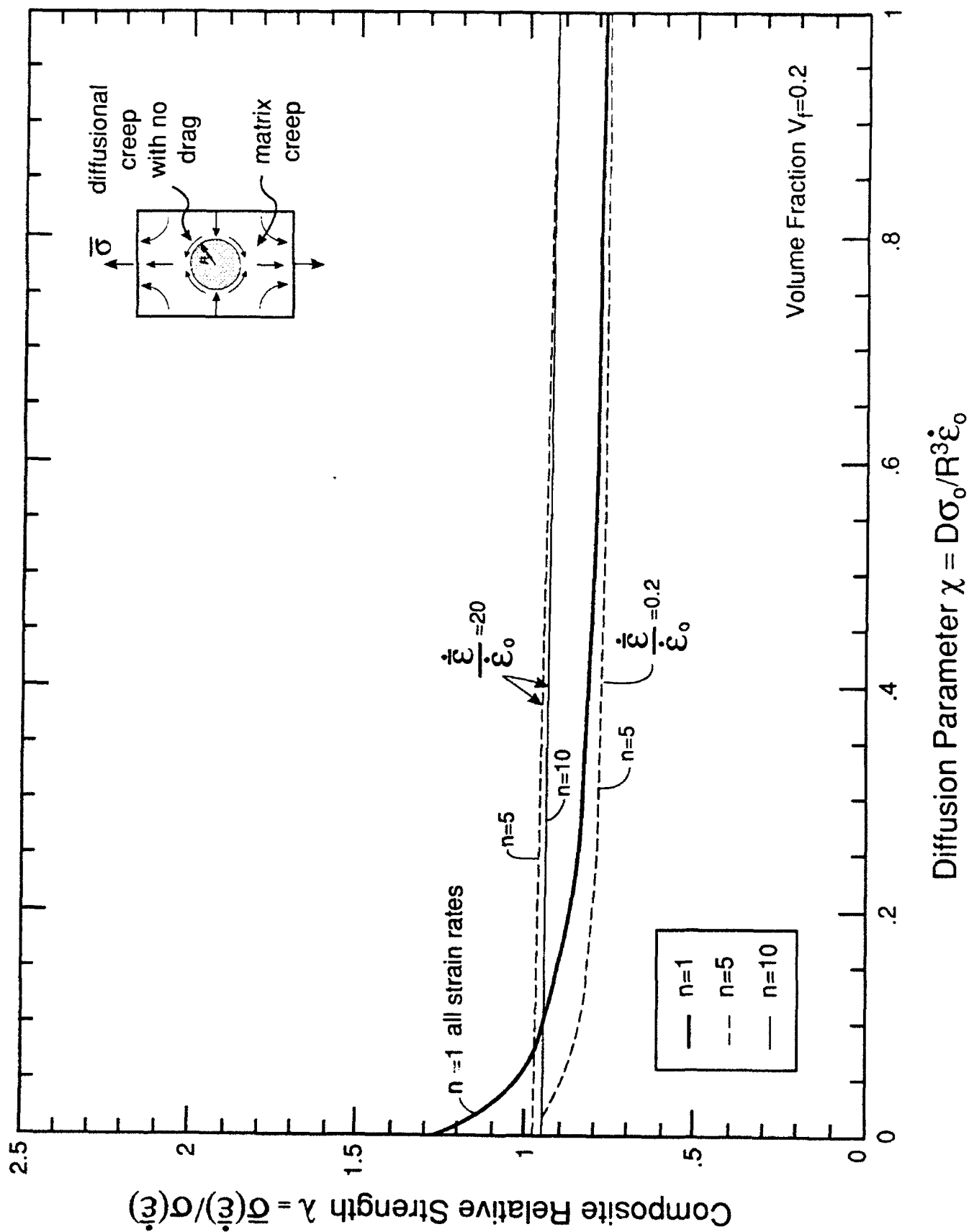
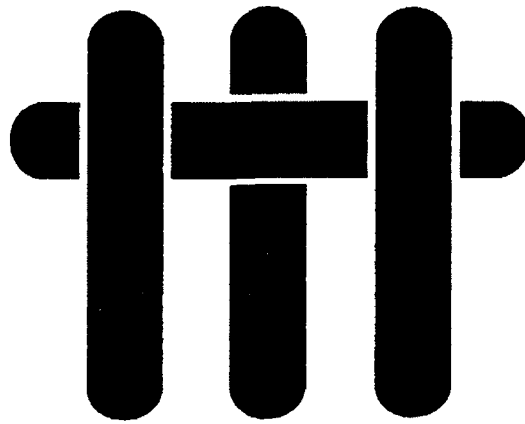


Figure 9

M A T E R I A L S



POWER LAW CREEP OF A COMPOSITE MATERIAL CONTAINING DISCONTINUOUS RIGID ALIGNED FIBERS

Robert M. McMeeking

Department of Materials and Department of Mechanical Engineering
University of California, Santa Barbara, California 93106

Submitted to International Journal of Solids and Structures

December, 1991

Revised, September 1992

Summary: An asymptotic analysis is presented for the power law creep of a matrix containing discontinuous rigid aligned fibers. The fibers analyzed have a high aspect ratio. As a result, the fiber length is much greater than both the fiber diameter and the spacing between neighboring fibers. For this situation, flow around the fiber ends can be neglected when the creep strength is being calculated. When the matrix is not slipping on the fiber surface or is nearly stuck, shearing flow dominates the behavior. The radial gradient of shear stress is balanced by the axial gradient of hydrostatic stress. Longitudinal, radial and circumferential deviatoric stresses are negligible. The resulting power law creep rate of the composite material is inversely proportional to the fiber aspect ratio raised to the power $1 + 1/n$ where n is the creep index. The fiber volume fraction also influences the creep rate. When the matrix slips freely on the fiber surface, or nearly so, stretching dominates the matrix flow. In this situation, the composite creep strength is not much better than the unreinforced matrix.

List of Symbols

Note: superposed carat indicates a physical variable; a symbol without a carat is normalized and dimensionless; e.g. \hat{a} is the fiber radius; a is \hat{a}/\hat{b} where \hat{b} is the unit cell radius.

\hat{a}	fiber radius
\hat{b}	unit cell radius
B	matrix creep rheology parameter
D	function of geometry and creep parameters; controls the creep strength
$\hat{\epsilon}$	axial strain rate
F	function for radial distribution of axial velocity
G	function controlling hydrostatic stress distribution
\hat{L}	fiber half length
m	interface drag exponent

n	matrix creep exponent
N	higher order term in creep strength
\hat{r}	radial coordinate
S	relative creep strength of composite material
\tilde{S}	scaled creep strength in excess of matrix strength
\tilde{S}_k	same as \tilde{S} evaluated from ref. [1]
\bar{S}	average radial stress
\underline{S}	stress deviator
\hat{v}	velocity
V_f	fiber volume fraction
\hat{z}	axial coordinate
α	\hat{L}/\hat{a} fiber aspect ratio
δ	\hat{b}/\hat{L} small parameter
ϵ_e	effective strain rate
η	$= z/\delta$
λ	$\hat{L}/\hat{b} = 1/\delta$
$\hat{\mu}$	interface drag parameter
ρ	integration variable
$\hat{\sigma}$	hydrostatic stress
$\hat{\underline{\sigma}}$	stress tensor
$\hat{\sigma}_a$	macroscopic axial stress
$\hat{\sigma}_f$	fiber axial stress
$\hat{\sigma}_m$	matrix axial stress
$\hat{\sigma}_c$	tensile equivalent stress
$\Sigma = (\hat{e}/B\delta)^{1/n}$	parameter for stress normalization
θ	circumferential coordinate

Introduction

Cell models are popular and effective for estimating the creep strength of metal matrix fiber reinforced composites and such an approach has been used by Kelly and Street (1972), Dragone and Nix (1990), Goto and McLean (1991) and Bao, Hutchinson and McMeeking (1991). For aligned discontinuous fibers, an individual reinforcement is considered embedded in a unit cell of the matrix material such that the volume ratio of fiber to matrix in the unit cell equals the average ratio in the composite material. Boundary conditions to cause the deformation are imposed on the perimeter of the unit cell to enforce periodicity and symmetry. For the creep response to tensile stresses aligned with the axis of circular fibers, it is sufficient to calculate the behavior of an axisymmetric cell such as shown in Fig. 1. The deformation imposed on the cell forces it to retain its circular cylindrical shape. Each point on the surface of the cell is free of shear traction. The average transverse stress on the cell is zero and appropriate conditions are imposed at the interface between the fiber and the matrix material. In the annotations on Fig. 1 the conditions appropriate to an interface around a rigid fiber without debonds but with a nonlinear viscous sliding behavior are stated. In general, however, any physical assumption can be incorporated into the cell model such as fiber elasticity or creep, debonding of the interface etc..

Cell models usually require a numerical treatment as undertaken by Dragone and Nix (1990) and Bao et al. (1991). However, in certain circumstances an approximate model is accurate and can be analyzed without recourse to complete numerical treatment. This approach has been used by Kelly and Street (1972) and Goto and McLean (1991). One such circumstance is when the fibers are aligned and have an aspect ratio which is high and a volume fraction that is moderate to high. Then the matrix segment around the fiber (with section ABCD in Fig. 1) is slender and can be readily analyzed with approximate flow fields. In addition, the flow in the remaining matrix segment at the fiber ends does not have to be analyzed accurately because it contributes little to the yield or creep strength compared to the matrix around the fiber. That is,

when the fiber aspect ratio is high, the energy dissipation in the fiber end regions during matrix creep is negligible compared to the energy dissipation rate in the matrix surrounding the fiber. The creep strength is directly related to the energy dissipation rate, so it can be analyzed by calculating the major contributions to the energy dissipation rate. In this paper, that is achieved by analyzing the creeping flow of the matrix adjacent to the fiber sides. If this approach is unsatisfactory in a particular case, it can always be rectified by considering longer fibers, thereby making the fiber end regions relatively less important. In this sense, the analysis can always be justified by taking the asymptotic limit of extremely long fibers. However, the analysis is proposed as being justifiable for fibers with a range of finite aspect ratios.

The issue has been studied by Bao et al. (1990) for layered composites with perfectly plastic matrices. Bao et al. found that less than 10% of the yield strength is due to the end region when the volume fraction of rigid reinforcements is 25% and their aspect ratio is 100. For smaller aspect ratios the contribution from the end region is a higher fraction but can be modelled in an ad hoc manner as was demonstrated by Bao et al. (1990). In addition, the aspect ratio of the cell relative to the aspect ratio of the fiber is known to affect the prediction of strength significantly which was demonstrated by Bao et al. (1991). Thus, it is likely that the choice of aspect ratio of the cell will also influence how much of the strength is due to the matrix material around the fiber compared to the amount due to the material at the fiber ends. For example, choosing the aspect ratio of the cell to be the same as the aspect ratio of the fiber, as Bao et al. (1990) did, is likely to exaggerate the importance of the fiber end region for high aspect ratio cases. A perhaps more sensible choice, in which the distance between the fiber and the cell edge is the same at the end and on the side is likely to diminish the importance of the matrix at the fiber ends and so the 10% contribution mentioned above is probably an overestimate. At the other extreme of the rheology, namely a linearly viscous matrix, an argument can be made that as well as fiber end regions occupying relatively small volumes of the total composite microstructure, any nonuniformity of flow which they induce will be confined to the fiber end

region by a St. Venant effect. Thus, for all types of matrix an analysis concerned only with the matrix material surrounding the fibers circumferentially can be justified in certain cases.

In particular, the problem of a high aspect ratio rigid fiber embedded in a power law creeping matrix can be analyzed in terms of the matrix material around the fiber. The cell shown in Fig. 1 will be used. The fiber is bonded to the matrix so that the radial velocity at the fiber is zero. However, it is assumed that the bond, or thin layer of interphase material at the interface, has a power law rheology of its own which allows slip of the matrix relative to the fiber. The end of the fiber is bonded strongly to the matrix as well, so that matrix incompressibility forces a net matrix flow parallel to the fiber. The axisymmetric quasistatic creeping response to an axial stress is considered. A power law rheology is assumed so that the analysis represents the steady state creep of metal or ceramic matrices around rigid (e.g. ceramic) fibers.

Problem Formulation

The domain of the problem is the axisymmetric region with section ABCD in Fig. 1 ($\hat{a} \leq \hat{r} \leq \hat{b}$; $0 \leq \hat{z} \leq \hat{L}$). In cylindrical polar coordinates, the governing equilibrium equations neglecting inertia and body forces are

$$\frac{\partial \sigma_{rr}}{\partial r} + \frac{\sigma_{rr} - \sigma_{\theta\theta}}{r} + \delta \frac{\partial \sigma_{rz}}{\partial z} = 0 \quad (1)$$

$$\frac{\partial \sigma_{rz}}{\partial r} + \frac{\sigma_{rz}}{r} + \delta \frac{\partial \sigma_{zz}}{\partial z} = 0 \quad (2)$$

where $\underline{\sigma}$ is a scaled stress such that

$$\hat{\underline{\sigma}} = \Sigma \underline{\sigma} \quad (3)$$

with $\hat{\underline{\sigma}}$ being the Cauchy stress and Σ a scaling parameter to be discussed later. The components r and z are scaled measures of position defined by

$$\hat{r} = \hat{b} r \quad (4)$$

and
$$\hat{z} = \hat{L} z \quad (5)$$

where \hat{r} , \hat{z} , \hat{b} and \hat{L} are specified in Fig. 1. The parameter δ is such that

$$\delta = \hat{b}/\hat{L} \quad (6)$$

and in the problems to be analyzed is much less than 1. The choice of differential scaling for r and z introduces a coordinate stretching transformation (van Dyke, 1975) which will be useful in the subsequent analysis.

The matrix creeps with a power law incompressible rheology given by

$$\hat{\underline{e}}_{ij} = \frac{3}{2} B \hat{\sigma}_e^{n-1} \hat{S}_{ij} \quad (7)$$

where $\hat{\underline{e}}$ is the strain rate, $\hat{\underline{S}}$ is the deviatoric stress given by

$$\hat{S}_{ij} = \hat{\sigma}_{ij} - \hat{\sigma} \delta_{ij} \quad (8)$$

where $\hat{\sigma} (= \hat{\sigma}_{kk}/3)$ is the hydrostatic part of the stress, $\hat{\sigma}_e$ is the effective stress such that

$$\hat{\sigma}_e = \sqrt{\frac{3}{2} \hat{S}_{ij} \hat{S}_{ij}} \quad (9)$$

and B is a material constant which is, however, dependent on temperature. Note that in uniaxial stress the axial strain rate equals B times the n th power of the stress. In terms of scaled variables, the creep law can be written as

$$\frac{\partial v_r}{\partial r} = \frac{3}{2} \sigma_e^{n-1} S_{rr} \quad (10)$$

$$\frac{v_r}{r} = \frac{3}{2} \sigma_e^{n-1} S_{\theta\theta} \quad (11)$$

$$\delta \frac{\partial v_z}{\partial z} = \frac{3}{2} \sigma_e^{n-1} S_{zz} \quad (12)$$

$$\frac{\partial v_z}{\partial r} + \delta \frac{\partial v_r}{\partial z} = 3 \sigma_e^{n-1} \sigma_{rz} \quad (13)$$

where $\hat{\underline{v}}$ is the velocity and

$$\hat{\underline{v}} = \hat{b} B \Sigma^n \underline{v}. \quad (14)$$

On AB ($z = 0$) the boundary conditions by symmetry are

$$v_z(r, 0) = 0 \quad (15)$$

$$\sigma_{rz}(r, 0) = 0. \quad (16)$$

On AD ($r = a = \hat{a}/\hat{b}$) one boundary condition is

$$v_r(a, z) = 0 \quad (17)$$

while the slip condition (see Fig. 1) becomes

$$v_z(a, z) = \sigma_{rz}^m / \mu \quad (18)$$

where

$$\mu = \hat{\mu} B \hat{b} \Sigma^{n-m}. \quad (19)$$

and $\hat{\mu}$ is a slip parameter for the interface. It should be noted that the last boundary condition can represent a variety of physical situations. One possibility is that there is a thin but distinct interphase of thickness t so that $V_z(a, z)/\hat{t}$ is the shear strain rate in the interphase. Eq. (18) then implies that the interphase is subject to power law creep but with an exponent m and the coefficient in the creep law is $1/(3^{\frac{m+1}{2}} \hat{\mu} \hat{t})$ replacing B in eq. (7). Another possibility is that there is no interphase but instead the fiber has a rough surface over which the matrix must flow even though the bond between the matrix and the fiber is relatively weak in shear. In that case, the index m would equal n and the slip parameter $\hat{\mu}$ would depend on the roughness of the fiber surface which would provide drag.

On BC ($r = 1$) the boundary conditions are

$$\sigma_{rz}(1, z) = 0 \quad (20)$$

and

$$v_r(1, z) = -\frac{1}{2} \delta \quad (21)$$

where

$$\hat{\dot{\epsilon}} = B \sum^n \delta \quad (22)$$

is the axial strain rate. The condition in eq. (21) means that the scaled axial strain rate is equal to δ . This choice is arbitrary, though convenient. As a consequence, eq. (22) establishes \sum in terms of $\hat{\dot{\epsilon}}$, the axial strain rate in physical variables. The boundary condition, eq. (21) states that the unit cell remains a cylinder of uniform diameter. As a result, the normal stress σ_{rr} is not uniformly zero on $r = 1$. However, the average of σ_{rr} on $r = 1$ can be set to zero so that

$$\int_0^1 \sigma_{rr}(1, z) dz = 0 \quad (23)$$

to ensure that the transverse stress is approximately zero. The approximation arises because the cell extends a small distance above C, but that portion is neglected. The boundary condition eq. (23) can be met through adjustment of the hydrostatic stress.

Note that no explicit boundary conditions are posed for CD. The average stress there will be of interest and determines $\hat{\sigma}_a$. The creep strength S of the composite material is defined as the average axial stress in the composite at a given axial strain rate divided by the stress in the matrix alone at the same axial strain rate. That is

$$S = \hat{\sigma}_a(\hat{\dot{\epsilon}})/(\hat{\dot{\epsilon}}/B)^{1/n}. \quad (24)$$

where $\hat{\sigma}_a$ is a function of the axial strain rate $\hat{\dot{\epsilon}}$.

Asymptotic Analysis

A perturbation series solution will be developed. It will have much in common with the outer solution for a plane strain power law squeeze film due to Johnson (1984). In addition, there are boundary layers, but fully matched solutions will not be established in them. In the

outer solution for the fiber problem, the matrix flow is dominated by shearing and the shear stress can be expanded in integer powers of δ , so that

$$\sigma_{rz} = \sigma_{rz}^{(0)} + \delta \sigma_{rz}^{(1)} + O(\delta^2). \quad (25)$$

As a consequence of eq. (13), v_z is $O(1)$ at leading order so

$$v_z = v_z^{(0)} + \delta v_z^{(1)} + O(\delta^2). \quad (26)$$

Incompressibility (i.e. the sum of eq. (10-12)) then implies that

$$v_r = \delta v_r^{(1)} + O(\delta^2). \quad (27)$$

and, apart from σ_{rz} , S_{ij} is $O(\delta)$, so

$$S_{rr} = \delta S_{rr}^{(1)} + O(\delta^2) \quad (28)$$

etc.. Any gradient of σ_{rz} in the r direction must be balanced by a gradient of σ_{zz} in the z direction. For this to be possible, the stress σ_{zz} must be $O(1/\delta)$ so that the contribution of the longitudinal gradient of σ_{zz} to eq. (2) is $O(1)$ which is the same order of magnitude as the contribution of the shear stress gradient in eq. (2). This suggests

$$\sigma = \frac{1}{\delta} \sigma^{(-1)} + \sigma^{(0)} + O(\delta) \quad (29)$$

so that the hydrostatic stress is an order of magnitude larger than the deviatoric stress.

The leading order governing equations can now be stated. With terms of higher order omitted, it is found that eq. (1) gives

$$\frac{\partial \sigma^{(-1)}}{\partial r} = 0 \quad (30)$$

while eq. (2) provides

$$\frac{\partial \sigma_{rz}^{(0)}}{\partial r} + \frac{\sigma_{rz}^{(0)}}{r} + \frac{\partial \sigma^{(-1)}}{\partial z} = 0 \quad (31)$$

The creep relationship of eq. (13) gives

$$\frac{\partial v_z^{(0)}}{\partial r} = 3 \left(\sigma_e^{(0)} \right)^{n-1} \sigma_{rz}^{(0)} \quad (32)$$

where

$$\sigma_e^{(0)} = \sqrt{3} \left| \sigma_{rz}^{(0)} \right| \quad (33)$$

while incompressibility provides

$$\frac{\partial v_r^{(1)}}{\partial r} + \frac{v_r^{(1)}}{r} + \frac{\partial v_z^{(0)}}{\partial z} = 0 \quad (34)$$

Equations (15-23) give the boundary conditions

$$v_z^{(0)}(r, 0) = 0 \quad (35)$$

$$\sigma_{rz}^{(0)}(r, 0) = 0 \quad (36)$$

$$v_r^{(1)}(a, z) = 0 \quad (37)$$

$$v_z^{(0)}(a, z) = (\sigma_{rz}^{(0)})^m / \mu \quad (38)$$

$$v_r^{(1)}(1, z) = -\frac{1}{2} \quad (39)$$

$$\sigma_{rz}^{(0)}(1, z) = 0 \quad (40)$$

$$\text{and} \quad \int_0^1 \sigma^{(-1)}(1, z) dz = 0. \quad (41)$$

Solution. Equation (30) shows that $\sigma^{(-1)}$ is independent of r . Therefore, integration of eq. (31) subject to eq. (40) gives

$$\sigma_{rz}^{(0)} = \frac{1}{2} \left(\frac{1}{r} - r \right) \frac{d\sigma^{(-1)}}{dz}. \quad (42)$$

It will be confirmed that $d\sigma^{(-1)}/dz$ is positive for $z > 0$ and thus so is $\sigma_{rz}^{(0)}$. Consequently eq. (32) shows that

$$\frac{\partial v_z^{(0)}}{\partial r} = \frac{3^{\frac{n+1}{2}}}{2^n} \left(\frac{1}{r} - r \right)^n \left(\frac{d\sigma^{(-1)}}{dz} \right)^n. \quad (43)$$

Integration of eq. (42) with eq. (37) provides

$$v_z^{(0)} = \frac{1}{\mu 2^m} \left(\frac{1}{a} - a \right)^m \left(\frac{d\sigma^{(-1)}}{dz} \right)^m + F(r, a, n) \left(\frac{d\sigma^{(-1)}}{dz} \right)^n \quad (44)$$

where

$$F(r, a, n) = \frac{3^{\frac{n-1}{2}}}{2^n} \int_a^r \left(\frac{1}{\rho} - \rho \right)^n d\rho \quad (45)$$

Differentiation of eq. (44) with respect to z provides the axial strain rate which is inserted into eq. (34). Integration of eq. (34) with respect to r combined with boundary condition eq. (37) then gives

$$\begin{aligned} v_r^{(1)} = & \frac{1}{\mu 2^{m+1}} \left(\frac{1}{a} - a \right)^m \left(\frac{a^2}{r} - r \right) \frac{d}{dz} \left(\frac{d\sigma^{(-1)}}{dz} \right)^m \\ & - \frac{1}{r} \int_a^r \rho F(\rho, a, n) d\rho \frac{d}{dz} \left(\frac{d\sigma^{(-1)}}{dz} \right)^n \end{aligned} \quad (46)$$

The boundary condition specifying the strain rate, eq. (38), then provides the nonlinear differential equation

$$\frac{d}{dz} \left[G(a, n) \left(\frac{d\sigma^{(-1)}}{dz} \right)^n + \frac{(1-a^2)^{m+1}}{\mu 2^{m+1} a^m} \left(\frac{d\sigma^{(-1)}}{dz} \right)^m \right] = \frac{1}{2} \quad (47)$$

where $G(a, n) = \int_a^1 \rho F(\rho, a, n) d\rho$. (48)

This can be integrated once and boundary condition eq. (36) along with eq. (42) used to give

$$G(a, n) \left(\frac{d\sigma^{(-1)}}{dz} \right)^n + \frac{(1-a^2)^{m+1}}{\mu 2^{m+1} a^m} \left(\frac{d\sigma^{(-1)}}{dz} \right)^m = \frac{z}{2} \quad (49)$$

This is hard to solve in general when $m \neq n$ except when $n = 2$ and $m = 1$ and vice versa. Substantial insight and a degree of generality can be retained by choosing $m = n$. As discussed previously, this case represents that of a well bonded fiber-matrix interface with a rough fiber surface at a temperature sufficiently high to give rise to a negligible shear strength of the bonded interface. The resistance to slip arises from the drag induced by the creep of the matrix along the rough fiber surface. Alternately, it could represent the case of an interphase with the same creep index as the matrix but with a different creep coefficient. The approach of using $m = n$ permits the study of the effect of a weak interface and some general insights are obtained. With $m = n$, eq. (49) provides

$$\frac{d\sigma^{(-1)}}{dz} = \left(\frac{z}{D}\right)^{\frac{1}{n}} \quad (50)$$

where

$$D(a,n) = 2G(a,n) + \frac{(1-a^2)^{n+1}}{\mu 2^n a^n} \quad (51)$$

Integration of eq. (49) and use of eq. (41) reveals that

$$\sigma^{(-1)} = \frac{z^{1+1/n} - \frac{n}{2n+1}}{\left(1 + \frac{1}{n}\right) D^{\frac{1}{n}}} \quad (52)$$

The remaining significant terms in the solution are then

$$\sigma_{rz}^{(0)} = \frac{1}{2} \left(\frac{1}{r} - r \right) \left(\frac{z}{D} \right)^{\frac{1}{n}} \quad (53)$$

$$v_z^{(0)} = \left[\frac{1}{\mu 2^n} \left(\frac{1}{a} - a \right)^n + F(r, a, n) \right] \frac{z}{D} \quad (54)$$

$$v_r^{(1)} = - \left[\frac{1}{\mu 2^{n+1}} \left(\frac{1}{a} - a \right)^n \left(r - \frac{a^2}{r} \right) + \frac{1}{r} \int_a^r \rho F(\rho, a, n) d\rho \right] \frac{1}{D}. \quad (55)$$

Thus the key assumption made by Kelly and Street (1972) that the velocity in the z direction is proportional to z is correct to leading order. However, now the dependence on r has been established too.

Boundary Layer. It is possible to proceed with the solution to higher order terms and so establish the small corrections involved. This will not be done. However, it should be noted that boundary layers are involved at $z = 0$ and at $r = 1$. The shear stress to leading order is zero at those locations and thus so is the effective stress σ_e . In the pure power law rheology being used in this problem, this makes the matrix rigid to leading order at $z = 0$ and $r = 1$. However, material is deforming at those locations and as a result the higher order terms in the deviatoric stress in the perturbation series diverge there. To correct this, a boundary layer analysis is required. However, the result of Johnson (1984) for the plane strain squeeze film indicates that the boundary layers are passive and so do not disrupt the leading order outer solution. Consequently, the leading order outer solution eq. (52-55) is valid. The boundary layer analysis provides a significant correction term at higher order in the outer solution. This correction term has not been worked out. However, the boundary layer at $z = 0$ can be analyzed and terms for the correction estimated there. An overall axial balance of stress then provides the net resultant

stress for the composite material and therefore an estimate to higher order of the creep strength of the composite. The details of the boundary layer results are developed in the Appendix.

Composite Material Creep Response

We now have an estimate for the average axial stress at $z = 1$ in the cell. This is given by eq. (52) at $z = 1$ divided by δ plus the correction $\delta^{\frac{1}{n}} N$ arising from the analysis of the boundary layer at $z = 0$ (see Appendix eq. (A16, A22 & A28)). The correction is required at $z = 1$ to balance the tension in the boundary layer at $z = 0$. Thus, the average stress at $z = 1$ in normalized variables is

$$\frac{n}{\delta(2n+1)D^{1/n}} + \delta^{\frac{1}{n}} N \quad (56)$$

Clearly, as long as D is not large, the first term will be the largest contribution to $\hat{\sigma}_a$ (see Fig. 1) which represents the creep stress of the composite material. Additional contributions to $\hat{\sigma}_a$ will arise from the effects of matrix flow around the fiber end. This term may be of the same order of magnitude as the boundary layer term N , but the fiber end flow term is difficult to estimate. Although it may be inconsistent, we will simply omit the fiber end flow term but include the boundary layer term. It is hoped that the result will then be meaningful for low fiber volume fractions where the fiber end flow term will tend to be small. In any case, as long as D is not large, the discrepancy relates only to a higher order term and the creep behavior predicted by the leading order term in eq. (56) is still reliable. The omission will be more serious in the case of low drag fiber-matrix interfaces with moderate to high volume fractions of fibers because D becomes large in that case. Then the fiber end term will be just as significant as the leading term in eq. (56). The validity of the model is then doubtful.

The estimate for $\hat{\sigma}_a$ is obtained from eq. (56) in physical variables. Accordingly

$$\begin{aligned}
\hat{\sigma}_a &= \frac{\Sigma \hat{L} n}{\hat{b}(2n+1) D^{1/n}} + \Sigma N \delta_n^{\frac{1}{n}} \\
&= \left(\frac{\hat{\epsilon}}{N} \right)^{\frac{1}{n}} \left[\frac{\lambda^{1+1/n} n}{(2n+1) D^{1/n}} + N \right]
\end{aligned} \tag{57}$$

where $\lambda = \hat{L}/\hat{b}$. In turn, the creep strength is

$$S = \frac{\lambda^{1+1/n} n}{(2n+1) D^{1/n}} + N \tag{58}$$

Note that the term S functions as a dimensionless reference stress (Leckie, 1986) for the creep behavior of the composite as in

$$\hat{\epsilon} = B (\hat{\sigma}_a/S)^n. \tag{59}$$

The results will be left in the form presented in eq. (57 & 58) even though the dependence on parameters like fiber volume fraction and fiber aspect ratio is not apparent. The forms presented, in terms of a and λ , are more versatile with the advantage that there is no assumption dependent conversion from a and λ to volume fraction and fiber aspect ratio. However, such conversions can be done easily by the user of the results. For example, Kelly and Street (1972) neglected the ends of the unit cell and assumed that \hat{b} is half the nearest neighbor center to center spacing in a hexagonal array of fibers. In that case

$$a = \frac{\hat{a}}{\hat{b}} = (2\sqrt{3} V_f/\pi)^{1/2} \tag{60}$$

where V_f is the fiber volume fraction. On the other hand, if the unit cell is assumed to have the same aspect ratio as the fiber, then

$$a = V_f^{1/3}. \quad (61)$$

Therefore, it is best to avoid any conversion and leave the user of the results to choose an approach which is appropriate to the material of interest.

In any case, since

$$\lambda = \hat{L}/\hat{b} = (\hat{L}/\hat{a})(\hat{a}/\hat{b}) \quad (62)$$

λ will be proportional to the aspect ratio of the fiber $\alpha = \hat{L}/\hat{a}$. Therefore, the creep strength S , eq. (58), depends relatively strongly on the fiber aspect ratio, being proportional to $\alpha^{1+1/n}$. This ranges from a quadratic dependence for linear viscosity to nearly linear for high n . This dependence was identified by Kelly and Street (1972). As the fiber volume fraction goes up, a will increase and be around unity for fiber volume fractions around unity. This will cause D to become very small or zero, predicting very large or infinite creep strengths. This locking up is present in the model of Kelly and Street (1972), occurring at $V_f = 0.91$ in that case, which is when fibers in a hexagonal array touch each other.

As the fiber volume fraction goes to zero with μ finite, a will disappear and so will the creep strength predicted by the first term in eq. (58). The second term, N , then provides the creep strength, which will be unity according to eq. (A22). Returning to the general case, consider what happens if $\mu \rightarrow 0$. This is the zero drag case and eq. (51) makes it clear that $D \rightarrow \infty$. Consequently, the creep strength is given then by N , expressed in this case by eq. (A28). Results for N for several values of n are plotted in Fig. 2. The values are less than or equal to unity, indicating that the composite will be weaker than the matrix alone. This effect occurs because the fibers act only to fill cylindrical holes in the matrix and the composite behavior represents the creep of a matrix filled with such cylindrical holes. It can be seen in Fig. 2 that N is approximately given by $1-f$, confirming this effect. This result is not exact

because the effect of flow around the fiber end has been neglected. The true result is probably $1-f$ plus a small amount accounting for the fiber end effect. However, the magnitude of the contribution due to flow around the very end of the fiber will not depend to any great extent on the aspect ratio of the fiber. Thus, for long, discontinuous fibers, the creep strength will be modest if the matrix is free to slip without drag relative to the fiber. This effect was apparent, although not emphasized in the model of Kelly and Street (1972).

It is difficult to know realistic physical values of μ . In addition, the model for interface drag with $m = n$ is of limited value although it is very similar to a form implied in the model of Kelly and Street (1972). As they pointed out (in terms of their interface sliding parameter but the implications are the same), a given value of μ (less than ∞) will have a stronger effect on the creep strength of a material with a low n compared to a high n . This arises because S is controlled by $D^{-1/n}$ and μ enters the creep strength to leading order through D . However, the effect of a more physically realistic slip law remains to be investigated. For example, interface diffusion tends to occur readily in metal matrix composites at creep temperatures. This will tend to induce slipping with a linear rheology; i.e. $m = 1$ in eq. (18).

Finally, we can consider the creep strength in detail for the no slip case $\mu = \infty$. This is accomplished by consideration of $\tilde{S} = (S - 1)/\alpha^{1+1/n}$ computed from eq. (58). This parameter is the excess creep strength over the matrix strength normalized to make it independent of α . The result is plotted as a function of a^2 in Fig. 3 for several creep exponents. For comparison, the equivalent parameter from the model of Kelly and Street (1972) is graphed as well. For the latter model, the volume fraction has been converted to a by use of eq. (60). The result has the form

$$\begin{aligned}\tilde{S}_K &= (S - 1)/\alpha^{1+1/n} \\ &= \left(\frac{2}{3}\right)^{\frac{1}{n}} \frac{n}{2n+1} \left(\frac{a}{1-a}\right)^{\frac{1}{n}} \frac{a^2}{1-a^2}.\end{aligned}\tag{63}$$

It can be seen in Fig. 3 that there are significant differences between the two models.

Fiber Stresses

Fiber stresses are important because the reinforcements can crack and degrade the creep strength when the stress exceeds the fiber strength as observed by Weber et al. (1991). In addition, Sancakter and Zhang (1990) have demonstrated that high shear stresses on the interface can cause interphase and matrix cracking. The shear stress at the interface between the matrix and the fiber is directly related to the gradient of the average axial fiber stress along the fiber. The average axial stress at any point in the fiber can be computed from a net balance of forces in the axial direction. This requires

$$\hat{\sigma}_a = a^2 \hat{\sigma}_f(\hat{z}) + (1 - a^2) \hat{\sigma}_m(\hat{z}) \quad (64)$$

at any position \hat{z} where $\hat{\sigma}_f$ is the average axial fiber stress at \hat{z} and $\hat{\sigma}_m$ is the average axial matrix stress at \hat{z} . From eq. (52) we have

$$\hat{\sigma}_m(\hat{z}) = \left(\frac{\hat{e}}{B}\right)^{\frac{1}{n}} \left\{ \frac{\left[\left(\frac{\hat{z}}{\hat{L}}\right)^{1+1/n} - \frac{n}{2n+1}\right] \lambda^{1+1/n}}{(1+1/n) D^{1/n}} + N \right\} \quad (65)$$

Given eq. (57), it follows that

$$\hat{\sigma}_f(\hat{z}) = \left(\frac{\hat{e}}{B}\right)^{\frac{1}{n}} \left\{ \frac{\lambda^{1+1/n}}{D^{1/n}} \frac{n}{n+1} \left[\frac{1}{a^2} - \frac{1-a^2}{a^2} \left(\frac{\hat{z}}{\hat{L}}\right)^{1+1/n} - \frac{n}{2n+1} \right] + N \right\} \quad (66)$$

The highest value is at $\hat{z} = 0$ where

$$\begin{aligned}
 \hat{\sigma}_f^{\max} &= \hat{\sigma}_f(0) \\
 &= \left(\frac{\hat{e}}{B} \right)^{\frac{1}{n}} \left[\frac{\lambda^{1+1/n}}{D^{1/n}} \frac{n}{n+1} \left(\frac{1}{a^2} - \frac{n}{2n+1} \right) + N \right].
 \end{aligned} \tag{67}$$

To the neglect of N , which will be small compared to other terms when λ is large, we find

$$\frac{\hat{\sigma}_f^{\max}}{\hat{\sigma}_a} = \frac{2n+1-a^2n}{a^2(n+1)}. \tag{68}$$

Thus the maximum axial fiber stress can be obtained approximately by multiplying the composite stress by a factor given by a fairly simple formula. For example, with a^2 equal to a quarter (i.e. the fiber diameter is equal to the fiber spacing), the ratio is $(7n+4)/(n+1)$ which, for example, is equal to 6.4 for $n = 4$. It is interesting that the ratio is independent of the aspect ratio of the fiber. This, however, only applies if the fiber is long enough, say with an aspect ratio of 5 or greater.

A further interesting point is that the minimum matrix stress (at $\hat{z} = 0$) is compressive. Expressed as a fraction of the composite stress, the minimum matrix stress $\hat{\sigma}_m^{\min} = \hat{\sigma}_m(0)$ is

$$\frac{\hat{\sigma}_m^{\min}}{\hat{\sigma}_a} = -\frac{n}{n+1} \tag{69}$$

independent of the volume fraction *and* the fiber aspect ratio (given that the fiber aspect ratio is high enough).

Comparison with Finite Element Results

There are few finite element results available in detail for comparison. The most useful is the analysis by Dragone and Nix (1990), who treated an aluminum alloy with 20% by volume of SiC fibers. A unit cell approach was adopted and calculations performed for $n = 4$. The fiber was perfectly bonded to the matrix and so the relevant comparison is with our results when $\mu = \infty$. A number of features found in the asymptotic analysis are apparent in their steady state solution for $\alpha = 5$, a somewhat lower aspect ratio than we would prefer for comparison. The stress in the matrix around the fiber is dominated by the hydrostatic stress with the hydrostatic component apparently 25 times the longitudinal deviatoric stress. The hydrostatic stress in the matrix varies almost linearly down the length of the fiber. (Our analysis predicts a variation with $z^{1.25}$, but it would be difficult to distinguish this from a linear behavior in numerical results). The hydrostatic stress adjacent to the fiber is independent of distance from the fiber. The axial stress at the fiber end is about 25% higher than the composite stress indicating an effect of flow around the end of the fiber which we have neglected. The aspect ratio of the cell is equal to the aspect ratio of the fiber. Therefore, by eq. (61), $a^2 = V_f^{2/3}$. For $V_f = 0.2$, this gives $a^2 = 0.34$. For this value of a^2 , we predict 4.5 for $\hat{\sigma}_f^{\max}/\hat{\sigma}_a$ from eq. (68) and -0.8 for $\hat{\sigma}_m^{\min}/\hat{\sigma}_a$ from eq. (69). Dragone and Nix (1990) find these ratios at steady state to be 4.9 and -1.2 respectively. Thus even for the low aspect ratio fiber the asymptotic analysis is reasonably good. We suspect that most of the discrepancy is due to the stress arising from flow around the fiber ends. When the difference between the composite stress and the stress at the fiber end is factored out, our ratios predict the Dragone and Nix (1990) stress values almost exactly. Thus, for longer fibers, we believe our estimates will be quite accurate even without adjustment.

The steady state strain rates computed by Dragone and Nix (1990) at 80 MPa for fibers with aspect ratios 5, 7 & 10 are listed in Table 1. Also given is a strain rate for an aspect ratio of 20 obtained by extrapolation of the transient results. The matrix steady creep law used by Dragone and Nix (1990) is our eq. (7) with $B = 2 \times 10^{-13}$ when strain rate is given in units of s^{-1} and stress in MPa. As noted before, $n = 4$. The finite element creep strength is computed from

eq. (24) and the asymptotic result from eq. (58) with $\mu = \infty$ and $a^2 = V_f^{2/3} = 0.34$ as used in the finite element results. N was taken to be 1 in eq. (58). There is reasonable agreement. The Kelly and Street (1972) prediction for creep strength, based on our eq. (63) with $N = 1$, are given in Table 1 as well under the heading "shear lag". They are well below the other results. Dragone and Nix (1990) provide additional results in which the aspect ratio of the cell is varied and the asymptotic solution agrees reasonably well with those as well.

Another comparison can be made with the finite element results of Bao et al. (1991). The comparison is made in Table 2. One feature in the results of Bao et al. (1991) is the contrast with the results of Dragone and Nix (1990). Bao et al. (1991) predict lower creep strengths as can be seen in the results for $n = 4$ in Table 2. This suggests that either Dragone and Nix (1990) are in error or Bao et al. (1991) are. However, the asymptotic analysis consistently predicts higher strengths than Bao et al. (1991). The substantial differences are probably due to the contribution to the creep strength in the finite element results arising from the fiber end region. The cell length in the finite element calculations is $1/V_f^{1/3}$ times the fiber length. The portion of the cell beyond the fiber ends as a fraction of the whole cell length is $1 - V_f^{1/3}$. This region of the cell experiences relatively unconstrained flow compared to the matrix material surrounding the fiber circumferentially. An estimate of the effect can be made by consideration of radial stressing. The portion of the cell around the fiber would require a radial stress S to produce the same strain rate as unit radial stress would produce in an unconstrained end region. Therefore, the average radial stress on the whole cell for the same strain rate is

$$\bar{S} = 1 + V_f^{1/3} (S - 1). \quad (70)$$

This can be converted to an axial stress result by addition of hydrostatic stress. Therefore eq. (70) with S given by the asymptotic solution provides an estimate for the axial creep strength of a unit cell with the same aspect ratio as the fiber. In Table 2 it can be seen that \bar{S} agrees better than S with the creep strength of Bao et al. (1991). There are still discrepancies, but the

conversion represented by eq. (70) is an approximation at best. It seems safe to conclude that the asymptotic results should be used for cases where the fiber aspect ratio is greater than 20 so that fiber end effects are less important.

Closure

An asymptotic solution has been presented for power law creep of a composite material containing aligned, rigid, discontinuous, well bonded high aspect ratio fibers. The solution exhibits several of the features assumed by Kelly and Street (1972) for their shear lag model. These features include the linearity of the axial velocity with distance along the fiber and the dominance of the creep strength by the shearing flow in the matrix. However, asymptotically exact forms for the velocity and stress are provided rather than the estimates used in the shear lag model. The asymptotic solution provides a model for the creep law of the composite material. Although the shear lag creep law of Kelly and Street (1972) exhibits several of the characteristics of the more exact asymptotic creep law, the shear lag model underestimates the creep strength of the composite material. We think this arises from a stress averaging procedure used by Kelly and Street (1972) which seems to be faulty.

The dominant characteristic of the creep law predicted by the asymptotic analysis is that the creep strength is proportional to the fiber aspect ratio raised to the power $1 + 1/n$ where n is the creep exponent. In addition, the model shows that fiber-matrix interface slip can have a disastrous effect on the creep strength of discontinuous fiber composites. If the interface has no shear strength, the creep strength of the composite is approximately equal to the creep strength of the matrix alone. This indicates that such a composite material would creep as fast as the unreinforced matrix at the same applied stress. However, modest levels of interface drag can be mitigated by very long fibers. The effect can be identified in eq. (58) where the interplay between interface drag and aspect ratio is evident. A low drag coefficient, μ , gives rise to a high value of D . However, very long fibers will have a large aspect ratio leading to high values of λ .

The resulting combination can lead to significant creep strengths. Thus continuous fibers, even with occasional breaks, can provide good strengthening even when some interface slip can occur.

The asymptotic solution agrees reasonably well with finite element analyses of the problem. The solution features in the matrix are very similar. Some adjustments have to be made to the creep strength for some of the comparisons to account for the fact that the finite element results were obtained typically for low aspect ratio fibers with unit cells containing substantial volumes of relatively unconstrained matrix beyond the fiber ends. With an appropriate adjustment, there is quite good agreement in terms of the creep strength.

Appendix:

Boundary Layer Analysis

According to Johnson (1984), the outer solution velocities eq. (54 & 55) prevail into the boundary layer at $z = 0$. Thus in terms of unstretched coordinates with $\eta = z/\delta$ in the boundary layer

$$v_z = \frac{\delta}{D} \left[\frac{1}{\mu 2^n} \left(\frac{1}{a} - a \right)^n + F(r, a, n) \right] \eta \quad (\text{A1})$$

and

$$v_r = -\frac{\delta}{D} \left[\frac{1}{\mu 2^{n+1}} \left(\frac{1}{a} - a \right)^n \left(r - \frac{a^2}{r} \right) + \frac{1}{r} \int_a^r \rho F(\rho, a, n) d\rho \right]. \quad (\text{A2})$$

An effective strain rate can be computed as

$$\epsilon_e = \sqrt{2/3} \left[\left(\frac{\partial v_r}{\partial r} \right)^2 + \left(\frac{v_r}{r} \right)^2 + \left(\frac{\partial v_z}{\partial \eta} \right)^2 + \frac{1}{2} \left(\frac{\partial v_z}{\partial r} \right)^2 \right]^{\frac{1}{2}} \quad (A3)$$

and then the constitutive law provides

$$S_{rr} = \frac{2}{3} \epsilon_e^{\frac{1-n}{n}} \frac{\partial v_r}{\partial r} \quad (A4)$$

$$S_{\theta\theta} = \frac{2}{3} \epsilon_e^{\frac{1-n}{n}} \frac{v_r}{r} \quad (A5)$$

$$S_{zz} = \frac{2}{3} \epsilon_e^{\frac{1-n}{n}} \frac{\partial v_z}{\partial \eta} \quad (A6)$$

and

$$\sigma_{rz} = \frac{1}{3} \epsilon_e^{\frac{1-n}{n}} \frac{\partial v_z}{\partial r} \quad (A7)$$

The hydrostatic stress can be computed from the two equilibrium equations

$$\frac{\partial \sigma}{\partial r} = -\frac{\partial S_{rr}}{\partial r} + \frac{S_{\theta\theta} - S_{rr}}{r} - \frac{\partial \sigma_{rz}}{\partial \eta} \quad (A8)$$

and

$$\frac{\partial \sigma}{\partial \eta} = -\frac{\partial \sigma_{rz}}{\partial r} - \frac{\sigma_{rz}}{r} \quad (A9)$$

According to Johnson (1984), on the scale of the boundary layer, the hydrostatic stress at leading order is uniform and given by eq. (52) with $z = 0$. It is sustained by tractions on the side of the cell enforcing the constraint that $v_r = -\frac{1}{2} \delta$ there. Therefore, the boundary condition for evaluation of the hydrostatic stress is

$$\sigma(1,0) = -\frac{n^2}{\delta(n+1)(2n+1)D^{1/n}} - S_\pi(1,0) \quad (\text{A10})$$

which ensures that eq. (23) is satisfied at higher order. At higher order, eq. (23) degenerates to a point wise condition on σ_π because S_π is uniform at $r = 1$ which is a boundary layer also.

Thus by solution of eq. (A8 & A9) subject to eq. (A10), the stresses can be established throughout the boundary layer at $z = 0$. In particular, σ_{zz} can be computed on $z = 0$. This stress at $z = 0$ plus the axial stress in the fiber at $z = 0$ must be balanced at the other fiber end by an appropriate average stress. The leading order term in eq. (52) at $z = 1$ plus a smaller correction arising from terms computed in eq. (A8) is required. This provides an estimate of the creep strength of the composite material to higher order.

The form of v_z is such that on $z = 0$

$$\frac{\partial \sigma_{rz}}{\partial \eta} = \frac{1}{3} \epsilon_e^{\frac{1-n}{n}} \frac{\partial^2 v_z}{\partial r \partial \eta} \quad (\text{A11})$$

because, through $(\partial v_r / \partial r)^2$, ϵ_e depends on η^2 . Therefore, on $z = 0$, eq. (A8) becomes

$$\frac{\partial \sigma_{rr}}{\partial r} = \frac{2}{3} \epsilon_e^{\frac{1-n}{n}} \left[\frac{v_r}{r^2} - \frac{1}{r} \frac{\partial v_r}{\partial r} - \frac{1}{2} \frac{\partial^2 v_z}{\partial r \partial \eta} \right]. \quad (\text{A12})$$

Since $\partial v_r / \partial r = 0$ there, on $z = 0$

$$\epsilon_c = \sqrt{2/3} \left[\left(\frac{\partial v_r}{\partial r} \right)^2 + \left(\frac{v_r}{r} \right)^2 + \left(\frac{\partial v_z}{\partial \eta} \right)^2 \right]^{1/2} \quad (\text{A13})$$

with v_z and v_r given by eq. (A1 & A2). To compute the higher order terms in σ_{rr} on $z = 0$, eq. (A12) can be integrated subject to

$$\sigma_{rr}(1, 0) = 0 \quad (\text{A14})$$

which is equivalent to eq. (A10) with the leading order term (i.e. the first term on the right hand side) omitted. The result for $\sigma_{rr}(r, 0)$ can be used to compute the axial stress from

$$\sigma_{zz}(r, 0) = \sigma_{rr}(r, 0) + S_{zz}(r, 0) - S_{rr}(r, 0). \quad (\text{A15})$$

The net resultant in the boundary layer is

$$2\pi \int_a^1 \sigma_{zz}(r, 0) r dr = \delta_n^{\frac{1}{n}} N\pi \quad (\text{A16})$$

which defines N . Two cases can be considered. One situation arises if μ is large or infinite and there is little or no slip at the fiber matrix interface. This is the high drag case. In that situation N only becomes important in the creep strength at small volume fractions of fibers. The other case is where μ is small or zero so that the matrix is free or almost free to slip against the fiber without drag.

High drag interface. In this case, D in eq. (51) is large only if a is small. With D large, the leading order stress estimate at $z = 1$ can be modest in magnitude and the higher order corrections are significant. Investigation of the velocities in eq. (A1 & A2) reveals that when a is

small, the term containing μ can be neglected and the effective strain rate $\dot{\epsilon}_e$ on $z = 0$ is almost uniform except when r is just slightly larger than a . However, the strain rates go rapidly to zero at $r = a$ and according to eq. (A4-A6) so do the deviatoric stresses. Consequently, the small region around the fiber with r slightly larger than a will contribute very little to the stress resultant N . In view of this, a treatment will be reasonably accurate with $\dot{\epsilon}_e$ taken to be uniform everywhere on $z = 0$ but with the strain rate components allowed to vary otherwise according to eq. (A1 & A2).

With the strain rates computed from eq. (A1 & A2) (with $\mu \rightarrow \infty$) eq. (A12) becomes

$$\frac{\partial \sigma_{rr}}{\partial r} = -\frac{2}{3} \dot{\epsilon}_e^{\frac{1-n}{n}} \frac{\delta}{D} \left[\frac{2}{r^3} \int_a^r \rho F(\rho, a, n) d\rho - \frac{1}{r} F(r, a, n) + \frac{1}{2} \frac{\partial F(r, a, n)}{\partial r} \right]. \quad (A17)$$

With $\dot{\epsilon}_e$ uniform, this integrates, subject to eq. (A14) to give

$$\sigma_{rr} = \frac{2}{3} \dot{\epsilon}_e^{\frac{1-n}{n}} \frac{\delta}{D} \left[\frac{1}{r^2} \int_a^r \rho F(\rho, a, n) d\rho - G(a, n) - \frac{1}{2} F(r, a, n) + \frac{1}{2} F(1, a, n) \right]. \quad (A18)$$

On $z = 0$, from eq. (A4 & A6)

$$S_{zz} - S_{rr} = \frac{2}{3} \dot{\epsilon}_e^{\frac{1-n}{n}} \frac{\delta}{D} \left[2F(r, a, n) - \frac{1}{r^2} \int_a^r \rho F(\rho, a, n) d\rho \right] \quad (A19)$$

so

$$\sigma_{zz} = \frac{2}{3} \dot{\epsilon}_e^{\frac{1-n}{n}} \frac{\delta}{D} \left[\frac{3}{2} F(r, a, n) + \frac{1}{2} F(1, a, n) - G(a, n) \right] \quad (A20)$$

which is valid for r close to 1 but suspect for r close to a . Calculation of N from eq. (A18) then gives

$$N = \delta^{-\frac{1}{n}} \epsilon_c^{\frac{1+n}{n}} \frac{\delta}{D} \left[\frac{2}{3} (2+a^2) G(a, n) + \frac{1}{3} (1-a^2) F(1, a, n) \right] \quad (A21)$$

This result is most readily utilized for even integer positive values of n . In that case, calculation of $F(1, a, n)$ and $G(a, n)$ can be carried out by binomial expansion. In addition, the leading terms in ϵ_c can be computed at $r = 1$. The result to leading terms is

$$N = 1 - \frac{(2n^2 - 2n - 7)(n-1)}{6n(n-3)} a^2 + \dots \quad (A22)$$

Low drag interface. In this situation, μ is close to zero. The limiting case of $\mu \rightarrow 0$ (no drag) will be considered. As a consequence, the velocities in eq. (A1 & A2) become

$$v_z = \frac{\eta \delta}{1-a^2} \quad (A23)$$

and

$$v_r = -\frac{\delta}{1-a^2} \frac{1}{2} \left(r - \frac{a^2}{r} \right) \quad (A24)$$

and $D = \infty$. This is a planar flow in the fiber direction, as would be expected when there is no drag. The effective strain rate is

$$\epsilon_e = \frac{\delta}{1-a^2} \left[1 + \frac{1}{3} \frac{a^4}{r^4} \right]^{\frac{1}{2}} \quad (A25)$$

and integration of eq. (A12) gives on $z = 0$

$$\sigma_{rr} = -\frac{2}{3} \left(\frac{\delta}{1-a^2} \right)^{\frac{1}{n}} \int_r^1 \left[1 + \frac{1}{3} \frac{a^4}{r^4} \right]^{\frac{1-n}{2n}} \frac{a^2}{r^3} dr \quad (A26)$$

The deviatoric stresses are such that

$$S_{zz} - S_{rr} = \frac{2}{3} \left(\frac{\delta}{1-a^2} \right)^{\frac{1}{n}} \left[1 + \frac{1}{3} \frac{a^4}{r^4} \right]^{\frac{1-n}{2n}} \left[\frac{3}{2} + \frac{1}{2} \frac{a^2}{r^2} \right] \quad (A27)$$

Finally, the stress σ_{zz} , the sum of eq. (A26 & A27), can be integrated to give

$$N = \frac{4/3}{(1-a^2)^{1/n}} \int_a^1 \left[1 + \frac{1}{3} \frac{a^4}{r^4} \right]^{\frac{1-n}{2n}} \left[\frac{3}{2} r + \frac{a^4}{2r^3} \right] dr \quad (A28)$$

Note that when $a = 0$, $N = 1$, as in eq. (A22).

Acknowledgment

This research was supported by the DARPA University Research Initiative at the University of California, Santa Barbara (ONR Contract N00014-86-K0753).

References

- Bao, G., Genna, F., Hutchinson, J.W. and McMeeking, R.M. (1991), "Models for the Strength of Ductile Matrix Composites," in Intermetallic Matrix Composites, MRS Symposium Proceedings, Vol. 194, (Eds. D. L. Anton, P. L. Martin, D. B. Miracle and R. M. McMeeking) MRS, Pittsburgh, pp. 3-15.
- Bao, G., Hutchinson, J.W. and McMeeking, R.M. (1991), "Particle Reinforcement of Ductile Matrices Against Plastic Flow and Creep," *Acta Metall. Mater.*, **39**, 1871-1882.

Dragone, T.L. and Nix, W.D. (1990). "Geometric Factors Affecting the Internal Stress Distribution and High Temperature Creep Rate of Discontinuous Fiber Reinforced Metals," *Acta Metall. Mater.*, **38**, 1941-1953.

Goto, S. and McLean, M. (1991). "Role of Interfaces in Creep of Fibre-Reinforced Metal-Matrix Composites-II Short Fibres," *Acta Metall. Mater.*, **39**, 165-177.

Johnson, R.E. (1984). "Power-Law Creep of a Material Being Compressed Between Parallel Plates: A Singular Perturbation Problem," *J. Engg. Math.*, **18**, 105-117.

Kelly, A. and Street, K.N. (1972). "Creep of Discontinuous Fibre Composites II. Theory for the Steady-State," *Proc. Roy. Soc. Lond.* **A328**, 283-293.

Leckie, F.A. (1986). "Micromechanics of Creep Rupture," *Engg. Fracture Mech.*, **25**.

Sancaktar, E. and Zhang, P. (1990). "Nonlinear Viscoelastic Modelling of the Fiber-Matrix Interphase in Composite Materials," *Trans. ASME, J. Mech. Design*, **112**, 605-619.

Van Dyke, M. (1975). Perturbation Methods in Fluid Mechanics, The Parabolic Press, Stanford, California.

Weber, C.H., Löfvander, J.P.A., Yang, J.Y., Levi, C.G. and Evans, A.G. (1991). "Microstructure and Creep of α -TiAl Reinforced with Al_2O_3 Fibers," to appear in Advanced Metal Matrix Composites for Elevated Temperatures, (Ed. M. N. Gungor) ASM Conference Proceedings.

TABLE 1

Comparison of steady state creep results from the finite element calculations of Dragone and Nix (1990) and the asymptotic solution. The results are for 20% SiC fibers in 6061 Al at 80 MPa. (____) \equiv extrapolated.

Fiber Aspect Ratio α	Steady Creep Rate	Creep Strength S		
		Finite elements (Dragone and Nix)	Asymptotic analysis	Shear Lag (Kelly and Street)
	s^{-1}			
5	3.5×10^{-8}	3.9	4.5	2.7
7	1×10^{-8}	5.3	6.4	3.6
10	1.5×10^{-9}	8.6	9.4	5.0
20	(7×10^{-11})	(18.5)	21	10.5

TABLE 2

Comparison of creep strength calculated by Bao et al. (1991) by finite elements with the asymptotic solution. The adjusted column lists $\bar{S} = 1 + V_f^{1/3} (S - 1)$ based on the asymptotic solution.

Fiber Volume Fraction V_f	Fiber Aspect Ratio α	Creep Index n	Creep Strength S		
			Finite Elements (Bao et al.)	Asymptotic Analysis	Adjusted \bar{S}
0.1	5	5	1.8	2.5	1.7
0.1	5	10	1.6	2.2	1.5
0.1	10	5	2.4	4.3	2.5
0.1	10	10	2.1	3.5	2.2
0.2	5	4	3.4	4.5	3.1
0.2	5	5	3.3	4.1	2.8
0.2	5	10	2.9	3.3	2.3
0.2	10	4	4.7	9.4	5.9
0.2	10	5	4.5	8.1	5.2
0.2	10	10	3.9	5.8	3.8

List of Figure Captions

- Figure 1 Unit cell for matrix creep analysis.
- Figure 2 Creep strength of a material with zero drag between the fiber and the matrix.
- Figure 3 Excess creep strength of a material with no slip between the fiber and the matrix.
The result is normalized by the fiber aspect ratio raised to the power $1 + 1/n$.

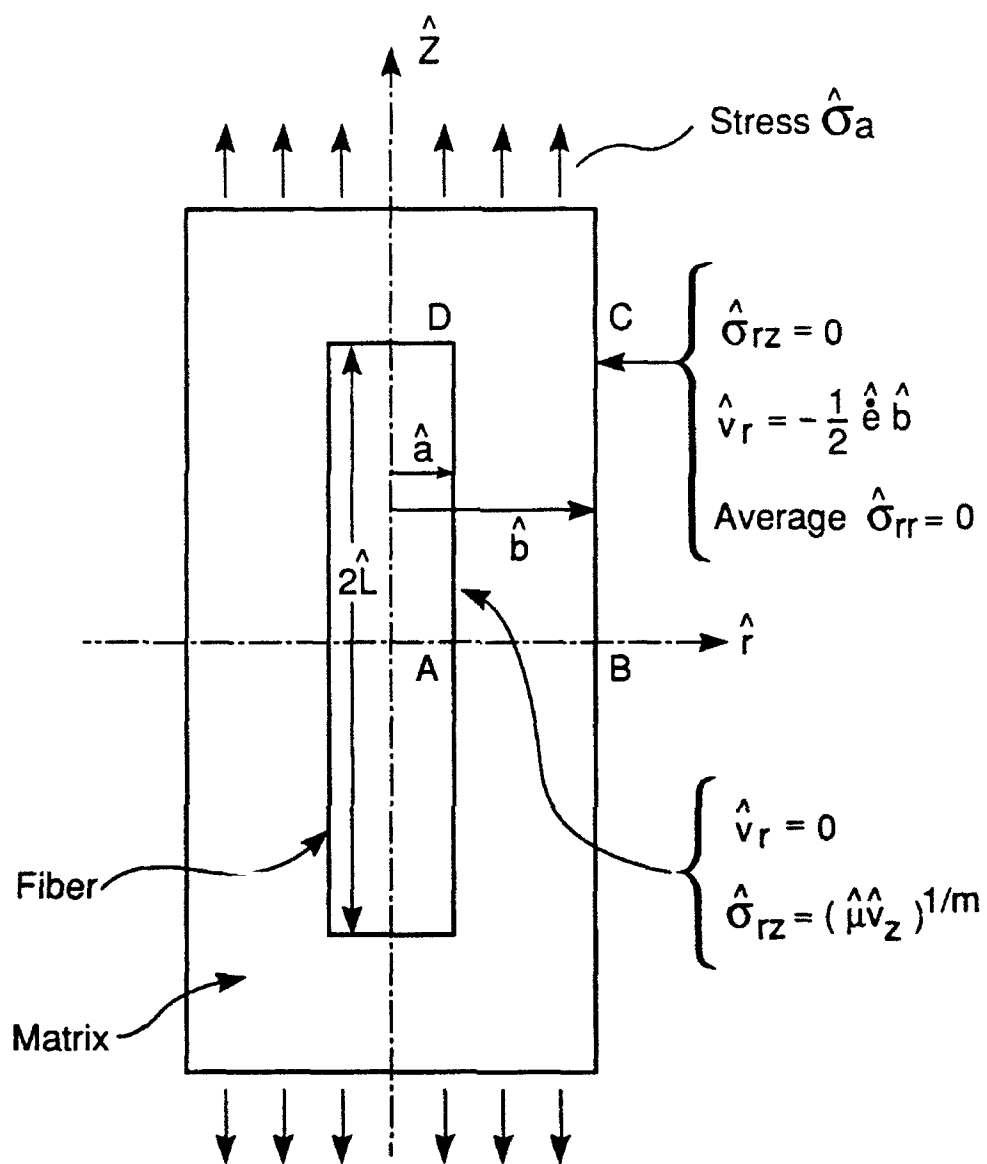


Figure 1

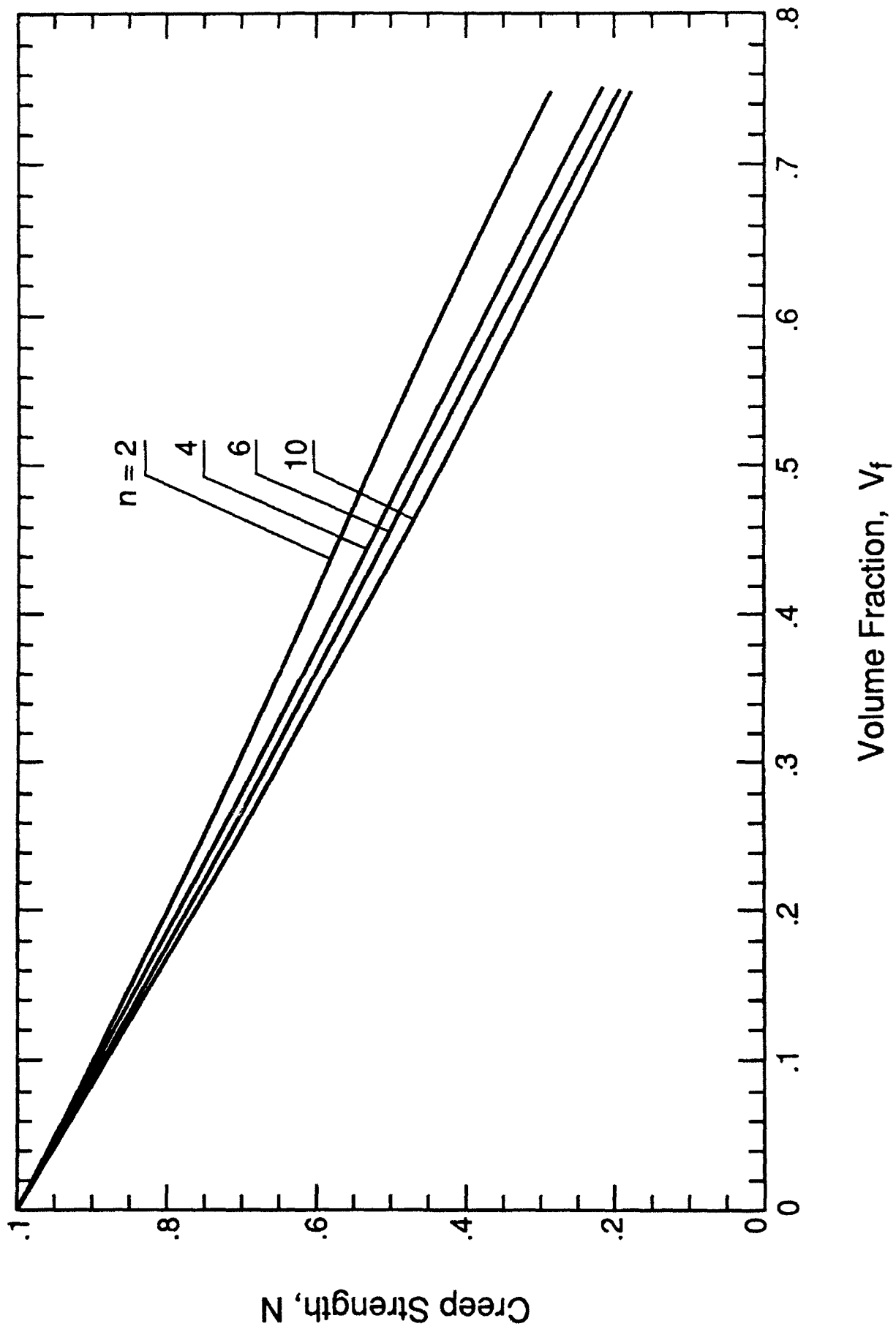


Figure 2

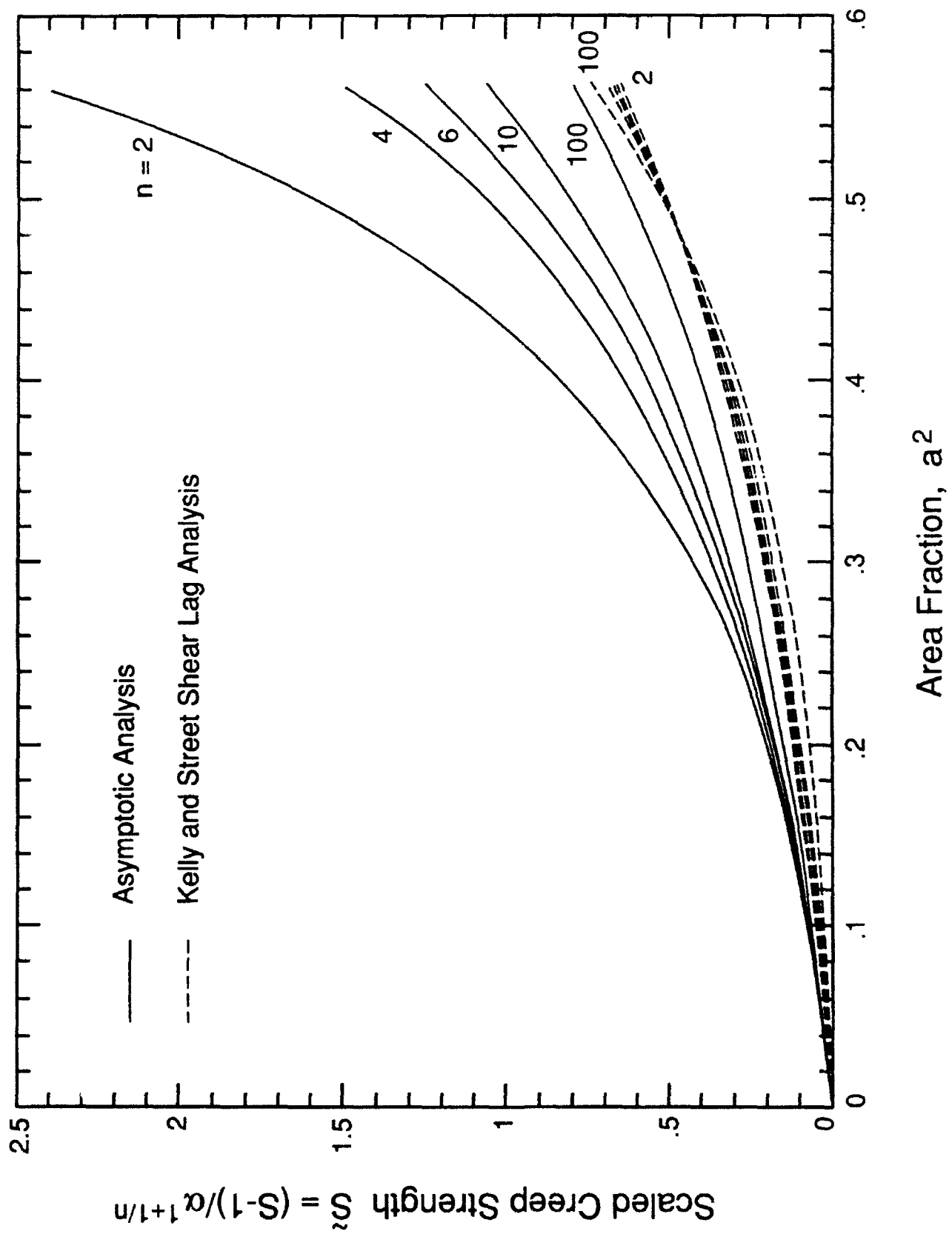
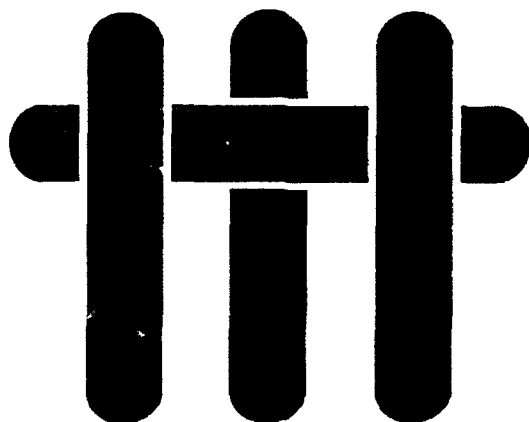


Figure 3

M A T E R I A L S



EFFECTS OF MISFIT STRAIN AND REVERSE LOADING ON THE FLOW STRENGTH OF PARTICULATE-REINFORCED Al MATRIX COMPOSITES

by

S.M. Pickard, S. Schmauder, D.B. Zahl and A.G. Evans

Materials Department
College of Engineering
University of California
Santa Barbara, California 93106

ABSTRACT

Experimental studies conducted on particulate-reinforced Al alloys are used to critically assess flow models. For this purpose, the influence of thermal expansion misfit and of reverse loading provide a particularly critical assessment. Comparison with models indicates that continuum cell calculations provide good predictions of trends, subject to an *in situ* matrix strength that may differ from that for the unreinforced alloy.

1. INTRODUCTION

For metal matrix composites with well-bonded discontinuous reinforcements (such as Al alloys with either SiC or Al₂O₃ particulates, platelets or whiskers), the dependence of the mechanical properties on such microstructural parameters as the matrix yield strength, the reinforcement volume fraction, shape, orientation and spacing are not well defined. However, a recent viewpoint set has clarified some of the issues.¹ There is now compelling evidence that at plastic strains exceeding the yield strain by a factor 3–5, the flow properties are dominated by plastic constraint in the matrix.^{2,3} Such constraints are governed by the flow incompatibility between the elastic reinforcements and the matrix and lead to important effects of the reinforcement volume fraction, f , aspect ratio A , work-hardening coefficient, N , and spatial arrangement S , as well as the thermal expansion mismatch with the matrix,⁴ but are independent of the reinforcement spacing (at fixed f , A and S). Comprehensive calculations concerning trends in flow properties now exist.³

At smaller plastic strains, the data are indicative of an explicit effect of reinforcement size, R (or spacing, l) on the initial flow strength.^{1,5,6} Such effects cannot be associated with plastic constraint, but are presumed to reflect the matrix substructure, on the scale of dislocation cells. Thermal expansion misfit, as well as deformation processing, have been regarded as important factors controlling the dislocation substructure.^{1,6,7} In a continuing attempt to quantify the realm wherein (continuum) plastic constraint approaches provide an adequate material representation, the present study selects material characteristics believed to provide a critical test of the utility of the approach. These are the effects of thermal *expansion misfit* as well as *reverse loading*, evident in the Bauschinger effect.

2. EXPERIMENTAL

Aluminum matrix composites containing SiC particulate reinforcements with volume fractions ranging from 0.2 to 0.5 were manufactured by squeeze casting.⁸ The particulates were incorporated into matrices of both pure Al and a Al-3 wt % Mg solid solution strengthened alloy. Some experiments were conducted with the material in the as-cast condition. Others were performed after the material had been subject to extrusion. Beams were cut from the as-cast and hot-worked billets using a high-speed diamond saw. The surfaces of the beams were polished using diamond media.

Various types of measurements have been made, using tensile, compressive and flexural loading, with emphasis on the latter, as needed to examine the *small strain*, non-linear behavior. These tests were conducted using strain gauges to measure strains and were performed under monotonic loading, as well as fully reversed loading at fixed strain-amplitude. Most tests were conducted on composites with small particles (9 μm) to minimize the influence of reinforcement cracking.^{8,9} In an attempt to systematically vary the residual stress induced by expansion misfit, specimens with 9 μm particles were annealed in a resistance furnace at 200–525°C for 10 minutes, followed by cooling at various rates to a range of low temperatures and then allowing the specimens to equilibrate at room temperature. Liquid nitrogen quenching (LNQ) provided the fastest cooling rate to the lowest temperature. Air cooling to room temperature was used as the reference condition. Effects of microstructural variability were minimized by conducting some tests at different cooling rates *on the same specimen* using an intermediate annealing step to revert the material to its *reference state*. Comparison calibrations of load/deflection curves ensured that this multi-cycle testing procedure did not induce damage and that the material had a well-defined reference state.

The microstructures of each material were characterized by transmission electron microscope (TEM) on thin foils prepared by ion beam milling. In some cases, quenching

was performed on the thin foils. For this purpose, the specimens were held at one corner to avoid mechanical constraint and inserted directly into either a hot or cold medium. This delicate handling minimized unintentional deformation of the foil. The foils were examined in a JEOL 200 CX operating at 200 kV.

3. MECHANICAL MEASUREMENTS

Some preliminary experiments provided the following important information. The flow properties were found to be *insensitive* to pre-quench annealing at all temperatures above $\sim 100^\circ\text{C}$. Specifically, flow strength changes induced by either quenching or deformation (monotonic or cyclic) could be *eliminated* by annealing at $\sim 100^\circ\text{C}$ and slow cooling to room temperature. Such annealing thus restored the material to its *reference strength*.

Cooling to different low temperatures gave reproducibly different monotonic flow curves at room temperature (Fig. 1a), although the effects are small. The *lowest* temperature gave the largest *initial* flow strength, but the strength differential diminished at large strains (Fig. 1b). The differential exhibited a maximum $\Delta\sigma_s$ at strains between 0.2 and 0.8%. Most of the data emphasize this strain range. Plots of the maximum strength differential (Fig. 2) reveal that $\Delta\sigma_s$ increases as either the reinforcement volume fraction f or the matrix yield strength increase (Fig. 2a) and as the cooling range ΔT increases (Fig. 2b). The reinforcement size does not have a systematic influence on $\Delta\sigma_s$ (Fig. 2c), except that a lower strength arises at the largest particle size (100 μm) caused by particle cracking.⁹

Reverse loading experiments have indicated several systematic trends (Fig. 3). An appreciable Bauschinger effect was evident. The differential between the forward and reverse flow strengths $\Delta\sigma_b$ (defined on Fig. 3) increased as the cyclic strain amplitude

increased and was larger for the composites with the higher yield strength matrix (Fig. 4).

To illustrate aspects of the effects of substructure on matrix strength, 'pure' Al materials were subjected to hot and cold extrusion to plastic strain of ~ 3 and tested. The extruded material exhibited flow strengths 2–6 times that for as-cast material (Fig. 5).

4. OBSERVATIONS

Examination of thin foils in the TEM using 2-beam imaging conditions provided the following information. In composites deformed and annealed to achieve the reference state, dislocation cells interconnect the SiC particulates (Fig. 6a). Quenching changed the dislocation substructure such that in the same area, the dislocation density was larger by a factor ~ 3 (Fig. 6b,c). The dislocations in the quenched material occurred predominantly around the SiC particles, where they formed tangles (Fig. 6c). However, slip lines present on the surface of the foil indicated that some dislocations were eliminated at the foil surface. Upon compressive deformation, the dislocation cells decreased in size, both in the transverse and longitudinal orientations. The cell interiors were well defined with a high level of dislocation storage in the walls. Such cell refinement contrasts with an absence of cells found upon deformation of the matrix. There was no TEM evidence of either precipitation in the matrix or of a reaction product at the interface.

5. CALCULATIONS

The predicted effects of thermal expansion misfit and of reverse loading on the flow strength of particulate reinforced composites are addressed within the framework of continuum plasticity by using finite element cell calculations. The procedures used have

been described elsewhere.^{2,3,4,10} The variables are f , A , N and S . The calculations are conducted for axisymmetric cells containing unit cylindrical reinforcements arranged within a regular array, subject to periodic boundary conditions. The imposed loading is uniaxial. The effects of thermal expansion misfit are simulated by imposing a misfit strain,

$$\epsilon_T = 3\Delta\alpha\Delta T/(1 - \nu)$$

where $\Delta\alpha$ is the thermal expansion coefficient difference between the particulate and the matrix, ν is Poisson's ratio and ΔT is the cooling range. The results of such calculations are presented in terms of normalized parameters

$$\Sigma = \sigma/\sigma_0; \quad E = \epsilon/\epsilon_0; \quad \lambda = \Delta\alpha\Delta T/\epsilon_0$$

where σ_0 is the uniaxial yield strength and ϵ_0 the yield strain of the matrix, σ is the stress and ϵ the strain. Calculations are performed for a work hardening exponent $N = 5$ with λ in the range 1–10, typical of the magnitudes applicable to the present composites, and for reinforcement volume fractions in the range 0.1 to 0.5 (Fig. 7). As noted in prior calculations,^{2,4} when $\lambda \gtrsim 1$, misfit induced yielding in the matrix *lowers* the initial flow strength. This occurs because the residual stress in the matrix is at yield and has sufficient magnitude to induce immediate plastic flow upon loading. However, when the matrix exhibits appreciable work hardening ($N \gtrsim 10$), *composite hardening occurs more rapidly in the presence of misfit*, because elastic unloading proceeds in some regions of the misfit deformation zone around the reinforcements. Finally, at large strains ($\epsilon \gtrsim 5 \epsilon_0$), when the deformation field becomes dominated by the applied loading, the flow curves tend to merge. Such behavior is characteristic of that found in

plasticity problems involving misfit.¹¹ The trends in the *maximum* strength differential, $\Delta\sigma_s/\sigma_0$, with f and λ , calculated for $N = 5$, are plotted on Fig. 8.

The behavior subject to *reverse loading* again involves consideration of the internal stresses. In this case, such stresses develop during forward deformation, which then influence the flow that occurs when the loading is reversed. Calculations of the effects of reverse loading for perfect plasticity ($N = \infty$), without misfit (Fig. 9), reveal that flow in compression, following initial tensile deformation, occurs at a reduced strength level (again because of the residual stress in the matrix) and diminishes at large strains. Furthermore, the flow strength differential $\Delta\sigma_b/\sigma_0$ also becomes larger as the reinforcement concentration, f , increases (Fig. 10). Calculations with work hardening have not been conducted. But the analogous effects of N on misfit induced changes in flow strength^{2,4} suggest that the differential would persist to larger strains as the hardening increases (N becomes smaller).

6. COMPARISON BETWEEN EXPERIMENT AND THEORY

6.1 Thermal Expansion Misfit

Comparison of the measured strength differentials with the continuum calculations is achieved by compiling the data from Fig. 2 and superposing on the calculated curves (Fig. 8), with the matrix flow strength, σ_0 , regarded as an *unknown*. For this purpose, it is noted that $\Delta\alpha \approx 2 \times 10^{-5} \text{ C}^{-1}$ and $\epsilon_0 \approx 10^{-3}$, such that λ varies between ~ 1 and 5 for the ΔT range used in the present experiments. The comparison commences with the experimental results for the effect of volume fraction. For the case $\lambda = 5$ (Fig. 2a), fitting the experiments to the calculations, at $f = 0.4$ (Fig. 8), *infers* matrix yield strengths, $\sigma_0 \approx 100 \text{ MPa}$ for the Al system and $\sigma_0 = 170 \text{ MPa}$ for the Al/3 Mg system. By *fixing these values for σ_0* , trends with f , ΔT and R can be compared with experiments, as shown on Figs. 2 and 8. Most of the key features predicted by the calculations are found to be

consistent with the data. Notably, the strength differential data $\Delta\sigma_s$ for both systems (Al and Al/3 Mg) *superpose when normalized with σ_0* (Fig. 8). Furthermore, $\Delta\sigma_s$ increases as either f increases (Fig. 2a) or ΔT increases (Fig. 2b), but is independent of R (Fig. 2c).

The *in situ* matrix yield strengths inferred using this approach are larger than those found for the monolithic matrices (Table I). Furthermore, the differential is greater for Al than Al/3 Mg matrices, as also found in other recent studies.^{12,13} The TEM studies provide no evidence that such matrix strengthening could be associated with compositional effects (such as solute and precipitate hardening). However, the dislocation substructure present in the composites in the reference state (Fig. 6a) may provide a forest hardening term that superposes on the *matrix strength*. This possibility is qualitatively supported by the strong substructure effects on flow strength found after extrusion (Fig. 5).

6.2 Reverse Loading

An assessment of the continuum predictions of reverse loading effects is made by normalizing the strength differential $\Delta\sigma_b$ data (Fig. 4) with σ_0 and replotting on Fig. 10. *The normalization again unifies the data for the same σ_0 used to rationalize the misfit data.* Furthermore, the experimental stress differentials are of the same order as the predictions. However, the peak stress is found to occur at much larger strains than predicted. Two factors influence this discrepancy. i) The calculations have not included work hardening, which should have a substantial effect, both on the magnitude of the stress differential ($\Delta\sigma_b/\sigma_0$) and especially on the relative strains at which this strength differential persists. ii) The measurements involve thermal expansion misfit which may also influence $\Delta\sigma_b$. Such misfit has not been included in the calculations. Further calculations would be needed to address these factors.

7. CONCLUDING REMARKS

Various trends in the flow strength of particulate reinforced metal matrix composites have been found to be consistent with finite element cell calculations. These include effects of thermal expansion misfit and of reverse loading.[‡] To achieve good correlations between experiments and calculations, it has been necessary to invoke a matrix reference strength σ_0 that differs from that for the unreinforced alloy. However, once the reference strength for a given matrix has been identified, the same σ_0 appears to apply throughout the range of reinforcements and testing variables associated with that matrix. It remains to understand the factors that dictate this matrix strength.

ACKNOWLEDGEMENTS

The authors are indebted to Dr. Y. Yang and Mr. C. Cady for preparation of the material. Dr. S. Schmauder acknowledges the partial support of the German Research Society for his part of the work. This work was supported by Defense Advanced Research Projects Agency (DARPA).

[‡] A widely invoked dislocation model does not have such good predictive ability (Appendix).

APPENDIX

Dislocation Approach For Misfit Strengthening^{5,6}

The thermal misfit strain in the matrix on cooling the composite through a temperature range ΔT is

$$\epsilon_m \approx \frac{3\Delta\alpha\Delta T f}{(1-\nu)} \quad (A1)$$

where $\Delta\alpha$ is the difference in thermal expansion between SiC ($\alpha = 4 \times 10^{-6} \text{ K}^{-1}$) and Al ($\alpha = 24 \times 10^{-6} \text{ K}^{-1}$) and ν is Poisson's ratio. The resulting dislocation density, ρ , is related to the thermal strain through

$$\rho = \epsilon_m / b\bar{l} \quad (A2)$$

where b is the Burgers' vector and \bar{l} is the mean slip distance in the matrix, given by

$$\bar{l} = R/f\% \quad (A3)$$

where R is the particle size.

The flow stress $\bar{\sigma}$ due to the presence of these dislocations is,

$$\bar{\sigma} = A\mu b\sqrt{\rho} \quad (A4)$$

where A is a constant of order unity and μ is the shear modulus of the matrix.

Combining Eqns. (A1) to (A4), the flow strength becomes,

$$\bar{\sigma} = \sqrt{3} \mu b f^{\frac{1}{2}} \left(\frac{\Delta \alpha \Delta T}{(1 - \nu) b R} \right)^{\frac{1}{2}} \quad (\text{A5})$$

Note that the flow stress is *independent* of the matrix yield stress, σ_0 and scales *inversely* with the particle size. Such characteristics are not apparent in the present experiments (Fig. 2).

REFERENCES

- [1] J.P. Hirth, Viewpoint Set, *Scripta Metall. Mater.*, **25** (1991) pp. 1-33.
- [2] T. Christman, A. Needleman and S. Suresh, *Acta Metall.*, **37**, 3029 (1989).
- [3] G. Bao, J.W. Hutchinson and R.M. McMeeking, *Acta Metall. Mater.*, **39**, 1071 (1991).
- [4] D.B. Zahi and R.M. McMeeking, *Acta Metall. Mater.*, **39**, 1117 (1991).
- [5] S.M. Pickard and B. Derby, *Acta Metall. Mater.*, **38**, 2537 (1990).
- [6] F.J. Humphreys, *Proc. 9th Risø Int. Symp. Metall. Mater. Sci.*, (edited by S.I. Anderson, H. Lilholt and O.B. Pederson) p. 51 (1988).
- [7] R.J. Arsenault, L. Wang and C.F. Feng, *Acta Metall. Mater.*, **39**, 47 (1991).
- [8] Y.L. Klipfel, M.Y. He, R.M. McMeeking, A.G. Evans and R. Mehrabian, *Acta Metall. Mater.*, **38**, 1063 (1990).
- [9] J. Yang, C. Cady, M.S. Hu, F.W. Zok, R. Mehrabian and A.G. Evans, *Acta Metall. Mater.*, **38** (1990) 2613.
- [10] J. Llorica, S. Suresh and A. Needleman, to be published.
- [11] M.Y. He and A.G. Evans, *Acta Metall. Mater.*, **39**, 1387 (1991).
- [12] B. Derby and J.R. Walker, *Scripta Metall.*, **22**, 529 (1988).
- [13] J. Yang, S.M. Pickard, C. Cady and A.G. Evans, *Acta Metall. Mater.*, **39**, 1863 (1991).

FIGURE CAPTIONS

- Fig. 1. a) Typical flow curves at small strains obtained on specimens cooled to different temperatures (Al matrix, $f = 0.3$, $R = 9 \mu\text{m}$).
 b) The effects of large strains on the difference between the flow curves in the reference state and when cooled to liquid nitrogen temperature (Al/3 Mg matrix, $f = 0.5$, $R = 9 \mu\text{m}$).
- Fig. 2. Trends in thermal expansion misfit strength differential $\Delta\sigma_s$ with
 a) reinforcement volume fraction for both Al and Al/3 Mg matrices ($R = 9 \mu\text{m}$, LNQ), b) cooling range ΔT for Al ($f = 0.4$, $R = 9 \mu\text{m}$),
 c) reinforcement size for Al/3 Mg ($f = 0.5$, LNQ). Also shown are predicted values for the uniaxial yield strengths, σ_0 , indicated on the figures.
- Fig. 3. A loading cycle conducted on a material cooled in liquid nitrogen. Comparison with the flow strength of the material in the reference state ($R = 9 \mu\text{m}$, $f = 0.5$).
- Fig. 4. Trends in the strength differential $\Delta\sigma_b$ with plastic strain amplitude for both Al/3 Mg and Al matrix materials in reference state ($f = 0.5$, $R = 9 \mu\text{m}$). Also shown is the curve predicted for a non-hardening matrix.
- Fig. 5. Effects of extrusion on the flow strength of 'pure' Al.
- Fig. 6. TEM observations of matrix dislocations a) hot-worked deformation cell substructure b) and c) same area of composite after annealing and quenching into water, respectively.
- Fig. 7. Calculated flow curves with and without thermal expansion misfit ($\lambda \equiv \Delta\alpha\Delta T/\epsilon_0 = 5$, $N = 5$).
- Fig. 8. Effects of reinforcement volume fraction and misfit strain, $\lambda \equiv \Delta\alpha\Delta T/\epsilon_0$, on the relative strength differential. Also shown are experimental results, plotted with matrix flow strength σ_0 *inferred* by fitting the data to the calculation at $f = 0.4$, with $\lambda = 5$. All other points are plotted using these σ_0 . The inferred σ_0 are 100 MPa for Al matrices and 170 MPa for Al/3 Mg matrices.

Fig. 9. Forward and reverse loading calculations for two different reinforcement volume fractions and a perfectly plastic matrix ($N = \infty$).

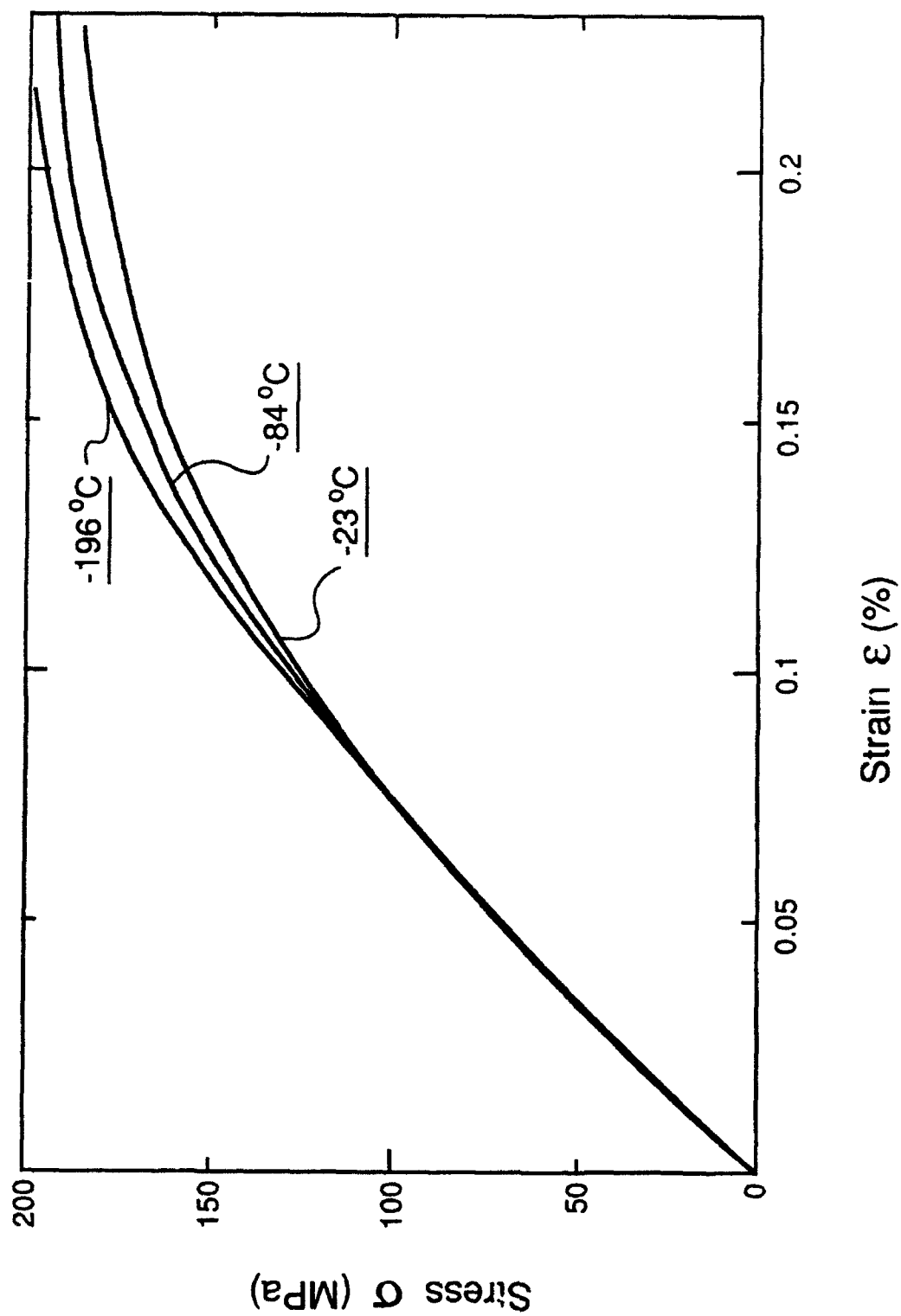


Fig. 1. a) Typical flow curves at small strains obtained on specimens cooled to different temperatures (Al matrix, $f = 0.3$, $R = 9 \mu\text{m}$).

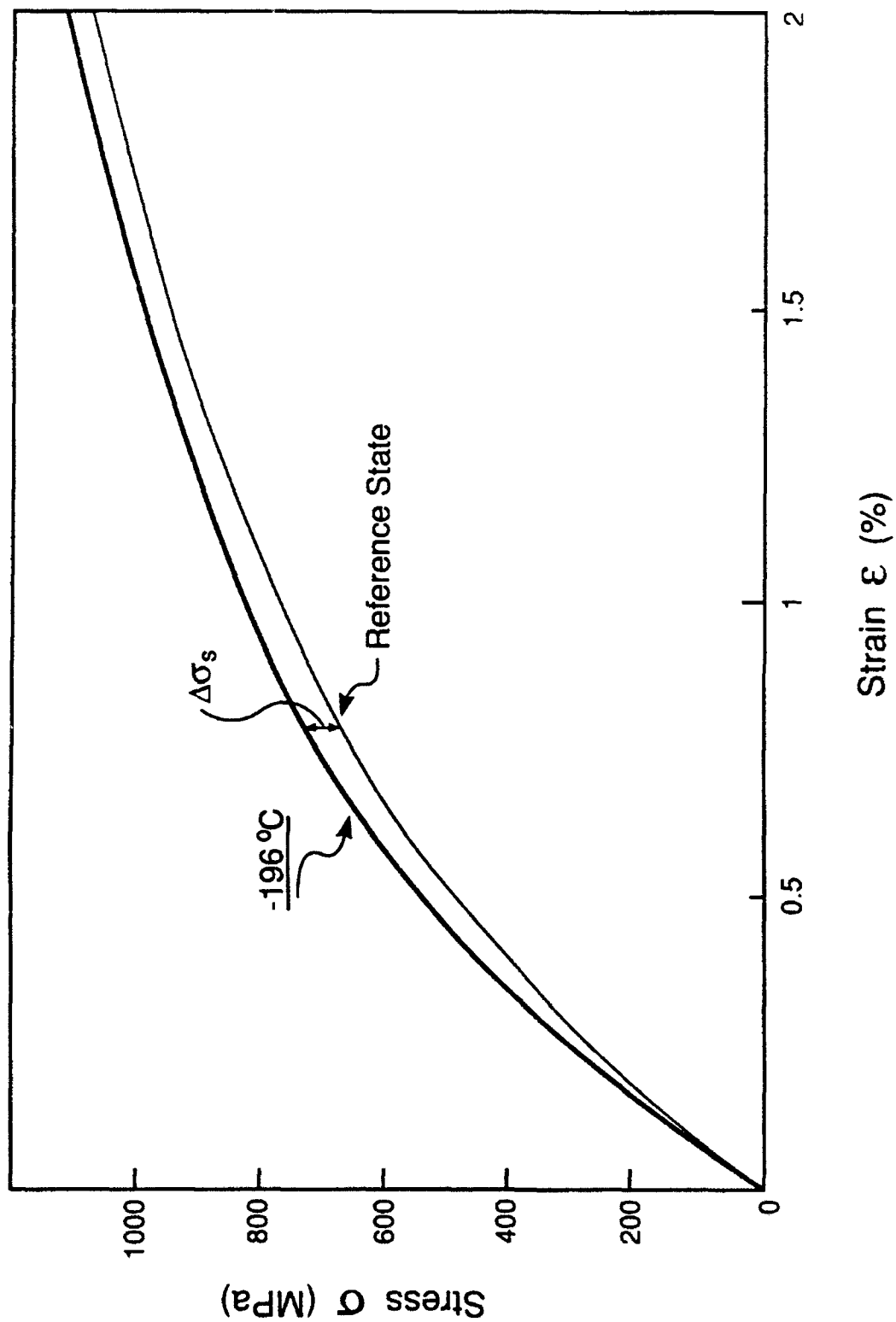


Fig. 1. b) The effects of large strains on the difference between the flow curves in the reference state and when cooled to liquid nitrogen temperature (Al/3 Mg matrix, $f = 0.5$, $R = 9 \mu\text{m}$).

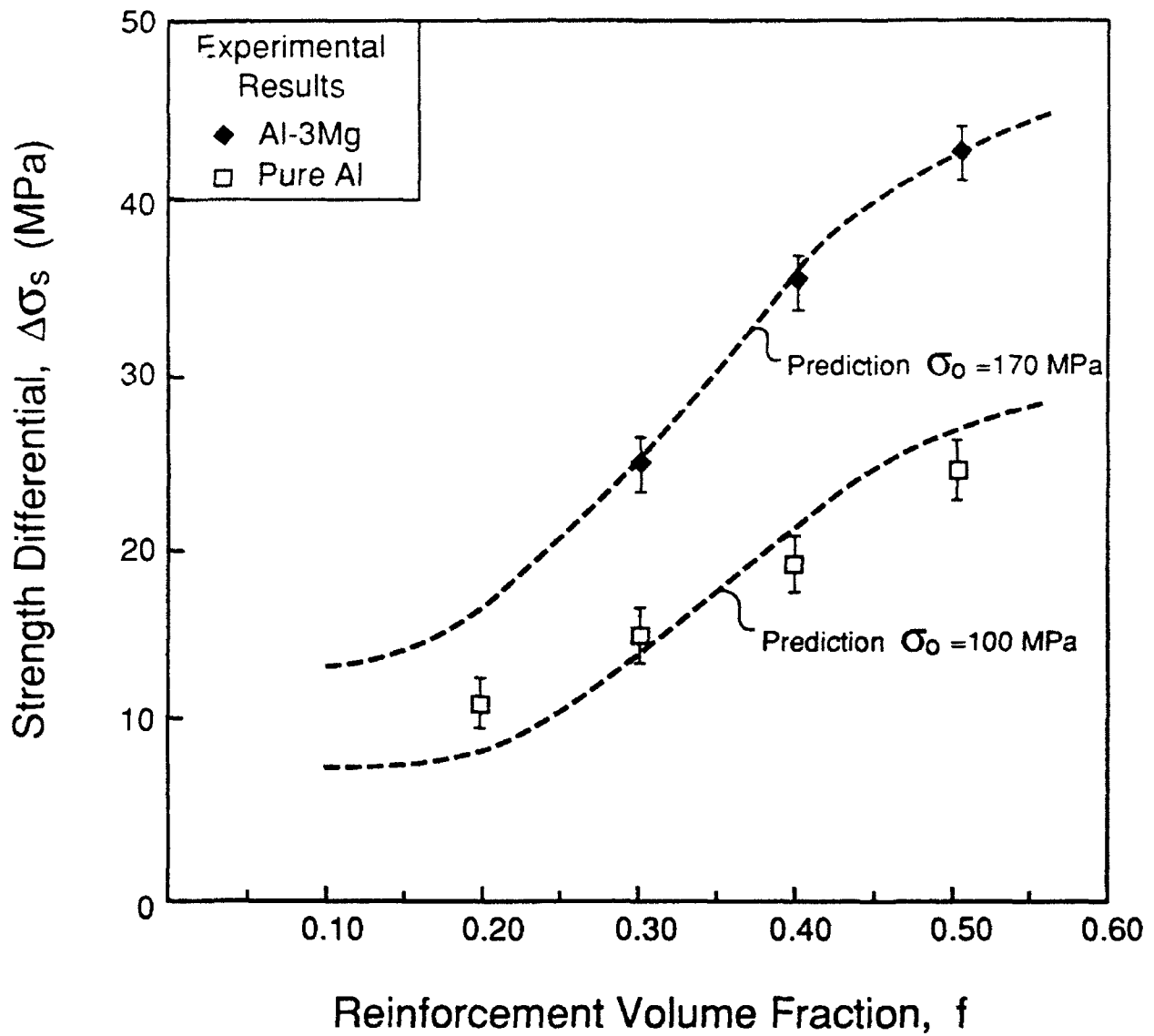


Fig. 2. a) Trends in thermal expansion misfit strength differential $\Delta\sigma_s$ with reinforcement volume fraction for both Al and Al/3 Mg matrices ($R = 9 \mu\text{m}$, LNQ)

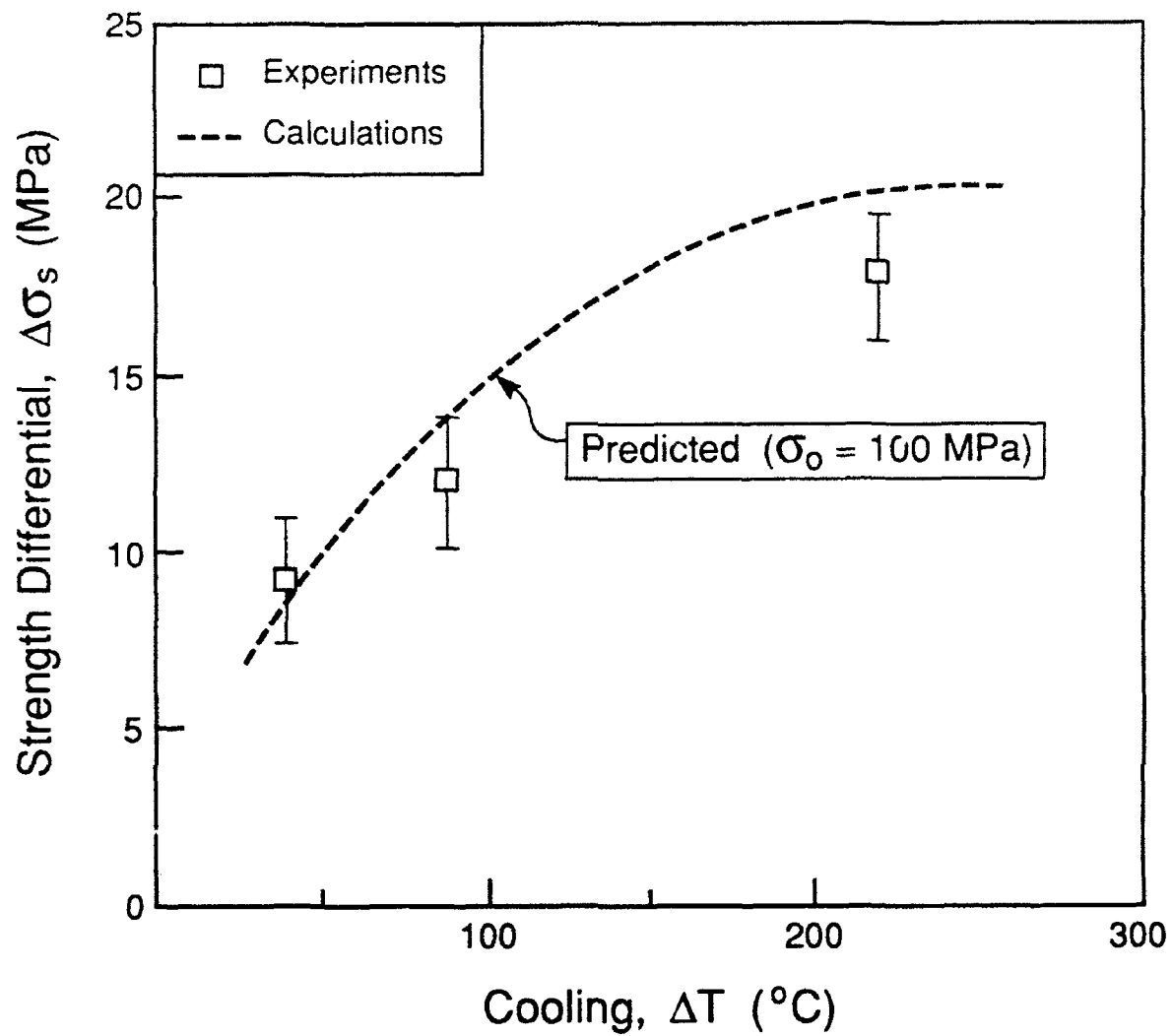


Fig. 2. b) Trends in thermal expansion misfit strength differential $\Delta\sigma_s$ with cooling range ΔT for Al ($f = 0.4$, $R = 9 \text{ mm}$)

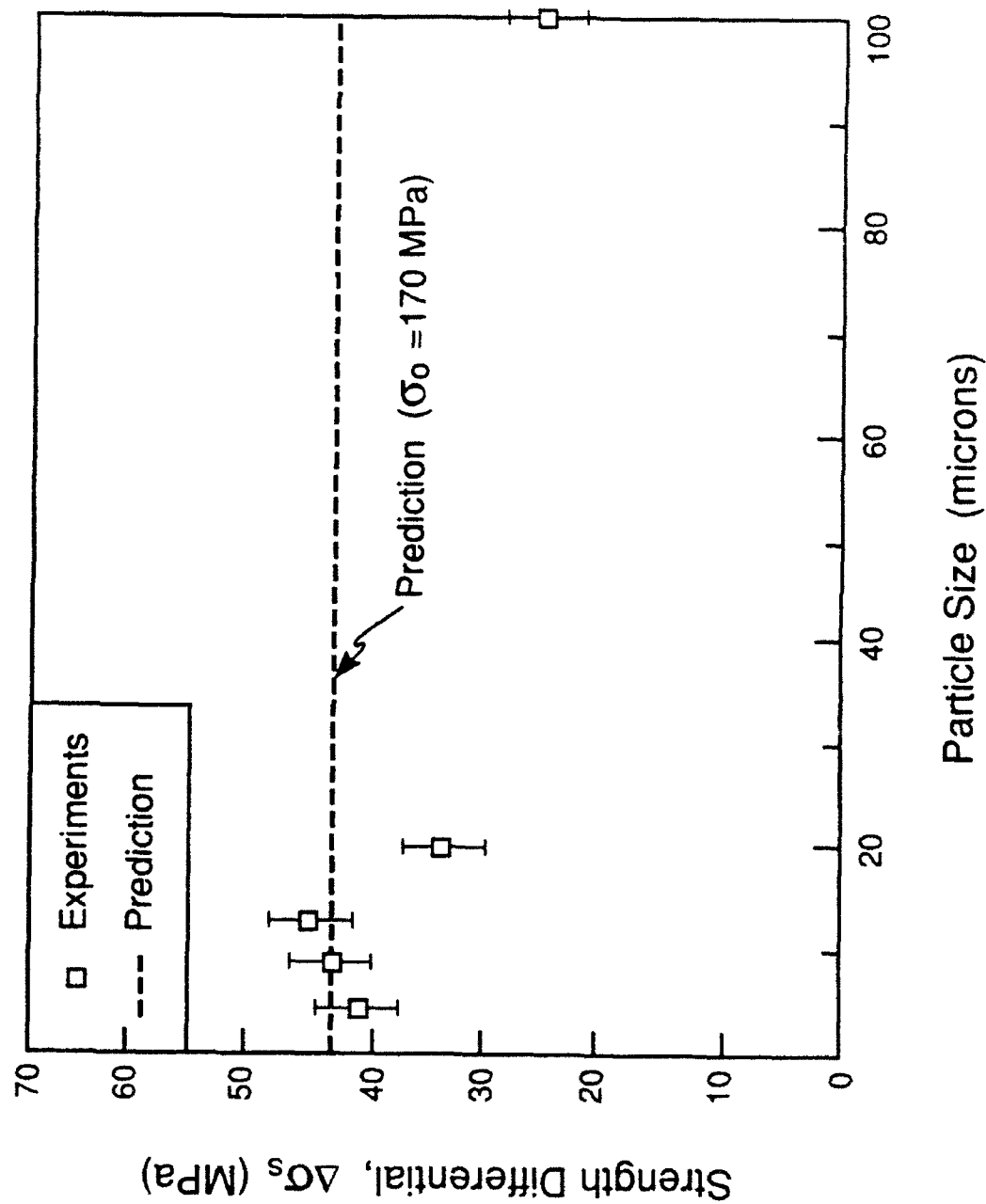


Fig. 2. c) Trends in thermal expansion misfit strength differential $\Delta\sigma_s$ with reinforcement size for Al/3 Mg ($f = 0.5$, LNQ). Also shown are predicted values for the uniaxial yield strengths, σ_0 , indicated on the figures.

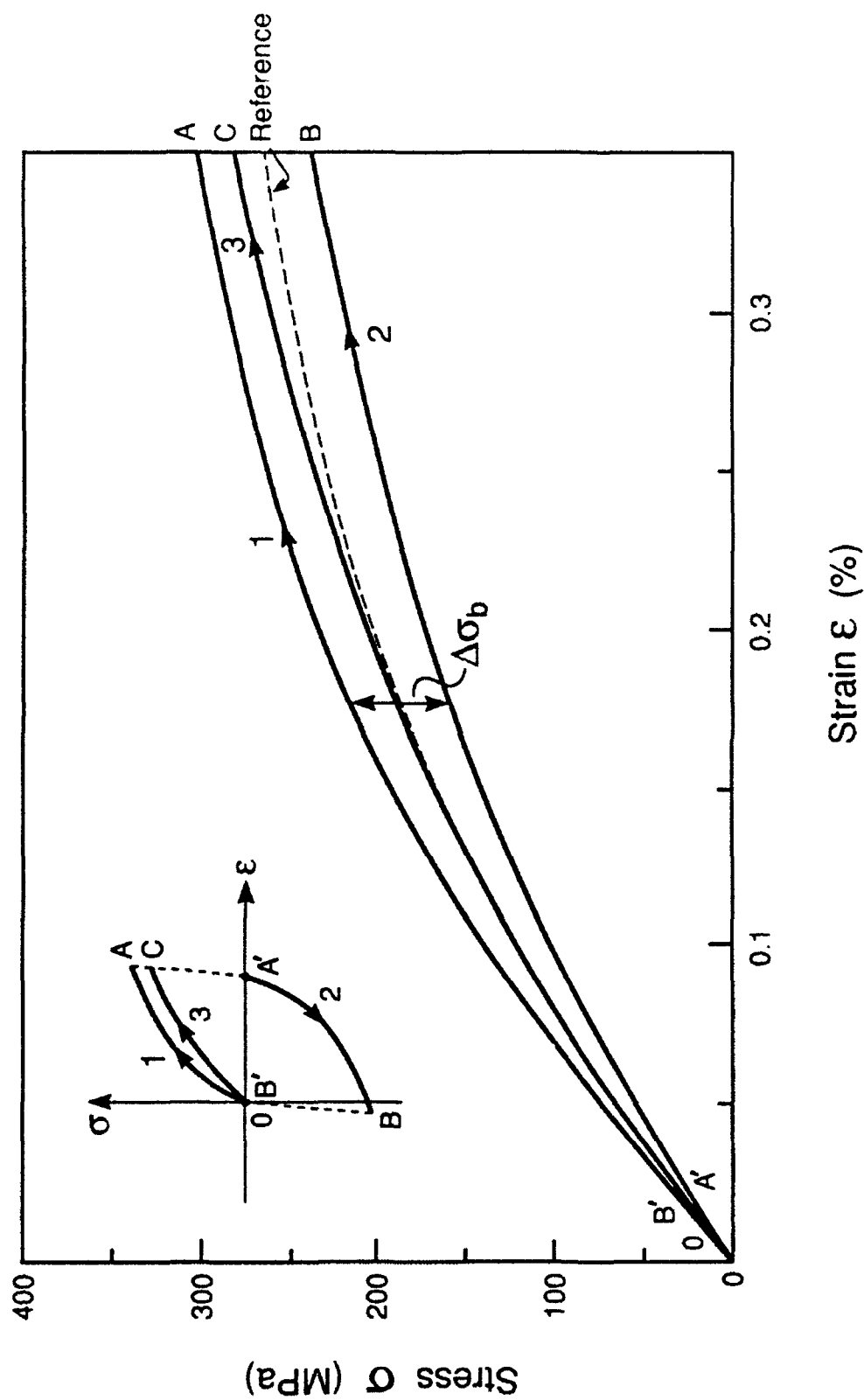


Fig. 3. A loading cycle conducted on a material cooled in liquid nitrogen.
Comparison with the flow strength of the material in the reference
state ($R = 9 \mu\text{m}$, $f = 0.5$).

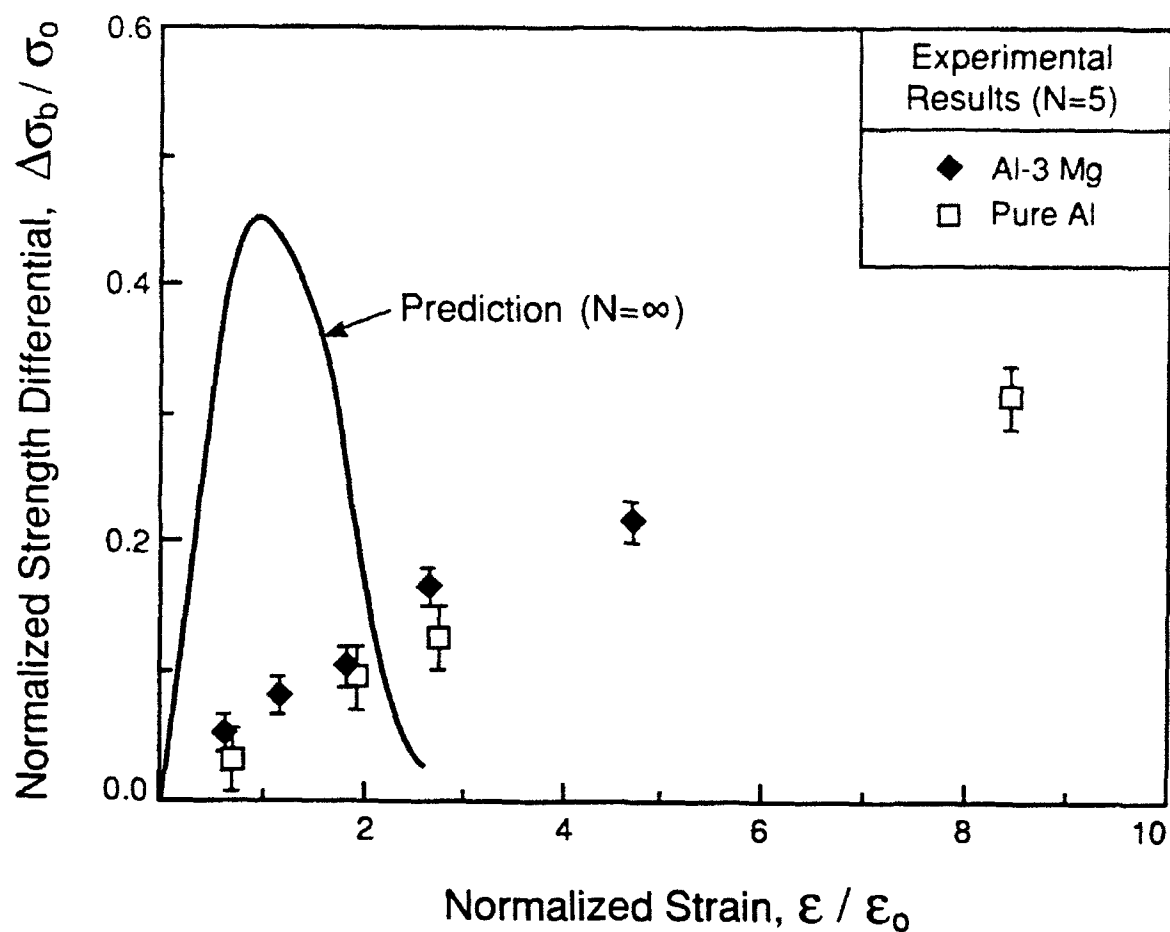


Fig. 4. Trends in the strength differential $\Delta\sigma_b$ with plastic strain amplitude for both Al/3 Mg and Al matrix materials in reference state ($f = 0.5$, $R = 9 \mu\text{m}$). Also shown is the curve predicted for a non-hardening matrix.

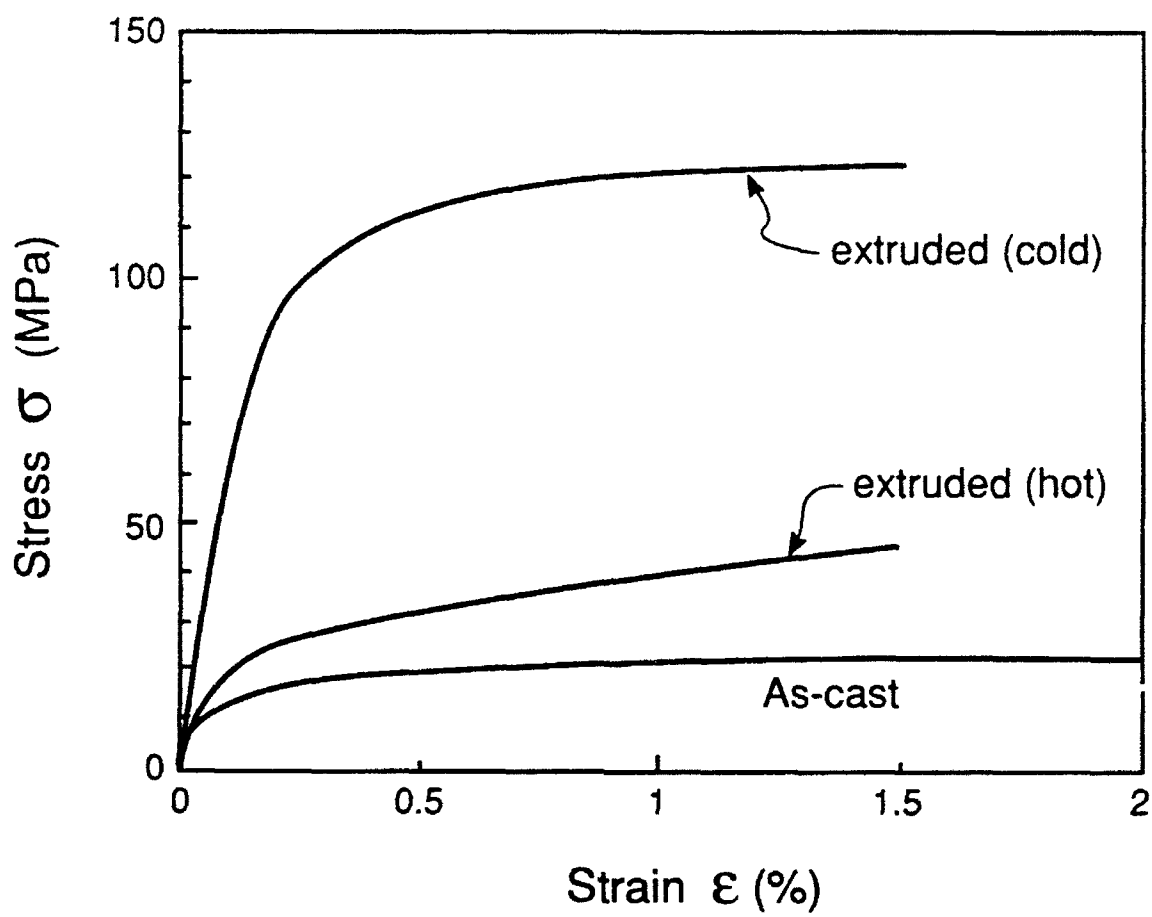


Fig. 5. Effects of extrusion on the flow strength of 'pure' Al.



Fig. 6. a) TEM observations of matrix dislocations a) hot-worked deformation cell substructure b) and c) same area of composite after annealing and quenching into water, respectively.



Fig. 6. a) TEM observations of matrix dislocations a) hot-worked deformation cell substructure b) and c) same area of composite after annealing and quenching into water, respectively.



Fig. 6. a) TEM observations of matrix dislocations a) hot-worked deformation cell substructure b) and c) same area of composite after annealing and quenching into water, respectively.

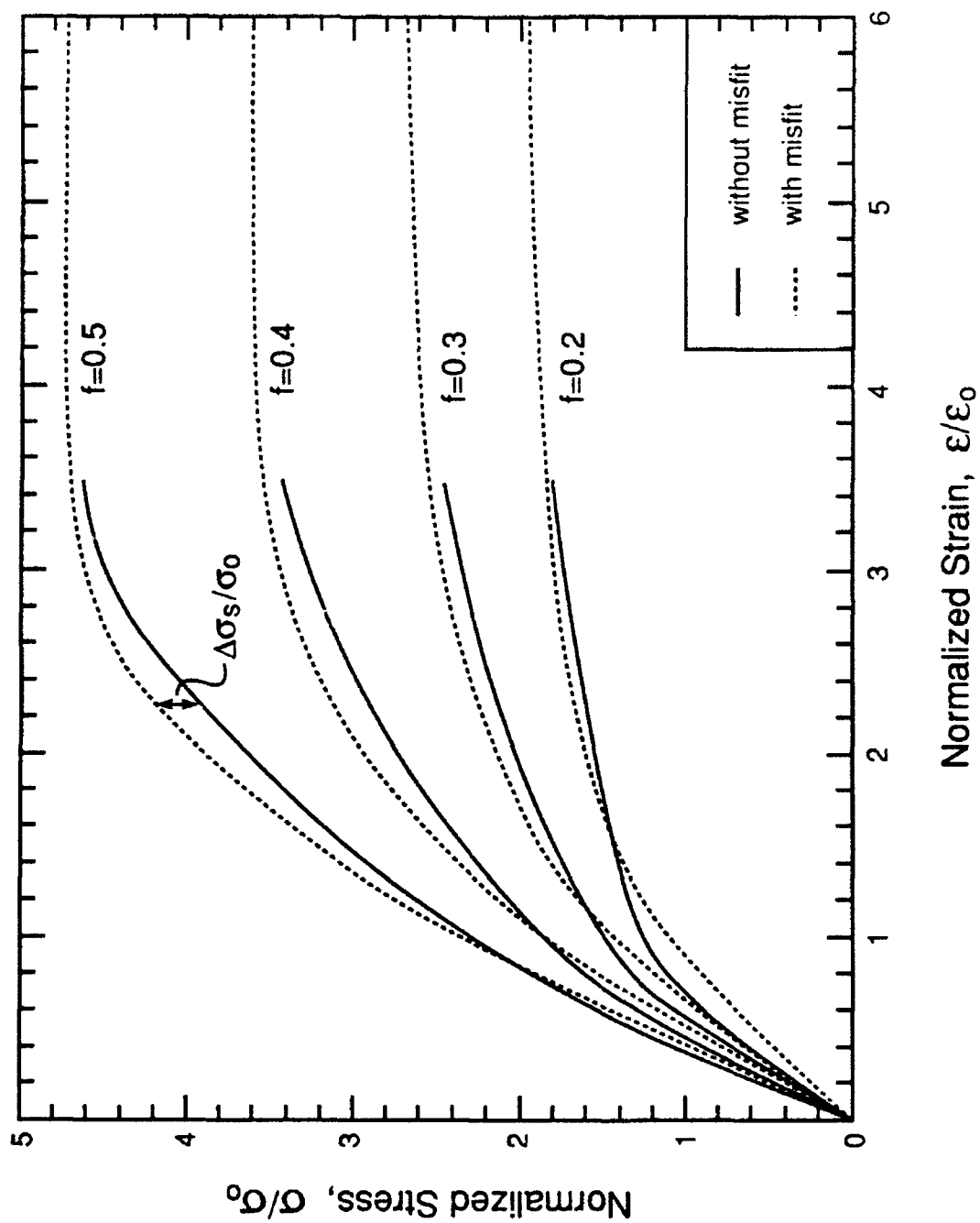


Fig. 7. Calculated flow curves with and without thermal expansion misfit
($\lambda \equiv \Delta\alpha\Delta T/\epsilon_0 = 5$, $N = 5$).

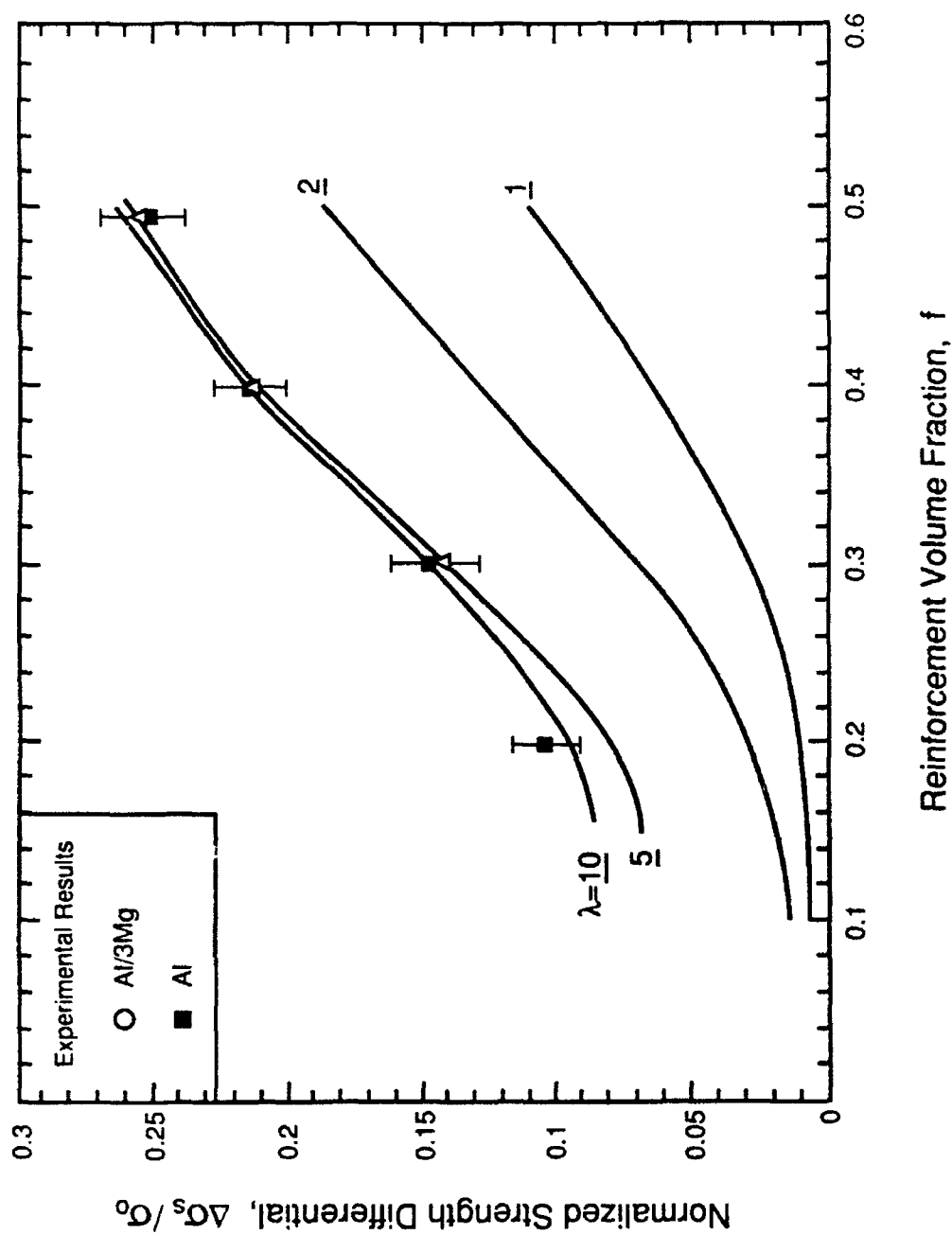


Fig. 8. Effects of reinforcement volume fraction and misfit strain, $\lambda \equiv \Delta\alpha\Delta T/\epsilon_0$, on the relative strength differential. Also shown are experimental results, plotted with matrix flow strength σ_0 *inferred* by fitting the data to the calculation at $f = 0.4$, with $\lambda = 5$. All other points are plotted using these σ_0 . The inferred σ_0 are 100 MPa for Al matrices and 170 MPa for Al/3 Mg matrices.

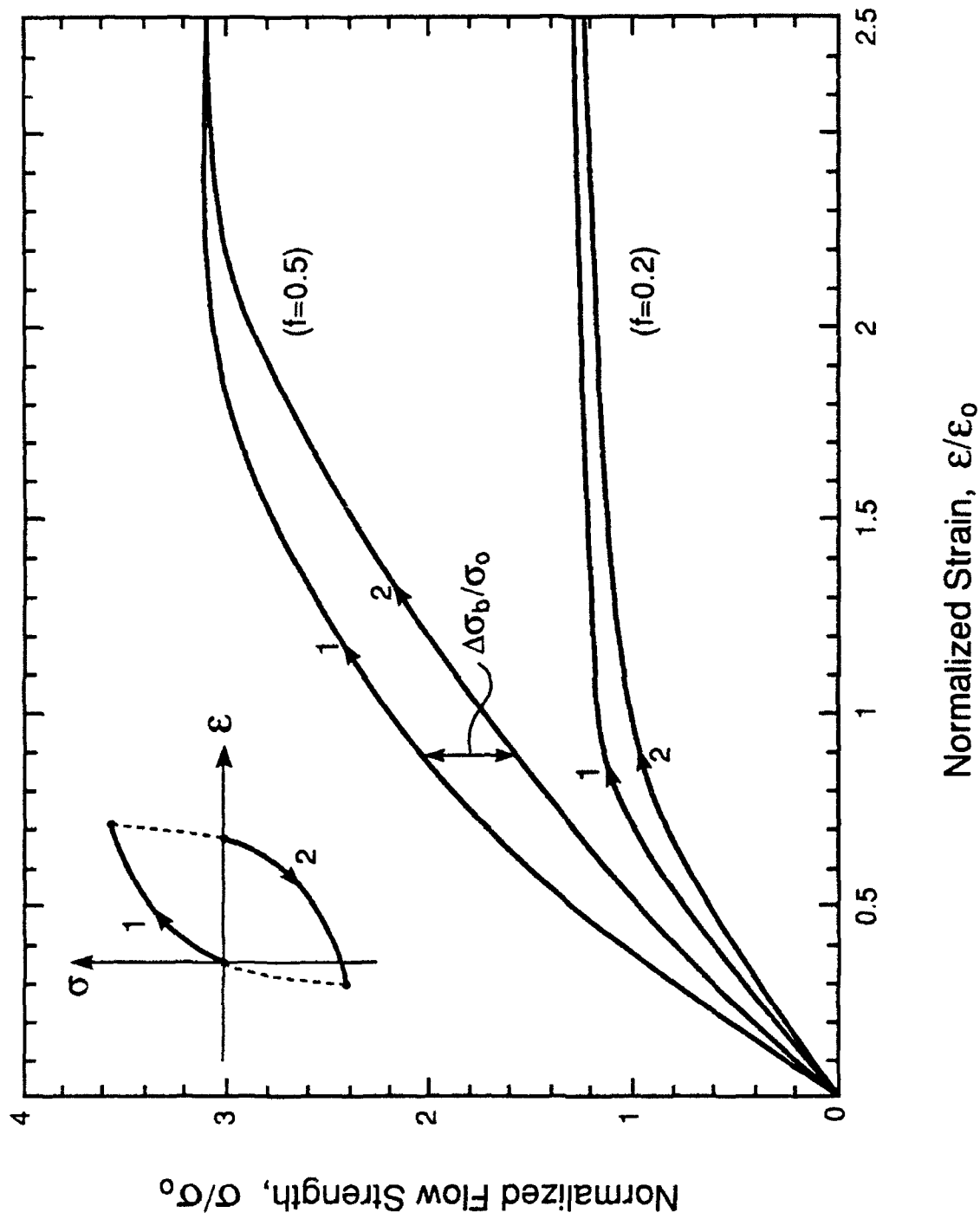


Fig. 9. Forward and reverse loading calculations for two different reinforcement volume fractions and a perfectly plastic matrix ($N = \infty$).

CHAPTER n

CONTINUUM MODELS FOR DEFORMATION: DISCONTINUOUS REINFORCEMENTS

J. W. Hutchinson and R.M. McMeeking

The assumption underlying the mechanics of particle reinforcement of ductile matrix materials presented in this chapter is that the size of the particles and the spacing between particles are sufficiently great such that continuum plasticity can be used to characterize the deformation of the matrix material. The continuum results discussed below are very different in character from dislocation-based models of precipitation hardening. For example, there is a strong size effect in precipitation hardening independent of particle volume fraction, while there is no size effect predicted by the conventional continuum models since the constitutive model for the matrix has no length scale associated with it. The length scale characterizing the transition between the two approaches has not been established and is undoubtedly material dependent and perhaps dependent on whether the description is for rate-independent plasticity or creep. For continuum plasticity to be valid it is necessary that the particle size and spacing be large compared to the dominant scale of the dislocation motion such as cell size. Generally, for typical metal matrix materials, it is felt that particle sizes and spacings of several microns or more should ensure that conditions are met for validity of the continuum description.

An independent issue is the assignment of insitu plastic properties of the matrix material such as the flow strength and strain hardening index. It is not uncommon for the insitu properties of the matrix to be altered from the bulk properties due to processing of the reinforced composite system. In the approach described below, the properties of the matrix must be regarded as insitu properties. Further discussion of this matter will be given in a later section in which comparisons of theory and experiment are made.

The chapter is organized as follows. The first section considers the flow strength of perfectly plastic matrix materials. In particular, the effects of particle shape, volume fraction, alignment and distribution will be discussed. The perfectly plastic idealization has a number of advantages for presenting and discussing the role of particle reinforcement. It isolates the primary strengthening effect and provides a setting for discussing the effect of matrix hardening in rate-independent materials, which is the topic of the second section. This chapter does not deal with the important question of damage development. It will be assumed that the reinforcing particles are well bonded to the matrix and that neither the interface separates nor the particles crack. Thus, the macroscopic stress-strain responses of the composites predicted here must be regarded as limiting responses for systems free of damage. Section n.3 deals with residual stress development and with the effect of these stresses on overall stress-strain behavior. Section n.4 discusses application of the approach to creep reinforcement, including the effect of diffusional relaxation of the reinforcement.

Much of the material presented in this chapter is drawn from two recent papers by the authors (Bao, Hutchinson and McMeeking 1991a, 1991b). The primary emphasis is on the role of particulate reinforcements but results on the *transverse* behavior of continuous aligned fiber reinforced composites will also be included since it falls naturally within the framework for discontinuous reinforcement. There are a number of relatively recent papers in the literature based on the continuum approach and other chapters in this book draw on this work. Papers especially relevant to the present chapter are those by Christman, Needleman and Suresh 1989; Levy and Papazian 1990; Tvergaard 1990; and Dragone and Nix 1990.

n.1 FLOW STRENGTH OF COMPOSITES WITH NON-HARDENING MATRICES

With the exception of creep behavior dealt with in Section n.4, the matrix material will be taken to be rate-independent. In this section the matrix will be further idealized to be elastic-perfectly plastic with a tensile flow stress σ_0 . A Mises yield condition is assumed such that $\sigma_e = \sigma_0$ where the effective stress depends on the deviator stress components s_{ij} according to

$\sigma_e = \sqrt{(3s_{ij}s_{ij}/2)}$. Plastic strain increments are directed along the outward normal to the yield surface, proportional to s_{ij} . The primary emphasis in this section is on the strengthening of the composite due to the discontinuous reinforcements, which is best reflected by the increase in the overall limit stress of the composite. Let $\bar{\sigma}$ denote the overall tensile stress applied to the composite in some direction. For aligned reinforcements we will be concerned with overall tension (or compression) applied parallel to the direction of alignment, except for some examples of continuous fiber reinforcement where the loading will be transverse to the direction of alignment. For an elastic-perfectly plastic matrix reinforced by discontinuous reinforcements which do not deform plastically, there is a limit value of $\bar{\sigma}$ which is denoted here by $\bar{\sigma}_0$. This overall limit yield stress does not depend on the elastic moduli of either the matrix or the reinforcement nor does it depend on the absolute size of the reinforcing particles. It does depend on the volume fraction of the reinforcement phase and on other details of the reinforcement such as shape and alignment. It is these dependencies which will be presented below.

n.1.1 Aligned Discontinuous Reinforcements

An axisymmetric cell model is used to calculate the overall limit stress. This method has been widely employed and is used by some of the authors in other chapters. The population of reinforcing particles is assumed to have identical size, shape and alignment and, in addition, is assumed to be uniformly distributed such that each particle and its surrounding matrix deforms in the same way as every other particle/matrix neighborhood. In this way, a single particle/matrix cell with special periodic boundary conditions can be used to compute the response of the entire composite. Usually, to reduce the computations, a cell with full 3D geometry will be replaced, as an approximation, by an axisymmetric cell under axisymmetric boundary conditions. This final step in the modeling process, which is illustrated in the insert in Figure n-1 for a 3D array of spherical particles, has been shown to introduce little error at moderate volume fractions (Hom, 1992). The volume fraction of the reinforcing phase in the cell is identified with the volume fraction of that phase in the composite. The height to diameter of the cell can be chosen to model

the axial to transverse spacing of the particulates in the composite. Some further discussion of the role of the cell aspect ratio can be found in Bao et al. 1991a; in this chapter all results for aligned reinforcements will have been calculated using a cell whose height to diameter ratio equals that of the reinforcing particles.

The results of the cell model computation for the strengthening ratio, $\bar{\sigma}_0/\sigma_0$, as a function of particle volume fraction f for spherical particle reinforcements in an elastic-perfectly plastic matrix is shown in Figure n-1. The limit yield stress of the composite becomes unbounded as the volume fraction approaches the value where the particles make contact, which for the cell model is $f=2/3$. The most notable feature of these predictions is how little strengthening effect spherical particles have. A ten percent increase in limit yield stress requires almost a twenty percent volume fraction of particles. This, of course, is in marked contrast with the relatively large strengthening possible from volume fractions of less than even one percent of equi-axed precipitates whose sizes are sufficiently small that discrete particle/dislocation interactions govern strengthening. Larger equi-axed particles, in the range in which continuum plasticity governs, are remarkably inefficient strengthening agents.

Elongated or disc-shaped particles can be effective strengthening agents, as seen in Figures n-2 and n-3. The effect of aligned ellipsoidal particles on the strengthening ratio is displayed in Figure n-2, where the prolate axisymmetric particles have aspect ratio $a/b < 1$ and the oblate particles have $a/b > 1$. The effect of either pronounced elongation or flattening of the particles is striking in comparison with the effect of the spherical particles, which is labeled in this figure by $a/b=1$. Particles in the shape of right circular cylinders (rods $a/b < 1$, unit cylinders $a/b=1$, or discs $a/b > 1$) are somewhat more effective than ellipsoids at the same volume fraction (Figure n-3). The unit cylinders are still not very efficient, but they are about twice as effective as spheres (Christman, et al. 1989). Thus, details of particle shape in addition to aspect ratio can be important. Arrangement of the reinforcing phase can also be important especially when the particles are highly elongated with significant strengthening capacity. The results for the elongated particles shown in Figures n-

2 and n-3 represent an arrangement where the particles are end-to-end with no overlap, by virtue of geometry of the axisymmetric cell model. Alternative arrangements of highly elongated particles allowing for varying degrees of particle overlap have shown that results such as those discussed above based on the simplest cell model usually predict the largest possible strengthening (Levy and Papazian, 1990; Tvergaard, 1990; and Dragone and Nix, 1990).

n.1.2 Transverse Strengthening of Continuous Fiber-reinforced Composites

A composite with aligned continuous fibers which do not deform plastically (nor fracture) will not have a limit yield stress for stressing parallel to the fiber direction, and nonlinear response of the composite for such loadings will be dealt with elsewhere in this book. The fibers have a strengthening effect for stressing in tension or compression in directions perpendicular to the fibers which is analogous to that described for the discontinuous particulate reinforcements with a well defined limit yield stress. For this reason, results of Jansson and Leckie, 1992 and unpublished work of Schmauder and McMeeking for the transverse strengthening of fiber-reinforced composites will be included in this chapter. As in the case of the discontinuous reinforcements, the fibers are assumed to be perfectly bonded to the matrix which is elastic-perfectly plastic with tensile yield stress σ_0 . The strengthening ratio $\bar{\sigma}_0/\sigma_0$ is plotted as a function of the fiber volume fraction f in Figure n-4 for round fibers in square and hexagonal arrangements. It should be noted that results for biaxial stress states can be obtained from Figure n-4 by superposition of a hydrostatic stress.

At small volume fractions there is very little strengthening except for the imposition by the fibers of plane strain flow in the matrix. Thus, the limit at zero volume fraction is a strengthening ratio of $2/\sqrt{3}$, consistent with plane strain. The minimal effect of fibers on the transverse strength is analogous to the situation with spherical reinforcements discussed previously. The results plotted in Figure n-4 make it clear that there is a strong effect of fiber arrangement, which has been observed previously in calculations by Brockenbrough, Suresh and Wienecke, 1991 and others. When the stress is applied parallel to the diagonal of the square packing, the strengthening is $2/\sqrt{3}$

for all the volume fractions studied by Schmauder and McMeeking which were as high as 75%. The lack of strengthening beyond the plane strain level occurs in this case because plastic shear strain can occur without constraint on planes parallel to the diagonal of the packing. This deformation is sustained by the yield stress in shear parallel to the diagonals and therefore by a transverse tension of $\bar{\sigma} = 2\sigma_0/\sqrt{3}$. This particular mechanism of deformation occurs when the square packed composite is loaded parallel to the diagonal. It is only precluded when the fibers touch each other which takes place when $f = \pi/4$. Thus, the strengthening ratio of $2/\sqrt{3}$ should prevail up to just below this volume fraction of fibers. When $f = \pi/4 = 0.79$ and the fibers touch, the square packed composite has an unbounded limit load in analogy to the behavior of the material reinforced with spheres.

When the material with fibers packed in a square arrangement is loaded parallel to the fiber rows, there is no strengthening beyond the plane strain level up to a volume fraction of $\pi/8 = 0.39$ as can be seen in Figure n-4. Below this volume fraction, shear strain can occur on uninterrupted planes at 45° to the tensile axis. Thus a shear stress, at 45° to the fiber rows, equal to the shear yield strength, is sufficient to ensure yielding of the square packed material at volume fractions below 39%. Consequently, the transverse limit strength in these circumstances is $2\sigma_0/\sqrt{3}$. When the volume fraction exceeds 39%, the planes at 45° to the square packed fiber rows are interrupted by the fibers. As a result, shear strain can no longer occur freely on those planes and the constraint leads to an elevation of the transverse strength. Figure n-4 shows that this constraint rises quite rapidly as the volume fraction is increased. Indeed, the strength would become unbounded at a volume fraction of $\pi/4 = 79\%$ when the fibers are touching. Therefore the strengthening ratio must rise rapidly between the volume fractions $\pi/8 = 39\%$ where it is $2/\sqrt{3}$ and $\pi/4 = 79\%$ where it is infinity. Comparison of the results in Figure n-4 for the square packed fiber composite loaded in the two orientations reveals a marked anisotropy at volume fractions above 39%.

In contrast, the material with the fibers arranged in a hexagonal array exhibits minimal anisotropy. This was noted by Brockenbrough et al. (1991) and Jansson and Leckie (1992) who cite unpublished work by Jansson. A single line has been used in Figure n-4 to represent all results for the hexagonal packed composites, though with a perfectly plastic matrix there is a small difference in the transverse strength if the stress is applied parallel to the fiber rows or at 30° to the fiber rows. At a given volume fraction, other results lie in between. It can be seen in Figure n-4 that there is little strengthening when the volume fraction of fibers is low. In this regard, the hexagonally packed fibers in terms of transverse strength are similar to spherical particulates in their ineffectiveness as strengthening agents. It requires 50% fibers to increase the transverse strength to 30% above the matrix uniaxial strength and about half of that effect comes from plane strain. In contrast to the square packed case, there is a small effect at low volume fractions of hexagonally packed fibers. This arises because there are no uninterrupted shear planes in the case of hexagonally packed fibers so that even a small number of fibers causes some constraint, although the net effect is quite modest. The strengthening ratio rises more strongly above volume fractions of 70%. Presumably, the more rapid rise occurs because the volume fraction is approaching the level of $\pi/2\sqrt{3} = 91\%$ at which the hexagonally packed fibers touch and the strength becomes unbounded.

n.1.3 Randomly Oriented Versus Aligned Discontinuous Reinforcements

Very few results are available to illustrate strengthening effects for other than aligned reinforcements. The computational cell models are not readily extended to other than aligned arrangements. One exception is the set of results obtained by Bao, et al. 1991a for randomly oriented elongated ellipsoidal and disc-shaped oblate ellipsoidal particles embedded in an elastic-perfectly plastic matrix. The composite was assumed to have a packet morphology with grain-like regions containing a number of aligned particles. The grain-like packets are randomly oriented such that the overall behavior of the composite is isotropic. The analysis of Bao, et al. involved two steps: a 3D cell model analysis was performed to obtain the multi-axial limit yield surface of

the grain-like packet; and then this result was used in conjunction with a Bishop-Hill procedure, averaging over all orientations of the "grains" relative to the tensile stressing axis, to obtain an upper bound to the limit yield stress $\bar{\sigma}_0$ of the composite. The strengthening ratios for such randomly oriented prolate ellipsoids ($a/b=0.1$) and oblate ellipsoids ($a/b=10$) are shown in Figure n-5. Included in this figure are the results from Figure n-2 for the same particles when they are aligned and stressed parallel to their direction of alignment. The particles are obviously not nearly as effective when they are randomly oriented as when they are aligned. Of course, the strengthening effect for the randomly oriented reinforcement holds for any orientation of the tensile axis, whereas the strengthening for the composite with aligned particles applies only for stressing parallel to the alignment. Its transverse yield strength is lower than the yield strength of the composite with the randomly oriented particles.

Relatively high aspect ratio disc-shaped particles packed to volume fractions of about twenty percent or more must assume a packet-like morphology if they are randomly oriented, but needle-shaped particles (e.g. chopped fibers) need not assume the packet morphology. A more common morphology involves little orientation correlation between neighboring particles. It is an open question as to whether morphologies giving isotropic behavior other than the packet morphology would give more significant strengthening than that observed in Figure n-5.

n.1.4 Spatial Distribution of the Reinforcement: Nonuniform Versus Uniform

The particle/matrix computational cells model a particle distribution which is necessarily uniform, both in space and with respect to the size and shape of the particles. Even when the cell is embellished to reflect details such as local arrangement of particles, the overall spatial distribution is uniform. Some methods for estimating the overall elastic moduli of composite materials do lend themselves to the study of the effect of nonuniformity (Toquanto 1991). Nevertheless, there is surprisingly little guidance available from the literature for material designers to go by in the form of simple "rules of thumb" on the role of nonuniformity, even for elastic properties. A recent study of the effect of a special form of nonuniform spatial distribution of

reinforcement on limit flow strength (Bao, Hutchinson and McMeeking 1991b) does lead to the clear-cut conclusion that nonuniformity increases the strength of the composite relative to its uniform counterpart, at least for the class of nonuniformities envisioned. The procedures leading to this result will now be described for the case of reinforcement of an elastic-perfectly plastic matrix with isotropic distributions of rigid spherical particles.

Self-consistent calculations were carried out for the overall limit flow stress $\bar{\sigma}_0$ for a two-phase elastic-plastic composite where each phase is isotropic and elastic-perfectly plastic with flow stress $\sigma_0^{(i)}$ and volume fraction $f^{(i)}$, $i=1,2$. Each of the two phases is assumed to be isotropically distributed so that the overall behavior of the composite is isotropic. The self-consistent calculations of $\bar{\sigma}_0$ of Bao, et al, 1991b, which will not be reported here, employed a three-shell model with an inner sphere representing the 'particulate' phase #1 (with $\sigma_0^{(1)}$ and $f^{(1)}$), an intermediate shell representing the 'matrix' phase #2 (with $\sigma_0^{(2)}$ and $f^{(2)}$), and an outer region extending to infinity endowed with the unknown properties of the composite. For ratios of $\sigma_0^{(1)}/\sigma_0^{(2)}$ differing from unity by less than a factor of two, the uniform strain rate upper bound (i.e. the rule of mixtures) to the overall limit tensile stress

$$\bar{\sigma}_0 = f^{(1)}\sigma_0^{(1)} + f^{(2)}\sigma_0^{(2)} \quad (n.1)$$

gives an excellent approximation.

The nonuniformity in the distribution of the spherical particles is also depicted in Figure n-6a. The average volume fraction of the spherical particles taken over the whole composite is \bar{c} . It is assumed that there are particle-rich sub-regions and particle-poor sub-regions. Moreover, it is assumed that the spacing between the particles in each of these regions is small compared to the size of the sub-regions. Thus within each of the respective sub-regions the results of Figure n-1 for a uniform distribution of spherical particles (sketched also in Figure n-6a and denoted by $\Sigma(c)$) can be used to specify the flow stress. Specifically, let c_1 be the volume fraction of the particles in the isolated sub-regions comprising volume fraction $f^{(1)}$ of the composite and whose flow stress $\sigma_0^{(1)}$ is read off the curve for the uniformly distributed particles at the value c_1 . The volume

fraction of the particles in the contiguous sub-regions is c_2 with associated values $f^{(2)}$ and $\sigma_0^{(2)}$, which is also read off the same curve. The relation between the local particle volume fractions, the average particle volume fraction, and the volume fractions of the two sub-regions ($f^{(1)}$ and $f^{(2)}=1-f^{(1)}$) is

$$\bar{c} = f^{(1)}c_1 + f^{(2)}c_2 \quad (n.2)$$

In this way, the self-consistent results for the two-phase composite can be used to estimate the effect of the non-uniformity.

An example of the outcome of the calculation just described is shown in Figure n-6b for three levels of average particle volume fraction \bar{c} . In this example the volume fraction of the isolated ('particulate phase') and contiguous regions ('matrix phase') are taken to be the same (i.e., $f^{(1)}=f^{(2)}=1/2$). The measure of the nonuniformity is taken as $c_1 - \bar{c}$, so that $c_1=c_2=\bar{c}$ gives the uniform distribution. Each curve in Figure n-6b corresponds to a fixed value of \bar{c} , and thus one notes that the uniform distribution gives the minimum estimate of $\bar{\sigma}_0$. Any nonuniformity, whether corresponding to particle-rich contiguous sub-regions or particle-rich isolated sub-regions, leads to an increase in limit flow stress relative to the uniform distribution. An analytical expression for the limit flow stress, valid for sufficiently small nonuniformities, brings out this feature very clearly, i.e.

$$\bar{\sigma}_0 = \Sigma(\bar{c}) + \frac{1}{2} \left(\frac{\partial^2 \Sigma}{\partial c^2} \right)_{c=\bar{c}} \left(\frac{f^{(1)}}{f^{(2)}} \right) (c_1 - \bar{c})^2 \quad (n.3)$$

Thus, as long as the curvature of the relation of flow stress to particle volume fraction is positive for the uniformly distributed case, any nonuniformity of the class discussed here will enhance the flow strength. This conclusion seems to be borne out by the numerical results for the transverse stress-strain behavior of continuous fiber reinforced metal matrix composites discussed by Suresh and Brockenbrough in Chapter 10. These authors have compared transverse behavior for various nonuniform distributions of circular fibers ('random arrays') with the corresponding behavior for uniform triangular arrays, which give rise to nominally isotropic transverse behavior. The

transverse stress-strain curves of the composites with the nonuniform distributions of fibers lie well above that for the triangular array at the same volume fraction of reinforcement.

n.2 ALIGNED REINFORCEMENT OF ELASTIC-STRAIN HARDENING MATRICES

Now consider isotropic matrix materials whose tensile stress-strain curve is specified by the Ramberg-Osgood relation

$$\varepsilon = \frac{\sigma}{E} + \alpha \frac{\sigma_0}{E} \left(\frac{\sigma}{\sigma_0} \right)^n \quad (n.4)$$

where E is the Young's modulus, σ_0 is now a reference yield stress, and n is the stress hardening exponent. Let $\bar{\sigma}$ and $\bar{\varepsilon}$ be the overall tensile stress and strain of the composite in the direction of the aligned reinforcement. An approximation to the tensile stress-strain curve of the composite developed by Bao, et al. 1991a is

$$\bar{\varepsilon} = \frac{\bar{\sigma}}{\bar{E}} + \alpha \varepsilon_0 \left(\frac{\bar{\sigma}}{\bar{\sigma}_N} \right)^n \quad (n.5)$$

where $\varepsilon_0 = \sigma_0/E$ is the reference yield strain of the matrix and $\bar{\sigma}_N$ is the reference stress of the composite elaborated on below.

The elastic modulus of the composite in the direction of alignment \bar{E} can be computed using a cell model or it can be estimated in a number of ways. The prediction of elastic properties of composites as dependent on the constituent properties is a well developed subject, and thus the estimation of \bar{E} will not be dwelt on in this chapter.

To understand the origin of the second term in (n.5), consider a pure power matrix material reinforced by rigid particles (or, in the case of the transverse behavior of a continuous fiber composite, a pure power law matrix surrounding by rigid fibers). The incompressible matrix has the following tensile and multi-axial behavior

$$\frac{\epsilon}{\epsilon_0} = \alpha \left(\frac{\sigma}{\sigma_0} \right)^n \quad \text{and} \quad \frac{\epsilon_{ij}}{\epsilon_0} = \frac{3}{2} \alpha \left(\frac{\sigma_e}{\sigma_0} \right)^{n-1} \frac{s_{ij}}{\sigma_0} \quad (n.6)$$

As discussed in detail by Bao, et al. 1991a, the composite with perfectly bonded rigid particles also has pure power law behavior. The uniaxial stress-strain relation for the composite for stressing in the direction of particle alignment is

$$\frac{\bar{\epsilon}}{\epsilon_0} = \alpha \left(\frac{\bar{\sigma}}{\bar{\sigma}_N} \right)^n \quad (n.7)$$

The composite reference stress $\bar{\sigma}_N$ depends on n as well as on the same parameters influencing $\bar{\sigma}_0$ for the perfectly plastic solid, i.e. f , particle shape, etc. In the limit for $n \rightarrow \infty$, $\bar{\sigma}_N \rightarrow \bar{\sigma}_0$. The dependence of the reference stress on n must be computed. A large number of such computations reported in Bao, et al. 1991a indicate that the dependence on $N \equiv 1/n$ is accurately approximated by

$$\bar{\sigma}_N \equiv \bar{\sigma}_0 + cN(\bar{\sigma}_0 - \sigma_0) \quad (n.8)$$

The coefficient c has a weak dependence on f and particle shape (see Figure n-7) but is in the range from 2 to 2.5 for most systems of interest. Stain hardening of the matrix enhances the flow strength of the composite as reflected by (n.7) in two ways: through the stress exponent n and through the increase of the reference stress above $\bar{\sigma}_0$.

Now consider again the composite with a elastically deforming reinforcement phase well bonded in the Ramberg-Osgood matrix (n.4). Neither the elastic properties of the reinforcement nor the elasticity of the matrix influence the asymptotic "large strain" behavior of the composite for overall strains which become large compared to ϵ_0 . Thus, the asymptotic behavior of the composite is given precisely by the pure-power relation (n.7). The approximate Ramberg-Osgood relation (n.5) for the elastic-plastic behavior of the composite was proposed as a formula to interpolate between the elastic limit and the asymptotic limit for "large strains". The formula reasonably accurately captures the response of the composite. This can be seen in Figure n-8

where results for an example for a composite with aligned disc-shaped cylindrical reinforcements ($f=0.2$ and $a/b=5$) are displayed for three levels of hardening. The matrix curves (n.4) are shown for reference, the dashed curves represent the approximation (n.5) with the relevant values of \bar{E} and $\bar{\sigma}_N$, and the solid line curves are the results of numerical calculations using a cell model with the complete Ramberg-Osgood relation (n.4) for the matrix. Other examples are shown by Bao, et al. 1991a. The example in Figure n-8 illustrates the point that the flow stress enhancement derives from both the exponentiation and the dependence of the reference stress $\bar{\sigma}_N$ on n . It should also be noted that the approximate formula (n.5) tends to overestimate the stress in the knee of the composite stress-strain curve. This may be of some consequence since for many metal matrix composites the strain range of interest may not significantly exceed the region of the knee. More accurate predictions will require more detailed computations such as those shown as solid line curves in Figure n-8 and as reported elsewhere in this volume.

A series of squeeze cast composites with a matrix of aluminum/magnesium and reinforced by silicon carbide particles were prepared and tested to obtain uniaxial stress-strain data by Yang, et al, 1990. This study was notable for the range of volume fractions, particle sizes and shapes considered, and for the careful attempt to establish the insitu matrix stress-strain behavior. Particle sizes ranged from several microns to more than a hundred microns. Over this size range it was established that there was very little dependence on particle size once the volume fraction and particle shape were fixed. Two sets of stress-strain data are shown in Figures n-9 where comparison with the Ramberg-Osgood estimation procedure just described is made. These Figures were taken from Yang, et al, 1991, where a fuller discussion of the composites and their preparation can be found. Figure n-9a shows tensile stress-strain data for the matrix and for composites reinforced by three volume fractions of equi-axed particles whose average size was 9 microns. The estimation scheme described above was applied by fitting the Ramberg-Osgood curve (n.4) to the matrix curve to obtain n and σ_0 (α was taken to be $3/7$). The value of \bar{E} in (n.5) was taken from the experimental curve (which in turn was shown to agree well with self-consistent predictions) and $\bar{\sigma}_N$ was determined from (n.8) using the results for $\bar{\sigma}_0$ from Figure

n-3 for the unit cylindrical particles. The dashed-line curves in Figure n-9a are the result of the estimation procedure. The same procedure was applied to the uniaxial compression data in Figure n-9b for composites reinforced by randomly oriented platelets whose average maximum diameter was 25 microns. In this case, the platelets are taken to have a 10 to 1 aspect ratio and the results for $\bar{\sigma}_0$ for the randomly oriented ellipsoidal platelets in Figure n-5 were employed to estimate $\bar{\sigma}_N$.

n.3 THE INFLUENCE OF RESIDUAL STRESS ON COMPOSITE YIELDING

The results presented so far in this chapter are for materials initially free of residual stress in the matrix and the reinforcements. Most metal matrix composites are processed at high temperature and upon cooling develop residual stresses due to thermal expansion mismatch between the matrix and the reinforcements. While the residual stresses have no effect on the purely elastic response of the composite, it is of interest to determine the effect on the yielding of reinforced materials. Such effects can occur because the residual stress can have a deviatoric component and therefore can influence the process of yielding in the matrix. The effect has been considered by several investigators including Povirk, Needleman and Nutt, 1990. However, Zahl and McMeeking, 1991, have provided a series of results for strongly bonded elastic reinforcements in perfectly plastic matrices showing the influence of the thermal strain mismatch relative to the volume fraction of reinforcements and the yield strain of the matrix.

The results of Zahl and McMeeking, 1991, were obtained by the unit cell method with finite elements used for the analysis. The residual stresses were first generated by cooling the material down while the matrix was permitted to respond elastoplastically. Thereafter the loads were applied to cause macroscopic deformation. The magnitude of the residual stresses generated were controlled by the parameter $\Delta\alpha \Delta T/\epsilon_0$ where $\Delta\alpha$ is thermal expansion coefficient of the reinforcement minus the thermal expansion coefficient of the matrix and ΔT is the current temperature minus the temperature at which the composite material is free of residual stress in both the matrix and the reinforcement. The parameter ϵ_0 is, as before, the yield strain in tension of the

matrix material. The calculations were carried out with an elastic modulus for the reinforcement which is 6.62 times the elastic modulus of the matrix.

Figure n-10 shows the stress-strain curves for spherical reinforcements in a perfectly plastic matrix with $\Delta\alpha \Delta T/\epsilon_0 = 1$. This case corresponds to SiC particles in an Al alloy matrix 256C below the stress free temperature. A softening of the composite response results at strains comparable to the matrix yield strain for both tension and compression with the effect much more pronounced in the compressive cases. The compressive stress-strain curve is up to 30% below the tensile one in terms of strength at the same strain magnitude. However, as the strain increases beyond $\epsilon_0 = \Delta\alpha \Delta T$, the compressive and the tensile stress-strain curves converge towards the curve for the material without initial residual stress. The limit strength is thus the same whether there are initial residual stresses or not. Since the compressive stress-strain curve also represents tension applied to a material with $\Delta\alpha \Delta T/\epsilon_0 = -1$ (i.e. the sign of the residual stresses reversed), the limit strength is unaffected by whether the residual stresses in the matrix are tensile or compressive. Since the limit strength of reinforced materials is independent of the initial residual stresses, the behavior of the composite material when the strain greatly exceeds $\epsilon_0 = \Delta\alpha \Delta T$ is correspondingly independent of them too. However, the limited ductility of particulate composites means that such large strains are rarely achieved in tension and are unusual in compression unless accompanied by internal damage. As a consequence tension-compression asymmetries in the yielding of particulate composites are to be expected and will generally persist until fracture of the material occurs.

The degree of yielding caused by thermal expansion mismatch between the matrix and the reinforcements depends on the magnitude of $\Delta\alpha \Delta T/\epsilon_0$. When this parameter equals 1 as in the case discussed above, about 50% of the matrix around spherical particles is yielded. When $\Delta\alpha \Delta T/\epsilon_0 = 2$, 60% of the matrix has yielded whereas when $\Delta\alpha \Delta T/\epsilon_0 = 5$, the entire matrix has deformed plastically upon cooling. The effect of these different degrees of yielding on a material with 20% of elastic spheres on the compression and tension stress-strain curves is shown

in Figures n-11 and n-12. It can be seen that in both tension and compression the greater thermal expansion misfit causes a softer response. Since the matrix is fully yielded when $\Delta\alpha \Delta T/\epsilon_0 = 5$, any larger magnitude of $\Delta\alpha \Delta T/\epsilon_0$ than 5 will give rise to the same tension and compression stress-strain curves as occur for $\Delta\alpha \Delta T/\epsilon_0 = 5$. It is of interest that the characteristic strain during which the thermally induced transient occurs is ϵ_0 rather than $\Delta\alpha \Delta T$. At a macroscopic strain of $2\epsilon_0$, the transient effect in each case has largely disappeared.

Zahl and McMeeking, 1991, have also given results for 20% by volume of aligned well bonded elastic short fibers in a perfectly plastic matrix. The aspect ratio of the fibers is 10 and they are circular cylinders. The stress-strain curves are shown in Figure n-13 for compression and n-14 for tension. As before, the thermal residual stresses cause a transient softening of the response which is more marked in compression than in tension. However, in both cases the effect is not great and in the tensile case is almost negligible. In compression, the maximum softening is only about 15%. In addition, the matrix is almost fully yielded by thermal stresses when $\Delta\alpha \Delta T/\epsilon_0 = 1$ and only a region beyond the fiber ends is still elastic. Increasing values of $\Delta\alpha \Delta T/\epsilon_0$ do not change this situation very much. It is likely that this effect is caused by the fact that in the calculations the fibers are modeled as being fairly close together side by side but far apart end to end. When there are no initial residual strains, the limit strength is reached in this case at a strain of about $5\epsilon_0$. When there are initial thermal stresses, the transient they cause is noticeable up to this strain. Thus it can be concluded that in general the transient persists up to the strain at which the limiting behavior sets in when there are no thermal residual strains.

n.4 REINFORCEMENT AGAINST CREEP

n.4.1 Steady-state Power Law Creep

A simple correspondence between behavior for pure power law plasticity and steady-state power law creep permits the results of the form (n.7) to be translated immediately to give insight into reinforcement against creep. It is again assumed that the particle/matrix bond is perfect and in

addition that the sole mechanism of inelastic deformation is power law creep. The consequences of interface sliding and diffusional relaxation of the reinforcement are taken up in the next subsection. In power law creep the tensile and multiaxial stress-strain rate relations are the exact counterparts to (n.6), i.e.

$$\frac{\dot{\epsilon}}{\dot{\epsilon}_0} = \alpha \left(\frac{\sigma}{\sigma_0} \right)^n \quad \text{and} \quad \frac{\dot{\epsilon}_{ij}}{\dot{\epsilon}_0} = \frac{3}{2} \alpha \left(\frac{\sigma_e}{\sigma_0} \right)^{n-1} \frac{s_{ij}}{\sigma_0} \quad (\text{n.9})$$

where now ϵ_0 is a reference strain rate and α is an adjustable constant which may be taken to be unity. The steady-state creep behavior of the composite also has a pure power law form, and the tensile behavior in the direction of the aligned particles converts from (n.7) to

$$\frac{\dot{\bar{\epsilon}}}{\dot{\epsilon}_0} = \alpha \left(\frac{\bar{\sigma}}{\bar{\sigma}_N} \right)^n \quad (\text{n.10})$$

where $\bar{\sigma}_N$ is precisely the same composite reference as for the rate-independent matrix. The strengthening in creep is reflected by the ratio $\bar{\sigma}_N/\sigma_0$, which in turn is given by (n.8) together with the plots of $\bar{\sigma}_0/\sigma_0$ for various forms of reinforcement presented earlier.

n.4.2 Diffusional Relaxation of the Reinforcement

At high temperature, in addition to matrix power law creep, mass transport by diffusion can occur within grains, on grain boundaries and on interfaces. Matter diffuses from regions of low stress to regions of high stress and the result is a macroscopic deformation which is proportional to the applied stress, usually in a linear manner (Frost and Ashby, 1982). This is known as Nabarro-Herring or Coble creep depending on the diffusion path. Macroscopically, it can be modeled as a continuum linear viscosity of the matrix or, in the cases where it is nonlinear, as a continuum power law creep with a low creep index. However, the presence of the interface between the reinforcement and the matrix in a composite material provides an additional path for mass transport which is not accounted for by matrix properties alone or reinforcement properties alone. Furthermore, the interface is typically a rapid path for mass transport and therefore

diffusion on the interface can lead to a relatively fast creep of the composite material. As a consequence, it is desirable to model this mode of creep and Rosler, Bao and Evans, 1991, have used this mechanism to explain trends in the creep strength of composite materials. There is reason to believe that when the temperature is sufficiently high an otherwise strongly bonded interface will be capable of sliding. Therefore, the sequence that is envisioned is that as the temperature is increased, the resistance to sliding on the interface diminishes and eventually disappears. As the temperature continues to increase, diffusion is activated in the interface and occurs in an environment of zero resistance to sliding.

Little comprehensive modeling has been done on this problem. However, Sofronis and McMeeking, 1992, have provided theoretical results for the creep strength of a material containing 20% by volume of rigid spheres of radius R . The results were obtained using the cell model method as described previously in this chapter but with interfaces which are capable of sliding or are capable of sliding and simultaneously subject to mass transport within the interface. In the results of Sofronis and McMeeking, 1992, the resistance to sliding in the form of a shear strength τ_s was considered to be proportional to the relative velocity v_s of sliding across the interface and thus

$$\tau_s = \mu v_s \quad (n.11)$$

where μ is an effective interface viscosity. As the temperature goes up, μ will diminish and eventually disappear. Mass transport is controlled by an effective diffusion parameter \mathcal{D} such that

$$v_n = - \mathcal{D} \nabla^2 \sigma_n \quad (n.12)$$

where v_n is the relative velocity normal to the interface of the matrix relative to the reinforcement, ∇ is the gradient operator in the surface of the interface and σ_n is the normal component of the stress across the interface.

A summary of the results of Sofronis and McMeeking, 1992, is shown in Figure n-15. The creep strength $\bar{\sigma}/\sigma$ is plotted against the inverse interface sliding viscosity and against the effective interface diffusion coefficient. The creep strength is the stress required to cause a given strain rate in the composite divided by the stress to cause the same strain rate in the matrix alone. In the left half of the figure $\mathcal{D} = 0$ so that no diffusion takes place on the interface and in the right half of the figure $\mu = 0$ so that shear free sliding occurs at the interface. In terms of the whole plot, the temperature is relatively low (but in the creep range) at the far left of the diagram and increases from left to right all the way across. However, the scale would almost certainly not be linear or continuous in terms of temperature from left to right as drawn in Figure n-15. It can be seen that the creep strength falls as the resistance to sliding diminishes and mass transport increases. When the matrix is linear ($n = 1$), the creep strength is independent of strain rate. However, the power law creeping matrix leads to an effect, in conjunction with interface sliding or mass transport, which is sensitive to strain rate. A slower strain rate leads to a lower creep strength indicating that the slow straining permits the sliding behavior or the diffusion process to become active relative to matrix creep whereas a fast strain rate seems to preclude these interface processes to some extent.

Sliding with no mass transport (the left half of Figure n-15) leads to a reduction of the creep strength of the composite material. The creep strength in each case reaches an asymptote as the sliding resistance diminishes and these asymptotic values represent the creep strength when there is no shear strength at the interface. In the linear case, the strength falls from over twice the matrix strength for a well bonded non-sliding interface down to only 30% above the matrix strength when the interface slides freely.

When mass transport by diffusion becomes active, the creep strength is diminished further. As before, an asymptotic value of the creep strength is approached as the diffusion becomes very fast. In each case, the asymptotic creep strength is below that of the matrix strength indicating that

due to the presence of the interface, the reinforcements actually weaken the composite material if the diffusion rate is high enough.

Another important feature of the results is a particle size effect. The material parameters μ and \mathcal{D} inherently contain length scales. As a result, the continuum analysis predicts a behavior which, in turn, depends on the particle size. For a given interface and volume fraction of reinforcements, a larger particle size improves the creep strength. In the case of sliding, the effect can be understood in terms of the reduction in the total area of particle surface as the size is increased thereby diminishing the effective strain produced by the same velocity of sliding. In the case of mass transport, the larger particle imposes greater diffusion distances, hence reducing the macroscopic strain rate. This effect in relation to grain size is well known in diffusion controlled creep of homogeneous materials (Frost and Ashby, 1982).

Acknowledgements

The work of JWH was supported in part by the National Science Foundation under Grant NSF-MSS-90-20141, by the DARPA URI (Subagreement P.O.#VB38639-0 with the University of California, Santa Barbara, ONR Prime Contract N00014-86-K-0753), and by the Division of Applied Sciences, Harvard University. The work of R.M.M. was supported by the DARPA URI at the University of California, Santa Barbara (ONR Contract N00014-86-K-0753).

- Bao, G., Hutchinson, J.W. and McMeeking, R.M. (1991a) *Acta Metall. Materialia* **39**, 1871-1882.
- Bao, G., Hutchinson, J.W. and McMeeking, R.M. (1991b) *Mech of Materials* **12**, 85-94.
- Brockenbrough, J., Suresh, S. and Wienecke, H.A. (1991), *Acta Metall. Materialia* **39**, 735-752.
- Christman, T., Needleman, A. and Suresh, S. (1989) *Acta Metall. Materialia* **37**, 3029-3047.
- Dragone, T.L. and Nix, W.D. (1990) in *Proc. TMS Int. Conf. on Advanced Metal and Ceramic Composites*, Anaheim, CA.
- Frost, H. J. and Ashby, M.F. (1982) Deformation Mechanism Maps, Pergamon Press, Oxford.
- Hom, C. L. (1992) *J. Mech. Phys. Solids* **40**, 991-1008.
- Jansson, S and Leckie, F. A. (1992) *J. Mech. Phys. Solids*, **40**, 593-612.
- Levy, A. and Papazian, J.M. (1990) *Metall. Trans.* **21A**, 411-420.
- Povirk, G.L., Needleman, A. and Nutt, R.S. (1990) "An analysis of the effect of residual stresses on deformation and damage mechanisms of Al-SiC composites," to be published.
- Rosler, J., Bao, G. and Evans, A.G. (1991) *Acta Metall. Materialia* **39**, 2733-2738.
- Sofronis, P. and McMeeking, R.M. (1992) "The effect of interface diffusion and slip on the creep resistance of particulate composite materials," submitted to *Mechanics of Materials*.

Torquato, S. (1991) Appl. Mech. Rev. **44**, 37-76.

Tvergaard, V. (1990) Acta Metall. Materialia **38**, 185-194.

Yang, Y., Pickard, S., Cady, C., Evans, A.G. and Mehrabian, R. (1991) Acta Metall. Materialia **39**, 1863-1870.

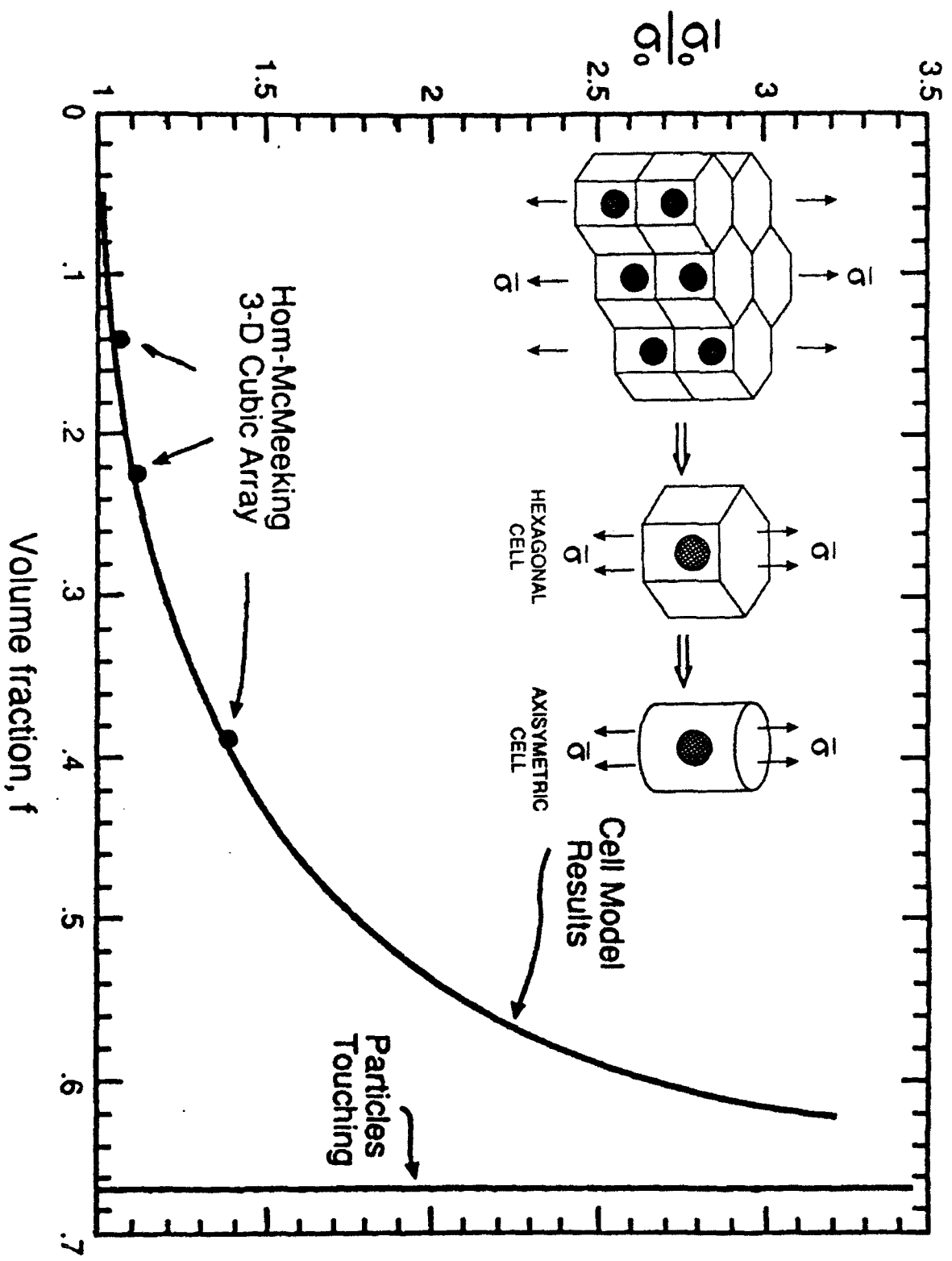
Zahl, D.B. and McMeeking, R.M. (1991) Acta Metall. Materialia **39**, 1117-1122.

Figure Captions

- Figure n-1 Strengthening ratio for an elastic-perfectly plastic matrix reinforced by rigid spherical particles. The insert illustrates the steps leading to a axisymmetric cylindrical cell for a uniform distribution of particles.
- Figure n-2 Strengthening ratio for an elastic-perfectly plastic matrix reinforced by aligned ellipsoidal particles (from Bao, et al, 1991a).
- Figure n-3 Strengthening ratio for an elastic-perfectly plastic matrix reinforced by aligned cylindrical particles (from Bao, et al, 1991a).
- Figure n-4 Strengthening ratio for the transverse loading of a perfectly plastic material reinforced by long rigid fibers.

- Figure n-5 Strengthening ratio for an elastic-perfectly plastic matrix reinforced by randomly oriented ellipsoidal needles ($a/b=1/10$) and randomly oriented ellipsoidal platelets ($a/b=10$) where the particles possess a packet-like morphology. The strengthening ratios for the corresponding aligned reinforcements from Figure n-2 are included for reference (from Bao, et al, 1991a).
- Figure n-6 a) Scheme for applying the results for a dual-phase composite to a matrix reinforced by equi-sized rigid particles which are nonuniformly distributed. b) Strengthening ratio as a function of nonuniformity for three levels of average particle volume fraction \bar{c} . In this example the volume fraction of each of the nonuniform 'phases' is taken to be $1/2$, and the tensile yield stress of the elastic-perfectly plastic matrix is taken to be σ_Y .
- Figure n-7 Computed dependence of the reference stress $\bar{\sigma}_N$ on the hardening index $N=1/n$ for a variety of particle shapes and volume fractions.
- Figure n-8 Tensile stress-strain curves for composites reinforced by aligned disc-shaped cylindrical particles ($a/b=5$ and $f=0.2$). The matrix material has the Ramberg-Osgood stress-strain curves shown. The solid line curves for the composite were computed using a cell model while the dashed line curves were obtained using the estimation scheme described in the text.
- Figure n-9 Comparison of experimental data for composites of an Al/Mg matrix material reinforced by SiC particles with stress-strain curves predicted by the estimation scheme described in the text (from Yang, et al 1991). a) uniaxial tensile curves for matrices reinforced by equi-axed particles. b) uniaxial compression curves for matrices reinforced by randomly oriented platelets.

- Figure n-10 Stress-strain curves for 10, 20, 40 and 50 volume % of spherical reinforcements in a perfectly plastic matrix with $\Delta\alpha \Delta T/\epsilon_0 = 1$.
- Figure n-11 Compressive stress-strain curves for 20 volume % of spherical particles with different amounts of thermal expansion misfit with the perfectly plastic matrix.
- Figure n-12 Tensile stress-strain curves for 20 volume % of spherical particles with different amounts of thermal expansion misfit with the perfectly plastic matrix.
- Figure n-13 Compressive stress-strain curves for 20 volume % cylindrical fibers with a 10 to 1 aspect ratio with different amounts of thermal expansion misfit with a perfectly plastic matrix.
- Figure n-14 Tensile stress-strain curves for 20 volume % cylindrical fibers with a 10 to 1 aspect ratio with different amounts of thermal expansion misfit with a perfectly plastic matrix.
- Figure n-15 Creep strength of a material containing 20% by volume of rigid spheres when sliding occurs on the interface and when shear free sliding and mass transport occur on the interface. The radius of the spherical reinforcements is R.



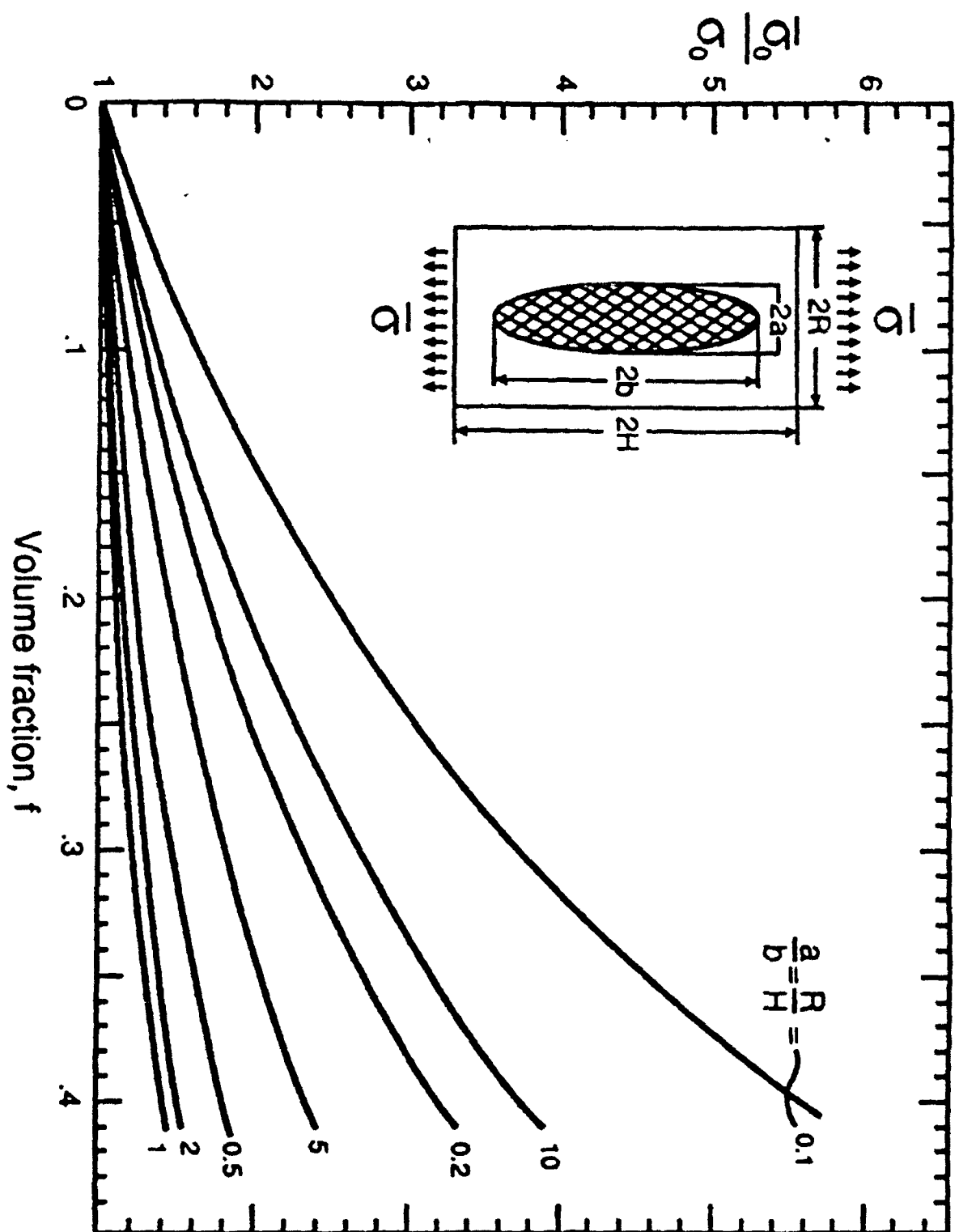


Fig 2

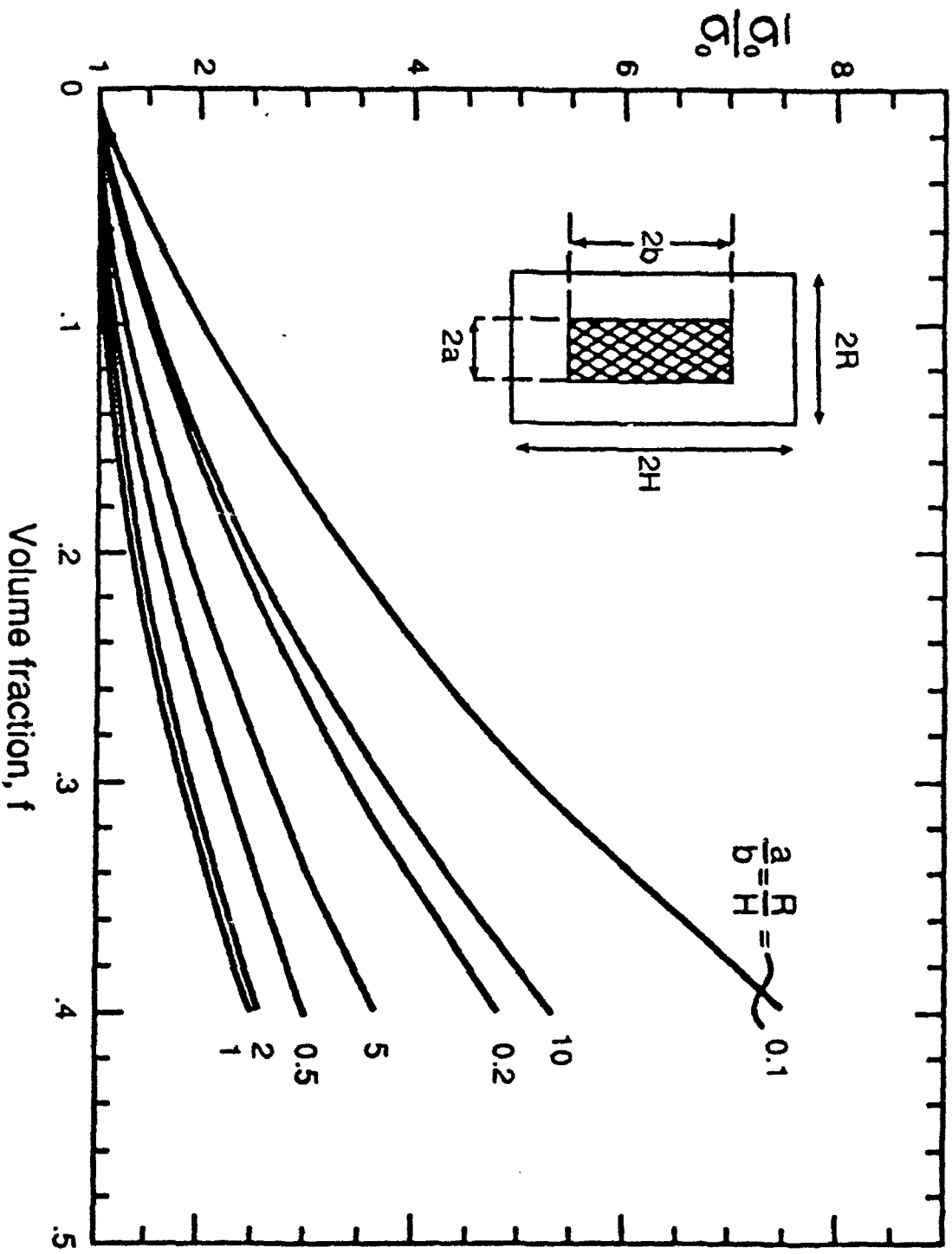


Fig 3

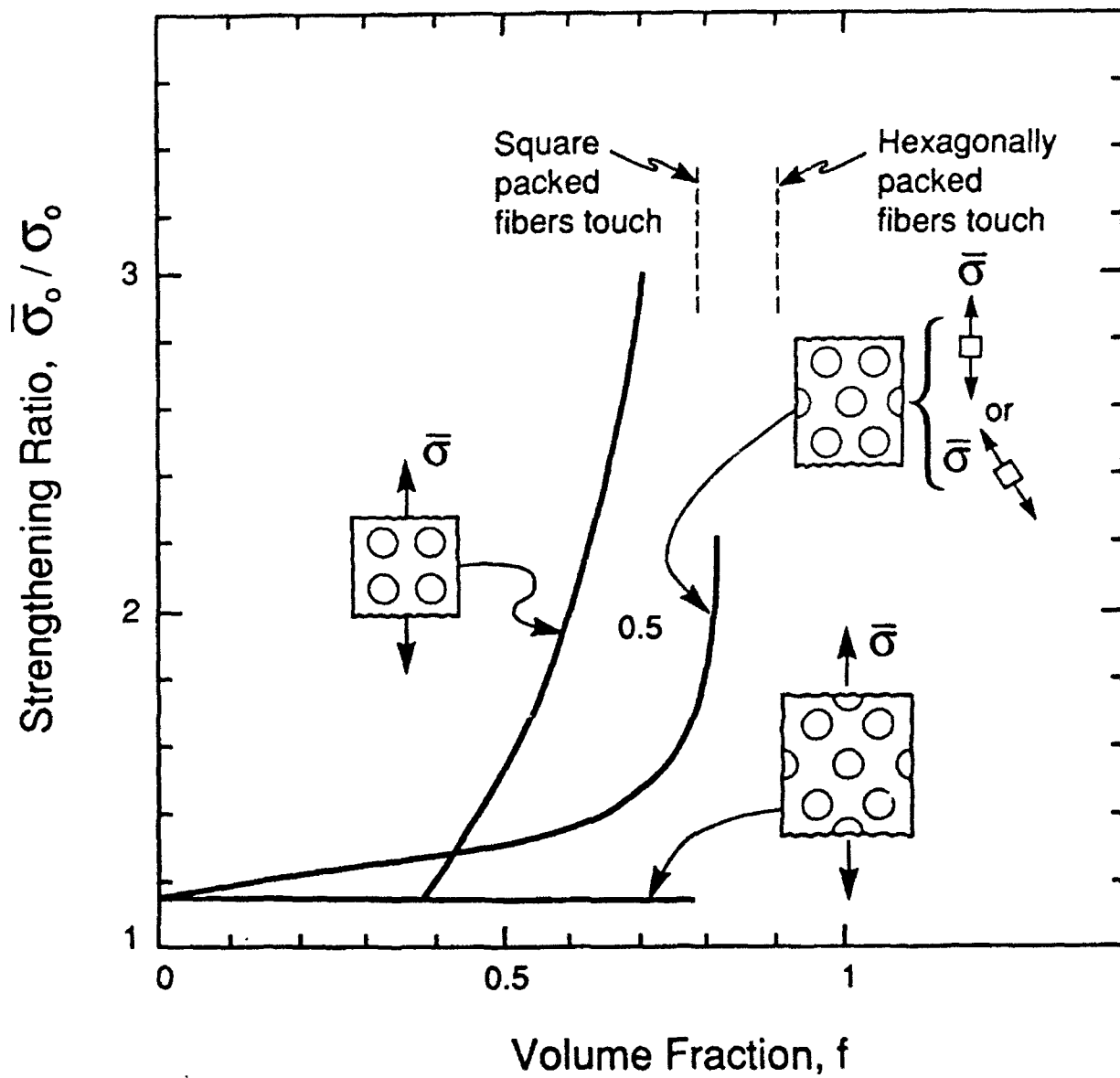


Figure n-4

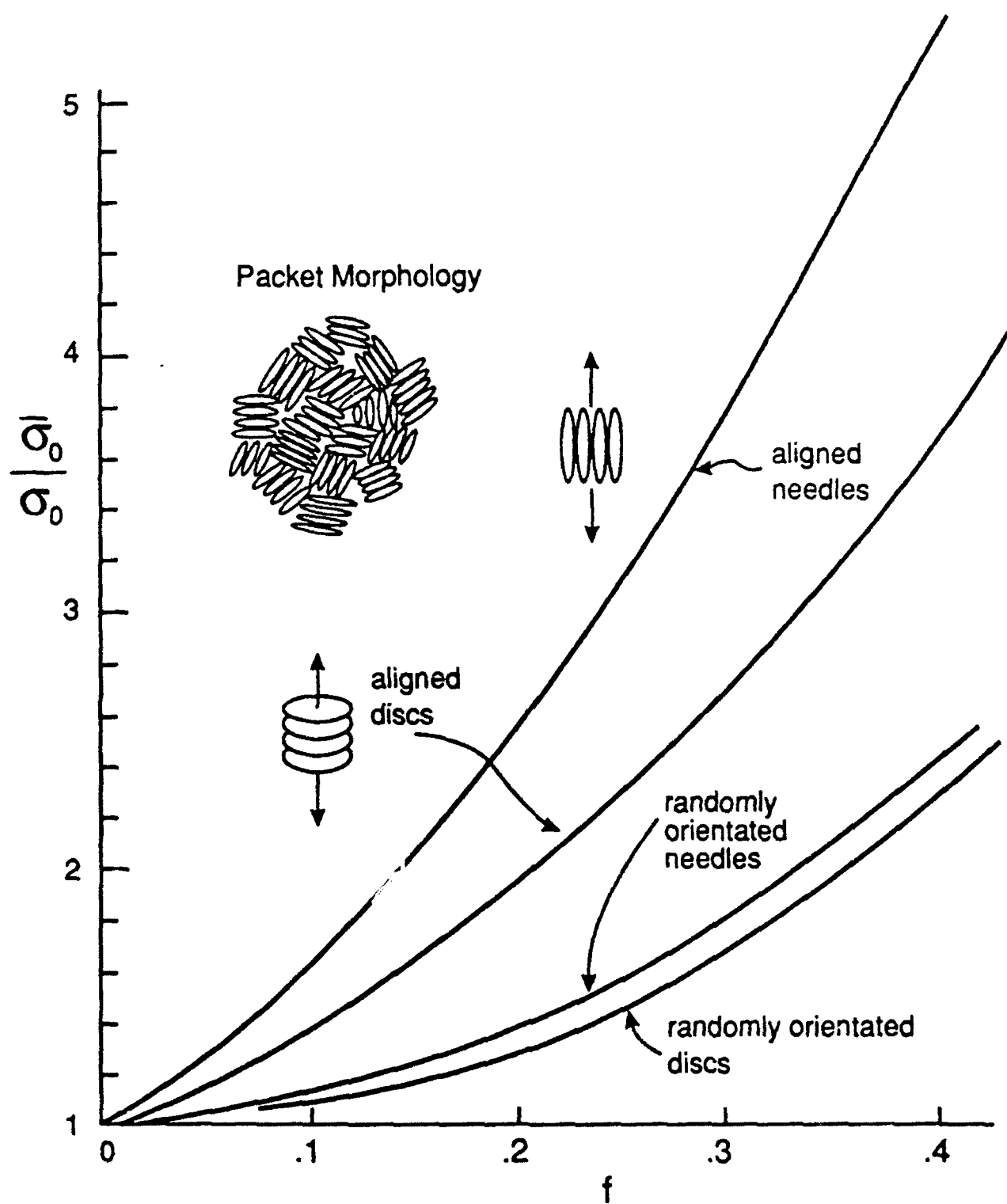
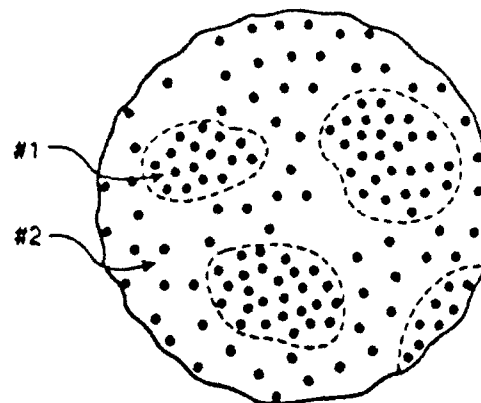
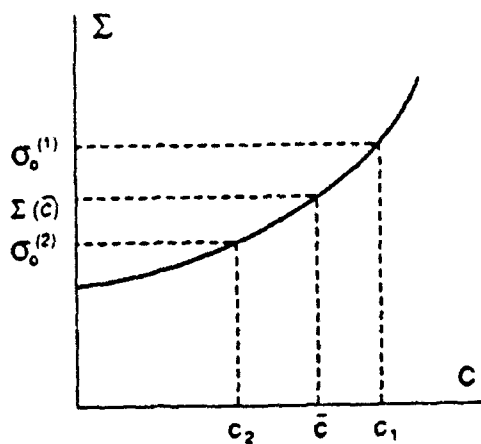


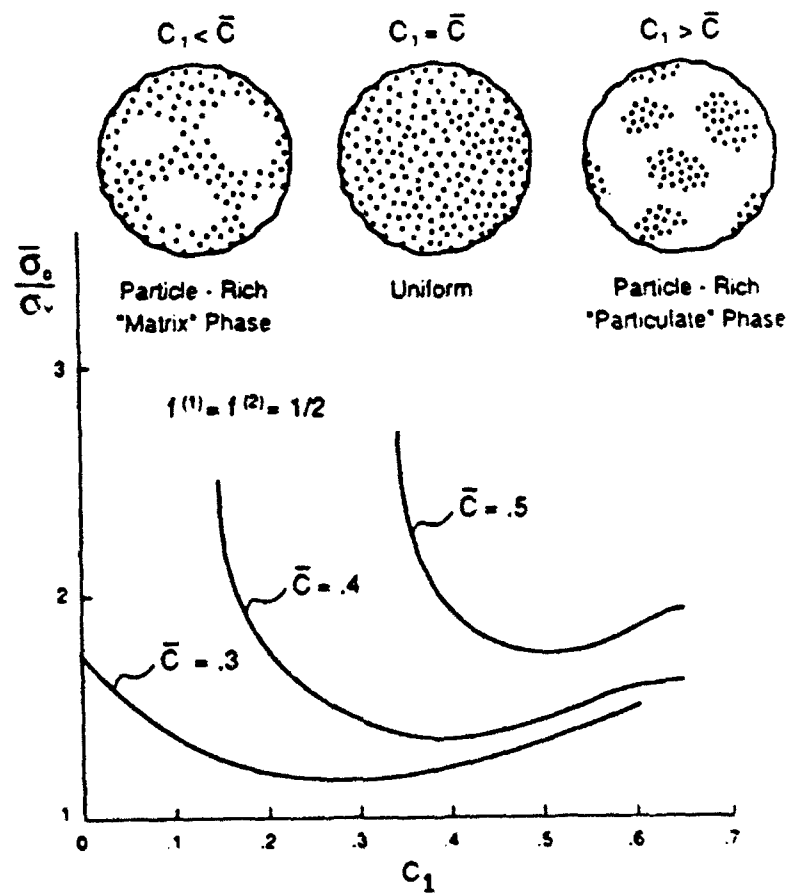
Fig 5



"Particulate" Phase: $f^{(1)}, c_1, \sigma_0^{(1)}$

"Matrix" Phase: $f^{(2)}, c_2, \sigma_0^{(2)}$

a)



b)

Fig 6

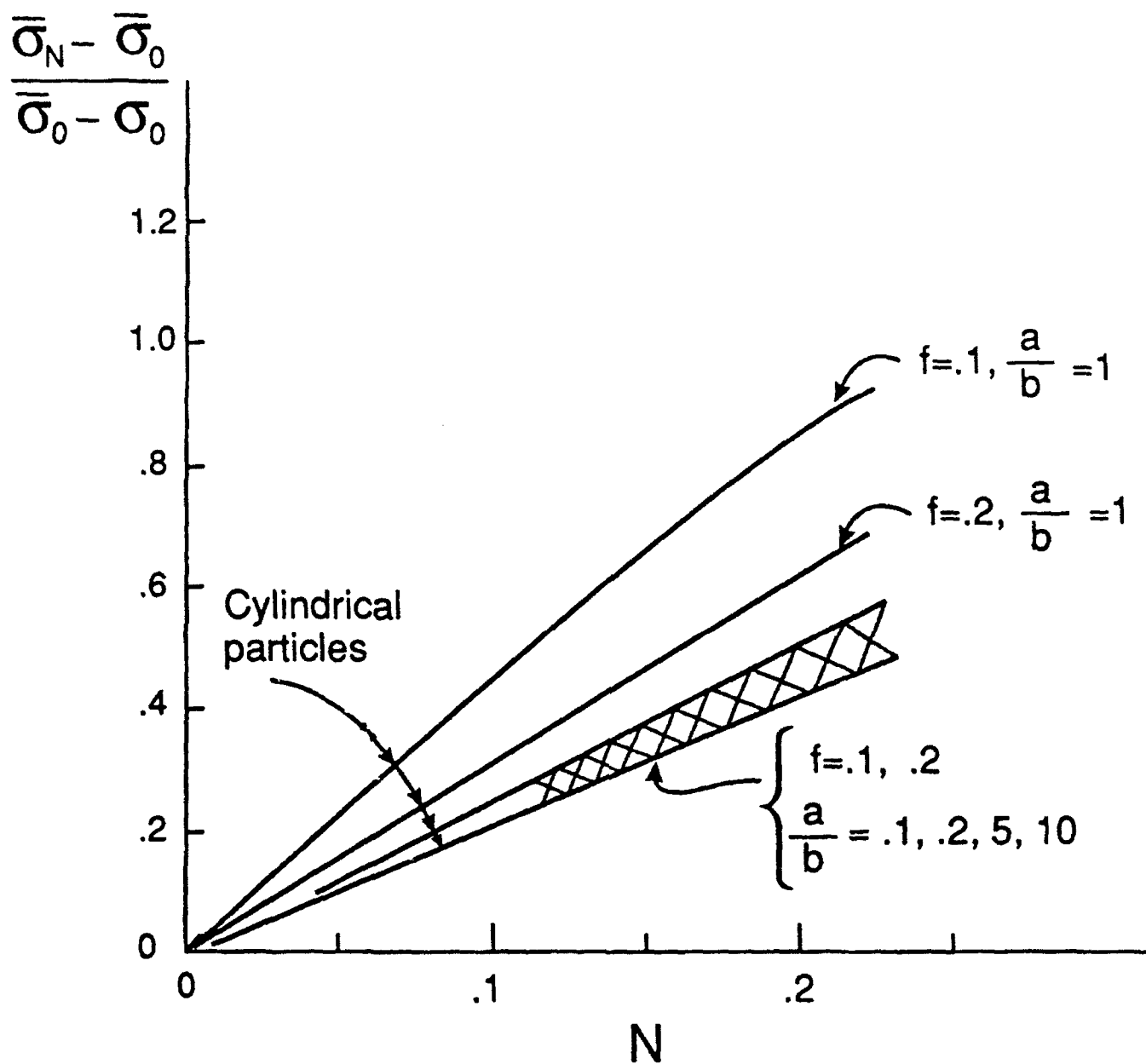


Fig 7

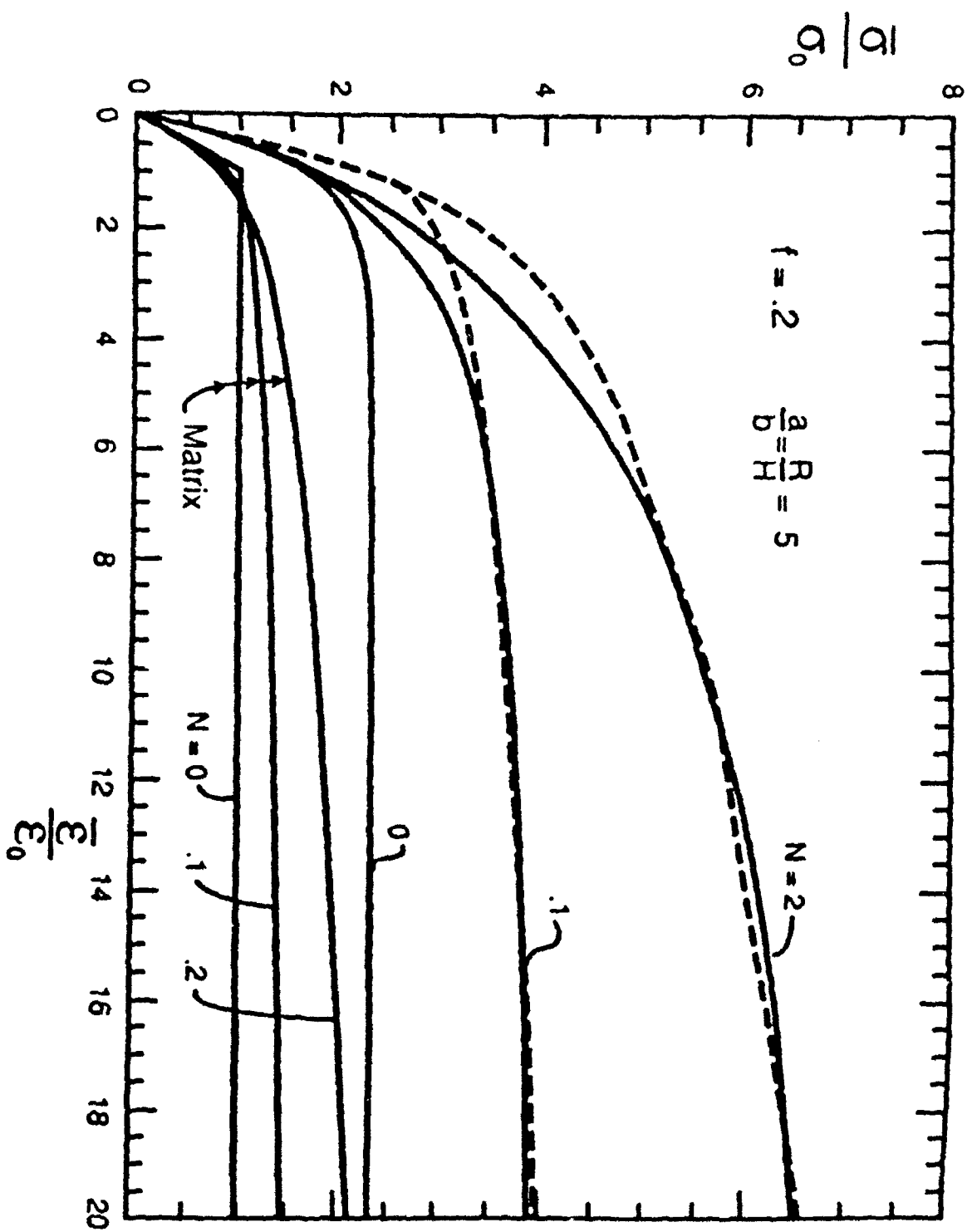


Fig 8

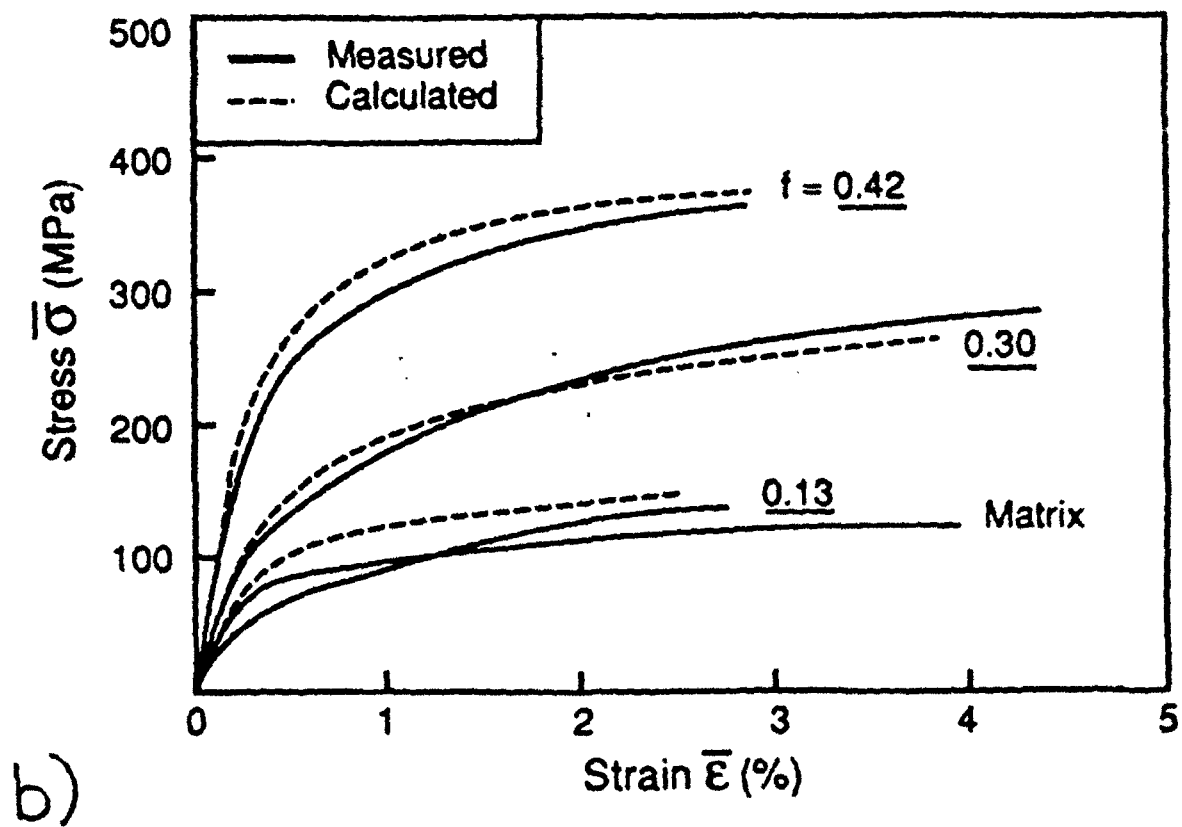
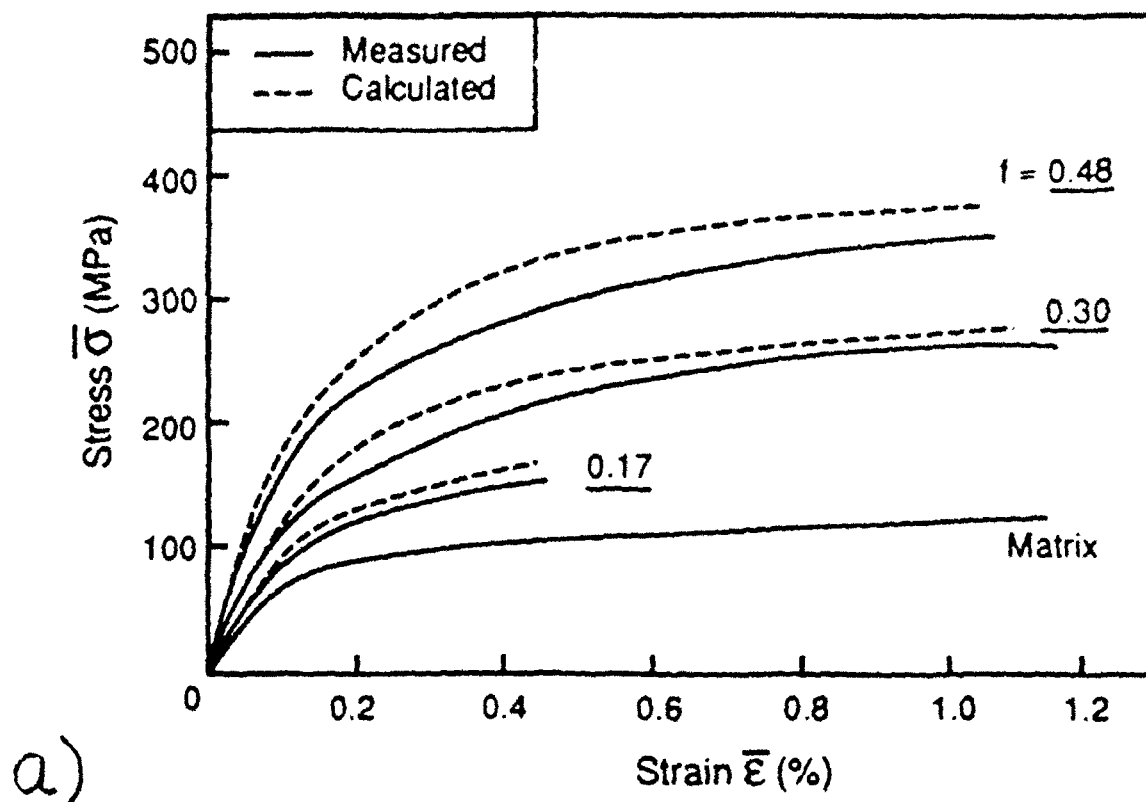


Fig 9

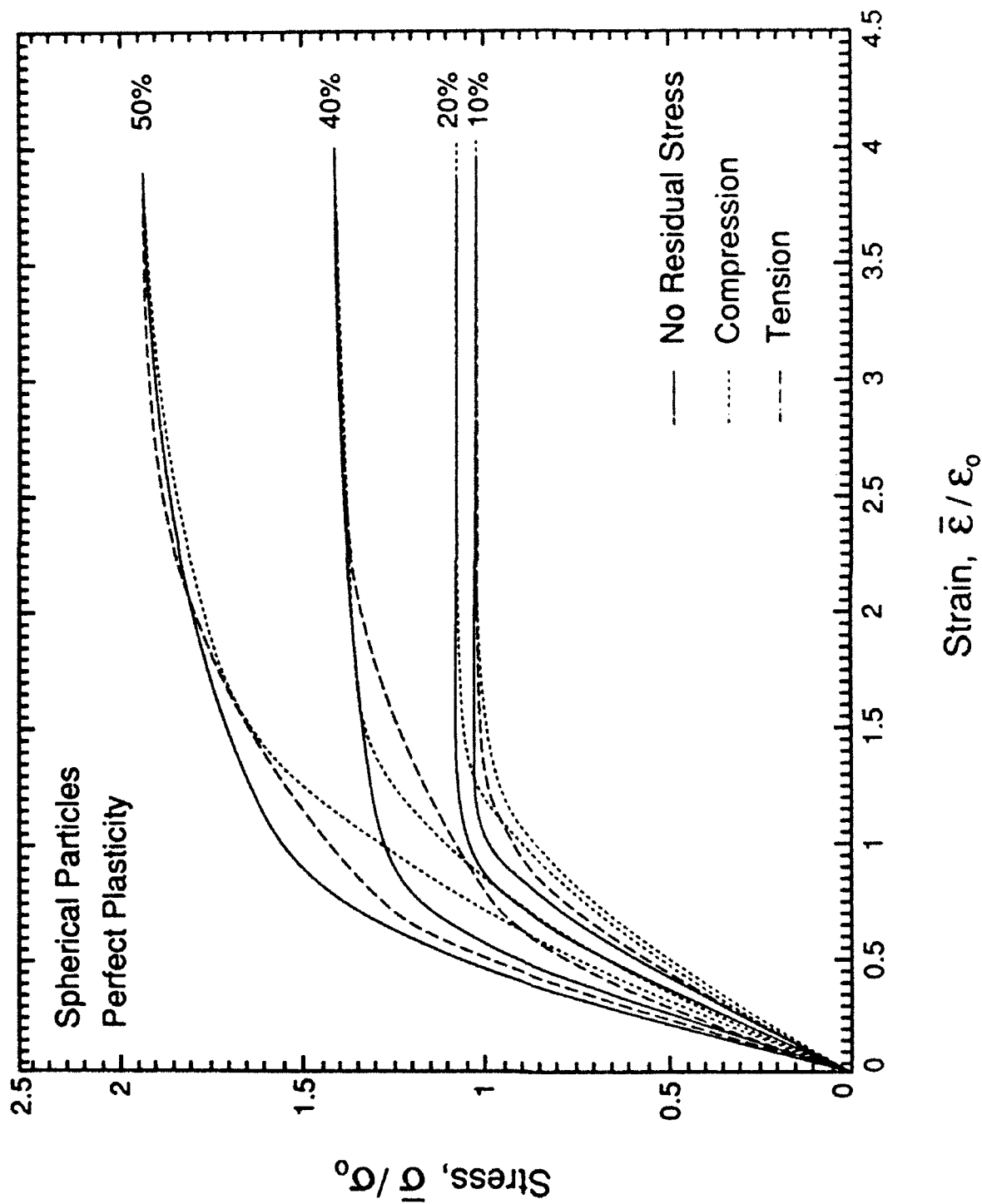


Figure n-10

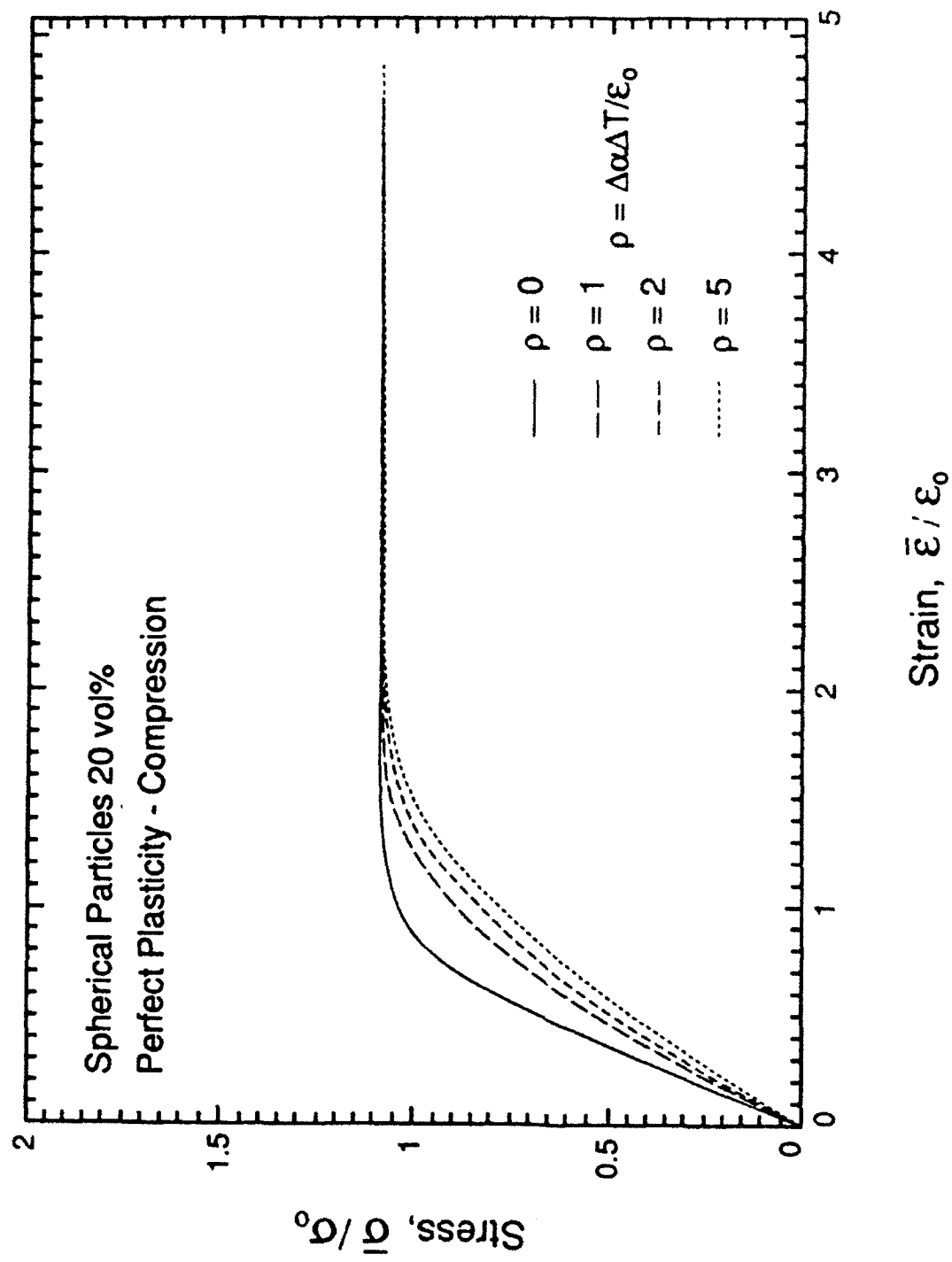


Figure n-11

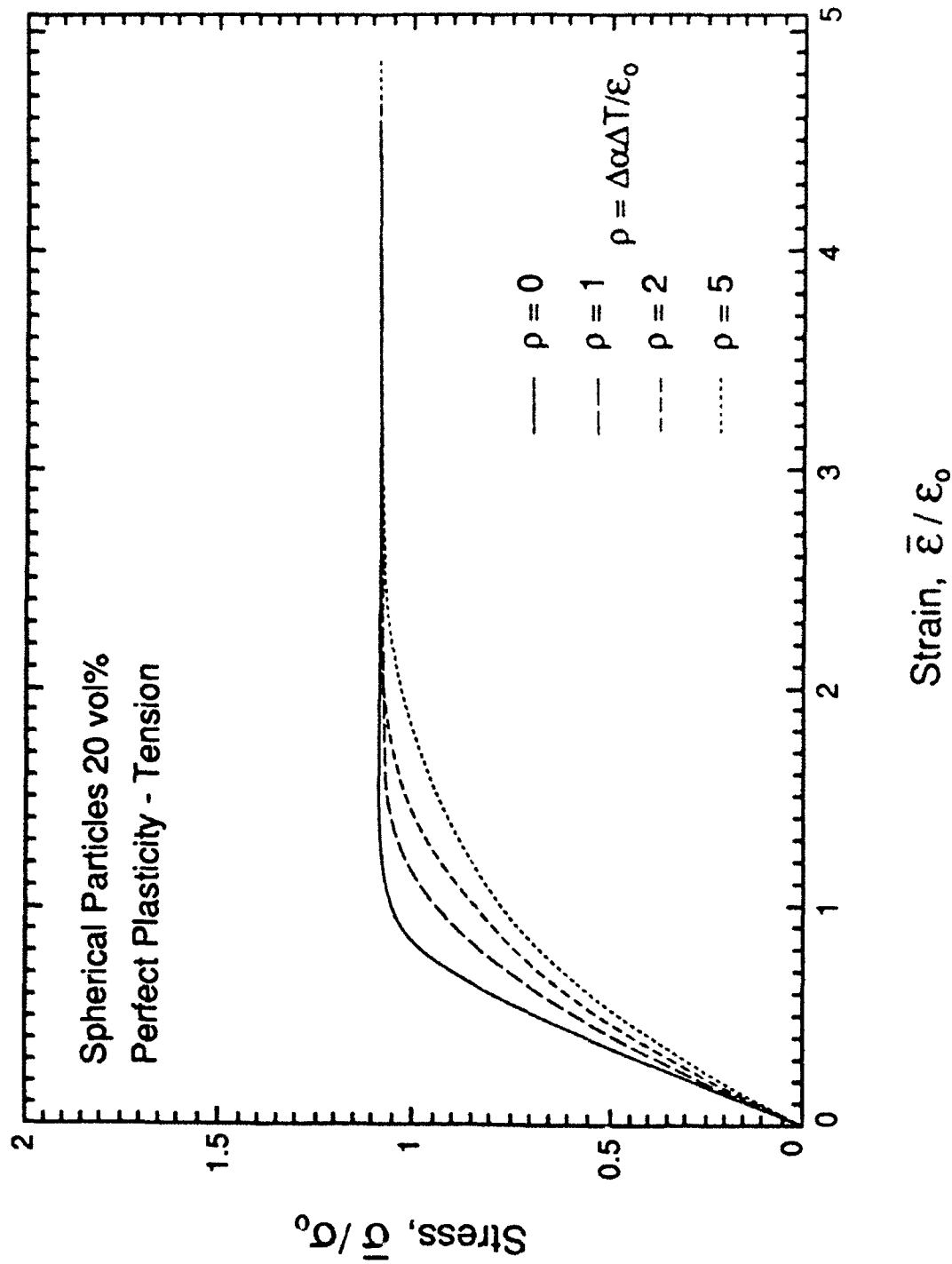


Figure n-12

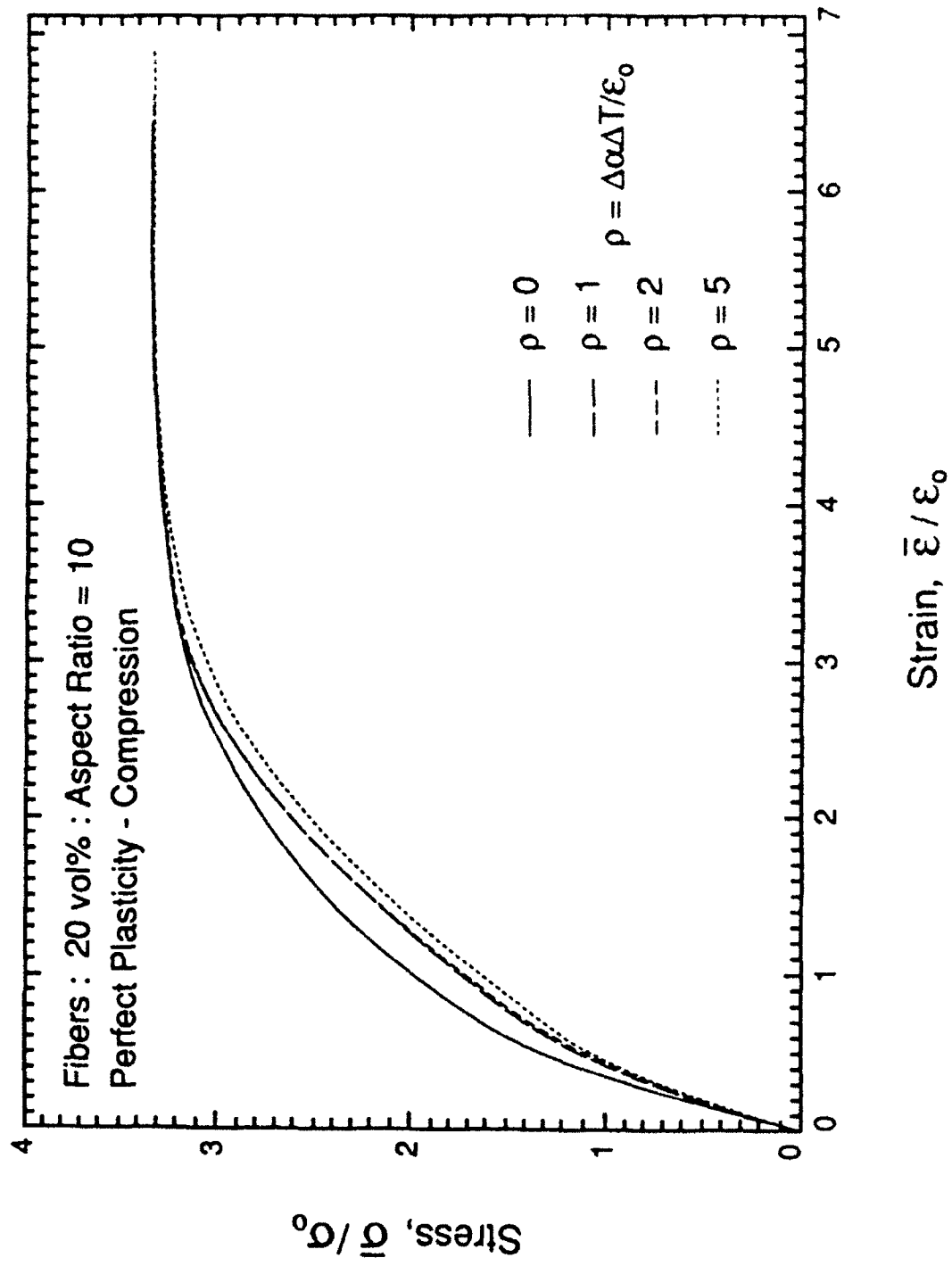


Figure n-13

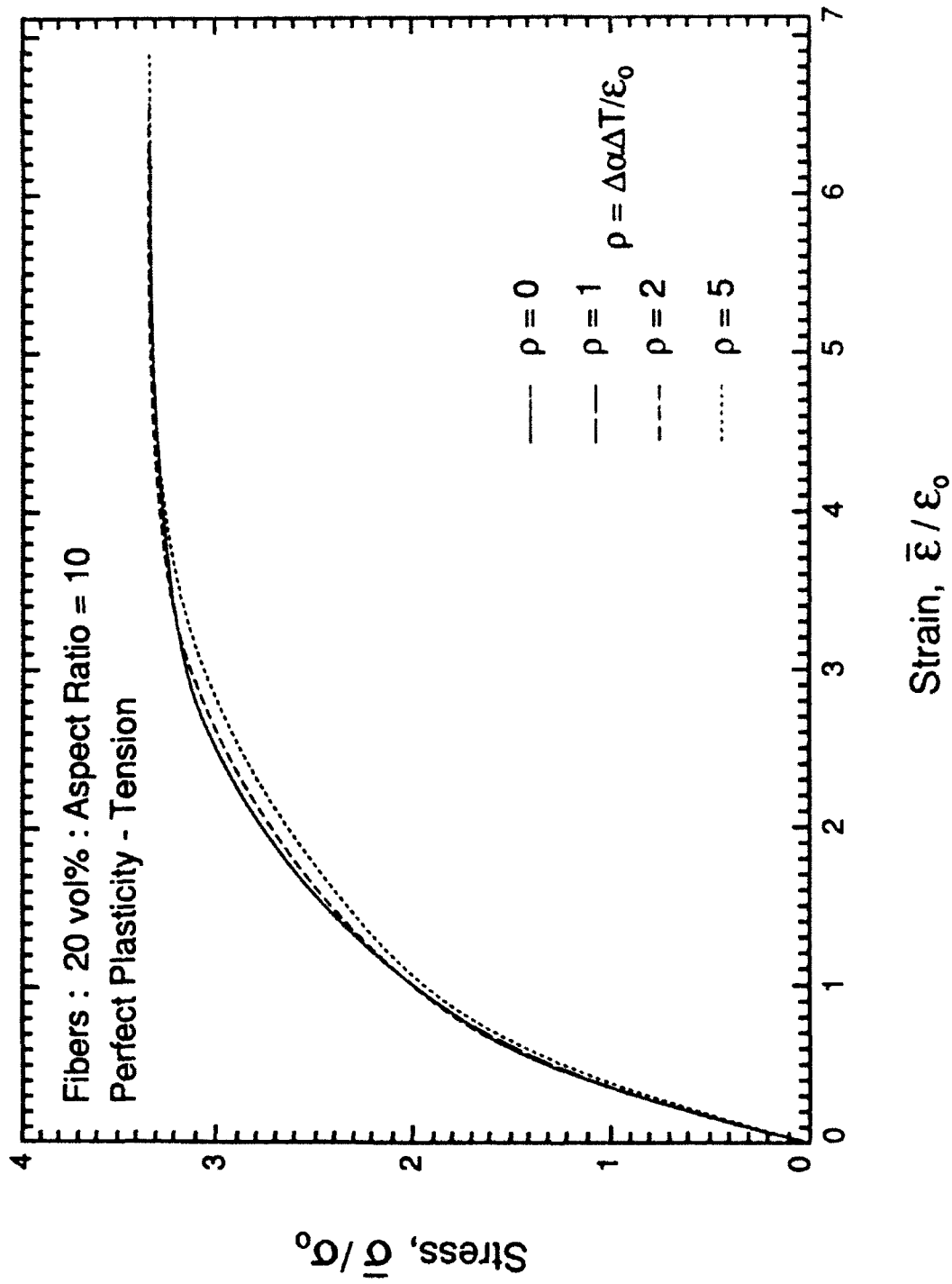


Figure n-14

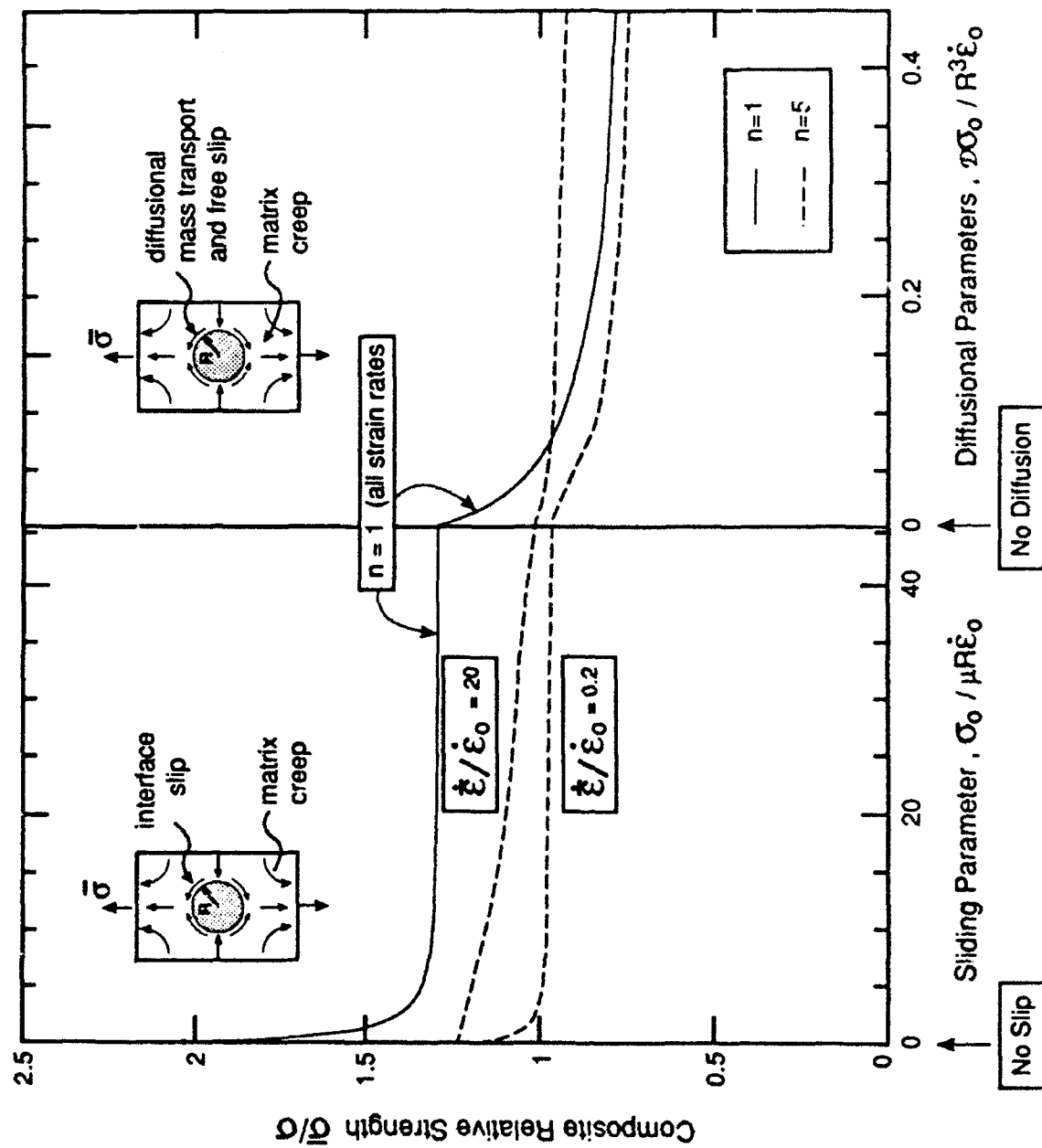


Figure n-15